Electric charge within volcanic plumes

on Earth and Io

A thesis by Michael R. James

BA (Hons.) Cambridge University

Submitted in partial fulfilment of the requirements for the degree of

Doctor of Philosophy

University of Lancaster, December 1998

Electric charge within volcanic plumes on Earth and Io

Michael R. James

Submitted for the Degree of Doctor of Philosophy

University of Lancaster, December 1998

Abstract

Field, experimental and theoretical investigations have been carried out into the electrification of volcanic plumes. At Sakurajima volcano, Japan, ground-level perturbations of the atmospheric electric potential gradient generated by particulate plumes were recorded. Simultaneous measurements, made at up to five sites around the volcano, are shown to be capable of detecting even very small quantities of volcanic particles, and tracking a continuously produced (over a period of several hours), dilute plume as it was dispersed by the wind. Data collected during one small Vulcanian eruption suggest that charges, about 1 C in magnitude, were generated and then separated, with the positive charge centre residing above the negative charge centre.

Experiments have been carried out in order to assess fracto-emission (the release of ions, neutral atoms and various frequencies of electromagnetic radiation from fracture surfaces) as a charging mechanism for the electrification of silicate particles in plumes. Silicate particles, generally less than 100 μm in diameter, were produced by colliding pumice samples together and were shown to have net specific charges of

approximately 10^{-5} to 10^{-6} C kg^{-1} (similar to previous field measurements on ashfall). Most (but not all) of the experimental samples produced net negatively charged ash, and demonstrated a positive-above-negative charge separation. Additional charge thought to have been released in the form of ions was also detected, supporting fracto-emission as the charging mechanism for volcanic plumes. The magnitude of the net ash charge is shown to be a function of the particle size, with relative humidity having only a small effect. The polarity of the net charge appears to be a function of a property of individual pumice types, possibly their geochemistry.

Experiments during which the particles were separated by their polarity indicate that the net charges reflect only a small imbalance in much larger, individual particle charges (10^{-3} C kg^{-1}) of both polarities. The particle charges are shown to vary with the sample impact velocity, the number of impacts carried out within an experiment and, to a lesser degree, relative humidity. Variation within the results appears to be partly an effect of particle aggregation within the experiment.

Investigation of any effects that this particle charging may have on the plumes observed on Io (one of Jupiter's moons) suggests that luminous discharges and particle aggregation are both probable in this environment. It is shown that the distinct asymmetries observed in plumes are unlikely to be a result of electromagnetic interactions, but probably represent decompression features and asymmetric vent or crater morphologies.

Acknowledgements

First and foremost, I indebted to my supervisors, Prof. Lionel Wilson, Dr. Jennie Gilbert and Dr. Steve Lane for their endless encouragement, support and helpful suggestions throughout the work involved in this thesis.

I also wish to thank to the staff of the Sakurajima Volcano Research Center, in particular Prof. K. Ishihara and Dr. M. Iguchi, for their generous provision of facilities and assistance during my stay in Japan. Prof. K. Ishihara must be further thanked for contributing SVRC geophysical data to this thesis. Prof. K. Kinoshita of Kagoshima University has also been of great help in supplying invaluable video and meteorological data.

The SEM work could not have been completed without the tenacity of Paul Williams (Lancaster University), and Colin Woof and Bernie Simon (Institute of Freshwater Ecology, Windermere) are thanked for their help during the particle sizing at IFE. Dr. Jennie Gilbert, Dr. Stuart Black, Saskia Marshall and Jane Toothill kindly provided some of the pumice samples and associated geochemical data. Thanks must also go to my parents for their continual support, particularly during construction of the experimental apparatus in Manchester.

Last, but by no means least, Lancaster would not have been the same without the friendship and support of the people there. I am particularly grateful to the members of the Volcanology and Planetary Science groups, and all the other residents of Alexandra Hall.

This research project was funded by the Particle Physics and Astronomy Research Council, award reference 95300872.

Contents

Figures

Tables

1. Introduction

Explosive volcanic eruptions have both terrified and fascinated man, and early written accounts (e.g. Pliny, 79AD) often gave details of the vivid electrical displays which frequently accompany the generation of particle-rich plumes. However, despite our understanding of the physical processes controlling such eruptions having increased substantially over the last three decades, research into the electrical properties of plumes has not progressed far. The production of extensive displays of lightning (and other effects such as St. Elmo's fire) during explosive eruptions demonstrates the large magnitude of the charges involved. These electrical phenomena are not observed during effusive eruptions, suggesting that the production or presence of small silicate particles is a key factor in plume electrification.

Plumes can contain a wide range of particle sizes, but large particles fall out relatively rapidly, leaving only small particles, generally less than a few millimetres in diameter (Sparks *et al.*, 1997). As a result, plumes are not always easy to detect and represent a potential hazard to aircraft. Increased knowledge of charge generation and distribution within plumes could provide insights into plume detection by electrostatic techniques. It could also aid understanding of aggregation processes, which are important when considering dispersion and ashfall hazards. The discovery of active plume volcanism on Io (Morabito *et al.*, 1979) has also led to the possibility of observing electrical effects within plumes on another planet. With Io's tenuous atmosphere and low gravity (approximately that of the Moon), the results of electrostatic interactions may be enhanced within its plumes, relative to those on Earth.

The aims of the research covered by this thesis were thus to record field-based

electrostatic measurements of volcanic plumes, and also to investigate the generation of electric charge during particle production, with the results to be applied to the plumes on Io. As such, this work can be separated into three different sections: measurement of atmospheric electric potential gradients at Sakurajima volcano (fieldwork), investigation of charge generation during particle production from pumice (laboratory experiments) and theoretical analysis of potential electrical effects within Io's plumes.

A brief introduction to volcanic plumes is provided in Chapter 2, and this is accompanied by a summary of mechanisms known to generate charge within both solid materials and liquids. These mechanisms are known as a result of research carried out into a wide variety of processes, from those used in industrial applications to thunderstorms and geoelectric phenomena. The maximum charge limits for a particulate medium (such as a volcanic plume) are also discussed.

The previous research into volcanic plume electrification is summarised in Chapter 3. The various approaches which have been used on volcanoes (atmospheric potential gradient measurements, ashfall charge measurement and lightning detection) are covered, along with previous laboratory investigations (including charging by boiling during phreatomagmatic eruptions).

Chapter 4 describes work carried out at Sakurajima volcano for this thesis, using the atmospheric potential gradient monitoring technique. A brief introduction to Sakurajima is given, and the monitoring sites and equipment are described. The data recorded are presented in the form of daily graphs. The periods of most interest are then discussed and charge distribution models are proposed for one of the plumes detected.

The experimental work carried out is introduced in Chapter 5 with a description of

the apparatus design and experimental procedures. Two different types of experiment were carried out, using different kinds of measurement apparatus. For both experiments, small silicate particles (generally less than 100 μm in diameter) were produced by colliding samples of pumice together, in an effort to assess fracto-emission processes as the charge generation mechanism in plumes (Gilbert *et al.*, 1991). In the first series of experiments, the net charge held on the silicate particles was measured using a Faraday cup. The second series used an electric field between two parallel plates in order to separate particles of different polarity and thus measure particles of only one sign. The results of both types of experiments are given and interpreted in Chapters 6 and 7.

The application of these results to the plumes on Io is examined in Chapter 8. Following a brief introduction to Io and its explosive volcanism, any possible observable effects of plume electrification are discussed. One of the questions regarding the plumes is the cause of the frequently observed asymmetry, and so other possible mechanisms to produce this effect are also examined.

Finally, conclusions drawn from both the fieldwork and the experiments are given in Chapter 9. The possible uses of potential gradient monitoring are discussed, and the application of the experimental results to volcanic plumes is examined. Appendices are provided which cover the specifications of equipment used, calibration of the experimental apparatus and tables and graphs of the experiments carried out. Geochemical analyses of the samples used are also given.

In this thesis, S.I. charge units have been used and, where alternatives have been given in previous work, conversions are provided. Engineering prefixes have been avoided in the presentation of the charge results. Instead, many of the graph axes are labelled as '$\times 10^{-12}$ C', which should be interpreted as 'in units of 10^{-12} C'.

2. Mechanisms of charge generation

2.1 Introduction

Prior to reviewing published electrostatic measurements of volcanic plumes (Chapter 3), this chapter will address the possible mechanisms and limitations of charge generation within plumes. Historically, numerous mechanisms have been proposed, but few of them have then been experimentally studied specifically for the volcanic case. Of the charging mechanisms reviewed here, many have been researched for industrial purposes. Some have also been incorporated into charging theories for the two other natural, terrestrially-sourced phenomena known to produce major ground and atmospheric electrical effects; earthquakes and thunderstorms. After observing lightning from ash clouds, Green (1944) compared the volcanic plumes created by eruptions of Paricutín to thunderstorm activity. Some thunderstorm charging mechanisms may indeed be relevant to plumes (especially to large ones), and it is for this reason that modern theories of thunderstorm electrification are reviewed in section 2.6. However, one obvious difference between thunderstorms and many volcanic plumes is the presence of solid silicate particles in plumes, produced during magma fragmentation. As many of the processes proposed to explain electrical effects from earthquakes involve rock fracture, some of them may be relevant to magma fragmentation during eruptions, and thus geoelectric phenomena are also discussed.

2.2 Volcanic plumes

Large scale terrestrial volcanic plumes are truly spectacular features of nature, but are also potentially destructive to humans, their infrastructure, and to plant and animal

life. They are generated by explosive volcanic eruptions and the collapse of lava domes, and consist of solid silicate foam particles, acidic aerosols and entrained air (Sparks *et al*., 1997). On Earth, volcanic activity produces many different styles of plumes, from gas-rich plumes (e.g. Caltabiano *et al*., 1994) to hydrothermal plumes at mid-ocean ridges (e.g. Lupton *et al*., 1980). Here, only explosively generated, particle-laden plumes are considered because these have already been shown to be highly electrically charged (see Chapter 3). This is frequently demonstrated during explosive eruptions by extensive displays of electrical phenomena, some accounts of which are given in Table 2.1. Further compilations of historical accounts describing electrical effects of volcanic plumes can be found in Pounder (1978, 1980b).

Particle-laden eruption columns can vary in size from a couple of kilometres in height (e.g. from small Vulcanian eruptions, Wilson and Self, 1980) to more than 30 km for major Plinian eruptions (e.g. Mt. Pinatubo, 1991; Lynch and Stephens, 1996). The dominant particle sizes transported in volcanic plumes range from micrometers to millimetres in diameter, although blocks, metres in size, can be ejected in eruptions. The smallest particle sizes may be transported for thousands of kilometres by wind, creating aviation and ashfall hazards far from the volcano (Sparks *et al*., 1997). Disturbances of the natural atmospheric electrical field from volcanic plumes have also been detected and observed at large distances from the volcano (Hobbs and Lyons, 1983; Hatakeyama, 1958) providing evidence that the electrical charge can reside for some time on the fine particles and droplets in plumes.

Major explosive eruptions may be the closest terrestrial analogue to the volcanic activity on Io which has been producing the plumes observed by Voyager (Strom *et al*., 1981) and Galileo (McEwen *et al*., 1998a). The lack of a stable atmosphere on Io allows erupted particles to follow nearly ballistic trajectories and, under the low

Table 2.1. Some observations of electrical phenomena associated with volcanic plumes.

Volcano	Year	Reported electrical phenomena	Reference
Vesuvius	79AD	A ‘fearful black cloud was rent by forked and quivering bursts of flame, and parted to reveal great tongues of fire, like flashes of lightning magnified in size’.	Pliny, 79AD
Vesuvius	1631	‘Men and beasts struck dead by lightning’.	Hamilton, 1772
Mayon	1814	Some of the 1200 deaths caused by electrical discharges.	COMVOL, 1975
Vesuvius	1872	Intra-cloud and cloud-to-ground lightning.	Palmieri, 1873
Krakatau	1883	First Point lighthouse on Sunda Straight was hit several times by lightning, breaking the conductor and burning 4 convicts. Many other reports originate from ships in the area: From the steamship Zeeland - ‘black cloud seen above island with continuous lightning accompanied by constant crackling, like machine gun fire, the lightning remained in the cloud and did not strike the earth’. Capt. W. Thomson of the Medea observed smoke (steam), and electrical displays including vivid lightning darting from and around column. Capt. T.H. Lindemann of the Governor General Louden reported that the mainmast lightning conductor had been struck 6 to 7 times. Capt. Logan of the Berbice reported ‘fearful electric phenomena’ and that ‘fireballs continually fell on the deck and burst into sparks’. St. Elmo's Fire was observed on the rudder and sailors received numbing shocks. Capt. Watson of the Charles Bal quoted the ‘incessant glare of varied kinds of lightning’ and Capt. Visman of the Princes Wilhelmina reported ‘nearly uninterrupted lightning’.	Verbeek, 1885; Simkin and Fiske, 1983
Tarawera	1886	Lightning travelling up, down, and horizontally, and ending in balls of fire. Fireballs landing in Wairoa.	Pond and Smith, 1886
Vesuvius	1906	Vertical, horizontal and ‘upwardsly curved’ lightning observed in the eruption plume, sounding like pistol shots. Lightning was also described as having a ‘rik-a-tak’ spark-like quality. St. Elmo’s fire covered pointed objects on people close to an ash plume not observed to display lightning.	Jaggar, 1906; Perret, 1924
Stromboli	1907	A bright blue ‘fire globe’ was observed to emerge horizontally near the base of the ash cloud. After a minute, it shot out a forked flash and then vanished.	Perret, 1924
Taal	1911	Lightning in plume observed to travel upwards, downwards and obliquely.	Pratt, 1911

Table 2.1 continued..

Volcano	Year	Reported electrical phenomena	Reference
Anak Krakatau	1929	A few electrical discharges in the tallest eruption columns. During the presence of thunderstorms, lightning was observed going to and coming from the top of columns 50 to 875 m high. Lightning was also seen flashing upwards from the top of columns 100 to 300 m high in the absence of thunderstorms.	Simkin and Fiske, 1983
Anak Krakatau	1933	Photograph of extensive intra-cloud lightning within the eruption plume above the vent.	Stehn, 1933
Paricutín	1944	Lightning and thunder observed every 1 to 5 minutes during some days, but absent on others.	Green, 1944
Myojin	1953	Fireballs, flashes of lightning and claps of thunder reported during the explosive eruptions that formed Myojin Island.	Dietz, 1954
Surtsey	1963 - 1964	Phreatomagmatic activity and steam plumes from lava entering the sea caused up to 10 discharges per minute, often starting about 10 seconds after the onset of eruption. Strikes to ground and discharges within the cloud were observed.	Anderson *et al.*, 1965
Taal	1965	Lightning reported as forked, branched or displayed as chain lightning.	Carroll and Parco, 1966
Fernandina	1968	Observations of straight sided lightning bolts, about 20 times the width of normal lightning, at intervals of 2 to 15 seconds, pointed down towards the volcano. Eruption cloud was 24 km high, and 175 km in diameter. Reports of the expanding plume suggested that it was a Vulcanian eruption.	Simkin and Howard, 1970
Heimaey	1973	Phreatomagmatic eruptions when lava entered the sea. Frequent lightning between cloud and the island occurred within 10 to 12 seconds after eruption sequence started. One discharge caught on time-lapse camera showed an upwards ‘v’, the base of which was about 100 m or less above the lava flow.	Brook *et al.*, 1974
Plosky Tolbachik	1975	In plumes up to 12 to 14 km high, strong lightning pierced the eruptive cloud at intervals of a few seconds, in all directions.	Fedotov *et al.*, 1980
Usu	1977	Numerous daytime and at night-time photographs taken of intra-cloud and cloud-to-ground lightning.	Kikuchi and Endoh, 1982
Soufière St. Vincent	1979	Intra-cloud and cloud-to-ground lightning observed, sometimes at rates of over 1 per second. Some strikes at distances of up to 9 km from the volcano.	Shepherd *et al.*, 1979

Table 2.1 continued..

Volcano	Year	Reported electrical phenomena	Reference
Mount St. Helens	1980	Observations of 'ordinary lightning', impressive only by size and frequency. Vertical lightning at 25,000 to 30,000 ft was constrained entirely to within the eruption column. Beneath any part of the plume, radios were useless due to static. Some red lightning and other unusual phenomena reported: 'first a white dot appeared in the cloud, and then a bolt would shoot out from it'. Several reports of ball lightning; 'streaking towards the ground, connected neither with the cloud nor with the ground. It was like a group of balls all going in the same direction, but going much too fast to have been projectiles'; 'big balls, big as a pickup and just started rolling across the ground and bouncing'. Climbers on Mt. Adams noted the air becoming electrically charged when ash overhead and one received a discharge on raising his axe.	Rosenbaum and Waitt, 1981
Anak Krakatau	1981	Plumes 400 m to 1 km high, with occasional lightning.	SEAN, 1981
Redoubt	1990	Lightning detected by AVO lightning detection system, accompanied by photographs and video footage of lightning strikes. Observed strikes were remote from the volcano summit and interpreted to be from coignimbrite plumes.	Hoblitt, 1994
Pinatubo	1991	Lightning in the main eruptive plume, pyroclastic surges exhibited beautiful firework displays like 'dancing lights'.	Sabit *et al*., 1996
Spurr	1992	171 lightning strikes recorded by AVO lightning detection system in 1 hour from 18 km high plume.	Paskievitch *et al*., 1993
Rabaul	1994	1 man killed by lightning (of only 2 fatalities in 53,000 displacements). Plume was 18 to 30 km in height and 2 km above Rabaul town.	SIBGVN, 1994
Grímsvötn	1996	Vertical lightning in ash and steam plume erupted through Vatnajökull glacier.	Assorted TV news footage.

gravity, produce plumes up to 400 km high. Observations of areas on Io's surface at temperatures of up to 2000 K (McEwen *et al*., 1998) strongly suggest the presence of silicate magmas, although the composition of the plumes is not certain (Collins, 1981). Electrostatic measurements on Io's plumes are not currently possible, so the results from terrestrial plumes have to be applied to Io's different environmental and volcanic conditions in order to assess any possible effects. Further description of Io's plumes, and discussion of electrostatic effects within them, is undertaken in Chapter 8.

In the early stages of eruption, volcanic plumes represent highly complex, high energy environments, consisting of a wide variety of chemical components and phases. The multitude of reactions and interactions which take place during an eruption provide many possible mechanisms for the generation and separation of electrical charge. As yet, no single process has been identified as a dominant charging process within volcanic plumes. Indeed, it is possible that different processes dominate in different styles of eruptions. Björnsson *et al*. (1967) and others (see Chapter 3) have shown the importance of boiling water in the electrification of phreatomagmatic plumes. The charging of ash particles during their production by fragmentation was suggested by Gilbert *et al*. (1991) and is experimentally examined as a potential plume charging mechanism in this work. Because fragmentation could be a dominant source of charge generation even in the presence of external water, charging mechanisms for solid materials are reviewed first in the following section.

2.3 Charging of solids

Understanding of solid-solid charging mechanisms has increased greatly over the last fifty years, but is still far from complete. Early experiments with materials rubbed by silk have been replaced with complex automated apparatus, often operating under high vacuums. Modern theories of charging mechanisms reflect current understanding of particle interactions within the atomic structure of solids. However, these ‘pure’ theories cannot always explain results obtained for real applications and ‘dirty’ systems. The solid-solid charging mechanisms reviewed here include contact charging and triboelectrification, fracto-emission, mobile charge carriers, piezoelectric effects and pyroelectric effects.

2.3.1 Contact charging and triboelectrification

Contact charging is a process by which charge is transferred between materials when they touch, and was initially recorded as long ago as 600 BC by Thales of Miletus. The process is still not fully understood and most theories are applicable only to contacts between clean material surfaces in a vacuum. When two materials are brought into contact, electrons flow across the contact surface to equalise the work function at the interface. A material’s work function can be defined as the energy needed to just remove an electron from the material. For metals, it represents the potential difference between the Fermi level and the vacuum energy level, and is around 4 eV. For insulators, predicting potential differences due to contact charging is highly complicated. Only the contacting surface layers are involved in the process and charges on the rest of the material depend on the time constant, t, where

$$t = \varepsilon\rho \tag{2.1}$$

and ε and ρ represent the material's permittivity and resistivity respectively.

Experiments on contact charging are extremely difficult to carry out and demonstrate the wide variety of factors that can influence the degree of charging. With polyethylene, PTFE and PET, Lowell (1976) showed that the magnitude of charge transfer from a single contact with metal was not a function of the metal's work function. However, for multiple impacts, a linear relationship was found and the charge transfer was also shown to increase as the logarithm of the number of contacts. Lowell found no dependence with the duration of contacts, but a time dependence has been shown for polystyrene (Furhmann and Kurshchner, 1981). Despite the experimental difficulties, several 'rules of thumb' have been developed. Coehn's rule states 'when two dielectric materials are contacted and separated, the material with the higher dielectric constant becomes positively charged' (Lawver and Dyrenforth, 1973). This was put in context with modern theories of solids by Zwikker (1954); 'the material with the greater number of energy levels will have the higher permittivity and will be more easily polarised so that it will give off electrons to the other contact material.' Whilst more than 400 materials have been shown to obey Cohen's rule, others do not. Although a large amount of research has been carried out into the contact charging of atomically clean surfaces, real surfaces are highly irregular and have coatings of adsorbed gases, water vapour and other contaminants. It is also rare that 'contacts' do not also incorporate a sliding component, which dictates that some of the charging must be attributed to triboelectrification, rather than to pure contact electrification.

Triboelectrification is the mechanism by which materials charge when they are rubbed together. Experimentally, it can be difficult to separate from contact

electrification and the term ‘triboelectrification’ is often taken to include also charges generated by contact electrification. It has been found that charge transfer between two samples of like material can be as large as between unlike materials. In the case of like materials, the polarity of charge transfer is dependant on which sample is doing the rubbing and which is being rubbed (Cross, 1987). Charge magnitudes depend on the materials, applied force and rubbing velocity, as well as temperature and relative humidity. Experiments carried out under vacuum can give misleading results because, in the atmosphere, high electric fields between separating surfaces can cause the air to ionise. Ions neutralise the surface charges but tend to overcompensate, leaving charged areas of opposite polarity to the initial frictional charge (Cross, 1987).

Triboelectric effects in industrial powders can present electrostatic hazards including the risk of major explosions (Eden, 1973; Cross, 1987). Powders are typically charged during sieving, pouring, scroll feed transfer and pneumatic transport. Boschung and Glor (1980) measured the charge on two hundred different powders using apparatus designed to simulate pneumatic transport. They recorded charges between 10^{-7} and 10^{-3} C kg^{-1}. Some of the difference was attributable to variations in specific area of the powders, with the higher charge densities on powders of higher surface area (about 500 m^2 kg^{-1}). Cross and Farrer (1982) showed how the polarity of charge on some powders generated by frictional effects can vary with the particle size. Passing the powders through either polymer or metal fans produced positive charges on smaller particles (50 to 200 μm) and negative charges on larger particles (200 to 2000 μm) of up to 10^{-4} C kg^{-1}.

Kanagy and Mann (1994) attributed the electrification of creeping and saltating sand grains to triboelectric effects due to the common grain-to-grain frictional

contacts. Similarly, the electrification of sand and dust storms, which can be sufficient to cause blue light emission, has also been associated with frictional electric effects (Nalivikin, 1983), even on other planets (Mills, 1977). As friction has been known to produce electrification for such a long time, early accounts of electricity in volcanic plumes (e.g. Perret, 1924) commonly suggested frictional effects as the charge generation mechanism. Electrification experiments on volcanic ash by Kikuchi and Endoh (1982) and Hatakeyama and Uchikawa (1952) have, by their design, probably been dominated by frictional effects (see Chapter 3).

2.3.2 Fracto-emission

Fracto-emission is the name given to the release of electrons, positive ions, neutral atoms and various frequencies of electromagnetic radiation from radio waves to light, from a material due to fracture. Typically, emission starts at the time of onset of crack generation, but can continue from the fresh surfaces for up to several seconds after the break (Dickinson *et al*., 1984). Research has been dominated by the physics and materials science communities, mainly on oxide coatings of metals (Dickinson *et al*., 1981b), crystals (Dickinson *et al*., 1981a) and adhesives (Dickinson *et al*., 1982) under high vacuum. Table 2.2 lists some of the experiments carried out and the emissions recorded.

Dickinson *et al*. (1981b, 1984) studied emission from a variety of materials including mica and quartz, and recorded electron releases of up to 7000 per second decaying rapidly over 3 seconds. Dickinson *et al*. (1988) observed long wavelength electromagnetic signals associated with the fracture of single crystal quartz that they attributed to microdischarges near the propagating crack tip. They proposed that the piezoelectric nature of the silica structure enhanced charge separation around crack

Table 2.2 Fracto-emission experiments. The abbreviations used are FE, fracto-emission; EE, electron emission; NCE, negative charge emission; PIE, positive ion emission; NE, neutral emission (i.e. atomic or molecular, excited or unexcited); phE, photon emission; RE, radio emission; cps, counts per second; and cpms, counts per millisecond.

Material	Emission types	Pressure, fracture technique	Ref.
various, including quartz, muscovite, fused silica	**EE, PIE** EE: for quartz, up to 10^6 electrons emitted per cm^2 of crack wall.	2×10^{-6} to 4×10^{-6} Torr tension and three point flexure	Dickinson *et al.*, 1981a
interfacial failure between: epoxy-brittle materials, polybutadiene-glass, pressure sensitive adhesives-polymers	**EE, PIE, phE** EE & PIE: up to ~10^5 cps. Fracture involving adhesive failure gives intense, long lasting EE & PIE.	1×10^{-4} to 4×10^{-4} Torr tension and delamination by peeling	Dickinson *et al.*, 1982
polybutadiene filled with small glass beads, Al_2O_3 filled epoxy, single-crystal sucrose, single crystal quartz	**EE, phE, RE, PIE** EE: for quartz, up to 7000 cps, decaying rapidly over 3 s.	10^{-5} Pa tension and three point flexure	Dickinson *et al.*, 1984
interface failure between Al and epoxy	**EE, phE, RE** EE: 2.5×10^3 cps, decaying over 300 s. Fracture caused electrical breakdown with an applied potential difference of a few 100 V over 1 mm.	10^{-5} Pa tension	Dickinson *et al.*, 1985a
polycrystalline 95/5 Pb zirconate-titanate	**EE, PIE, phE** EE: up to 400 cpms.	10^{-5} Pa three point flexure, a variety of orientations	Dickinson *et al.*, 1985b
interface failure between Au, Al and glass	**EE, phE** EE: up to 1700 cpms; over 10^5 counts over 400 s.	10^{-5} Pa peeling	K'singham *et al.*, 1985

Table 2.2 continued..

Material	Emission types	Pressure, fracture technique	Ref.
single-crystal pentaerythritol tetranitrate	**EE, PE, PIE** EE: up to 31,000 cps, total ~2.1×10^6 counts over 400s. Highest emission rates from impact loading, no FE for cleavage fracture.	10^{-5} Pa compression, three point knife edge cleavage fracture, impact loading	Miles *et al.*, 1985
clear, single-crystal MgO, cloudy MgO	**phE, EE, PIE** EE: up to ~5000 cps, decaying within tens of seconds. Peaks not well correlated with phE peaks.	$<10^{-6}$ Pa three point flexure	Langford *et al.*, 1987
many, including Si, quartz, fused silica	0.1 to 500 μm ejecta studied, individual particles had charges of 10^{-14} C; total fracture debris: 10^{-13} to 10^{-12} C.	atmospheric pressure; three point flexure and other geometries	Donaldson *et al.*, 1988
fused silica, sodium trisilicate glass	**phE, EE, PIE, NE** (O, O_2) PIE: ~10^3 cps, decay monitored for 400 s. EE: most from trisilicate glass, max. being 70 nA.	10^{-7} Pa three point flexure	Dickinson *et al.*, 1988
single-crystal LiF, MgO	**EE, PIE** Intense post-fracture emission from areas observed under SEM to be covered in a high density of dust-like particles. Off-axis fracture and damaged areas produced increased post-emission (measured up to 600 s).	~10^{-5} Pa tension, cleavage and three point flexure	Mathison *et al.*, 1989
polycrystalline Ti, deuterated Ti	**phE, RE, NCE, PIE, NE** (D_2) NCE: ~$4x10^3$ cps, decay monitored over 20 s, 105,000 counts in total. PIE: ~2×10^2 cps, decayed over ~5 s, 1300 total count.	10^{-6} to 10^{-8} Torr, and atmospheric pressure tension and three point flexure, in various orientations	Dickinson *et al.*, 1990
Au films peeled from oxidized Si	**EE, phE** EE: ~10^4 cps, can last > 8 s (0.3 cm^2 peeled).	10^{-7} Torr peeling	Doering *et al.*, 1990

Table 2.2 continued..

Material	Emission types	Pressure, fracture technique	Ref.
quartz, feldspar, 11 rocks including granite, andesite, dolerite and basalts of various water contents	**NCE, PIE** Charges of -2×10^{-12} C and $+6 \times 10^{-13}$ C released during loading of feldspar. Increasing water content of hygroscopic rocks up to 0.05 wt%, increased total emission (up to ×1000). Andesite produced a net negative charge of about -10^{-11} C s^{-1} during loading.	indentation fracture (loads of 9.8 to 490 N) atmospheric pressure, temperatures up to 400 °C	Enomoto and Hashimoto, 1990
Au, Ag and Cu films peeled from oxidised Si	**EE** EE: correlated to work function of the metal. Post fracture emission for a few seconds.	peeling	Xiong-Skiba *et al*., 1991
sodium trisilicate glass, soda lime glass	**NE** (Na^0), **phE, EE, PIE** NE: set a lower limit of 10^{12} atoms released per cm^2 of fracture surface. EE & PIE: counts of $<10^4$ cps, decaying within ~50 ms.	<1 mPa three point flexure; measurements made by quadrupole mass spectrometry and surface ionisation techniques	Langford *et al*., 1991
Ge	**NE** (Ge, Ge_2)	$<10^{-6}$ Pa three point flexure	Dickinson *et al*., 1991a
NaCl, LiF	**NE** (alkali atoms, molecules including NaCl, $(LiF)_{1-3}$)	undescribed vacuum three point flexure	Dickinson *et al*., 1991b
calcite	**NE** (CO_2) NE: CO_2 emission caused by all processes.	<1 mPa; three point flexure, diamond abrasion and thermal stimulation of deformed material	Dickinson *et al*.,1991c
interfacial failure between epoxy and stainless steel	**EE, phE, RE** EE: around 10^4 cps.	10^{-5} Pa tension, rotational	Ma and Dickinson, 1991
alkali feldspar	**NE** (K, Na, and H_2O, KOH attributed to fluid inclusions) NE: at least 6×10^{14} K atoms per cm^2 of crack surface.	10^{-7} Pa probably three point flexure	Dickinson *et al*., 1992

tips, producing large electric fields. These fields were also responsible for accelerating some emitted electrons back towards surface regions of positive charge and causing secondary emission of positive ions and neutral atoms by electron stimulated desorbtion (Ohuchi and Holloway, 1982). Wollbrandt *et al*. (1983) detected charge densities on cleavage planes of LiF crystals which created electric field strengths of 10^7 V m^{-1}. They hypothesised that these fields were sufficiently strong for some of the electrons observed to represent field emission from surface regions by the tunnel effect (a quantum mechanism whereby a finite chance exists that a particle could escape, even if it had not been given enough energy to do so by classical theory).

The high surface charge densities measured suggest the presence of dislocations at the surface (Wollbrandt *et al*., 1983). Dickinson *et al*. (1991b) also explained delayed and intermittent emission of neutral species from fractured NaCl crystals as the arrival of dislocation avalanches at the surface. This delay is not always observed in the case of silicate glasses where significant neutral emission can occur during the fracture event (Dickinson *et al*., 1988). Immediate neutral emission can be explained by bond breaking decomposition. Delayed emission of Na^0 from sodium silicate glasses is thought to reflect the diffusion of Na^+ towards the fracture surface under pressure gradients near the crack tip (Langford *et al*., 1991). Near the surface, ions are neutralised by trapped holes and then thermally emitted. Langford *et al*. (1991) recorded 10^{12} atoms released per square centimetre of fracture surface (which equates to approximately 0.1 % of a monolayer). Because they were unable to detect all the emitted atoms, the estimated total release was several orders of magnitude higher. Dickinson *et al*. (1992) recorded emission of at least 6×10^{14} potassium atoms per

square centimetre of fracture in an alkali feldspar (which equates to approximately 30 % of a monolayer). These experiments have demonstrated that the upper regions of fracture surfaces represent a low density, highly strained layer with many strained and broken bonds exposed at the surface.

Donaldson *et al*. (1988) broke minerals and other materials and measured the charge on the macroscopic particles produced. They explained charges of around 10^{-14} C per particle on the fracture debris as being caused by fractoemission. The total net charge on ejecta produced from fracturing a sample several square millimetres in cross section was in the range of 10^{-13} to 10^{-12} C. Mathison *et al*. (1989) showed that the amount of fracto-emission increased with the degree of damage caused around the fracture site. On SEM examination of fracture surfaces, they found them to be covered with dust-like particles adhering by electrostatic forces.

Some fracto-emission experiments have been carried out on rocks. Brady and Rowell (1986) observed a brief light emission during the compressional fracture of granite, which they interpreted as excitation due to electrons emitted from the fresh surfaces. Enomoto and Hashimoto (1990) indented rocks and found that they released positive and negative charges as a result. Andesite, dolerite and basalt were found to increase their total amount of emission with increasing water contents up to 0.05 wt% H_2O. By estimating the volume of the fractured zone, they calculated that loads of 294 N released net charges of about -0.6 C m^{-3} from andesite with approximately 0.05 wt% H_20.

The fracturing of materials can thus produce charged particles, electromagnetic radiation and charged debris fragments. Because particle-laden volcanic plumes are the result of extreme fragmentation of magma, they represent a very large, freshly

fractured, surface area. For this reason, Gilbert *et al*. (1991) suggested fractoemission as the dominant charging mechanism for plumes.

2.3.3 Mobile hole charge carriers

Studies of MgO single crystals have led to the discovery of defect electrons on the O^{-2} sublattice (called positive holes) at temperatures as low as 200 °C (Freund *et al*., 1989; 1994a). Originally known only as the product of radiation bombardment, the production of these holes at such low energy levels suggested that they were being produced by thermal dissociation of some type of unknown defect. Freund *et al*. (1994a) proposed that these defects were self-trapped positive hole pairs called peroxy anions, O_2^{2-}, consisting of two positive holes (O^-) residing in adjacent sites next to an Mg^{2+} vacancy. Although the O^- are bound by a strong covalent bond, its short length actually renders it labile due to nuclear-nuclear repulsion (Freund, 1994b). Thus, peroxy anions can be disassociated by moderate temperatures and even by shock (Borucki and Freund, 1998b). Once activated, the O^- can propagate as holes (defect electrons) through the O2p-dominated valence band. They thus represent highly mobile positive charge carriers, able to flow through otherwise insulating matrices and cross grain boundaries with ease (Borucki and Freund, 1998b).

In rocks and minerals, peroxy could be formed by the reaction

$$(OH^-)_{structure} + (OH^-)_{structure} = (H_2)_{structure} + (O_2^{2-})_{structure} \qquad (2.2).$$

Experiments have provided evidence for this by detecting mobile charge carriers in olivine (Freund *et al*., 1988), fused silica (Freund, 1985), diorite and anorthosite (Freund *et al*., 1998), gabbro (Borucki and Freund, 1998a, 1998b) and obsidian (Batllo *et al*., 1988).

Due to their high mobility, electrostatic repulsion between the holes rapidly disperses them from the material bulk, producing large charges at the material surface. During impact experiments on gabbro, Borucki and Freund (1998a, 1998b) measured surface potentials of up to +1.5 V, and also observed light emission due to breakdown of the surrounding air in the high electric fields produced. Using a series of electrodes, they were able to detect the charge 'cloud' as it travelled along the samples at speeds of approximately 300 m s^{-1}. Because the positive charge appears on the surface, the holes can be neutralised by electrons from outside the sample, thus imparting a net negative charge to the sample. Although no field evidence has yet been obtained, Freund *et al*. (1994b) proposed that these highly mobile charge carriers could be responsible for such geoelectric phenomena as earthquake lights (see section 2.5).

2.3.4 Piezoelectric effects

Due to a lack of symmetry in their crystal structure, piezoelectric materials generate electric fields within them when they are placed under mechanical stress. Thus, surface charges can develop on stressed samples before they undergo cleavage or fracture. The magnitude of this effect is measured with the piezoelectric constant which, for quartz, has a value of 2×10^{-12} C N^{-1}. Due to this relatively high value, it has been suggested that piezoelectricity in quartz could be the cause of the charge generation in rocks (Ogawa *et al*., 1985) linked to the production of earthquake lights (Finkelstein and Powell, 1970).

During particle collisions, piezoelectric charges are also a function of the impact duration. Hard particles rebound quickly, so experience larger forces and thus greater piezoelectric effects than softer particles. Because quartz is highly piezoelectric and

has a hardness of 7 on Mohs scale, piezoelectric charging during the collision of quartz particles is a potentially important effect. However, although charges are generated, they are not necessarily transferred. Charge transfer can be achieved if an electrically conductive material is present (as in piezoelectric gas lighters) or an induced charge in a remote conductor is removed by being earthed (charging by induction).

2.3.5 Pyroelectric charging

The pyroelectric effect causes the generation of unlike charges within crystals undergoing heating. Quartz charges along the *a* crystallographic axis, as noted by Simpson (1966), on heating to only 100 ºC. Just as for the piezoelectric effect, charge is not necessarily transferred, but other particles could potentially charge by an induction process. Industrially, pyroelectric materials (often lithium tantalate single crystals and lead zirconate titanate ceramics) are used in the manufacture of various types of temperature sensors and thermal imagers (Cross, 1987).

2.4 Charging by particles

Although charging by (atomic) particles has not been suggested for terrestrial plumes, it is an important factor for dusts in space and on other planets (e.g. Bibhas and Criswell, 1977), and could be a charging mechanism acting on Io's plumes. The surface of the Earth is protected from almost all particle bombardment by the magnetosphere and atmosphere. However, particle charging is employed extensively in industry, especially using corona in electrostatic precipitators (Cross, 1987). Short

reviews are given here of charging by particle bombardment, photoelectric and field emission, radioactive decay and thermionic emission.

2.4.1 Bombardment charging

Materials will become charged if they are subject to bombardment by charged particles. Industrial applications often make use of corona charging where high voltages at a point electrode cause partial breakdown of the surrounding gas. The ions produced which are repelled by the electric field can then be collected on other materials, often dusts in electrostatic precipitators (DuBard and Nichols, 1990). This application in particular has generated volumes of research on the charging and discharging of particles by unipolar or bipolar space charges (e.g. Williams and Bailey, 1989; Robinson, 1973). Particle charge is a function of ion mobilities, charges and number densities, the magnitude of the electric field, treatment time and particle diameter. Due to the random thermal motion of ions, ion-bombardment works simultaneously with diffusion charging. (In the absence of external electric fields, a neutral particle will still charge as a result of ions attracted to it by their image charges). Robinson (1973) showed that, for typical discharge conditions in atmospheric air, with an electric field of 2×10^5 V m^{-1} and an ion number density of 5×10^{13} m^{-3}, diffusion charging is only important for particles less than about 0.2 μm in diameter.

An alternative bombardment charging technique is the use of ion and electron beams. The charged particles (ions or electrons) are accelerated towards the target by strong electric fields. The final charge on the target is a function of its time in the beam and the energy of the particles. Complications in calculating the exact charge

are caused by the repulsion of the particles once the target is partially charged. If the charging particles have sufficient energy they may cause secondary emission from the target. This will also be a function of the current charge on the target.

Due to the lack of a protective atmosphere, dust particles on the surface of the moon are susceptible to charging by bombardment of particles from the solar wind (Inculet and Criswell, 1979). The absorbed particles can generate large space charges in dielectric materials, leading to fields of 10^5 to 10^6 V m^{-1}. However, they are also subject to photoelectric charging, which can be highly important in the lunar environment, and also on Io.

2.4.2 Photoelectric charging

In contrast to bombardment charging (charging due to absorption of charged particles), photoelectric charging is caused by the ejection of electrons due to the absorption of uncharged particles (photons). However, this will only occur if each incident photon is sufficiently energetic to allow an electron to escape from its potential well.

On Earth, ultra-violet light is heavily attenuated by the atmosphere. Thus, because visible light is not sufficiently energetic to cause photoemission, little charging occurs by this process on the surface of the Earth. However, photoelectric charging is much increased at high altitude, in space and on the surface of planets where little or no atmosphere is available to filter out ultra-violet radiation and soft x-rays. Electrostatic levitation of charged lunar dust on the surface of the moon has been suggested as an explanation of 'lunar horizon glow' observations (Rennilson and Criswell, 1974). Electric fields large enough to produce this phenomenon could be generated by photoemission of electrons from illuminated portions of lunar regolith and re-

entrapment of those electrons in shadowed areas (Criswell and De, 1977; De and Criswell, 1977). In space, the shape of Jupiter's ring can be reproduced by considering the fate of dust particles subjected to positive charging due to photoelectron emission and negative charging from collecting electrons released from Jupiter's atmosphere (Horányi and Cravens, 1996).

2.4.3 Field emission charging

A neutral particle entering an electric field will become polarised into a dipole. If the field is strong enough, emission of positive and negative ions will occur from sharp points on the particle. For electron emission the local field must be at least 10^{10} $V\,m^{-1}$ and for positive ion emission, 10^{11} $V\,m^{-1}$ (Moore, 1973).

These field strengths cannot be produced in a gas due to its electrical breakdown (Earth's atmosphere breaks down at about 3×10^{6} $V\,m^{-1}$ at sea level). However, field emission on a small scale may be induced from particles in a vacuum or insulating liquid, because higher field strengths can be supported.

2.4.4 Charging by radioactive decay

Because α, β and β^{+} particles are charged, their emission leaves the parent body with an equal and opposite charge. A β particle (a single electron) holds a charge of -1.6×10^{-19} C. Therefore, each emission leaves the sample with a charge of $+1.6 \times 10^{-19}$ C. The less common β^{+} particle (positron) has an equal but opposite charge to the β particle and thus leaves the sample with a -1.6×10^{-19} C charge. α-emission leaves the sample with a -3.2×10^{-19} C charge. As decay and emission

proceed, charge on the parent material increases until the environment's breakdown level is reached, or field emission starts at asperities.

2.4.5 Charging by thermionic emission

This effect occurs in environments where temperatures are sufficiently high that electrons obtain enough energy to escape from the surface of a material. This process is highly temperature dependant and occurs in gases from furnaces and in high temperature chemical reactors (Moore, 1973). The effect does occur at low temperatures, but only to an insignificant degree. The Richardson equation allows calculation of the current density, *J*, from a surface at a temperature, *T*, (in Kelvin,) given by

$$J = A_0 T^2 \exp\left(\frac{-e\phi}{k\,T}\right) \qquad (2.3),$$

where *e*, is the electronic charge, *k*, the Boltzmann constant, ϕ, the material's work function, and A_0 is a universal constant with a theoretical value of 1.2×10^6 A m^{-2} K^{-2}.

2.5 Charging with liquids

As with dust charging, electrostatic effects in liquids are industrially important due to the potential hazards involved. Stirring, spraying and pipe transport of volatile, highly insulating liquids are all potentially dangerous if electrostatic precautions are not taken (Cross, 1987). Several of the listed liquid charging mechanisms have been used to explain various naturally occurring electrification phenomena, from thunderstorms to earthquake lights.

2.5.1 Streaming currents

Streaming currents can be found in industrial environments within liquids transported by pipe. If the liquid behaves like a weak electrolyte, a Helmholtz double layer (Hunter, 1981) can form on the pipe wall due to preferential adsorption of one ionic species. The charge on these bound ions (the Helmholtz layer) induces a diffuse mobile zone of oppositely charged ions (the Gouy-Chapman zone) within the liquid next to the wall. The potential at the plane of slip between these two layers is used to assess the degree of possible charging and is known as the zeta potential. Downstream flow of the free ions constitutes an electrical current, the magnitude of which is extremely hard to predict due to the large number of unknown parameters. In industrial applications it can be of order 10^{-10} to 10^{-7} A, sufficient to produce sparks from ungrounded pipework. Disruption of the liquid after leaving the pipe can then produce charged droplets. This charging mechanism creates a hazard especially when using low conductivity, highly volatile liquids, for example, during aircraft refuelling.

Streaming currents have also been studied in saline solutions flowing through rocks (e.g. Jiang *et al*., 1998). Annual magnetic anomalies beneath La Fournaise volcano have been attributed to streaming currents, as have other magnetic anomalies preceding eruptions (Zlotnicki and Le Mouël, 1990).

2.5.2 Charging of particles in a liquid

A similar effect can charge solid particles within insulating liquids. A contact potential at the particle surface-liquid interface can be produced as a result of surface effects in the liquid and selective or dipole adsorption onto the particle surface. This contact potential produces a Helmholtz double layer consisting of one layer of charge

tightly bound to the particles, surrounded by a diffuse layer of the opposite charge within the liquid. This effect is used during electrophoresis to separate particles from a liquid using an electric field.

2.5.3 Waterfall electrification (Lenard charging)

Charged waterdrops produced by the mechanical disruption of water were first noticed by Lenard (1892). Larger particles carried a positive charge while smaller particles and the air carried a negative charge. Geysers, breaking waves and waterfalls all demonstrate electrification by this process, which is now known as Lenard splashing. Electrification is produced by the rapid formation of new water surface area, and does not occur if water disruption is not violent and production new surface area is gradual. Theory and experiment have shown that a relationship exists between the charge per unit mass of the larger droplets and their number density. For seawater, droplets with specific charge of about 10^{-14} C kg^{-1} correspond to number densities of 10^{5} droplets cm^{-3} and space charge densities of about 10^{-8} C m^{-3} (Eden, 1973). These magnitudes can be potentially hazardous and it has been suggested that electrostatic discharges due to Lenard charging whilst spray cleaning were responsible for five supertanker explosions in 1969 (Pierce, 1970).

2.5.4 Charging by freezing and boiling

Workman and Reynolds (1948, 1950) discovered electric potentials of up to 232 V between ice and water in the process of freezing. The ice was negative with respect to the water, and this ‘freezing potential’ was much larger than the potential generated between ice and water in a steady state. Workman and Reynolds studied a variety of different solutions, including ones found as natural rainwater. The potentials produced

varied widely with dissolved species and concentrations, and proved especially sensitive to ammonia. However, using highly purified water, Gill and Alfrey (1952) produced potentials of the opposite polarity, with the ice being positive with respect to the water.

Boiling saline solutions have also been shown to produce charge separation (Blanchard, 1964; Björnsson *et al*., 1967; Pounder, 1978) and these results have been used to explain atmospheric potential gradient measurements of steam plumes (see Chapter 3). However, the exact mechanism of charge separation can be explained in terms of shearing double electric layers in the water and solid-solid charging of salt crystals rather than any distinct boiling phenomenon (Pounder, 1980a).

2.6 Thunderstorm electrification

Despite some differences, there are several similarities between volcanic plumes and thunderstorms which make a comparison worthwhile. Both represent extensive, electrified atmospheric phenomena, and consist of solid particles and liquid droplets. Both are also known to discharge by lightning to the ground or between different parts of the cloud or plume. A typical thunderstorm may produce a lightning discharge once every 20 s, with tens of Coulombs of charge being neutralised (Uman, 1984). Although much more frequent lightning has been observed from volcanic plumes (Anderson *et al*., 1965; Shepherd *et al*., 1979) the amount of charge neutralised is not known. The possibility exists that some charge generation mechanisms in thunderstorms could also occur in volcanic plumes.

Extensive research has been carried out during this century into the nature of processes involved in the electrification of thunderclouds. Repeated observations

using varied techniques have placed constraints on possible charging mechanisms by locating the main charge densities. Figure 2.1 shows this typical charge distribution within a thundercloud. The lower main charge, located at temperatures between -10 and -20 °C, is usually the source of cloud-to-ground lightning, lowering negative charge to Earth.

Despite the large number of theories that have been proposed during this century, the exact mechanism of thunderstorm charging is still unknown. Current theories can be divided into two groups: convective mechanisms and charging due to particle interactions. Convective processes involve particles becoming charged by ion capture and then being distributed by convection currents. Particle interaction mechanisms involve gravitational separation of particles of different sizes that have been charged during collisions. They can be further subdivided into inductive processes, relying on the particles being polarised by an external electric field, and non-inductive processes.

2.6.1 Convective charging

This is the only charging process proposed that does not involve direct gravitational separation of particles of opposite polarity in order to separate charge. It relies on charges produced in spatially separated areas then being transported by air currents in the cloud. Positive ions are drawn into a growing cloud's updraft from below the cloud base. The ions are quickly trapped onto water droplets which are then carried upwards in the updrafts to areas close to the cloud top. The positive charge of these regions attracts negative charge from outside the cloud which becomes trapped on cloud particles at the edge of the cloud. This negative screening layer is then entrained and descends in downdrafts, where it attracts further positive charge to the

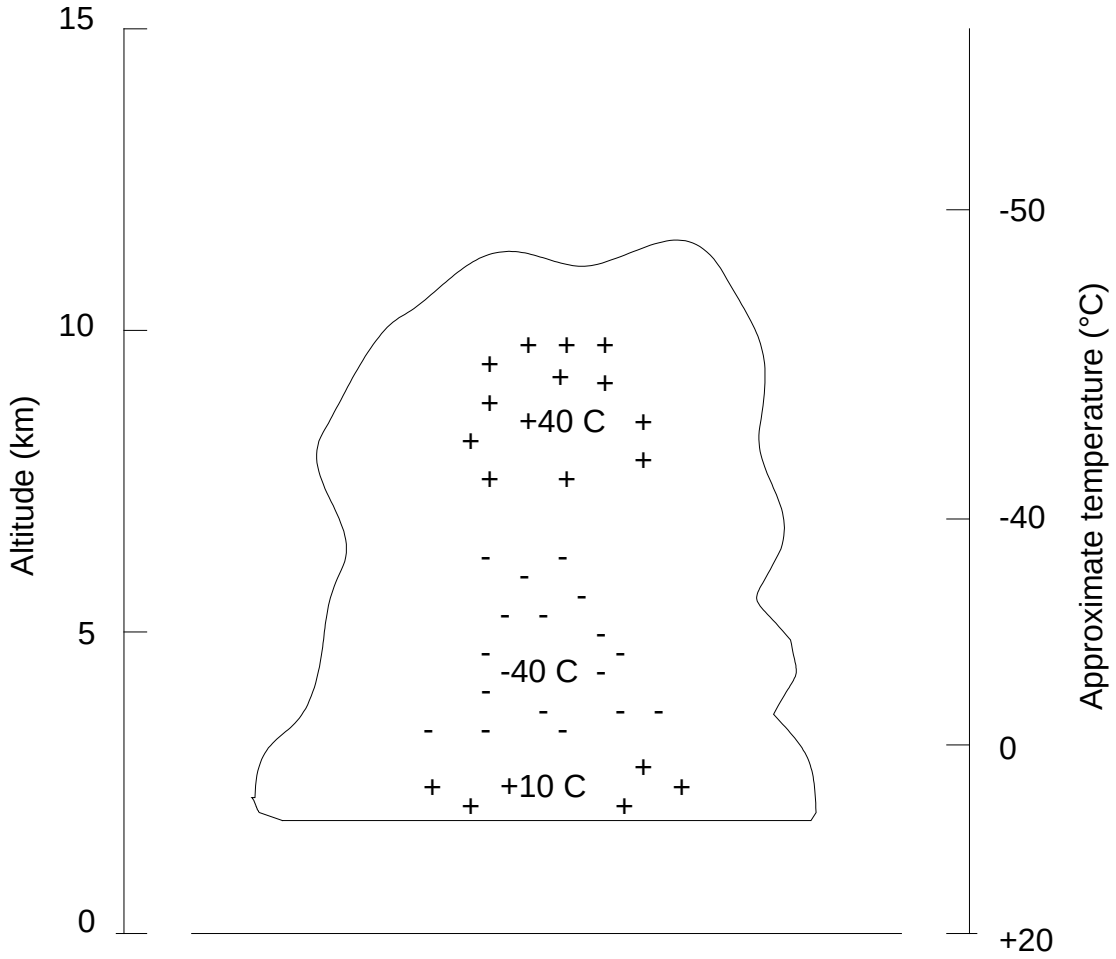

Figure 2.1 Schematic diagram of charge distribution within thunderstorms.

base of the cloud. Wagner and Telford (1981) showed that latent heat effects in a descending parcel of cloud make it neutrally buoyant and thus stop decent at around the -10 °C level.

By introducing negative ions into the base of a growing cloud, Moore *et al*. (1989) demonstrated that space charge near the ground can be transported into clouds. The negative charge was swept aloft and attracted sufficient positive charge to reverse the local potential gradient and produce positive cloud to ground lightning. Further evidence in support of convective charging comes from the measurements made by Marshall *et al*. (1989) of the charges held in the anvil tops of thunderclouds. From balloon data they showed that the anvil was formed from positively charged ice crystals which had been sheared out from the top of the cloud. Upper and lower screening layers then formed round the anvil as the positive charge attracted negative ions which were trapped on to cloud particles. Doppler radar measurements showed the downward movement of cloud near the lower screening layer, potentially transporting negative charge further into the cloud.

2.6.2 Inductive particle charging

This mechanism was originally suggested by Elster and Geitel (1913) as a charging process between raindrops (hydrometeors) and cloud droplets. The existing vertical electric field (see Chapter 4) polarises hydrometeors, producing a net positive charge at the base, and negative at the top. Any cloud droplet that collides with, but then rebounds from, the falling hydrometeor will contact the positively induced base of the drop. The droplet will thus donate electrons, become positively charged and leave the hydrometeor with a net negative charge. This separation of charge will enhance the original electric field. However, calculations have shown that it could

only account for a small fraction of the fields present in thunderclouds. Electrostatic forces from the droplet polarisation would also promote coalescence during impact, rather than rebound.

To avoid the coalescence problem, the original idea was extended in the 50's and 60's for the case of ice crystals rebounding from graupel (soft hail). However, Latham and Mason (1962) showed that the magnitude of charge separation was still small due to the low conductivity of ice and the short contact time during collisions. More recently, Mason (1988) showed that appreciable charge separation may be possible with small, low density graupel and cloud droplets, but further investigations of collision efficiencies and separation probabilities are needed.

Inductive particle charging cannot account for the large charge detected on some particles in the early stages of storm electrification (Christian *et al*., 1980; Marshall and Winn, 1982). Particles less than 3 mm in diameter have been detected with up to -400×10^{-12} C of charge. This can only occur by inductive processes once large electric fields have been developed. Despite several problems with inductive theories, the fact that they are relatively easy to model quantitatively has led them to be incorporated into several thunderstorm models.

2.6.3 Non-inductive particle charging

Non-inductive particle charging processes involve charge transfer which is independent of the local electric field. These processes are poorly understood and very difficult to model quantitatively. The highest charging rates are observed from interactions between vapour-grown ice crystals and graupel pellets in the presence of supercooled water droplets. Reynolds *et al*. (1957) showed that riming graupel (growing by accretion of freezing supercooled cloud droplets) would become

negatively charged by collisions with vapour-grown ice crystals at -25 °C. Without the presence of ice crystals, charge separation could not be detected. Takahashi (1978) showed that the sign of charge transfer is dependent on the temperature and liquid content of the cloud. At temperatures greater than -10 °C he was able to charge ice spheres (representing graupel) positively from collisions. At lower temperatures, the direction of charge transfer depended on the liquid water content of the cloud, with graupel charging negatively at intermediate values of water content. Similar experiments by Saunders *et al*. (1991) reproduced the polarity change with temperature between -10 and -25 °C, but did not show the same dependence on water content as observed by Takahashi (1978).

Jayaratne *et al*. (1983) demonstrated that the magnitude of the charge transferred during impacts of ice crystals and graupel is a function of impact velocity and the size of the ice crystals, with charge transfer increasing rapidly with crystal size. Crystals between 10 to 100 μm in diameter produced charges between 10^{-18} to 10^{-15} C per impact, which varied as a function of the crystal diameter to the power 3.4. Keith and Saunders (1990) used ice crystals up to 800 μm in size and suggested that, at high values of charge transfer, the actual measured charge magnitude was limited by reverse transfer when the particles separated. By studying collisions in the dark, Keith and Saunders (1988) observed this reverse charge transfer in the form of light emission from coronae. The mechanism of the initial charge transfer is not known. However, there are several different theories.

Relative growth rates.

Baker *et al*. (1987) explained the polarity reversal with temperature of graupel-ice particle collisions in terms of relative particle growth rates. Unlike ice particles that

grow only from environmental vapour, a riming graupel grows from diffusion from the environmental vapour and from vapour released from droplets freezing on its surface. The freezing time of a droplet depends on the temperature; at low temperatures, droplets freeze quickly and release little vapour producing low growth rates. Comparison of the growth rates of graupel and ice particles suggested that below the temperature of charging polarity reversal, ice particles grew faster and charged positively during collision. Baker and Dash (1989) suggested that this was due to an excess of negative ions in the disordered melt layer on top of the ice. Rapid growth produces a thicker melt layer and thus can provide more negative charge during impacts. However, the presence of this layer at low temperatures is not certain and the effects of impurities in the ice are not yet understood.

Growing or evaporating ice surfaces.

In the absence of cloud water droplets, ice particles colliding with an ice surface growing by vapour diffusion charge the surface positively (Gaskell and Illingworth, 1980). If the ice surface is subliming, it becomes negatively charged. In confirming these results, Jayaratne *et al*. (1983) observed that the charge magnitudes were typically an order of magnitude smaller than those obtained in the presence of water droplets. Caranti *et al*. (1991) explained these results in terms of a thermoelectric effect. The extremities of a growing ice structure are warmed by latent heat and, during fracture, protons on hydrogen bonds tend to remain on the colder material. The extremities of a graupel pellet undergoing sublimation will be colder than the rest of pellet and positive charge will be lost during collisions which remove part of the surface. Thermoelectric effects were originally invoked for thunderstorm electrification by Latham and Mason (1961) but were rejected as inadequate to obtain

the necessary charge transfer. The enhanced temperature gradient mechanism of Caranti *et al*. (1991) has yet to be proven.

Contact potential charging.

Caranti and Illingworth (1983) showed that a rimed ice surface has a negative contact potential compared to the unrimed surface, irrespective of whether it is growing or subliming. Thus, a riming graupel pellet in collision with an ice crystal would receive a negative charge due to the contact potential, but a positive charge if part of the growing surface was lost in the contact. As both processes are likely to occur, the net charge will be determined by the surface condition of the graupel pellet. At low temperatures and growth rates contact potential dominates because there is little vapour to enhance the growth rate. At temperatures greater than the polarity reversal temperature, growth rates are sufficiently rapid for charge loss on fragments to dominate and graupel will become positively charged.

Charges on dislocations.

Keith and Saunders (1990) suggested that positively charged dislocations in the ice structure could be the source of charge transfer between ice crystals and graupel during collisions. For a typical dislocation number density, the charge held on an area of 55×55 mm^2 is $+5 \times 10^{-14}$ C. The density of dislocations increases with the vapour deposition rate, allowing negative charge to be transferred to the more rapidly growing graupel during collisions with ice crystals. Although charge values are of the right order of magnitude to explain the observed charging, the actual mechanism of charge transfer is not clear.

It is probable that some charge transfer occurs by all the different charging mechanisms, but the world-wide consistency of thunderstorm electrification suggests that one mechanism must dominate. If this is a particle interaction mechanism, then it may also operate in volcanic plumes sufficiently cool to produce ice. However, because lightning is observed close to the vent during many eruptions, it is clear that neither ice particle interactions nor convective processes are the only charge generating mechanisms active in volcanic plumes.

2.7 Geoelectric phenomena

The association of earthquakes with electrical effects has prompted research that could also be relevant to some aspects of plume electrification. Electromagnetic disturbances between radio and ultra-low frequencies have been shown to occur before or during large earthquakes (Warwick *et al*., 1982; Gokhberg *et al*., 1982; Varotsos and Alexopoulos, 1984a; Tate and Daily, 1989) and volcanic eruptions (Fujinawa *et al*., 1992; Fujinawa and Takahashi, 1990; Yoshino and Tomizawa, 1990). Disturbances have also been observed as luminous phenomena in the form of fireballs, fire-tongues, diffuse light and aurora-like stripes (Ouellet, 1990; Tsukuda, 1997), collectively known as earthquake lights (EQLs). In order to explain these phenomena, previous research has been carried out on a variety of charge generation mechanisms, many involving rock fracture.

2.7.1 Earthquake lights

Early reports of luminous phenomena directly preceding earthquakes were often anecdotal and largely ignored by the scientific community. However, more recently,

photographs and compilations of observations (Yasui, 1968, 1971; Derr, 1973; Huang and Hanzen, 1979) have verified that earthquake lights are a real feature of many large ruptures.

Some theories concerning the production of EQLs involve light emission directly from rocks. After experiments imparting mechanical damage to minerals, Schloessin (1985) proposed phosphorescence (light emission that persists after the excitation of a material), thermoluminescence (light emission due to a body's temperature) and chemiluminescence (light emission due to a non-heat producing chemical reaction), either from ground rocks or fine particles ejected into the air at faults, as possible mechanisms. Light emission would be stimulated by either ultra-violet exposure or water adsorption onto fresh mineral surfaces. Chemiluminesce of gases such as phosphine, released from underground and then reacting with oxygen, has also been suggested (Hedervari and Noszticzious, 1985). Brady and Rowell (1986) observed brief light emission during the compressional fracture of granite. By analysing the spectrum of the light, they concluded that it was produced from the atmosphere, probably as a result of being excited by exoelectrons emitted from the fresh surfaces. Direct light emission has been shown to occur from the fracture of quartz and has also been suggested as a possible EQLs source (Hadfield, 1996; Kawaguchi, 1995).

As an alternative to direct light emission, luminosity may represent an atmospheric response (a type of glow-discharge) to ground-based electrical disturbances. This would require a mechanism to generate large magnitudes of charge within the ground, and maintain them for a suitable length of time. Finkelstein and Powell (1970) proposed that piezoelectric effects in quartz could do this. However this would have required the crystals to be somehow aligned. Lockner *et al*. (1983) argued that the conductivity of the Earth's crust is generally too high to maintain

charges for any length of time. They proposed a solution that involved water, boiled during fault movement, creating an electrically insulating sheath around the conductive fault plane. They invoked ‘violent boiling’ (Blanchard, 1964) as a charge generation mechanism to produce enough charge for corona discharge on the surface. The greater degrees of charging produced by Leidenfrost boiling would allow even larger electric fields to be developed (Pounder, 1984) if this mechanism does operate. As an alternative mechanism for charge flow through crustal rocks, Freund *et al*. (1994b) suggested that mobile hole-type charge carriers could be released by seismic activity and rapidly diffuse to the surface. In experiments involving impacting igneous rocks, sufficient charge flow is generated to produce light from atmospheric discharge at the surface of the sample (Borucki and Fruend, 1998a, 1998b).

2.7.2 Electromagnetic emission

Unlike earthquake lights, electromagnetic anomalies at radio and lower frequencies are already being used as a (albeit highly controversial) predictive tool for earthquakes (Varotsos and Alexopoulos, 1984a, 1984b; Geller, 1996). Although it appears that anomalous emissions occur over a wide frequency range (Gokhberg *et al*., 1982), measurements are usually made at specific frequencies in order to avoid background noise, particularly from industrial sources. Fujinawa and Takahashi (1990) recorded anomalous underground vertical electrical signals in the 1 to 9 kHz range during the seismic swarm and undersea eruption off the coast of Ito, in 1989. At higher frequencies, anomalies recorded by 18 MHz radio receivers were associated with the great Chilean earthquake of 1960 by Warwick *et al*. (1982). The lead time for anomaly detection before seismic activity has varied from less than an hour (e.g. Gokhberg *et al*., 1982) to several days (e.g. Tate and Daily, 1989).

Electromagnetic emissions have also been detected as possible precursors to volcanic activity. Yoshino and Tomizawa (1990) recorded impulsive bursts at 82 kHz between 4 to 28 hours before eruptions of Mt. Mihara, 1986. Fujinawa *et al.* (1992) recorded the underground electric field and detected anomalies in the vertical component, dominantly in the ULF band (0.01 to 0.6 Hz) a few days before, and a month after, the 1990 eruptions of Mt. Mihara. Self potential variations have also been detected before eruptions (Dzurisin, 1980) as well as earthquakes (Corwin and Morrison, 1977).

Laboratory experiments on rocks have successfully reproduced electromagnetic phenomena from DC to high frequencies (Nitsan, 1977; Warwick *et al*., 1982; Ogawa *et al*., 1985; Khatiashvili and Perel'man, 1989; Yamada *et al*., 1989). Nitsan (1977) detected electromagnetic emission only from quartz-bearing rocks and suggested the piezoelectric effect as a source mechanism. However, others (e.g. Cress *et al*., 1987) have observed emissions from quartz-free rocks and proposed alternative mechanisms such as fractoelectric effects (Yamada *et al*., 1989; Warwick *et al*., 1982), movement of charged dislocations and point defects (Hadjicontis and Mavramatou, 1994), oscillation of double electric layers (Khatiashvili and Perel'man, 1989) and varying streaming potentials (Jouniaux and Pozzi, 1997). Most of these theories assume that high rates of micro-fracturing before the main shock are responsible for the generation of precursors.

2.8 Maximum particle charges

Whatever process is employed to charge particles, the maximum charge that can be maintained may be limited by factors which are independent of the charging

mechanism. The charge on liquid droplets can be limited by the repulsive electrostatic force of the surface charge. When the surface charge density reaches a value defined by the Rayleigh limit, σ_R, the repulsive forces are strong enough to overcome the surface tension, causing disruption of the droplet. For a droplet with diameter D of a liquid with surface tension γ in the atmosphere (permittivity ε), the Rayleigh limit is

$$\sigma_R = \left(\frac{8\varepsilon\gamma}{D}\right)^{\frac{1}{2}} \qquad (2.4).$$

For liquid or solid particles in the atmosphere, the maximum charge is also limited by the breakdown field strength of air, E_B. If the electric field exceeds this limit, breakdown of the air produces ions in a corona discharge, which neutralise the excess charge. The maximum uniform surface charge density, σ_m, that can be held on a flat plane is given by

$$\sigma_m = \varepsilon E_B \qquad (2.5)$$

thus, for $E_B \approx 3 \times 10^6$ V m^{-1}, $\sigma_m \approx 2.6 \times 10^{-5}$ C m^{-2}. When considering particles, it is usually easier to measure the specific charge (charge per unit mass, q_{sp}), than to calculate the surface area. Thus, the maximum specific charge for a sphere of radius r and density ρ can be given as

$$q_{sp\,max} = \frac{4\pi r^2 \sigma_m}{\frac{4}{3}\pi r^3 \rho} \qquad (2.6),$$

$$= \frac{3\sigma_m}{r\rho} \qquad (2.7).$$

For industrial applications, this gives a valuable guide to the amount of charge carried by particles, especially if a slightly reduced value of $\sigma_m = 1 \times 10^{-5}$ C m^{-2} is used (Blythe and Reddish, 1979). Note that on a solid surface, the atomic density is on the order of 2×10^{19} atoms m^{-2}, so charge densities of about 10^{-5} C m^{-2} are

equivalent to only a few charged atoms per million in a surface monolayer. Thus, surface impurities and heterogeneities can be expected to change significantly the charging properties of materials.

For particles of radii less than about 1 mm, the electric field is highly divergent, and the maximum field strength acts over a much reduced distance. This has the effect of increasing the maximum surface charge density possible before atmospheric breakdown occurs (analogous to the Paschen Law increase in breakdown strength of air for small gaps). To account for this apparent increasing breakdown strength, Harper (1967) developed a semi-empirical formula for particles from corona inception data for fine wires. Assuming spheres of diameter D (in metres), σ_m can be found (in coulombs per square metre) by

$$\sigma_m = 1.03 \times 10^{-5} D^{-0.3} \qquad (2.8).$$

However, Hamamoto *et al*. (1992) pointed out that this has yet to be experimentally demonstrated and, in fact, the data used by Harper (1967) for diameters less than 100 μm were actually proportional to $D^{-0.5}$, not $D^{-0.3}$. By evaporating charged liquid drops (with high surface tensions), Hamamoto *et al*. (1992) showed that surface charge densities of up to 10^{-3} C m^{-2} are possible. Their data for particles with diameters of 1 to 5 μm were also proportional to $D^{-0.5}$.

Liquid droplets do not have sharp corners or edges, so surface charge is distributed more or less evenly over the droplet. Conducting, angular, solid particles have lower maximum charge limits due to the concentration of charge in areas of high surface curvature. The high fields produced at these points cause premature discharge by local breakdown of the surrounding air. If the particles are insulating, then charge will not be able to flow to asperities, and the maximum charge limit will be determined by the original distribution of charge over the surface. In a vacuum, much

higher charge densities are possible because there is no surrounding dielectric to allow discharge by breakdown. Particle charge can continue to increase until field emission occurs.

2.9 Summary

Possible mechanisms for volcanic plume electrification have been reviewed, along with processes invoked to explain anomalous electrical effects created by earthquakes, and to account for thunderstorm charging. Because this thesis is concerned with charge generation during the fracture of pumice, it is interesting to note that fracto-electric effects are also invoked in some of the current theories for electrical earthquake precursors. Charging mechanisms for thunderstorms may influence any plumes containing ice but, because electrical effects are often seen in low altitude plumes, this cannot be the dominant process for charge generation. In the next chapter, research dedicated to plume electrification is reviewed, and the current ideas of charging mechanisms assessed.

3. Previous investigations of volcanic plume electrification

3.1 Introduction

Research into the electrical charging of volcanic plumes has been previously carried out through both field investigations and laboratory experiments. Attempts to measure the magnitude and polarity of charges within plumes have been complemented with experiments aimed at reproducing particle charging in the laboratory. Most of the early work was carried out in Japan, with the aim of discovering more about the nature of volcanic plumes. More recently, research has been aimed at the possibility of being able to detect and track plumes remotely by their electrical and electrostatic properties. As an introduction to the fieldwork described in Chapter 4 and the experiments described in Chapters 5 to 7, previous studies are reviewed here. Field investigations have employed remote techniques, such as lightning detection and measurement of electric potential gradients created by plumes, and have also recorded the charge on falling volcanic particles. Although only a few experiments have been carried out so far, some have been relatively successful at reproducing the charges detected in steam plumes. Condensing gases are similarly present in all explosively generated plumes, so these experiments are also reviewed here.

3.2 Electrical measurements of volcanic plumes

Electrical measurements of volcanic plumes have been obtained by three different techniques. The majority of research has been carried out by detecting the perturbations of the atmospheric electric potential gradient created by plumes, a

technique which has good potential as a remote sensing tool for plume monitoring. However, lack of understanding of the charging process and the lack of a large, consistent potential gradient data set currently prevent this technique from being used with confidence.

A more direct approach involves measuring the charge on ash (particles less than 2 mm in diameter) being deposited by a plume. Although accurate data on particle charges can be obtained by this technique, it cannot provide information about the charge held in non-sedimenting parts of the plume, which is very important when attempting to interpret potential gradient data. Charge magnitudes in plumes are often sufficiently large to produce lightning discharges and lightning studies have provided another avenue for research into plume electrification. The use of modern equipment allows stroke frequency, magnitude, polarity and location to be ascertained (Paskievitch *et al*., 1995) which can aid understanding of overall charge distributions. Results obtained by these three techniques are summarised in Table 3.1.

3.2.1 Perturbations of the atmospheric electric potential gradient

The electric potential difference between two points is defined as the work done per coulomb to move a small positive test charge from one point to the other (Duffin, 1990). Electric potential V, thus represents a scalar field in which moving a positive test charge to a higher potential requires the input of work. The spatial rate of change of potential (potential gradient) then denotes a vector quantity, the magnitude of which is the force per coulomb acting on the test charge, but which acts in the opposite direction to that force. The force per unit charge on a small positive test charge is also the definition of electric field strength $\boldsymbol{E}$, thus it can be seen that

Table 3.1 Summary of previous measurements of plume electrification.

Reference	Volcano	Electrical and electrostatic measurements of plume
Hatakeyama, 1943	Asama-yama	**Charge:** Plume modelled using a charge of -1.4 C.
Hatakeyama, 1949	Yake-yama	**Potential gradient:** Data from single potential gradient monitoring station as the particulate plume moved overhead. Maximum: -1.2 $kV\,m^{-1}$. **Charge:**. Modelled as a row of single charges, at 4 km height, total charge -0.55 C.
Ishikawa *et al*., 1951	Azuma	**Plume:** Particle-bearing or steam? **Charge:** Modelled as a net positive charge, with a maximum charge density of 5 $esu\,m^{-3}$ ($+2 \times 10^{-7}\,C\,m^{-3}$) and total of 0.006 C. Distributed as a cylinder, 10 km long, surrounded by a thin, negative, induced layer of -0.5 $esu\,m^{-3}$ ($-2 \times 10^{-8}\,C\,m^{-3}$).
Hatakeyama and Uchikawa, 1952	Aso	**Potential gradient:** Observed positive (maximum of 88 $kV\,m^{-1}$) and negative (maximum of -4.3 $kV\,m^{-1}$) potential gradients. Negative gradients only observed when the plume front was directly overhead. Positive gradients recorded during ashfall. **Charge:** Modelled by +11.7 $esu\,m^{-3}$ ($+5 \times 10^{-7}\,C\,m^{-3}$) and -0.46 $esu\,m^{-3}$ ($-2 \times 10^{-8}\,C\,m^{-3}$). Laboratory experiments showed that during collisions, large ash particles charged positively, and small ash particles charged negatively.
Hatakeyama, 1958	Yake-yama	**Potential gradient:** 2.5 $kV\,m^{-1}$. **Charge:** Net specific charge on ash of $-4 \times 10^{-7}\,C\,kg^{-1}$.

Table 3.1 continued..

Reference	Volcano	Electrical and electrostatic measurements of plume
Anderson *et al*., 1965	Surtsey	**Charge:** Phreatomagmatic activity. Ash bearing plume charged to $+2 \times 10^4$ e cc^{-1} ($+3.2 \times 10^{-9}$ C m^{-3}). Plume modelled with 2 lines of charge: +1 C km^{-1} at 2500 m high, -0.7 C at 1500 m high with the positive charge having a wider widthways distribution. Steam cloud from lava/sea contact charged to ~$+10^4$ e cc^{-1}, calculated to be ~$+10^6$ e cc^{-1} at source. **Lightning:** Positive lightning neutralised +0.1 to +0.5 C per strike, strike rate indicated an average cloud charging current of ~30 mA. **Potential gradient:** Maximum potential gradient 60× fair weather value (fwv). Usually returned to fwv by lightning after increasing to about 30× fwv.
Brook *et al*., 1974	Heimaey	**Potential gradient:** Greater than +7 kV m^{-1} measured due to steam clouds. **Lightning:** Positive cloud-to-ground lightning recorded in plume 7 km high.
Cobb, 1980	Mt. St. Helens	**Potential gradient:** +20 kV m^{-1} measured due to plume 18 km high. **Lightning:** Positive and negative cloud-to-ground strikes, mainly to mountain top, at up to 11 per minute.
Kikuchi and Endoh, 1982	Mt. Usu	**Potential gradient:** Rapidly varying potential gradients with maxima of both polarities exceeding ±15 kV m^{-1} during ashfall from one eruption. Potential gradients also reported for blowing volcanic ash. **Lightning:** Photographs of cloud-to-ground and intra-cloud lightning.
Gilbert *et al*., 1991	Sakurajima	**Charge:** Measured the specific charge of falling positive and negative ash particles, and the net specific charge on falling ash as a whole. (ash particles with positive charge) $+3 \times 10^{-4}$ to $+6 \times 10^{-4}$ C kg^{-1} (ash particles with negative charge) -2×10^{-4} to -5×10^{-4} C kg^{-1} (net ash specific charge) $+2 \times 10^{-5}$ to $+5 \times 10^{-5}$ C kg^{-1}
Lane and Gilbert, 1992	Sakurajima	**Potential gradient:** Positive (up to +2.5 kV m^{-1}) and negative (~-3 kV m^{-1} during ashfall) potential gradients recorded. **Charge:** Modelled as a $+10 \times 10^{10}$ e m^{-3} net charge in gas cloud, separated from particulate cloud by 10 m. Assumed that the net charges on the gas and particulate clouds were equal and opposite.

Table 3.1 continued..

Reference	Volcano	Electrical and electrostatic measurements of plume
Hoblitt, 1994	Redoubt	**Lightning:** Only cloud-to-ground flashes could be detected. After an eruption, earlier flashes were negative, later flashes positive. Flashes followed seismicity by up to 15 minutes and were located away from the volcano, suggesting that they were from coignimbrite plumes. Discharges often occurred to the local highest ground. Eyewitness accounts suggested that intra-cloud lightning was more common than cloud-to-ground strikes.
Lane *et al*., 1995	Sakurajima	**Potential gradient:** Measured simultaneously at 4 locations. Positive perturbations recorded during the fall of acid liquid drops and plume approach. Negative perturbations recorded during ashfall, and only very small perturbations recorded during and after ash-free explosion. **Charge:** A vertical dipole of 10 C (positive charge above negative) used to model potential gradient data during plume ascent. A horizontal 10 C dipole (positive charge leading negative) models potential gradient data recorded as the plume was dispersed overhead.
Miura *et al*., 1995	Sakurajima	**Potential gradient:** Mainly positive perturbations recorded during explosions, up to +1.5 $kV\,m^{-1}$. **Charge:** Specific net charge on falling ash $+2.0 \times 10^{-5}\,C\,kg^{-1}$. Particles also separated by polarity in an electric field demonstrate distributions suggesting net positive charge for one eruption and net negative charge for another. Recorded potential gradients for one eruption were modelled by several point charges of total charge +0.64 C.
Paskievitch *et al*., 1995	Mount Spurr	**Lightning:** 171 lightning strokes detected and located by AVO lightning detection system. All strokes were positive, and their horizontal locations formed a ring-like pattern, 10 km in diameter, displaced from the vent by about 5 km. Lightning was not detected during two other eruptions, despite been visually observed during one of them.
Miura *et al*., 1996	Unzen	**Potential gradient:** Measured simultaneously at 2 locations during the dispersal of two coignimbrite plumes. Mainly negative perturbations of up to -150 $V\,m^{-1}$. **Charge:** Potential gradient data modelled with dipoles of magnitudes 0.45 C and 0.2 C, with positive charge above and ahead of negative charge.
James *et al*., 1998	Sakurajima	**Potential gradient:** Measured simultaneously at 4 locations during Vulcanian explosion and periods of continuous ash and gas emission. See Chapter 4 for details.

$$\boldsymbol{E} = -\text{ grad } V \qquad (3.1).$$

Fortuitously, the surface of the Earth acts as a conductor for electrostatic measurements, thus all electric field lines are perpendicular to it at ground level. In areas of low topographic gradient, this allows the magnitude and sign of the surface potential gradient to be measured by recording only its vertical component (as all other components are zero). Using the convention that height is measured positively upwards (Chalmers, 1967), then positive charge in the atmosphere produces a positive potential gradient at the ground.

All early work on atmospheric electricity was dedicated to the extreme electrical effects produced by thunderstorms. It was only during the 1750's that a small atmospheric electric field was finally detected during periods of undisturbed weather, and this became known as the fair-weather field. The action of thunderstorms is believed to maintain this field (Chalmers, 1967), although details of the exact mechanism are still not fully understood (Bering, 1995). The atmosphere is electrically bounded by the conducting surface of the Earth below, and a conducting electrosphere above. Thunderstorms provide an electrical generator between these two conducting areas, lowering negative charge to Earth and effectively injecting positive charge high up into the atmosphere. It is this separation of charge, with a positive charge maintained at high altitude, that produces the fair-weather field. As an average value on the surface of the Earth, it is represents a potential gradient of about +100 V m^{-1} (Duffin, 1990).

Local charge in the atmosphere (such as from a thunderstorm or a volcanic plume) produces perturbations of this fair-weather field which can be detected. Excess positive charge enhances the fair-weather field, and so is measured as a positive perturbation of the potential gradient. If excess negative charge is present in the lower

atmosphere, the negative perturbation produced can easily reverse the direction of the fair-weather potential gradient measured at the ground. Measuring the potential gradient at different sites simultaneously can allow detection of the excess charge magnitude, polarity and location (Vereshagin *et al*., 1989).

Early work using the potential gradient technique to detect volcanic plumes was dominated by Japanese meteorologists such as H. Hatakeyama (Hatakeyama, 1943; 1949). Most experiments collected potential gradient data from single locations as a function of time as particle laden plumes passed nearby or overhead. Data from Asama volcano (Hatakeyama, 1943), Sakurajima (Nagata *et al*., 1946) and Yake-yama (Hatakeyama, 1949) all demonstrated negative perturbations from the eruption plumes. However, during 1950, Hatakeyama and Uchikawa (1952) recorded mainly positive perturbations from eruptions of the volcano Aso, with only one negative disturbance. This negative perturbation was detected when the tip of one plume was directly over the measurement station. The potential gradient then rapidly returned to a positive perturbation as ashfall commenced. Hatakeyama and Uchikawa (1952) explained these data by assuming that the larger particles in the lower portions of the plume held a positive charge, and smaller ones in the upper portions held a negative charge. They calculated that the space charge densities responsible for the perturbations were about ± 0.5 esu m^{-3} ($\pm 2 \times 10^{-10}$ C m^{-3}). As a result of a more vigorous eruption, they recorded potential gradients of more than +88 kV m^{-1} during heavy ashfall only 400 m from the centre of the crater. The calculated space charge density for this eruption was more than +11 esu m^{-3} ($+5 \times 10^{-9}$ C m^{-3}).

Kikuchi and Endoh (1982) recorded perturbations of the potential gradient of up to thirty times the background level during an eruption of Mt. Usu. The plume deposited

a thickness of 6 cm of ash at the recording site (5 km from the vent), during which time the polarity of the potential gradient had varied continuously and rapidly. The falling ash current was also recorded and was observed to maintain an opposite polarity relationship with the potential gradient data (deposition of negatively charged ash produces negative potential gradients, but represents an upwards, thus positive, electric current). This correlation suggested that the sudden polarity changes were not an effect of lightning discharges (which were observed close to the vent), but did represent changes in the polarity of the falling ash. They also noted changes in the particle size distribution and the degree of particle aggregation, but no clear relationships were apparent with the measured polarity of the ash.

Rapid changes in atmospheric potential gradients due to lightning were recorded by Hobbs and Lyons (1983) during the eruption of Mount St. Helens, 1980 (see section 3.2.3). These authors measured the vertical component of the potential gradient from an aircraft which flew both inside and outside of the plume, at distances of 9 to 260 km downwind of the volcano, and at altitudes of about 2.9 to 3.4 km. Within 60 km of the mountain, the potential gradient was generally negative, with a maximum of -3.5 kV m^{-1}. Further from the mountain, the potential gradient was generally positive and up to about 10 kV m^{-1}. The best match to these data was provided by assuming that fallout of negative charge dominated near the mountain and, further away, positive charge dominated. Hobbs and Lyons (1983) ascribed this to negatively charged ‘heavy’ ash particles, and positively charged ‘lighter’ ash particles.

Thus, several workers have recorded both positive and negative perturbations due to volcanic plumes, and have ascribed these polarity variations to different particle sizes. However, Lane and Gilbert (1992) could find no physical explanation for

polarity changes as a function of particle size. They proposed a fracto-emission mechanism as the charge generation process in plumes, which gives ash a net negative charge during fragmentation as ions with a net positive charge are released to the environment. Due to the settling velocity of particles, the upper portions of plumes become dominated by the gas and thus have a net positive charge. The particle-rich lower regions then contain an equal magnitude of net negative charge. This separation of plumes into particle-rich and particle-poor regions has also been observed experimentally (Holasek *et al*., 1996).

Lane and Gilbert (1992) reported potential gradient perturbations created by eruptions from Sakurajima volcano, Japan, which they detected with a rotating-chopper field mill. They recorded both positive and negative perturbations representing ground-level gradients of up to ± 3 kV m^{-1} from dark particle-laden plumes, but no perturbations from explosions generating white plumes of condensing gases. Lane and Gilbert interpreted their results from one particle-rich eruption column as being produced by a dipole (a positive charge above a negative charge) rising above the volcano before being dispersed downwind. Assuming a 10 m separation between the charges (calculated from a fall velocity of 0.35 m s^{-1} over about 30 s), a charge density of $+10^{10}$ e m^{-3} ($+1.6 \times 10^{-9}$ C m^{-3}) was calculated for the gas-rich portion of the plume. The fracto-emission hypothesis was also supported by positive potential gradients recorded during the fall of liquid acid droplets. The droplets had formed from condensing volcanic gases and were produced after a period of light ashfall (Lane and Gilbert, 1992).

Perturbations of the atmospheric potential gradient produced by plumes have been measured simultaneously at four sites by Lane *et al*. (1995) and James *et al*. (1998). Both of these sets of experiments were carried out at Sakurajima volcano. The James

et al. (1998) work is presented as part of this thesis in Chapter 4. The plume detected by Lane *et al*. (1995) was produced by a Vulcanian explosion and created both positive and negative perturbations of the atmospheric potential gradient. The initial vertical ascent of the plume could be modelled using a dipole with a 10 C positive charge above a -10 C negative charge. Positive perturbations were recorded as the plume approached the downwind measurement site, but these changed to negative perturbations as ashfall commenced. Lane *et al*. (1995) interpreted this as wind shear accelerating the upper, positively charged portions of the plume ahead of the negatively charged, particle-rich, lower portions.

Evidence for net positively charged silicate particles from Sakurajima was obtained by Miura *et al*. (1995) who recorded positive potential gradient perturbations of up to +1.5 kV m^{-1} as a white-grey ash plume passed directly over their measuring site. They calculated a total charge of +0.64 C, and provided further evidence (by measuring the charge on falling ash) that the net ash polarity of Sakurajima is not always the same.

The eruption of Surtsey in 1963 allowed the electrification of phreatomagmatic plumes to be studied. Anderson *et al*. (1965) recorded potential gradients and point discharge currents as well as taking time-lapse photographs during periods of intense electrical activity over the volcano. Black, particle laden plumes and white steam plumes were observed, producing both positive and negative perturbations of up to 60 times the fair-weather potential gradient. During one period, potential gradient data were obtained from a boat as it passed under the eruption plume 2 km, then 3 km, downwind from the vent. Both traverses showed positive perturbations either side of the plume but negative perturbations directly beneath it, during periods of slight

ashfall. They modelled this as two horizontal lines of charge, one containing +1 C km^{-1}, above the other containing -0.7 C km^{-1}. However, close to the crater, plumes showed no detectable dipole structure and contained, on average, positive charge densities with magnitudes of 10^5 to 10^6 e cc^{-1} ($+1.6 \times 10^{-8}$ to $+16 \times 10^{-8}$ C m^{-3}). Similar charge densities were deduced for white, predominantly steam plumes, produced from lava flows entering the sea. Brook *et al*. (1974) also studied the electrification of condensing plumes generated at lava–sea interfaces. Working at Heimaey in 1973, they detected positively charged plumes producing surface atmospheric potential gradients in excess of +7 kV m^{-1}.

There is only one published account of potential gradient measurements being made of plumes created from pyroclastic flows. This is by Miura *et al*. (1996) who recorded small positive and negative potential gradients from two such plumes produced at Unzen in 1993. They modelled the perturbations using charges of ±0.45 C and ±0.2 C. In a similar manner to the perturbations recorded at Sakurajima, small positive perturbations preceded larger negative ones and were modelled best by a higher, positive charge moving faster than a lower, negative charge.

3.2.2 Charge measurements on falling ash

In 1941, using apparatus designed to measure the electric charge on rainfall, Hatakeyama (1958) measured the net charge on falling ash from Asama volcano, Japan. An average specific charge of -1.2 esu g^{-1} (-4×10^{-7} C kg^{-1}) was recorded for ash falling at a location 50 km from the vent, and a total of -6.4 C was estimated for the total ashfall. At distances less than 10 km from the vent, Gilbert *et al*. (1991) and Miura *et al*. (1995) have carried out similar experiments with an electrometer-

monitored Faraday cup on ash falling from eruptions of Sakurajima volcano. During May 1990, Gilbert *et al*. (1991) collected ash with an average net charge of $+2 \times 10^{-5}$ to $+5 \times 10^{-5}$ C kg^{-1} and, during August 1991, Miura *et al*. (1995) collected ash with a net charge of $+2.0 \times 10^{-5}$ C kg^{-1}. Note that the net positive charges conflict with the majority of the potential gradient data obtained at Sakurajima (Lane and Gilbert, 1992; Lane *et al*., 1995; James *et al*., 1998), which demonstrate a net negative charge on the ash. However, the potential gradient data of Miura *et al*. (1995) did offer evidence that ash fall at Sakurajima is not always of the same net polarity.

Gilbert *et al*. (1991) also used a horizontal electric field to separate falling particles by their charge polarity and thus made measurements of absolute particle charges. Values for the specific charge of positive particles collected at 2.5 to 5 km from the vent were between $+3 \times 10^{-4}$ to $+6 \times 10^{-4}$ C kg^{-1} and, for negative particles, -2×10^{-4} to -5×10^{-4} C kg^{-1}. Gilbert *et al*. (1991) calculated the approximate surface charge density of the particles, obtaining results of order 10^{-5} C m^{-2} (assuming spherical particles 25 μm in diameter). Although this is about an order of magnitude smaller than the theoretical maxima for particles of that size (see Chapter 2), it is very similar to the value quoted by Blythe and Reddish (1979) as a realistic maximum surface charge density carried by a stream of insulating particles. Gilbert *et al*. (1991) thus suggested that the particles were close to their charge limit, so that they were nearly 'saturated' in charge. Using this result for a Sakurajima plume containing net charge densities of 10^{-9} C m^{-3}, Lane and Gilbert (1992) calculated that this excess charge was held on a mass loading of 10^{-6} kg m^{-3}. Comparing the calculated net specific charge with previously measured values (Gilbert *et al*., 1991), they suggested that only 0.1 % of the total ash was responsible for the charge excess. Thus, the mass

loading of the Sakurajima plume may have been of order 10^{-3} kg m^{-3} (Lane and Gilbert, 1992), an estimate similar to the 8.5×10^{-3} kg m^{-3} calculated by Harris *et al.* (1981) for the initial eruption cloud of Mount St. Helens, 18 May, 1980.

Separation of particles in a horizontal electric field was undertaken by Miura *et al.* (1995), who studied the particle distribution on a base plate rather than measuring charge magnitudes. During two eruptions on 12 February, 1993, they observed that the maximum particle number density of the collected ash was perturbed in the direction of positively charged particles for one eruption, and negatively charged particles for the other. Although they calculated net specific charges of order $\pm 10^{-5}$ C kg^{-1} from the data, the number of assumptions needed to convert particle distributions into net specific charges limits the accuracy of these results. However, the experiment did demonstrate the variable nature of particle charge distributions in ashfall, even from the same volcano.

The polarity variations observed by Kikuchi and Endoh (1982) in their ashfall current data were recorded during ashfall from a single eruption of Mt. Usu. Electric currents to Earth due to the charge on the ash were recorded with magnitudes of up to 4×10^{-4} esu s^{-1} cm^{-2} (1.3×10^{-9} C m^{-2} s^{-1}). Unfortunately, because mass data were not published for the collected ash, the net specific charge cannot be calculated. Thus, in agreement with some of the atmospheric potential gradient data, charge measurements on falling ash have shown variations in the net polarity. Ash being deposited less than 5 km from a volcano has been shown to have net specific charges of order $\pm 10^{-5}$ C kg^{-1}, produced as a result of a small imbalance in the individual charges on ash particles, of order $\pm 10^{-4}$ C kg^{-1}.

3.2.3 Lightning in volcanic plumes

Lightning produced by volcanic eruptions has not received the same degree of scientific attention that has been lavished on thunderstorm lightning. Although historical accounts of eruptions often include vivid descriptions of lightning displays (see Table 2.1), very few data have actually been recorded in order to discover more about these discharges. The effect of volcanic lightning on the atmospheric potential can be seen in the data of Anderson *et al*. (1965) from Surtsey, and Brook *et al*. (1974) from Heimaey.

At Surtsey, lightning events in phreatomagmatic plumes were observed to produce sawtooth-like decreases in the measured electrical potential gradient. A very rapid decrease in potential gradient would accompany the lightning, and would be followed by a gradual recovery before the next discharge. These abrupt transients were recorded in both directions, indicating neutralisation of both positive and negative excess charge. Frequent lightning was observed to follow the phreatomagmatic eruption of 'black clouds' by 10 to 60 seconds. Many of these discharges occurred between the cloud and the ground, with most (but not all) of these striking close to the crater. Frame-by-frame analysis of motion picture film showed that most of the intra-cloud lightning was located in the upwind side of the plume. For many of the discharges observed, Anderson *et al*. (1965) estimated that between 0.1 to 0.5 C of charge was neutralised, up to a height of 200 to 300 m into the plume. With discharges occurring between 10 to 40 s, they inferred plume charging currents of about 30 mA.

At Heimaey, Brook *et al*. (1974) observed lightning in plumes created as lava flowed into the sea. Using an electric field-change meter, Brook *et al*. (1974) were able to study the rapid variations in potential gradient due to the lightning. These results showed that the lightning was created by a slowly rising positive charge (in the

plume) being rapidly neutralised by negative charge that originated at the base of the column and travelled upwards. Charge neutralisation appeared to occur only in the lowest 100 m of the column. Their data showed no structure in the rapid unidirectional gradient changes suggesting that, in effect, positive charge was lowered to ground in a single stroke. The field-change meter had a temporal resolution of 10 ms, so it is possible that undetected stroke leaders did occur. However, none of the 8 observed changes could be interpreted as the multiple strokes that typify thunderstorm lightning strikes.

The 1980 eruption of Mount St. Helens provided extensive electrical displays (Rosenbaum and Waitt, 1981). Close to the vent, extensive plume-ground lightning was observed, mainly to the mountain top, at rates of up to 11 strikes a minute (Cobb, 1980). Further away, the aircraft-mounted potential gradient meter recorded frequent spikes (Hobbs and Lyons, 1983), interpreted as produced by lightning discharges. The frequency of spikes decreased away from the volcano, from a maximum of more than one every five seconds inside the plume at 9 km from the vent. The spike magnitudes similarly decreased from 5 to 6 kV m^{-1} to less than 1 kV m^{-1} at distances greater than 100 km. At distances of less than 50 km from the mountain, spikes were predominantly positive (equivalent to lowering negative charge to the ground), changing to predominantly negative (equivalent to lowering positive charge to the ground) at distances greater than 50 km. Closer than 40 km, the potential gradient recovered to pre-spike values within 10 to 30 s after each spike, but further away, this occurred in less than 5 s. This change appeared to coincide with a significant decrease in the spike frequency, and occurred at a distance from the volcano similar to that at which the largest vertical electric fields changed direction (section 3.2.1).

The spike data tend to support the hypothesis suggested by the general sign of the atmospheric potential gradient data. Close to the volcano, coarse, negatively charged ash was falling out, and 'negative' lightning was apparently recorded due to the proximity of the negative charge to Earth. Further away, the plume consisted of smaller particles which were positively charged and weak 'positive' lightning was detected.

In 1990, the Alaska Volcano Observatory deployed a lightning detection system (LDS) during the eruption of Redoubt Volcano (Hoblitt, 1994). This initial deployment was of a commercially-available system owned by the Bureau of Land Management's Alaska Fire Service, which was normally used to help detect lightning-induced forest-fires. As such, it was tuned to detect radio emissions from thunderstorm-generated ground strikes. In the subsequent eruptions, the LDS detected lightning in 11 of 13 eruptions, and provided locations in 9 of them. This success demonstrated that some volcanic lightning gives a similar radio signature to 'normal' lightning. The LDS also showed that, for each eruption, lightning polarity usually started as 'negative', but often then turned 'positive'. Hoblitt (1994) interpreted this in the same manner as the Mt. St. Helens data, with coarse, negatively charged particles falling out first, leaving the finer positively charged particles to produce the delayed 'positive' lightning. The first detected strikes always lagged behind the onset of seismicity by 5 to 15 minutes and were located away from the volcano's summit (often in an area of rugged highlands 15 km to the northeast of the summit). This was interpreted as evidence that the plumes were spawned from pyroclastic flows which had followed topographic lows away from the summit of Redoubt. Naturally, strike locations were also controlled by wind dispersion of the plumes, and temporal variations of azimuth data from the closest detector were often shown to be consistent

with wind-induced plume motion (Hoblitt, 1994). For night-time eruptions and events occurring during periods of bad weather, the association of seismicity and lightning proved to be a valuable tool for the detection of ash cloud production.

After using this temporary system, the AVO installed a permanent LDS which allowed the detection of intra-cloud lightning as well as cloud-to-ground strikes. Data recorded by this system during the eruptions of Crater Peak, Mount Spurr, have been reported by Paskievitch *et al*. (1995). The August 18, 1992, eruption produced 171 locatable lightning strokes, all of positive polarity. Their horizontal spatial distribution defined a rough circle, 10 km in diameter and displaced to the east of Crater Peak by about 5 km (in agreement with plume dispersion by the westerly winds). 70 % of the strokes were classified as intra-cloud. However, because the classification model was based on thunderstorm lightning, this may be a minimum figure. The ground strikes had amplitudes between 15 to 40 kA, which lie in the range of amplitudes from local thunderstorms. Despite these successful locations, lightning observed in another Spurr eruption during September was not detected. Paskievitch *et al*. (1995) suggested that 'subtle factors' in the eruptions, or atmospheric and meteorological conditions may have prevented lightning detection during this event.

3.3 Experiments on charging

The positive charge detected in steam plumes created at lava-seawater interfaces on Surtsey (Anderson *et al*., 1965) prompted several attempts to reproduce this effect in the laboratory. Experiments produced electrified steam clouds by boiling droplets of seawater on hot samples, but did not attempt to reproduce any phreatomagmatic explosions. Similarly, the potential gradient measurements made of particle laden

volcanic plumes in Japan lead to experiments attempting to reproduce charging of particulate plumes. Experiments emphasised differences in charge magnitude and polarity as a function of grain size. However, by design, the experiments were limited to charging effects due to frictional contacts as particles moved over one another. More recently, experiments on electrification due to phreatomagmatic explosions have been carried out by Büttner *et al*. (1997).

3.3.1 Water-lava interactions

Much of this work was initially driven by interest in the nature of atmospheric electrification and the rate of atmospheric nuclei production (Woodcock and Spencer, 1961). Experiments were carried out by letting water drop onto insulated heated samples. Charge separation was then detected by either measuring the charge flow to Earth from the sample, or by detecting the charge of the condensing cloud produced by the droplet. Using apparatus of this type, Blanchard (1964) obtained positive charges of +125 esu g^{-1} ($+4.2 \times 10^{-5}$ C kg^{-1}) from boiling droplets of seawater falling on a hot metal block. After replacing the metal block with a sample of molten 'pahoehoe-type lava' he estimated that charge separation increased by about an order of magnitude and suggested that mechanical pulverisation of the drops during their violent boiling was important for charge generation. Thus, charging could be due to shearing of the double electric layer at the water surface during the rapid increase in surface area.

Björnsson *et al*. (1967) carried out similar experiments specifically to explain the data from Surtsey (Anderson *et al*., 1965). Lava samples from Mauna Loa and Kilauea were heated until they had a molten layer a few millimetres in depth. Seawater droplets falling on this surface produced charges of order $+10^{-8}$ C cm^{-3} ($+10^{-5}$ C kg^{-1}).

Charge separation was also shown to decrease slightly with increasing size of the drops. When rough lava was heated so that only the protuberances melted, charge separation was increased by about an order of magnitude. For a droplet of volume 3×10^{-2} cm^3 a cloud of about 2000 cm^3 was produced, with a charge of $+2 \times 10^{-9}$ C. This represents a space charge density of 10^{-6} C m^{-3}, which was in the range calculated for the source regions of the Surtsey steam plumes (Anderson *et al*., 1965). Björnsson *et al*. (1967) considered salt particles as the charge carriers, and a solid-solid process between these particles and the sample as a possible charge generation mechanism. They supported this with experiments on rock surfaces contaminated by organic materials (possibly only monolayers thick). The results confirmed data obtained earlier by Blanchard (1964), that even the smallest degree of contamination could reverse the charging polarity. Because surface contamination of the hot block altered the results so much they suggested that charging was controlled by a solid surface process.

Charge magnitudes were confirmed by Pounder (1972) who re-emphasised that the physical disruption of drops was important and showed that solution concentration was also a factor. He reported positive charges of +40 to +220 esu ml^{-1} ($+1 \times 10^{-5}$ to $+7 \times 10^{-5}$ C kg^{-1}) for saline solutions of up to 30 % NaCl on brass and molten lead samples. Further quantitative results were given by Sheldon (1974) who varied solution concentrations, drop volumes and surface temperatures. On steel at about 660 K, he also recorded maximum charges of order of $+10^{-5}$ C kg^{-1}. Pounder (1978, 1980a) extended his work into an investigation of charge generation during Leidenfrost boiling. This contact boiling phenomenon involves a liquid drop supported above a hot surface by a vapour layer. Periodically, the vapour layer collapses due to

crystallisation at the base of the droplet. The surfaces contact, and charged particles are emitted during decrepitation of the crystal layer. Liquid vapourisation rapidly forms another insulating vapour layer, and the process starts again. Charge generation could be from solid-solid charging (by contact, frictional or fracture effects) or shear of the double layer in the liquid. Pounder showed that the average specific charge of particles produced by Leidenfrost boiling was $+2 \times 10^{-3}$ C kg^{-1}.

Shear of the electrical double layer at a water-magma interface has also been inferred as the charge generation mechanism during experimental molten fuel coolant interaction (MFCI) explosions by Büttner *et al*. (1997). These authors studied the electrification of the ejecta produced when a crucible of melted olivine melilitite was injected with purified water. The resulting explosion created an expanding particle cloud which travelled towards a sensor mesh. The electric potential of the mesh was then recorded as the particle cloud approached. From MFCI explosions, potentials of up to +335 V were recorded, in contrast to potentials of less than +5 V generated when the melt was disrupted by pressurised inert gas.

3.3.2 Ash charging

In order to explain their potential gradient data, Hatakeyama and Uchikawa (1952) carried out electrification experiments using particles collected from Aso and Asama volcanoes. Some of the particles were adhered to a earthed tin plate and more particles were then placed on top. As the inclination of the plate was increased, the loose particles moved over the fixed ones, and fell onto a copper dish monitored by an electrometer. The particles collected from Aso were classed as either ‘larger’, with an average diameter of 0.3 mm, or ‘smaller’ with an average diameter of 0.04 mm. With larger particles adhered to the plate, the smaller particles were collected in the dish.

Without exception, a negative charge with an average of -0.108 esu g^{-1} (-3.6 × 10^{-6} C kg^{-1}) was measured on the smaller particles. When the larger particles were run over the smaller particles, the charge collected was usually positive with an average of +0.004 esu g^{-1} (+1.3 × 10^{-9} C kg^{-1}). To explain their potential gradient measurements, Hatakeyama and Uchikawa (1952) had assumed that lower portions of the plumes held a net positive charge and the upper portions a net negative charge. They used the experimental results to support this hypothesis, assuming that similar grain-to-grain contacts occurred within the plume and that the lower portions of the plume were dominated by the larger particles.

The experiments were repeated using particles collected from Asama volcano. Larger particles from Asama had an average diameter of 1.3 mm, and smaller particles 0.03 mm. The Asama sample also had a very fine ash fraction of mean diameter 1.6 μm. No data for the smaller particles and the fine ash were given, but the larger particles were found to hold a net negative charge of -0.027 esu g^{-1} (-8.9 × 10^{-9} C kg^{-1}) after the experiment. The authors offered no hypothesis to explain the opposite polarity held on the larger grains of the Aso and Asama samples.

Similar frictional experiments were carried out by Kikuchi and Endoh (1982) using volcanic particles collected during an eruption of Mt. Usu, Japan, in August, 1977. Particles were poured onto the upper end of an inclined aluminium trough and allowed to slide down until they fell into a Faraday cup located underneath the lower end of the trough. Experiments were carried out using different size fractions of the particles, ranging from 10 to 1000 μm, all of which became negatively charged. Smaller particles were found to receive -50 esu g^{-1} (-1.7 × 10^{-5} C kg^{-1}), and larger particles -2 esu g^{-1} (-6.6 × 10^{-7} C kg^{-1}). In further experiments, during which the trough

was lined with particles adhered to it by water, the small particles tended to obtain a negative charge, but larger particles a positive charge.

Unlike Hatakeyama and Uchikawa (1952), Kikuchi & Endoh (1982) did not use their experimental results to explain potential gradient measurements made on volcanic plumes. They noted that, because lightning and thunder were witnessed near the crater only during active eruptions, the main charge generation mechanism probably occurred only during the eruption itself. They did not consider their experiments to represent conditions during eruption, thus they used their results to explain only the negative atmospheric potential gradients from wind-blown ash, and not the charges present in volcanic plumes.

3.4 Summary

Detection of perturbations of the atmospheric potential gradient due to volcanic plumes have confirmed that they are highly electrically charged. Data showing perturbations of both polarities demonstrate that areas of net positive and net negative charge usually exist within plumes. This has been supported by detection of both ‘positive’ and ‘negative’ lightning during eruptions. The development of areas of net charge in plumes has been ascribed to gravitational separation of particles of different size, or to volcanic gases being charged equally and oppositely to the ash by fracto-emitted ions. Although no explanation for a size effect can be given, experiments on charging ash by frictional effects have reproduced polarity changes by using different particle sizes.

Measurements of the charge on falling ash have shown that very high charge densities exist on individual particles. Because ashfall consists of particles of both

polarities, the net ash charge is produced by only a small imbalance in the particle charges. Variation of the net ash charge polarity has been shown between different volcanoes, between different eruptions from the same volcano, and even during ashfall from a single eruption.

Both lightning detection and atmospheric potential gradient measurements have advantages as techniques for monitoring volcanic plumes. Although a lightning detection system is employed at Alaska Volcano Observatory, no observatory currently uses the potential gradient method. Chapter 4 describes fieldwork undertaken in an attempt to extend the understanding of perturbations of the atmospheric electric field from volcanic plumes, and to investigate further the potential of this technique as a monitoring tool.

4. Atmospheric electric potential gradients at Sakurajima volcano

4.1 Introduction

This chapter describes fieldwork undertaken in an attempt to record the effect of particle-laden volcanic plumes on the natural atmospheric electric potential gradient. One of the main aims was to record data from multiple eruptions in order to assess any variations and to test the reliability of the system as a monitoring tool.

The work was carried out at Sakurajima volcano, in south Kyushu, Japan, during October and November, 1996, and the results have been summarised in James *et al*. (1998). Sakurajima has many advantages for this type of study and has been the site of previous research into potential gradients (Lane & Gilbert, 1992; Lane *et al*., 1995; Miura *et al*., 1995). Unfortunately, despite the recent very active eruptive history of Sakurajima, the volcano was relatively quiet during the field season and a complete data set was recorded for only one explosion during this period.

This chapter introduces Sakurajima volcano, and describes the apparatus and monitoring array used. Graphs are provided for all data recorded by the array. Selected results are then analysed after the 'background' data have been discussed.

4.2 Sakurajima volcano

Sakurajima is an andesitic stratovolcano which forms a 'half-island' in Kagoshima Bay, southern Kyushu (Figure 4.1a). It lies on the southern rim of the Quaternary Aira caldera which bounds the north end of the Bay and is about 14 km east-west and 8 km north-south. Sakurajima's twin summits rise just over 1000 m above sea level, with

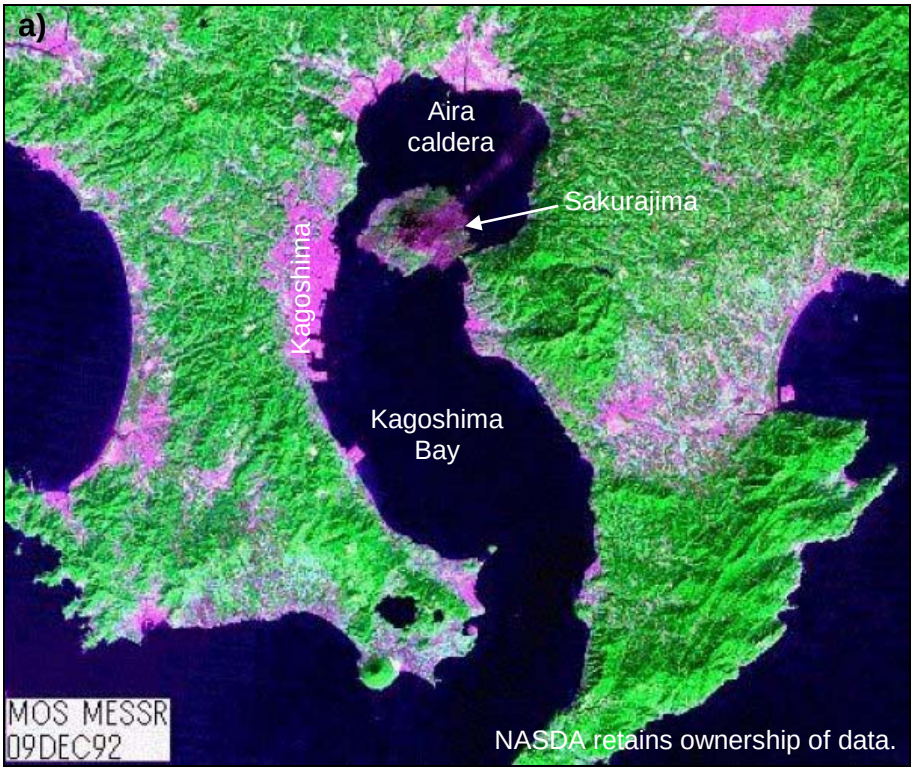

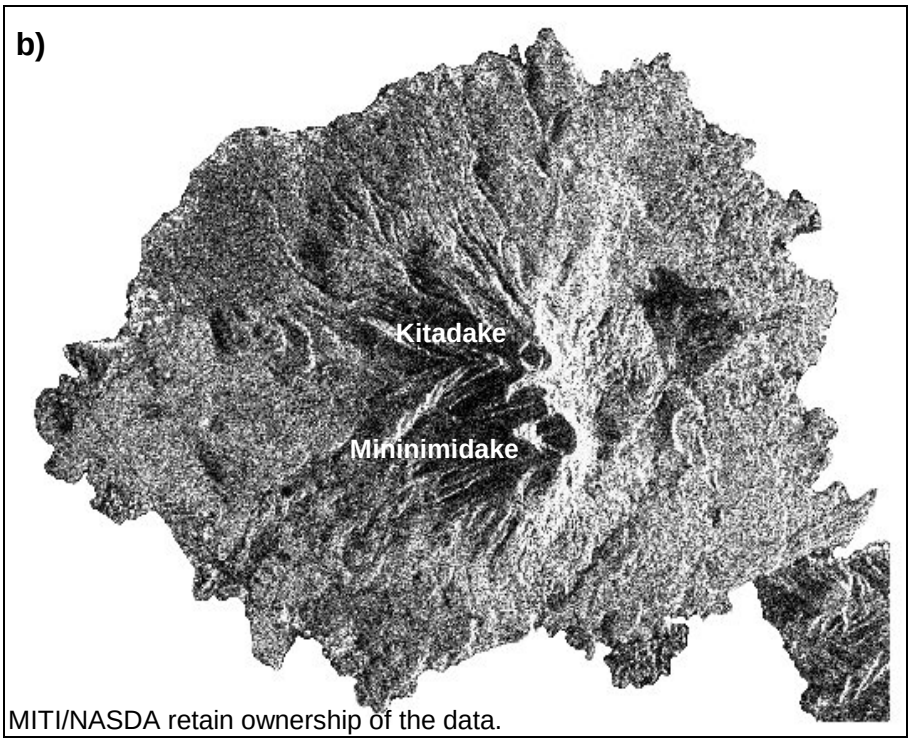

Figure 4.1 Satellite images of Sakurajima volcano. **a)** MOS (Marine Observation Satellite) image, 95 km × 80 km, coloured such that vegetated areas appear green and urban or unvegetated areas, pink. Note the plume extending to the northeast of Sakurajima. **b)** Excerpt from SAR image of Sakurajima, showing the twin cones. Images acquired from SiNG Kagoshima web site.

the northern Kitadake overlain by the younger, and currently active, Minimidake to the south (Figure 4.1b).

Activity began at Sakurajima approximately 13,000 years ago and three major eruptions have been produced within historical time. One of these, the Taisho eruption in 1914, produced a Plinian column, pyroclastic flows and lava emission from central and flank vents. The eruption killed 78 people, buried 5 villages and joined the island to the Osumi peninsula with a lava flow (Figure 4.1b). The current style of activity started abruptly on 13 October, 1955, with an explosion from the central Minimidake crater. Since then, frequent Vulcanian eruptions have occurred and, by December 1996, there had been 7,097 recorded explosions. A circular exclusion zone, 2 km in radius and centred on the active crater, prevents people from approaching the upper slopes of Minimidake. The frequent production of particle-laden plumes, along with easy access around the island and extended periods of stable weather, makes Sakurajima an ideal volcano for the study of atmospheric potential gradients.

4.3 Measurement network for atmospheric potential gradients

The definition of electric potential gradient and an introduction to the atmospheric electric field have been given in section 3.2.1. The work described in this chapter was aimed at recording multi-point atmospheric potential gradient data using the technique and site locations of Lane *et al*. (1995). A network of four fixed potential gradient measurement locations was augmented by a 'mobile' site that could be moved quickly in response to changing wind directions. The fixed sites were located at points with the aim of providing uniform azimuthal coverage around the volcano (section 4.3.2.1).

The mobile site enabled downwind measurements to be taken during most of the monitoring periods.

4.3.1 Measurement equipment

The equipment at each measurement location consisted of a mast or tripod-mounted electrostatic fieldmeter, a data logger and a power supply. The fixed sites all used identical equipment and mast-mounted fieldmeters, but a different model fieldmeter, mounted on a tripod, was used for the mobile equipment. With the potential gradient technique still under development as a monitoring tool, installation of the measurement apparatus was necessarily low-cost and temporary. One of the main implications of this was that the equipment could not be weather-proofed, with the result that it could not be deployed during periods of precipitation.

4.3.1.1 Sensors and mounting

The sensors used were rotating chopper type electrostatic field mills (Chubb, 1990), configured to detect electric potential gradient. Two different models were employed, model JCI 121 (Appendix I) at fixed sites, and a model JCI 111 (Appendix I) at the mobile site. These fieldmeters were auto-ranging with ranges of ± 2, 20, 200 and 2000 kV m^{-1} full scale deflection. JCI 121 meters have an analogue output which defines the measurement signal level and a 2-bit binary output which provides the range data. The analogue output (specified as ±2 V) had been modified to ±1.0 V by the manufacturer for compatibility with the data loggers. The JCI 111 meter had similar outputs to the JCI 121 meters with the exception of the range data, which were provided by the potential of one line (0.25, 0.5, 0.75 or 1.0 V).

The sensors were elevated above the ground (on right-angled masts at fixed sites and on a tripod for the mobile site, Figure 4.2) in order to provide noise-free amplification of the atmospheric potential gradient (Lane and Gilbert, 1992; Lane *et al*., 1995). Equipment at the fixed sites was left unattended, so the sensors were mounted inverted to help prevent the ingress of any precipitation or ash. This was not necessary for the mobile sensor as it was usually manned continuously and also had a relatively open sensing aperture which allowed easy removal of contaminant particles. The operator could also make notes on the weather and plume type, and record the times of any periods of ashfall.

Mast-mounting (fixed sites).

At fixed sites, semi-permanent masts were constructed out of right-angle steel shelving scaffold (Figure 4.2a). The masts consisted of two pieces of scaffold, bolted together and then attached to a metal stake which was embedded in the ground. Three wire cables provided further support, and were also anchored to the ground by metal stakes which ensured that all of the mast structure was maintained at Earth potential. The logging equipment and batteries were stored in a plastic box at the foot of the vertical post. This was then covered in metal foil to prevent measurements from being influenced by the plastic if it became electrically charged by wind-blown dust. The sensing apertures of the fieldmeters were 1.65 m above the ground.

Tripod-mounting (mobile site).

The JCI 111 fieldmeter was mounted upright on a tripod (Figure 4.2b). Logging equipment and batteries were stored in a foil-covered box placed between the legs of the tripod. The tripod was anchored to the box to increase its stability in windy

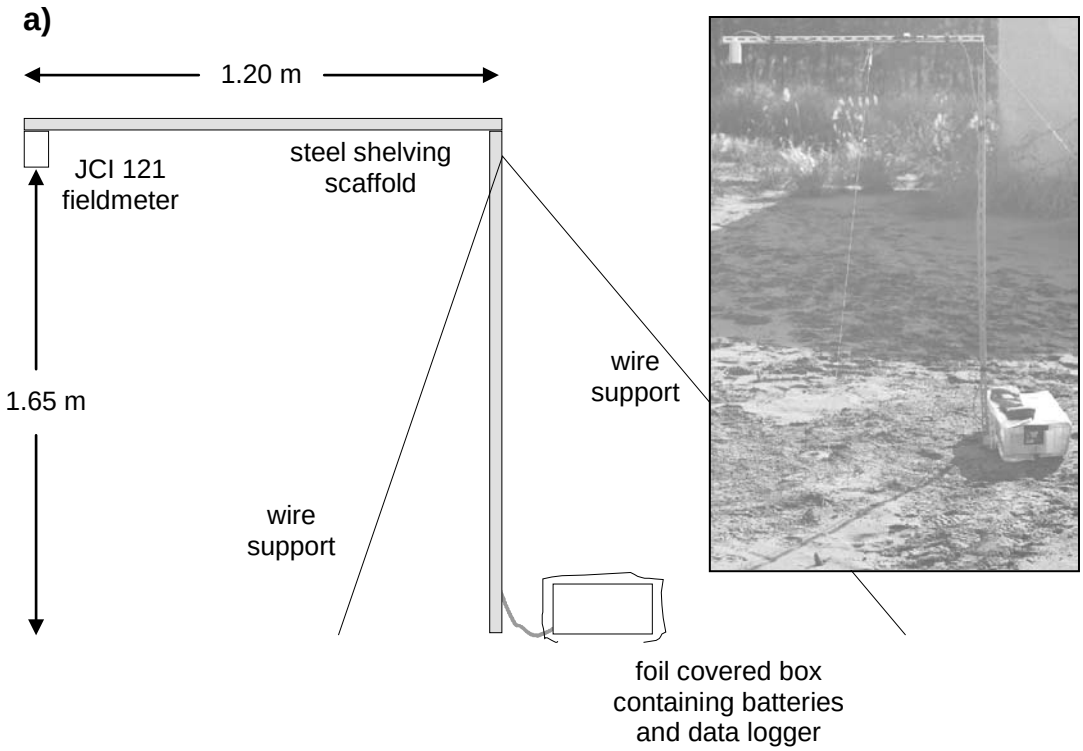

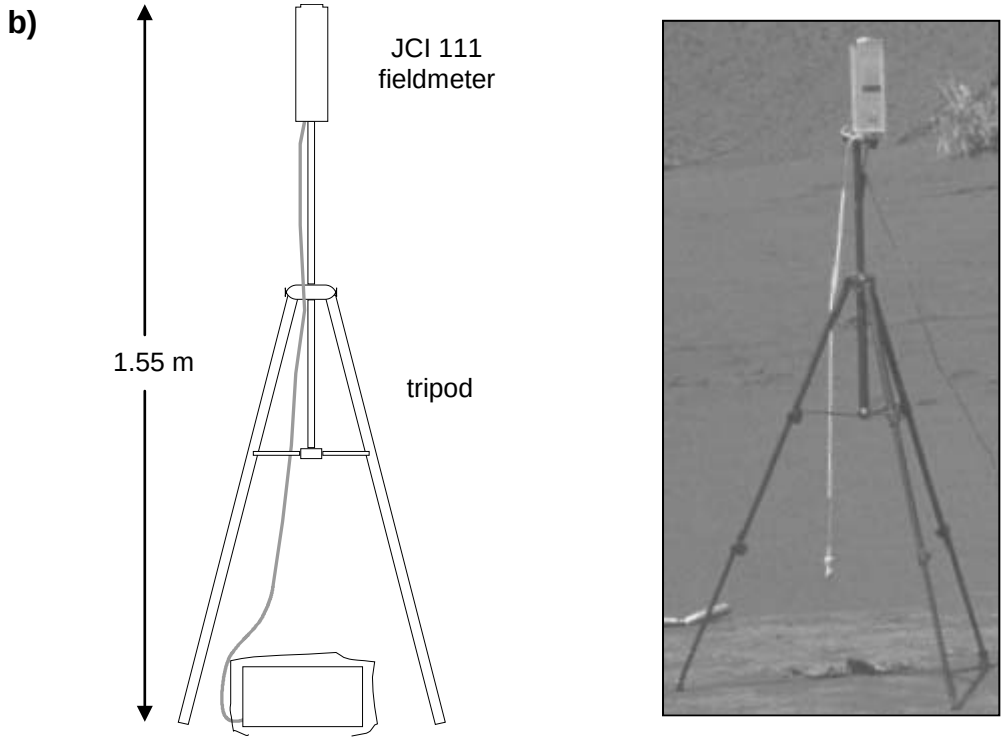

Figure 4.2 Fieldmeter mounts for atmospheric potential gradient measurements. **a)** Semi-permanent mast mounting used at fixed sites (diagram and photograph). **b)** Tripod mounted fieldmeter used at mobile sites. Note that the equipment box is not present in the photograph.

conditions. With this arrangement, the sensing aperture of the fieldmeter was 1.55 m above the ground level. Use of a tripod made the equipment easy to transport and assemble, but did not provide the necessary ground connections available at the fixed sites.

4.3.1.2 Earth connections

In order to measure the atmospheric potential gradient, the fieldmeters had to be earthed. At fixed sites, the sensor was earthed via its case to the mounting frame and supporting wires. The mobile fieldmeter could not be earthed via the tripod as it did not provide a good connection to ground. In this case, earthing was achieved by a 2 m length of woven ribbon cable which was connected to the Earth terminal on the power supply unit. The ribbon cable was then buried and, in order to provide additional surface area and depth penetration, it was also wrapped around three metal pegs which were driven further into the ground. In dry conditions, the ribbon trench was watered before being covered to increase further the conductivity to Earth.

4.3.1.3 Power supply and data loggers

Power for each fieldmeter was provided by rechargeable batteries contained in a power supply unit specifically designed for this application (Lane, 1994; Figure 4.3). Each unit provided a ±7.5 V supply with an Earth connection and had two BNC plugs for data output to the data logger. Units designed for the JCI 121 fieldmeter had a 12-way D-type socket which connected the unit to the fieldmeter, and a small resistor network in the unit which combined the binary scale data into a single output of 0, 0.3, 0.6 or 0.9 V. The unit designed for the JCI 111 fieldmeter was identical, with the

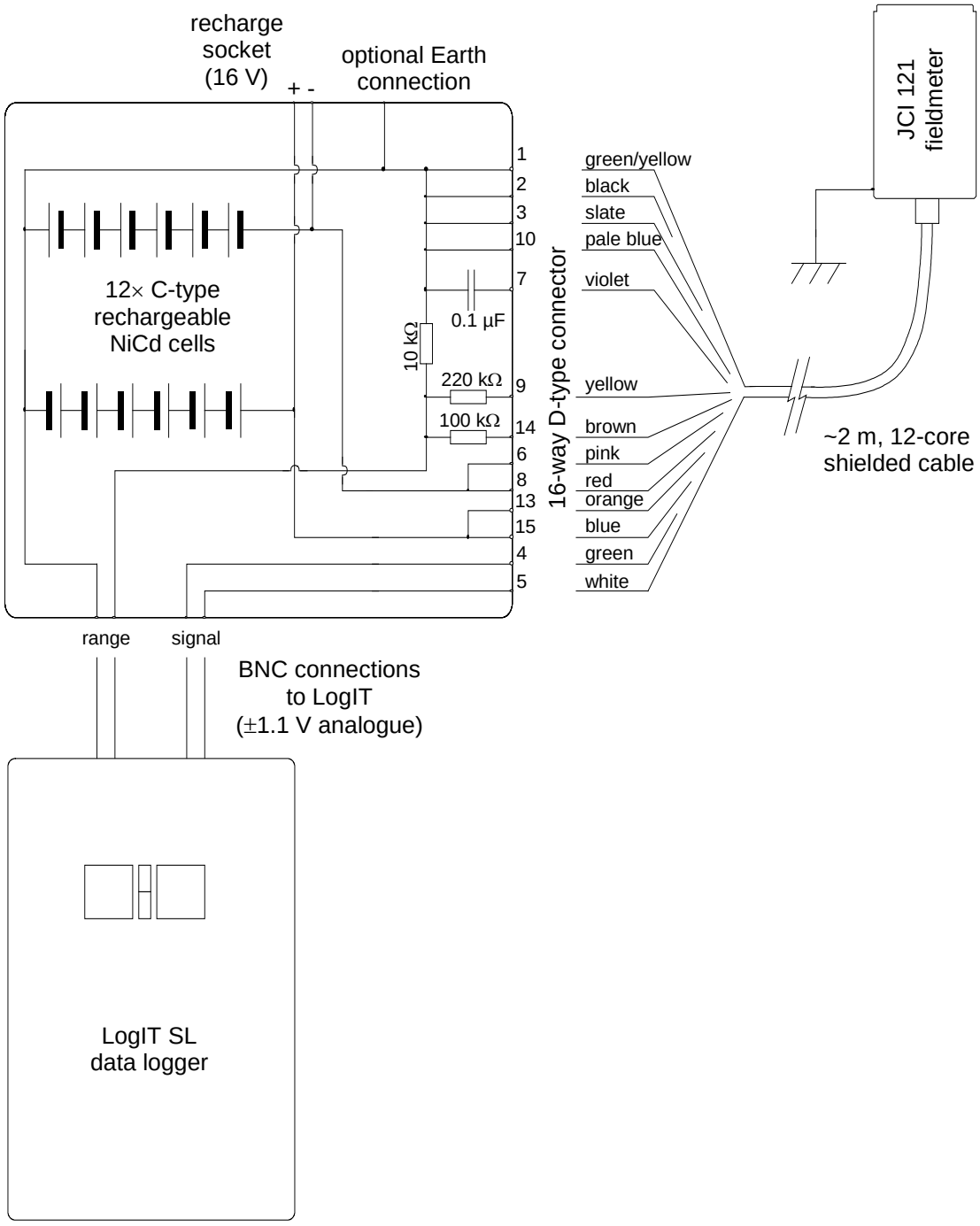

Figure 4.3 Electrical diagram of the power and signal box used at fixed sites. Dashed line encloses contents of the box. LogIT data logger has internal 8.3 V rechargeable battery.

exception of using a 9-way D-type connector and not requiring the resistor network to combine binary scale data.

LogIT data loggers (Lane, 1994; Appendix I) were employed at all sites, and were powered by four internal, rechargeable, 8.3 V NiCd batteries. The loggers had a 'sleep' mode to facilitate power conservation and, with the logging regime used, batteries were capable of lasting for several days. However, as equipment was installed and collected daily, the LogIT batteries were recharged every night. The data loggers used two ±1 V voltage sensors, which connected directly to the power supply unit.

4.3.2 Monitoring sites

The locations of the fixed sites had been previously selected by Lane *et al*. (1995) in order to optimise measurements of the atmospheric potential gradient. The requirements for a good site are detailed below.

Ground surface.

A relatively flat, horizontal ground surface is needed for accurate measurement of the vertical component of the potential gradient. The ground surface also has to be sufficiently soft to allow the supporting stakes to be driven in, or an earthing trench to be dug to provide a good Earth connection. However, the ground is required to be firm enough to provide mechanical stability for the equipment.

Vegetation.

Any monitoring site should have little or no surrounding vegetation, especially trees or tall bushes. The problems created by vegetation generally involve reduction of the measured ground-level potential gradient. As a result of the electrically conducting

nature of trees, at ground level, the surrounding area is shielded to some degree from the full potential gradient. When large potential gradients are present, point discharge currents can also be induced from trees (Chalmers, 1967), due to the strong electric fields which develop close to the tree-tops. Point discharges effectively inject charge into the local atmosphere (of the polarity to oppose the inducing field), thus further reducing the measured potential gradient.

On Sakurajima, ashfall collecting on the leaves of trees is readily remobilized by wind and this can produce local potential gradients which mask other perturbations. When selecting monitoring sites on Sakurajima, the vegetation cover is a much greater problem than either the ground surface or the topography.

Isolation and exposure.

The equipment should be located in a quiet spot where it is unlikely to be approached or disturbed by animals or people. Although vandalism or theft are not problems on Sakurajima, the recorded data could potentially be disturbed by inquisitive tourists approaching the apparatus. To minimise this, several sites were located on Sakurajima Volcano Research Center (SVRC) property. Equipment at other sites were accompanied by notices requesting that the apparatus not be disturbed.

Locating equipment on exposed sites can produce problems due to the generally windy conditions in these areas. Wind-blown dust and remobilized ash has been shown to produce potential gradients reminiscent of ashfall (Kikuchi and Endoh, 1982). Hilltops also have increased background potential gradients because, on a geographic scale, they are not ‘flat’ sites, and the atmospheric electric field is concentrated by the relief.

4.3.2.1 Fixed measurement sites

The four fixed sites used were Harutayama, Mochiki, Arimura and Kurokami. Their locations are marked in Figure 4.4 and photographs of each site are shown in Figure 4.5a, b, c and d, respectively. The locations of the sites were chosen to provide the best azimuthal coverage possible around the volcano. However, as can be seen from Figure 4.4, the topography and lack of access to the northern and northeastern slopes of the volcano dictated that these sectors were poorly monitored. The road to site Y was being used for construction access so, although Y could not be used as a fixed site, it was available at weekends.

Harutayama.

The Harutayama site was at the old Sakurajima Volcano Observatory building, on the top of a hill about 2.7 km west-northwest of the active vent. The area is inaccessible to the public, but frequently windy and this location has topographically-enhanced background potential gradients. As a result of Sakurajima's relative quiescence during the months preceding the monitoring period, wind-blown dust was not an excessive problem at Harutayama. However, data collected at this site tended to show elevated values when compared with those from other sites, and also demonstrated the most variation of the background level.

Mochiki.

The Mochiki site, at only 2.3 km southwest of the Minimidake summit crater, was the closest fixed site to the volcano. The equipment was located on the side of a mudflow channel. Due to its proximity to the exclusion zone around the volcano it was frequented by few people. The site was prone to gas emissions from the volcano, and corrosion of the mounting points on the mast was a problem.

Figure 4.4 Map of Sakurajima and potential gradient monitoring sites. Fixed sites are marked with a filled black circle with the associated site name. Mobile sites are marked by the designated site letter alone.

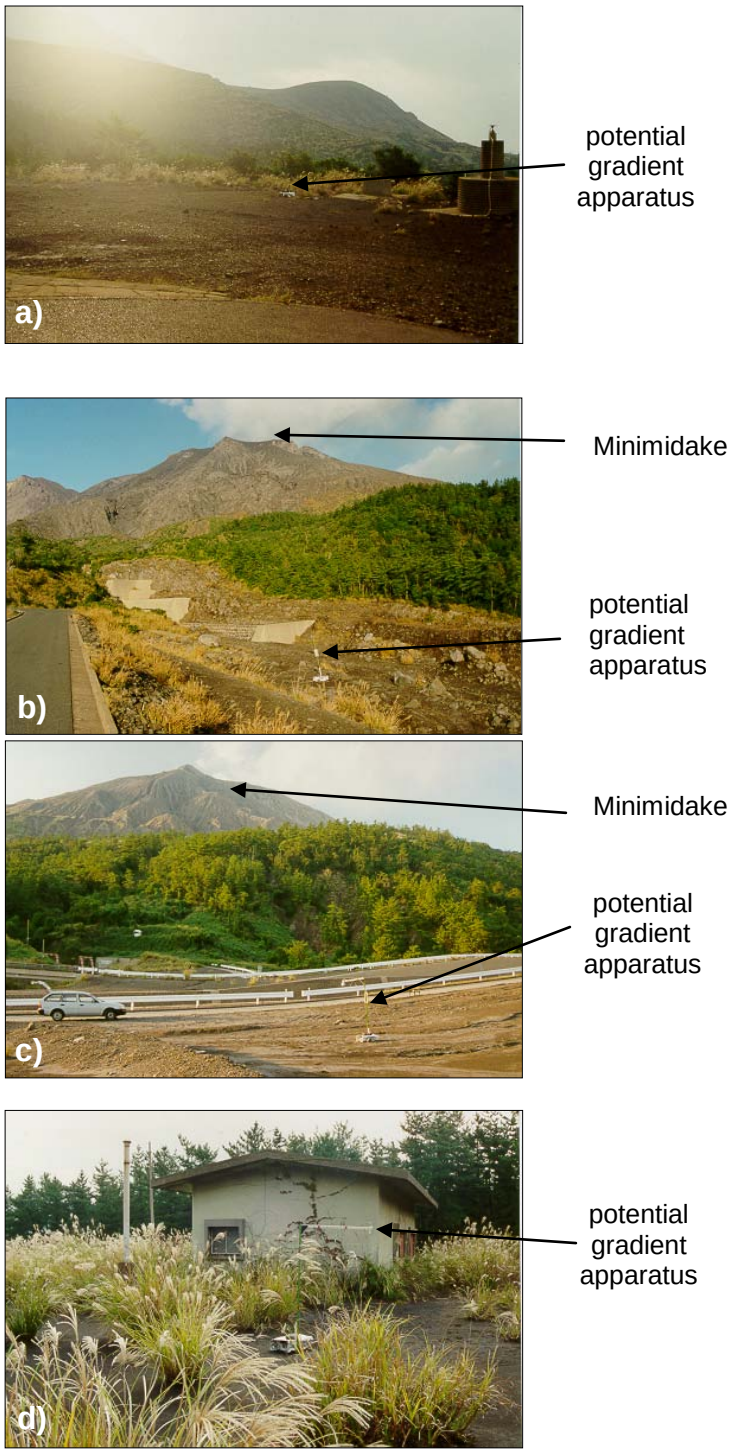

Figure 4.5 Photographs of the potential gradient apparatus at the fixed site locations. **a)** Harutayama. **b)** Mochiki. **c)** Arimura. **d)** Kurokami. For scale, masts are approximately 1.7 m high at each site. The foil-covered boxes containing the power unit and data logger can be seen at the base of each mast.

Arimura.

The Arimura site was a flat area next to a mudflow drainage channel. The edge of a lava flow, about 4 m high, was present 10 m from the equipment. The main disadvantage of the site was that the flat topography had been created by the accumulation of ash deposits so, despite the low level of activity preceding the monitoring period, the site was still prone to wind-blown ash. The Arimura site was located 2.7 km south-southeast from the vent.

Kurokami.

The Kurokami site was in the grounds of a SVRC building, and thus secure from visitors. Unfortunately, the site was surrounded by trees, and tall grass was present close to the apparatus. These factors reduced the measured potential gradients considerably. The Kurokami site was 4.0 km due east of the vent.

4.3.2.2 Mobile measurement sites

Over the monitoring period, eight locations were used as sites for the mobile equipment. These were designated letters A 1, T, U, V, W, X, Y, and Z, as shown in Figure 4.4. The equipment at mobile sites was manned continuously, so the need for the location to be isolated was reduced. With this exception, all mobile sites would also have been suitable for use as fixed sites.

4.4 Data acquisition and processing

The limited data capacity of the loggers and the possible susceptibility of the equipment to rain dictated that monitoring was not carried out overnight. Thus, the apparatus at each fixed site (with the exception of the semi-permanent masts) was

installed and removed every day. The equipment for each site was individually labelled and maintained in a named box. This enabled records to be kept of individual battery performance and any problems with the different sensors.

In order to install the network efficiently, the LogITs were loaded with the time and logging program at the SVRC. Each logger was programmed for 'interval' logging, sampling once every 15 s (Lane, 1994). Two channels were recorded; one recorded the analogue output of the fieldmeter at high resolution (12-bit), and the other logged the range data at low resolution (8-bit). With a memory capacity of about 7 kb, this allowed approximately 9.8 hours of data to be recorded. Once the program was installed, the loggers went into 'sleep' mode. Logging could then be initiated at any time by button press.

The equipment was then taken by car to each site, a round trip of 55 km. At each location, the sensor was bolted to the mast and the cable secured with insulation tape. The Earth connection between the sensor case and the wire supports was then checked with an ohm-meter. Corrosion of the metal frames, especially at the Mochiki site, which was frequently exposed to the gas plume from Sakurajima, sometimes prevented a good connection. To ensure a high conductivity to Earth, the mounting points were cleaned with a metal file before the sensor was installed. The box containing the data logger and battery unit was placed by the base of the mast and the sensor plugged in to the battery unit. Once the data logger had been started, the lid was replaced on the box and it was then wrapped in a foil cover. Rocks were used to prevent the foil from vibrating in the wind or blowing away. For the first two minutes of logging, a zero-check chamber was placed over the sensor. This provided a field-free environment to allow the zero-offset of the sensor to be checked. The logging start time, and time of removal of the zero-check chamber, were recorded, along with

the ambient temperature and relative humidity. Unfortunately, failure of the meter providing temperature and relative humidity measurements over a period of 10 days prevented these data from being taken for the whole monitoring period.

In order to try to maintain even discharge of all the power supplies, the equipment was retrieved in the same rotational order as it was installed. At each site, the zero-check chamber was placed on the sensor for a further two minutes before stopping the data acquisition. Again, the time, temperature and relative humidity were recorded. Once back at the SVRC, data from the loggers were downloaded onto the PC. The raw data could then be easily converted to measured potential gradients by means of a spreadsheet. The raw data and converted results from one logger are shown in Figure 4.6.

4.4.1 Timing

Care was taken to ensure accurate timing of all the measurements. The LogIT data loggers have a programmable internal real-time clock which can also record the date. Initially, both the time and date were set every day from the internal clock on the PC. Although this ensured that all the logger clocks were synchronous, drift of the PC clock prevented the logger clocks from being calibrated to Japan Standard Time (JST). Attempts to reset the PC clock with any accuracy failed. Accuracy of the internal logger clocks was checked against a digital Casio watch, manually calibrated to JST from radio broadcasts. After test logging overnight, no drift could be detected on any of the LogITs.

To ensure that logging timing was accurate to JST, an alternative procedure was employed to set the LogIT time. Each logger was initially set to the PC clock to allow the date to be uploaded. The time was then reset manually from the digital watch. This

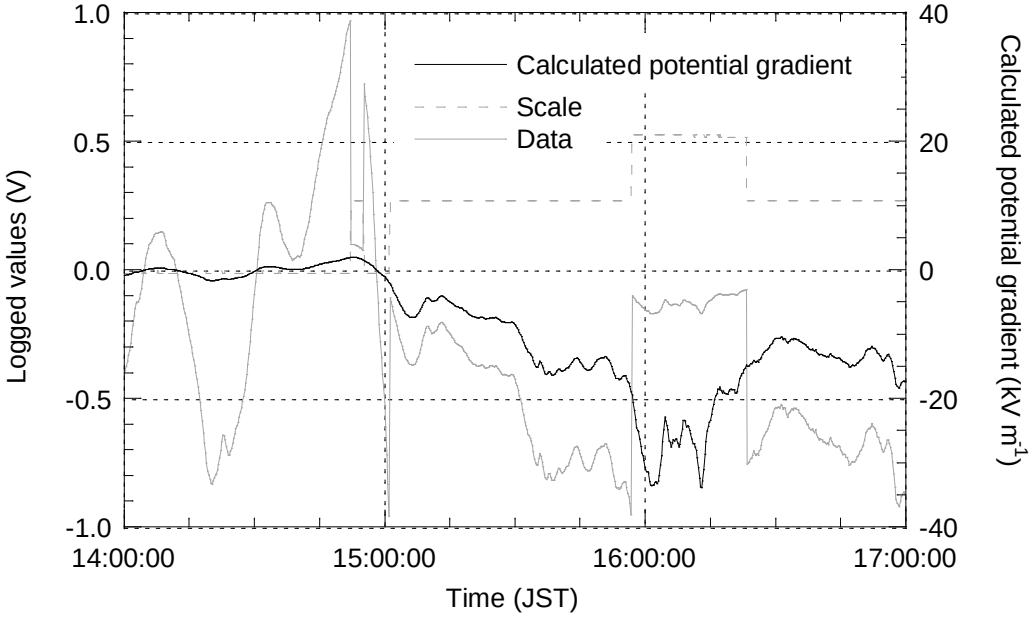

Figure 4.6 Raw and processed potential gradient data. Data were collected at Mochiki on 10 November, 1996. Note the range changes at approximately 14:51, 14:55, 15:02, 15:56 and 16:22. JST is Japan Standard Time.

allowed the LogIT times to be to set to JST with an accuracy of greater than a second. Any drift of the watch could be detected easily from the hourly broadcasts and a suitable correction back to JST applied.

With the LogITs programmed to sample every 15 seconds, logging at each site was initiated at 0, 15, 30 or 45 seconds past the minute. This synchronised all the readings so that each meter was logged simultaneously. A laptop 486 PC was used to program and download the data from the loggers. The software allowed data to be recorded as a simple comma-separated ascii file, or as a '.SID' text file which included logging details in a header.

4.4.2 Calibration

The mast-mounting of the fieldmeters produces a noise-free amplification of the actual potential gradient. This is a result of the concentration of fieldlines towards the elevated and earthed surface of the sensing aperture. For the equipment and masts used, Lane and Gilbert (1992) and Lane *et al*. (1995) had previously deduced an amplification factor of twenty. Unless otherwise stated, data quoted in this chapter are the measured potential gradients; they thus represent the actual potential gradient multiplied by twenty.

Ideally, for calibration purposes, the linearity and accuracy of the fieldmeters would have been monitored. However, to do this usefully, it would have had to be carried out periodically throughout each day as the environmental conditions varied. Equipment to do this automatically could be designed, and this approach would be adopted if a permanent monitoring network were ever constructed. Although this was not feasible for the temporary network, the linearity of one fieldmeter (fieldmeter 'F',

see Appendix III) was later assessed in the laboratory as part of the calibration of the experimental apparatus (Chapter 5). This showed that, over a period of about a year (albeit not outdoors), the calibration of the fieldmeter varied less than ±0.5 %.

In order to obtain absolute values from the fieldmeters, the calibration also involved the zero-field offsets. Very small amounts of contamination of the sensing surfaces in the sensor head can alter the offset considerably. However, the zero-check chamber was usually applied both before and after the collection of each data set, so the zero offset could be calculated and removed from the data. Where the offset changed over the monitoring period, a linear interpolation between the two values was used to correct the data. As a further check, the zero was re-taken most evenings at the SVRC to ensure that the fieldmeters were performing as expected. The recorded zero offsets are listed in Appendix II.

4.4.3 Data loss

The main cause of data loss was low fieldmeter battery power during monitoring periods. Due to age, the main power supply units had developed variable capacities, with useful lives varying from approximately 17 hours to more than 27 hours. Because recharging facilities were limited to only one full recharge per night, an optimum recharging system was developed whereby one unit received a short ‘top-up’ charge before another was left overnight. During periods of inclement weather, when no monitoring was possible, full use was made of the time to ensure that all units were fully charged. Batteries in the data loggers gave few problems because up to six could be recharged overnight. Consequently, only one data set was ever lost due to logger failure from power loss.

Several data sets are thought to be unreliable due to a fault that developed in one of the fieldmeters. After several days of use, the rotating chopper of fieldmeter 'D' was observed to be not rotating freely. Examination of the data recorded by 'D' suggested that the fault may have also caused low readings and intermittent noise in previously recorded data. The fieldmeter was replaced with another JCI 121, designated 'F'.

The final equipment problem encountered was a loose connection to a data logger. This problem had been caused by a screw coming loose in a plug and, once this had been tightened, the connection caused no further trouble.

4.5 Results

Data were successfully recorded on thirty one days between 16 October and 21 November, 1996. Poor weather prevented the experiment from being carried out on the other days. During the monitoring period, Sakurajima was relatively quiet. A variety of plumes were observed, varying from white plumes of condensing gases being blown from the summit crater by the wind, to particle-rich plumes generated from Vulcanian explosions. On most days, only plumes of condensing gases were produced. These sometimes rose energetically from the crater, but usually ascended only a few hundred metres before reaching their equilibrium height and being blown downwind.

In the following pages, Figures 4.7 to 4.37 display the potential gradients recorded and give atmospheric data, the equipment status and descriptions of the plumes observed. The descriptions are taken from field observations and also from video footage taken from Kagoshima city, supplied by K. Kinoshita, Kagoshima University.

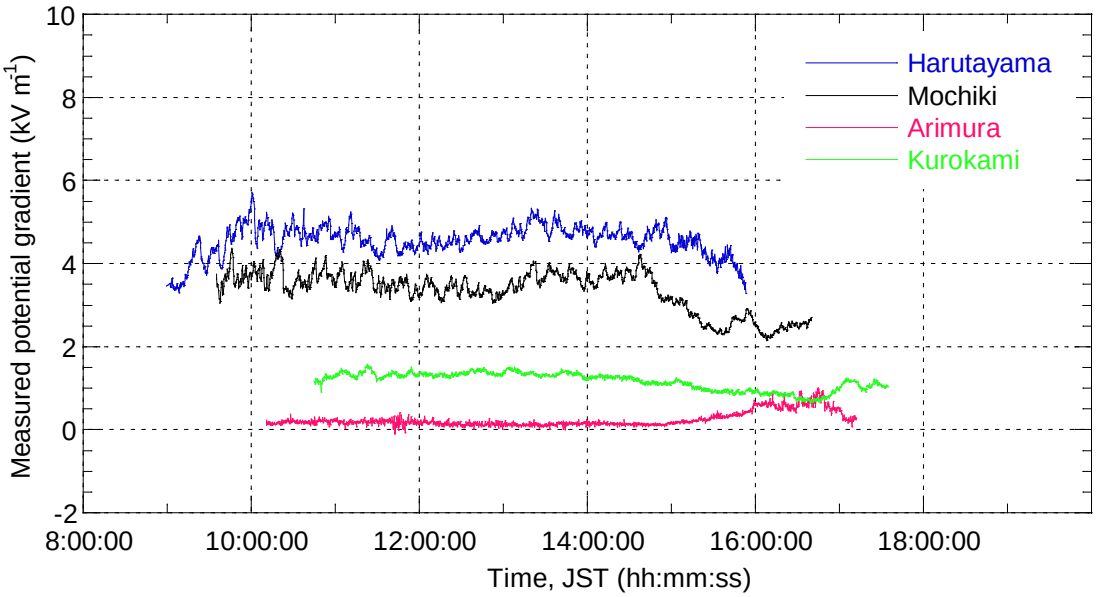

Figure 4.7 Atmospheric potential gradients, Sakurajima, 16 October, 1996.

Air temperature and relative humidity:

Harutayama	08:56	16°, 67 %	15:50	27°, 29 %
Mochiki	09:32	20°, 44 %	16:45	25°, 28 %
Arimura	10:07	23°, 37 %	17:07	22°, 30 %
Kurokami	10:42	25°, 37 %	17:32	17°, 50 %

Sky: Cloudless

Equipment: Fieldmeter D used at Arimura; later diagnosed as faulty. Timing of data accurate to only ±1 minute, data loggers were not calibrated to JST.

Plumes: None observed.

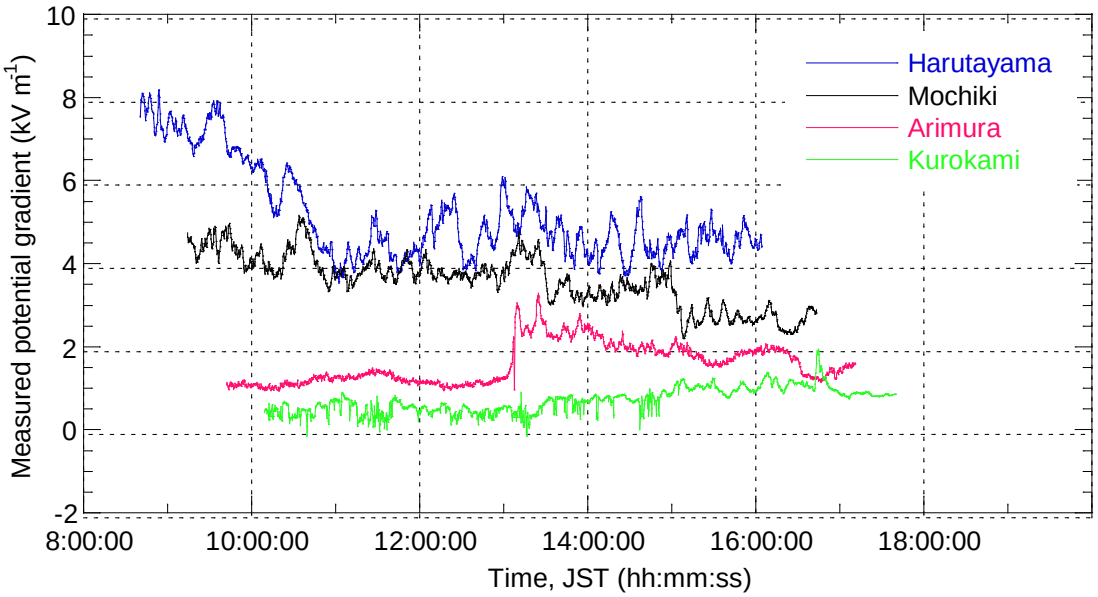

Figure 4.8 Atmospheric potential gradients, Sakurajima, 17 October, 1996.

Air temperature and relative humidity:

Harutayama	08:37	21°, 52 %	16:08	22°, 44 %
Mochiki	09:10	22°, 45 %	16:47	22°, 52 %
Arimura	09:35	24°, 38 %	17:17	22°, 59 %
Kurokami	10:07	26°, 39 %	17:49	19°, 80 %

Sky: ~40 % cloud cover, increasing to ~80 % at about 12:00.

Equipment: Fieldmeter D used at Kurokami; later diagnosed as faulty.

Plumes: A series of condensing gas plumes produced at 09:39, several hundreds of metres high, blown west.

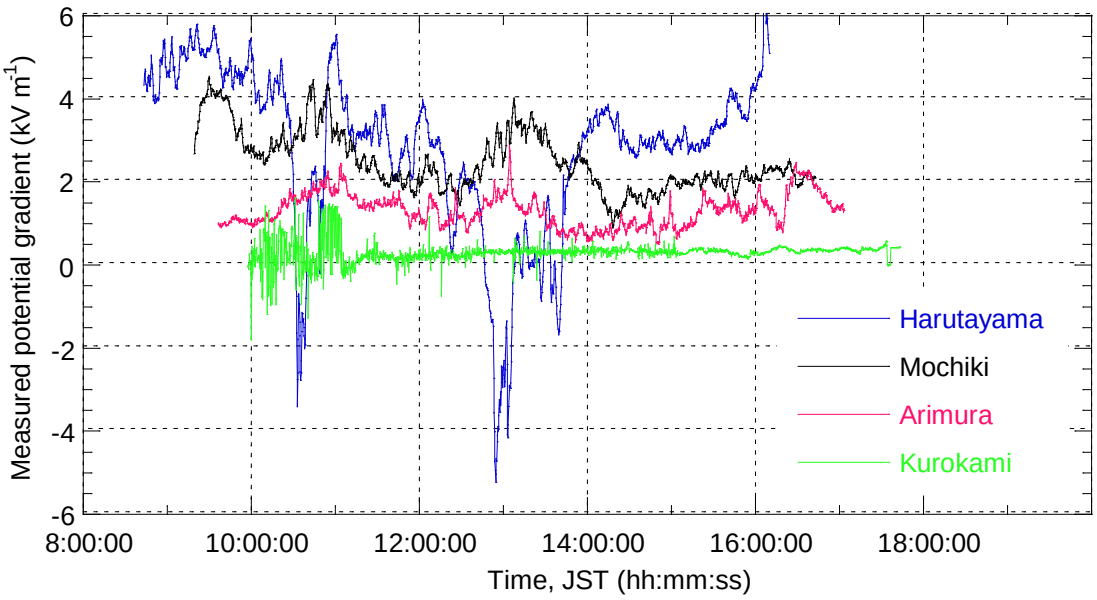

Figure 4.9 Atmospheric potential gradients, Sakurajima, 18 October, 1996.

Air temperature and relative humidity:

Harutayama	08:42	21°, 78 %	16:12	26°, 50 %
Mochiki	09:10	25°, 44 %	16:44	26°, 51 %
Arimura	09:33	27°, 45 %	17:10	24°, 58 %
Kurokami	09:58	26°, 51 %	17:35	22°, 68 %

Sky: Cloudless.

Equipment: Fieldmeter D used at Kurokami; later diagnosed as faulty.

Plumes: Condensing gases only. Size of plume increased during the day, becoming reasonably well developed towards end of monitoring period. Very little wind; plume remained over the top of Minimidake.

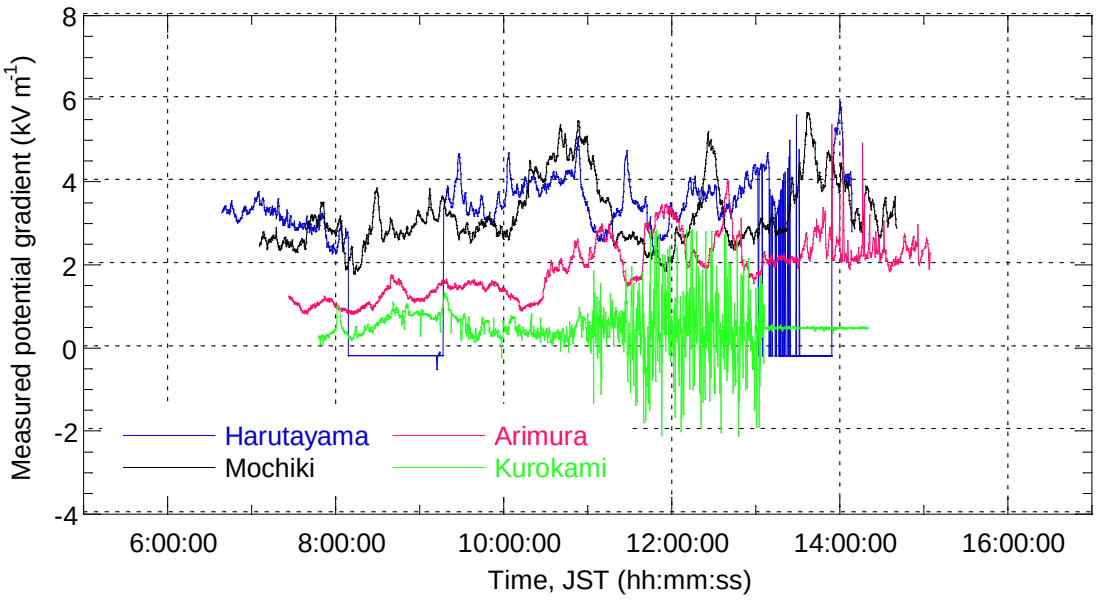

Figure 4.10 Atmospheric potential gradients, Sakurajima, 19 October, 1996.

Air temperature and relative humidity:

Harutayama	06:36	17°, 80 %	14:11	27°, 46 %
Mochiki	07:01	17°, 82 %	14:43	27°, 38 %
Arimura	07:24	19°, 82 %	15:06	27°, 40 %
Kurokami	07:45	21°, 78 %	15:30	26°, 48 %

Sky: Started clear, but overcast by 08:00. Cloud cover varied between 0 and 100 % until about 12:00. Cloudless afternoon.

Equipment: Fieldmeter D used at Kurokami; diagnosed as having a fault. Sensor was dead on collection, and data showed high noise. Equipment at Harutayama demonstrated intermittent fault between approximately 08:00 and 09:00, and 13:00 and 14:00.

Plumes: Condensing gases only. Plumes being blown over Kurokami while network was being installed.

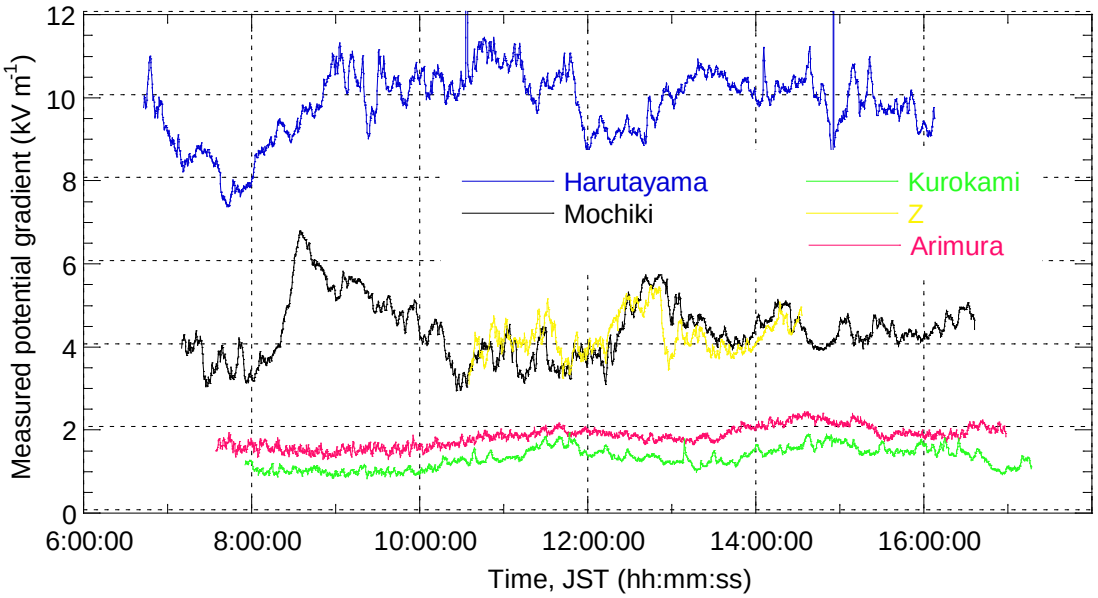

Figure 4.11 Atmospheric potential gradients, Sakurajima, 21 October, 1996.

Air temperature and relative humidity:

Harutayama	06:40	15°, 64 %	16:10	24°, 56 %
Mochiki	07:08	16°, 68 %	16:39	21°, 52 %
Arimura	07:31	17°, 59 %	17:01	20°, 56 %
Kurokami	07:51	17°, 58 %	17:24	19°, 62 %
Z	10:33	25°, 32 %	14:35	26°, 36 %

Sky: Cloudless.

Equipment: No problems.

Plumes: Condensing gas only. While network was being installed, a plume was present over the summit. Wind-blown dust at Arimura. At 10:30, a white plume, less than 1 km in length, was being blown towards Harutayama.

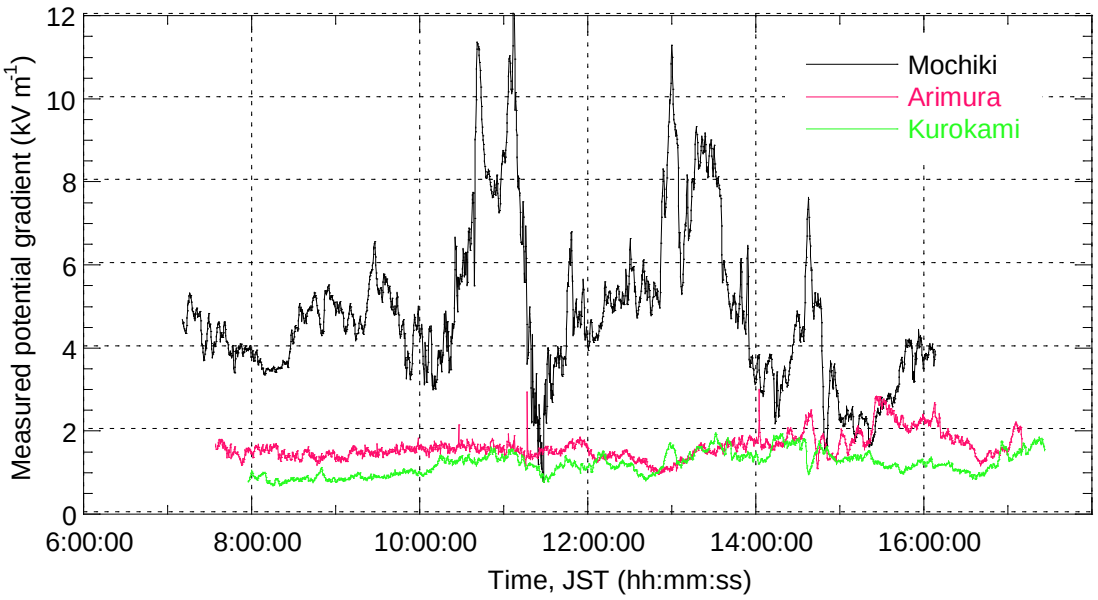

Figure 4.12 Atmospheric potential gradients, Sakurajima, 22 October, 1996.

Air temperature and relative humidity:

Harutayama	06:42	18°, 72 %	15:03	21°, 62 %
Mochiki	07:08	18°, 74 %	16:47	21°, 60 %
Arimura	07:32	19°, 69 %	17:13	22°, 74 %
Kurokami	07:55	22°, 60 %	17:35	21°, 75 %

Sky: Started clear, before clouding over and starting to rain at about 15:00.

Equipment: Logging problem at Harutayama prevented data from being recorded.

Plumes: Only condensing gases. Wind fairly constant from the northeast and north-northeast. Summit wind speeds of over 10 m s^{-1} (K. Kinoshita, *pers. comm.*) produced a mountain lee wave which brought the plume to the ground. Plume directly over Mochiki for most of the day, but moved slightly clockwise at 14:30 such that it was over X.

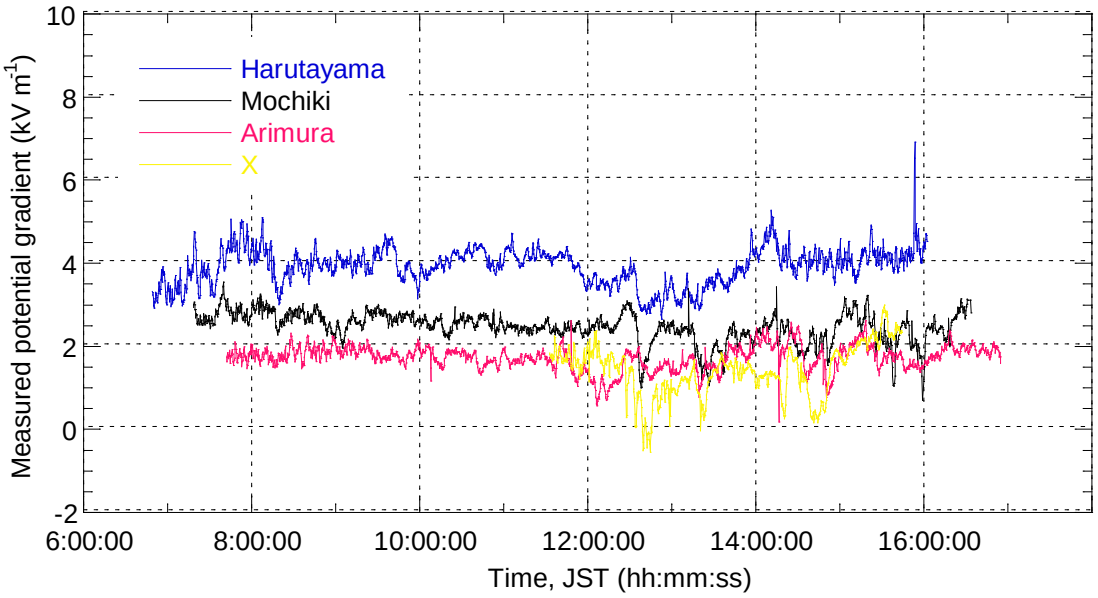

Figure 4.13 Atmospheric potential gradients, Sakurajima, 23 October, 1996.

Air temperature and relative humidity:

Harutayama	06:47	18°, 80 %	16:04	21°, 65 %
Mochiki	07:15	20°, 76 %	16:33	23°, 69 %
Arimura	07:40	21°, 76 %	16:57	25°, 54 %
Kurokami	08:00	23°, 71 %	17:18	
X	11:33	28°, 45 %	15:47	25°, 36 %

Sky: ~10 % cloud cover, increasing to ~40 % at 10:00, with some orographic cloud. Some high altitude cloud in the afternoon, which cleared by 17:00.

Equipment: LogIT battery failure prevented data collection at Kurokami.

Plumes: Condensing gases only. Plume overhead or slightly clockwise of X all day. Plume appeared very dense in the morning, but gradually reduced and had almost disappeared by about 15:30.

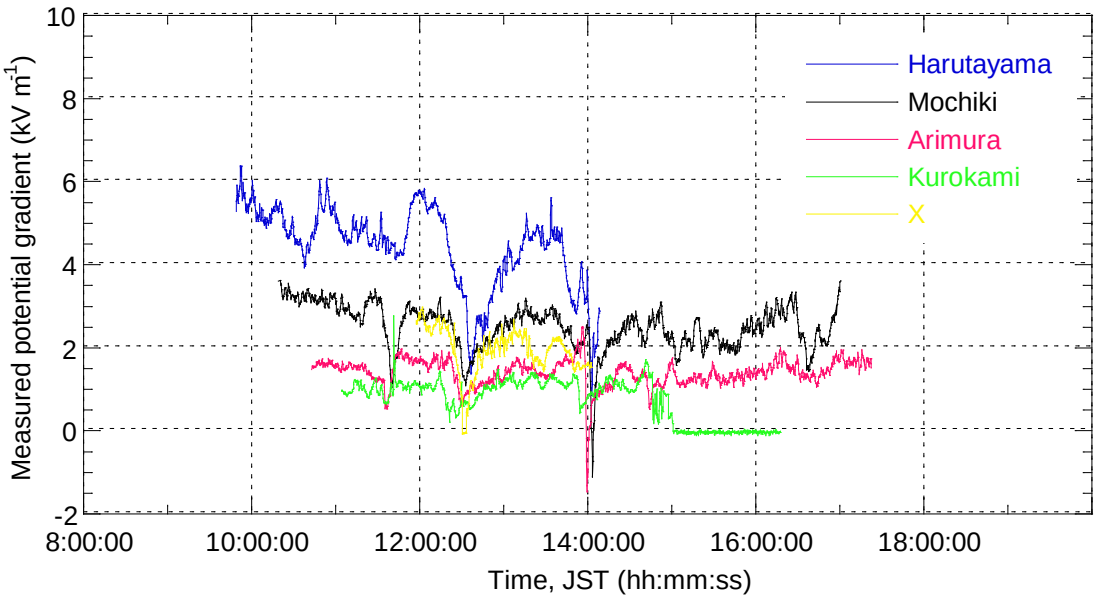

Figure 4.14 Atmospheric potential gradients, Sakurajima, 24 October, 1996.

Air temperature and relative humidity:

Harutayama	09:46		16:10	
Mochiki	10:17		16:39	22°, 66 %
Arimura	10:40		17:01	23°, 66 %
Kurokami	11:01	31°, 58 %	17:24	
X	11:54	27°, 32 %	14:35	25°, 60 %

Sky: Clear except for orographic cloud, increasing to about 20 % cloud cover by 10:00. Increasing further by 14:00, with rain showers.

Equipment: Kurokami site lost power at about 15:00 and Harutayama site lost power at about 14:00.

Plumes: Condensing gases only. Plume variable in strength, being blown over X.

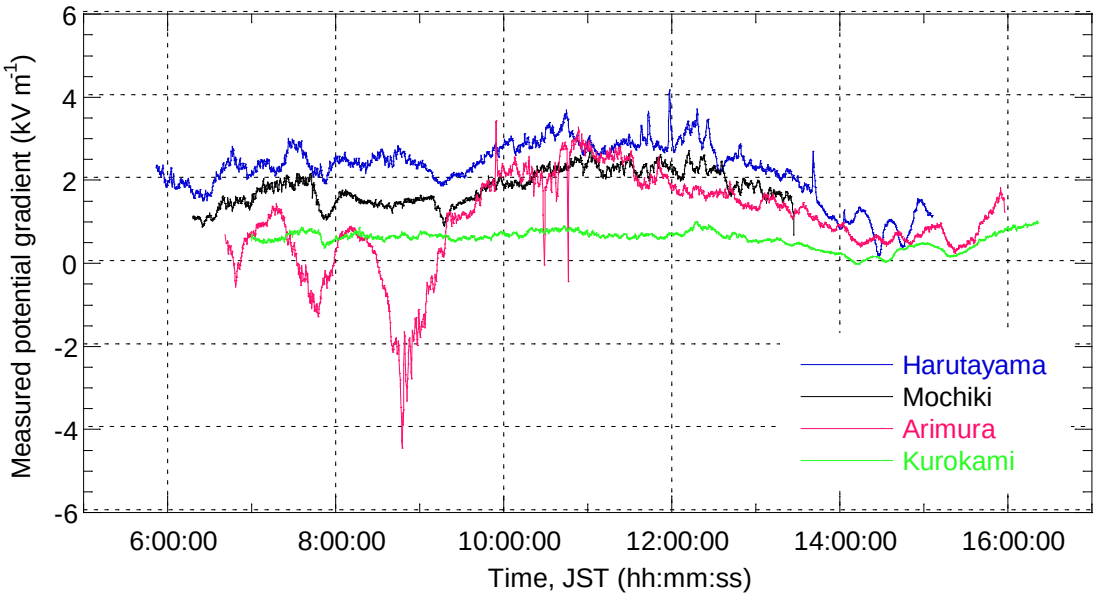

Figure 4.15 Atmospheric potential gradients, Sakurajima, 26 October, 1996.

Air temperature and relative humidity:

Harutayama	05:49	16°, 69 %	15:08	17°, 60 %
Mochiki	06:16	17°, 62 %	15:34	17°, 51 %
Arimura	06:39	19°, 56 %	16:00	19°, 45 %
Kurokami	06:58	19°, 63 %	16:22	19°, 51 %

Sky: Overcast with low cloud.

Equipment: Manual setting of the LogIT clocks started, maximum error of ±1 s.

Plumes: Very little visible, restricted to some light steaming in the afternoon. No observations to correlate with negative gradients at Arimura, but construction work observed being carried out in the vicinity when the apparatus was removed.

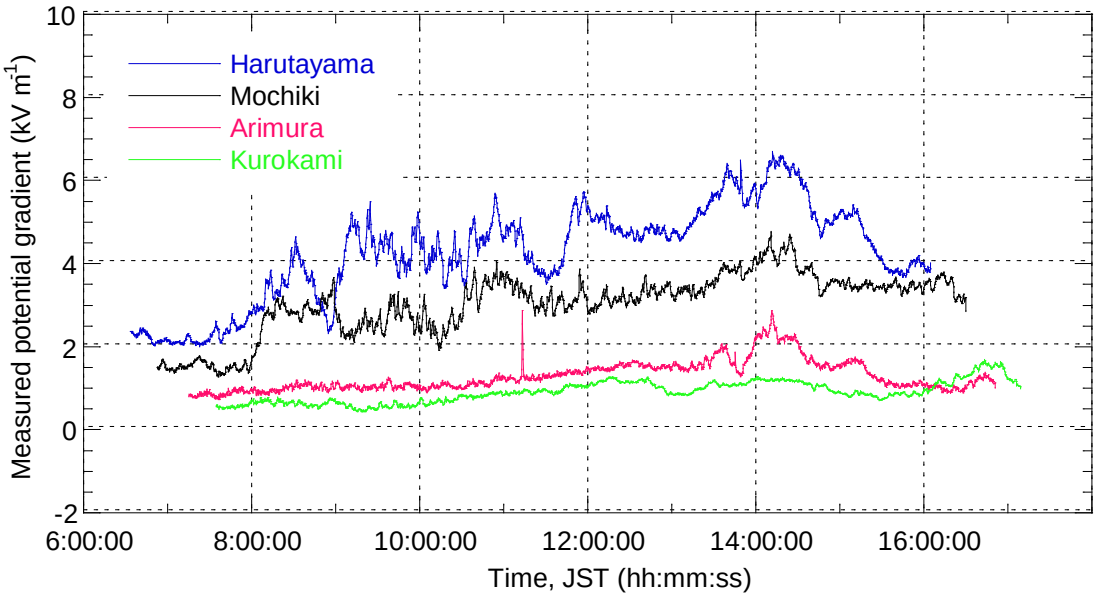

Figure 4.16 Atmospheric potential gradients, Sakurajima, 27 October, 1996.

Air temperature and relative humidity:

Harutayama	06:23	12°, 72 %	16:08	24°, 44 %
Mochiki	06:50	14°, 72 %	16:32	22°, 41 %
Arimura	07:13	14°, 67 %	16:54	22°, 41 %
Kurokami	07:32	15°, 70 %	17:11	19°, 62 %

Sky: Overcast start, clearing at 08:00. Some high altitude cloud.

Equipment: No problems.

Plumes: Condensing gases only. Fairly continuous plume heading approximately northeast all day.

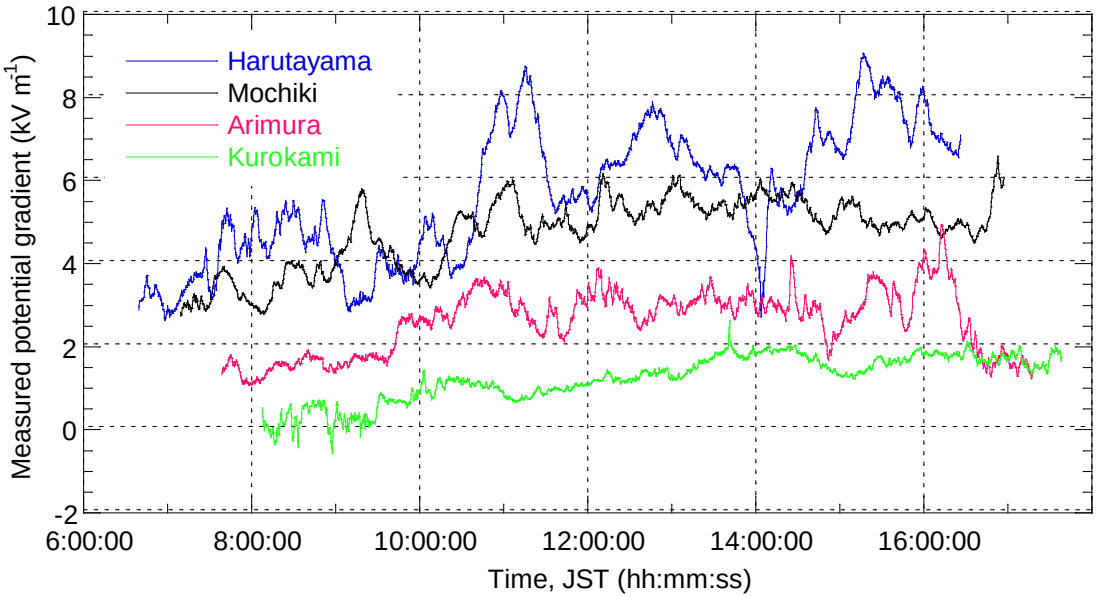

Figure 4.17 Atmospheric potential gradients, Sakurajima, 29 October, 1996.

Air temperature and relative humidity:

Harutayama	06:35	16°, 81 %	16:24	20°, 67 %
Mochiki	07:06	17°, 81 %	16:43	21°, 70 %
Arimura	07:32	18°, 88 %	17:01	21°, 78 %
Kurokami	07:54	18°, 88 %	17:24	21°, 75 %

Sky: Clear initially, but low cloud obscured the summit by about 09:00 and remained for the rest of the monitoring period.

Equipment: No zeros taken at Harutayama or Mochiki because loggers were full on collection.

Plumes: Condensing gases only. A small plume, slightly distorted eastwards by the wind, was observed before being obscured by the cloud.

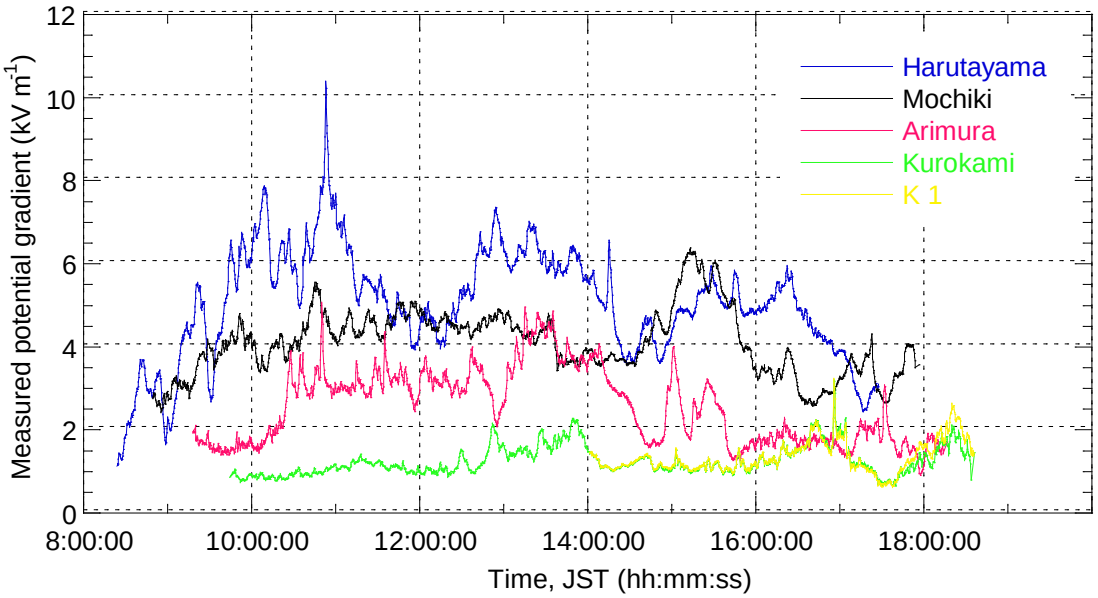

Figure 4.18 Atmospheric potential gradients, Sakurajima, 30 October, 1996.

Air temperature and relative humidity:

Harutayama	08:21	20°, 80 %	17:30	23°, 75 %
Mochiki	08:47	23°, 71 %	17:56	23°, 76 %
Arimura	09:15	26°, 60 %	18:16	23°, 74 %
Kurokami	09:41	28°, 59 %	18:36	22°, 78 %
K 1	13:59	30°, 51 %	18:40	22°, 78 %

Sky: An early cover of about 90 % high altitude cloud cleared after 11:00. Low cloud formed at about 14:00 and obscured summit for the afternoon, clearing again at about 17:00.

Equipment: No problems. Site K 1 located 1 m from the fixed apparatus at Kurokami.

Plumes: Condensing gases only.

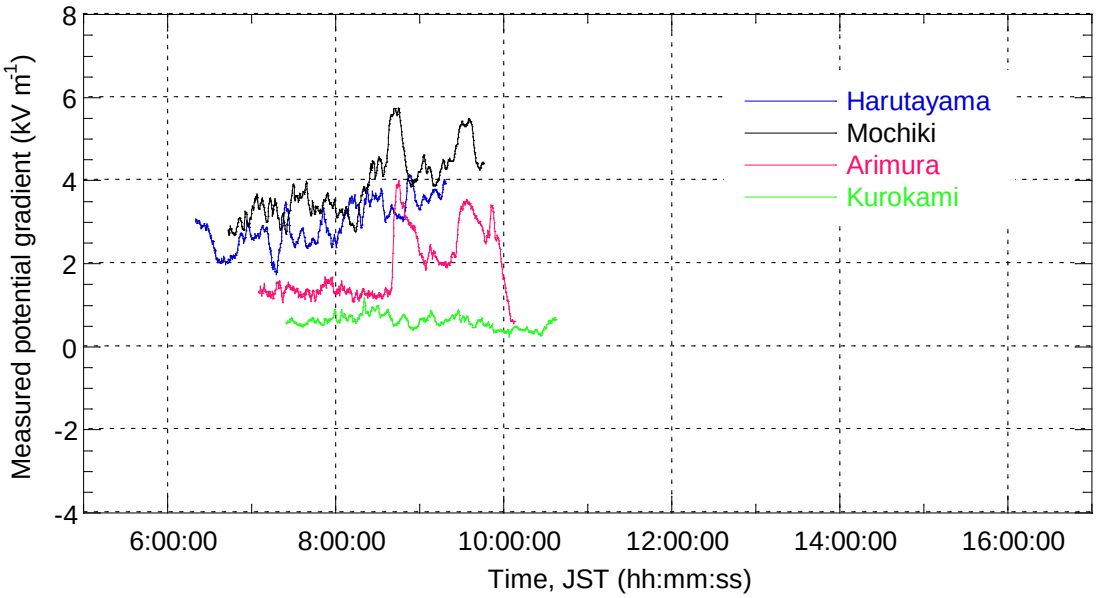

Figure 4.19 Atmospheric potential gradients, Sakurajima, 31 October, 1996.

Air temperature and relative humidity:

Harutayama	06:16	21°, 87 %	09:21	23°, 80 %
Mochiki	06:41	21°, 84 %	09:28	23°, 83 %
Arimura	07:02	22°, 79 %	10:10	24°, 78 %
Kurokami	07:22	22°, 79 %	10:38	25°, 77 %

Sky: Started clear, rapidly clouded over.

Equipment: Apparatus withdrawn due to rain.

Plumes: Condensing gases only.

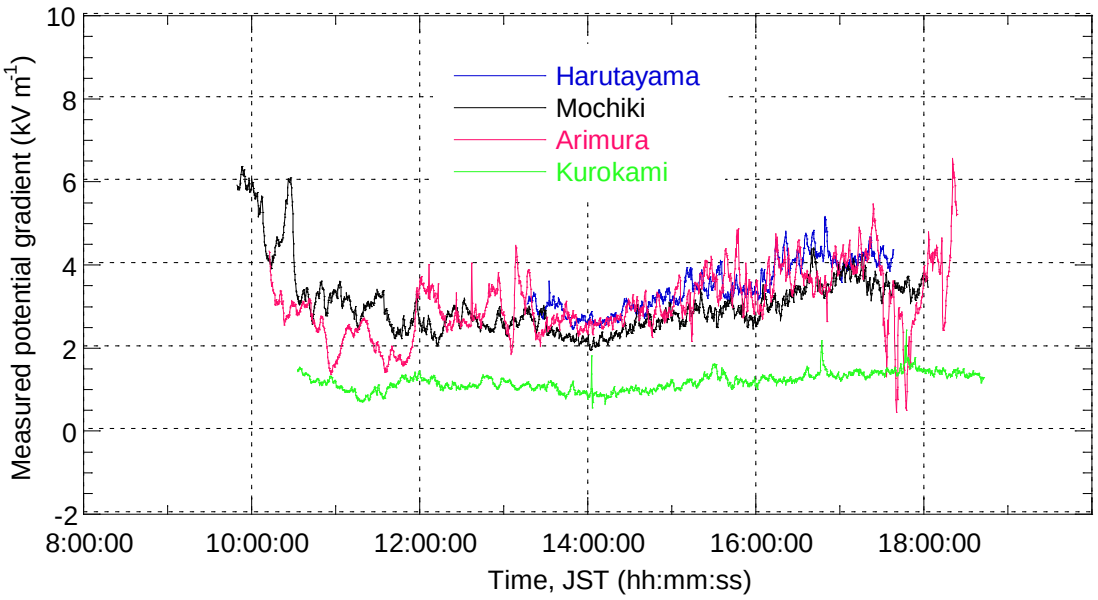

Figure 4.20 Atmospheric potential gradients, Sakurajima, 2 November, 1996.

Air temperature and relative humidity:

Harutayama	09:18	24°, 68 %	17:40	18°, 72 %
Mochiki	09:47	24°, 69 %	18:05	19°, 72 %
Arimura	10:10	25°, 65 %	18:26	21°, 65 %
Kurokami	10:30	27°, 59 %	18:45	20°, 71 %

Sky: Overcast start, but cleared by 08:00.

Equipment: No problems.

Plumes: Condensing gases only for most of the day. In the morning, the plume was to the north of Kurokami, but rotated clockwise during the afternoon until it was low over Arimura when the apparatus was collected. Some very light brown, ashy parts to the plume observed between 15:45 and 15:50.

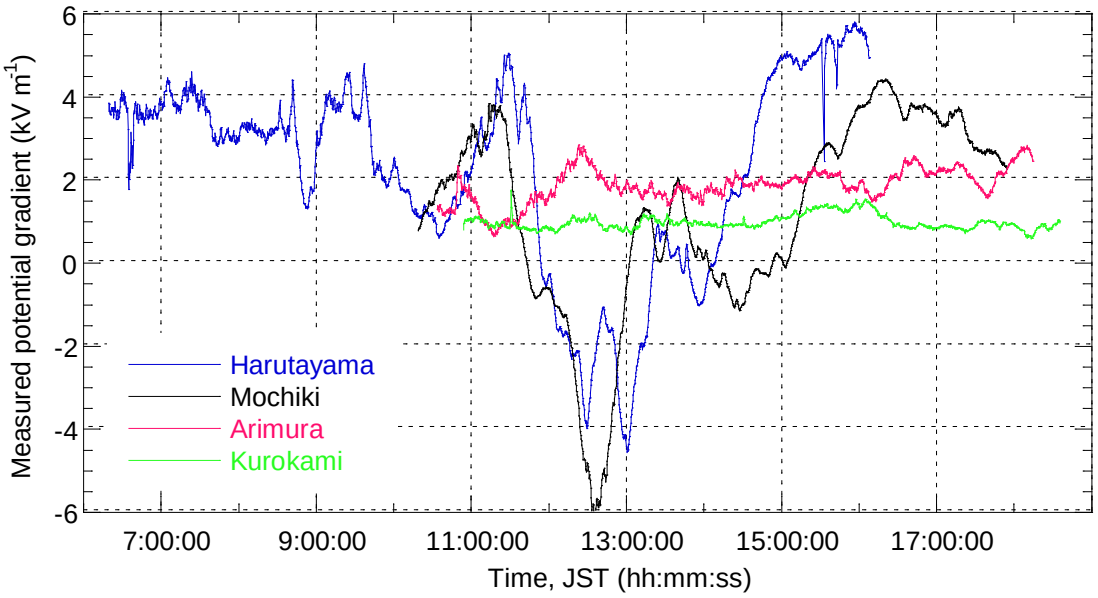

Figure 4.21 Atmospheric potential gradients, Sakurajima, 3 November, 1996.

Air temperature and relative humidity:

Harutayama	06:17	16°, 70 %	17:30	18°, 63 %
Mochiki	10:08	24°, 48 %	17:57	19°, 61 %
Arimura	10:31	28°, 40 %	18:17	19°, 70 %
Kurokami	10:51	27°, 46 %	18:37	18°, 79 %

Sky: Mainly clear sky with exception of some high altitude hazy cloud. Generally hazy, clearing by 15:00.

Equipment: Logger full at Harutayama on retrieval.

Plumes: Only condensing gases observed. Plume being blown between Arimura and Mochiki at 06:30. A small plume only, restricted to summit region was present between 10:00 and 11:00. Observations not possible for most of the day, so negative gradients recorded at 12:30 are unaccompanied by visual report. Video gave some evidence of ash production between 12:30 and 13:00.

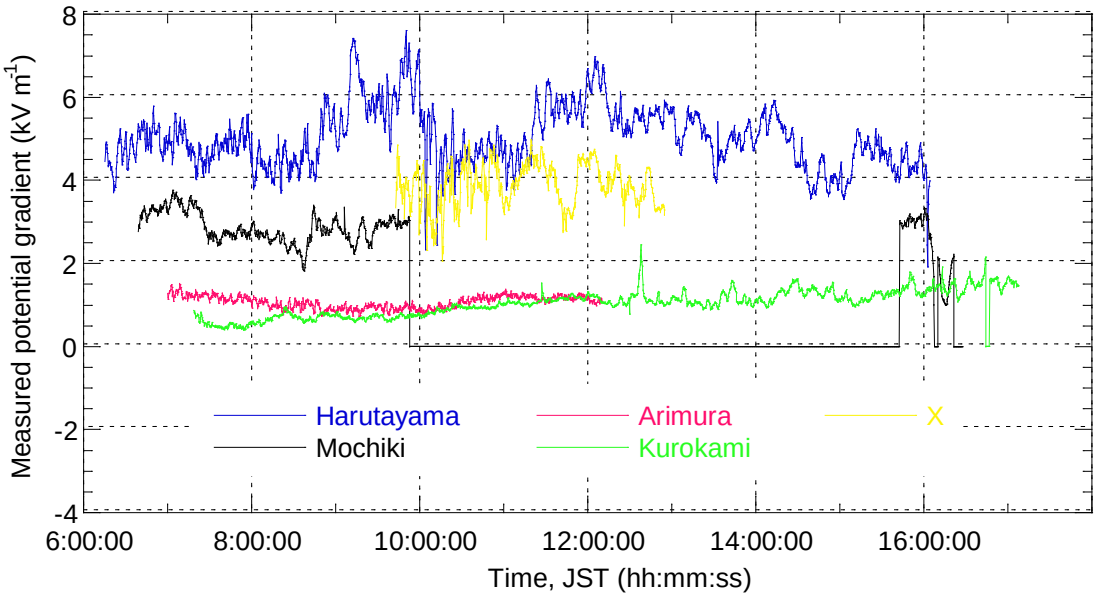

Figure 4.22 Atmospheric potential gradients, Sakurajima, 4 November, 1996.

Air temperature and relative humidity:

Harutayama	06:13	18°, 69 %	16:42	20°, 61 %
Mochiki	06:37	18°, 74 %	17:07	21°, 62 %
Arimura	06:58	19°, 67 %	17:26	23°, 58 %
Kurokami	07:17	18°, 71 %	17:44	20°, 73 %
X	09:40	24°, 58 %	13:00	27°, 60 %

Sky: ~40 % cover before 07:00, clearing to cloudless. ~5 % at 12:00 with some orographic cloud over the summit.

Equipment: Data loggers full at all fixed sites. Logging problem at Mochiki prevented data from being taken between ~10:00 and 15:30.

Plumes: Mainly condensing gases. White plumes observed through the orographic cloud at 07:24, 07:47, 07:58, 08:01 and 08:04. Wind direction from the summit, towards X. Heavy odour of SO_2 at X, at 09:30. Fairly vigorous production of white plumes from 10:00 to 12:40. Plumes observed to rise convectively up to about a kilometre above the vent. Further production of white plumes observed up to about 13:30. Very small ash-rich plume produced at 16:10, ascended less than a kilometre and was then blown low over Mochiki and Harutayama.

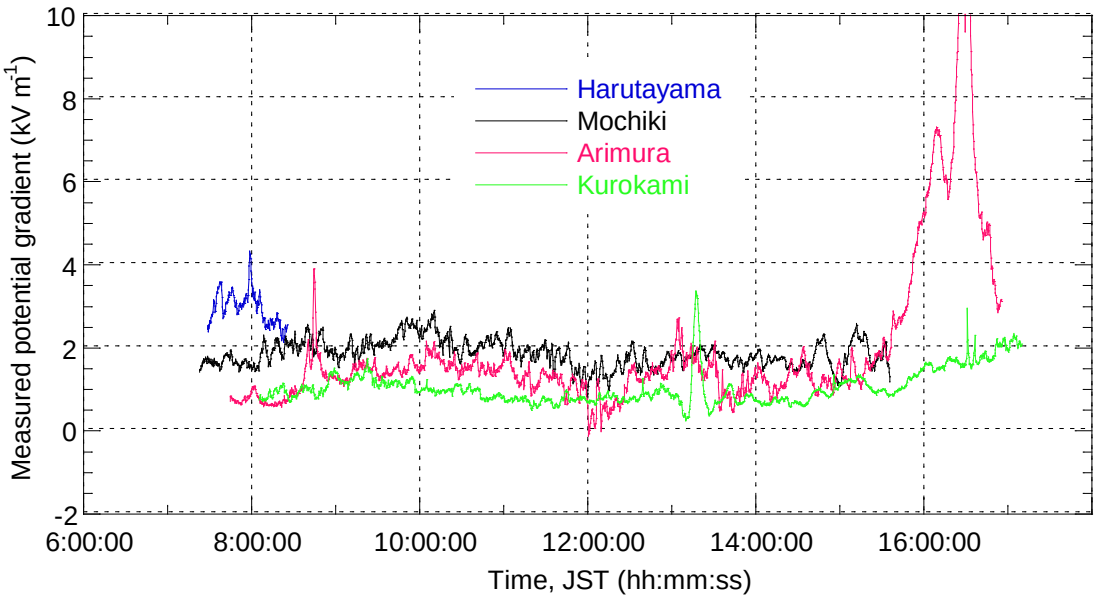

Figure 4.23 Atmospheric potential gradients, Sakurajima, 5 November, 1996.

Air temperature and relative humidity:

Harutayama	06:53	19°, 80 %	16:17	22°, 77 %
Mochiki	07:20	19°, 81 %	16:40	23°, 74 %
Arimura	07:42	21°, 77 %	16:59	24°, 77 %
Kurokami	08:03	22°, 78 %	17:17	23°, 79 %

Sky: Clear start, some high altitude cloud forming at 10:00. Cloud cover increased rapidly at 15:00, covering summit by 16:00.

Equipment: Mochiki site lost power at about 15:30. Logger problem at Harutayama prevented data from being recorded for most of the day.

Plumes: Mainly condensing gases observed, but video showed eruption of particle-rich plume at 13:10. Wind dispersed plume to the north for most of the day. Higher portions of the plume taken east due to wind shear. Plume from explosion at 13:10 blown east-northeast.

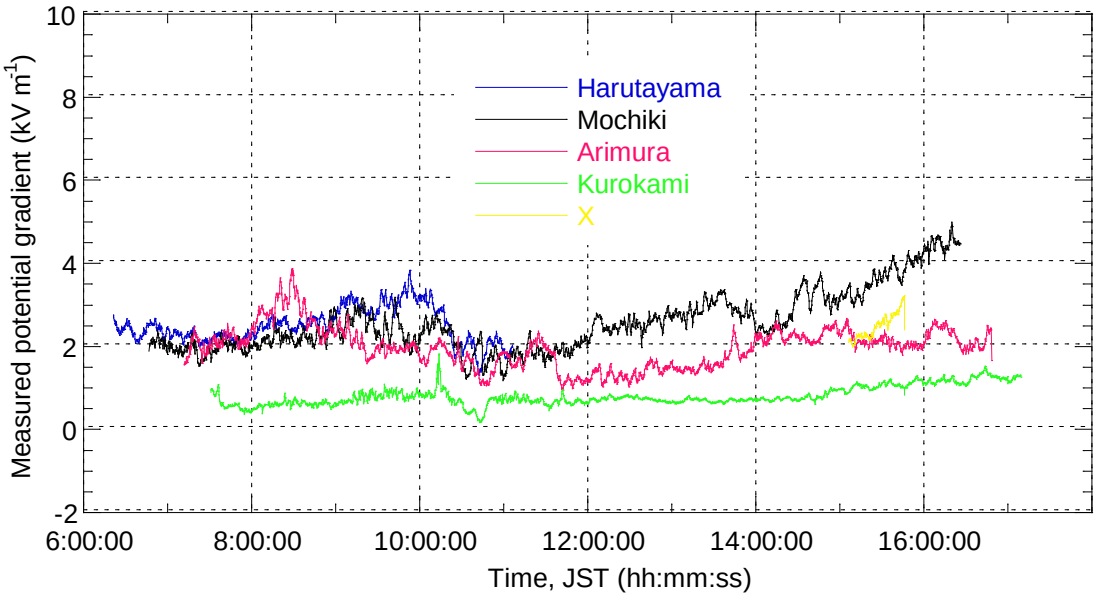

Figure 4.24 Atmospheric potential gradients, Sakurajima, 6 November, 1996.

Air temperature and relative humidity:

Harutayama	06:19	19°, 82 %		
Mochiki	06:44	20°, 79 %	16:28	21°, 52 %
Arimura	07:07	21°, 80 %	16:51	20°, 56 %
Kurokami	07:28	21°, 82 %	17:12	19°, 62 %
X	15:03	23°, 44 %	15:49	23°, 44 %

Sky: Overcast start, cloud lowering to obscure summit by 09:00. Cleared at 12:00 to produce cloudless conditions.

Equipment: Harutayama site lost power at about 11:00.

Plumes: Condensing gases only. During the morning, a small plume was being blown towards Arimura. Plume decreased in size until about 15:00 when virtually no plume was visible and the wind had rotated to the northeast. Wind decreased and, when apparatus was collected, only a small plume was visible vertically above the vent.

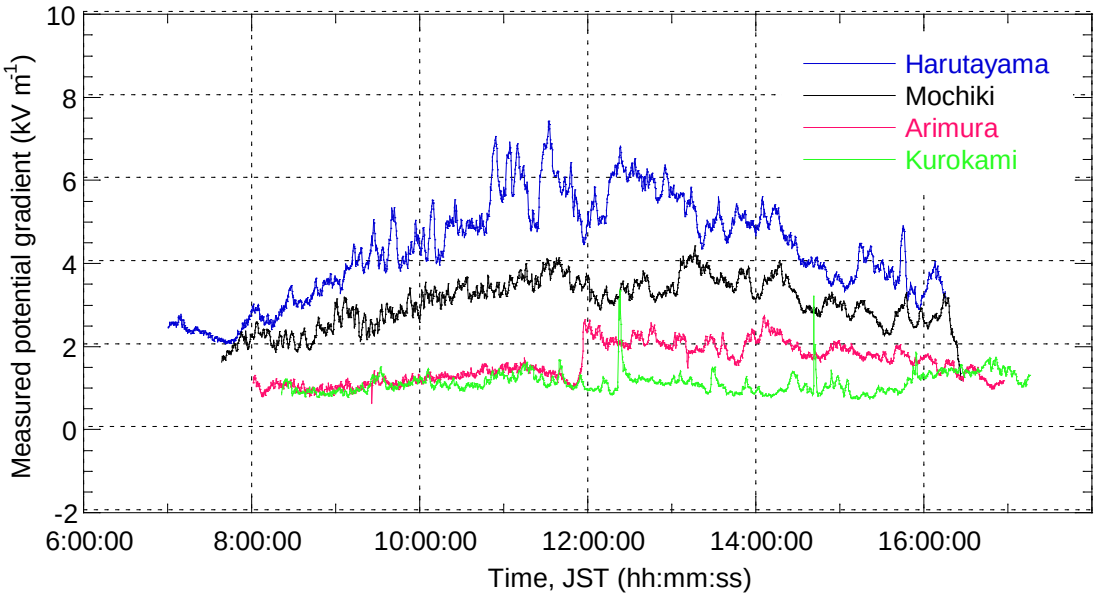

Figure 4.25 Atmospheric potential gradients, Sakurajima, 7 November, 1996.

Air temperature and relative humidity:

Harutayama	06:58	12°, 73 %	16:10	21°, 61 %
Mochiki	07:36	16°, 64 %	16:39	19°, 68 %
Arimura	07:58	17°, 60 %	17:01	21°, 64 %
Kurokami	08:19	17°, 65 %	17:24	19°, 70 %
W	10:35	25°, 44 %	14:22	27°, 40 %
T	14:33	25°, 48 %	17:30	19°, 71 %

Sky: Clear start, high altitude cloud forming after 10:00 to give 100 % cover for the afternoon.

Equipment: Mochiki site on low power when equipment was retrieved.

Plumes: Condensing gases only. Small plume observed being blown to the north between 07:00 and 11:30. Wind direction gradually changed and plume rotated round to the northeast. Elongate plume dispersed over W at 14:45.

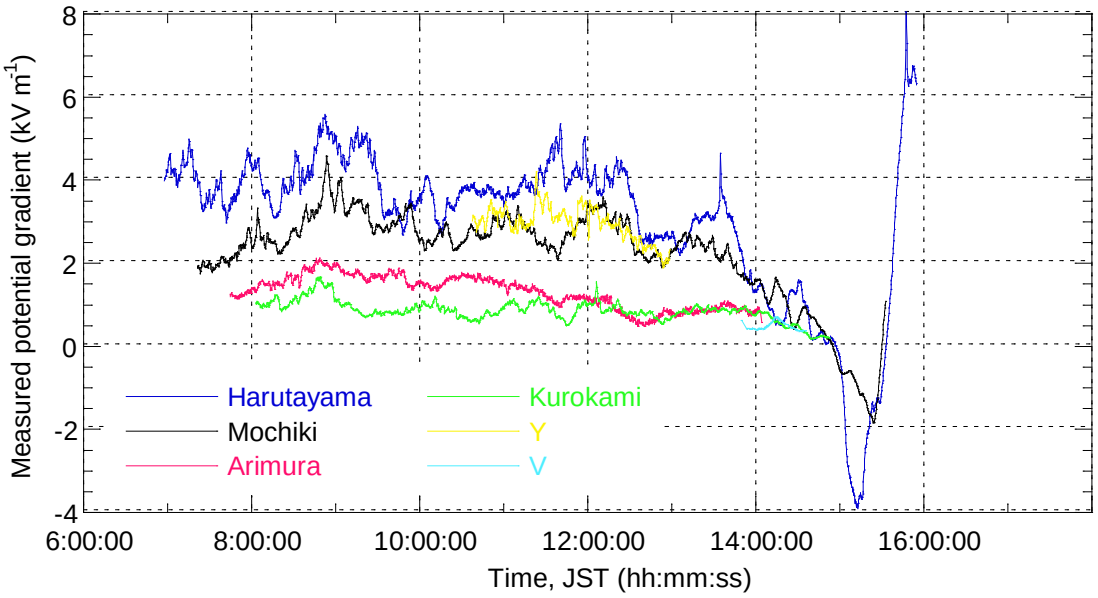

Figure 4.26 Atmospheric potential gradients, Sakurajima, 8 November, 1996.

Air temperature and relative humidity:

Harutayama	06:55	19°, 70 %	16:00	
Mochiki	07:20	20°, 68 %	15:35	
Arimura	07:42	20°, 71 %	15:16	23°, 67 %
Kurokami	07:01	21°, 71 %	14:56	22°, 70 %
Y	10:35	24°, 66 %	13:00	22°, 65 %
V	13:46	27°, 60 %	14:39	23°, 67 %

Sky: Overcast, began to rain at 15:15.

Equipment: Arimura site lost power at about 14:00. Zero offsets not recorded during equipment collection due to the rain.

Plumes: Condensing gases only. Small plume being blown north as equipment was being set out. Decreased in size to small, discrete puffs by 10:00.

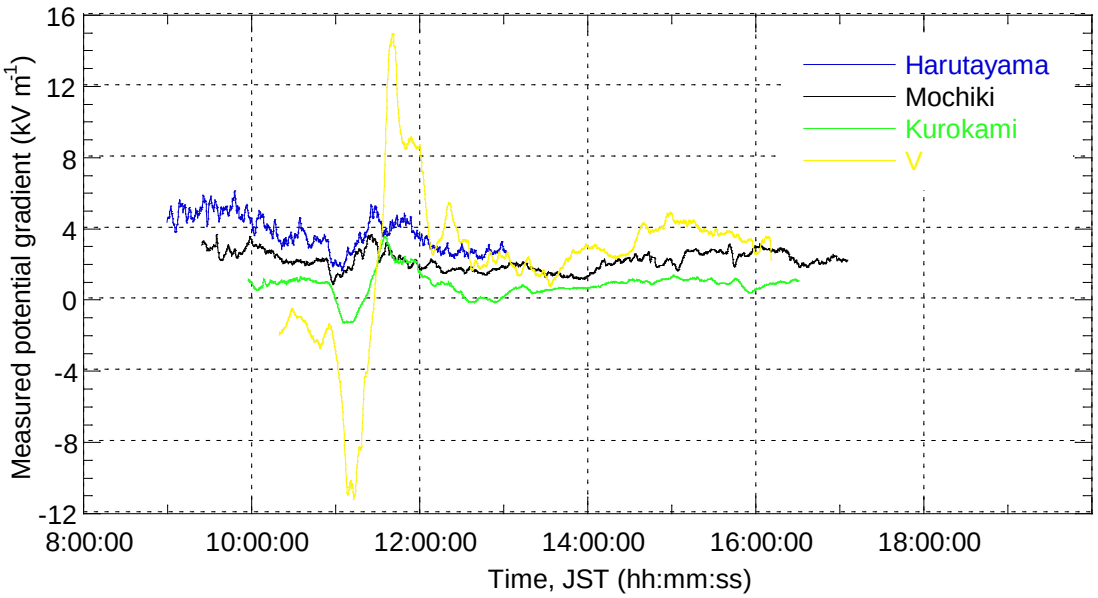

Figure 4.27 Atmospheric potential gradients, Sakurajima, 9 November, 1996.

Air temperature and relative humidity:

Harutayama	08:57	24°, 76 %	17:25	24°, 76 %
Mochiki	09:22	25°, 67 %	17:06	25°, 67 %
Kurokami	09:55	27°, 64 %	16:31	27°, 64 %
V	10:17	29°, 65 %	16:13	24°, 78 %

Sky: Overcast with low cloud initially, clearing steadily, but overcast most of the day.

Equipment: Harutayama site lost power at about 13:00.

Plumes: Gentle emission of dirty brown coloured plumes indicating some ash component in plumes still dominated by condensing gases. Light brown plume ascended, dispersed north-northeast, between V and Y at 10:41. The more ash-rich portions of the plume rose higher, and dispersed just to the east of V. Dirty brown coloured plume produced at 10:59. Further slightly ash-rich plumes produced were fanned out by wind shear. More ashy portions dispersed to the east of the rest of the plumes. Dirty brown plume present between V and W at 11:11.

At 11:35, some light ashfall was visible within 2 km of the vent, with cloud obscuring the summit region. Little ash

Figure 4.27 continued..

production visible by 11:39. A lightly ashy plume seen heading for V at 11:48. An ashy plume over V at 12:01, but no ashfall. General decrease in apparent ash proportion in plume being produced and low cloud started to obscure white plumes. Some extremely light ashfall at V, at 13:10. Cloud base lifted by 15:00 and a small white plume was blown towards Kurokami.

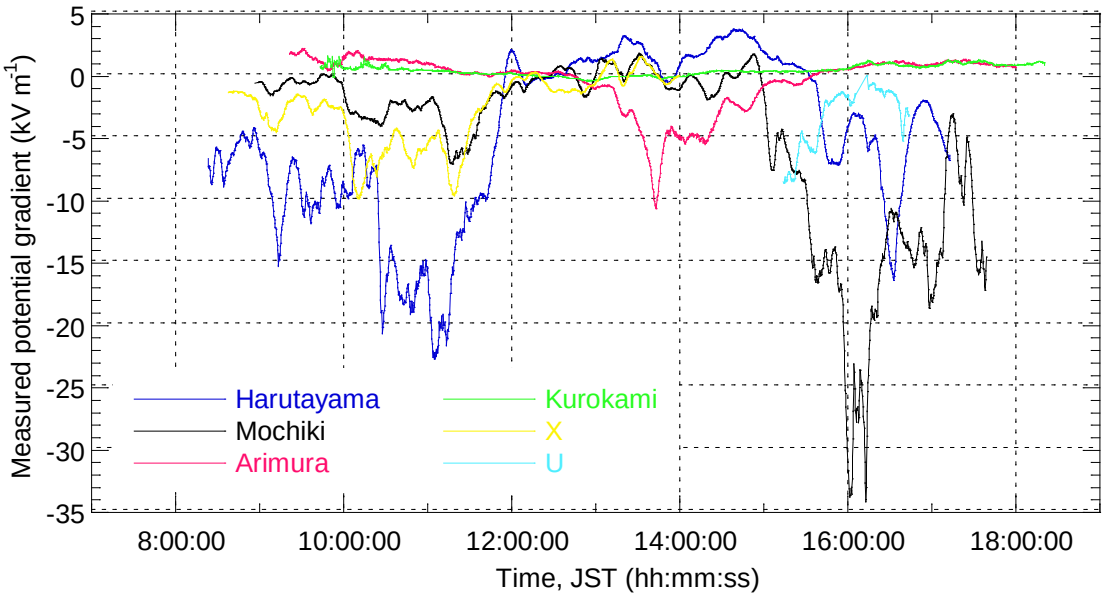

Figure 4.28 Atmospheric potential gradients, Sakurajima, 10 November, 1996.

Sky: Overcast but no precipitation.

Equipment: No temperature or relative humidity measurements due to equipment failure.

Plumes: Near-continuous emission of light brown coloured plumes of condensing gases, indicating some particulate content. A light brown plume, mainly over the crater between 8:40 and 10:15. Increasing wind speed dispersed plume over Harutayama at 10:30. Evidence for light ashfall at Harutayama since 8:30. Plume over X at 11.15, but very light ashfall at Harutayama at 11:38. Cloud obscured summit area between 11:50 and 13:00, with more light ashfall at Harutayama at 12:09. A vertical, diffuse, light brown plume over the crater at 13:00. An increasing wind appeared to disperse plume towards Arimura and Mochiki at 13:10. By 13:20, complex wind shear to be separated plume into a more particle-rich portion (dispersed over Arimura) and a higher altitude, particle-poor portion (dispersed towards Harutayama). A light brown plume between U and Mochiki at 15:00. From 15:15 to 16:20, variously

Figure 7.28 continued..

coloured (between white and light brown) plumes produced and dispersed intermittently between U and Mochiki. Wind direction gradually changed to bring plume over Mochiki. Light brown portion of the plume over Harutayama at 16:30. On collection of the apparatus at Mochiki (17:40) there was evidence that some light ashfall had occurred during the day.

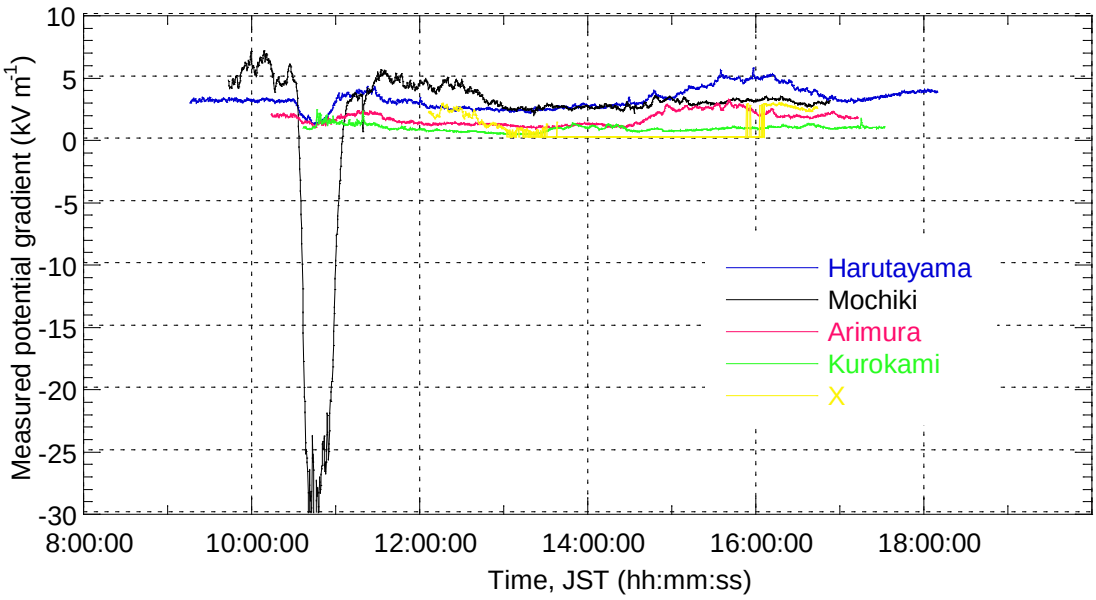

Figure 4.29 Atmospheric potential gradients, Sakurajima, 12 November, 1996.

Sky: Overcast, clearing by 11:00, cloudless at 12:00.

Equipment: LogIT problem prevented data being taken from mobile unit for most of the day.

Plumes: Mainly condensing gases. Plume blown over X, with the summit obscured by low cloud at 08:24. Crater observed to be full of slightly ashy steam (light brown) 10:22. Plume did not rise much out of the crater, but was blown towards Mochiki. Generally reducing ash content in plume between 11:10 and 12:00, when there was very little plume visible at all. Between 12:00 and 13:00 an intermittent roaring sound was produced by the volcano, accompanied by varying intensity ash-free plumes of condensing gases. Plume rotated slightly to pass between X and U at 13:10. Roaring sound accompanied by reasonably vigorous emission of white plume at 14:43. Plume was blown towards X, overhead at 14:47. From 15:00 until collection of the network; periodic emission of variously sized white plumes continued.

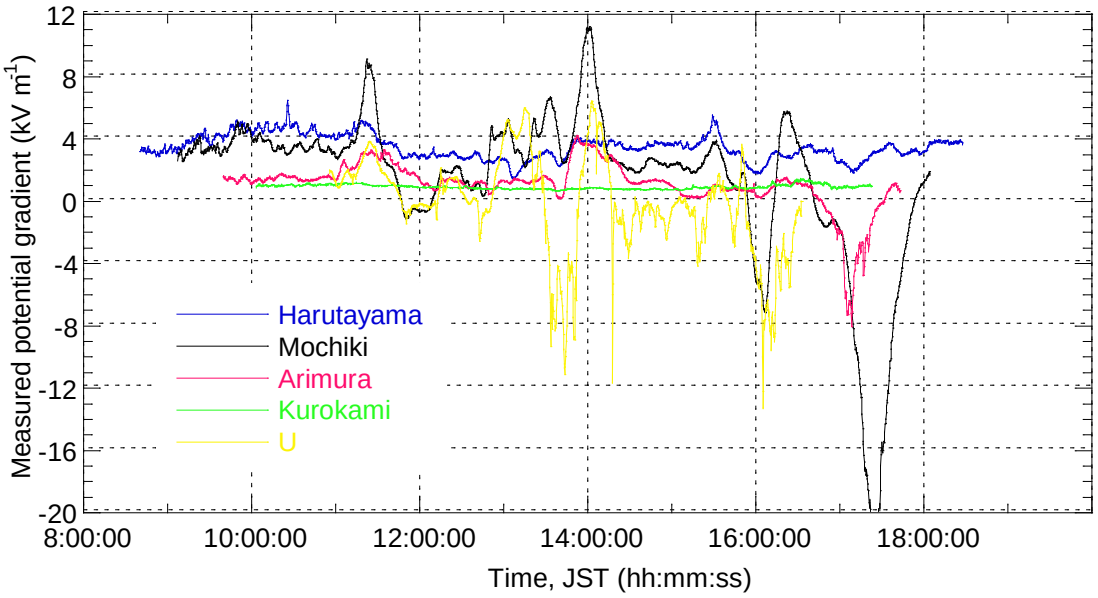

Figure 4.30 Atmospheric potential gradients, Sakurajima, 13 November, 1996.

Sky: Cloudless.

Equipment: No problems.

Plumes: Mainly condensing gases, variable ash component. White plume blown over U between 08:00 and 09:00. A light brown plume produced at 10:56. Very light ashfall at U between 11:04 and 11:23. Plume then returned to white colour (condensing gases only). Plume increased in ash component between 11:45 and 11:49, and was blown between U and Mochiki. Fairly continuous emission of light brown plumes of varying intensity. Further gentle ashfall at U, at 13:19. Ash-poor part of plume observed to be blown slightly further north, between U and Arimura. Fallout of sub-millimetre dry, spherical, aggregates at U between 13:40 and 13:46. Variable amounts of light ashfall at U between 14:08 and 14:29. Plume being swung around by varying wind directions, but generally close to U. Gentle, ashy emissions, varying in intensity and ash content, produced up to 16:30. Very light ashfall at U between 15:40 to 16:08. White plume observed to be over Arimura at 16:50, with light brown plume approaching Arimura.

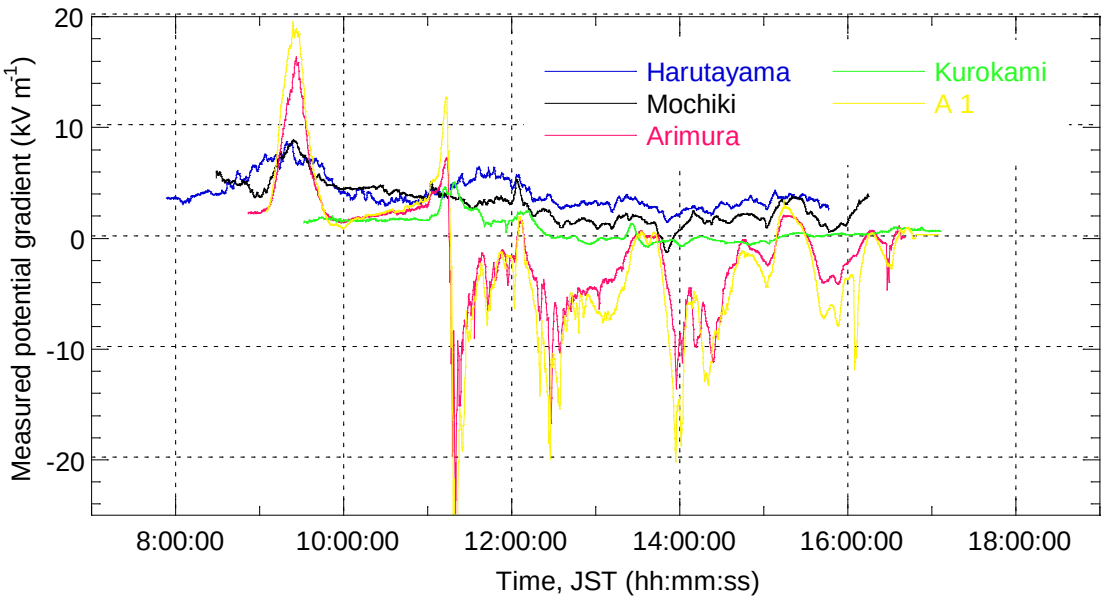

Figure 4.31 Atmospheric potential gradients, Sakurajima, 14 November, 1996.

Sky: Cloudless.

Equipment: No problems.

Plumes: While network was being installed, a white plume of condensing gases was blown between Mochiki and Arimura. Small amount of ash produced at 09:06, decreasing at 09:20. By 09:50, plume again consisted only of condensing gases. Small Vulcanian explosion produced particle-rich plume at 11:00. Several ashy 'bursts' produced over the next 5 minutes. Ash emission practically stopped by 11:07. Most of ash plume blown slightly north of Arimura. Ash overhead at site A 1, at 11:10, with ashfall between 11:13 to 11:21. Some of the plume observed to have been blown north towards Kurokami at 11:50. Emission of plumes with very low ash content continued. Plumes blown over Arimura.

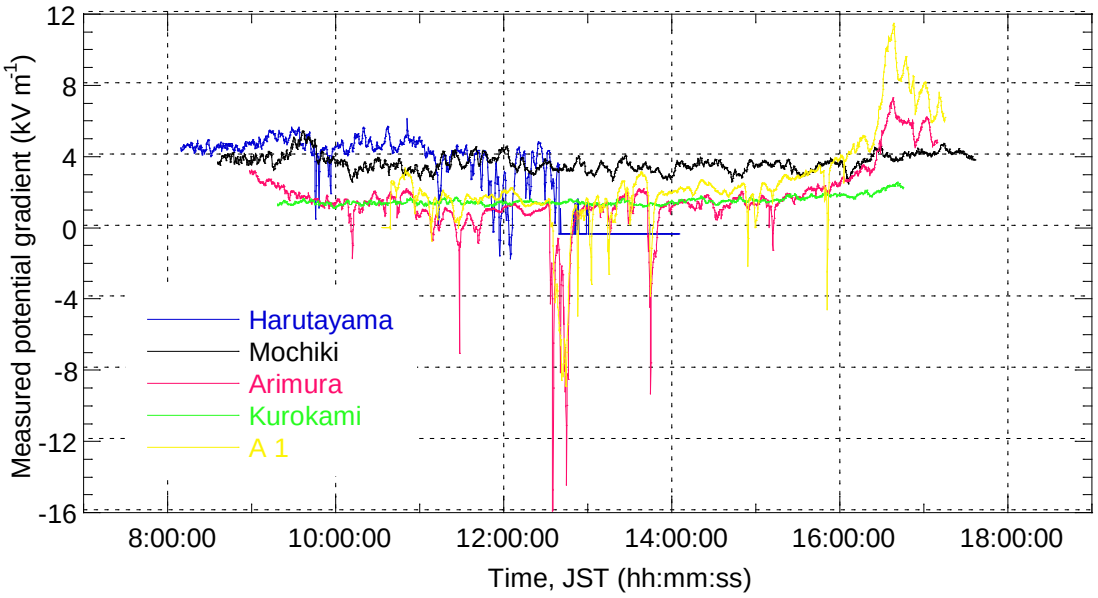

Figure 4.32 Atmospheric potential gradients, Sakurajima, 15 November, 1996.

Sky:	~5 to 10% cloud cover, increasing slightly in the afternoon.
Equipment:	Harutayama site lost power at about 12:30.
Plumes:	Condensing gases only. Windy conditions, blowing the plume fairly constantly over Arimura. Wind raising ash at the Arimura sites.

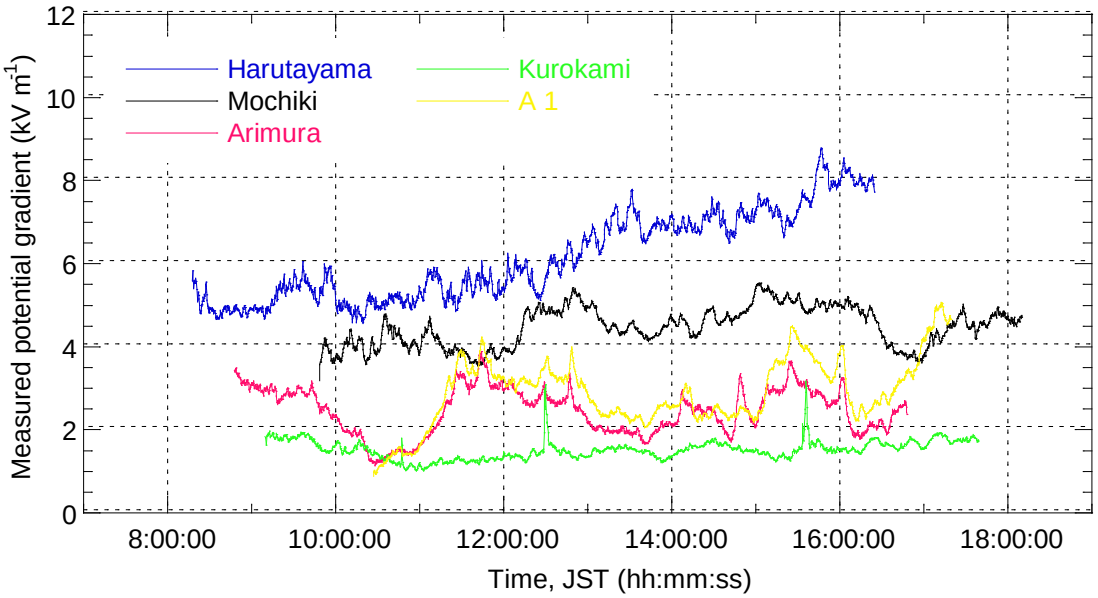

Figure 4.33 Atmospheric potential gradients, Sakurajima, 16 November, 1996.

Sky:	Cloudless.
Equipment:	Arimura site lost power at about 16:45.
Plumes:	Mainly condensing gases. Before 09:00, only very small plume observable. Increased slightly after 09:00, blown over Arimura. Larger white plumes produced at 11:54, 12:20 and 12:43. Small detonation heard at 13:29, very light brown plume produced. Very lightly ashy plume overhead at Arimura at 13:33, emission of just white plumes again. Decrease in visible plume production at 14:20.

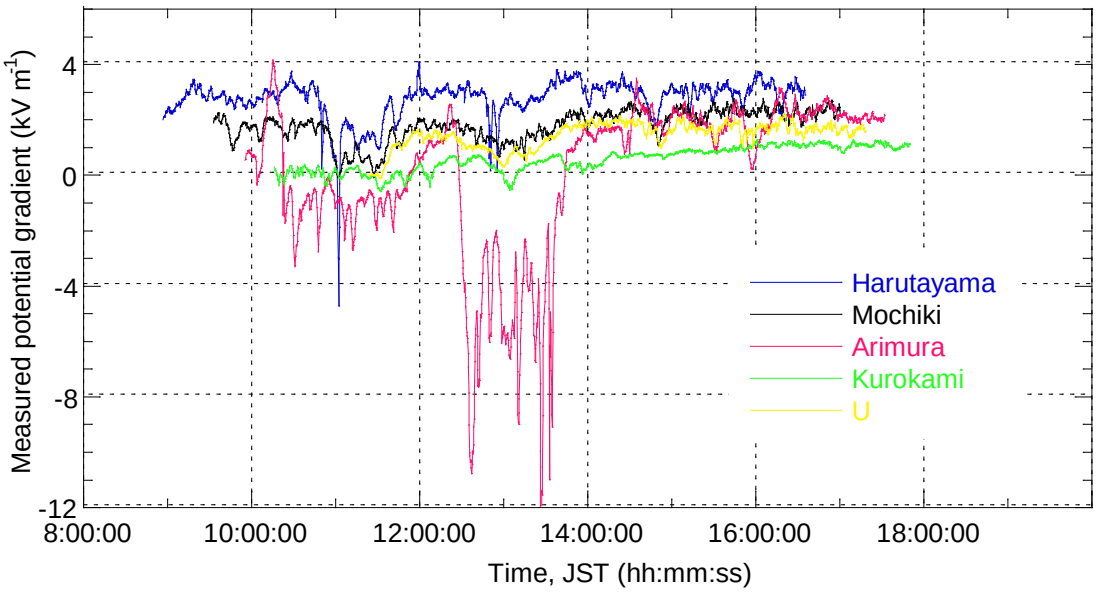

Figure 4.34 Atmospheric potential gradients, Sakurajima, 18 November, 1996.

Sky:	Overcast, low cloud at about the summit altitude.
Equipment:	No problems.
Plumes:	Mainly condensing gases, blown in the direction of Arimura all day. Visibility obscured by low cloud until about 11:30. At 12:23, plume production increased after period of relative quiescence. Visibility at A 1 reduced by the plume being blown to the ground. At 12:37, occasional ash particle deposited at A 1, with the plume still on the ground, obscuring the volcano and producing SO_2 odour. Plume lifted off the ground at 12:45. Plume on the ground at A 1 again between 14:25 and 14:55. During equipment collection, a small plume extended over Arimura.

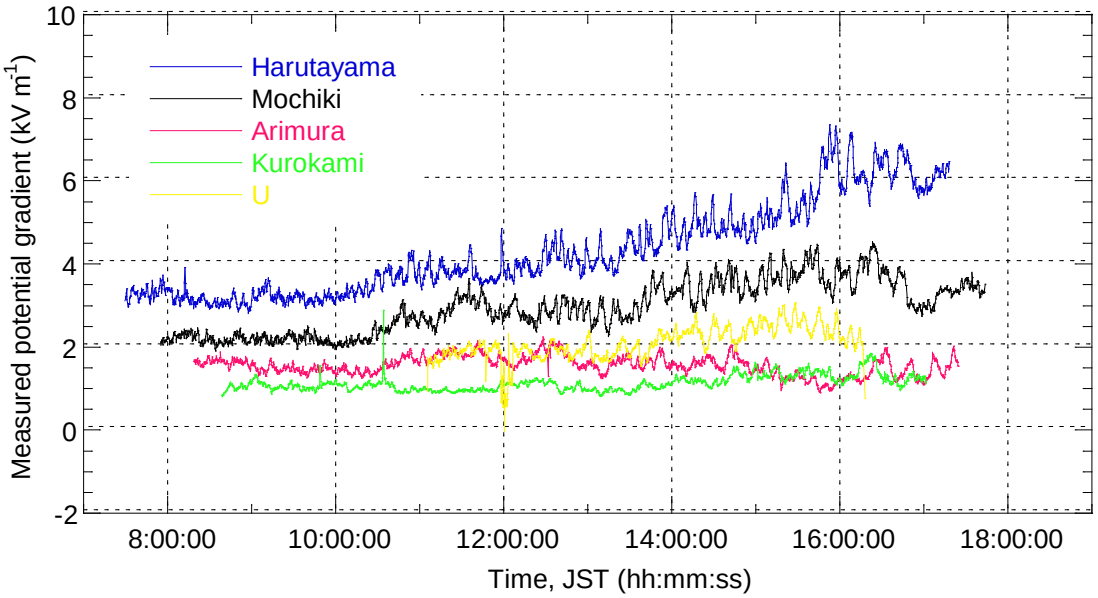

Figure 4.35 Atmospheric potential gradients, Sakurajima, 19 November, 1996.

Air temperature and relative humidity:

Sky: Morning overcast, clearing by 11:00 to cloudless sky.

Equipment: Logger full at Harutayama site. Between 12:00 and 12:05, equipment at U being inspected by SABO (civil engineering) workers.

Plumes: Condensing gases only, plumes of variable intensity. Up to 11:30, plume blown over Arimura. Then rotated to U, and remained between U and Arimura for remainder of monitoring period.

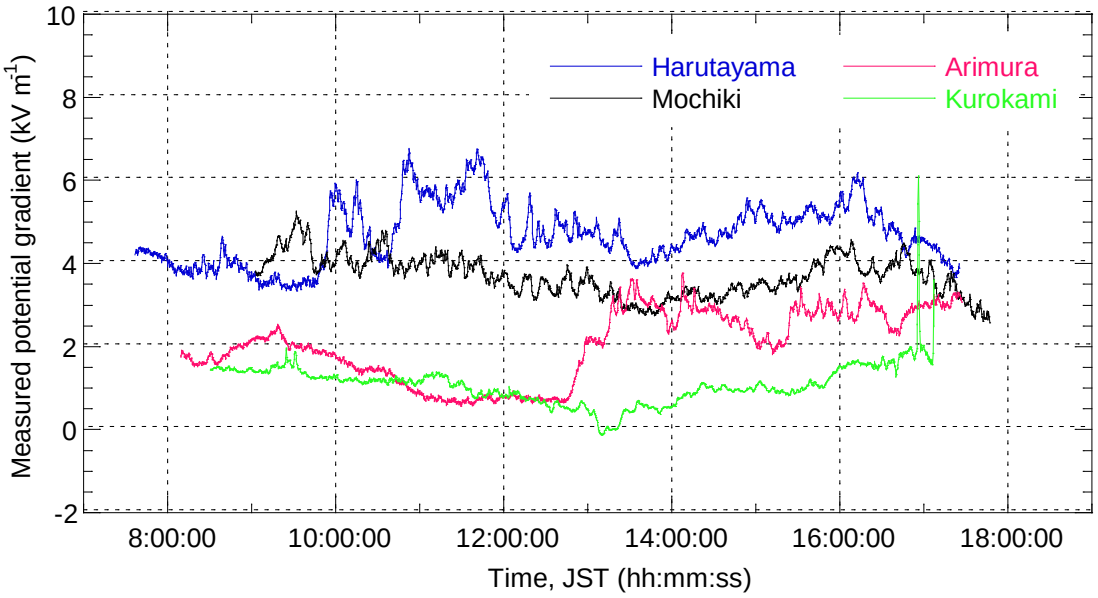

Figure 4.36 Atmospheric potential gradients, Sakurajima, 20 November, 1996.

Air temperature and relative humidity:

Harutayama	07:35 9°, 45 %	16:10 12°, 45 %
Mochiki	08:07 12°, 58 %	16:39 13°, 48 %
Arimura	08:28 13°, 53 %	17:01 15°, 45 %
Kurokami	09:00 15°, 50 %	17:24 15°, 46 %

Sky: Started clear, at 15:00 about 5 % cloud cover, increasing later from the west at 16:00.

Equipment: Logger full at Harutayama.

Plumes: Condensing gases only. Observations from 15:00 onwards only. Loud rumblings preceded production of a dense white plume over 1000 m in height at 16:40. Evidence for very light ashfall of relatively coarse ash (greater than 0.1 mm in diameter) at Kurokami earlier on during the day, with an approximate number density of 1 particle cm^{-2}. Plume created by 16:40 event overhead at Kurokami at 16:52.

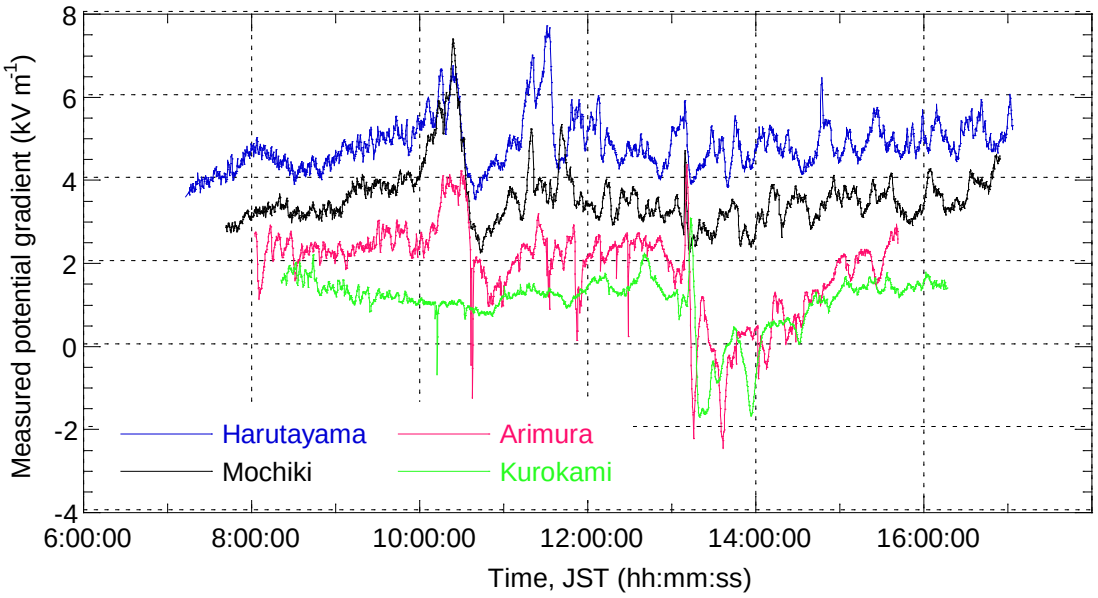

Figure 4.37 Atmospheric potential gradients, Sakurajima, 21 November, 1996.

Air temperature and relative humidity:

Harutayama	07:14	14°, 47 %	17:05	20°, 50 %
Mochiki	07:40	16°, 47 %	16:19	21°, 52 %
Arimura	08:00	18°, 47 %	16:44	20°, 56 %
Kurokami	08:19	19°, 47 %	15:45	21°, 45 %

Sky: ~10 % cloud cover, increasing to ~40 % by 12:00, then decreasing again.

Equipment: When equipment was collected, Harutayama logger was full.

Plumes: Mainly condensing gases.

During the morning, exclusively white plumes, of variable strength, being blown between Arimura and Kurokami. Generally windy conditions. Light brown plume close to Arimura at 13:11. Production of plume not observed. Ashfall visible on upper slopes of volcano at 13:13. At 13:16, ashfall to the north of Arimura, and continuing gentle emission of light brown plume containing low concentrations of ash. Much less ash being produced by 13:50, with no ash visible in plume by 14:00.

4.6 Interpretation and modelling

The data recorded and shown in Figures 4.7 to 4.37 demonstrate potential gradient variations with a wide range of wavelengths. In order to understand the perturbations produced by a plume it is essential to be able to discern them from other changes in the atmospheric potential gradient.

4.6.1 Background potential gradients

The data recorded on 21 October (Figure 4.11) represent a relatively noise-free example of the average potential gradients present at the sites during fair-weather conditions. The highest gradients were measured at Harutayama due to the topographically enhanced electric field. The exposed position at Harutayama also produced a high amplitude of noise, probably as a result of wind-blown dust. Lower amplitude gradients were recorded at Arimura and Kurokami. The consistently low potential gradients recorded at the Kurokami site are the result of the surrounding vegetation. The Arimura values are close to +2 kV m^{-1}, which represent actual ground-level potential gradients of about +100 V m^{-1} (the value often quoted for the fair-weather potential gradient). Data from Mochiki represent intermediate values between those of Harutayama and Arimura, reflecting the intermediate amount of exposure at the site. Note that precipitation can change the recorded background atmospheric potential gradients. Due to the equipment being retrieved if rain were likely, only one data set (8 November, Figure 4.26) was collected during which the effect of rain can be observed. The weather is thought to be the cause of the positive and negative perturbations recorded after approximately 15:30. Clearly, the effect of bad weather

on monitoring capabilities would have to be investigated if a permanent array were constructed.

It is believed that wind was the primary source of the high levels of noise often recorded at the Harutayama site. Gusts of wind produce perturbations of the natural atmospheric field by generating raised dust. Depending on the strength and extent of the wind, this can produce local noise (as observed in the data from Sakurajima) or large perturbations, as have been observed during dust storms (Kamra, 1969a, b). Space charges created by the dispersion of dust into the air have also been detected in the laboratory (Kamra, 1973).

As an example of the effect of wind on the measured potential gradient at Arimura, Figure 4.38 shows data recorded on still and windy days. The windy day was 21 November, with noticeably gusty conditions at 11:30 to 11:35, 11:50 and 12:30, during which dust was observed to be raised in areas close to the fieldmeter. These times were closely correlated with sharp decreases in the measured potential gradient, indicating the presence of negative charge in the atmosphere. The potential gradient technique is very sensitive to space charge close to the sensor (Chalmers, 1967), so even a small amount of charged dust close to the apparatus can easily be detected. Negative perturbations of the atmospheric electric gradient as a result of wind-blown ash have also been recorded by Kikuchi and Endoh (1982).

4.6.2 Comparison of mobile and fixed site data

In order to confirm that the amplification factor was identical (or similar) for the different styles of fieldmeter mounting, data were collected at the Kurokami site with the mobile apparatus placed 1 m from the fixed apparatus. The results, shown in Figure 4.39, show excellent agreement for the majority of the data. The reduced

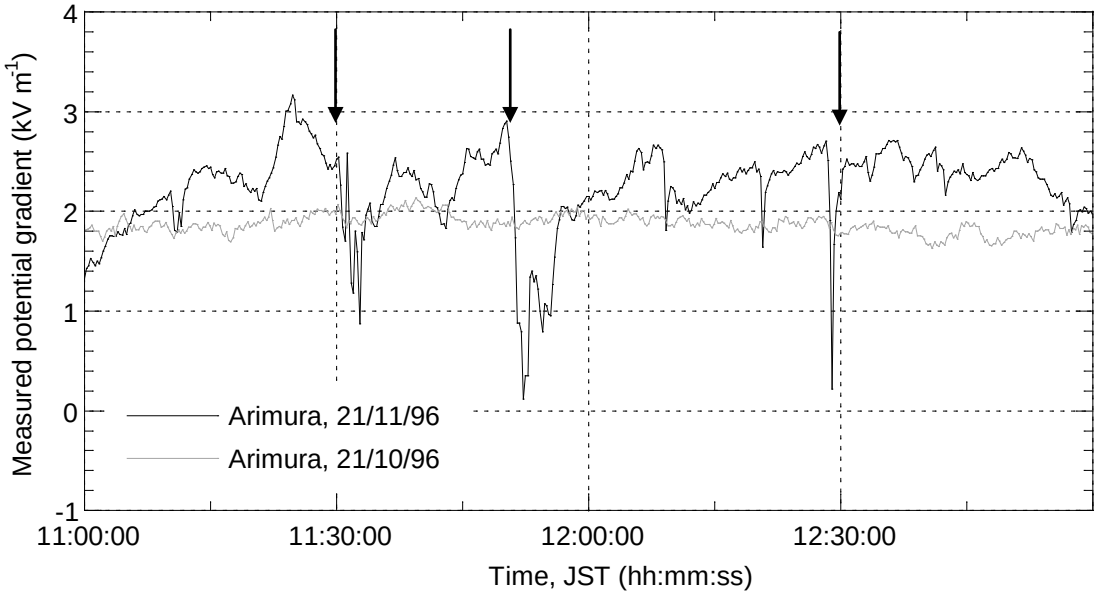

Figure 4.38 The effect of wind on potential gradient measurements. Data taken over two days are shown, on 21 November (black trace), during gusty conditions, and on 21 October (grey trace), during still conditions for comparison. The arrows indicate periods of particularly gusty conditions on 21 November, during which, dust was observed to be raised in the area close to the apparatus.

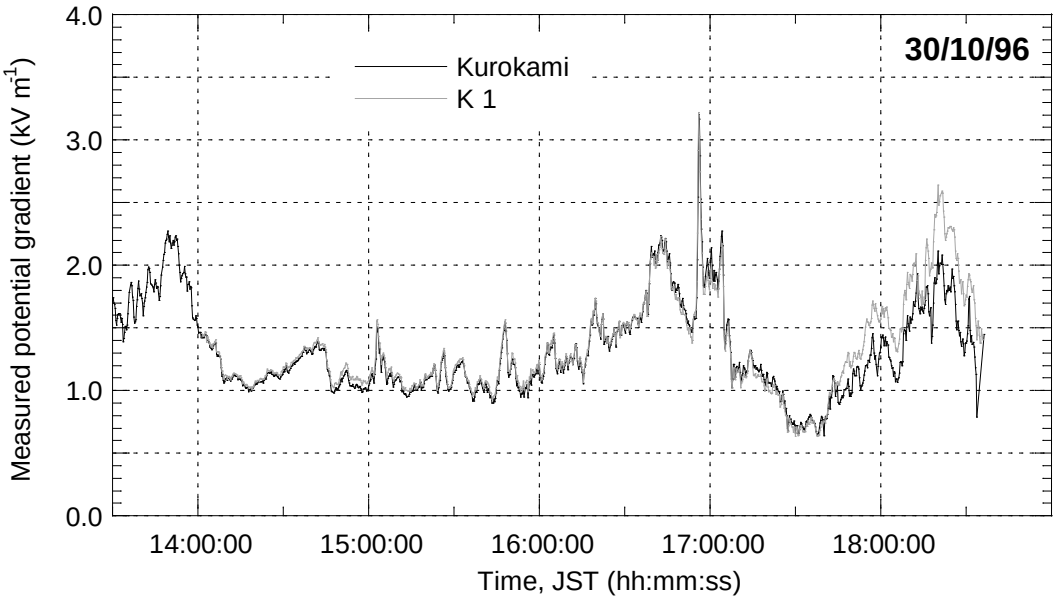

Figure 4.39 Comparison of data collected by a fixed site and the mobile apparatus. The mobile apparatus (grey trace, designated K 1) was located 1 m away from the fixed apparatus at Kurokami (black trace). The different sets of equipment produced similar results up to about 17:30, after which data from the fixed apparatus recorded reduced values. This was a direct effect of decreasing battery power at the fixed site.

potential gradients recorded by the fixed site towards the end of the test are a result of low battery power. The correlation observed also indicates that any noise produced within the apparatus was minimal, and that recorded variations in the potential gradient are not localised to less than a metre around the apparatus.

Further tests were carried out in an attempt to observe any decrease in the correlation of results between two sites as the distance between them increased. The results are given in Figure 4.40, and show few differences up to separation distances of 35 m. Thus, variations of the potential gradient (recorded during 'average' weather conditions) are not due to noise in the apparatus or charges localised to within a few tens of metres of the apparatus.

4.6.3 Perturbations due to particulate volcanic plumes

The variety of plumes produced over the monitoring period included several which were dominated by condensing gases, but which also had a particulate component. Although plumes of condensing gases alone were white in colour, the low concentration of particles produced a light brown colour. In general, these plumes were not energetically emplaced, and rose from the crater at similar velocities to plumes of condensing gases alone. Examples of these low concentration, particle-laden plumes were produced on 2, 3, 9, 10, 12, 13, 16, 18, and 21 November. Most of these produced perturbations at one monitoring site, all of which were of negative polarity. During light ashfall, the negative perturbations were of sufficient amplitude to reverse the natural potential gradient. The near-continuous emission of a lightly-particulate plume between approximately 10:00 and 17:00 on 10 November is discussed further in section 4.6.4. Although these lightly-particulate plumes appeared to be relatively easy to detect with the fieldmeters, white plumes of condensing gases

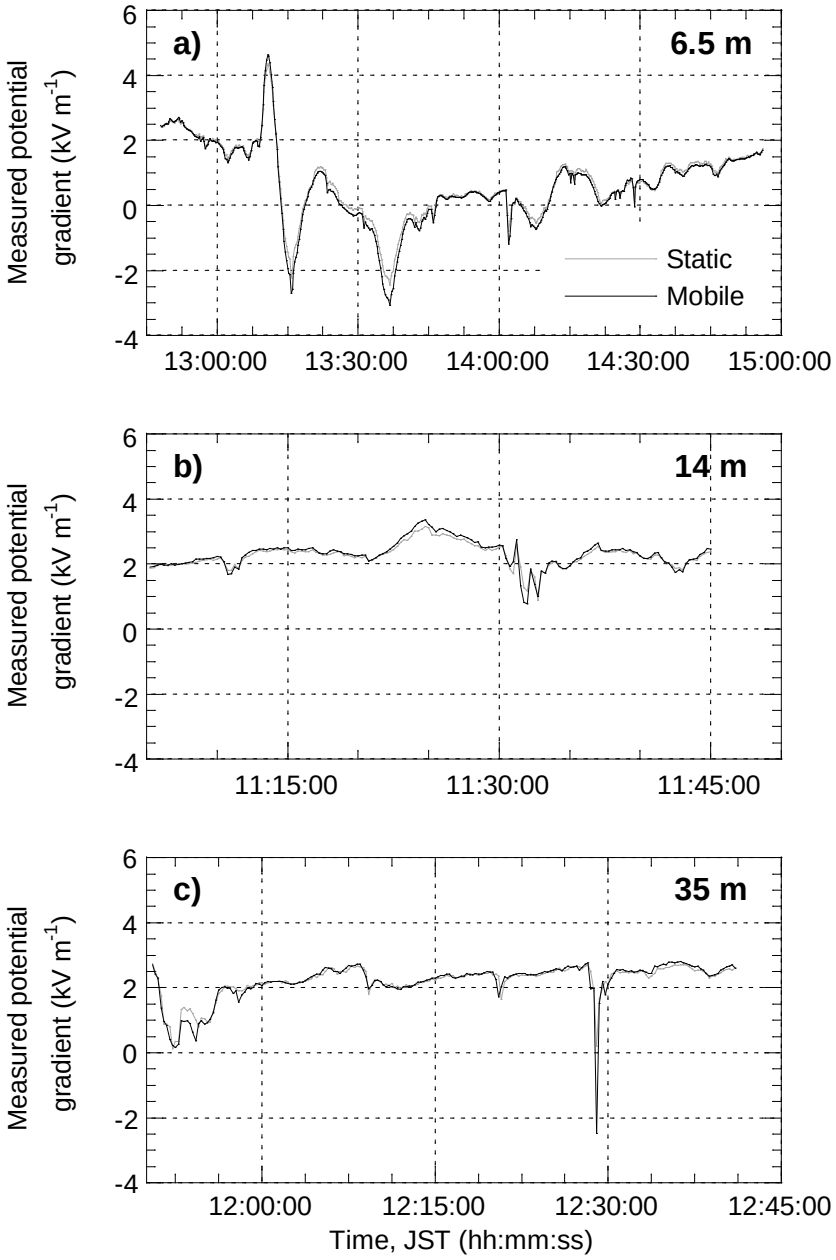

Figure 4.40 Correlation of the potential gradients recorded at two sites. Data collected by the fixed apparatus at Arimura (grey lines) are plotted along with data collected by the mobile apparatus (black lines) for different values of separation distance between the two fieldmeters. Even though the data were recorded on a windy day (producing the negative perturbations), little decrease in the correlation can be observed up to separation distances of 35 m.

alone never produced detectable perturbations of the potential gradient. This is in line with the results of Lane and Gilbert (1992), who also detected particle-rich plumes but could not detect condensing gases.

Over the monitoring period, only three particle-rich plumes produced by Vulcanian explosions were observed. These occurred on 4, 5 and 14 November. Dispersal directions of these plumes (as indicated by the ash deposition) are given in Figure 4.41. The 4 November plume was very small and ascended to a maximum altitude of only ~1720 m a.s.l. (~720 m above the crater). It was dispersed to the west, but was not detected by the monitoring network due to power and data logging problems. The 5 November plume was larger and rose to ~2900 m a.s.l.. However, it was dispersed to the east-northeast, over the poorly monitored sector of the volcano. The nearest fixed monitoring site to this dispersal direction, Kurokami, detected positive perturbations during the dispersion of the plume (Figure 4.42) but, unfortunately, the mobile monitoring equipment was not deployed and no visual observations of the dispersing plume were made. Thus, no detailed modelling of this plume has been carried out. However, some qualitative modelling is given in section 4.6.3.3 in order to show that the positive nature of the recorded perturbations cannot be used to imply a net positive ash charge.

The 14 November plume was observed from Arimura, with the mobile apparatus located at site A 1. Data for this eruption were recorded at all five sites and are reproduced in Figure 4.43a. Figures 4.43b and c show meteorological data collected at 09:00 over Kagoshima (K. Kinoshita, *pers. comm.*). Observations were made of the plume, and its dispersal direction was favourable for analysis by video footage taken from Kagoshima (courtesy of K. Kinoshita).

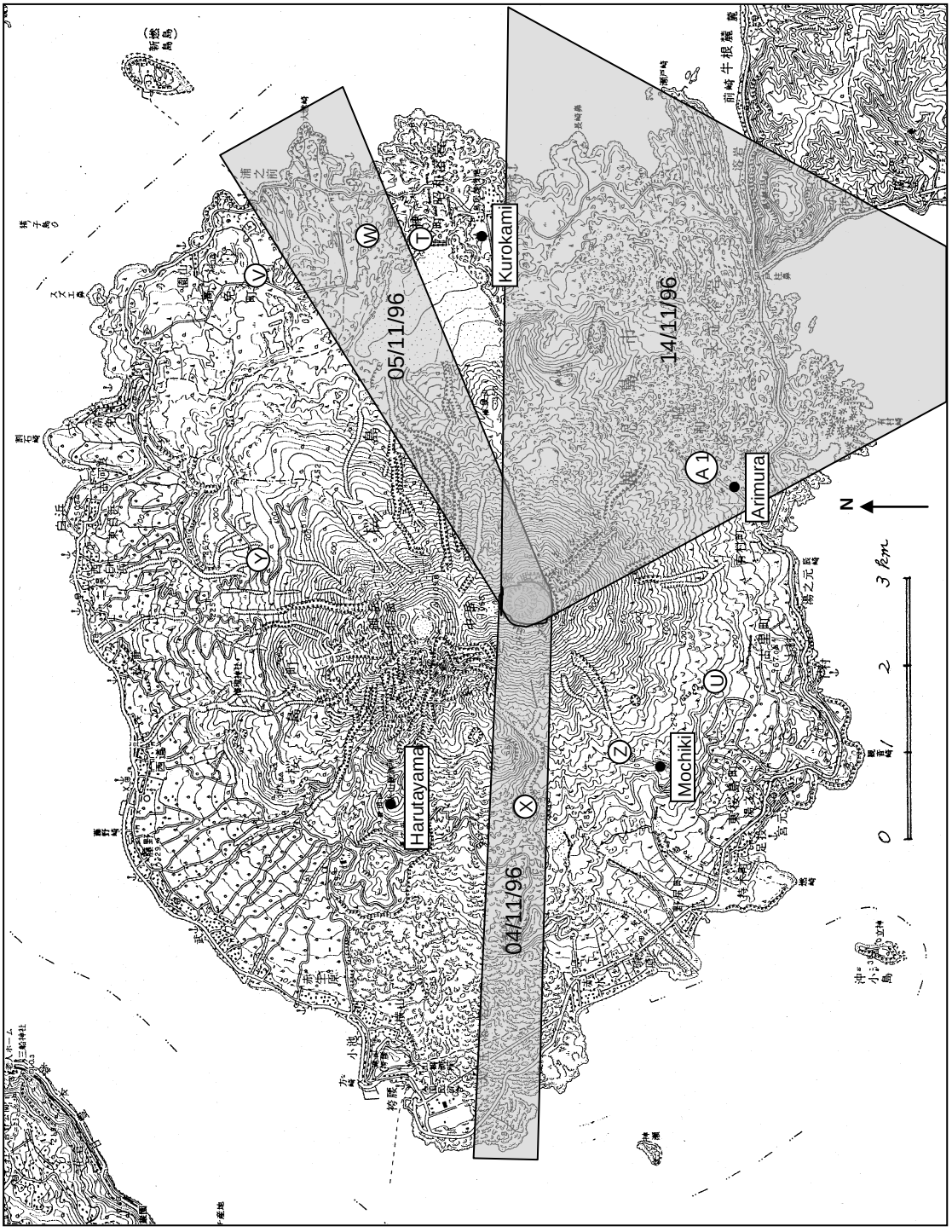

Figure 4.41 Topographic map of Sakurajima showing areas of ash deposition from observed particulate plumes. The shaded regions represent areas of deposition inferred from intersection of the edge of each ash deposit with the Sakurajima perimeter road. The dates indicate the eruption date. The monitoring sites are also shown.

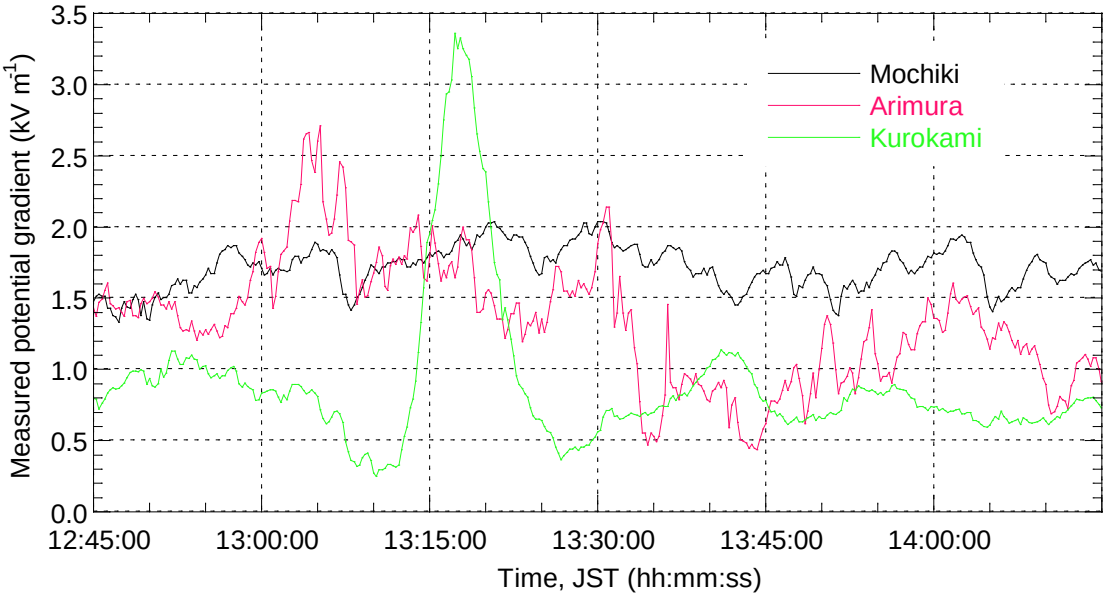

Figure 4.42 Potential gradients recorded after an explosion on 5 November, 1996. The explosion occurred at approximately 13:10 and produced a plume that was dispersed to the east-northeast. The closest site to the dispersed plume was Kurokami, which recorded a positive perturbation as the plume passed nearby. The initial, vertical ascent of the plume was not obviously detected. A logging problem at Harutayama prevented data from being recovered from that site.

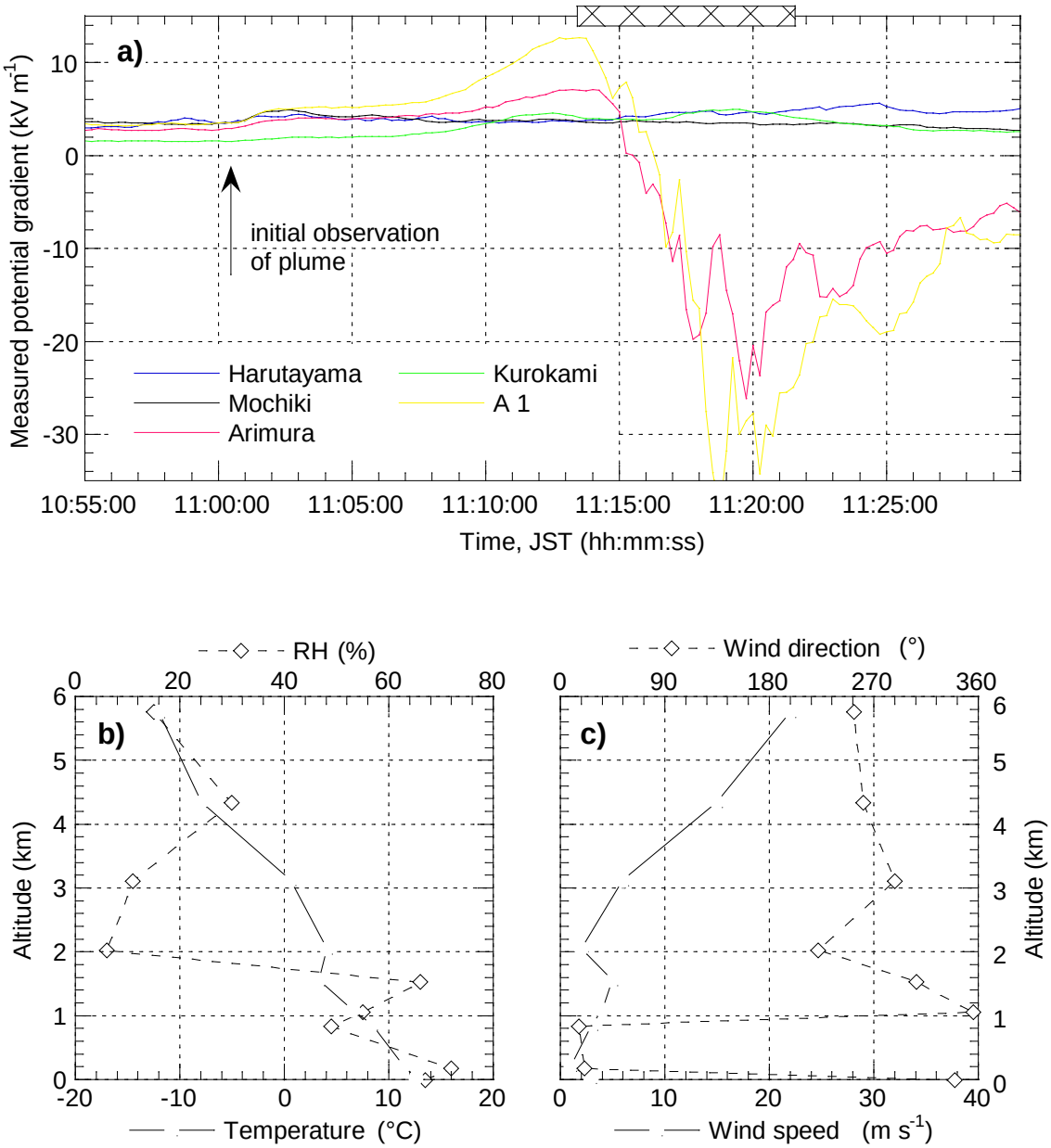

Figure 4.43 14 November, 1996. **a)** Potential gradient data. Hatched period indicates time during which ash fell at location A 1. Meteorological data acquired from Kagoshima Local Meteorological Observatory by K. Kinoshita is given in **b)** and **c)**. These data were collected by balloon, released from Kagoshima at approximately 09:00. Note that wind direction represents the clockwise angle from north from which the wind was blowing.

The observed plume motion can be divided into two different sections: the initial, vertical ascent, and then the following horizontal dispersal. During the eruption, the proximity of the Arimura site to the volcano prevented good observation of the plume dispersal. However, the video footage proved invaluable and enabled the spatial and temporal evolution of the plume to be reconstructed. It also showed the way in which the plume was generated in three discreet pulses, over a period of several minutes. Although the pulses produced plumes which initially appeared to merge into one, each separate pulse rose to a different height, and was subsequently dispersed in a different direction. Figure 4.44 shows two stills (courtesy of K. Kinoshita) taken from the video and a photograph taken from Arimura. Figure 4.44a shows the vertical ascent of the plume and Figure 4.44b clearly demonstrates the three distinct dispersal directions of different parts of the plume. In Figure 4.44c it can be seen that the main body of the plume was not dispersed towards Arimura. The last pulse (which was the weakest, and ascended less than a third of the distance travelled by the first pulse) deposited ash over Arimura and over the coast of Sakurajima (Figure 4.41).

Figure 4.45a shows the altitude of the plume top as calculated from the video. The horizontal distance (from the vent) of the front of the lower portion of the plume as it was dispersed towards Arimura is shown in Figure 4.45b. The best-fit lines in both figures were used to describe the plume motion in the subsequent modelling sections.

4.6.3.1 Potential gradient modelling

In order to model the recorded potential gradients, the effect of an airborne charge on the potential gradient at the Earth's surface must be calculated. From electrostatic theory, the potential V at a distance r from a point charge q is given by

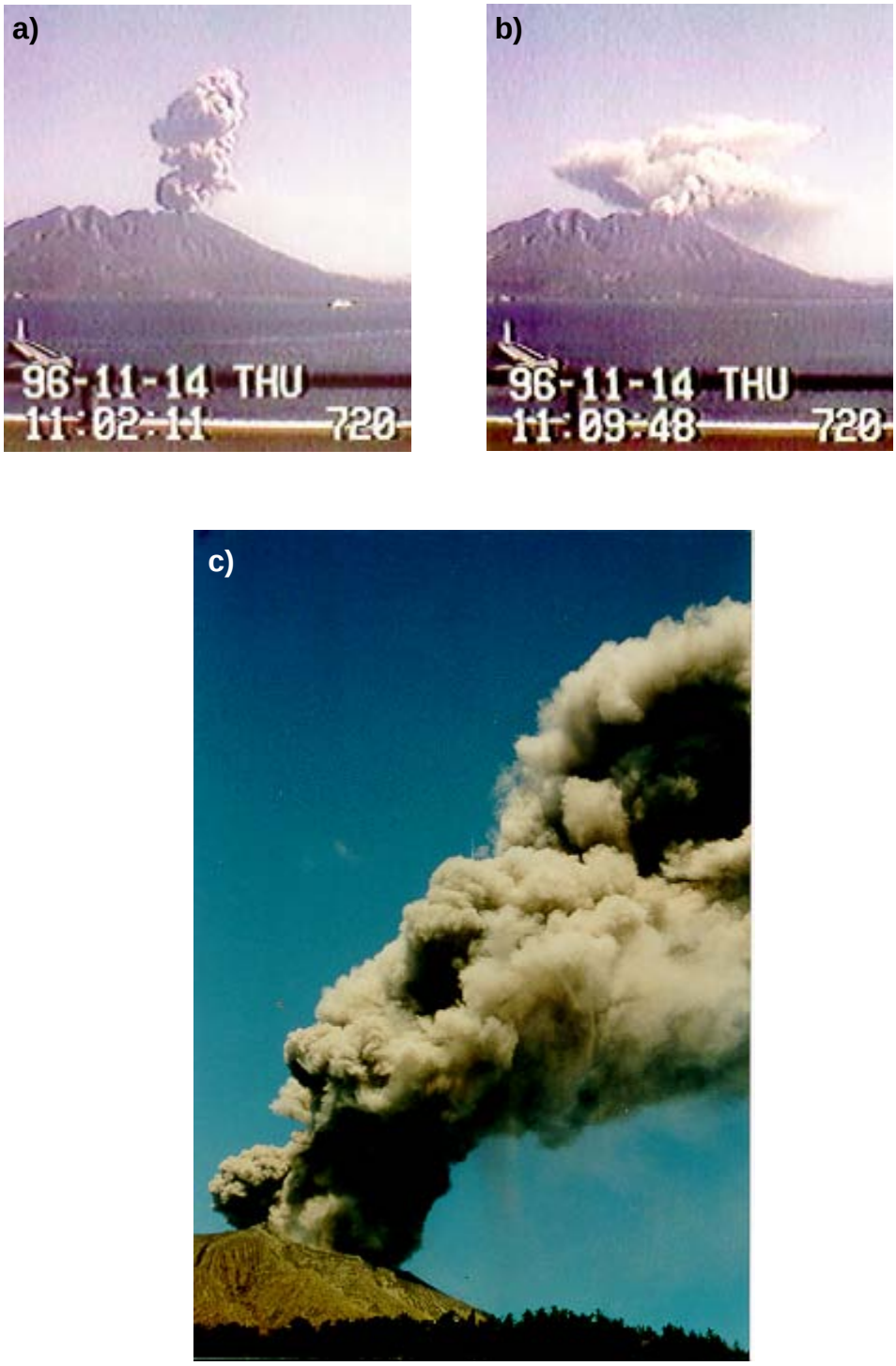

Figure 4.44 Images of the plume produced on 14 November, 1996. **a)** and **b)** are stills taken from a video filmed from Kagoshima (add 59 s to the times for JST). Courtesy of K. Kinoshita. **c)** Photograph taken from Arimura at 11:04:33 JST. The final pulse of the eruption can be seen just above the crater.

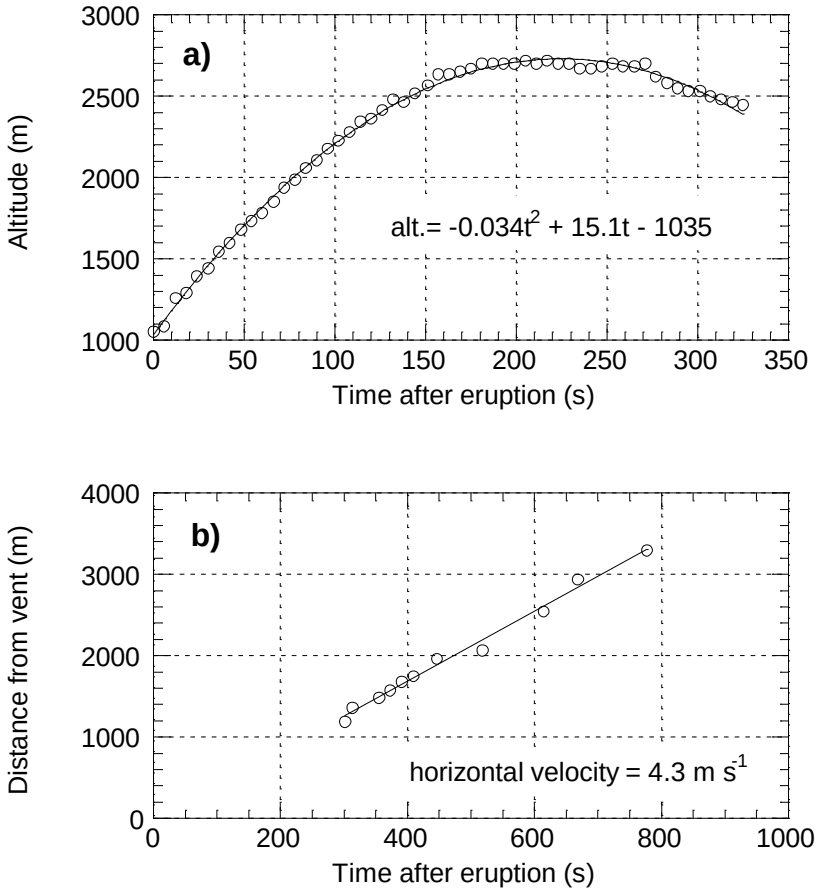

Figure 4.45 Rise and dispersal rates of the 14 November, 1996 plume. Circles represent data calculated from analysis of the video provided by K. Kinoshita (taken from Kagoshima). The lines represent best fits to the data. **a)** Altitude of the top of the plume. **b)** Horizontal distance from the vent of the lower portion of the plume, which deposited ash over Arimura.

$$V = \frac{q}{4\pi\varepsilon r} \qquad (4.1),$$

where ε is the permittivity of the environment. In Cartesian coordinates, the potential gradient is defined by

$$\text{grad}V = \frac{dV}{dx}\hat{\mathbf{x}} + \frac{dV}{dy}\hat{\mathbf{y}} + \frac{dV}{dz}\hat{\mathbf{z}} \qquad (4.2),$$

and r can be given as

$$r = \left(d_{\mathrm{x}}^2 + d_{\mathrm{y}}^2 + d_{\mathrm{z}}^2\right)^{\frac{1}{2}} \qquad (4.3),$$

where d_{x}, d_{y} and d_{z} are the distances in the directions $\hat{\mathbf{x}}$, $\hat{\mathbf{y}}$ and $\hat{\mathbf{z}}$, respectively, between the charge and the point of measurement.

In the presence of a conducting surface, the potential gradient is given by the vector sum of the gradient produced by the charge, and that produced by an equal and opposite image charge located below the surface. The contribution of each charge to the potential gradient can be found by combining equations 4.1, 4.2 and 4.3. For the simple models described below, the surface of the Earth was represented as a flat, conducting, **x**-**y** planar surface at $z = 0$, and z was defined to increase positively upwards. On any conducting surface, the induced image charge cancels out any along-plane potential gradients. Thus, on the surface of the Earth, the contribution to the potential gradient from a real charge is given by only the $\hat{\mathbf{z}}$ term of equation 4.2,

$$\left(\frac{dV}{dz}\right)_{z=0} = \frac{-qd_{\mathrm{z}}}{4\pi\varepsilon\left(d_{\mathrm{x}}^2 + d_{\mathrm{y}}^2 + d_{\mathrm{z}}^2\right)^{\frac{3}{2}}} \qquad (4.4).$$

If the charge is located at (x_{q}, y_{q}, z_{q}) then $d_{\mathrm{x}} = x - x_{\mathrm{q}}$, $d_{\mathrm{y}} = y - y_{\mathrm{q}}$ and $d_{\mathrm{z}} = -z_{\mathrm{q}}$ for measurements taken at coordinates (x, y, 0). The image charge $-q$, would thus be located at (x_{q}, y_{q}, $-z_{\mathrm{q}}$). Summing the potential gradients from both the charge and its

image, and using ε_0, the permittivity of free space, as a close approximation to the permittivity of the atmosphere, gives

$$\frac{dV}{dz} = \frac{qz_q}{2\pi\varepsilon_0\left(d_x^2 + d_y^2 + z_q^2\right)^{\frac{3}{2}}} \qquad (4.5).$$

In the next section, the charges held within the plume are represented by a vertical dipole. From equation 4.5, the potential gradient produced by a vertical dipole with charges of magnitude q, located a horizontal distance l away from the measurement point, is then

$$\frac{dV}{dz} = \frac{q z^+}{2\pi\varepsilon_0 (z^{+2} + l^2)^{\frac{3}{2}}} - \frac{q z^-}{2\pi\varepsilon_0 (z^{-2} + l^2)^{\frac{3}{2}}} \qquad (4.6),$$

where z^+ is the altitude of the positive charge and z^- is the altitude of the negative charge. Combining equation 4.6 with positional data and models of charge evolution within the plume allowed estimates of the charge magnitudes to be made.

4.6.3.2 The vertical ascent of the plume

All sites showed an initial positive perturbation as the plume ascended. However, at Harutayama this was somewhat hidden by high levels of noise and these data have not been included in the modelling. At other sites, the perturbations caused by the eruption can be estimated by removing the background level immediately preceding the eruption (calculated as the average over the previous 5.5 minutes). The positive sign of the perturbations indicates that they could be reproduced by assuming a net positive charge in the plume. However, charge balance and also the following negative perturbations recorded at Arimura suggest that areas of net negative charge

were also present. For these reasons, a dipole model has been used to reproduce the recorded potential gradients.

It was found that the perturbations could not be reproduced by a simple dipole model as used by Lane *et al*. (1995) if the plume rise data from the video were taken into account. Instead, a model with evolving charge magnitudes was required. This can be envisaged as two vertical lines of charge, one representing the gas portion of the plume and the other, of opposite polarity, representing the ash portion of the plume (Figure 4.46). Gradual vertical separation of these lines of charge due to the fall velocity of the ash produces a net positive charge at the top of the plume, and a net negative charge at the base. Assuming that these portions of net charge can be modelled as point charges, their magnitude represents the vertical charge density of the plume and the degree of separation of the ash and gas. Figure 4.47 shows the results of fitting this 'simple evolving dipole' model to the data. The Arimura potential gradients can be matched reasonably well, and the Mochiki data demonstrate a similar curve. Note that a smaller charge magnitude was used to fit the Kurokami data. However, it is known that the potential gradients at Kurokami were somewhat reduced due to the vegetation surrounding the site.

If the stability of the background gradient before the eruption is considered, data collected at Mochiki should be the most reliable because they demonstrated very low noise. If the fit to the Mochiki data is to be improved, then the rate of charge magnitude increase is required to vary. This can be thought of as an increasing separation velocity during the plume ascent as a result of decreasing convective 'stirring' or aggregation. However, this 'complex evolving dipole' model produces poorer fits to the data recorded at the other sites (Figure 4.48). The potential gradients

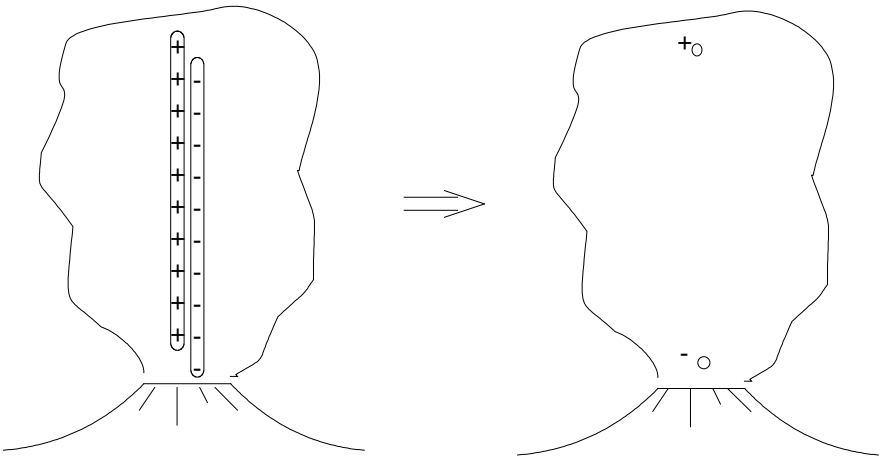

Figure 4.46 Model of charge distribution within a plume. The charge distribution in the plume can be represented as vertical columns of charge. Where the charges overlap no net charge is produced. However, due to gravitational separation, net charges are produced at opposite ends of the plume. When measuring from a suitable distance, these areas can be modelled as point charges.

produced were calculated from equation 4.6 where, for both models, q, z^+ and z^- were described by

$$q = \rho_q \int_0^t v_s \left(\frac{t}{t_{mx}} \right)^a dt \tag{4.7}$$

$$z^+ = z_{pt} - z_0 + \int_0^t v_s \left(\frac{t}{t_{mx}} \right)^a dt \tag{4.8}$$

$$z^- = 1000 - z_0 + \int_0^t v_s \left(\frac{t}{t_{mx}} \right)^a dt \tag{4.9}.$$

Within the equations, the vent is assumed to be at an altitude of 1000 m, z_0 is the altitude of the measuring site, z_{pt} is the altitude of the plume top, v_s is the maximum rate of separation, ρ_q is the vertical charge density in the plume, t is the time after the start of the eruption and t_{mx} is the duration of the plume ascent (approximately 220 s). The parameter a (where $a \geq 0$) is used to determine the way in which the rate of separation increases with time over the duration of the ascent (for times $t \leq t_{mx}$). For $a = 0$, the rate is constant at v_s, thus this represents the 'simple evolving dipole' model. For $a > 0$, the rate of separation is initially zero and increases to v_s at $t = t_{mx}$. If $0 < a < 1$, the rate of separation initially increases rapidly before slowing, and for $a > 1$, the rate of separation accelerates as the eruption proceeds. At $a = 1$, the rate of separation increases linearly with time. The site altitudes, z_0, are ~0 m for Arimura, 260 m for Mochiki and 75 m for Kurokami. The horizontal radial distances, l, have been given in section 4.3.2.1. The parameters used to produce Figures 4.47 and 4.48 are listed in Table 4.1.

Despite the differences between the models, both imply similar charge densities and maximum charges. Due to the fact that the charges deduced in Table 4.1 still include the twenty times amplification of the potential gradient, the actual values of

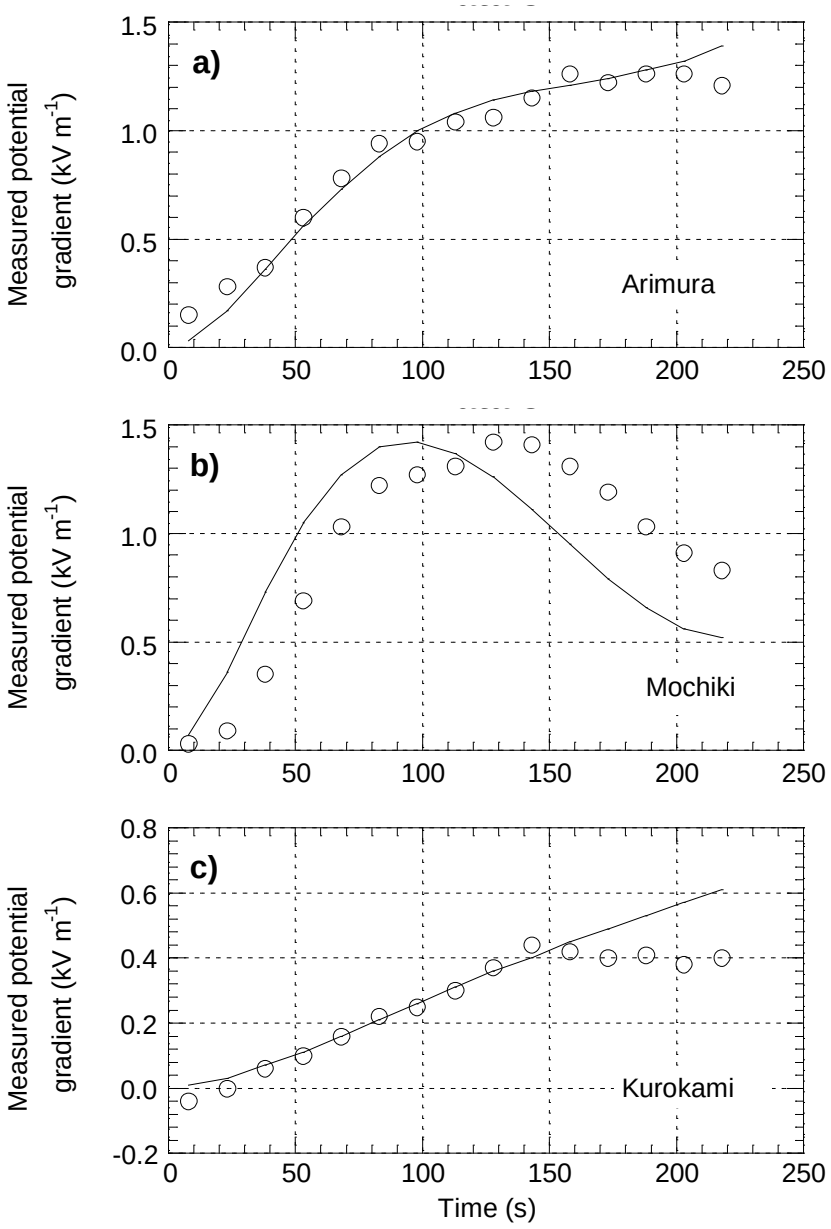

Figure 4.47 Simple evolving dipole model for the ascent of the 14 November, 1996 plume. The line shows the results of the model, and the recorded data are given by the circles. The time is the time after the observed onset of plume rise.

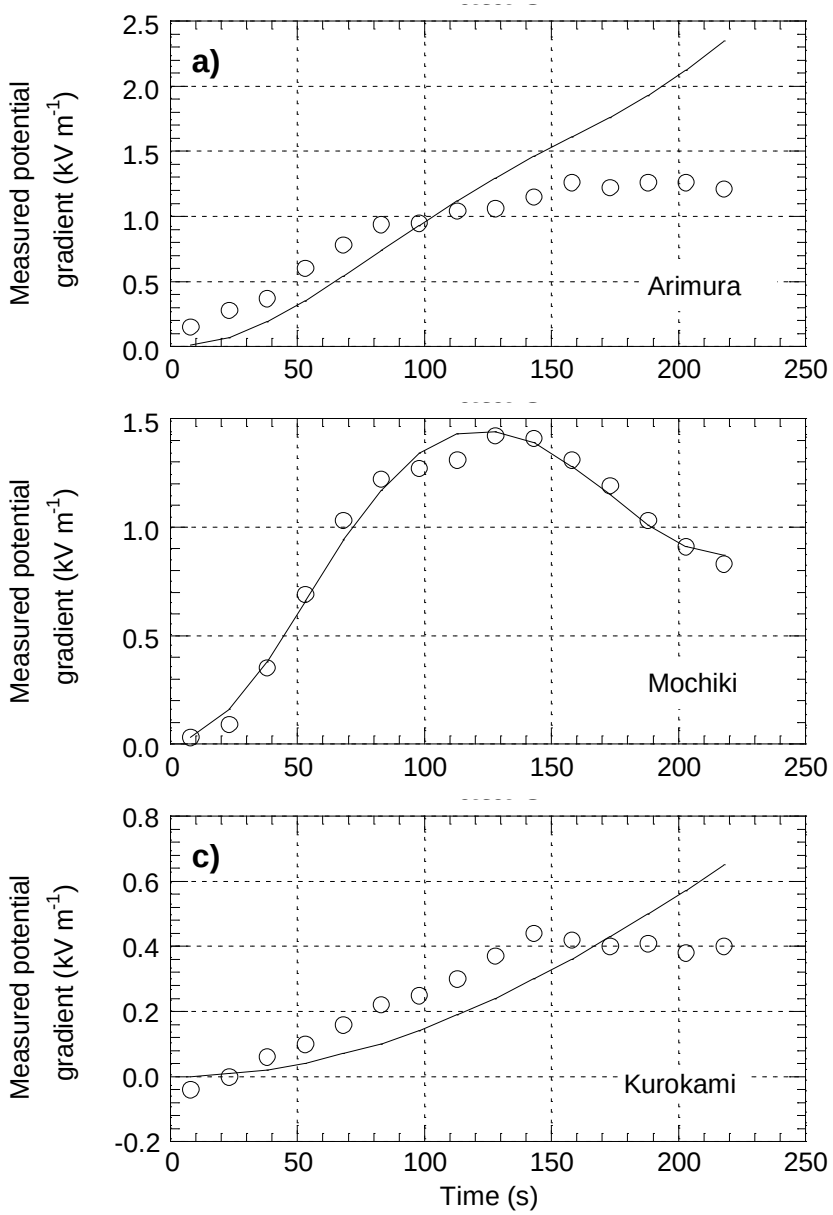

Figure 4.48 Complex evolving dipole model for the ascent of the 14 November, 1996 plume. The line shows the results of the model, and the recorded data are given by the circles. The time is the time after the observed onset of plume rise.

Table 4.1 Parameters used to model the potential gradient perturbations recorded on 14 November, 1996.

	Simple evolving dipole	Complex evolving dipole
Vertical charge density, ρ_q	1.4 C m^{-1}	0.99 C m^{-1}
Vertical separation velocity, v_s	0.04 m s^{-1}	0.17 m s^{-1}
Maximum charge separated, q_{mx}	21 C	13 C
Delay coefficient, a	0	0.87
Kurokami values: ρ_q	0.36 C m^{-1}	0.7 C m^{-1}
Kurokami values: q_{mx}	3.2 C	3.4 C

the total charges are of the order 1 C. This is much smaller than the charges of 10 C used by Lane *et al*. (1996) to model the ascent of a plume from Sakurajima on 27 December, 1993. However, both plumes can be modelled by positive-above-negative charge distributions. The rates of separation used in the models are relatively small when compared with particle fall velocities previously estimated for plumes. For example, Carey and Sigurdsson (1982) assumed that, in the 1980 eruption of Mount St. Helens, all particles smaller than 63 μm in diameter fell as aggregates with a fall velocity of 0.35 m s^{-1}. To reproduce potential gradient observations previously made at Sakurajima, Lane *et al*. (1995) used a gas-particle separation velocity of 0.50 m s^{-1}, and also assumed that aggregation would efficiently scavenge the slow-falling, small particles (less than 100 μm in diameter).

Table 4.2 provides geophysical data on these two explosions of Sakurajima (seismic amplitudes and airshock pressures), collected by the SVRC. Although both explosions were small for Sakurajima, the 1993 explosion was more intense and a little larger then the 1996 explosion (K. Ishihara, *pers. comm.*). Thus, the larger eruption appeared to be associated with greater charge separation than the smaller one.

Lightning was not observed during either eruption, but is frequently seen during larger eruptions of Sakurajima, suggesting that charge magnitudes do increase with eruption size.

Table 4.2 Geophysical data from two explosions of Sakurajima volcano. Notes: 1. Time represents the onset of explosion at the crater bottom (estimated from seismic data with an error of less than ±0.5 s). 2. Measured at Harutayama. 3. Volume represents depression of ground surface as estimated by tilt and strain data. All data from K. Ishihara, SVRC.

	27 December, 1993	14 November, 1996
Explosion time[1]	12:52:42.9 JST	10:59:52.5 JST
Airshock[2]	190 Pa	80 Pa
Max. amplitude of explosion-quake[2] (N-S, E-W and vertical components)	38, 35, 12 μm	15, 15, 5 μm
Depression volume[3]	11000 m^3	8000 m^3

4.6.3.3 Horizontal dispersal

The horizontal dispersal of the lower part of the plume was detected by the fieldmeters at Arimura and A 1 as initially positive and then negative perturbations as ashfall commenced. However, any attempt to reproduce these potential gradients is limited by the unknown contribution from the rest of the plume, which was being simultaneously dispersed in various directions. Note that the data collected at Kurokami, which was slightly off axis, demonstrated small positive perturbations during the plume dispersal. Figure 4.49 shows the result of one model for the Arimura data using a positive charge at an altitude of 1200 m, travelling away from the crater along the dispersal axis at 2.7 m s^{-1}, and a negative charge initially at 1200 m but

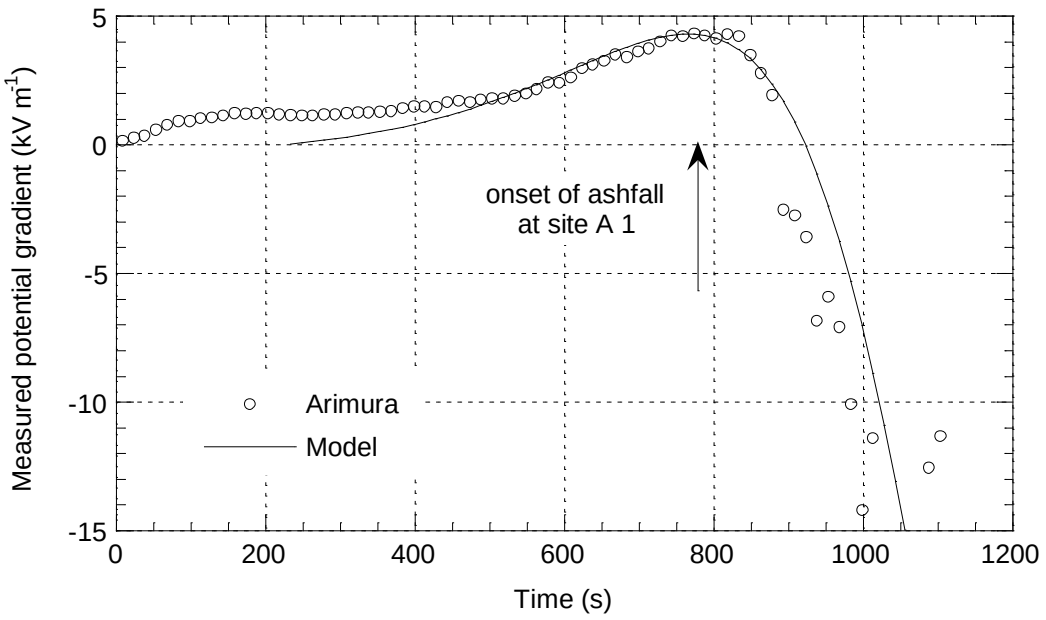

Figure 4.49 Model for potential gradients recorded at Arimura during dispersal of the 14 November, 1996 plume. The line shows the results of the model, and the recorded data are given by the circles. The time is the time after the observed onset of plume rise, and the modelled portion of the data is dominated by perturbations produced by the final pulse of the eruption which was dispersed over Arimura and A 1. The increase in scatter of the data after about 900 s is probably due to the onset of ashfall at the Arimura site.

descending at 0.3 m s^{-1}, with a horizontal velocity of 0.25 m s^{-1} in the same direction as the positive charge. Each charge has a magnitude of 0.43 C, representing actual charges of about 0.02 C. This is considerably smaller than the charges required to model the vertical ascent of the plume, so it appears that the majority of the charge in the plume was produced during the initial explosion of the eruption (and was thus not dispersed over Arimura). If this 'pulse' was classified as a separate eruption then it would certainly appear to follow the trend of diminishing charge magnitude with decreasing size of eruption. These data also imply a positive-above-negative separation of charge, in agreement with much of the work carried out previously at Sakurajima (Lane and Gilbert, 1992; Lane *et al*., 1995).

Figure 4.50 shows an SEM image and grain size data for ashfall deposited at the A 1 site. The thickness of the deposit at site A 1 was less than 1 mm, which fell as individual particles and loosely bound aggregates, over a period of about 10 minutes. The estimated specific surface area of the particles is 179 m^2 kg^{-1} (see Chapter 5 for details on the particle size analysis technique and specific surface area calculations).

The positive, followed by negative, perturbations detected during the horizontal dispersal of the plume are convincing evidence of its electrical dipole structure. By using a dipole model, it is also possible to explain qualitatively the positive perturbations recorded at Kurokami due to the dispersal of the plume on 5 November. Kurokami was off the axis of the plume dispersal direction, and Figure 4.51a shows the way in which a vertical dipole produces small positive potential gradients off-axis. The graphs were produced by assuming two point charges of magnitude 1 C, with a positive one at an altitude of 1000 m, and a negative one at altitudes of 990, 950, 900 and 850 m, respectively, for the four curves. Figure 4.51b shows the way in which the magnitude of the positive perturbations can be greatly enhanced if some degree of

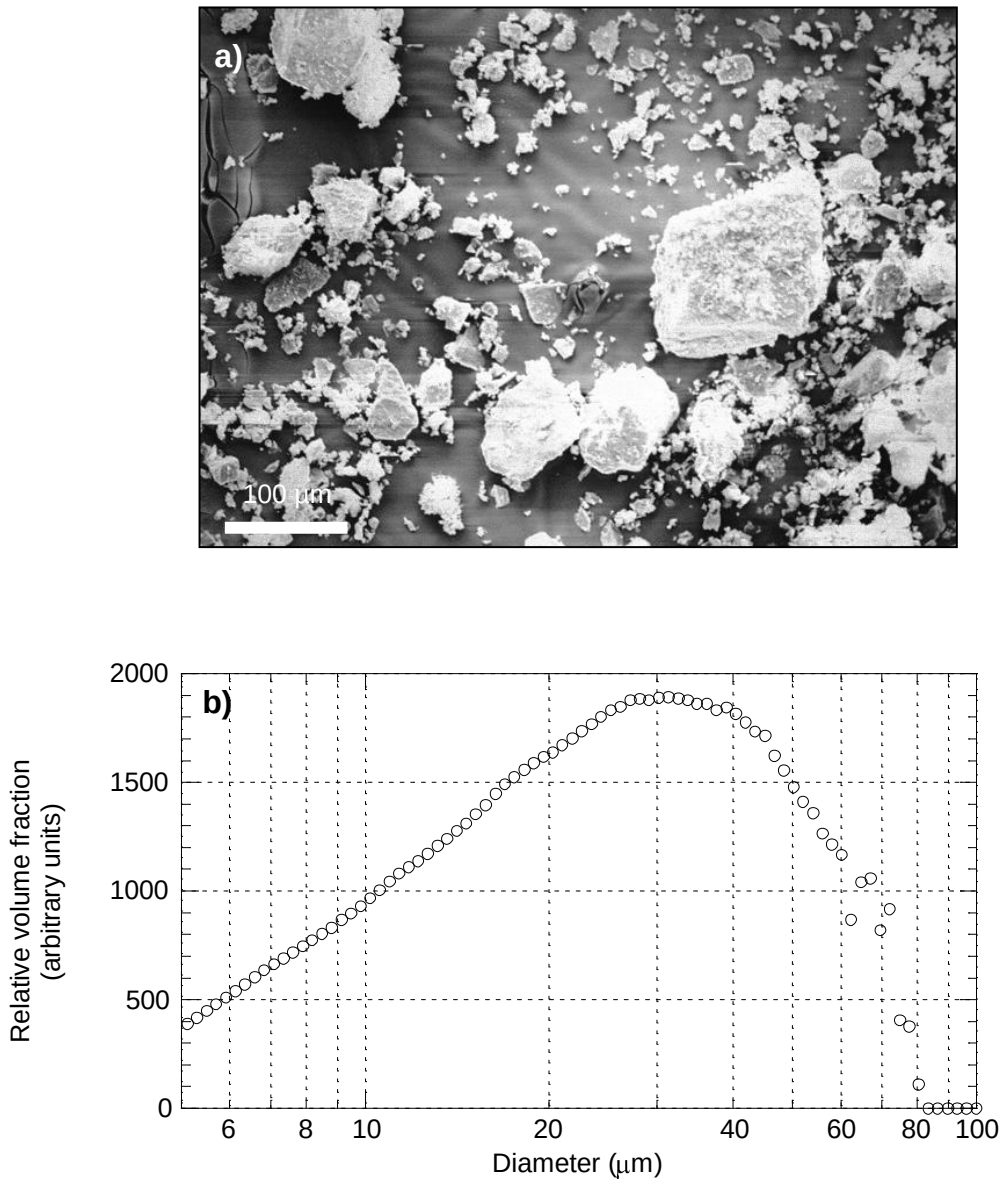

Figure 4.50 Ashfall collected from the 14 November, 1996 eruption. The sample was collected at site A 1. **a)** SEM photograph showing the non-vesicular nature and blocky morphology of the coarser particles. The large particles are also covered in a layer of fine shards. **b)** Particle size distribution. The coarse end of the distribution had to be removed before analysis by a 70 µm mesh. See Chapter 5 for details of sample preparation and the analysis technique.

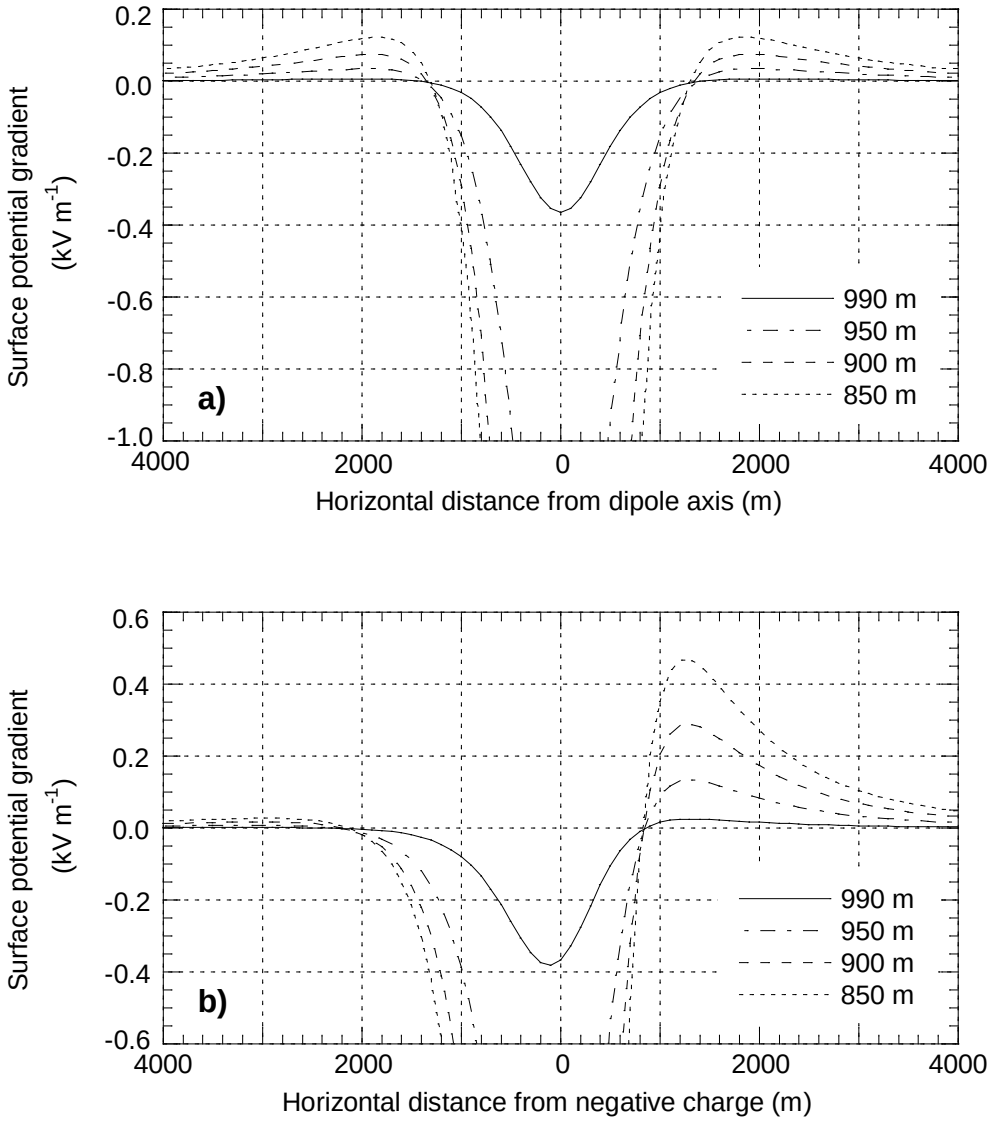

Figure 4.51 Potential gradients generated by electrical dipoles. **a)** The lines represent the surface potential gradients produced by a +1 C charge located at 1000 m above the surface of the Earth, and -1 C charges at 990, 950, 900 and 850 m altitude directly below the positive charge. Small positive potential gradients are produced either side of the dipole. **b)** The positive perturbations are greatly enhanced if the dipole is not vertical. In this graph, for every metre of vertical separation between the charges, the positive charge has been moved half a metre to the right. Thus, much enhanced positive potential gradients could be easily produced by small amounts of wind shear.

wind shear is present. For this second model, the positive charge has been horizontally offset (to the right of the negative charge which is still located over the origin) by a distance given by half of the vertical separation between the charges. Thus, the positive perturbations recorded at Kurokami cannot be assumed to represent evidence of a net positively charged plume.

4.6.4 Perturbations due to gentle ash emission

To emphasise the way in which a plume can be tracked, rather than just detected, Figure 4.52 reproduces data collected on 10 November, during which gentle ash emission from Sakurajima created a sustained, dilute plume. Over the day, the plume's propagation direction rotated around the volcano as a result of varying wind directions. At 10:00 there was very little wind and the plume formed an ashy column that rose gently into the clouds just above the crater. By 10:30 a light breeze was blowing the plume over the Harutayama measurement site, creating the increasingly negative potential gradients recorded at this site. The wind then began to shift anticlockwise, increasing the negative potential gradient at Mochiki, before it subsided again just before 13:00, allowing another vertical plume to form. This was visible up to the cloud base, approximately 1000 m above the crater. At 13:20, visual observations showed complex wind shear blowing ash towards Arimura and volcanic gases towards Harutayama. This produced small positive potential gradients at Harutayama and negative perturbations at Arimura. The particle-rich portion of the plume was then observed to rotate back clockwise, first over Mochiki (at 16:00) and then Harutayama (at 16:30). This ability to track such a dilute plume demonstrates the sensitivity of the potential gradient technique and shows that volcanic ash (and also

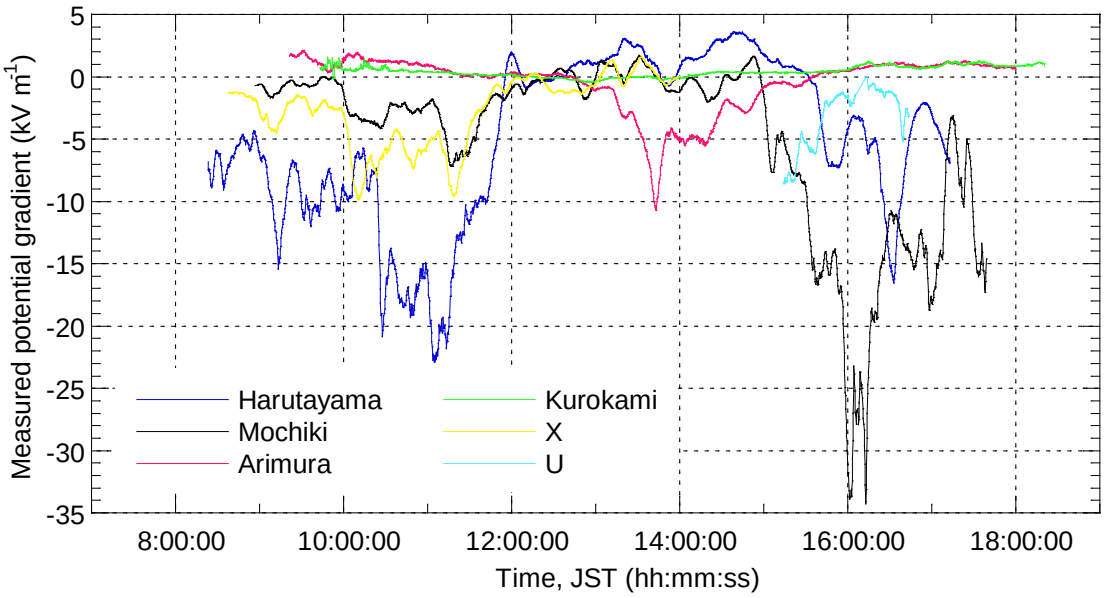

Figure 4.52 Potential gradients recorded during periods of continuous ash emission. Data recorded on the 10 November, 1996, see Figure 4.28 for further details.

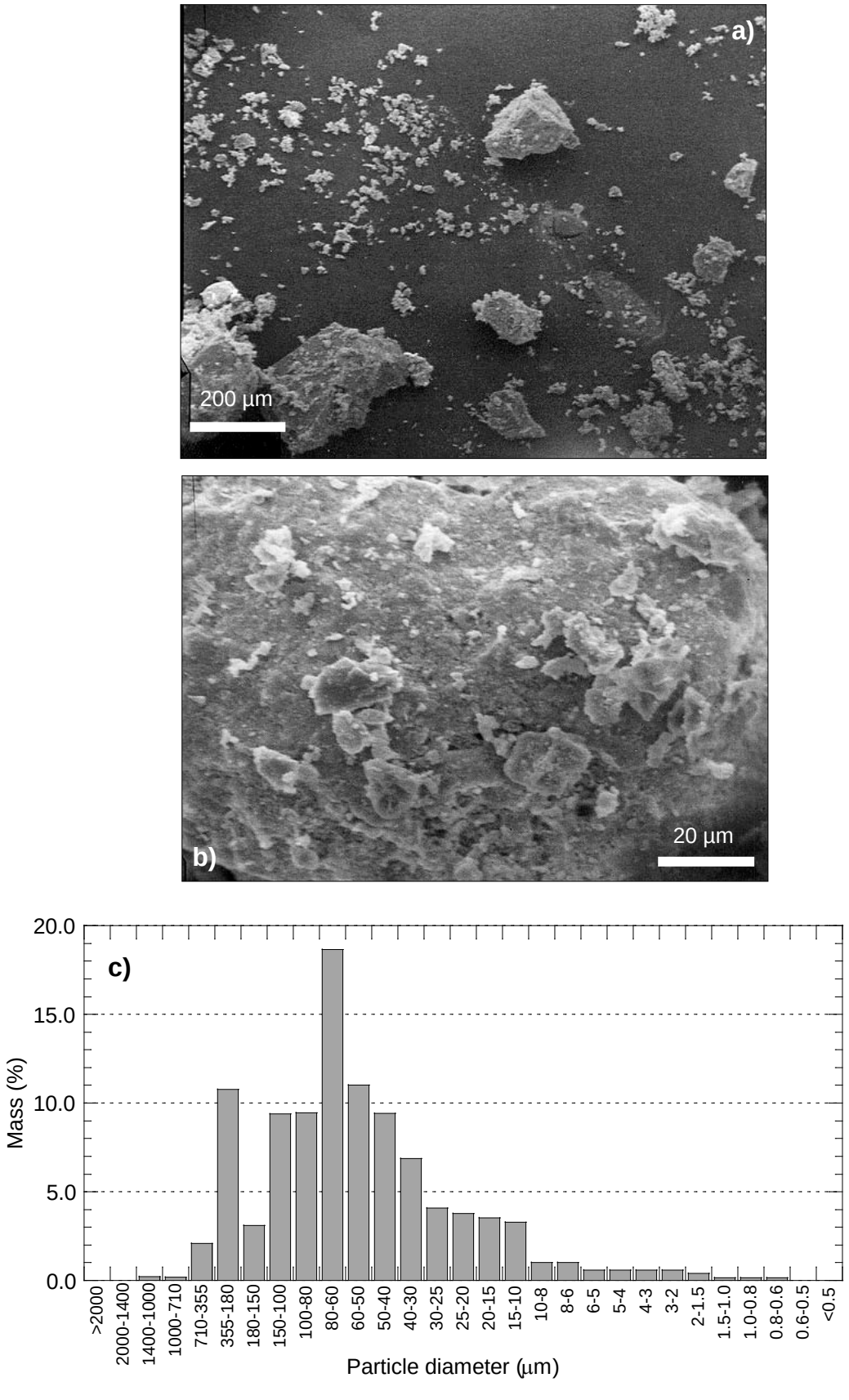

Figure 4.53 Particles collected from fallout from a lightly-particulate plume. **a)** An SEM image of particles collected at Harutayama (10:30, 10 November, 1996).

Figure 4.53 continued..

The image shows some large, blocky particles larger than 200 μm in diameter, and smaller particles, much more shard-like in their morphology. **b)** A close-up of one of the large, blocky particles, showing small particles (less than 20 μm in diameter) adhering to its surface. The irregular surface suggests that the large particle has been subject to alteration and thus may not be juvenile material. **c)** Particle size distribution of a similar ashfall collected at site U, between 13:15 and 16:00 on 13 November, 1996 (sufficient deposit could not be collected for analysis on 10 November). The data was collected using a sedigraph (analysis by S. Black) because the deposit was too coarse for analysis with the Elzone equipment discussed in Chapter 5. The data are presented in a different style to that of Figure 4.50c and the graphs provided in Chapter 5 due to the different data outputs of the two techniques.

volcanic gas under these conditions) must be highly charged, even when it has not been produced by a noticeably explosive event.

Very light, intermittent ashfall (of relatively coarse ash) was experienced at Harutayama between 11:40 and 12:00, and also at location U at about 16:40. Figure 4.53 gives the size distribution and an SEM photograph of a sample obtained at Harutayama.

4.7 Summary

The data collected at Sakurajima have further demonstrated the possible use of the potential gradient technique for detecting and tracking volcanic plumes. One good data set was recorded of a Vulcanian explosion, and models which reproduce the recorded potential gradients demonstrate the same positive-over-negative charge separation as has been previously inferred (Lane and Gilbert, 1992; Lane *et al*., 1995) at Sakurajima. The charge magnitudes required to model these eruptions indicate that there is a probable relationship between the size of the eruption and the amount of charge separated. However, due to the small number of data sets, this cannot yet be investigated in any detail. The potential gradient modelling has demonstrated the value of video footage in order to monitor the ascent and dispersion of plumes.

5. Ash charging experiments: Apparatus design and experimental method

5.1 Introduction

Published experimental investigations concerning volcanic plume electrification (reviewed in Chapter 3) have concentrated on frictional effects between particles (Hatakeyama and Uchikawa, 1952; Kikuchi and Endoh, 1982) and boiling mechanisms within steam plumes (Blanchard, 1964; Björnsson *et al*., 1967; Pounder, 1978, 1980a). An exception to this is the work carried out by Büttner *et al*. (1997) in which they detected charge on ejecta produced from small phreatomagmatic explosions. Although fracto-emission during fragmentation had been previously proposed as a charging mechanism (Gilbert *et al*.,1991; Lane and Gilbert, 1992), Büttner *et al*. (1997) explained their results purely in terms of shearing the electrical double layers of water surfaces. The experiments described here were designed to maximise any fracto-charging effects over frictional, or any other, charge generation mechanisms. As such, they represent the first experimental attempt to assess fracto-emission as the main charge generation mechanism within volcanic plumes.

During explosive eruptions which generate volcanic plumes (and pyroclastic flows), volcanic ash is generated by the fragmentation of magma. For this study, ash-grade silicate particles (i.e. particles less than 2 mm in diameter) were produced by colliding samples of pumice in the laboratory. In two different types of experiment, the net charge on the particles produced and the individual ash particle charges were measured. The results of these experiments are discussed in Chapters 6 and 7. In this

chapter the design, construction and calibration of the experimental apparatus are described, and the experimental methods explained.

5.2 Experimental aims

The primary aim of the experiments was to measure the charge on small silicate particles produced in the laboratory by fragmenting pumice. Both the net charge on the particles, and the individual particle charges, were measured for comparison with published results of experiments on ashfall from volcanic plumes (Hatakeyama, 1958; Gilbert *et al*., 1991; Miura *et al*., 1995). By generating the particles during collisions between pumice samples, it was hoped that evidence would be obtained for fracto-charging during pumice fragmentation. When considering the charge magnitudes produced, it would then be possible to assess fracto-emission processes as a charging mechanism for volcanic plumes.

As discussed in Chapters 3 and 4, the atmospheric potential gradients produced by plumes are thought to be a result of gravitational separation, either between charged silicate particles and volcanic gasses or, between silicate particles of different sizes. To investigate the separation of charge in plumes, the experimental apparatus was also designed to allow detection of any gravitational separation and, in particular, to collect any evidence for the production of ions. By carrying out particle size analysis it would be possible to address the question of charge polarity as a function of particle size, and also to observe any effect that specific surface area had on charge magnitude.

A variety of different pumice samples were used so that any effects due to differences in geochemistry, physical structure or phenocryst content of the pumice could be observed. The objective was to investigate the possible causes of charge

polarity variations observed between different volcanoes (Hatakeyama and Uchikawa, 1952) and even within ashfall from one plume (Kikuchi and Endoh, 1982). In order to allow some tentative extrapolation of the results to other planetary environments, many experiments were also carried out under vacuum. During plume-producing eruptions, the majority of the ash is probably produced within the conduit and the jet region of the plume, immediately above the vent. Thus, ideally, some experiments would have also been carried out at near-magmatic temperatures, however this would not have been possible without much more elaborate apparatus.

5.3 Net ash charge experiment

A schematic diagram of the experimental apparatus used to measure the net charge on particles produced by pumice–pumice collisions is shown in Figure 5.1. The sample impacts were initiated by a small solenoid. One sample was attached to the armature of the solenoid, and the other was mounted on a sprung anvil. On activation of the solenoid, the armature was accelerated towards the anvil until the samples collided. A small spring then separated the samples and allowed the ash produced during the collision to fall under gravity. This simple design was chosen to maximise the charge generated due to sample fracturing over any triboelectric effects between the samples or particles. As a comparison, for some experiments the solenoid was replaced by a small electric motor allowing ash particles to be produced by rotational motion (grinding) of the samples. This arrangement allowed the relative importance of frictional charge generation (triboelectric effects) to be assessed.

Net charge measurements were carried out by allowing the particles to fall into a Faraday cup. This standard technique is especially suited to charge measurements on

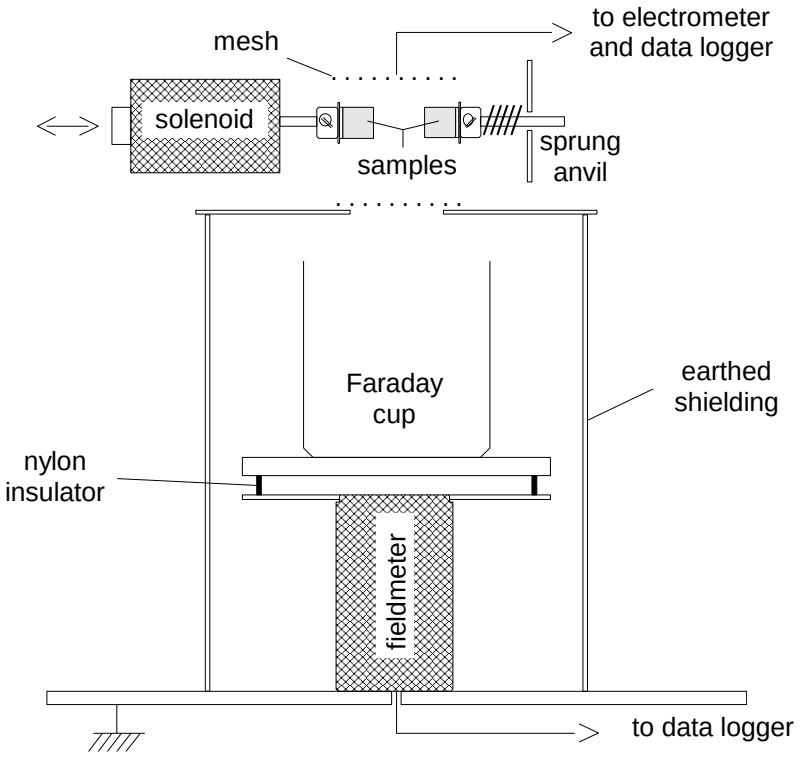

Figure 5.1 Schematic diagram (cross section) of the apparatus used for net ash charge experiments. Ash particles produced during collisions of the samples fell into the Faraday cup. The voltage induced on the outside of the cup due to charge on the ash particles was then detected by the fieldmeter. Charge collected on the mesh above the samples was monitored to assess any evidence of ion production.

small or insulating samples (Cross, 1987). The Faraday cup is a double walled vessel into which the sample is placed (although in this text, for clarity, 'Faraday cup' will refer to only the inner section). The grounded outer wall acts as an electrical screen which prevents stray charges from affecting the measurement. The inner cup is also constructed from a conducting material. Since charge can only reside on the outer surface of conductors, any charged material placed inside the cup induces an identical charge on the outside of the cup. The conducting material of the cup then allows the charge to be easily measured, and this is often carried out with an electrometer. However, electrometers are extremely sensitive to electrical noise and they are also prone to drift. To avoid these problems, an alternative approach was used in which the electric potential of the Faraday cup was detected by an electrostatic fieldmeter. The capacitance of the cup then directly related its potential to the charge held inside it.

In order to assess any gravitational separation of charge during the pumice collisions, a small mesh was placed above the samples. This was designed to collect any charge released as ions and also any charged ash particles for which electrostatic forces dominated over gravitational forces. Charge on the mesh was measured directly by an electrometer (other complications with the mesh data, detailed in Chapter 6, ensured that the problems associated with electrometer measurements were acceptable in this case).

5.3.1 Apparatus

The apparatus was constructed in two main sections, the particle charge measurement section (Faraday cup and fieldmeter) and the particle production section (sample collider). Both were mounted inside a vacuum chamber (Figure 5.2) to provide a low pressure environment for some experiments, and to eliminate draughts

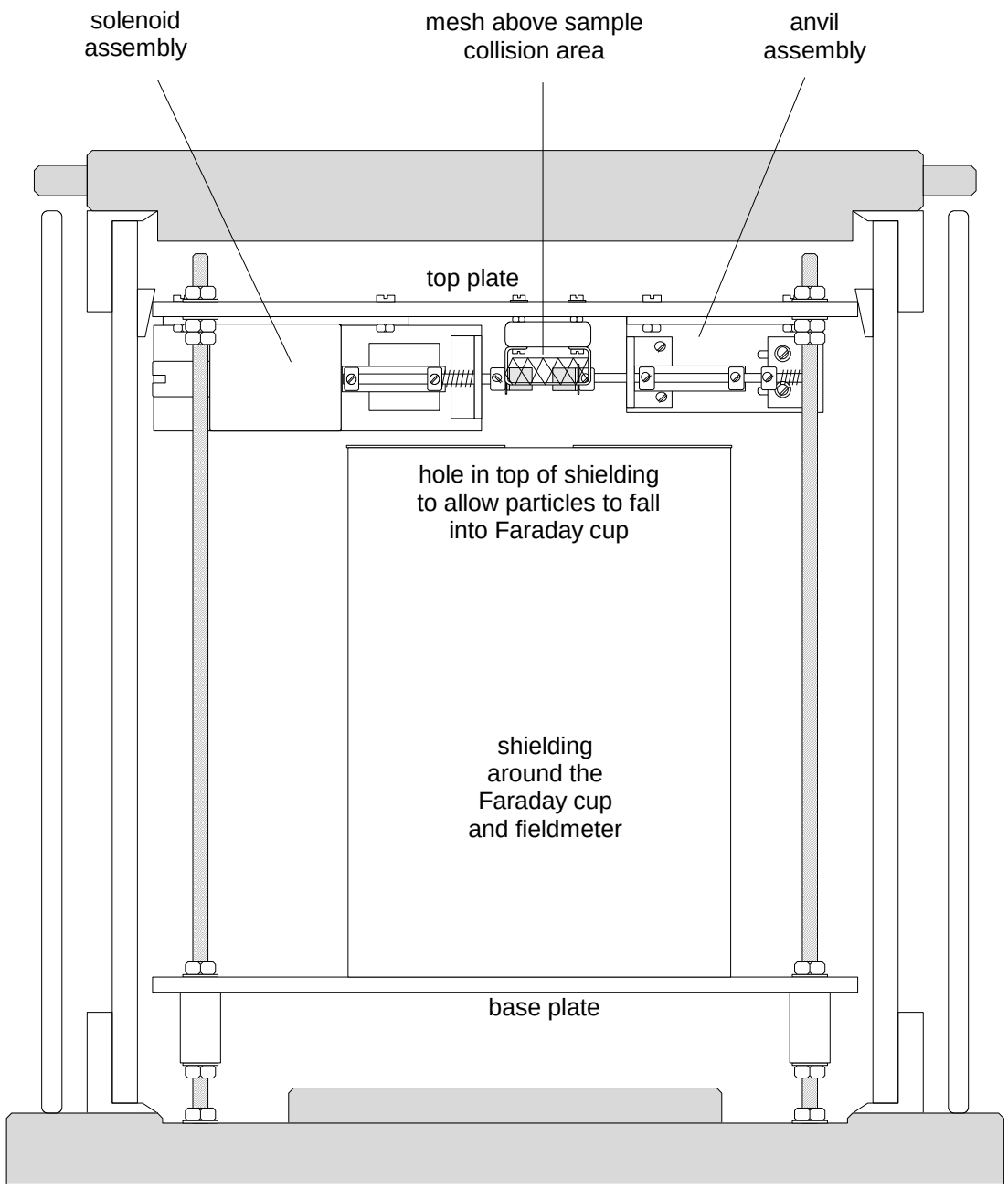

Figure 5.2 Cross sectional diagram of the net ash charge apparatus in the vacuum chamber. Shaded areas represent the aluminium lid and base of the chamber, and the chamber is approximately 40 cm tall. The chamber lid rests on a cylindrical glass tube and is sealed with L-shaped rubber seals. A perspex safety screen surrounds the chamber. Electrical connections have been omitted for clarity.

during experiments carried out at atmospheric pressure. Low pressure experiments, carried out at pressures of order 10^{-3} Torr (approximately 10^{-1} Pa), also had the advantage of much reduced charge loss from the Faraday cup. This was a result of decreased charge flow over the insulators (an effect of adsorbed water) and from prevention of any corona discharge in the atmosphere. The equipment was mounted on three studded rods threaded into the vacuum chamber floor. A lower base plate secured onto the rods held the Faraday cup and electrostatic fieldmeter. A similar top plate supported the sample collider and mesh (Figure 5.2). To prevent the top plate from vibrating during the collisions, it was locked to the vacuum chamber wall with rubber sash wedges before each experiment. Figure 5.3 shows photographs of the sample collider and mesh, and also of the Faraday cup mounted on the base of the vacuum chamber.

5.3.1.1 Particle production

Particle production was achieved by a sample collider consisting of a solenoid 'hammer' and a sprung anvil. The solenoid section of the collider is shown in Figure 5.4a. The solenoid was a 'pull' type but had a threaded hole drilled into the closed end. This allowed a rod to be attached which then provided the 'push' motion. (The first experimental design had used a pivot to convert the 'pull' into 'push', but the added complexity reduced the repeatability of the action). To ensure secure, repeatable actions of the solenoid with minimum friction, the rod was mounted on a high quality linear ball-slide. A small spring on the rod returned it to the original position after power was removed from the solenoid. The 'hammer sample' was secured onto the solenoid rod by a mounting collet. The solenoid unit was constructed on a length of 3 mm aluminium L-section which was then bolted to the top plate (Figure 5.2). The

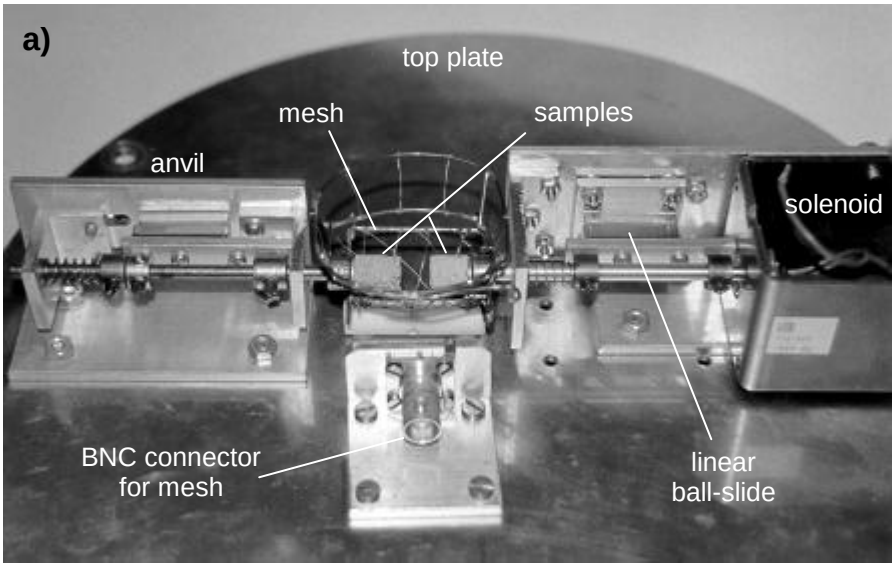

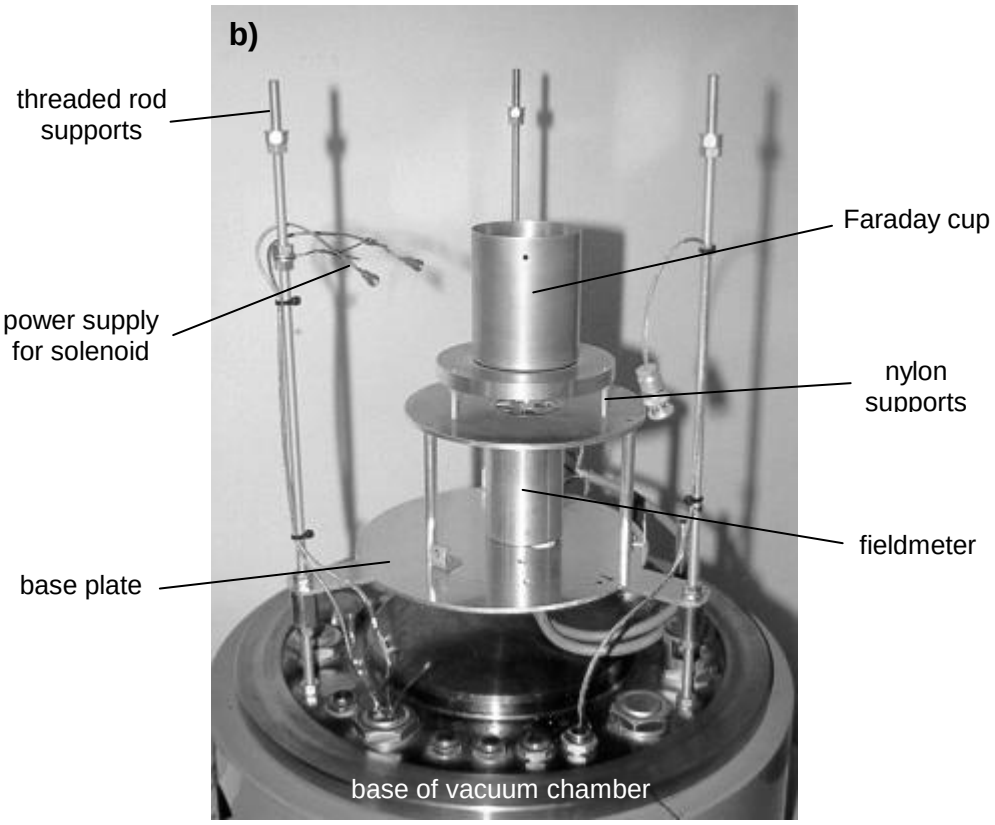

Figure 5.3 Photographs of net ash charge experimental apparatus. **a)** Sample collider; solenoid, anvil and mesh mounted on the top plate. Note that in this photograph, an extension has been added to the mesh to allow the attachment of a horizontal mesh below the samples for some experiments. **b)** The fieldmeter and Faraday cup, revealed by removal of the top plate and the shield.

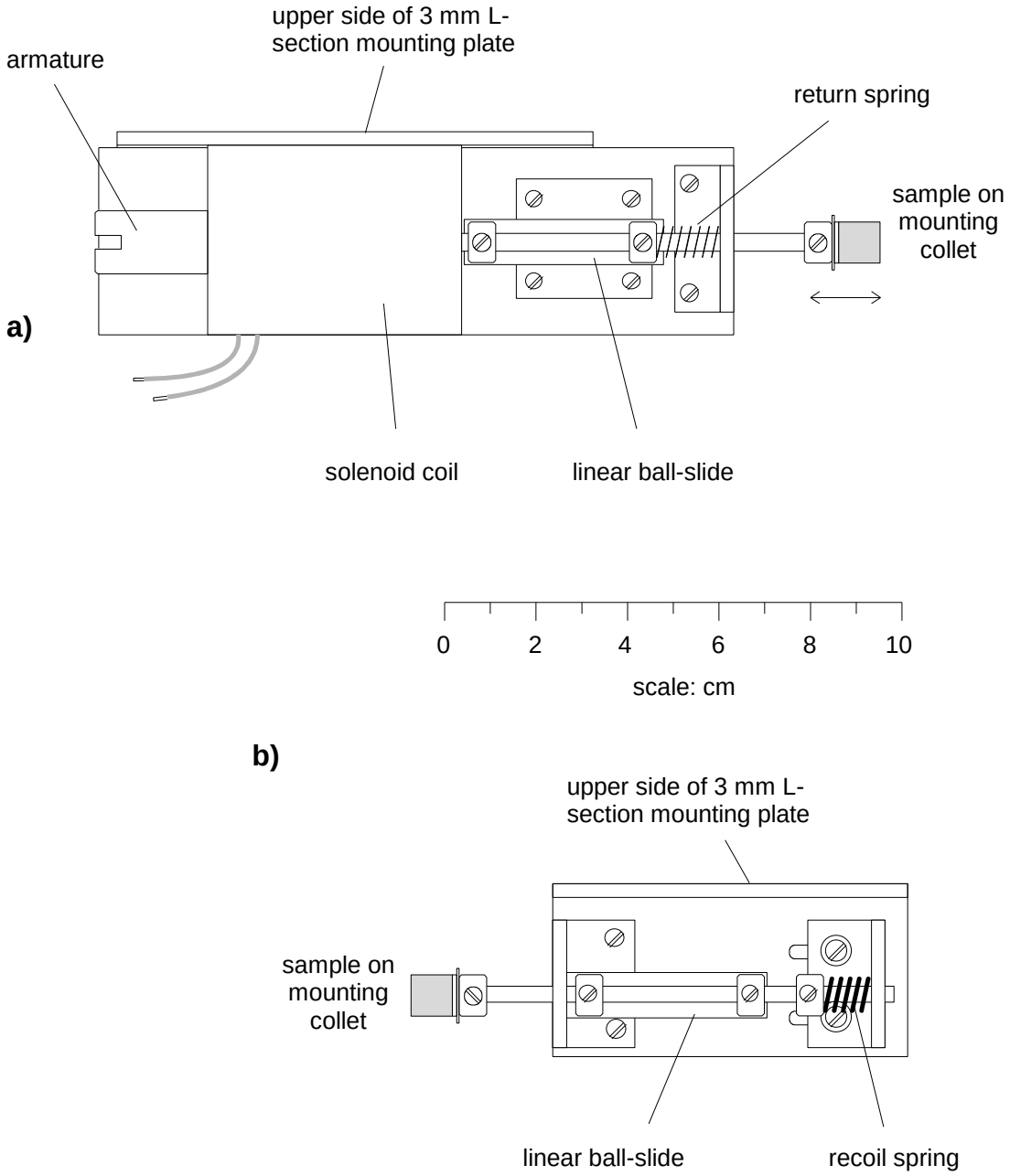

Figure 5.4 Components of the sample collider. **a)** The solenoid 'hammer'. **b)** The sprung anvil. Pumice samples are shown mounted on the ends of the rods.

motor used for rotational ‘grinding’ particle production was similarly mounted on 3 mm L-section. This modular approach allowed the solenoid and motor to be easily interchanged. Internal gearing of the motor produced a rotational speed of 60 rpm, and both motor and solenoid required a 12 V power supply.

The second sample was supported on a sprung anvil (Figure 5.4b). This sample was also mounted on a rod secured to a linear ball-slide, which allowed recoil during impacts. The spring could be changed or pre-compressed to allow a variety of return forces. The anvil was constructed on 3 mm aluminium L-section which was then bolted to the top plate.

Figure 5.5 shows the electrical connections for the experiment. To reduce electrical interference, the 12 V solenoid supply was not earthed to the vacuum system, which provided a system earth for the measurement circuits. The power supply was brought into the vacuum chamber by standard lead-throughs (single core copper wires embedded in insulation and epoxy). Inside the chamber, the leads were screened to further reduce interference primarily caused by the large back e.m.f. created when power to the solenoid was removed. This voltage spike had an amplitude of more than 50 V and was believed to cause minor arcing within the manual switch used to control the 12 V supply. Interference from the arcing produced large offsets in the mesh electrometer data, which were eliminated by putting a suppressor (100 Ω, 0.01 μF) in parallel with the solenoid coil.

The mesh over the collision area was constructed from fine steel wire, in a half-cylindrical shape. This was supported by thicker copper wire and mounted to the top plate by a PTFE insulator and nylon bolts. A BNC connector (bolted to the top plate) and shielded cable were used to provide an electrical connection from the mesh to the electrometer. Inside the vacuum chamber, the cable was supported by a threaded rod

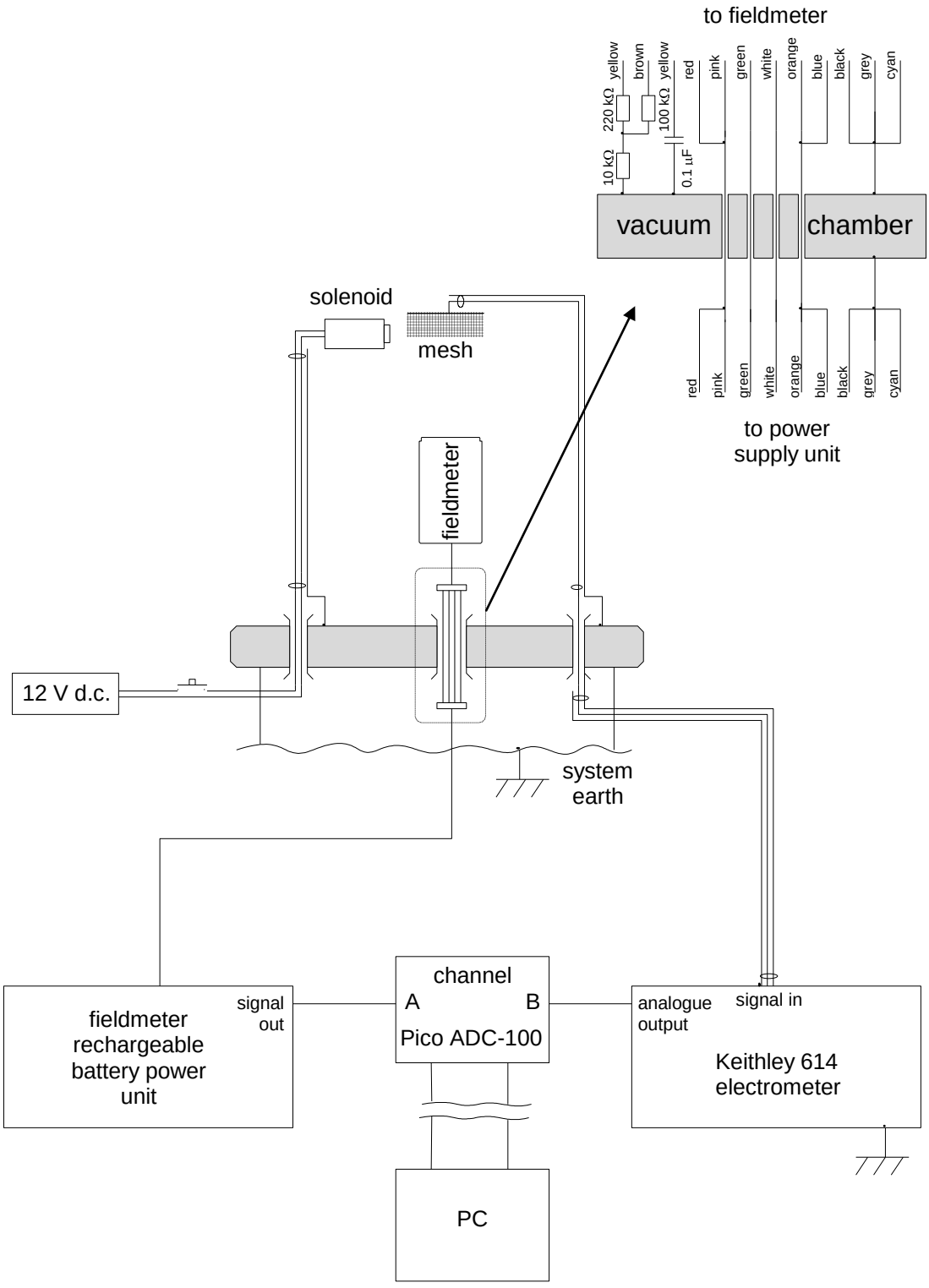

Figure 5.5 Schematic diagram of the electrical and data connections for the net ash charge experiment. The shaded area represents the base of the vacuum system through which the electrical connections are taken. The connections through the vacuum chamber for the JCI 121 fieldmeter are shown in detail at the top right.

and copper wire to prevent noise due to vibration of the cable. A PET 100 plug and socket formed the connection out of the chamber, the socket being mounted directly onto the triaxial electrometer lead. Careful shielding of the mesh connections was essential to prevent interference from operation of the solenoid. Figure 5.6a shows the effect of using an unshielded 'standard' lead-through rather than the PET connector. The operation of the solenoid (despite the presence of the suppressor) was recorded as offsets of about -6.1×10^{-13} C per activation by the electrometer (Figure 5.6a). With the PET connector, no offsets are observed over the drift of the electrometer (Figure 5.6b).

5.3.1.2 Faraday cup

The preliminary design of the ash charge measurement apparatus is shown in Figure 5.7. The fieldmeter was initially installed outside the vacuum chamber, due to the limited space inside the chamber. This design had a major drawback in that lengths of coaxial cable and connectors had to be attached to the charge sensitive part of the circuit (the Faraday cup). This produced unacceptably high rates of charge loss from the cup, which would have prevented any quantitative measurements from being taken. By installing the fieldmeter inside the vacuum chamber, the need for the cables and connectors attached to the Faraday cup was removed. Disconnecting the cables also decreased the capacitance of the cup and thus increased the sensitivity of the apparatus (see section 5.3.5.1). The effect of connecting cables on the rate of charge decay from the Faraday cup is shown for the apparatus in this configuration by the two decay curves in Figure 5.8. With a single cable attached to the Faraday cup (for fieldmeter calibration purposes) charge decay rates were very much enhanced. The graph also shows that a 'background' potential gradient (equivalent to a potential of

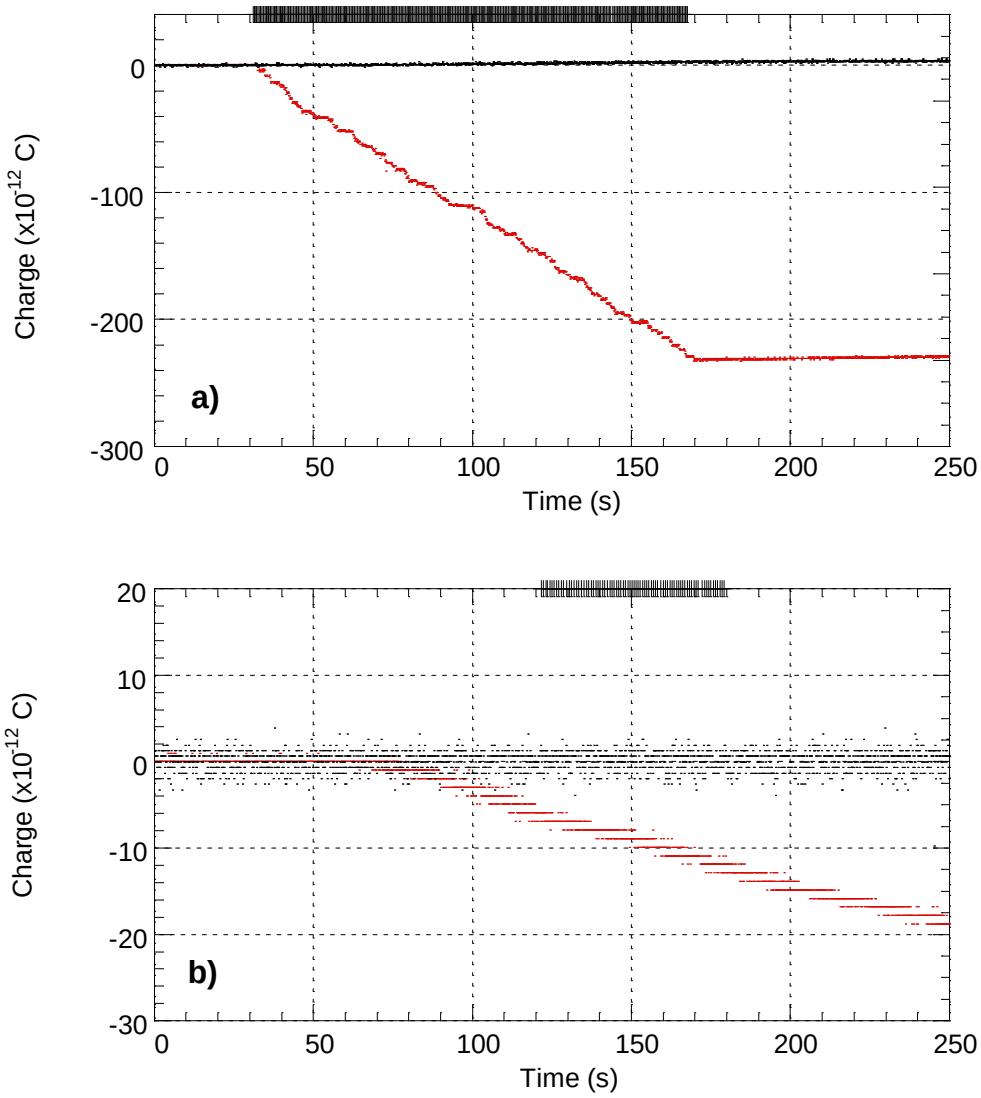

Figure 5.6 Shielding effects for the electrical connection to the mesh. **a)** Data collected using an unshielded, standard lead-through, with 376 solenoid activations. **b)** Data collected using the PET 100 connectors, with 86 solenoid activations. Black points represent charge on the Faraday cup, red points represent charge measured on the mesh. Individual activations of the solenoid are indicated by marks on top axis. In **b)**, the electrometer's zero-check was released after 60 s, and drift of the electrometer then produced a steady rate of apparent charge collection. No change in this steady drift rate was observed due to the solenoid activations.

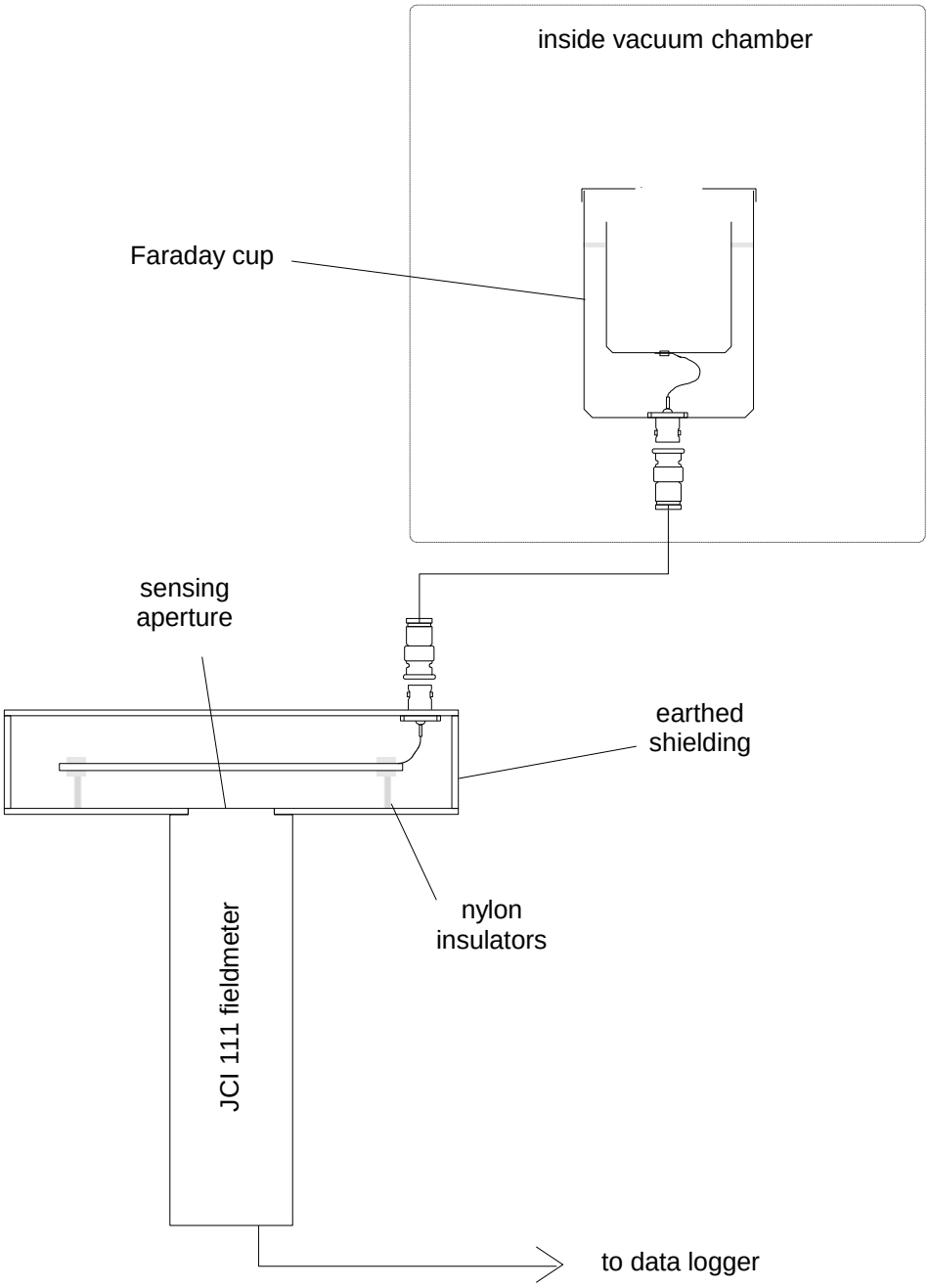

Figure 5.7 Original design of the net charge measurement apparatus. The Faraday cup was mounted inside the vacuum chamber, but the fieldmeter located outside. The fieldmeter detected the voltage of a plate mounted above its sensing aperture. The plate was connected to the Faraday cup by coaxial cable.

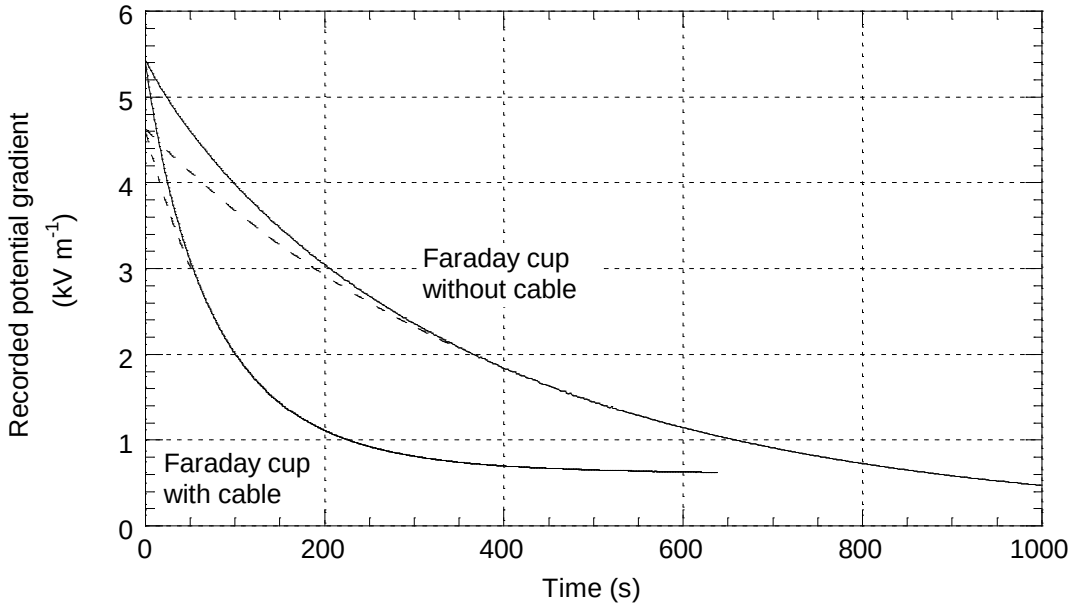

Figure 5.8 The effect of attached cables on the charge decay rate of the Faraday cup. The dashed lines represent best fit exponential curves (with $R > 0.99$) fitted for zero-corrected data less than 3 kV m^{-1}. Departure of the curves from the exponential fits demonstrates that the system was not acting as a pure resistance–capacitance circuit. The curve for the Faraday cup with an attached cable does not appear to tend to zero, demonstrating that a contact potential (of about 1.8 V) was present in the system. The distance between the base of the Faraday cup and the fieldmeter was 3 mm during the experiments.

about 1.8 V on the Faraday cup) was present in the system with this arrangement. This was undoubtedly a contact potential somewhere in the cables or connectors and was highly undesirable.

Details of the design used are shown in Figure 5.9. The Faraday cup (constructed from a 0.4 litre aluminium Sigg fuel bottle) was mounted on a circular, 10 mm thick, aluminium plate which formed the upper plate of a parallel-plate capacitor. This was supported by three nylon bolts (nylon 6,6) securely fastened into an earthed lower plate, which had the sensing aperture of a JCI 121 fieldmeter mounted flush within it. The bolts located into three holes in the 10 mm plate which then rested on nuts threaded on to the bolts. This allowed easy removal of the Faraday cup assembly for sample retrieval and precise re-positioning afterwards. Care was taken to ensure that the bolts were as clean as possible at all times to reduce charge dissipation over their surfaces. The Faraday cup assembly had rounded edges and was polished to reduce any surface roughness which would have increased charge decay through the atmosphere. The fieldmeter and Faraday cup were mounted inside an aluminium shield to protect them from electrical interference. A 5 cm diameter, mesh-screened hole in the top of the shield allows particles to fall into the cup. The mesh was constructed with a 10 mm hole size which allowed easy access for silicate particles, but prevented any ions from entering the assembly. The particles entering the cup fell onto a circular aluminium foil insert at the base. This was removed at the end of each experiment to allow the particles to be retrieved.

The fieldmeter was powered by a rechargeable battery power unit (also used during the fieldwork, see Figure 4.3), which was located outside the vacuum chamber. The use of battery power isolated the fieldmeter from mains-borne interference and

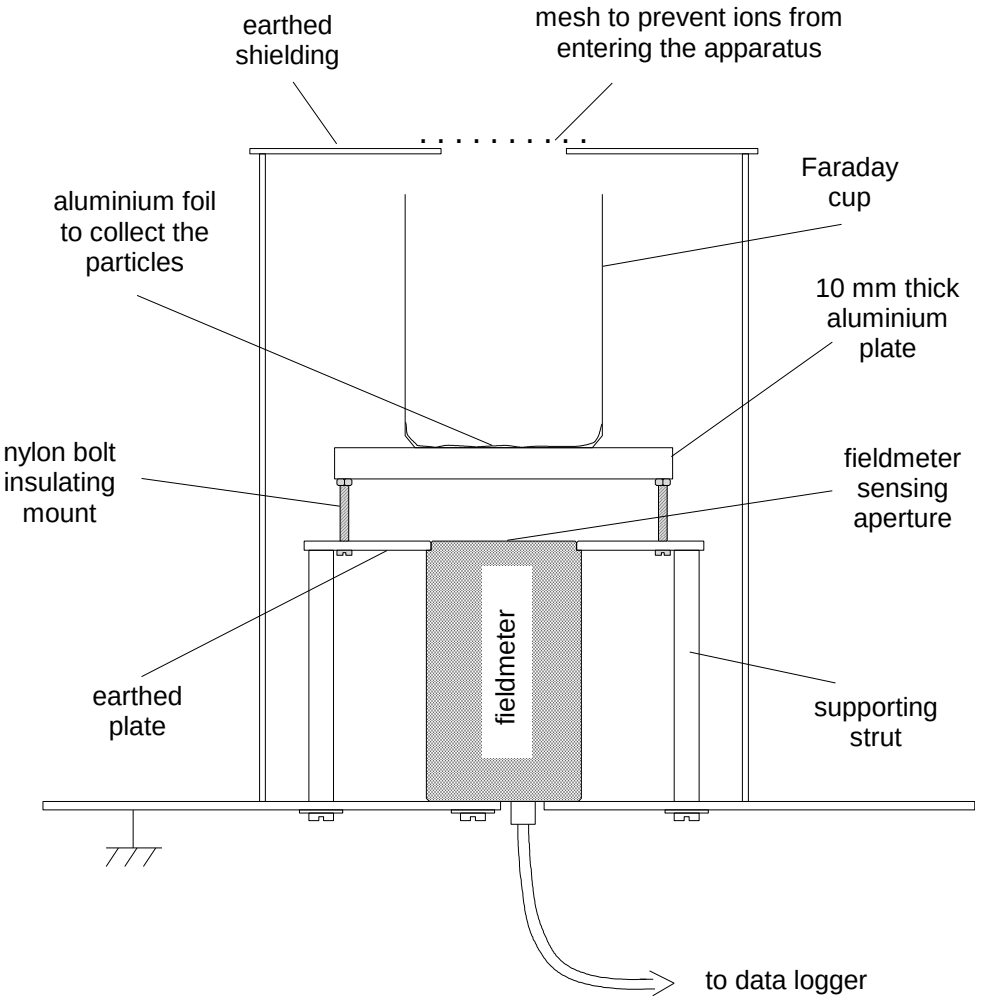

Figure 5.9 The net charge measurement apparatus. Diagram is to scale and the height of the surrounding shield was 210 mm.

allowed it to be earthed to the system earth provided by the vacuum chamber (Figure 5.5).

5.3.2 Data logging

The electrometer and fieldmeter readings were logged to a 486 PC using a Pico ADC-100 analogue to digital converter (Appendix I). This two channel, 12-bit ADC transferred data to the PC in real-time down a parallel cable. PicoLog software provided control of the converter and recorded the data. The DC voltage option was used, providing scales between ±200 mV to ±20 V. Data were normally recorded as ADC counts (i.e. as an integer between ±2047). However, for some calibration experiments it proved more convenient to record voltages directly.

Timing events during experiments were logged using a LogIT data logger (Appendix I). The 'mark' capability of the logger was used to indicate activation of the solenoid and the release of the electrometer zero-check facility. The starting and stopping of the LogIT, and the 'marks', were manually controlled because the precise timing of events was not critical to experiments. Even so, times were accurate to within a few tenths of a second.

5.3.2.1 Mesh data logging

The Keithley Model 614 electrometer (Appendix I) is equipped with a ±2 V analogue output which was used to record the charge measurements made from the mesh. This output provides a ratio of the full scale deflection (fsd). The measurement function (either charge or voltage), and the scale being employed were manually recorded.

The charge and voltage measurement functions of the electrometer have ranges of 20, 2, and 0.2 nC or V. The 4½-digit display gives a resolution of 5×10^{-5} of the full scale deflection, and a zero-check facility allows verification of any zero-offsets in the reading or output. Accuracy of the 20 V voltage range is quoted as ±(0.08 % + 1 mV), and for the 2 nC charge range as ±(5 % + 0.5 pC). Twelve-bit logging with the Pico ADC-100, reduced the recorded resolution to 1/2047 of the full scale deflection, i.e. to about 5×10^{-4} fsd.

Preliminary tests of logging the electrometer output demonstrated two problems: a low signal to noise ratio, and non-linearity with respect to the electrometer display (Figure 5.10a). The noise had a distinct peak at 9 kHz, and appeared to be generated by the logger (Pico or LogIT type) when it was connected to the electrometer. The problem was effectively eliminated by connecting a 100 nF capacitor across the output terminals of the electrometer. This also restored the output linearity (Figure 5.10b). With the parallel capacitor, noise amplitude was reduced to about 1 ADC count, or 2 to 3 counts if the fieldmeter was being logged simultaneously.

5.3.2.2 Faraday cup data logging

The potential of the cup was detected by the JCI 121 fieldmeter which had a quoted accuracy of better than 1 % of the full scale deflection at any scale, and internal noise less than 10 V m^{-1} in amplitude. The ±1.1 V analogue output was logged with the Pico ADC-100 on a ±2 V range. This gave a recorded resolution of about 1 V m^{-1} when the fieldmeter was on its lowest range (2 kV m^{-1}). Resolution could have been increased by logging over a ±1 V range, but data could have been lost during any

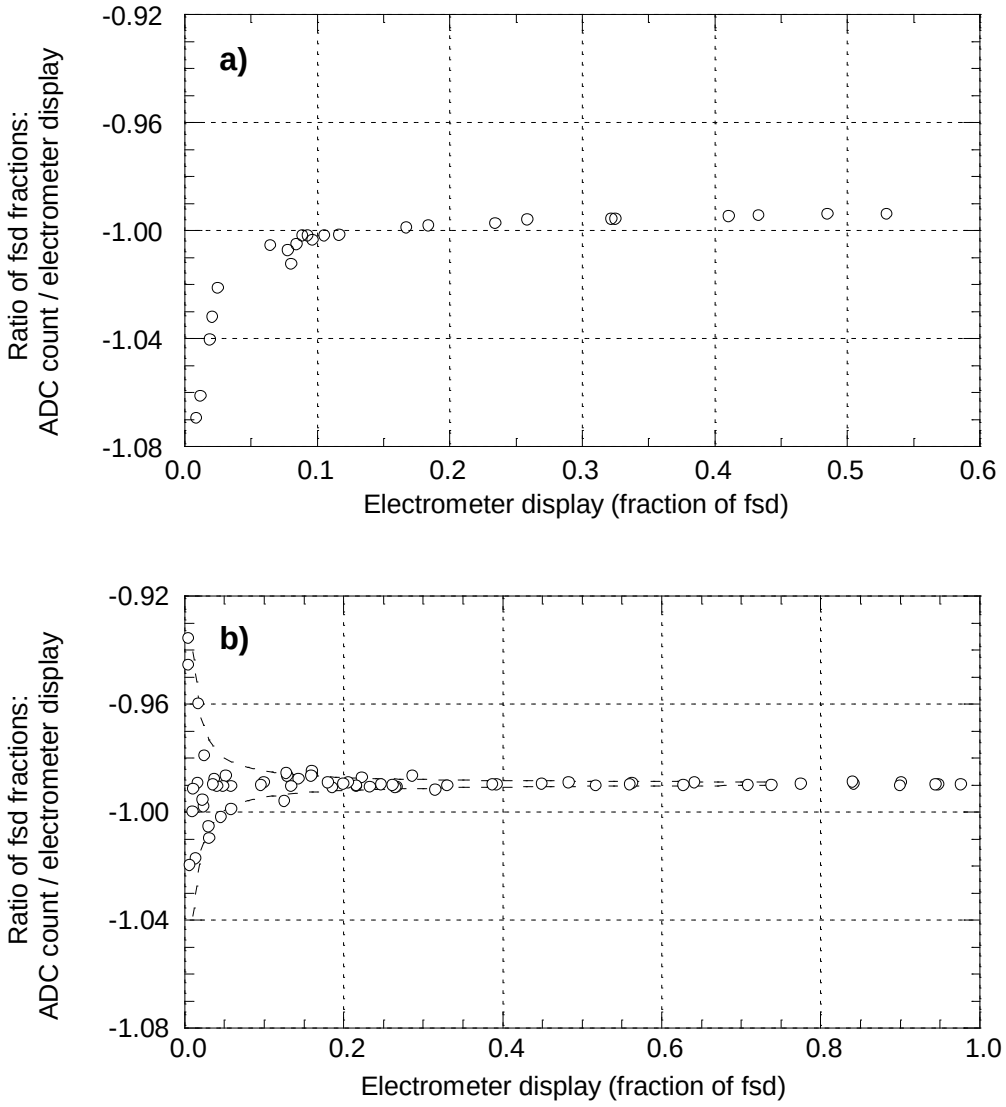

Figure 5.10 Linearity of logging the electrometer output. The plots show ratios of the ADC logged output of the electrometer to the electrometer display. Both values have been scaled to their full scale deflection (fsd) value. (The negative values are due to the output polarity of electrometer being inverted when using the voltage function). **a)** Non-linearity produced when no extra capacitance is applied to the electrometer output. At low output values, the ADC count is no longer a linear function of the electrometer display. **b)** Good linearity with an additional 100 nF capacitance applied across the electrometer output. The dashed lines show the expected spread of points from a ±1 digit variation in the ADC count. Note that the determined ratio was actually -0.99 rather than -1.00.

fieldmeter range changes. Although range data were not recorded, fieldmeter range changes were obvious when they occurred due to large step changes in the data values.

5.3.3 Sample impact velocities

The impact velocity of the samples could be altered by varying the voltage applied to the solenoid. Voltages between 6 V and 13 V were used and Figure 5.11a shows the way in which the velocity of the hammer, after 8 mm of travel, was determined (8 mm was the standard separation distance of the samples used during experiments). The velocities produced by different solenoid voltages are shown in Figure 5.11b. Kinetic energy was also calculated, using a hammer mass (the total of solenoid plunger, rod, slider of the ball-slide and collets) of 71.6 g. It must be noted, however, that this these figures do not represent impact energies, because power was still drawn by the solenoid during impacts of the samples. This proved to be necessary in order to fragment the pumice at a reasonable rate, but does prevent analysis of the actual amount of energy involved in each collision.

5.3.4 Electrometer calibration

The logged ADC count of the electrometer analogue output was calibrated to the electrometer display reading by applying voltages to the electrometer in the voltmeter mode (20 V range). The voltmeter function allowed accurate measurement of many different input potentials to provide further linearity checks as well as scaling. The output was logged by the Pico ADC-100, as different voltages were applied to the input. The ADC count, *adc*, was then compared to a manual record of the digital display reading. Figure 5.12 shows the results of one calibration experiment. The inversion of the output polarity is an internal feature of the electrometer when using

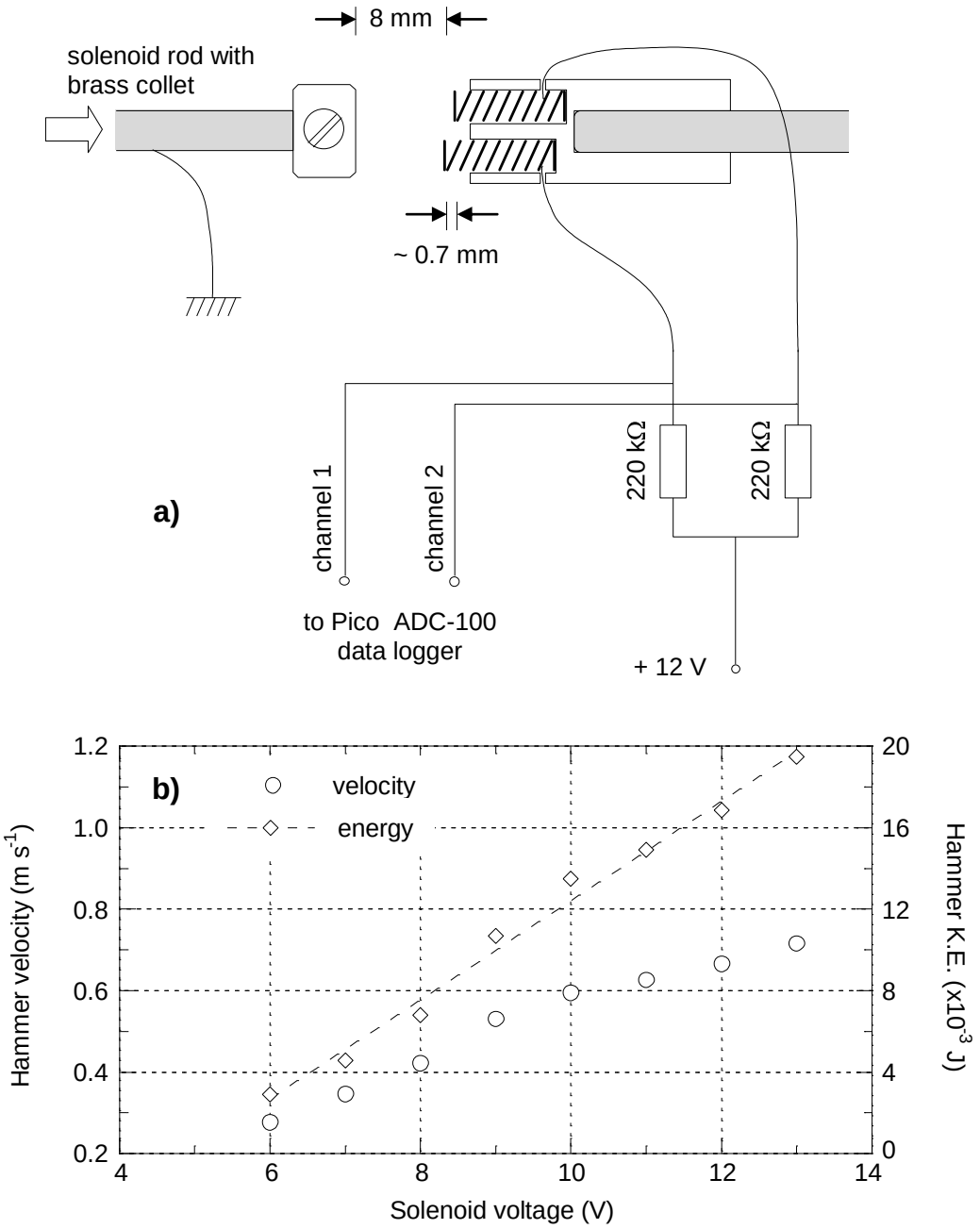

Figure 5.11 Hammer velocity and energy. The apparatus used to measure the velocity is sketched in **a)**. Soft spring contacts, held in a PTFE rod were used to time the brass collet over a distance of about 0.7 mm. Contact of the collet with each spring was detected as a downwards going edge by oscilloscope software for the Pico data logger. The results for different solenoid voltages are shown in **b)**. Each point represents the average of ten measurements, and the timed distance was measured accurately by micrometer before and after each ten measurements. The dashed line shows a best fit straight line for the kinetic energy results.

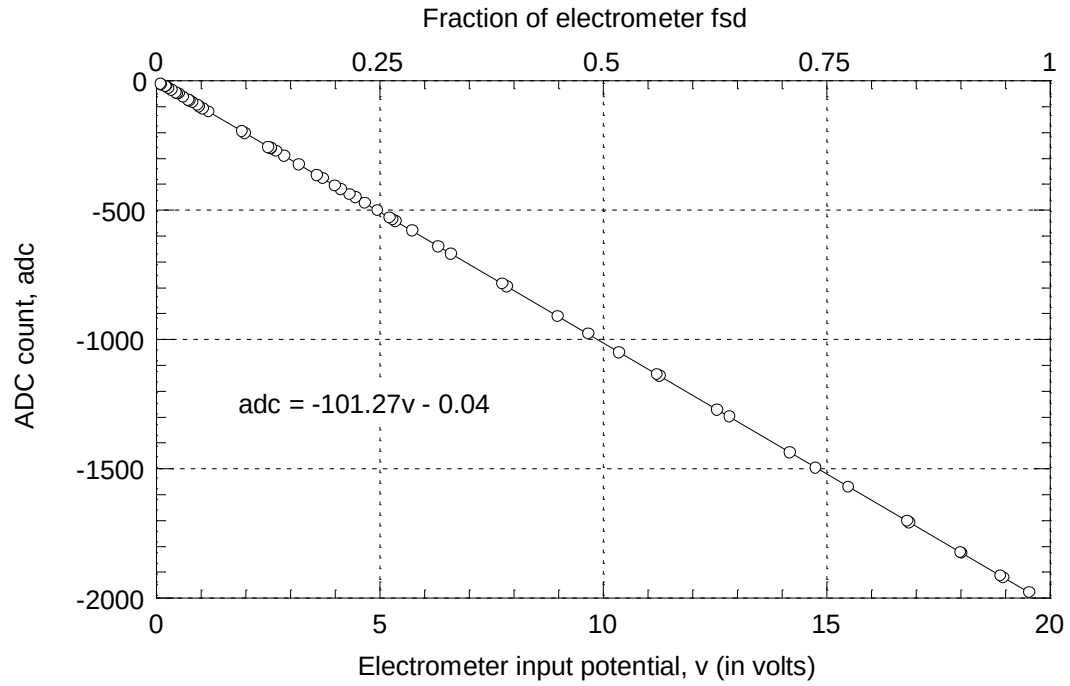

Figure 5.12 Calibration of logging the electrometer output. The plot shows the recorded ADC count when a potential was applied to the electrometer input. The inverted output polarity is an internal feature of the electrometer when using the voltage function; when measuring charge, positive ADC counts reflected positive charge readings.

the voltage scale. If the polarity is corrected and the small offset neglected then the reciprocal of the gradient gives the relationship needed. Converting this to a generic expression representing fraction of the full scale deflection gives

$$\text{fraction of fsd} = 4.94 \times 10^{-4}\, adc \qquad (5.1).$$

This scale was then adapted for logging the mesh data because the internal accuracy of the electrometer charge measurements was higher than could be experimentally tested. (Note that charge measurements made with the electrometer were also used to determine the capacitance of the Faraday cup (see section 5.3.5.3). This approach produced a value confirmed by finite element modelling, reflecting confidence in both the electrometer internal calibration and the charge conversion from logged values). During most experiments the 2 nC range was used, so the mesh charge, Q_m (in coulombs), was determined as

$$Q_m = 9.9 \times 10^{-13}\, adc \qquad (5.2).$$

Noise in the mesh data (produced within the electrometer, ADC or cables) thus had a maximum amplitude of between 2×10^{-12} and 3×10^{-12} C. The electrometer was also prone to drift at an approximate rate of 0.2×10^{-12} C s^{-1}.

5.3.5 Faraday cup calibration

To calculate the amount of charge collected in the Faraday cup, the potential of the cup, V_{fc}, and its capacitance, C_{fc}, are required. The charge on the cup, Q_{fc}, is then given by

$$Q_{fc} = C_{fc}\, V_{fc} \qquad (5.3).$$

Calibration was thus divided into two operations, determination of V_{fc}, from the fieldmeter output, and obtaining the Faraday cup capacitance. Both of these were

dependant on the separation distance between the base of the cup and the fieldmeter. However, this distance also controlled the sensitivity of the apparatus and the rate of charge loss from the cup.

5.3.5.1 Sensitivity and decay rate considerations

Given the fixed response of the fieldmeter, the charge sensitivity of the apparatus was determined by the capacitance of the Faraday cup. By modelling the Faraday cup and shield as simple parallel plate and coaxial capacitors (see section 5.3.5.3), the effect of varying the separation distance between the fieldmeter and the base of the Faraday cup was investigated. Figure 5.13 shows the results of this theoretical analysis. The top line shows the apparatus sensitivity if the Faraday cup was unshielded (thus all its capacitance would be between the base plate and the fieldmeter). In this case, the capacitance is inversely proportional to the separation distance (if edge effects are neglected), and thus the potential of the cup, for any particular charge, is proportional to the distance. This produces a constant potential gradient for different separations. If the cup is shielded (Figure 5.13, lower line), some capacitance is independent of the separation (see the dashed line), and increasing separation then decreases the potential gradient produced per unit charge. Thus, considering the sensitivity of the apparatus alone, the best system would use a small separation distance.

As charge builds up in the cup and its potential rises, some charge is lost to the surroundings. This charge flow can be over or through the insulating mounts, or through the atmosphere, and represents unmeasured (lost) charge. Thus, the Faraday cup can be considered as a resistance–capacitance circuit. If the effective resistance to

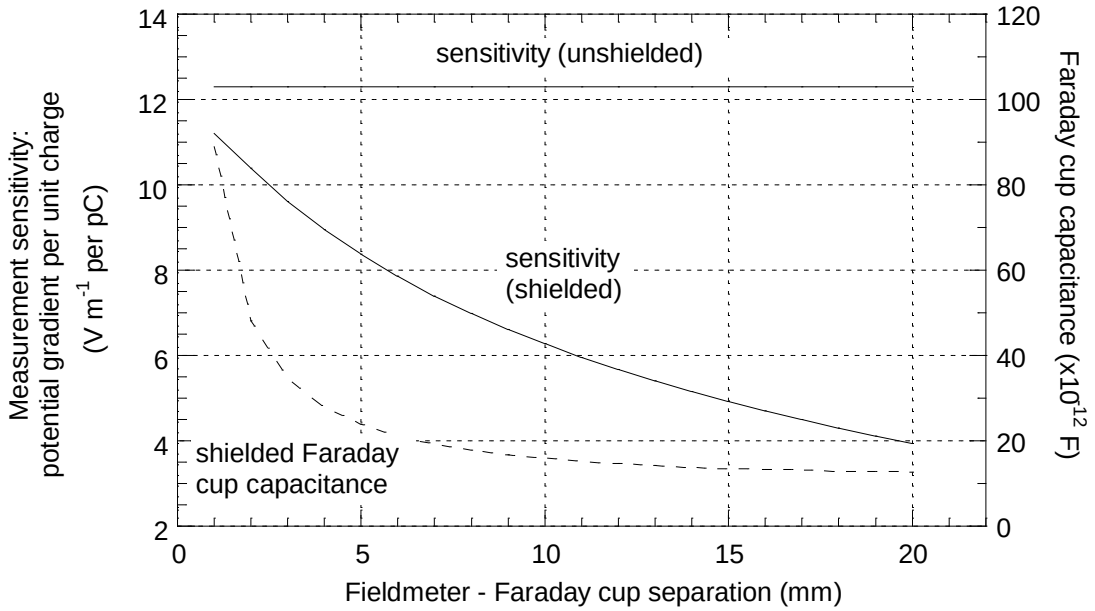

Figure 5.13 Theoretical sensitivity of measurements made by the Faraday cup. The solid lines represent the sensitivity of shielded and unshielded Faraday cups as a function of the cup to fieldmeter separation distance. The dashed line shows the way in which the capacitance of a shielded cup varies with the separation.

earth is R_{fc}, a charge, Q_0, placed on the resistance–capacitance circuit (given that R_{fc} obeys Ohm's law) decays as

$$Q_{fc} = Q_0 \exp\left(\frac{-t}{R_{fc}C_{fc}}\right) \qquad (5.4).$$

Thus, to record accurately the initial charge placed within the cup over a period of time, the decay constant, $R_{fc}\,C_{fc}$, must be as large as possible to reduce charge loss. Changing the Faraday cup–fieldmeter distance varies both R_{fc} (due to the changing length of the insulators) and C_{fc} (Figure 5.13). Increasing the separation distance increases the resistance, but decreases the capacitance.

Figure 5.14a shows decay data obtained by applying 20 V to the Faraday cup, then removing the supply, for different separation distances. The data can be fitted with exponential curves (with R > 0.99) and the $R_{fc}\,C_{fc}$ values obtained are plotted in Figure 5.14b. The increasing $R_{fc}\,C_{fc}$ with separation distance demonstrates that the resistance term dominates over the changes in capacitance of the cup. The anomalously low value of $R_{fc}\,C_{fc}$ at 3 mm separation is due to the fact that, to produce this distance, the nylon nuts supporting the Faraday cup had to touch the lower plate, and this increased the effective nylon surface area over which charge could flow. The calculated reduction in resistance, compared to similar lengths of nylon bolt, is close to a factor of ten.

Thus, when charge loss from the Faraday cup is considered, larger separation distances are better. Excessive charge losses during an experiment would have been difficult to quantify, so low decay rates were given priority over sensitivity. Thus, a separation of 20 mm was used, the distance being limited by the length of the bolts and the physical stability of the Faraday cup. Further consideration of charge decay,

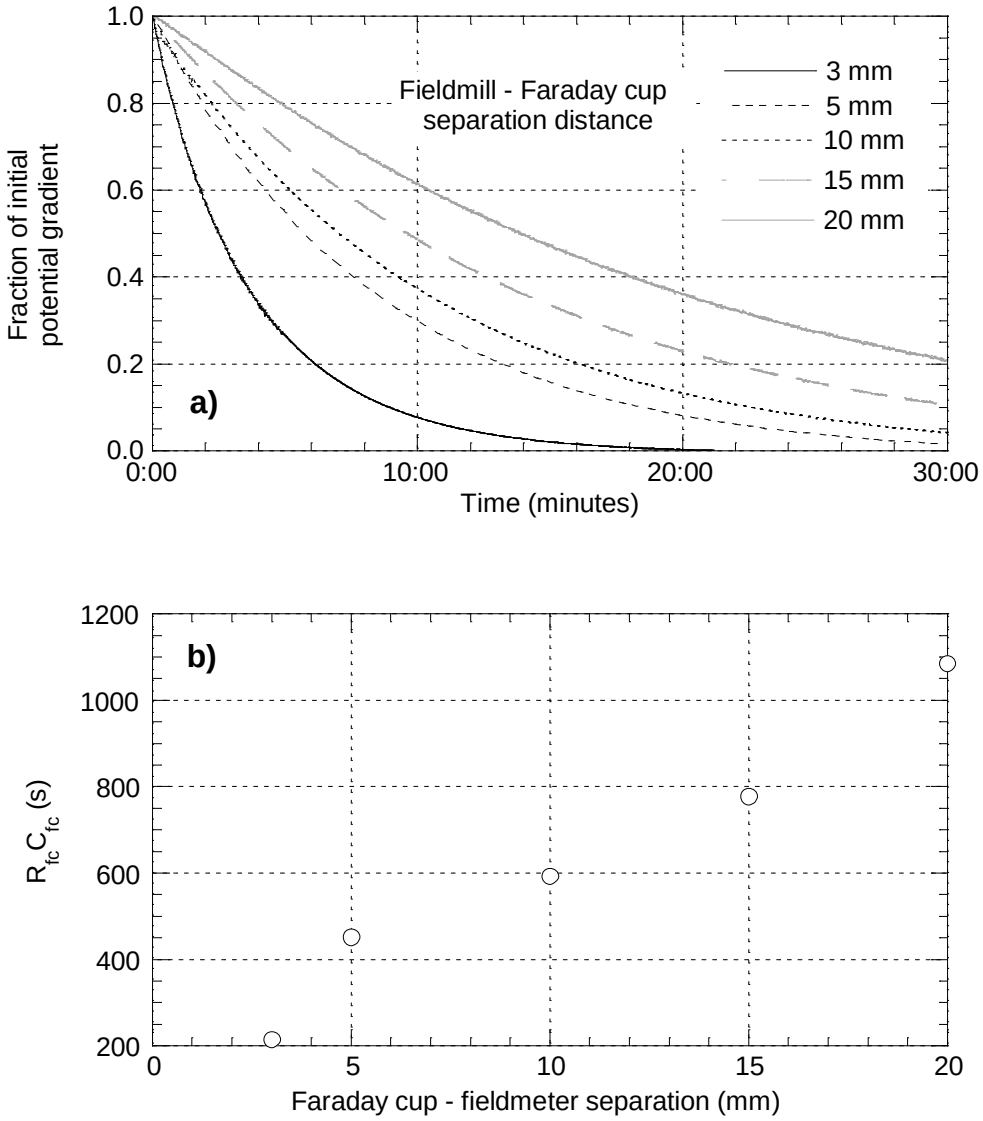

Figure 5.14 Charge decay from the Faraday cup. **a)** Decay curves recorded after a potential of 20 V was applied to the Faraday cup. (22.9 to 23.2 °C, 36 % RH). **b)** $R_{fc}\,C_{fc}$ values for the decay curves.

and theoretical analysis of the charge loss during a typical experiment is given in section 5.3.5.4.

5.3.5.2 Fieldmeter output

The fieldmeter output was calibrated by applying known voltages to the Faraday cup and recording the ADC count of the potential gradient measurements made. This technique thus correlated the ADC count directly to the potential of the Faraday cup. It avoided calculation of actual potential gradients and measurement of the effective gap between the fieldmeter sensing aperture and the base plate of the Faraday cup.

Figure 5.15a shows the data logged during a typical calibration experiment. Plotting the average ADC value for each applied voltage against the voltage produced the straight line shown in Figure 5.15b. To retrieve the ash sample after each experiment, the Faraday cup had to be removed, and new foil inserted before it was replaced. To ensure that this did not affect the charge sensitivity of the apparatus, the calibration was rechecked several times over the period during which experiments were being carried out. Calibration data are presented in Appendix III, including data from one experiment carried out under vacuum. Any zero-offset of the fieldmeter output could be removed individually for each experiment, so offsets were not required as part of the calibration. For calculating the Faraday cup potential from the response of the fieldmeter, the reciprocal of the gradient was needed. Using the average value from the experiments gave the potential, in volts, as

$$V_{fc} = 0.03968\, adc \qquad (5.5).$$

Differences in the reciprocal gradient were less than 0.8 % of this average.

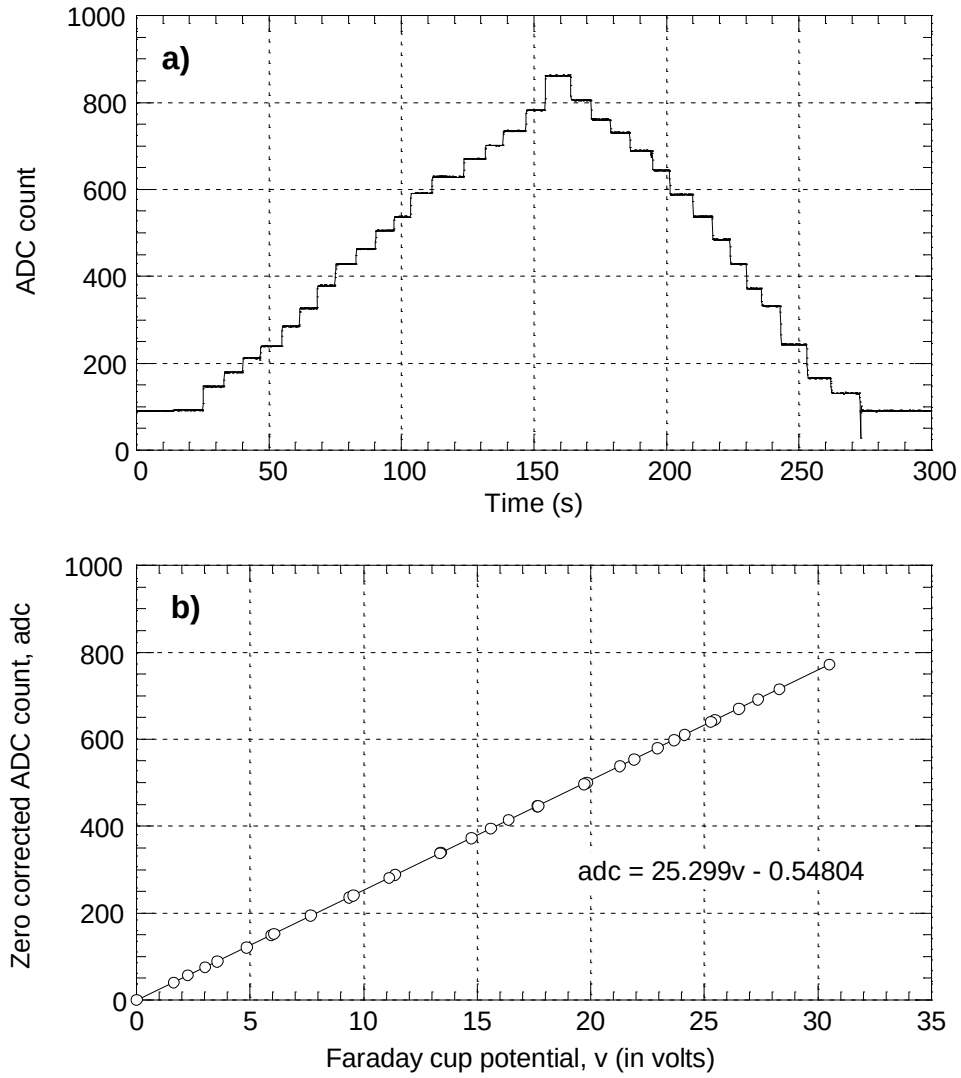

Figure 5.15 Fieldmeter output calibration. **a)** The raw data recorded from the fieldmeter when different potentials were applied to the Faraday cup (02/06/98). Plotting the Faraday cup potential against the zero-corrected ADC values produces the relationship shown in **b)**.

5.3.5.3 Faraday cup capacitance

The capacitance of the Faraday cup was assessed using four independent methods: by direct measurement using a multimeter; experimentally (by recording the charge stored on the cup as a voltage was applied); by theoretical calculations; and by numerical modelling.

Direct measurement.

The multimeter used (an Iso-tech 103) had a resolution of 1×10^{-12} F and a quoted accuracy of $\pm(1\ \% + 40 \times 10^{-12})$ F for its most sensitive scale. Repeated capacitance measurements were taken of a coaxial cable, and then of the cable attached to the Faraday cup. All measurements produced the same values for the cable only, 223×10^{-12} F, and for the cable and Faraday cup, 239×10^{-12} F. The cable and Faraday cup represented capacitors connected in parallel, therefore C_{fc} was found by simple subtraction, giving 16×10^{-12} F. Assuming that this subtraction removed any non-percentage error (offset of the meter), the accuracy of the result should have been limited by the meter resolution, and thus can be given as $\pm 0.5 \times 10^{-12}$ F.

Experimental.

The electrometer was used to detect the charge flowing into the system when a potential of 20.00 V was applied (Figure 5.16a). Again, measurements were taken of the switch and coaxial cable, and then repeated with the cable attached to the Faraday cup. To compensate for drift in the electrometer, the ±2 V analogue output was logged continuously over the time during which the potential was applied and best-fit lines were then used to obtain the charge that flowed onto the system (Figure 5.16b). Ten reading were taken for both the cup, and the cup with cables (Table 5.1), but up to

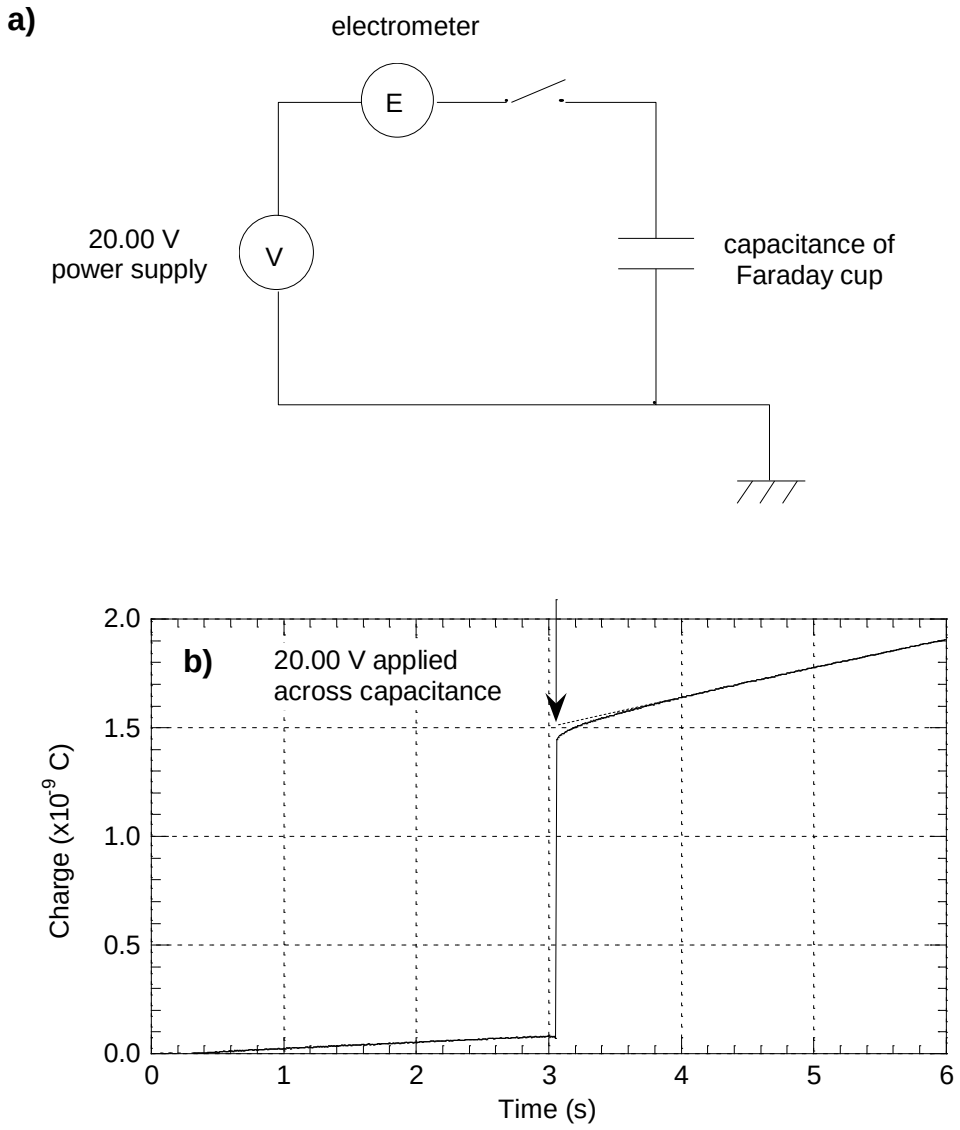

Figure 5.16 Experimental determination of the Faraday cup capacitance. The charge flow onto the Faraday cup was measured using the circuit shown in **a)** when a potential of 20.00 V was applied. Data logged from the electrometer during one of these experiments are shown in **b)**. When the potential was applied, charge flowed rapidly onto the Faraday cup. Note the increase in drift rate of the electrometer after this time, when the extra components (cables and Faraday cup) were connected into the circuit. The dashed extrapolation of these data show the line used to calculate the charge flow onto the cup (about 1.4×10^{-9} C). The delayed convergence of the data to the line between 3 and 4 s was probably due to the extra capacitance put on the output of the electrometer.

Table 5.1 Results of calibration experiments to determine the Faraday cup capacitance. Charges marked with a 'd' were thought to be unreliable due to bounce in the switch applying the voltage to the Faraday cup. Results from these runs were thus discarded, and not included in the averages.

Run Number	Charge flow into apparatus (units of 10^{-9} C)	
	Faraday cup and cables	Cables only
1	1.4631 d	1.0957
2	1.4266	1.0900
3	1.4355 d	1.1024
4	1.4382 d	1.0991
5	1.4497 d	1.1199 d
6	1.4205	1.0888
7	1.4253	1.0965
8	1.4261	1.0891
9	1.4179	1.0919
10	1.4252	1.1192 d
Average	1.4236	1.0942
σ_{n-1}	0.0035	0.0050
Charge flow onto cup in units of 10^{-9} C		0.3294 ± 0.0061
Cup capacitance in units of 10^{-12} F		16.47 ± 0.31

four (labelled ‘d’) of each were discarded due to bounce in the switch producing unreliable results. Averages of the remaining results were then used to calculate the capacitance of the Faraday cup, which was found to be $(16.47 \pm 0.31) \times 10^{-12}$ F.

Theoretical calculation.

Representing the Faraday cup assembly as a combination of two parallel plate capacitors and two coaxial capacitors allowed a very simple theoretical calculation of its capacitance. The top of the Faraday cup was represented as a flat plate, and all end effects were neglected. The summation used was

$$C_{\mathrm{fc}} = \frac{\pi r_1^2 \varepsilon_0}{d_1} + \frac{\pi r_2^2 \varepsilon_0}{d_2} + \frac{2\pi \varepsilon_0 l_1}{\ln\left(\frac{r_0}{r_1}\right)} + \frac{2\pi \varepsilon_0 l_2}{\ln\left(\frac{r_0}{r_2}\right)} \qquad (5.6),$$

for which, with the exception of ε_0, the permittivity of free space (8.85×10^{-12} F m^{-1}), the symbols are defined in Figure 5.17. Using the appropriate dimensions, also provided in Figure 5.17, gives

$$C_{\mathrm{fc}} = (2.16 + 3.48 + 5.32 + 1.23) \times 10^{-12} \qquad (5.7)$$

$$= 12.2 \times 10^{-12} \text{ F}.$$

Numerical modelling.

The electrostatic field generated by the Faraday cup inside the shield was modelled with ‘QuickField’ (a PC application, Student’s QuickField 4.0; free via http://www.tera-analysis.com/). The program determines the potential field over a finite element mesh (using Poisson’s equation), with either planar or cylindrical symmetry. Figure 5.18 shows the potential field generated by a model of the Faraday cup using cylindrical symmetry. The cup has been given a charge of 100×10^{-12} C and

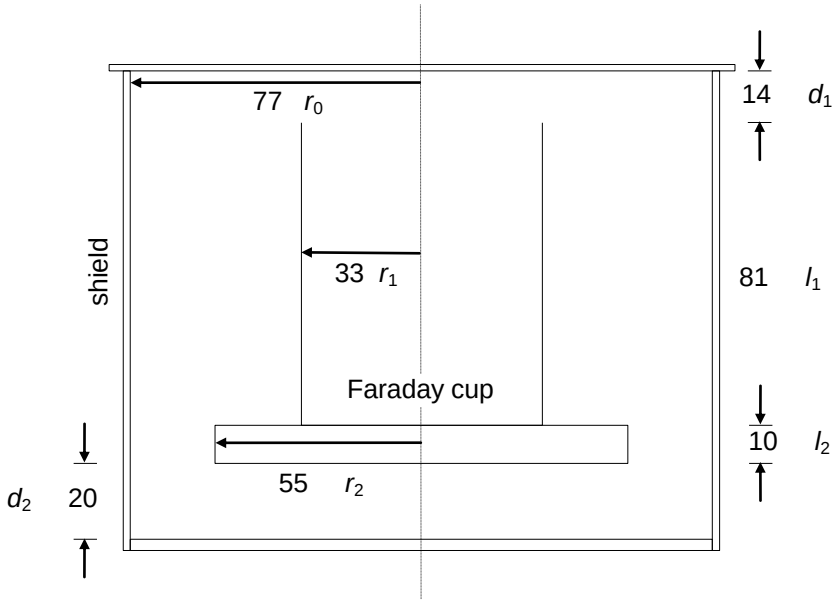

Figure 5.17 Theoretical determination of the Faraday cup capacitance. The diagram shows the distances (in mm) used to model the apparatus as two coaxial capacitors and two parallel plate capacitors. The top of the Faraday cup was modelled as a flat plate for simplicity. See text for the equations used.

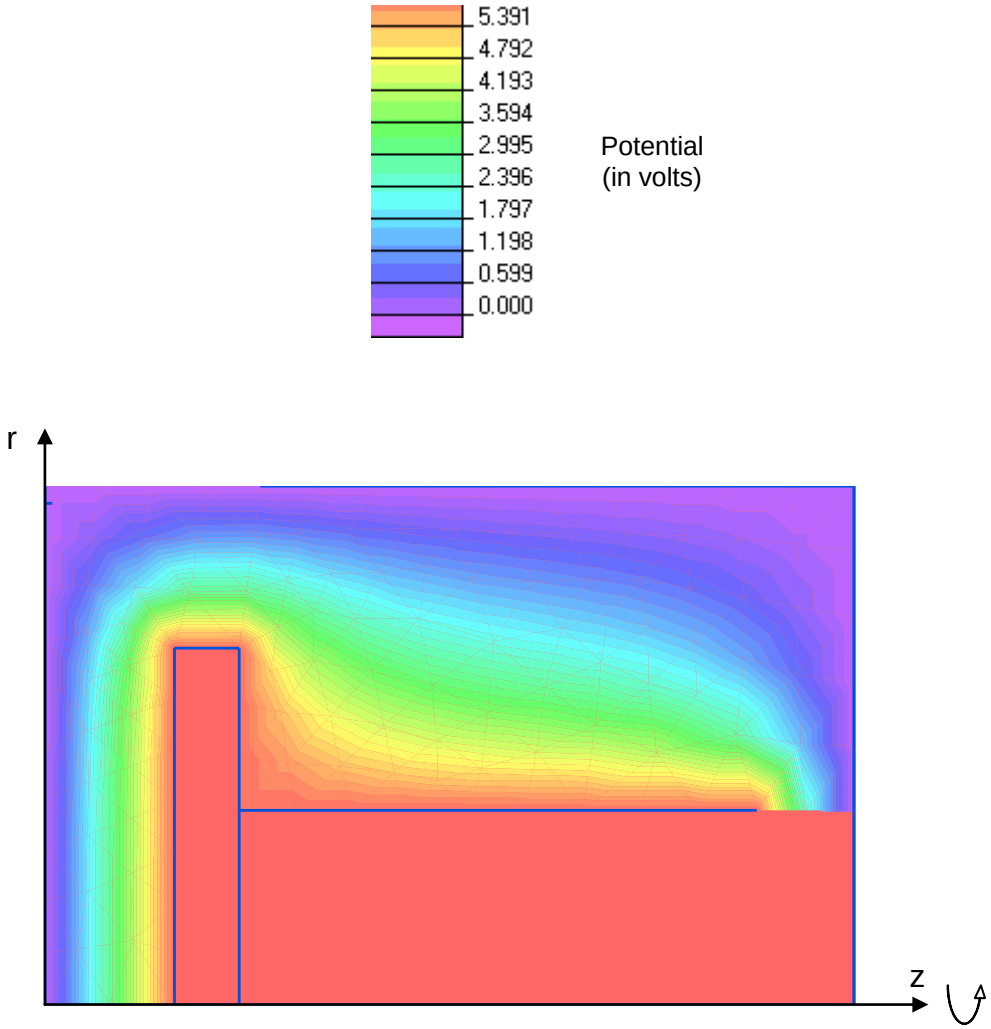

Figure 5.18 Determination of the Faraday cup capacitance by numerical modelling. The diagram shows the model used to represent the apparatus and displays the results of the potential field determination. The model is cylindrically symmetric around the z axis.

its calculated potential is 5.9929 V, implying a capacitance of 16.86×10^{-12} F (from equation 5.3).

With the exception of the most simplistic approach (theoretical calculation) the estimates of capacitance are all close to the value obtained experimentally. Due to this being the method which also provided the best idea of its error, the capacitance was taken as $(16.47 \pm 0.31) \times 10^{-12}$ F. As mentioned in section 5.3.4, the close correlation between all the values also gives confidence in charge measurements performed by the electrometer. Returning to equations 5.3 and 5.5, the charge inside the cup (in coulombs) is then given as

$$Q_{fc} = 0.6535 \times 10^{-12}\, adc \qquad (5.8).$$

The accuracy of the data was thus about ±2 %, and data were subject to noise with an amplitude of less than 2×10^{-12} C.

5.3.5.4 Charge decay rate

Under dry conditions, nylon 6,6 has a bulk resistivity of greater than 10^{17} Ω m. However, it is hygroscopic and absorbs water from the atmosphere and under 50 % relative humidity (RH) conditions the bulk resistivity of nylon is decreased to 10^{15} to 10^{16} Ω m (Brydson, 1982). The calculated resistance along a nylon bolt (represented as a cylinder, 20 mm long and 3 mm in diameter) would then be a minimum of 3×10^{18} Ω. The Faraday cup rests on three of these (in parallel), producing a combined bulk resistance which should be greater than about 10^{18} Ω.

The surface resistivity of nylon 6,6 is 10^{11} Ω. Assuming a smooth surface on each cylinder, each bolt should have a surface resistance of about 2×10^{11} Ω. For three bolts in parallel, this gives 7×10^{10} Ω. Clearly, surface flow should dominate any

charge loss over the insulators. If R_{fc} is thus estimated as about 10^{11} Ω, and C_{fc} was of order 10^{-11} F, then R_{fc} C_{fc} was approximately unity. However, the charge decay experiments shown in Figure 5.14 demonstrate that for a 20 mm separation, R_{fc} C_{fc} was of the order 1000 s. This suggests that, for some reason, charge flow over the surface of the insulators was not occurring, or if it was, that it occurred at a much reduced value from that expected.

The decay rate was also affected by environmental conditions; the temperature, RH and the presence or not of a vacuum. Figure 5.19a shows the variation of R_{fc} C_{fc} with temperature and RH. The results obtained at 35 % RH suggest that a small decrease in temperature significantly increases R_{fc} C_{fc}. However, the similar R_{fc} C_{fc} values recorded at about 22 °C and 40 % RH demonstrate that R_{fc} C_{fc} must also be a strong function of RH. Figure 5.19b shows the effect of a vacuum on the rate of charge decay. Under vacuum, the calculated values of R_{fc} C_{fc} were increased by up to an order of magnitude, demonstrating that charge loss through the atmosphere (or more likely, via adsorbed water on the insulator surfaces) must be occurring at atmospheric pressure.

During an experiment, the measured charge at any one time, Q_{fc}, represents the actual charge on the collected particles, Q_p, plus the total charge lost so far through dissipation during the experiment, Q_l. The rate of charge loss, I_l, changes as a function of the potential of the Faraday cup, thus it must be integrated over the duration of the experiment.

$$Q_p = Q_{fc} + Q_l \tag{5.9}$$

$$= Q_{fc} + \int I_l dt \tag{5.10}.$$

If the loss current I_l, is assumed to follow Ohm's Law, then

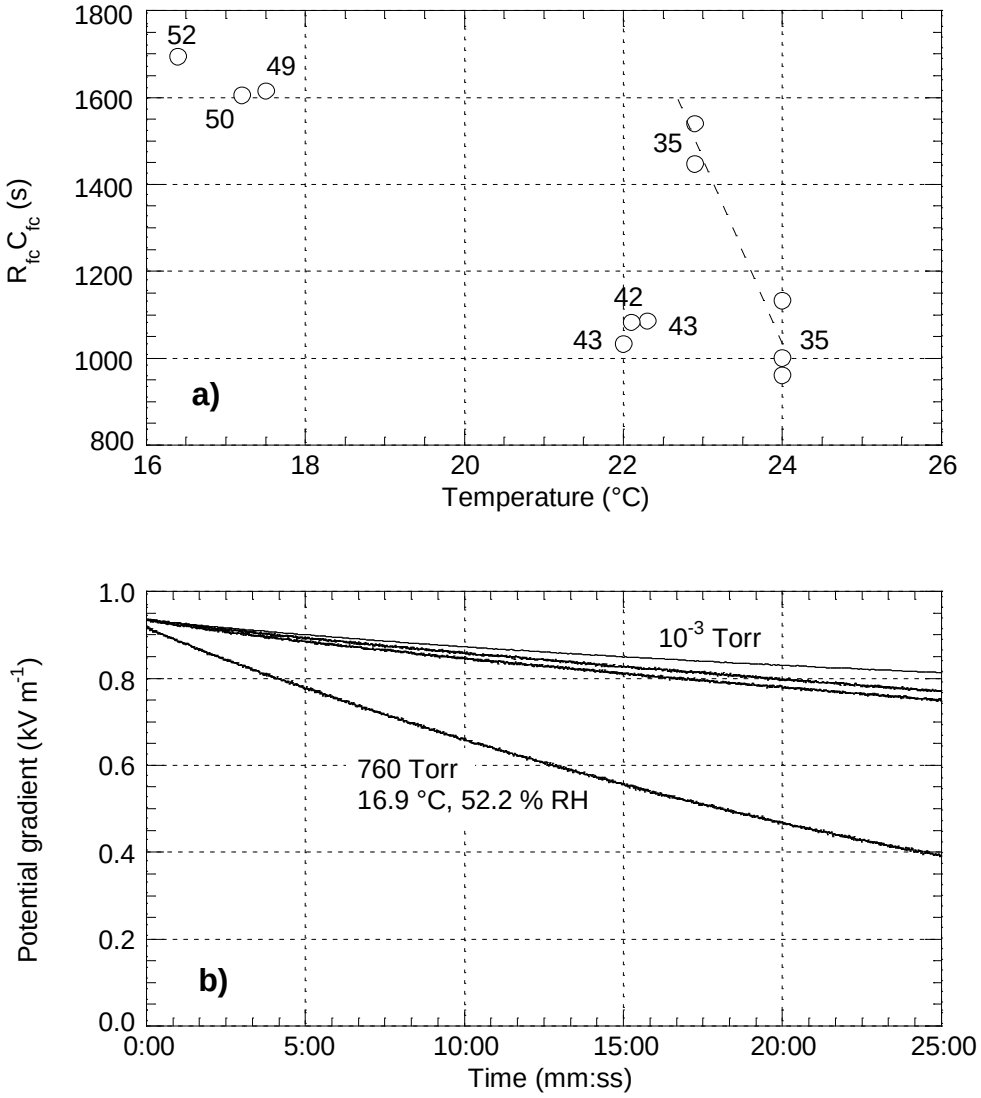

Figure 5.19 Variation of $R_{fc}\,C_{fc}$ with environmental conditions. **a)** The results of charge decay experiments carried out at atmospheric pressure. The numbers next to the data points give RH values (in percent). As shown by the data obtained at 35 % RH, increasing the temperature decreased $R_{fc}\,C_{fc}$. However, the other points demonstrate that $R_{fc}\,C_{fc}$ must also be a function of RH. **b)** Under a vacuum (10^{-3} Torr, approximately 10^{-1} Pa), decay rates are much reduced. The three curves shown here have $R_{fc}\,C_{fc}$ values between 7000 and 10000 s. The decay curve with the highest value of $R_{fc}\,C_{fc}$ recorded at atmospheric pressure (760 Torr) is also shown for comparison.

$$Q_p = Q_{fc} + \int \frac{V_{fc}}{R_{fc}} dt \qquad (5.11).$$

From equation 5.3, the potential of the Faraday cup can be expressed in terms of its charge and capacitance, giving

$$Q_p = Q_{fc} + \int \frac{Q_{fc}}{R_{fc} C_{fc}} dt \qquad (5.12).$$

Thus, an expression for the recorded charge accumulation as a function of time is required. A reasonable assumption could be that the actual charge accumulation occurred at a constant rate. However, if the measured charge was assumed to be a linear function of time, then an estimation of the charge loss could be made. This would imply that the actual charge accumulation was only linear in the case of no charge loss. Assuming that the measured charge can be given as $Q_{fc} = \alpha t$, gives

$$Q_p = Q_{fc} + \int \frac{\alpha t}{R_{fc} C_{fc}} dt \qquad (5.13)$$

$$= Q_{fc} + \frac{\alpha t^2}{2 R_{fc} C_{fc}}$$

$$Q_p = Q_{fc} \left(1 + \frac{t}{2 R_{fc} C_{fc}} \right) \qquad (5.14).$$

Monitoring charge decay at atmospheric pressure produced a minimum value for $R_{fc}\, C_{fc}$ of the order 1000 s (Figure 5.19). For charge accumulation over a maximum of 200 s during a typical experiment, the recorded charge would thus be 10 % less than the actual particle charge. The maximum values of $R_{fc}\, C_{fc}$ measured at atmospheric pressure were about 1600 s, which implies charge losses of about 6 %. Under vacuum, $R_{fc}\, C_{fc}$ was increased to above 7000 s (Figure 5.19), suggesting that charge losses during experiments carried out at low pressure (10^{-3} Torr, approximately 10^{-1} Pa) were of the order 1 %.

5.4 Ash particle charge experiment

The second set of experiments was designed to obtain the specific charge of the individual particles, rather than the net charge on the ash sample as a whole. Particles were produced by the sample collider apparatus used for the net charge experiments, but they were then collimated into a narrow beam by allowing them to fall through a narrow slit between two flat plates. The small proportion of particles that passed through the slot fell down the centre of a horizontal electric field produced by two vertical, parallel plates. Figure 5.20 shows a cross section through the parallel plates apparatus with the relative position of the collimating slot shown for reference. Highly charged particles adhered to the plates and the charge accumulated on one plate was measured by an electrometer. The parallel plates apparatus used was a slightly modified version of apparatus originally designed and used by S. J. Lane (Gilbert *et al*., 1991). The experiment was also mounted in the vacuum chamber to provide a draught-free environment at atmospheric pressure and to allow low pressure runs.

5.4.1 Apparatus

The plates which produced the electric field were mounted 38 mm apart inside an earthed aluminium box. Each plate was 180 mm × 101 mm in size and constructed from 0.66 mm thick copper sheet. The top 9 mm of the plates were bent outwards by 4 mm to maintain them in holding slots cut into PTFE insulators. Electrical connection was made to each plate by a terminal block located on one of the top corners. All corners and edges were rounded and polished to reduce the possibility of ion production.

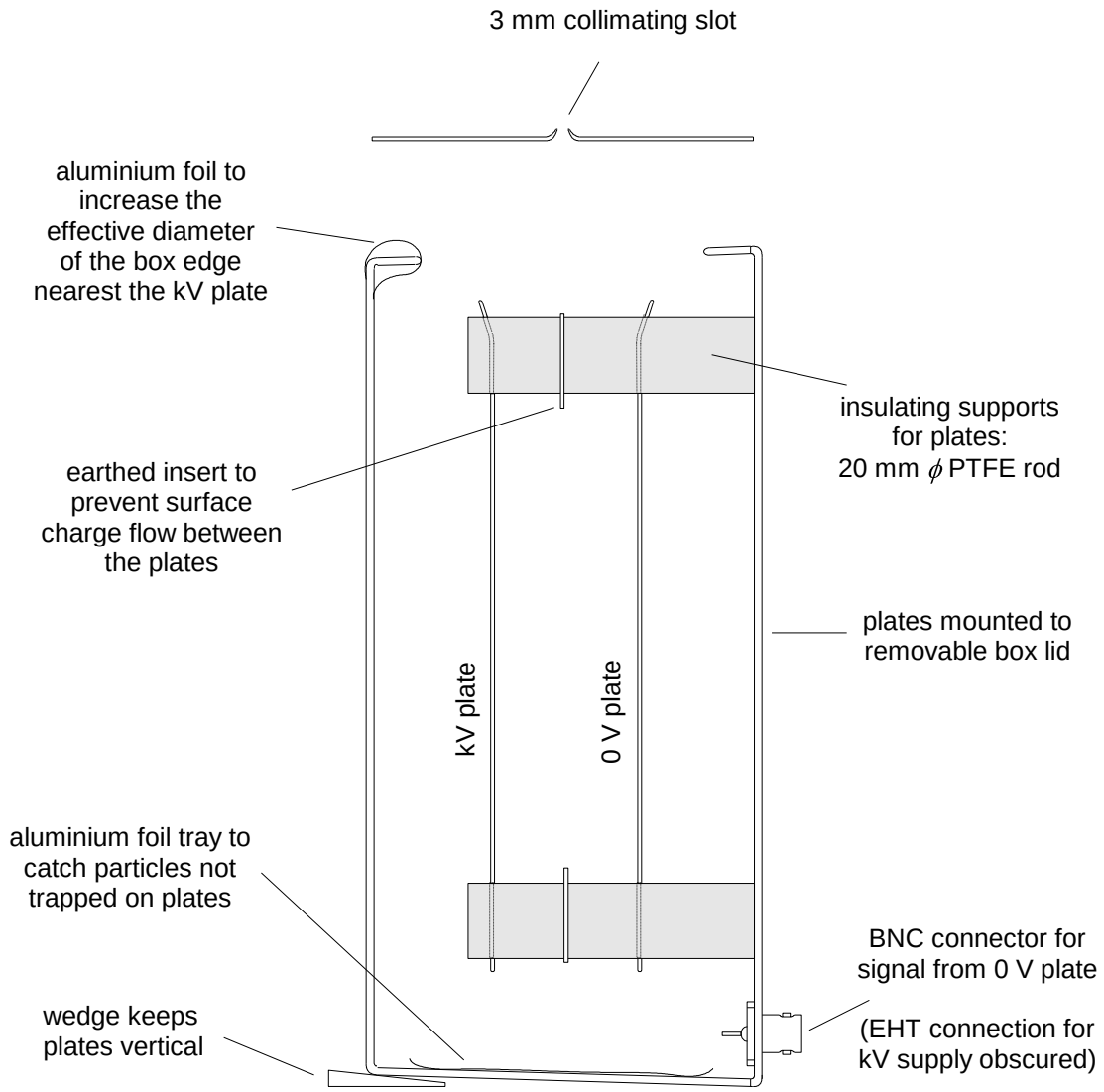

Figure 5.20 The parallel plates used for the particle charge experiments. Diagram is to half-scale and the electrical connections and supports for the collimating slot have been omitted for clarity.

To generate the electric field, one of the plates (the kV plate) was maintained at a potential between 0 and ±3.5 kV by one of two (one positive, one negative) Brandenburg 390 series miniature high voltage supply modules (Appendix I). The output potential of these EHT supplies was adjustable by potentiometer. The potential of the kV plate was detected using a 1:1000 voltage drop probe connected to an electrometer on a 20 V scale, which allowed the plate potential to be set to within about a volt of the desired level. The EHT modules were located outside the vacuum chamber and the supply was brought into the chamber by a high voltage lead-through.

The other plate (0 V plate) was earthed through a Keithley 614 electrometer to allow measurement of the charge deposited on the plate. The connection out of the chamber was made via a coaxial cable and the shielded PET 100 plug and socket used for the mesh data during the net charge experiments. When the kV plate was maintained at a negative potential, negatively charged particles were accelerated towards the 0 V plate by the electrostatic field. Thus, with the kV plate at a negative potential, negative charge was collected on the 0 V plate. With the kV plate at a positive potential, particles with a positive charge were collected on the 0 V plate. To prevent charge from flowing directly from the kV plate to the 0 V plate over the surface of the PTFE insulators, the insulators were broken by earthed copper inserts midway between the plates. Any charge flowing from the kV plate thus went to earth without interfering with measurements on the 0 V plate. The electrical and data connections for the experiment are shown in Figure 5.21.

Strips of aluminium foil taped onto the plates were used to collect the particles. The electrostatic forces created by image charges within the foil were sufficient to adhere the particles to it, even after the external electric field had been removed. The mounting slots and removable box lid allow the plates to be removed easily for

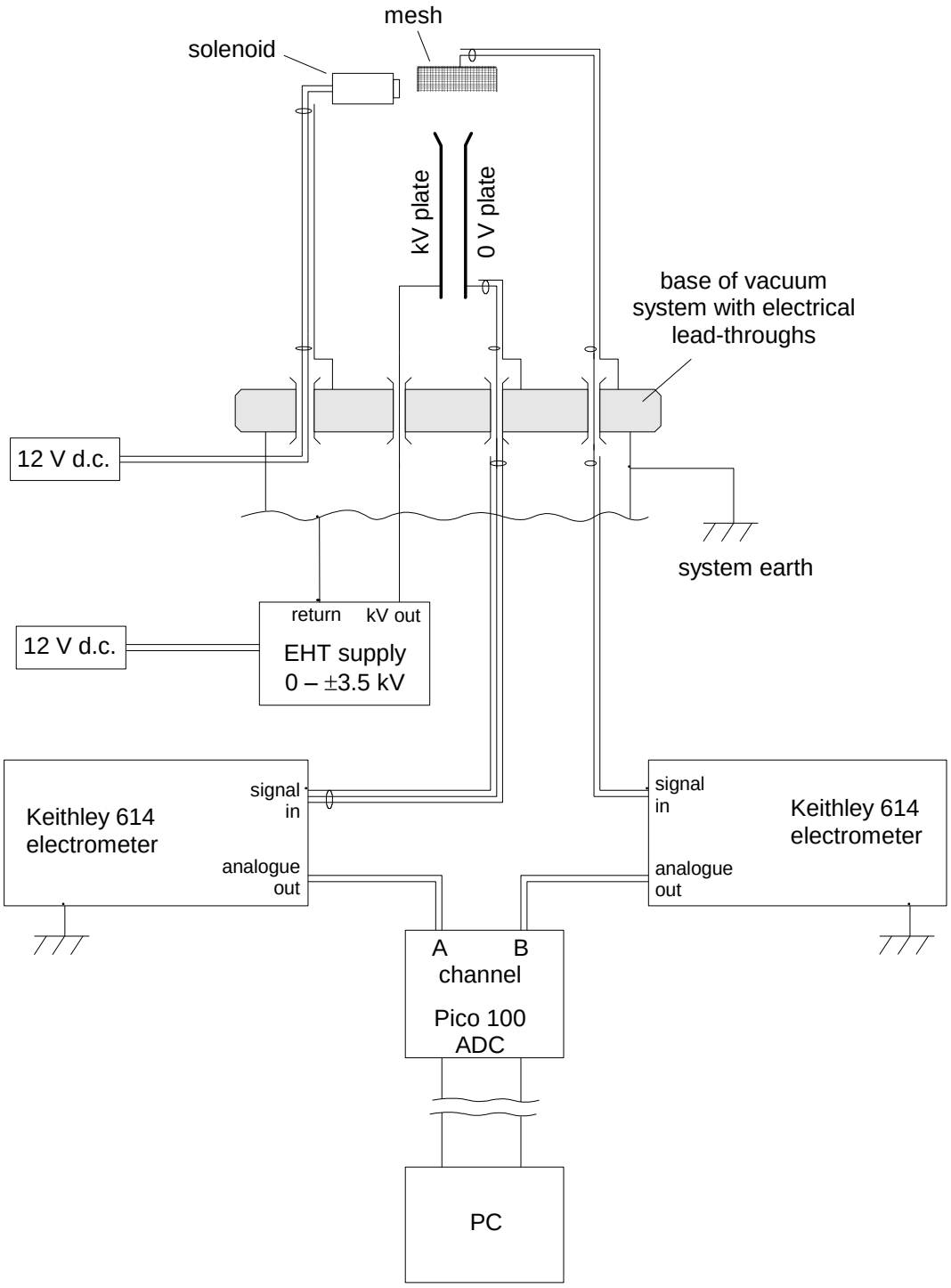

Figure 5.21 Schematic diagram of electrical and data connections for the particle charge experiments. Only one of the two EHT supplies is shown. To change the EHT polarity, one supply was substituted for the other.

preparation or retrieval of the foils. A foil tray was also placed below the plates to catch any particles which had passed through the electric field without being trapped on either plate.

5.4.2 Particle distribution on the plates

The first design of the experiment used a slot cut into the top of the earthed box as the collimating slit. The advantage of this design was that particle collimation occurred close to the plates. However, it brought the top of the kV plate closer to the earthed box than to the 0 V plate. This generated large electric fields between the kV plate and the top of the box and ion production from the sharp edges of the slit could have been possible. Experiments carried out with this apparatus demonstrated an unexpected particle distribution pattern on the kV plate. Figure 5.22 shows a schematic diagram of the particles collected on the plates after an experiment. The 0 V plate collected particles in a vertical stripe along its entire length, with a maximum number density somewhere near the top of the foil (Figure 5.22a). The kV plate did not demonstrate the same simple pattern (Figure 5.22b). A central stripe of highly aggregated particles (aggregates of several hundred microns in diameter) would be surrounded by a ‘halo’ of extremely fine particles. This halo would expand laterally towards the top of the deposit and then be abruptly cut off close to the flex in the plate.

The causes of the visual differences in the deposits on the plates are not fully understood. One possible explanation is that the particles were being charged by ions produced at the collimating slot due to the high field strengths developed at the slot edges. For this reason, a higher slot position (shown in Figure 5.20) was used during all further experiments. As a result, in all but a few cases, the pattern of unusual mass

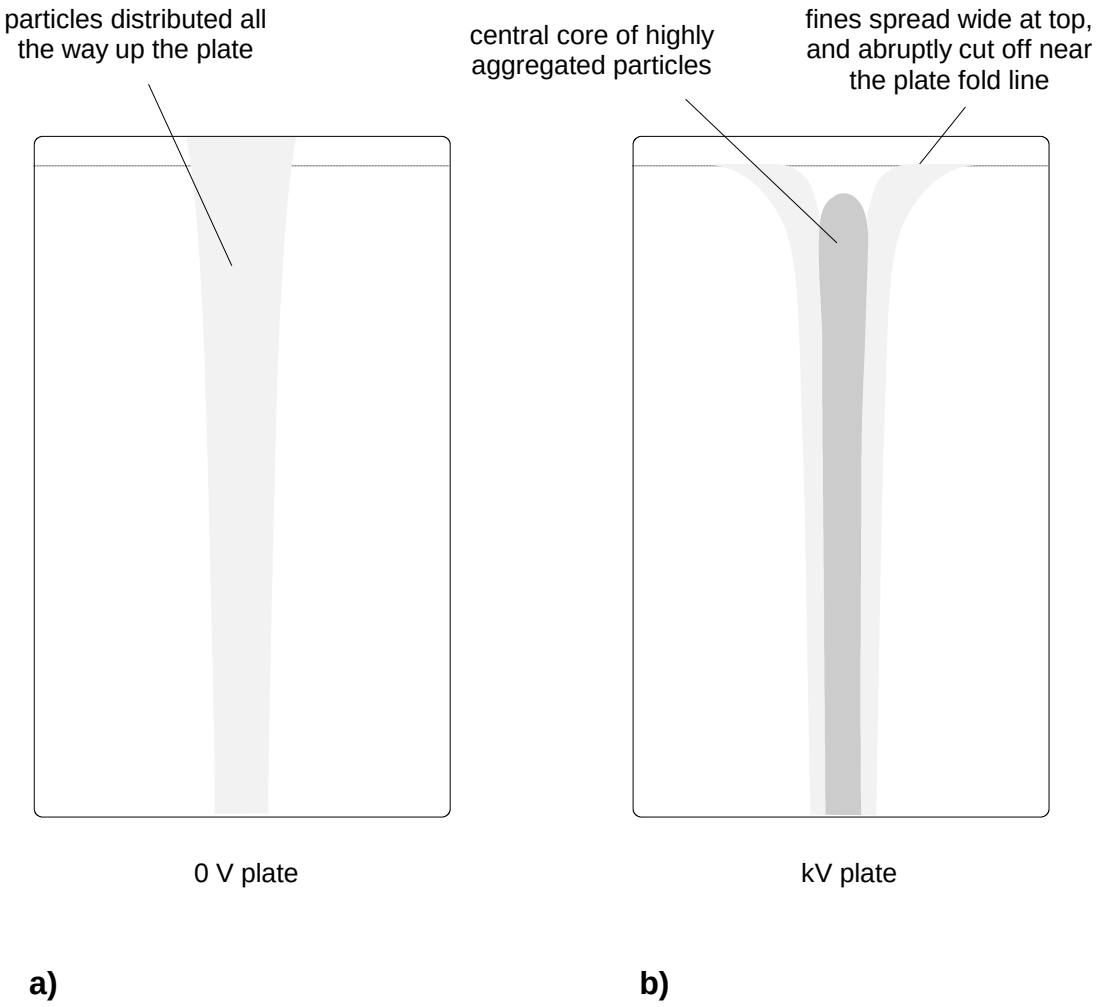

Figure 5.22 Particle distributions produced on the parallel plates during experiments with a low collimating slot. **a)** Particles collected on the 0 V plate show a distribution seen in most other experiments with the raised collimating slot. **b)** The particle distribution on the negatively charged kV plate is complex and difficult to interpret. Particles are absent from the uppermost part of the plate, where it is bent outwards slightly. Towards the base of the plate, the distribution resembles that on the 0 V plate, but with enhanced aggregation of the particles.

distribution seen on the kV plate was not observed. Both plates then produced particle distributions resembling that shown in Figure 5.22a.

5.4.3 Data logging

During each experiment, an electrometer continuously measured the charge accumulating on the 0 V plate. The mesh above the samples was still attached to the collider apparatus, so was also available for data collection and was monitored by an electrometer. However, only one shielded PET 100 connector was available (and was being used for the 0 V plate), so the signal from the mesh had to be taken out of the vacuum chamber by a standard lead-through. Care was taken to ensure it was as shielded as possible, but some uncertainty existed as to whether the data were always free of interference. Data taken during an experiment were recorded in real time on a PC via the Pico ADC-100, and a LogIT data logger was used to mark the time of impacts.

5.4.3.1 Noise generated within the measurement apparatus

Generally, the signal to noise ratio for the plate data was very low. The main exception to this was in data obtained from some experiments carried out at high values of RH. Figure 5.23a shows the raw data obtained from such an experiment. Processing with a 9-point running average removes most of the high frequency noise from the plate data, but low frequencies of considerable amplitude remain (Figure 5.23b). The onset of charge deposition on the plate from particles is clear, but obtaining an accurate figure for the total charge collected is not possible. The noise is thought to be due to varying leakage currents over the insulators from condensation or adsorption of water onto their surfaces (note also the high drift rate of the mesh data).

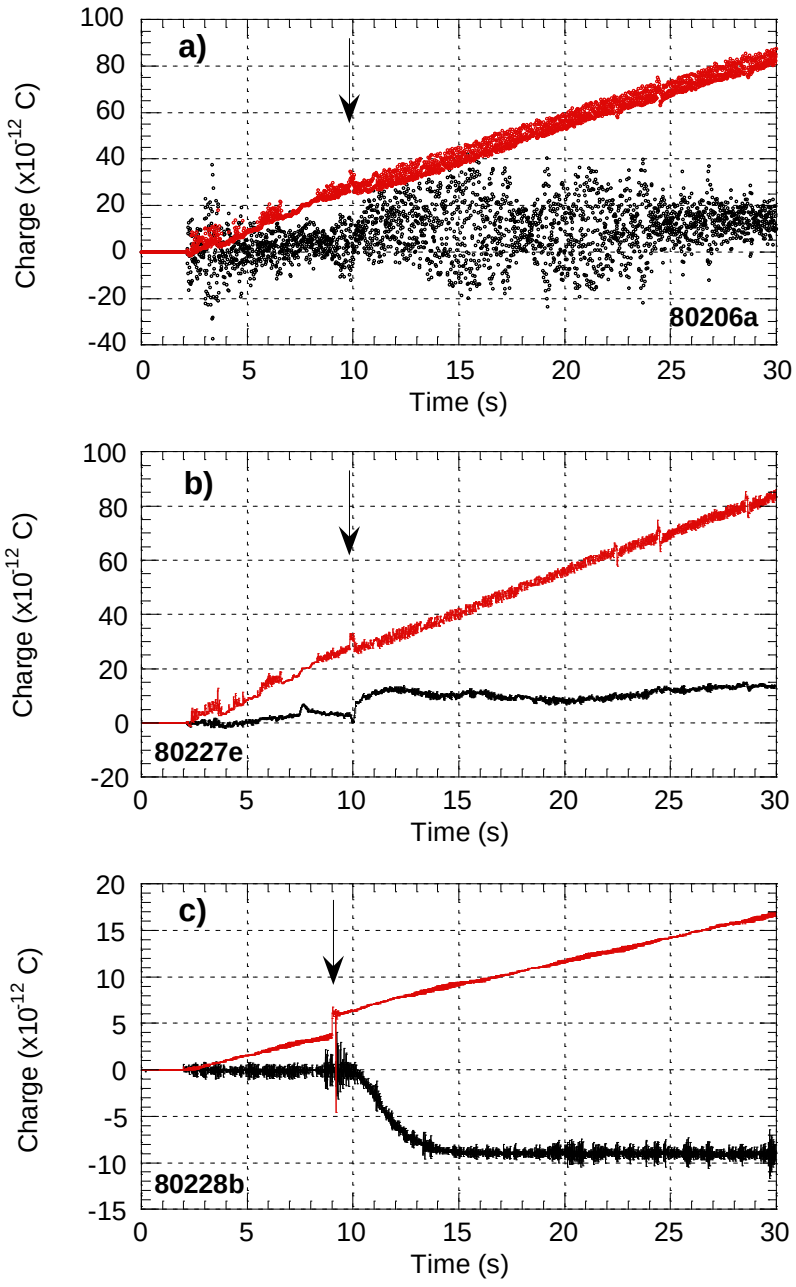

Figure 5.23 Data taken during experiments carried out at high humidity. **a)** Raw data from an experiment at 90 % RH, during which a single impact was made (arrowed). Mesh data (red) show a very high drift rate and the plate data (black) are dominated by noise. **b)** A 9-point running average removes the high frequencies from the plate data, but still does not allow quantitative measurements of charge to be made. **c)** Raw data from a similar experiment carried out after the apparatus was desiccated overnight before the relative humidity was raised to 90 %. Drift in the mesh data and noise in the plate data are greatly reduced.

Both noise and drift rates could be drastically reduced by maintaining the apparatus in a dry (< 10 % RH) environment overnight, before rapidly increasing the RH (over approximately 15 minutes) to the level required for the experiment. This is demonstrated in Figure 5.23c which shows the raw data from an experiment identical to that of Figures 5.23a and 5.23b, with the exception that the apparatus had undergone the low humidity treatment.

Interference generated by operation of the solenoid could also be detected in the mesh and plate data. Figure 5.24a shows data recorded during an activation of the solenoid (without allowing the samples to collide). The time scale is expanded in Figure 5.24b to show more detail during the period of solenoid operation. The mesh data demonstrate the usual trace produced as a charged sample is moved inside the mesh (see Chapter 6). The noise produced in the plate data is probably a consequence of small vibrations of the apparatus as the hammer slider hits its stop. The noise rapidly dies away, leaving no net offset in the plate data. Experiments during which the samples did collide show less noise in the plate data because the hammer slider did not hit its stop. In these cases, hammer motion was absorbed more slowly by the sprung anvil and the sample collision, producing less vibration of the apparatus.

5.4.3.2 Susceptibility to external noise

The sensitivity of the apparatus was demonstrated during experiments carried out at about 5 p.m. Data from these experiments show occasional spikes (particularly evident in the plate data, Figure 5.25) which were not recorded at other times. It is believed that these represent interference (either transmitted down the mains supply or as radio frequencies) from other electrical appliances being switched on or off.

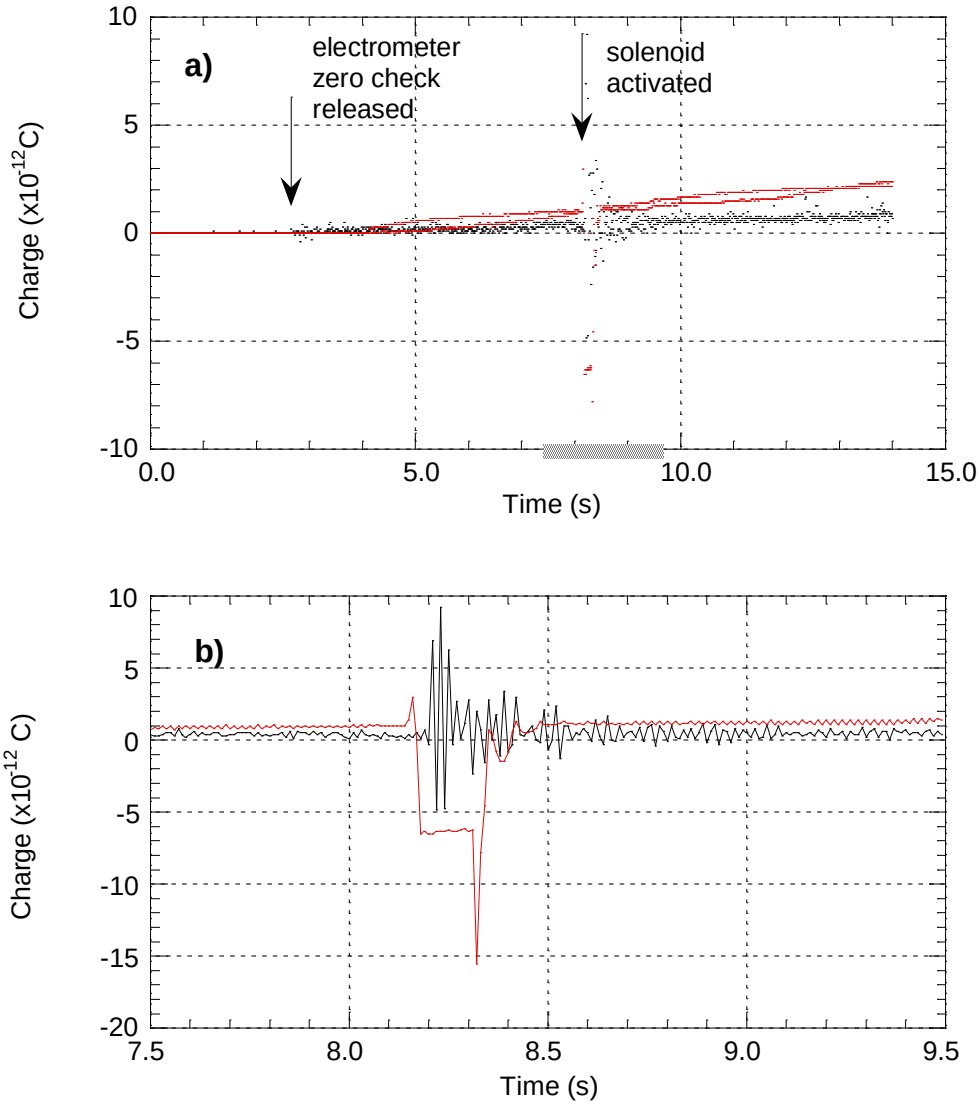

Figure 5.24 Noise produced by operation of the solenoid. **a)** Raw data logged at 10 ms intervals over a period with one solenoid activation (without collision of the samples). The red points show mesh data and the black points, the plate data. The kV plate was earthed. The time period indicated by the hashed line is expanded in **b)** and plotted as a line diagram. The onset of solenoid activation is shown by a small upwards peak in the mesh data. Collapse of the magnetic field when the supply is removed creates a larger downwards peak. Noise in the plate data is likely to be caused by small vibrations in the apparatus produced by the solenoid hammer hitting its stop.

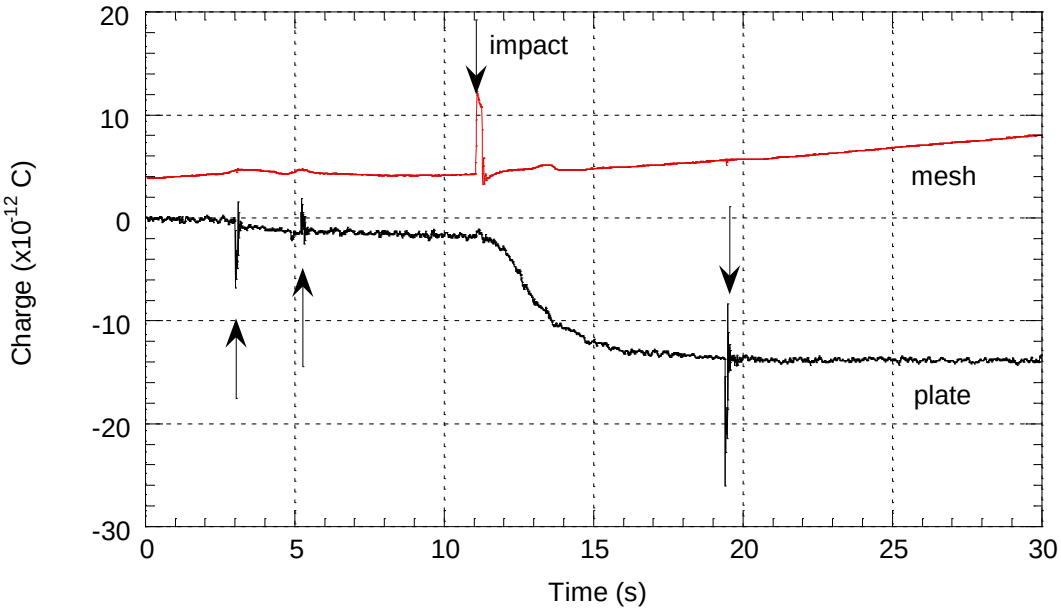

Figure 5.25 Noise spikes recorded during an experiment carried out close to 5 p.m. This experiment, consisting of one impact (arrowed in the mesh data) shows three noise spikes in the plate data (also arrowed). The mesh data have been vertically offset for clarity. The experiment was conducted at atmospheric pressure and humidity conditions.

Another undesirable signal became apparent during logging of single impact experiments at 10 ms intervals. The mesh data were observed to record beats representing a frequency close to 200 Hz. Figure 5.26 demonstrates this in raw data logged over 30 s (with no operation of the solenoid). The source of this frequency was not determined, but it appeared to be picked up by the cables connecting the mesh to the electrometer. Simple averaging of successive data points satisfactorily removed the frequency as shown by the displaced 'smoothed mesh' data in Figure 5.26.

5.4.4 Calibration

The method for calibrating and converting ADC counts of the electrometer output has been previously described for the mesh data in the Faraday cup experiment (section 5.3.4). The charges collected on the 0 V plate and on the mesh were both measured directly by electrometer, so this method was appropriate for both data sets. The electrometers were used on all charge scales (0.2, 2.0 and 20 nC full scale deflection), depending on the type of experiment undertaken. This was easily accounted for when processing the ADC data.

5.4.5 Ion production

With up to ±3.5 kV on the kV plate, electric fields in the order of 100 kV m^{-1} were generated between the plates (calculated as a uniform field between plates separated by 38 mm). Concentration of the electric field near corners and edges of the plates will have produced much larger field strengths in these areas. The production of ions by these high fields had to be prevented in order to avoid further charging or discharging the particles before they were collected on the 0 V plate. Checking for ion production was carried out by several methods.

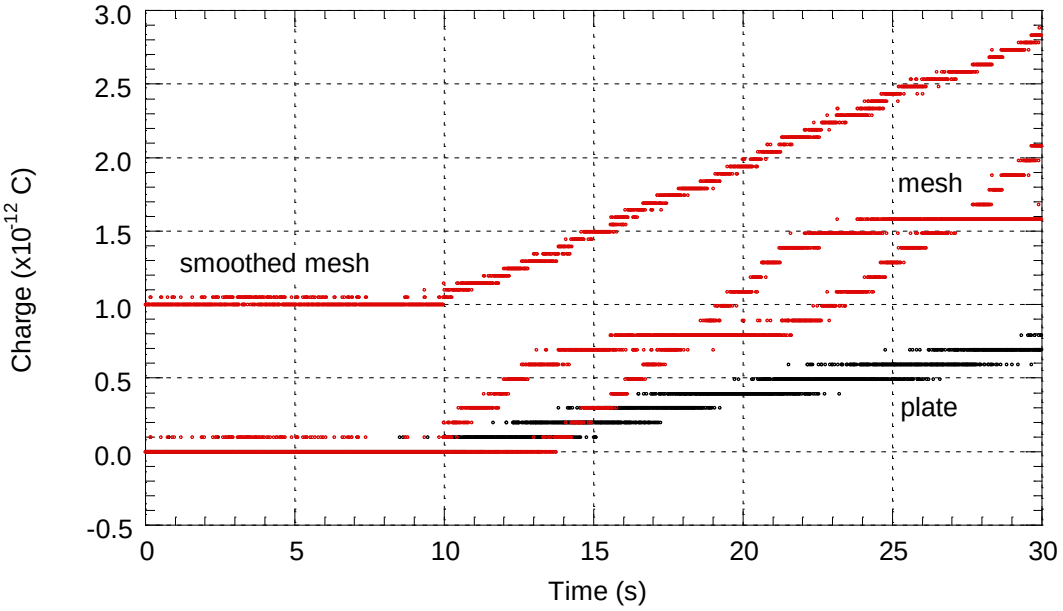

Figure 5.26 Beats in the mesh data produced when sampling every 10 ms. The zero checks on the electrometers were released after 10 s, and data were recorded for the next 20 s. The plate (black) and mesh (red) traces show individual raw data points, adjusted only to show charge in Coulombs. The digitisation of the analogue signal from the electrometers creates the discrete 0.1×10^{-12} C jumps in the plate and mesh data (electrometers on 2.0 nC scale). The interference frequency produces beats with a period of approximately 17 s in the mesh data. These can be removed from the data by averaging successive data points to produce the smoothed mesh data shown (offset by 1×10^{-12} C for clarity).

5.4.5.1 Charge accumulation on 0 V plate

If ions were being produced inside the apparatus, it is likely that some would be attracted to the 0 V plate. This would be detected as a (large) drift current. Although these experiments were subject to drift currents, these can be attributed to sources other than ion production:

Equipment drift.

Internal losses within the electrometer and its cables produce drift, but these are generally very low and could be identified easily by observing the drift rate when the electrometer was disconnected from the plate.

Surface charge flow over the insulators.

Despite the precautions of central earthed washers and acetone cleaning, the insulators (constructed from 20 mm diameter PTFE rod) supporting the plates sometimes caused drift by allowing charge flow over their surfaces. It is thought that under 'normal' atmospheric conditions this was mainly due to small amounts of contaminants on these surfaces producing a limited number of charge carriers. Thus, by allowing charge flow to continue for about 30 minutes, the number of available charge carriers became severely reduced, and drift currents returned to negligible values.

Simple calculations were carried out in order to assess the amount of charge flow that could theoretically occur through and over the insulators. With the bulk resistivity of PTFE being greater than $10^{20}\ \Omega$m and a distance between the plates and the earthed central inserts of 18 mm, each insulator represented a bulk resistance of $6 \times 10^{21}\ \Omega$.

For four insulators, this produced a bulk resistance of 1×10^{21} Ω which, for a potential difference of 3.5 kV, would have given a leakage current of 2×10^{-18} C s^{-1}. The surface resistivity of PTFE is 10^{17} Ω, so each insulator also represents a surface resistance of about 3×10^{16} Ω, producing a total surface resistance of 7×10^{15} Ω. For the 3.5 kV potential difference between the kV plate and the inserts, this gives a leakage current of 5×10^{-13} C s^{-1}. Thus, charge leakage would be dominantly by surface flow, and the low drift currents usually recorded (10^{-14} C s^{-1}) demonstrate the value of the earthed inserts.

These low detected drift currents suggested that under normal conditions ions were not being produced. The sensitivity of the 0 V plate to the production of ions was demonstrated at low pressure.

5.4.5.2 Observation of ion production

Significant ion currents were observed when the vacuum chamber was evacuated with an EHT supply switched on. As the pressure is decreased, the mean free path of any charged particle (ion) increases until it reaches a critical length and a significant ion current is produced. Onset of this current was observed as almost instantaneous off-scale recording of the 0 V plate electrometer, and the current taken by the EHT supply increasing to the unit limit.

Reducing the pressure to about 3×10^{-4} Torr (4×10^{-2} Pa) allowed the EHT supplies to be used at ±3.5 kV with little drift recorded. However, a small pressure increase, which could be produced by closing the diffusion pump, immediately initiated discharge. This was observed as the symptoms described above, accompanied

by a flash of blue light between the top of the kV plate and the rounded foil edge of the box.

Thus, under 'normal' conditions, silicate particles generated during the experiments were not being charged by ions produced by the apparatus. A possible exception to this was at high (~90 %) RH, where large drift currents were recorded. Although the drift is thought to be mainly due to charge flow in water condensed onto the insulators, the production of 'airborne' charge cannot be ruled out. It is possible that small water droplets could become charged by ions, and then drift into the path of falling ash particles due to their momentum.

5.4.5.3 Drift experiments

As a direct check of any possible ion production along the path of the falling silicate particles, a 'Y'-shaped copper wire attachment was added to the mesh. This hung down through the slot and into the electric field between the plates. The drift rate of the mesh electrometer was then recorded over a period of 200 s. Figure 5.27a shows the relative drift currents at various degrees of RH. This represents the drift recorded with the kV plate at ±3.5 kV, minus the drift recorded with the kV plate earthed.

Both absolute drift rates and relative drift rates were greatly increased at high RH. Even with an earthed kV plate, small amounts of condensation on the insulators produced large drift rates. This interpretation is supported by the drift rate data shown in Figure 5.27b. This was obtained from the copper wire attachment and demonstrates the way in which the drift rate increased with time after the RH had been rapidly raised. The apparatus had been dried out using silica gel for a couple of days before the RH was raised by means of a warm, damp cloth at time 0:00. The RH increased to

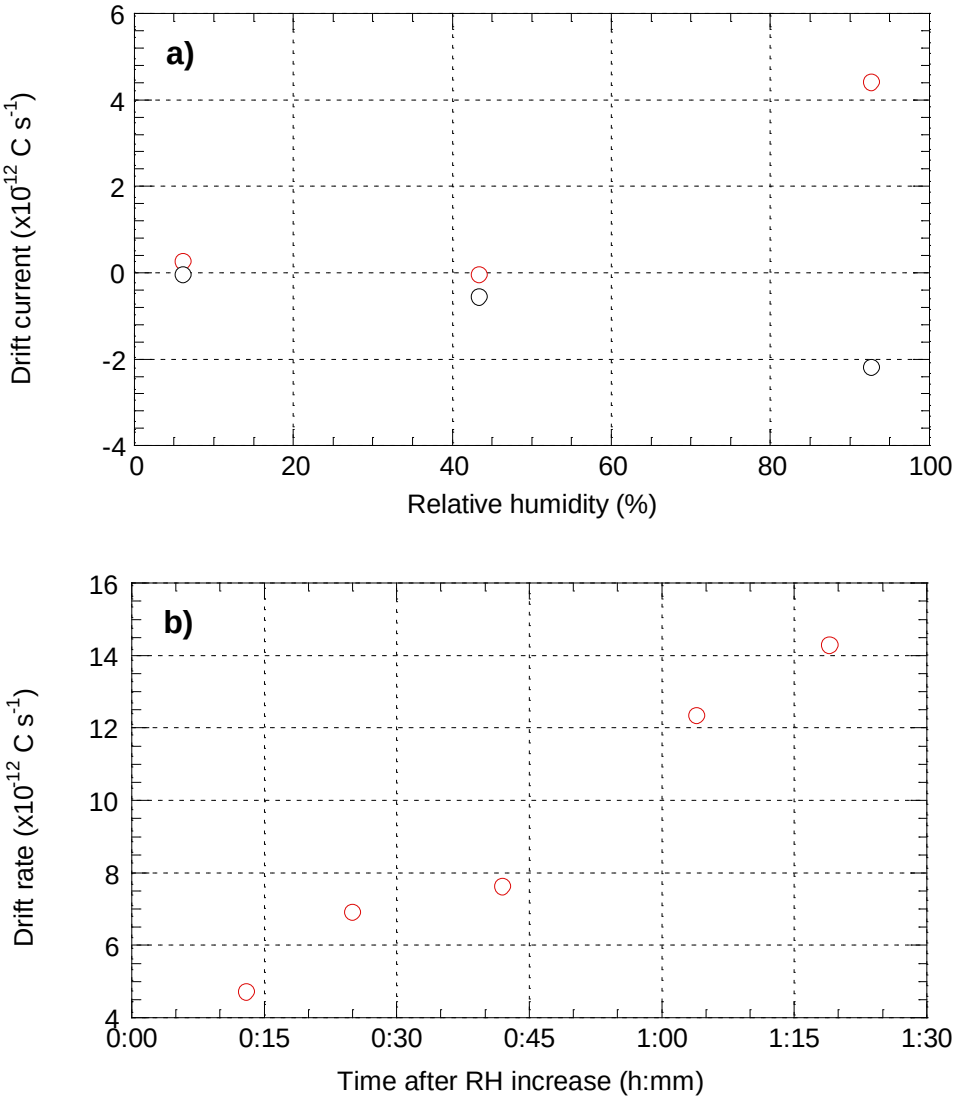

Figure 5.27 Charge accumulation on a wire probe inserted between the plates. Black symbols indicate experiments with a kV plate potential of -3.5 kV; red symbols for +3.5 kV. The probe was connected to the mesh, and charge accumulation was measured by the mesh electrometer. Addition of the probe to the mesh greatly increased the 'normal' drift rate. Therefore, data shown here have been normalised to data recorded with the kV plate at earth potential. **a)** With the exception of the high RH results, charge accumulation rates (drift currents) are very small. **b)** Further data taken at high RH demonstrate the way in which leakage currents increase with time. This can be interpreted as due to increasing condensation on the insulators.

about 90 % in the first ten minutes after which, during the experimental period, RH increased only from 90.5 % to 91.8 %. It is not thought that this increase in RH was sufficient to increase the drift rate by the amount observed, rather that the increasing amount of condensation on the insulators was responsible.

Although the presence of free space charge has not been demonstrated, the high drift rates indicate that the results of experiments carried out at high humidity (approximately 90 % RH) should be interpreted with some caution.

5.5 Experimental methods

Experiments using the equipment described above were carried out with a variety of different parameters. The net ash charge experiments were the first to be undertaken, and consequently many of these were dedicated to understanding effects of the apparatus itself. The pumice samples for both types of experiment were prepared and mounted in an identical manner. The samples were cut from central portions of pumice clasts, in a cylindrical shape approximately 10 mm in length and 8 mm in diameter. A mounting plate, consisting of a metal washer (M4 size), was attached to one end of the cylinder with a cyanoacrylate adhesive. During the first nineteen net ash charge experiments, the washer was then glued directly to a collet for mounting onto the solenoid or anvil rod. However, it was discovered that insulation tape and double-sided adhesive tape also secured the sample sufficiently for impacts. For this reason, the remaining experiments used a double layer of insulation tape and a layer of double-sided adhesive tape to attach the mounting plate to the collet. This technique had the advantage of allowing easy removal of the samples for storage and

possible re-use in later experiments. It also guaranteed that no charge could be lost over the sample to the solenoid rod or anvil.

5.5.1 Net ash charge experiments

With the exception of only a few experiments, data were logged at 100 ms intervals over 250 s. However, due to a problem in the PicoLog program, 200 ms intervals had to be specified to the software in order to produce logging at 100 ms intervals. This problem did not occur when logging at other frequencies. Each experiment was started with the electrometer's zero-check on, which was released after 10 s (this time was marked in the LogIT data). Sample impacts were not initiated until 30 s after the start of logging. This allowed 300 data points to be taken in order to establish the zero-offset of the fieldmeter, and to check its stability. Impacts were then initiated at a frequency of about 2 Hz, with the total number during an experiment varying up to a maximum of about 400. After an experiment, the Faraday cup was removed to retrieve the particles on the aluminium foil. The foil was folded to seal the particles inside it. The mass of the particles was then determined and, for many experiments, the sample was also analysed for particle size. This allowed the net specific charge and the net surface charge density to be calculated.

As described in section 5.2, particles were produced by colliding pumice samples together, or alternatively by a rotational grinding motion. During the grinding experiments, the LogIT data logger was used to record the release of the zero-check of the electrometer, and the stop and start times of the grinding. To check for the production of mobile charge (ions) during some experiments, one sample was replaced by a brass collet, either earthed or insulated from Earth. Grinding experiments with a brass collet used a collet that had a serrated edge to promote

fracturing of the sample. Table 5.2 lists the parameters that could be controlled during experiments, and the data types recorded.

Table 5.2 Summary of the parameter and data types for the net ash charge experiments.

Net ash charge experiments		
Experiment parameters	environment	pressure, relative humidity
	sample type	pumice or brass collet
	particle production	linear impact or rotational grinding impact energy
Results	mass	loss from 'hammer' sample loss from 'anvil' sample collected in Faraday cup
	charge	accumulation in Faraday cup with time accumulation on mesh with time

5.5.2 Ash particle charge experiments

For ash particle charge experiments, particles were only produced by linear pumice–pumice impacts. Experiments were undertaken with varying numbers of impacts, impact velocities and magnitudes of the separation electric field, and at different values of RH. Table 5.3 shows the parameters controlled and the type of data obtained from each experiment. Most experiments were carried out over 250 s, and logged at 100 ms intervals. Some experiments, involving only a single collision of the samples, were logged at 10 ms intervals over 30 s.

The charge on the 0 V plate was continuously recorded throughout each experiment. However, only the total charge accumulated was required. Where necessary, the time series data were used to remove any component of this which was

attributable to drift. The specific charge for the particles collected on the 0 V plate could then be calculated once their mass was determined. The particle mass was also recorded for the kV plate foil and the tray, so that the relative mass distributions could be analysed. All particle samples were retained after each experiment for particle size analysis. Although the mesh data were also recorded, they were not considered to be a reliable indication of charge collected on the mesh. However, the data were used to indicate the timing of operation of the solenoid, and this was especially useful during single impact experiments.

Table 5.3 Summary of the parameter and data types for the individual ash particle charge experiments.

Individual ash particle charge experiments		
Experiment parameters	environment	pressure, humidity
	impact	pumice sample, impact energy number of collisions
	particle separation	kV plate potential, plate separation
Results	mass collected	on 0 V plate on kV plate on tray
	charge	accumulation on 0 V plate with time accumulation on mesh with time

5.5.3 Particle masses

The mass of each particulate sample was determined by weighing the aluminium foils directly before and after an experiment, using a Mettler AT120 mass balance. The balance was internally calibrated and provided readings in grams to five decimal places. The internal calibration was verified to four decimal places with a check

weight of 1.0024 g (results are given in Appendix III). Weighing was carried out on a levelled concrete bench in an air-conditioned, closed room, and the measuring plate of the balance was fully shielded from draughts.

Foils were visually inspected before weighing to ensure that no contaminant particles were present. The circular foils used in the Faraday cup for net charge measurement experiments produced no problems during mass measurements. The mass collected during one experiment was usually greater than 1 mg, so weighing was carried out to only four decimal places. During repeated measurements of the same foil, identical masses were consistently obtained, and folding up empty foils did not produce any detectable change. However, problems were encountered during mass measurements for the particle charge experiments.

Plate foils were too long for the measuring plate of the balance and had to be gently folded over for weighing. The foils could not be creased due to the sharp points that this would have created producing problems when they were applied to the parallel plates. However, care was taken to ensure that the centre of mass was directly over the centre of the balance. Tray foils were sufficiently short to lie flat on the balance plate, but overhung by approximately a centimetre at each end. Again, care was taken to ensure alignment of the centre of mass and also that the ends were not resting on any of the surrounding areas of the balance. Before and after each measurement, the balance's zero was checked (to five decimal places). If it did not zero after a foil had been weighed, the measurement was discarded, and then retaken after the balance had been reset.

During an experiment, the plate foils frequently collected less than 1 mg of particles, so all weighing had to be carried out to five decimal places. After each experiment, the foils were folded up to contain the particles before re-weighing. Care

was taken during folding to ensure that a minimum of foil contamination occurred by touching, that no extra particles (e.g. dust) had been collected and that no silicate particles were lost. To assess the repeatability of the five decimal place foil mass measurements, a plate foil and a tray foil were repeatedly weighed. The results are listed in Appendix III, and statistics of those results are given in Table 5.4.

Table 5.4 Foil mass determination: measurement errors.

Foil masses (mg)	Plate foil	Tray foil
Range	641.39 to 641.42	464.04 to 464.09
No. of measurements	6	10
Standard deviation	0.012	0.015
Mean	641.412 ± 0.005	464.068 ± 0.005

Thus, mass measurements of individual foils apparently had an error of less than ±0.02 mg. However, the change in foil geometry due to folding after an experiment was found to produce a recorded mass increase in the foils. Factors such as contamination from contact during folding were eliminated by using clean spatulas to fold the foil. It is thought that electrostatic interaction between the foils and the interior of the balance was the cause of the apparent mass increase. Unfortunately, this was unavoidable because the size of the foils was dictated by the shape of the apparatus, and they could not be pre-folded before being applied to the plates. In order to assess the apparent mass increase, twenty further experiments were carried out with plate foils and ten more with tray foils. In each case, the foil was weighed, folded and re-weighed and the increase in mass calculated. Statistical analyses of the results (which are listed in Appendix III) are given in Table 5.5.

Table 5.5 Foil mass determination: apparent mass increases due to folding.

Increases in foil mass after folding (mg)	Plate foils	Tray foils
Range	0.13 to 0.26	0.14 to 0.24
No. of measurements	20	10
Standard deviation	0.033	0.033
Mean	0.185 ± 0.007	0.194 ± 0.010

The increases found were then subtracted from the measured 'foil + particles' mass before the mass of the particles could be determined.

5.5.4 Particle size analysis

Particle samples from the experiments varied in mass from tens of milligrams to only a few tenths of a milligram. These low masses precluded the use of sedimentation or diffraction techniques for particle sizing due to the small number of particles available. SEM microscopy was also not a viable solution, because the extreme aggregation of the particles would have prevented accurate particle counts and measurements. However, the density (comparable to that of water) and physical robustness of the particles were ideal for particle size analysis using an electrozone method. This technique can also be employed on small particle masses and, with the choice of a suitable electrolyte, particles are easy to disaggregate before analysis.

5.5.4.1 Elzone system

The electrozone technique measures particle volumes as they are drawn through a small hole (the sensing orifice) whilst suspended in an electrolyte. Each particle is

detected by the disturbance it creates to an electric field in the orifice produced by electrodes placed either side of it. Signal processing and PC software then assigns the particle a 'diameter', which represents the diameter of a sphere of equivalent electrozone response. The size bin into which this diameter falls is then incremented. Thus, the raw data obtained by the technique consist of individual numbers of counted particles. By using orifices of different sizes, this system can measure particle diameters in the range 0.15 to 900 μm, with each different orifice size being capable of detecting particle diameters spanning a range of 25 to 1.

5.5.4.2 Particle samples

Visual, optical microscope and SEM work on the particle samples showed that particle sizes ranged from hundreds of microns to sub-micron in diameter. Trial runs with the Elzone system showed that the majority of particles were in the 1 to 70 μm range. Any one orifice is only effective for particle sizes between about 10 to 60 % of its diameter. Therefore, a 120 μm orifice tube was used and, in order to prevent this from being blocked by an occasional large particle, the samples were wet sieved with a 75 μm mesh before analysis. Particles were disaggregated with an electrolyte dispersant of 4 % sodium metaphosphate. The electrolyte was prepared with all the usual precautions to provide a particle-free solution, and was filtered at 0.2 μm.

5.5.4.3 Data acquisition and processing

The equipment used was an Elzone 280PC connected to a 486 PC. The PC ran PDI280 analysis software under Windows 3.11, which was used for all the data collection and processing. The software also calibrated the equipment from a database of orifice sizes at the start of each set of analyses. This internal calibration is highly

accurate between all runs carried out with the same orifice tube and has an absolute accuracy, with any tube, of about 1 μm (C. Brown, Particle Sizing Systems Ltd., *pers. comm.*). Before each analysis, the orifice was checked for cleanliness and bubbles using the Elzone microscope. During analyses the 'fast' audio output was selected which allowed blockages to be detected and removed rapidly. Each sample was sieved directly into the analysis beaker using the filtered electrolyte. The degree of sample dilution was chosen in order to keep coincidence levels (the likelihood of more than one particle entering the orifice at any one time and being sensed as one, larger particle) to about 1 %, and always below 4 %. Analyses were run for a minimum of 300 s; however, for samples of very low mass, up to 900 s were required to provide statistically acceptable results. The repeatability of the results was checked by analysing a sample produced from Mount St. Helens pumice several times (Figure 5.28). The statistics and calculated specific surface areas (see below) of these distributions are given in Appendix III.

After acquisition, each distribution was exponentially extrapolated to zero at 1 μm diameter (from 5 μm) by the software, to complete the fine end of the distribution. This allowed calculation of the specific surface area (using a particle density of 2600 kg m^{-3}) once the data had been normalised to a total particle volume of 10^{-13} m^3 (the PDI280 software uses units of 10^{-18} m^3). For the finest distributions measured, the extrapolated portion accounted for no more than 50 % of the calculated surface area. The range in the calculated surface areas for the distributions shown in Figure 5.28 is ±5 % of the mean (Appendix III). During checks of the conversions carried out by the software between particle numbers, volumes and surface areas, it became apparent that there was an error in the calculation of surface area. Where the surface area of a sphere is given as $4 \pi r^2$, the software was using πr^2, so the surface areas given were

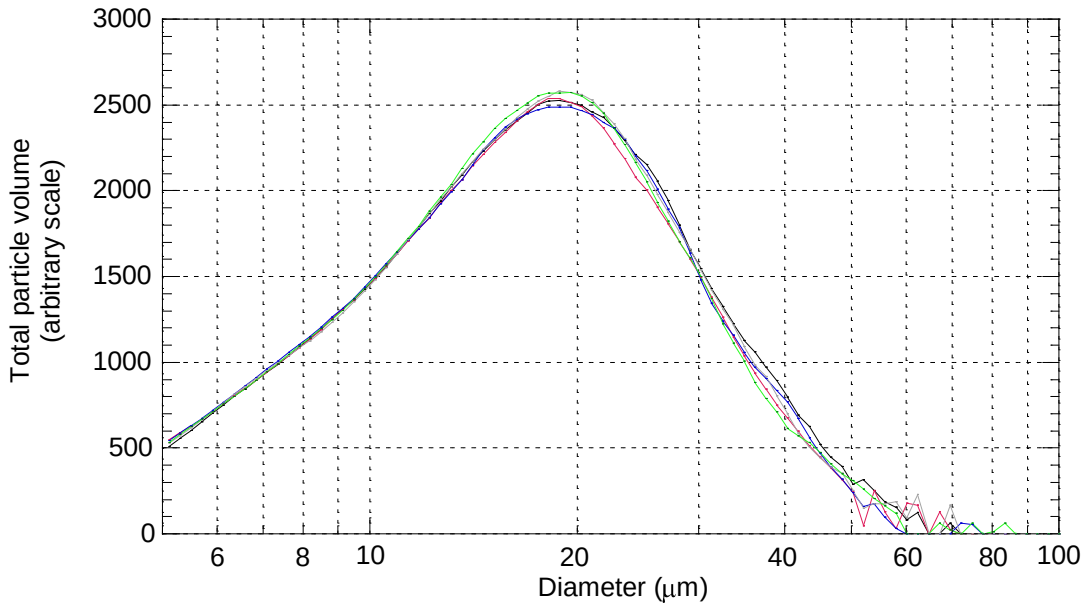

Figure 5.28 Repeated particle size analyses of the same sample produced from Mount St. Helens pumice. Each curve represents 82 data points. Noise is only observable in the data collected for particles larger than 50 μm in diameter. The noise is generated by the very small numbers of particles collected in these diameter ranges making each individual particle a large volume proportion of final count. 'Apparent' large particles can also be produced by several smaller particles traversing the orifice at the same time, an effect known as coincidence.

then multiplied by four before interpretation. This error was admitted by the current owners of the Elzone technology, and will be corrected in the next software release (P. Webb, Micromeritics, *pers. comm.*).

5.6 Summary

The experimental apparatus and procedures have been described for producing small silicate particles in the laboratory and measuring their charge. Data from selected experiments are shown in Chapters 6 and 7, and the results discussed. A full list of all the individual experiments is given in Appendix IV, along with graphs showing the results of the net ash charge experiments.

6. Experimental results and interpretation: Net ash charges

6.1 Introduction

The Faraday cup apparatus (described in Chapter 5) was used to measure the net charge on silicate ash particles from fragmenting pumice samples during 182 experiments. Experiments were carried out at either atmospheric pressure (labelled as 760 Torr in some figures) or at low pressure, which was 10^{-3} Torr (approximately 10^{-1} Pa). In Appendix IV the parameters and results of all the experiments carried out are listed, and graphs of the charge accumulation during each experiment are also provided. In this chapter, selected graphs are reproduced to demonstrate the data recorded during pumice–pumice impact experiments (section 6.4), and also during the other types of experiments (sections 6.5 to 6.8). For all these graphs (and for those in Appendix IV), mesh data are represented by red points and Faraday cup data by black points. The results of experiments are discussed in terms of the specific net ash charge generated, charge separation, and evidence for ion production. However, before the experimental results are given, the characteristics of the pumice samples are presented, with SEM images of the ash produced, and some of the charging phenomena which have been recorded are discussed.

6.2 Pumice samples and the particles produced

Six different pumice types were investigated and these are listed in Table 6.1. Further information and geochemical data for the samples are given in Appendix V. For the samples to be suitable for the apparatus, the individual clasts were chosen to be low density (less than 1000 kg m^{-3}), with a maximum vesicle diameter of about 1

mm. SEM investigation showed that all samples appeared to have a similar minimum vesicle diameter, of approximately 10 μm. Phenocrysts had a maximum size of less than about 1 mm.

Table 6.1 Pumice samples used during net ash charge experiments. For further details and sample geochemisty, see Appendix V.

Sample	Volcano	Composition	Eruption or formation
MSH	Mount St. Helens	rhyolitic	Plinian pumice fall, May 18, 1980
Sak 13I	Sakurajima	andesitic	Bunmei (1471 to 1476 A.D.)
Sak 14	Sakurajima	dacitic	Osumi (25,000 B.P.)
SMN 31	Gorge Farm (Naivasha, Kenya)	rhyolitic (peralkaline)	3,280 to 9,150 B.P.
StV 519	Soufrière St. Vincent	andesitic	Yellow Tuff formation (4,500 to 3,600 B.P.)
Santorini	Santorini	rhyodacitic	Minoan (1500 to 1550 B.C.)

The bulk of the particulate samples produced during the experiments were fine grained, with particle diameters less than 100 μm. Occasionally a 'chunk' of pumice was broken off and also fell into the Faraday cup. These larger (millimetre-sized) particles were never observed in the charge data (they did not produce visible offsets); thus it was assumed that they were a poor representation of the average charge to mass ratio. For this reason, large 'chunks' of pumice were removed before the particulate mass was determined. Descriptions of the pumice samples are given below.

MSH (Figure 6.1).

This is a white pumice, containing phenocrysts of hornblende, plagioclase, orthopyroxene and oxides, less than 1 mm in length. Vesicles vary widely in size, but are generally less than 500 μm in diameter and equant. Samples proved easy to fracture, and appeared to do so in a relatively repeatable fashion.

Sak 13I (Figure 6.2).

The Sak13I pumice is tan coloured, with elongate vesicles, many up to 1 mm long. The pumice contains phenocrysts of clinopyroxene, orthopyroxene and plagioclase, up to 1 mm long. The elongate vesicles occasionally made the pumice too weak to withstand the solenoid impacts, and several samples broke during experiments.

Sak 14 (Figure 6.3).

The Sak 14 pumice contains clasts varying in colour from very light grey to tan-grey. Phenocrysts consist of plagioclase, alkali feldspar in small amounts, quartz, clinopyroxene, orthopyroxene and oxides. Vesicles are generally very fine, with only a few up to 1 mm long.

SMN 31 (Figure 6.4).

This is a light grey pumice with mainly small vesicles (tens of micrometres in diameter). A few of the vesicles are highly elongated and up to 1 mm long. No visible phenocryst phases exist, but small amounts of sanidine, quartz and amphibole (up to about 100 μm in length) were observed in another pumice erupted from the same Gorge Farm centre (S. Marshall, *pers. comm.*).

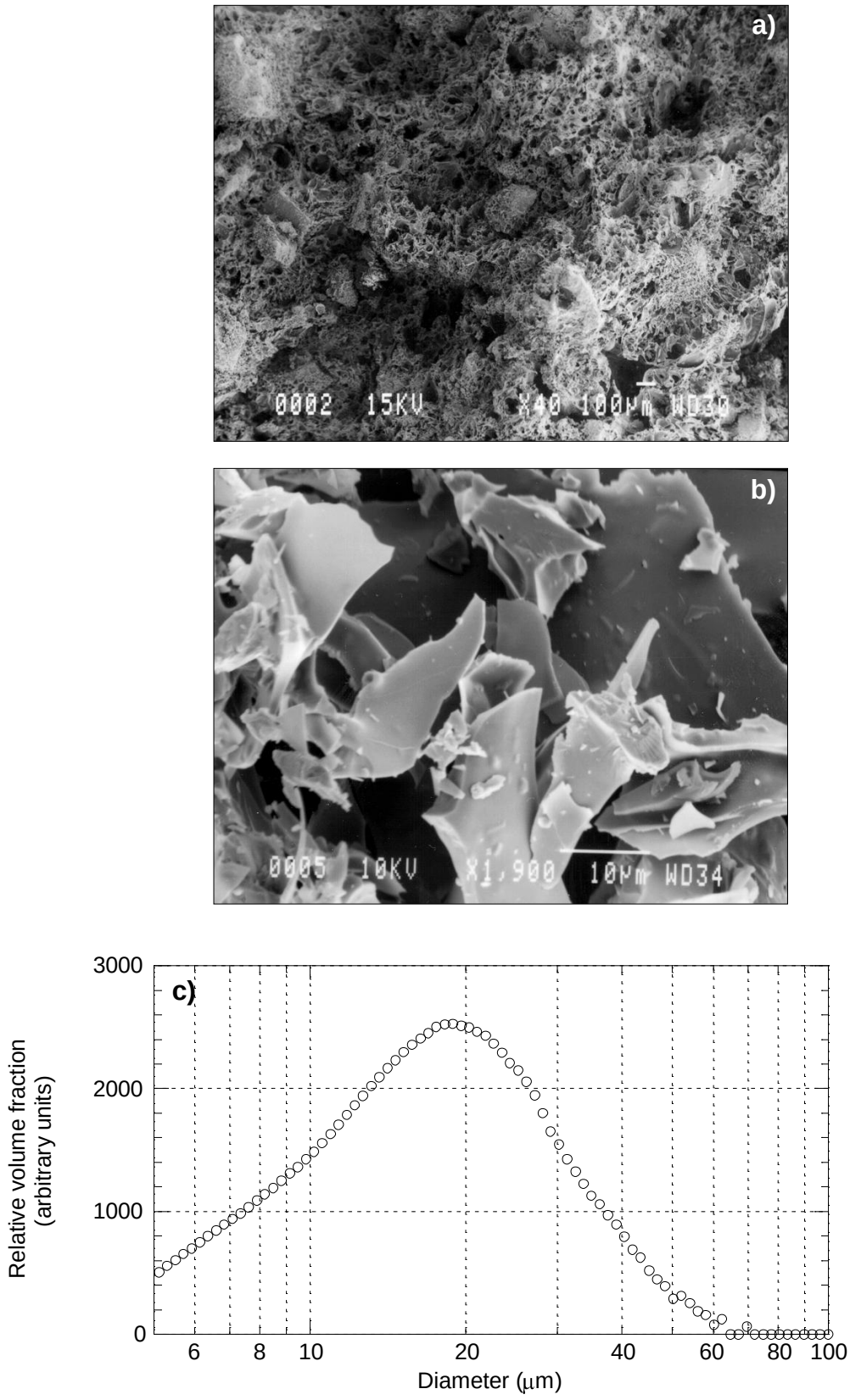

Figure 6.1 MSH sample. **a)** SEM image of fracture surface produced by pumice–pumice impacts. **b)** SEM image of particles generated from pumice–pumice impacts. **c)** Particle size distribution of particles shown in **b)**.

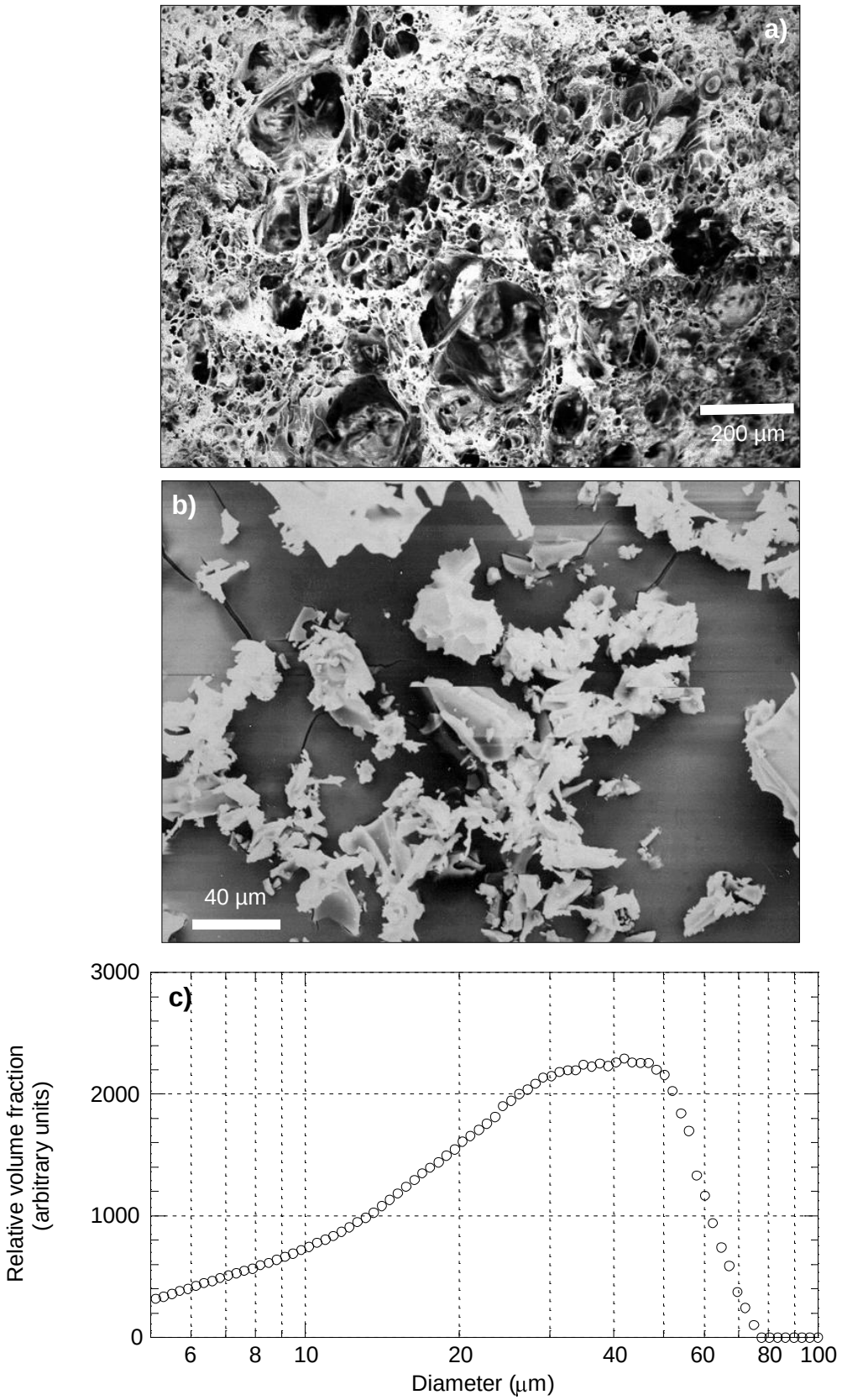

Figure 6.2 Sak 13I sample. **a)** SEM image of fracture surface produced by pumice–pumice impacts. **b)** SEM image of particles generated from pumice–pumice impacts. **c)** Particle size distribution of particles shown in **b)**.

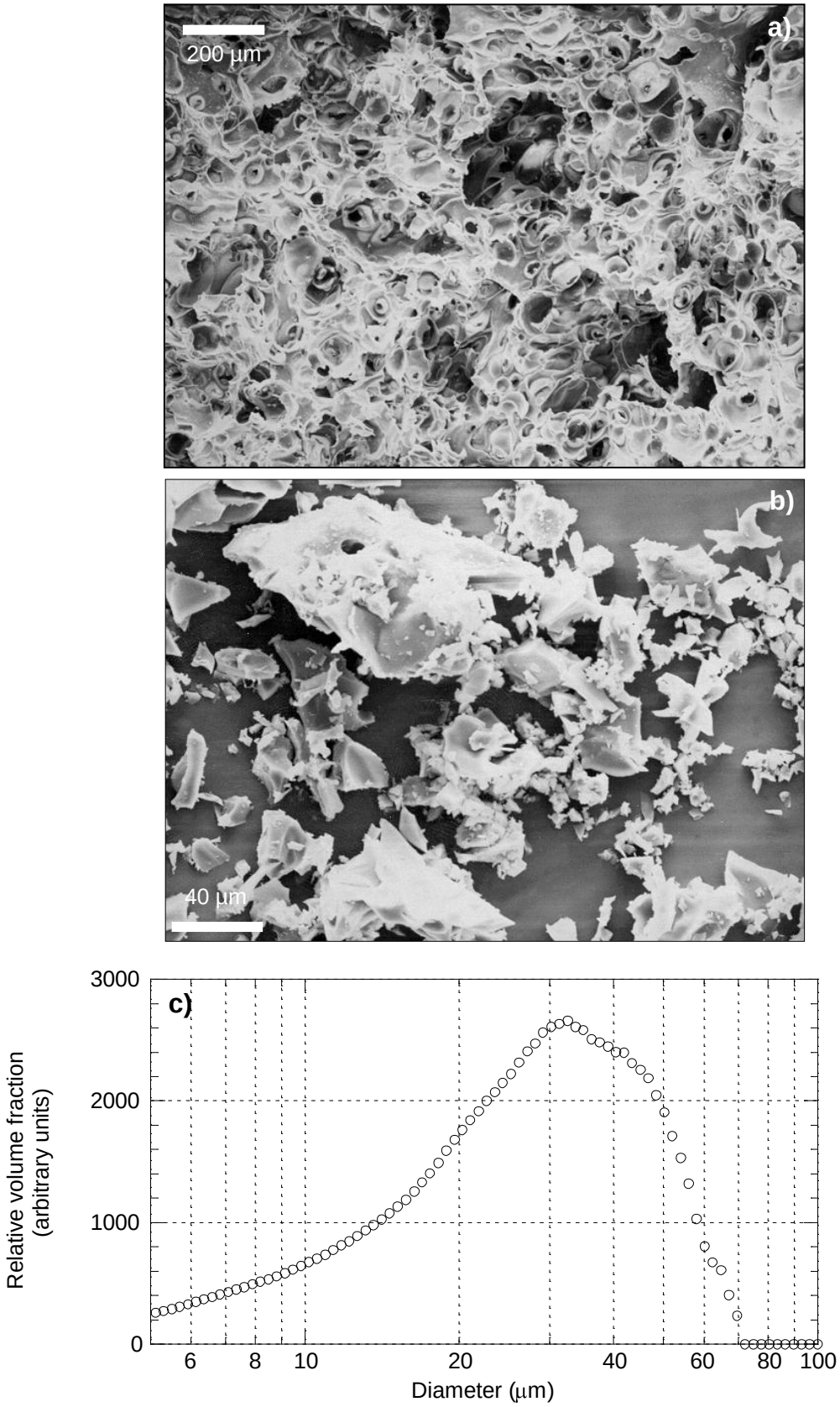

Figure 6.3 Sak 14 sample. **a)** SEM image of fracture surface produced by pumice–pumice impacts. **b)** SEM image of particles generated from pumice–pumice impacts. **c)** Particle size distribution of particles shown in **b)**.

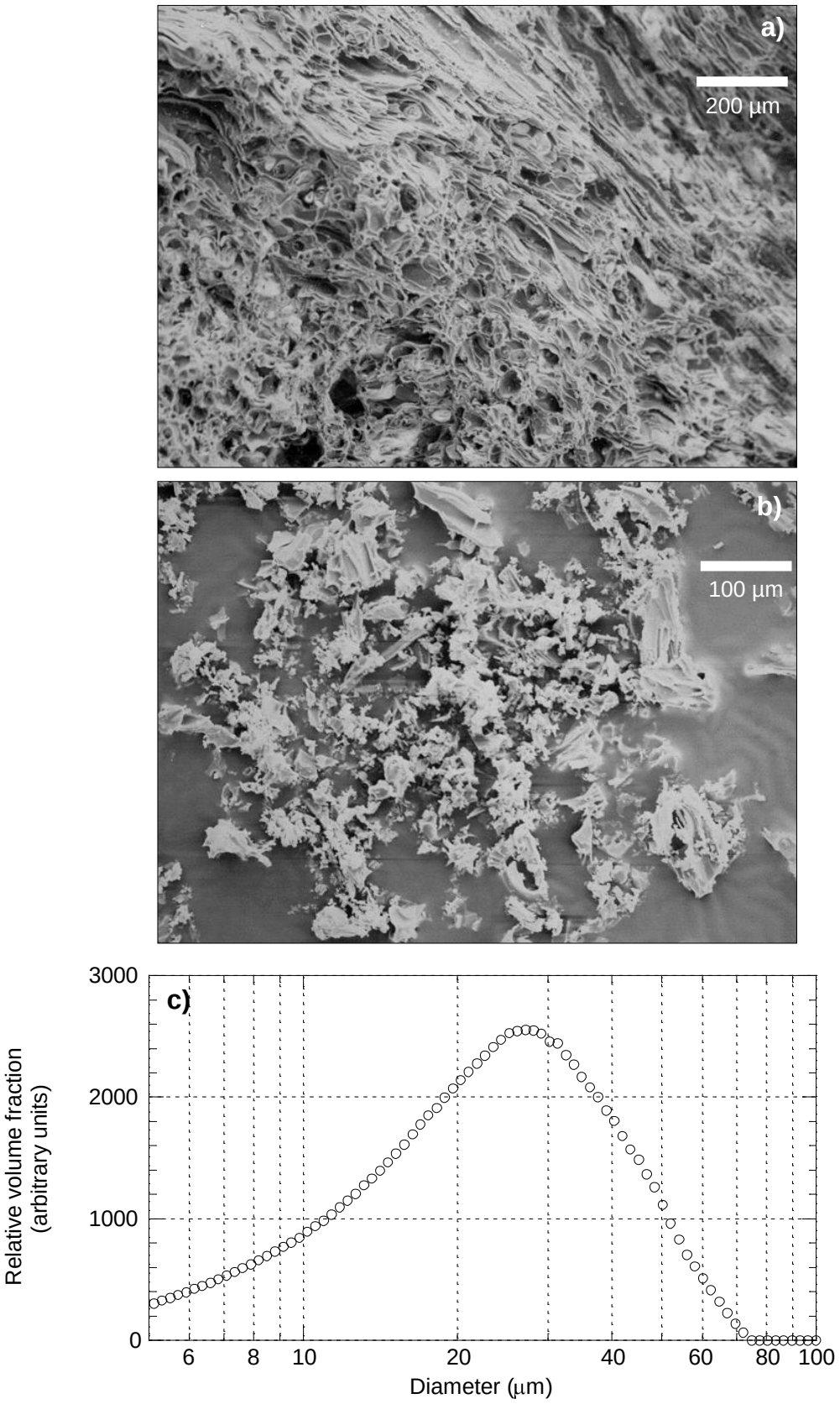

Figure 6.4 SMN 31 sample. **a)** SEM image of fracture surface produced by pumice–pumice impacts. **b)** SEM image of particles generated from pumice–pumice impacts. **c)** Particle size distribution of particles shown in **b)**.

StV 519 (Figure 6.5).

This is a pink coloured pumice with many vesicles up to 100 μm in diameter and several over 1 mm. Phenocrysts consist of plagioclase, orthopyroxene, clinopyroxene and oxides, and have a maximum length of about 500 μm.

Santorini (Figure 6.6).

The Santorini pumice is a white pumice containing some highly elongate vesicles up to 1 mm in length and a few plagioclase, orthopyroxene and clinopyroxene phenocrysts, most of which are much less than 1 mm in size. Considerable heterogeneity was observed in the strength of the samples cut from Santorini clasts, from those which could not be made to fracture in the apparatus to others that would produce particles relatively easily during impacts.

6.3 Charging phenomena observed during experiments

Recording data continuously during each experiment revealed several complex phenomena. Data from the fieldmeter reliably represented the net charge deposited in the Faraday cup. Changes in the data thus represented either addition of charge to the cup, or charge decay from it, mainly over the insulators. Charge decay produced characteristic decay curves, and so could be easily detected. The data were occasionally more noisy that expected, and this was attributed to some silicate particles managing to enter the sensing aperture of the fieldmeter. In contrast, interpretation of the mesh data was more complex as a result of the measurements being sensitive to charge not actually deposited on the mesh. The various charges detected by the mesh are discussed in the next section.

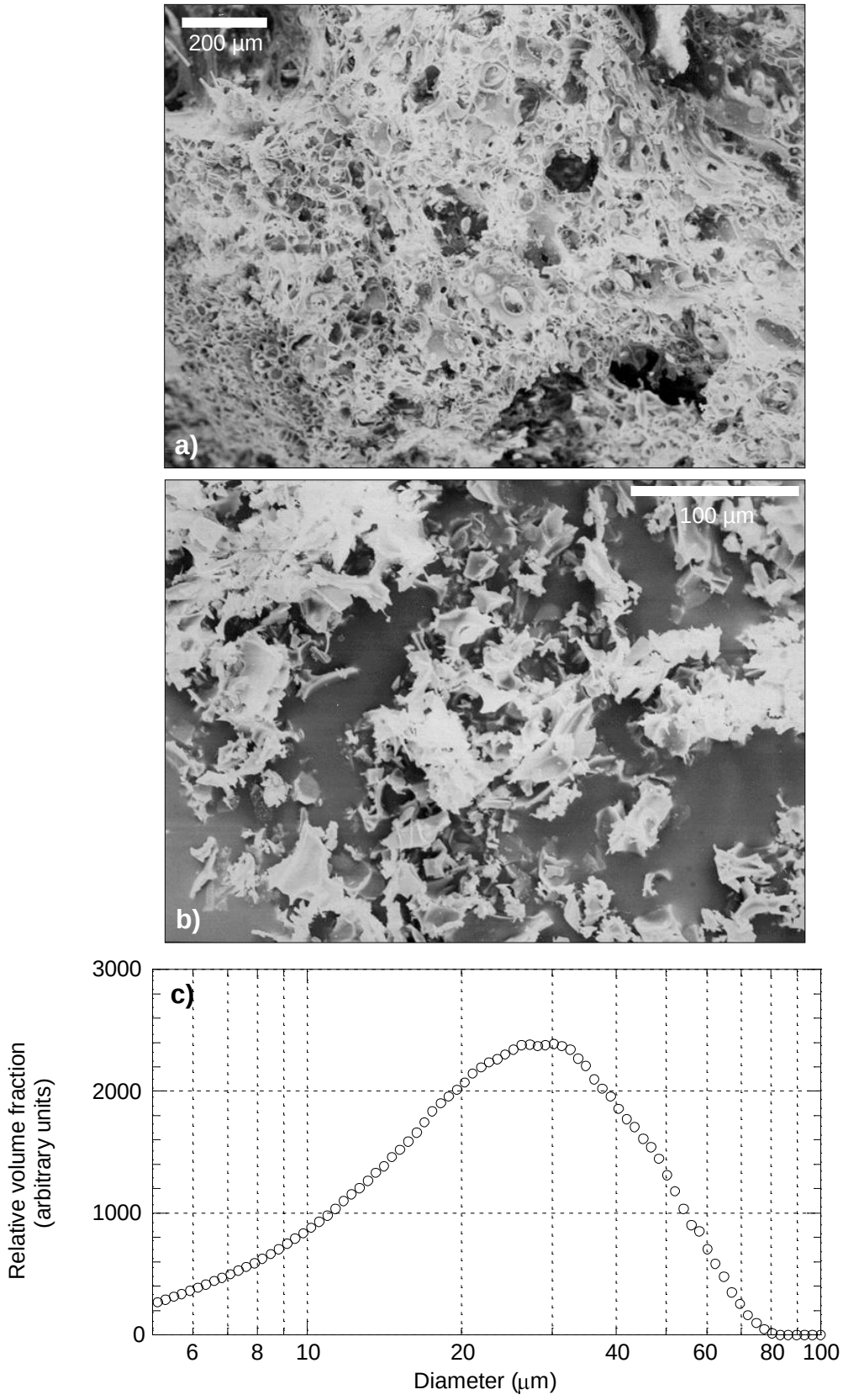

Figure 6.5 StV 519 sample. **a)** SEM image of fracture surface produced by pumice–pumice impacts. **b)** SEM image of particles generated from pumice–pumice impacts. **c)** Particle size distribution of particles shown in **b)**.

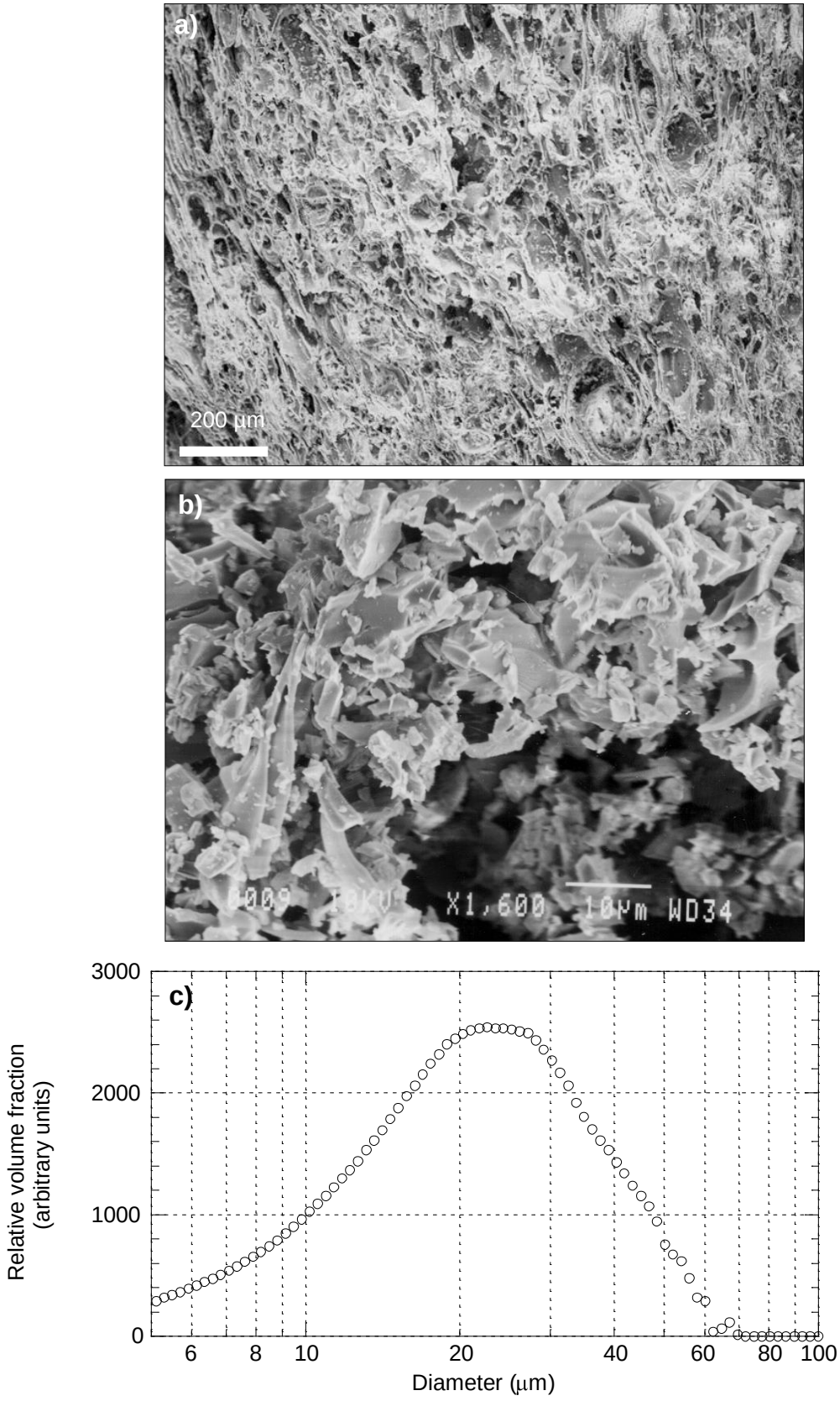

Figure 6.6 Santorini sample. **a)** SEM image of fracture surface produced by pumice–pumice impacts. **b)** SEM image of particles generated from pumice–pumice impacts. **c)** Particle size distribution of particles shown in **b)**.

6.3.1 Data recorded from the mesh

Keithley 614 electrometers measure charge by maintaining the input at Earth potential and integrating any current flow required to do so. Thus, charge collected on the mesh was detected directly by producing charge flow through the electrometer. However, the electrometer also detected charge flow due to variations in the electric potential of the mesh's environment. If the potential around the mesh was raised (by the presence of positive charge), negative charge flowed from the electrometer onto the mesh, in order to maintain its 0 V potential. This flow of negative charge out of the electrometer would be detected as representing a positive charge flow into the electrometer, and so would produce a positive 'induced' reading. The magnitudes of induced readings were a function of the inducing charge magnitudes and their positions relative to the mesh.

In order to display this effect, Figure 6.7 shows the results of applying various voltages to an insulated collet mounted on the end of the solenoid rod. The apparent charge detected on the mesh is demonstrated (within error) to be a linear function of the collet potential. The ability of the mesh to detect charges in its vicinity, as well as those deposited on it, implies that there were several sources of charge possibly responsible for the mesh data (Table 6.2). These are shown in a cartoon of the mesh section of the apparatus (Figure 6.8) and are discussed below.

Table 6.2 Types of charge detectable by the mesh.

'Induced' readings	**'Real' readings**
charge on the samples	ions collected by the mesh
space charge in the local environment	small charged silicate particles adhering to the mesh

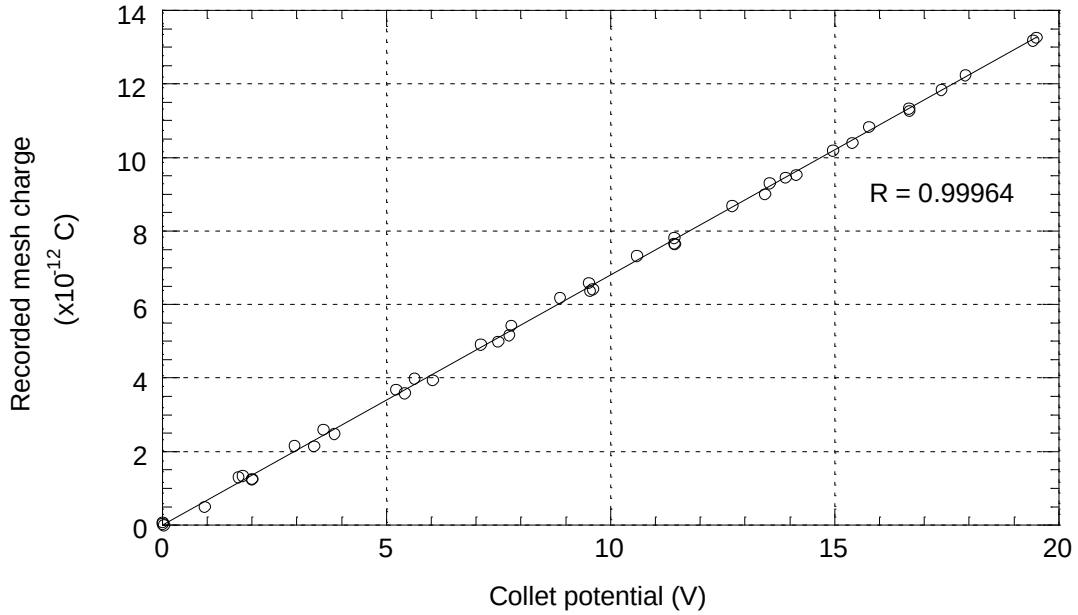

Figure 6.7 Detection of induced charge on the mesh. The plot shows the apparent charge recorded from the mesh as voltages were applied to a collet on the end of the solenoid rod. Data are shown by circles and the line represents a best-fit straight line with the given R value. The magnitude of the readings are also a function of the collet position and the of the charge distribution over it. The electrical connection to the collet was made by a fine wire, the presence of which also exerted an effect on the magnitude of the induced charge readings.

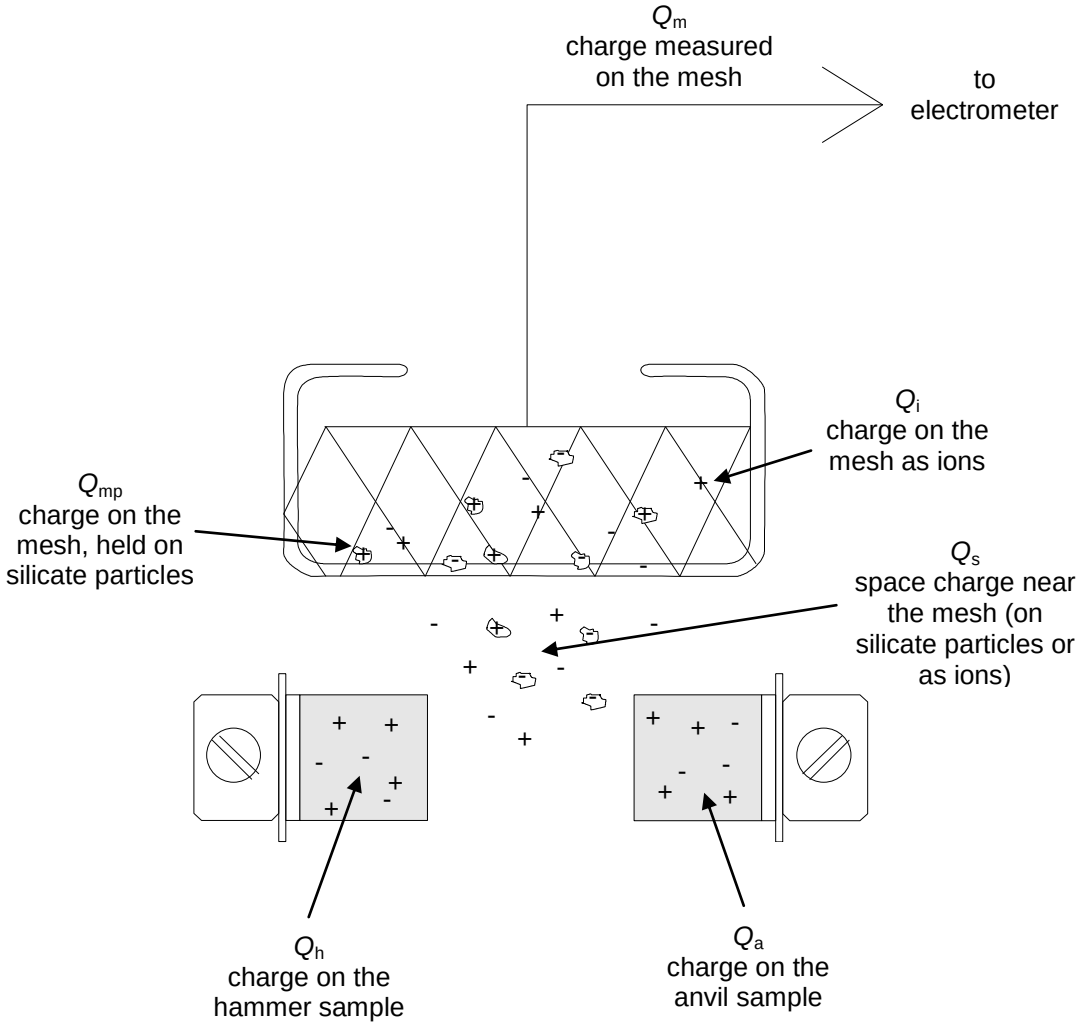

Figure 6.8 Charges influencing the mesh data. Note that charge on the samples will be held on the surface of the pumice. As a result of high surface resistivity, it will also probably be concentrated near the impact surfaces.

Charge on the samples.

Most experiments involved two pumice samples, thus any induced charge was a function of the net charge on the two samples. The effect of the changing position of the hammer sample during impacts is discussed in section 6.3.1.1. Although Figure 6.7 showed that induced charge readings could be produced from a collet, the presence of the wire used to apply the potential to the collet meant that the results could not be used to determine the magnitude of possible readings during experiments. Figure 6.9a shows the way in which the approximate magnitude of induced readings was determined. To investigate the effect of different charge distributions, three types of 'sample' were constructed, as shown in Figure 6.9b. One consisted of a standard pumice sample with a circular piece of aluminium foil attached to the impact surface to allow charge to be placed on the end. Another 'sample' consisted of only the aluminium foil adhered to the mounting collet by insulation and double-sided adhesive tape. An insulated anvil (brass collet) was also used. The electrometers monitored the charge that flowed onto the sample and the induced charge detected on the mesh (Figure 6.9a). This allowed the ratio of the induced charge to the applied charge to be calculated for the different charge distributions and positions provided by the three samples. The results of ten experiments with each sample are given in Table 6.3.

These data demonstrate that, for a pumice sample holding a charge on its impact surface, the mesh detected an induced charge representing approximately 25 % of the actual charge. The foil-only sample produced much smaller induced readings (4 %). Thus, it is likely that with decreasing sample length, the detected fraction of charge on a sample would also decrease. The ratio of induced charge for the brass collet (insulated anvil) was between these two extremes, at about 10 %.

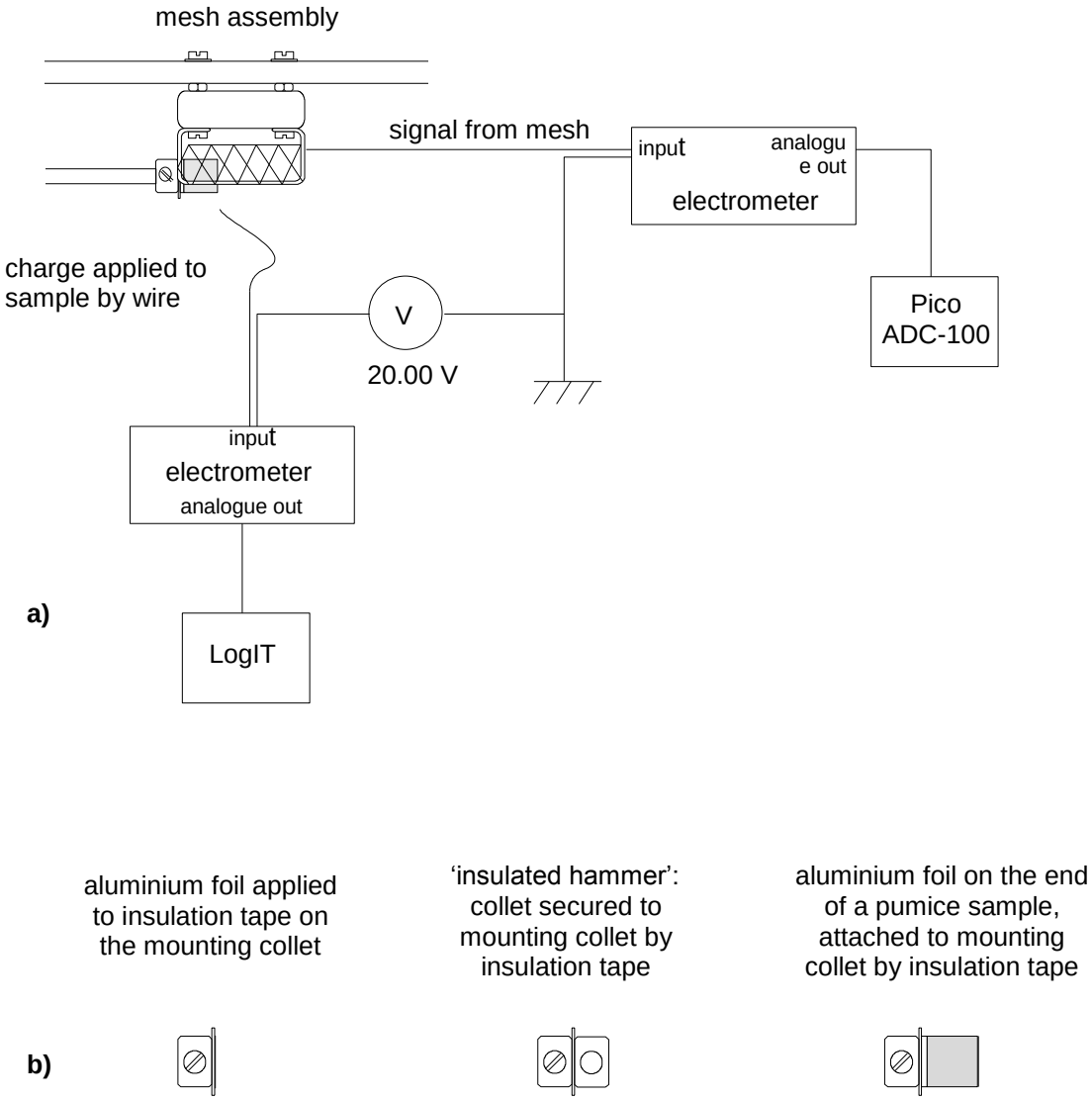

Figure 6.9 Measurement of the magnitude of induced charges on the mesh. **a)** The apparatus used to record the charge flow onto a sample (with the LogIT data logger) when a potential of 20.00 V was applied, and also to record the induced charge on the mesh (with the Pico ADC-100 data logger). **b)** The different types of sample used in these experiments.

Table 6.3 Induced charge detected by the mesh as a ratio of charge on the sample. The table shows the results of the experiments carried out with the apparatus and samples shown in Figure 6.9.

Test no.	Sample type (charge in units of 10^{-12} C)								
	Foil			Brass collet			Foil on pumice		
	Applied charge	Induced charge	Ratio	Applied charge	Induced charge	Ratio	Applied charge	Induced charge	Ratio
1	55.5	2.9	0.05	94.0	10.9	0.12	91.6	22.8	0.25
2	53.8	2.0	0.04	97.7	10.9	0.11	92.8	22.8	0.25
3	56.2	2.0	0.04	96.4	10.9	0.11	91.6	21.8	0.24
4	55.6	3.0	0.05	96.5	10.9	0.11	92.2	21.8	0.24
5	57.3	3.0	0.05	97.1	10.9	0.11	93.4	22.8	0.24
6	54.3	2.0	0.04	95.9	10.0	0.10	91.0	22.8	0.25
7	55.0	2.5	0.05	95.2	10.0	0.11	91.6	22.8	0.25
8	54.9	2.0	0.04	93.4	11.9	0.13	91.0	22.8	0.25
9	53.1	2.5	0.05	95.9	11.0	0.11	89.7	22.8	0.25
10	56.8	2.5	0.04	96.5	10.0	0.10	89.7	21.8	0.24
Average ratio:			0.04			0.11			0.25

Space charge in the local environment.

At any one time, a net space charge close to the mesh could have been produced by the presence of ions or charged silicate particles, or a combination of both. However, it is unlikely to have been long-lived. Most silicate particles would be removed from the area by gravity, and ions would be quickly attracted to either the mesh, the samples, or to other areas of earthed metal surface. Electrostatic forces may dominate over gravitational forces for small silicate particles with high charge to mass ratios. Thus, fine ash may also be attracted to the mesh, and small amounts of very fine silicate particles were indeed observed on the mesh after some experiments.

Ions collected by the mesh.

The mesh was designed to collect any ions produced by fracto-emission. However, if charge accumulation on the samples became sufficient to produce corona discharge, then ions generated by this process would also have been collected. It is likely that interference (voltage spikes) would also be detected by the mesh if corona discharges were occurring. Visual evidence for corona was never observed during an experiment, and spikes were only recorded in a few experiments (section 6.3.1.2).

Silicate particles collected on the mesh.

Due to the insulating properties of silicate particles, most of the charge on particles adhering to the mesh would actually be detected as an induced charge. However, the small size of the particles, and thus the proximity of the charge to the surface of the mesh, would produce an induced charge of almost identical magnitude to the actual charge. The particles are also effectively removed from the environment (because they will remain on the mesh) so it is convenient to consider charge on them to be detected as a 'real' charge rather than by an 'induced' mechanism.

If all these factors are taken into account, the detected mesh charge, Q_m, can be given as

$$Q_m = Q_i + Q_{mp} + \alpha Q_h + \beta Q_a + \gamma Q_s \qquad (6.1),$$

where Q_i represents the cumulative ion charge collected, Q_{mp}, the charge on fine particles adhering to mesh, Q_h, the charge on the hammer sample, Q_a, the charge on the anvil sample, and Q_s, the space charge influencing the mesh. α, β and γ are factors which are functions of the position and distribution of the relevant charge. However, for a typical experiment, some simplifying assumptions can be made.

After collisions stopped, free particles or ions would have been removed from the mesh area by gravitational or electrostatic forces, so Q_s can be assumed to be negligible. Also, many experiments did not produce any visible particles on the mesh. For this reason, and also because it would not be possible to distinguish between charge detected as a result of particles on the mesh or ions, Q_{mp} was neglected. It is thus assumed that, for a few experiments, Q_i may include some charge held on fine particles. Finally, if the effective position and distribution of the charges on the samples are assumed to be similar, then $\alpha \approx \beta$. The final measured charge can be represented as

$$Q_m \approx Q_i + \alpha\left(Q_h + Q_a\right) \qquad (6.2).$$

The results given in Table 6.3 provide estimates for values of α for several different types of sample (mounted on the solenoid rod), the values varying from 0.1 to 0.25.

The complications discussed in this section demonstrate that precise measurements of mobile charge were not possible from interpretation of the mesh data. However, the data provided by the electrometer were sufficiently accurate to provide good evidence for the production of some mobile charge (see section 6.10.1), and they also demonstrated various charging effects which would have not otherwise been observed. These effects are described and discussed in the following sections.

6.3.1.1 Double line effect

Many of the experiments carried out demonstrated a feature in the mesh data which was determined to be a result of charge accumulating on the moving 'hammer' sample. This was expressed in the data as coherent offsets which produced an apparent splitting of the line generated when plotting the mesh data against time. The

feature was thus called the ‘double line’ effect, and average and extreme examples are shown in Figures 6.10a and 6.10b respectively. Figure 6.10c shows a portion of mesh data taken from Figure 6.10a, which has been enlarged to demonstrate the offsets of individual data values. Each low value correlates to an impact event (to within the accuracy of the of the manually controlled timing, see Chapter 5).

In order to investigate this effect, mesh data (Figure 6.11) were recorded during solenoid activations with an insulated collet mounted on the solenoid rod. For the first three activations, the collet was at Earth potential. A potential of 20 V was then momentarily applied to the collet before the solenoid was operated a further three times. The data shown in Figure 6.11 clearly demonstrate that the apparent charge detected by the mesh varied with the position of the collet, with a reduction of the induced charge during the periods of solenoid operation. During periods of non-operation of the solenoid, the collet was closer to the edge of the mesh and the copper supporting wire (Figure 5.2). It is thought that proximity of charge to this supporting wire elevated the magnitude of the induced charge. Thus, when the solenoid was operated and the collet moved away from the edge of the mesh, the induced charge decreased. Similar experiments were also carried out with the collet at a negative potential, and they demonstrated the same result, but with reversed polarity.

Figure 6.12 shows data recorded at 1 ms intervals with a charged collet, and with solenoid operations at the approximate frequency used during experiments. The circles represent the same data sampled at 100 ms (as during experiments). This closely reproduces the patterns recorded during ‘real’ experiments as shown in Figure 6.10c. Thus, the double line effect has been shown to be a result of charge accumulation on the hammer sample. The polarity of this charge is given by the direction of the offsets (the induced charge decreases during solenoid operation), and

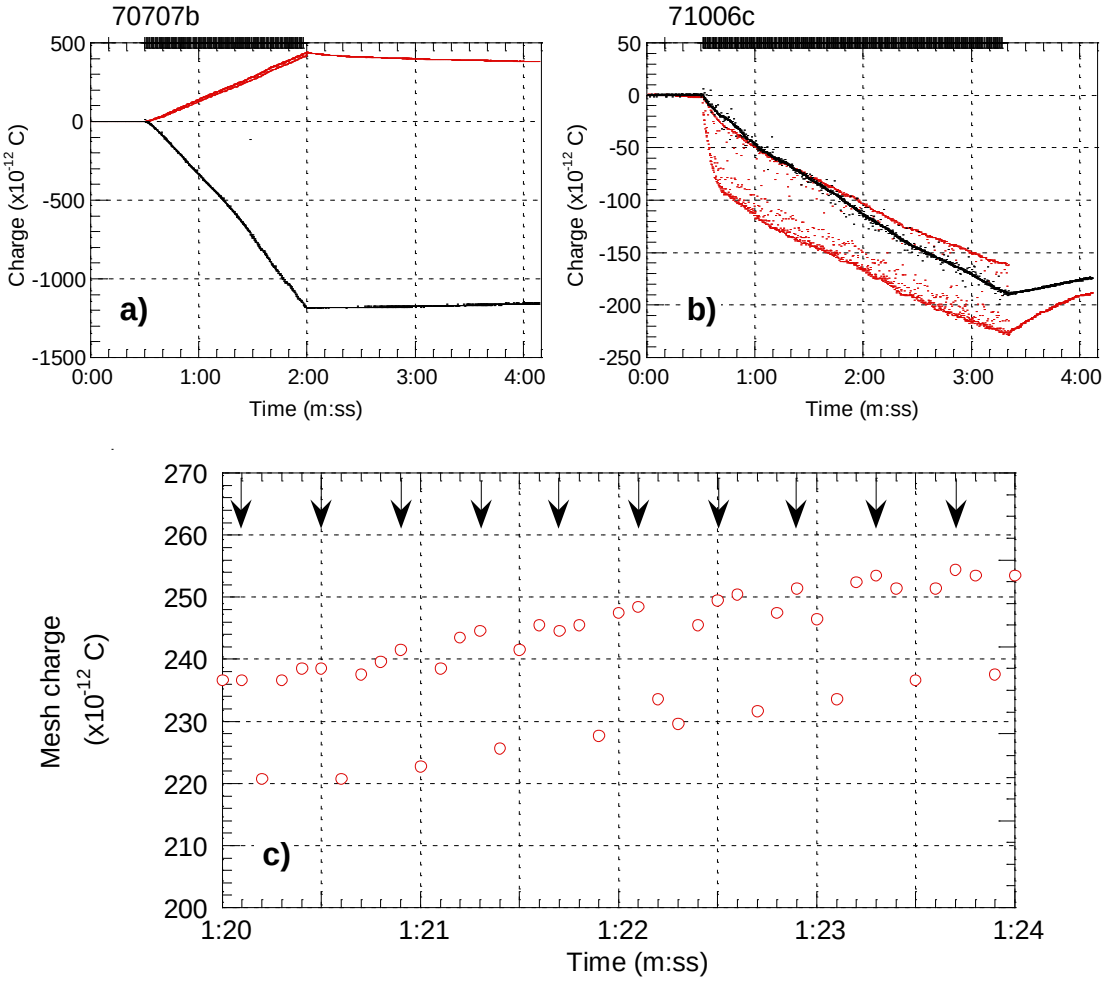

Figure 6.10 The 'double line' effect. The diagrams show two examples of 'double lines' recorded in mesh data during experiments. In **a)** and **b)**, with the exception of the first line (release of the electrometer zero-check), vertical lines on the top axes represent individual impacts; mesh data are in red, Faraday cup data in black. **a)** 207 pumice–pumice impacts with samples of Santorini pumice (atmospheric pressure, 24.3 °C, 47 % RH). **b)** 233 impacts between a pumice sample (Sak 13I) and an earthed anvil at low pressure. **c)** Expanding part of **a)** demonstrates the structure of the 'double line' in the mesh data. The arrows show the timing of the impacts, but are not necessarily exactly synchronised with the other data due to the manual starting of the LogIT data logger. For each impact, only one of the mesh data points is usually reduced in amplitude.

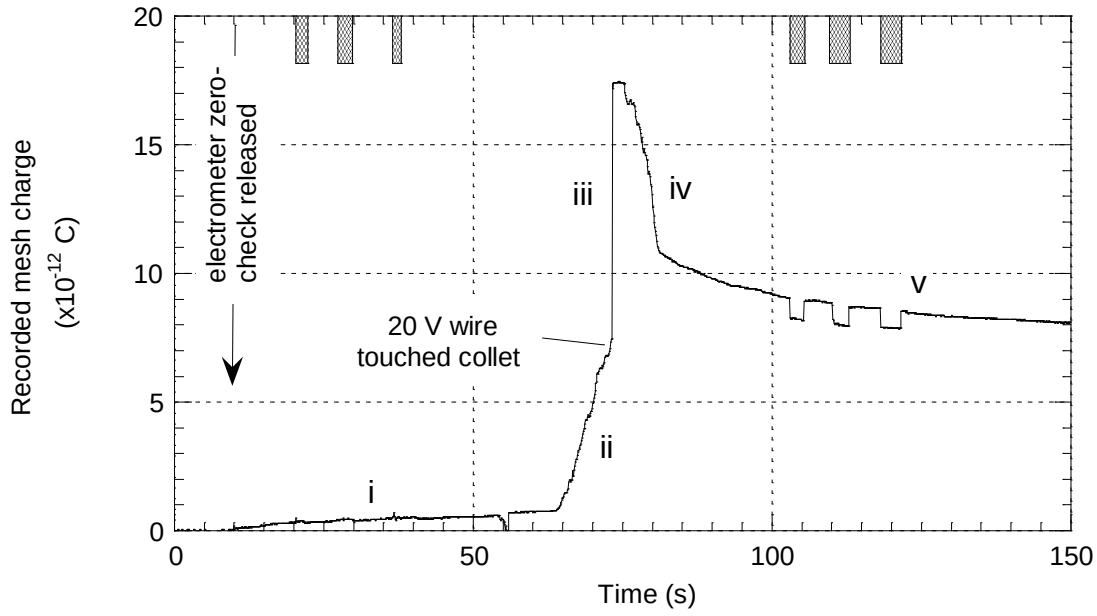

Figure 6.11 Investigation of the 'double line' effect. The plot shows data recorded from the mesh during a period in which operations of the solenoid are indicated by hatched bars on the top axis. An insulated collet attached to the solenoid rod was initially at 0 V, but was then raised to a potential of 20 V. During section i, with the collet at 0 V, operation of the solenoid was not detected by the mesh. During section ii, a wire at 20 V approached the mesh and collet, and the increase in the local electric potential was detected by the mesh. Section iii shows the instantaneous rise in the apparent mesh charge recorded when the wire touched the collet and raised it to 20 V. This was followed by a rapid decrease in the detected charge (section iv) as the wire was removed from the vicinity of the mesh. The final time section (v) demonstrates charge decay from the collet and periods of decreased detected charge during solenoid operation.

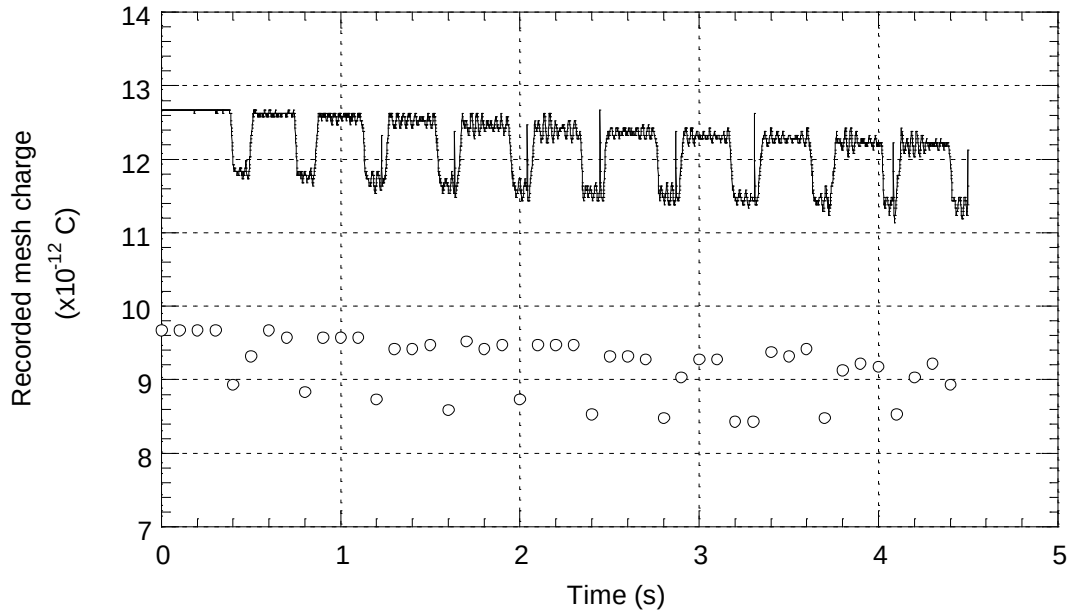

Figure 6.12 Reproduction of the 'double line' effect. The line shows mesh data logged at 1 ms intervals over a period during which the solenoid (with a charged collet secured on the rod) was operated at a similar frequency to that used in the experiments. The circles represent the same data re-sampled at 100 ms (and offset by -3×10^{-12} C). Note the similarity between these points and those shown in Figure 6.10c. The 1 ms data also demonstrated an increase in the recorded noise after the first solenoid operation, attributable to vibration of the apparatus. During some operations of the solenoid a transient spike was observed towards the end of the period of reduced data values. This is interpreted as interference from the solenoid due to the voltage spike generated when power was removed.

its magnitude could be inferred from the amplitude of the offsets. However, this would be of little use without also knowing the charge on the anvil sample, because the total induced charge on the mesh was a function of both.

6.3.1.2 Unusual (rapid) charge variations in mesh data

Another effect was also observed to be directly related to operations of the solenoid. However, unlike the double line effect (which was observed during many experiments), this effect was observed only during low pressure experiments involving collisions between a collet (earthed or insulated) and samples of StV 519 (experiments 71020e, 71021a, 71021d, 71021f, 71021l and 71022a). The effect produced offsets in the mesh data which were observed to be superimposed on perturbations from the double line effect. Figure 6.13a shows data from one of the experiments in which the effect was initially detected. During this standard experiment (logging at 100 ms intervals), many data points have been offset below the points forming the standard double line.

Figure 6.13b shows the results of an experiment logged at 1 ms intervals to display more detail of the phenomenon. The negative spikes in the mesh data (responsible for the displaced data points in Figure 6.13a) peak within approximately 1 ms. Data from Figure 5.11 show that the hammer velocity after 8 mm of travel was approximately 0.7 $m\,s^{-1}$ for the solenoid on 12 V. Thus 'outward' journeys of the hammer must have occurred over an absolute minimum time of 11 ms. The hammer return velocity was slower (it was not being driven by the solenoid), so the negative spikes in the mesh data peak on a time-scale much smaller than that of the hammer return.

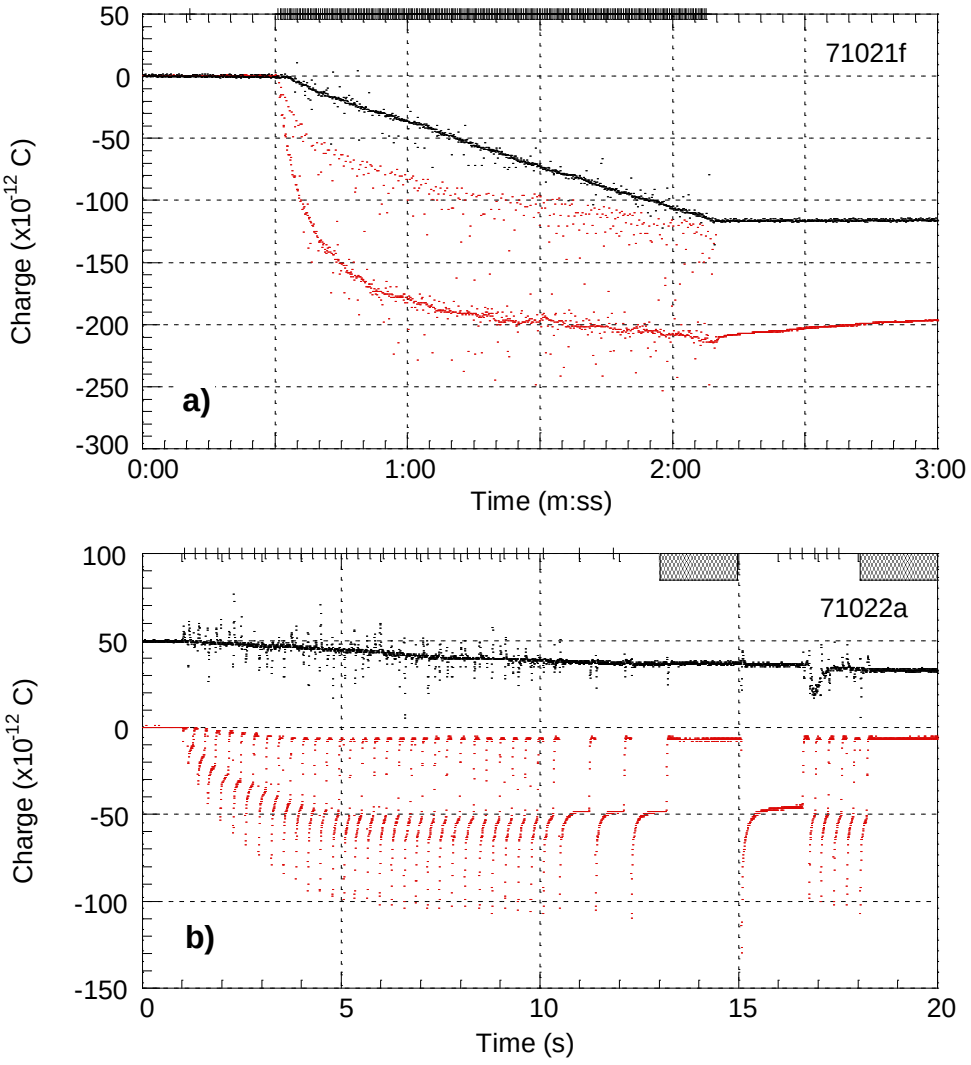

Figure 6.13 Unusual (rapid) charge variations recorded from the mesh. Vertical lines on top axes represent individual impacts; mesh data in red; Faraday cup data in black. **a)** 267 collisions between an earthed anvil and an StV 519 sample at low pressure (logged at 100 ms). The mesh data recorded shows a high amplitude 'double line', but also some unexplained points below the lower line. **b)** 40 impacts between the same sample and an earthed anvil under the same conditions, but logged at 1 ms. Periods during which the hammer was held against the sample are marked by hatched areas on the top axis. The 'double line' is observed along with further detail of the rapid negative transient spikes. The downwards edge of each spike occurred within approximately one sample interval (1 ms). The Faraday cup data have been offset by $+50 \times 10^{-12}$ C for clarity.

Although the cause of this effect is not fully understood, it is thought that it represents the generation of a short-lived electric field (or possibly a small discharge) immediately upon separation of the samples. A field change is the only mechanism which can be envisaged to operate over the very short time-scale necessary, and then decay rapidly afterwards. This interpretation is supported by the fact that the magnitude of the spikes increased with the charge held on the sample, as indicated by amplitude of the double line effect. Why the effect was limited to one specific pumice type, under vacuum, is not known.

6.3.1.3 Unusual (slow) charge variations in mesh data

During an experiment, after impacts had ceased, it was expected that changes in the mesh data would only reflect drift of the electrometer. However, several experiments displayed changes which could not be explained by this mechanism. Figure 6.14 shows three examples of this effect, which was also observed during experiments involving pumice–pumice collisions of Santorini (70730c), SMN 31 (70804d, 70804f, 70925b), Sak 13I (70805c), StV 519 (71020d) and MSH (71001c) samples, and collisions of Sak 13I (70808d), Santorini (70918b), StV 519 (71021g) and SMN 31 (71027c, 71027d) samples with an earthed collet, all at atmospheric pressure. There were only two possible similar examples from experiments carried out at low pressure; one for impacts with an earthed collet and Santorini pumice (71006a) and the other for pumice–pumice impacts of Sak 14 (70730b).

One possible explanation for the changes is that they reflect the removal of charge from the mesh area, on particles falling either from the samples or from the mesh itself. However, these particles would then collect in the Faraday cup and would produce similar (but opposite polarity) changes in the Faraday cup charge. Where

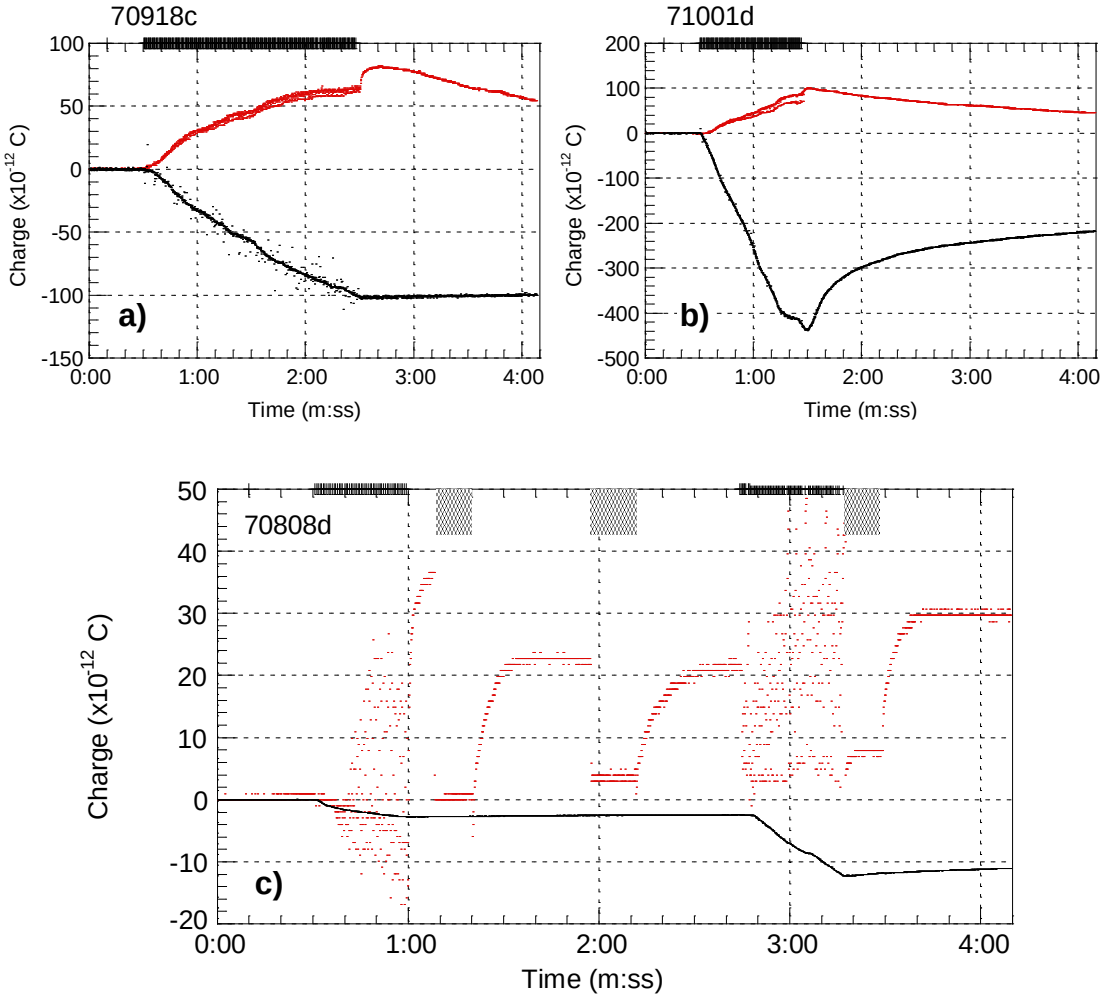

Figure 6.14 Unusual (slow) charge variations recorded from the mesh. With the exception of the first line (release of the electrometer zero-check), vertical lines on top axes represent individual impacts; mesh data in red; Faraday cup data in black. **a)** 267 pumice–pumice impacts between samples of Santorini pumice at low pressure. **b)** 136 pumice–pumice impacts between MSH samples at atmospheric pressure (17.2 °C, 61 % RH). **c)** 130 impacts between a sample of Sak 13I and an earthed hammer at atmospheric pressure (27.1 °C, 43 % RH). Periods during which the hammer was held against the sample are marked by hatched areas on the top axis. To allow detail in the mesh data to be observed, the Faraday cup data has been divided by a factor of fifty before plotting.

changes are observed in the Faraday cup data (Figure 6.14b), they are usually of the same polarity, so cannot be used to account for the mesh data.

The experiment 70808d (Figure 6.14c) was carried out to investigate the effect further. The increases in the recorded mesh charge were observed to occur (to some degree) after each impact, and only peak after approximately 20 s. This relatively slow time-scale suggests that the changes could be a result of redistribution of charge over the sample. During periods of solenoid activation, the elevated charge values are absent. Thus, with the samples together, the effect is being 'masked', suggesting that it is an induced charge. (If the charge were being detected directly on the mesh, for example, as ions from corona discharge, then there could be no decrease in the data values while the samples were together). Because the effect is also observed predominantly at atmospheric pressure, the presence of adsorbed water on the sample may be a relevant factor. The conductivity of the samples is likely to be dominated by surface conductivity and, without adsorbed water, could be too high for the effect to be observed.

Thus it is thought that the pressure, time-scale and 'masking' evidence suggests that the effect is a result of changes in charge distribution on the impact surfaces of the pumice, promoted by the presence of adsorbed water. The fact that not all experiments demonstrated this effect could be due to different amounts of adsorbed water or different initial charge distributions on the sample surfaces.

6.3.2 Charge balance and apparent charge loss

Only a few of the experiments carried out produced mesh and Faraday cup data which represented approximately equal and opposite charges. Thus, most experiments appeared to either lose or gain charge from the apparatus. The double line effect

demonstrated that samples could become charged during experiments, and it has also been shown that only a proportion of the net charge on the samples was detected by the mesh (section 6.3.1). Thus, sample charge can account for some of the 'lost charge'. However, in order to be able to consider the charge balance during an experiment, it was necessary to take account of any other possible sources of lost or undetected charge.

Particle loss.

Most experiments exhibited some degree of recorded mass loss (the difference between the mass reduction of the samples and the mass of the collected particles), mainly as a result of particles falling onto the shield rather than into the Faraday cup. The 'lost' mass can be expressed as a fraction of the particle mass collected, and given as the fractional mass loss λ, where

$$\lambda = \left(\frac{\text{mass decrease of samples}}{\text{particle mass collected in cup}} \right) - 1 \qquad (6.3).$$

At atmospheric pressure, λ was usually approximately 0.1 or less, but increased at low pressure up to about 0.5 (Appendix IV). This was a direct result of particles produced by impacts under vacuum dispersing more widely than those produced at atmospheric pressure due to the greatly reduced air resistance.

Conduction through the sample.

In the experiments for which the sample mounting plates had been adhered directly to the mounting collet, charge could have been lost to Earth if charge flow over or through the sample occurred. Attempts to measure the resistance across samples with the electrometer produced readings which were off the scale, indicating resistances greater than $2 \times 10^{11}\ \Omega$.

It could have been possible that some samples exhibited semiconductor characteristics, allowing charge flow only when the potential of the sample had reached a critical value (possibly suggested by some experiments which produced variable polarity ash). However, experiments carried out with samples mounted on insulation tape demonstrated no distinct differences, so charge loss over the samples is thought to have been unlikely. Some degree of charge flow is thought to be responsible for the changes in the mesh data shown in section 6.3.1.3. However, this is believed to be due to changes in the charge distribution only, and the insulation mounting would have prevented any flow to Earth.

Charge flow to the shield.

Particles falling into the Faraday cup fell through the mesh over the hole in the shield. In order to assess if any charge from these particles was flowing to Earth via the mesh, during some experiments, this horizontal mesh was elevated off the shield and electrically connected to the mesh above the samples. The results from these experiments did not demonstrate any coherent differences to results obtained with the mesh on the shield. Thus, it was assumed that only a negligible amount of charge was lost to the shield.

If the total charge within each experiment is assumed to be constant, the sum of the charges on the samples, the particles and any ions produced will be zero at the end of an experiment. If unrecovered particles (particles produced which were not collected in the Faraday cup) are assumed to hold the same net charge as the ones that did fall into the cup, then charge balance for an experiment gives

$$0 = Q_{\mathrm{i}} + Q_{\mathrm{p}}(1+\lambda) + Q_{\mathrm{h}} + Q_{\mathrm{a}} \qquad (6.4)$$

where Q_i, Q_p, Q_h, Q_a, Q_i, and λ are defined in Figure 6.15. Using equation 6.2 to produce an equation for the charge held on the samples leads to

$$Q_h + Q_a = \frac{1}{\alpha}\left(Q_m + Q_i\right) \qquad (6.5),$$

which can then be substituted into equation 6.4. Thus, the ion charge is given by

$$Q_i = \frac{\alpha(1+\lambda)Q_p + Q_m}{1-\alpha} \qquad (6.6).$$

So, even if the mesh data cannot be used directly as the charge collected in the form of ions, the presence of ions may be inferred in some cases by considering charge balance with sensible limits for α and λ.

6.3.3 Polarity reversals

The data recorded from some experiments showed that the net charge of the ash being collected could change polarity during the experiment. The most obvious polarity variations were produced during experiments carried out under vacuum, involving pumice–pumice collisions of Sak 13I samples. Data from a selection of such experiments are shown in Figure 6.16. The changes in the net ash polarity were usually mirrored to some degree by the data recorded from the mesh. This produced a variety of apparent charging styles from almost symmetric α-shaped graphs (Figure 6.16a) and those with multiple sign changes (Figure 6.15b) to the asymmetric graphs shown in Figures 6.16c and 6.16d. These data demonstrate that not only does the net ash polarity change but, during some experiments, considerable amounts of charge must be undetected. Several different scenarios were investigated to explain these phenomena.

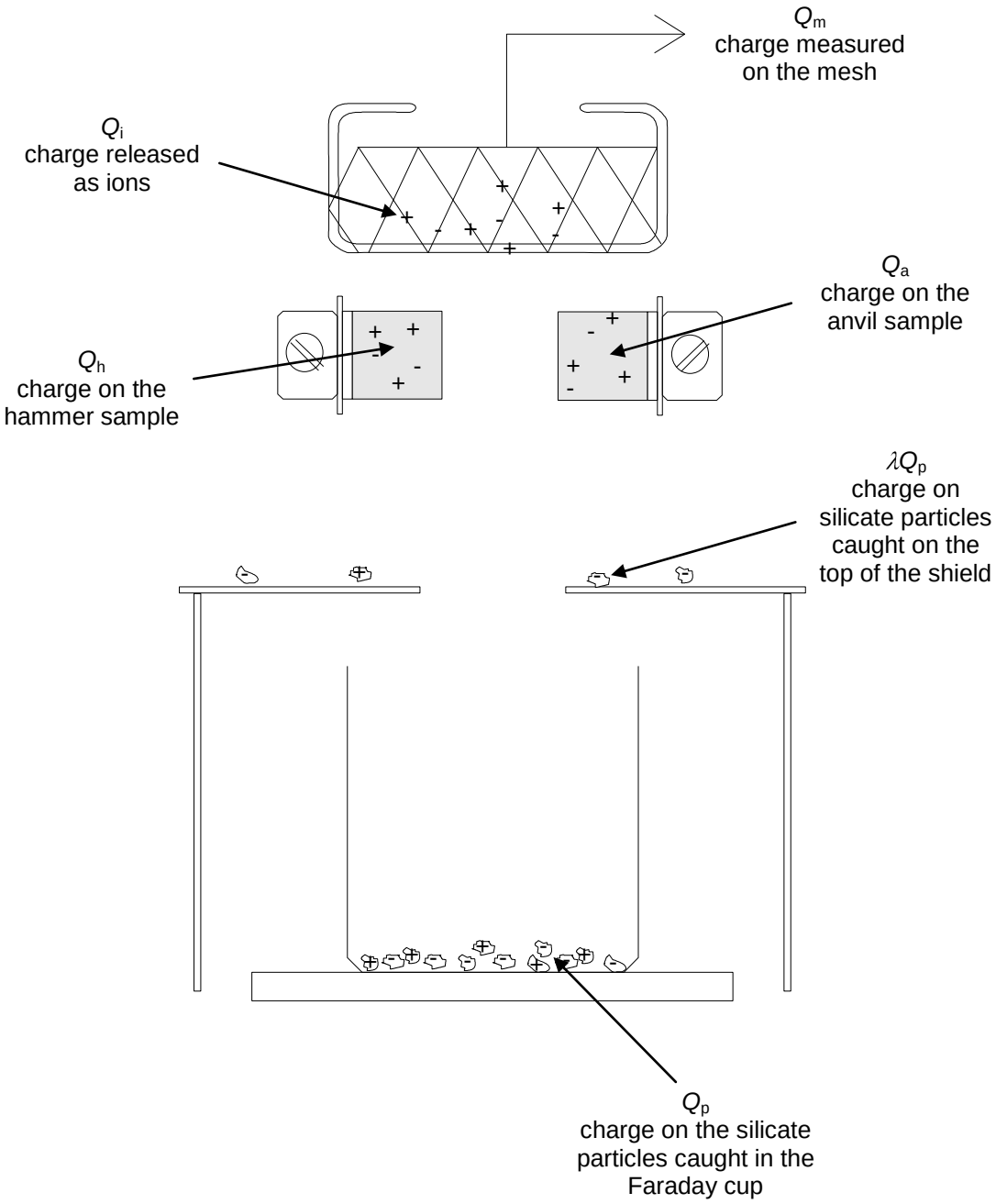

Figure 6.15 Assumed charge distribution for charge balance analysis.

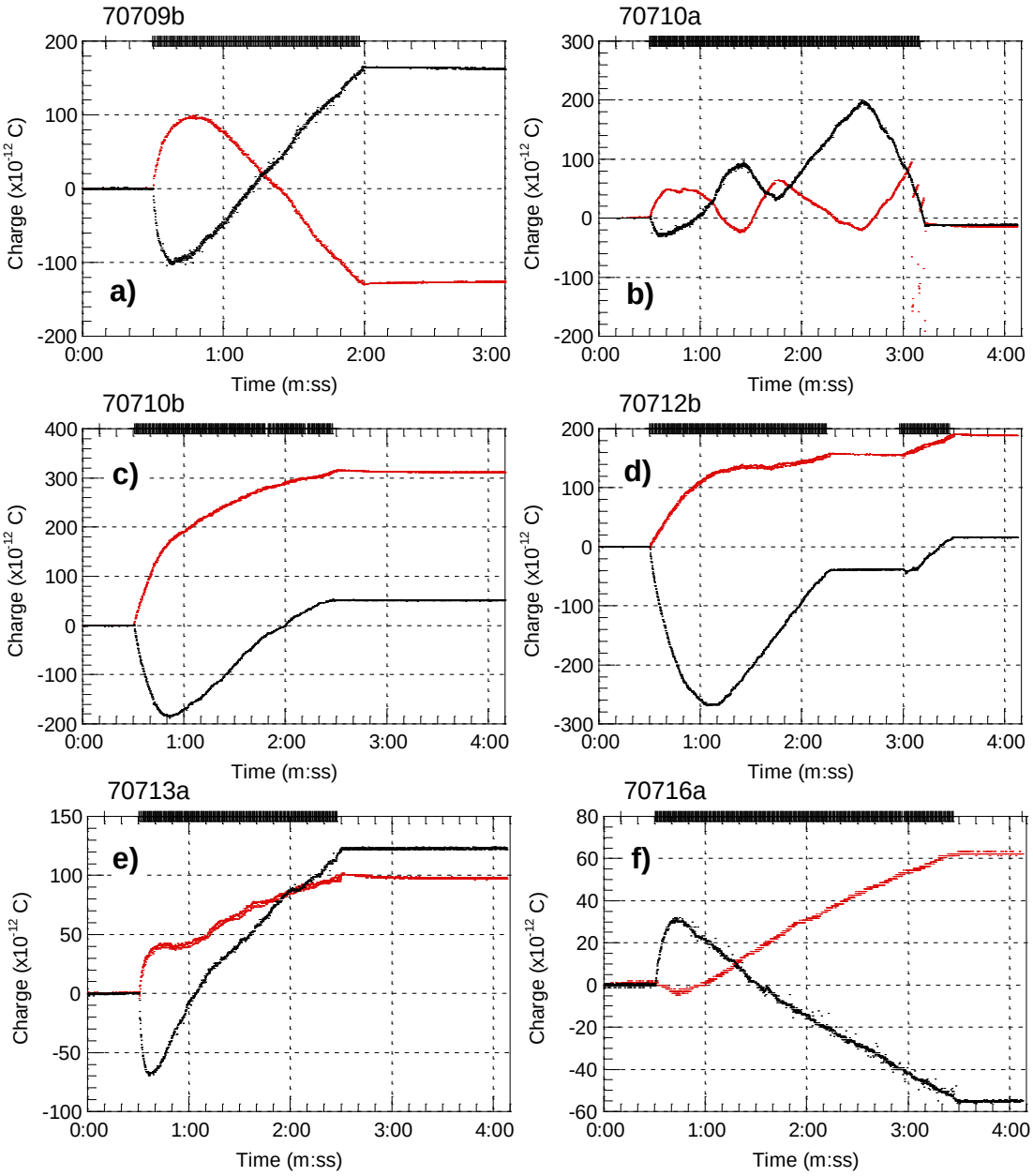

Figure 6.16 Experiments demonstrating variable net ash polarity. With the exception of the first line (showing the release of the electrometer zero-check), vertical lines on top axes represent individual impacts; mesh data in red; Faraday cup data in black. With the exception of **f)**, all experiments shown involved pumice–pumice collisions with samples of Sak 13I, carried out at low pressure. **a)** 193 impacts producing semi-symmetric charge data with one change in polarity. **b)** 368 impacts producing multiple polarity changes in semi-symmetric charge data. Asymmetric data are shown in **c), d)** and **e)** for 271, 306 and 269 impacts respectively. **f)** A similar experiment involving 408 impacts between Sak 14 samples which also showed variable net ash polarity.

Effect of water on the sample.

Small amounts of water adsorbed onto the surface of the pumice may alter its electrostatic properties and could also affect fracto-emission processes. As fresh surface is being produced by impacts, material with different charge generation properties may start to be fractured with resulting polarity variations. However, samples dried under vacuum (10^{-3} Torr, experiments 70710a, Figure 6.16b, and 70716a, Figure 6.16f) for several hours before the experiment (or overnight) showed no difference in their behaviour from those prepared just prior to the experiment.

Interlocking impact surfaces.

The ends of the pumice samples were observed to 'bed-in' rapidly after the start of collisions, producing highly interlocking surfaces. Because this often appeared to coincide with a change in the net polarity of the ash, it was possible that the effects were connected.

In order to investigate any possible link, two experiments (70712b, Figure 6.16d and 70713a, Figure 6.16e) were carried out with the samples left undisturbed between the runs. The first experiment produced initially net negative ash which then changed to being net positively charged. The second experiment, with the interlocking surfaces already formed, demonstrated the same pattern again, with initially net negative ash, followed by a polarity reversal. After one of the samples had been rotated by 90° to disrupt the interlocking nature of the fracture surfaces, the net ash polarity was again negative (experiment 70713b). It was thus concluded that interlocking surfaces alone were not the controlling factor determining net ash polarity.

Sample charging.

The accumulation of charge on samples has been demonstrated by the double line effect. It is likely that, if the impact surfaces become sufficiently charged, the net charge of particles produced from them would change. The period before the change in net ash polarity could then be seen as the time during which charge was accumulating to a critical level. Changes in polarity were often apparently associated with a decrease in the rate of particle production. (This was itself possibly due to the development of the interlocking impact surfaces, after which the impact load would be more evenly distributed over the sample surface, producing less fracturing). A low particle production rate could imply that particles were only being produced from the outermost surface layer of the pumice (where the sample charge would be held), in which case particles would be most susceptible to a change in net polarity.

The effect of surface charge on particle polarity is also supported by experiments 70712b and 70713a (Figure 6.16). Impacts were stopped for more than 40 s during 70712b (after the polarity change had occurred, Figure 6.16d). When they restarted, the net ash polarity remained positive. However, after being left overnight at air pressure (allowing all surface charge to dissipate), the net ash polarity had reverted back to negative (Figure 6.16e).

Polarity reversals of the net ash charge were thus thought to be a result of charge accumulation on the sample impact surfaces, although the development of interlocking surfaces may also be a factor in the transfer of charge. Some sample types (Sak 13I) were much more prone to this polarity reversals than others. Observations of the double line effect demonstrated that charge still did accumulate on the surface of other samples, without producing changes in net ash polarity. Thus, sample type is a

factor in the polarity changes (rather than in the accumulation of charge on the samples), and probably reflects differences in surface conductivity.

6.3.4 Charge accumulation after impacts cease

Most of the experiments carried out at atmospheric pressure detected changes in the charge on the Faraday cup which occurred for some time after sample impacts had ceased. Examples of this are shown in Figure 6.17. These changes can be explained as demonstrating either charge loss from the Faraday cup, or continuing charge accumulation in it.

Charge decay from the Faraday cup.

As shown in Chapter 5, the Faraday cup represents a resistance–capacitance circuit which produces exponential decay curves. Although some variation of the collected charge can be ascribed to decay, this should be observed to decrease exponentially. Because charge decay can only reduce the magnitude of the remaining charge, the only experiment shown in Figure 6.17 for which it could be a possible explanation is 70804f (Figure 6.17a). The dashed line represents an example of how the detected charge would vary if it decreased as a result of exponential charge decay alone (the effective resistance to Earth of the Faraday cup, and its capacitance, $R_{fc}\,C_{fc}$ = 1000 s). The differences between this and the recorded data strongly suggest that positive charge was accumulating in the cup rather than just negative charge being lost.

Continuing charge accumulation.

Figures 6.17b and 6.17c support the theory that the ‘delayed’ changes in Faraday cup charge were a result of continuing charge accumulation. In the case of Figure 6.17b, this can be the only explanation because the magnitude of the detected charge

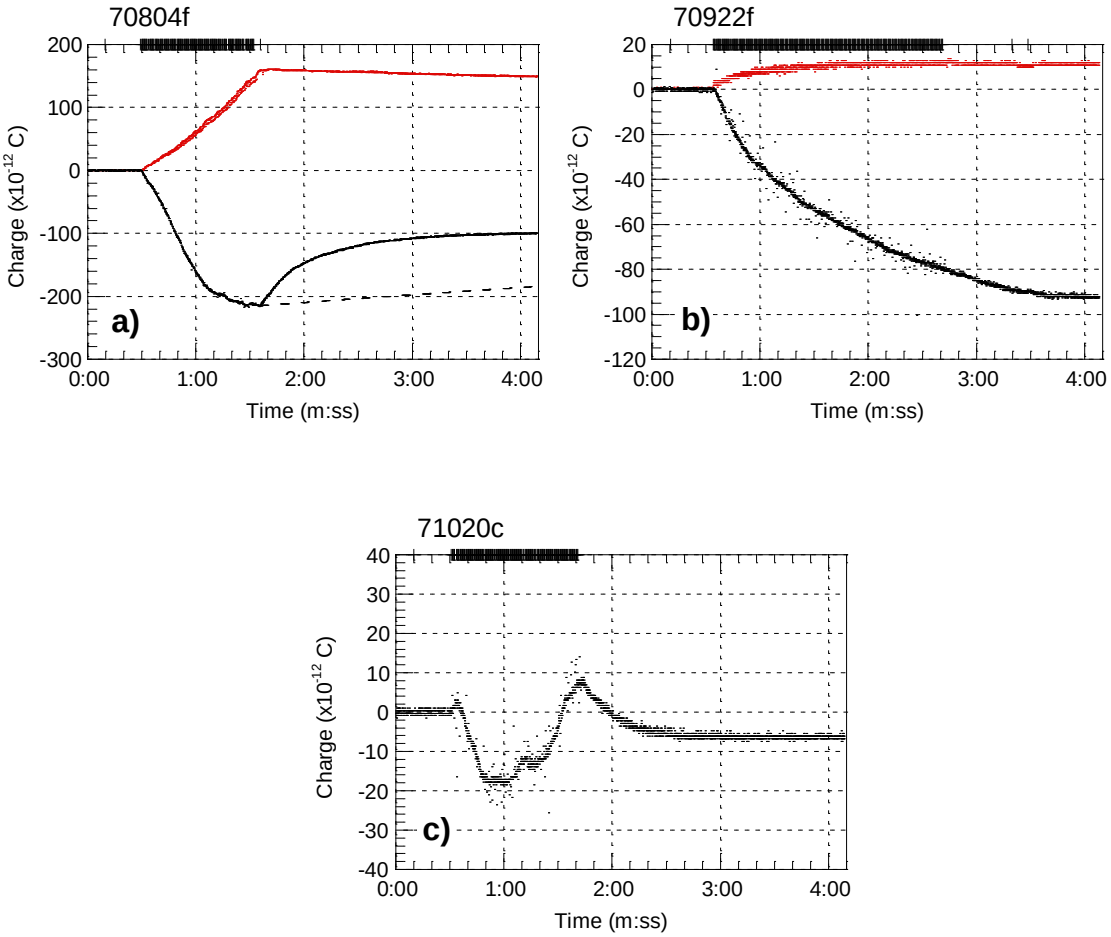

Figure 6.17 Changes in Faraday cup charge after impacts have ceased. With the exception of the first line (showing the release of the electrometer zero-check), vertical lines on top axes represent individual impacts; mesh data in red; Faraday cup data in black. **a)** 150 impacts between samples of SMN 31 (22 °C, 44 % RH). The dashed curve represents the expected exponential decay for a Faraday cup resistance to Earth and capacitance, $R_{fc}C_{fc}$ = 1000 s. **b)** 296 impacts between a sample of Sak 14 and an insulated hammer (19 °C, 42 % RH). **c)** 173 impacts between samples of StV 519 (16 °C, 41 % RH). Mesh data have not been shown for this experiment because they were corrupted by an equipment problem.

increased continuously. Similarly, for Figure 6.17c, because the data indicate that the Faraday cup changed polarity, charge decay cannot be the dominant effect. However, ‘delayed’ particles were not observed during any of these experiments (or any other) so several further experiments were carried out to investigate the hypothesis.

The data recorded during three of these experiments are given in Figure 6.18. Figure 6.18a shows the accumulating charge after impacts between an insulated hammer and an StV 519 sample. Repeating the experiment, with a foil placed over the hole in the shield above the Faraday cup after impacts had stopped, produced the data shown in Figure 6.18b. Although the charge accumulation was observed to be practically stopped by the foil, no particles were observed on it afterwards. The experiment was repeated once more, but with the glass of the vacuum chamber removed. The data recorded are shown in Figure 6.18c, and demonstrate very little charge accumulation after impacts ceased. This is interpreted as indicating that air circulation in the laboratory was sufficient to prevent the particles from entering the cup. This could also explain why no particles were observed on the foil, because it had to be extracted from the vacuum chamber to be examined. Thus, the experiments suggest that the ‘delayed’ charge variations are a result of charges held on very small silicate particles.

The source of the particles could have been the mesh or the samples, or they could represent particles (produced by the impacts) with very small fall velocities. If the particles were falling from the mesh or the samples, then the charge loss from these areas would be shown in the mesh data. The data from experiments shown in Figure 6.17 demonstrate that this was not the case. The presence of particles with very small fall velocities are supported by the experiment carried out without the glass vacuum chamber, and also by the fact that the effect was not observed during experiments

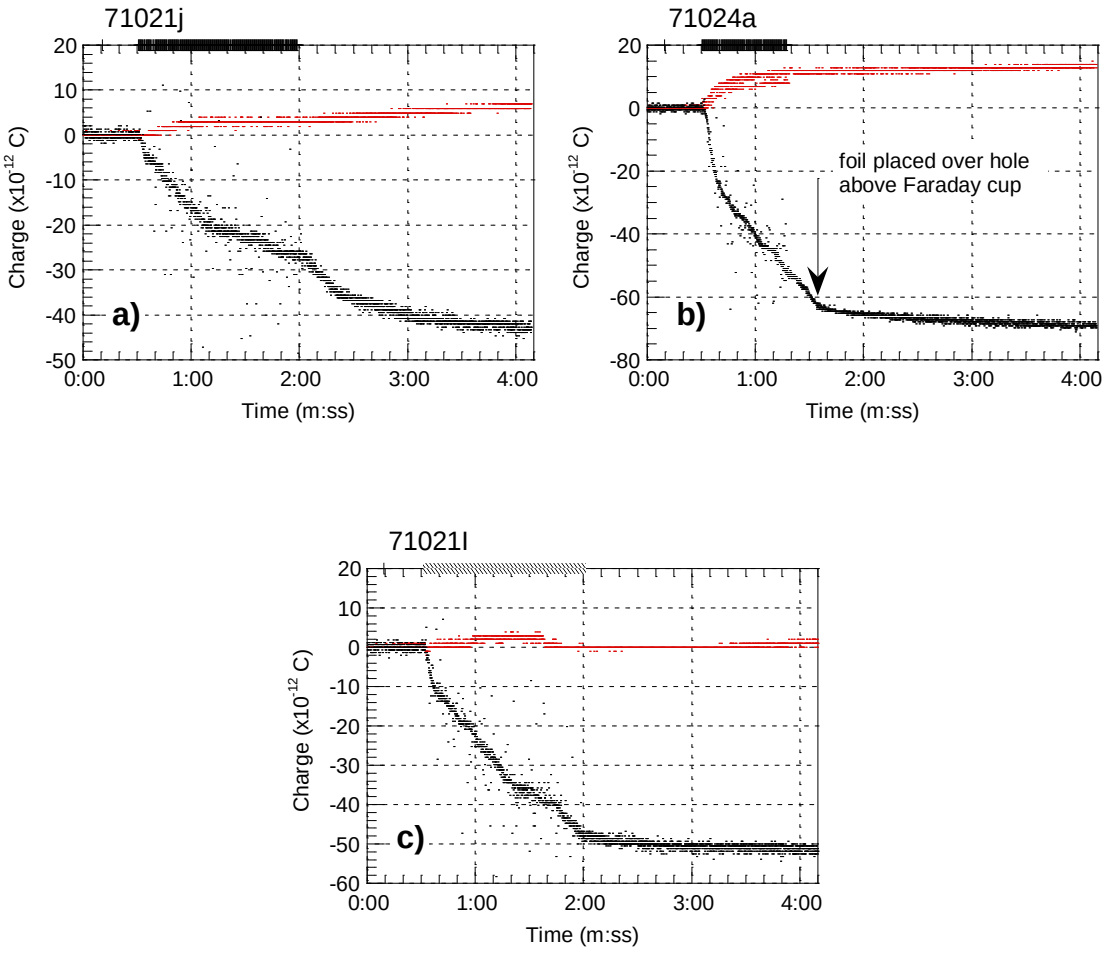

Figure 6.18 Investigation of charge accumulation after impacts have ceased. With the exception of the first line (showing the release of the electrometer zero-check), vertical lines on top axes represent individual impacts; mesh data in red; Faraday cup data in black. The plots show data collected during three experiments carried out at atmospheric pressure with an insulated hammer in collision with a pumice sample (StV 519). **a)** 239 impacts using the standard apparatus (17.7 °C, 36 % RH). **b)** The same experiment repeated with 136 impacts (16.1 °C, 37 % RH). After impacts ceased, the hole through which particles fall into the Faraday cup was covered by foil. **c)** The experiment carried out without the surrounding glass of the vacuum chamber (17.7 °C, 36 % RH). Individual impacts were not recorded, but their duration is shown by the shaded portion of the top axis. The particles prevented from entering the Faraday cup by the foil in **b)** appear to be sufficiently small that air circulation around the apparatus could also prevent them from entering the cup.

carried out at low pressure (where fall velocities for all the particles were approximately identical). If a fall distance of about 3 cm is assumed (the approximate distance between the samples and the top of the shield), which was covered in a time of about 30 s then, assuming Stokes' law, the equivalent sphere radius is of order 2 μm.

If it is assumed that the changes are due to charge held on very small silicate particles, then this should be included when calculating the net charge of the ash sample. However, due to difficulties in some experiments in quantitatively separating this effect from charge decay, the maximum charge magnitude reached was generally used to calculate specific charge.

6.4 Pumice–pumice impact experiments

A total of 97 experiments involving pumice–pumice impacts were carried out, 34 of which were at atmospheric pressure and 63 at low pressure. Experiments were carried out with all the different pumice types and representative graphs are given in Figure 6.19 (for experiments carried out at atmospheric pressure), and in Figure 6.20 (for experiments carried out at low pressure).

During low pressure experiments, samples of both MSH and Santorini pumice produced net negatively charged ash. As discussed in section 6.33, experiments with Sak 13I samples demonstrated varying net ash polarity. SMN 31 and StV 519 samples produced net positively charged ash, as did samples cut from one clast of Sak 14, whereas another clast produced net negative ash. Experiments carried out at atmospheric pressure produced negatively charged ash from all samples except StV 519. These results are summarised in Table 6.4.

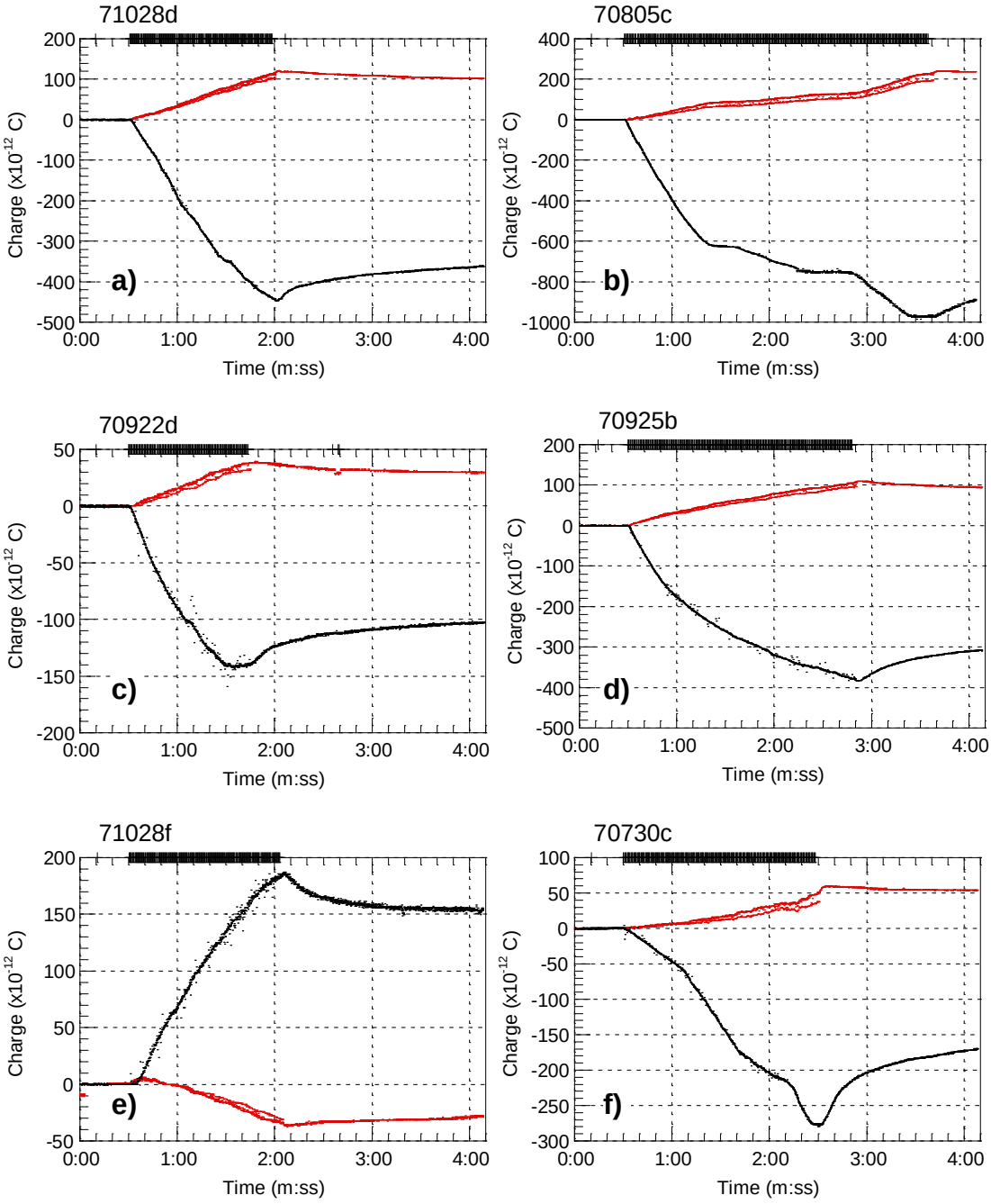

Figure 6.19 Results of pumice–pumice impact experiments carried out at atmospheric pressure. With the exception of the first line (release of the electrometer zero-check), vertical lines on top axes represent individual impacts; mesh data are in red; Faraday cup data in black. One example is given for each pumice sample. **a)** MSH. **b)** Sak 13 I. **c)** Sak 14. **d)** SMN 31. **e)** StV 519. **f)** Santorini.

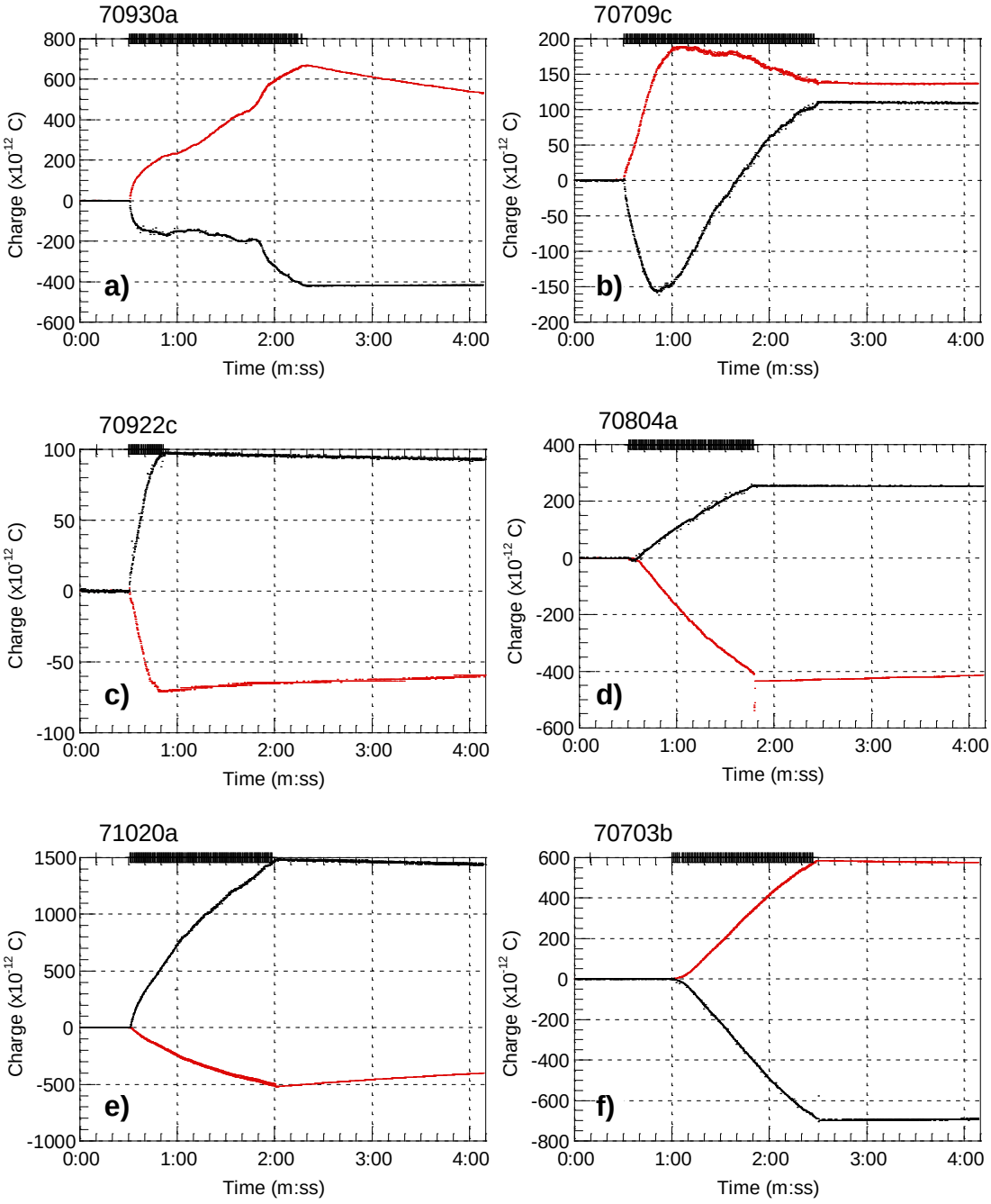

Figure 6.20 Results of pumice–pumice impact experiments carried out at low pressure. With the exception of the first line (release of the electrometer zero-check), vertical lines on top axes represent individual impacts; mesh data are in red; Faraday cup data in black. One example is given for each pumice sample. **a)** MSH. **b)** Sak 13 I. **c)** Sak 14. **d)** SMN 31. **e)** StV 519. **f)** Santorini.

Table 6.4 Summary of the polarity of the net charge collected on silicate particles produced from pumice–pumice collisions. Where ± is shown, net ash charges of both polarity have been recorded (although this may have been a product of sample charging).

Pumice type	Net polarity of collected particles	
	Atmos. pressure	Low pressure
StV 519	+	+
Sak 14	-	±
SMN 31	-	±
Sak 13I	-	±
MSH	-	-
Santorini	-	-

Plots of the net charge results are given in Figure 6.21. In Figure 6.21a the specific net charge of the particles are plotted against their specific surface area (calculated from the particle size distribution, see Chapter 5). The finer particle distributions (represented by the larger specific surface areas) are observed to hold the larger specific net charges. Plotting the surface charge density against the specific surface area (Figure 6.21b) shows that higher surface charge densities also reside on the smaller particles. Net surface charge densities and specific net charges are generally lower for experiments carried out at atmospheric pressure than for those carried out at low pressure (but not generally by as much as an order of magnitude).

The data suggest that the magnitude of the specific net charge is a function of the size of the particles produced. The theoretical maximum surface charge that can be held on a particle in the atmosphere increases with decreasing particle diameter (Chapter 2). Although the net surface charge density experimental results are less than the theoretical maxima, their dependence on particle size suggests that some of the

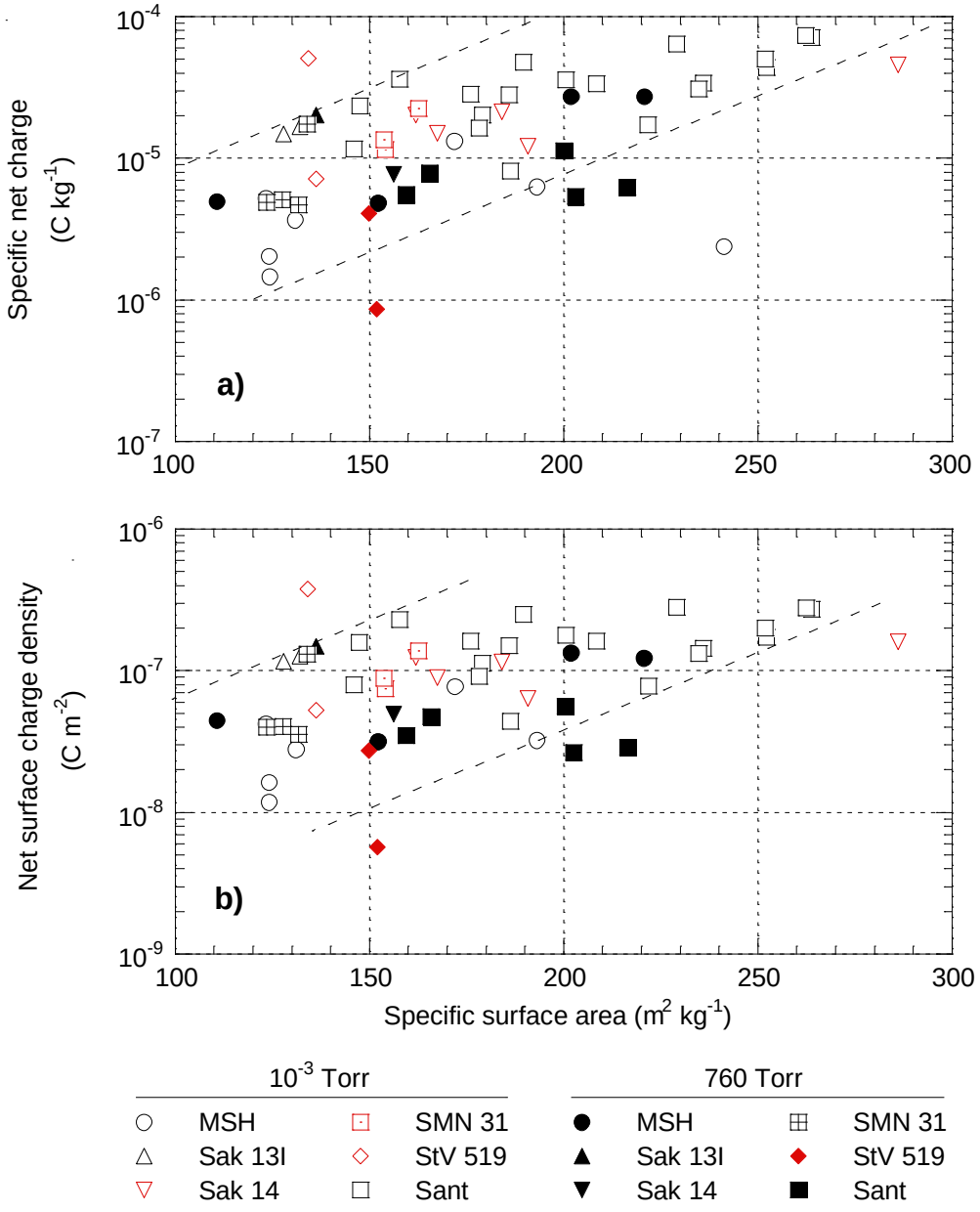

Figure 6.21 Net charge results for pumice–pumice collisions. Charges are given as magnitudes, the polarity is indicated by the colour of the symbol. Red symbols for net positively charged particles, black for net negatively charged. Charges are plotted against the specific surface area of the particles.

particles may be charged to their limit. However, it must be remembered that these are net charges and thus do not represent the actual maximum particle charges. In Chapter 7, it is demonstrated that the net charge is only a result of a small imbalance in much larger, individual particle charges of both polarities.

6.4.1 Net charge variation as a function of sample geochemistry

Geochemical data for the pumice samples are given in Appendix V. The net charge results from pumice–pumice impact experiments carried out at atmospheric pressure are plotted against the silica and total alkali contents of each pumice in Figure 6.22. The points represent the average charge values from all the relevant experiments undertaken, and the bars denote the range in the values. The variation in magnitude of the average net specific charge values is similar in size to the range of values obtained from individual samples, so no variation in charge magnitude as a function of geochemistry can be observed (as suggested by Figure 6.21).

However, note that the only pumice (StV 519) to consistently produce net positively charged ash also contained a markedly lower silica content than the other samples.

6.4.2 Net charge variation in results from one pumice type

Figures 6.21 and 6.22 demonstrated that there was a considerable range of specific net charge results from experiments on any one sample type. Differences were observed in the results obtained from experiments carried out with samples from different clasts, with different samples from the same clast and also between experiments carried out with the same samples.

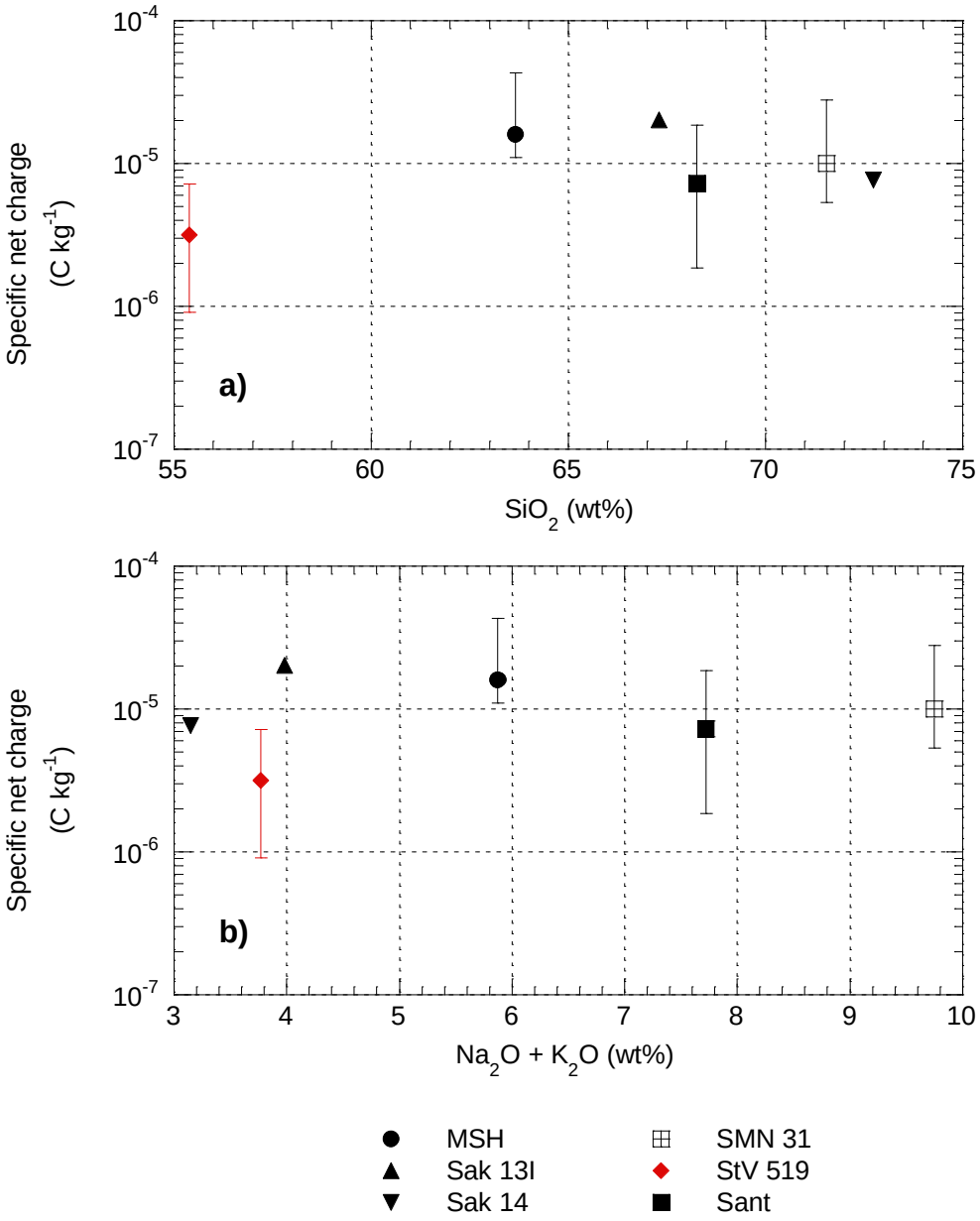

Figure 6.22 Variation of specific net charge results with sample geochemistry. The results shown are all from pumice–pumice impacts carried out at atmospheric pressure. The red symbol represents net positively charged ash; all the black symbols are net negatively charged ash. Where more than one experiment has been carried out, the average is shown, and the bars represent the range of values. **a)** Net specific charge plotted against silica content. **b)** Net specific charge plotted against total alkali content.

Figure 6.23 shows the variation in the specific net charge results from impacts between different MSH samples cut from a single clast (Clast 1). Samples 70930a generated noticeably more particle mass per impact than was produced by samples 71025c. This higher mass per impact was also associated with a coarser particle distribution (and thus lower specific surface area, Figure 6.23a) than produced by the 71025c experiments. The coarser particles from 70930a experiments held a smaller specific net charge and net surface charge density than the finer ones from 71025c experiments.

Figure 6.24 shows the results of pumice–pumice impacts between Sak 14 samples, carried out at low pressure. Unlike the MSH experiments shown in Figure 6.23, there appears to be little consistent variation in the magnitude of net charge produced, but rather there is a change in net polarity of the ash generated. However, colour differences between the clasts may indicate that there may be also a geochemical difference between them.

Another interesting polarity change was observed in the results of pumice–pumice impact experiments carried out with SMN 31 samples. These results can be seen in Figure 6.21 and show a net positive ash charge for experiments carried out under vacuum, and a net negative ash charge for experiments carried out at atmospheric pressure. Possible processes to account for this polarity change are surface charge flow or ion scavenging. If the movement of charge over the impact surfaces is of importance then the increased presence of adsorbed species at atmospheric pressure may be a factor (due to changing the surface conductivity of the pumice). If the net ash polarity is a function of ion scavenging, then the pressure will have a direct effect due to its control over the drift speed of ions.

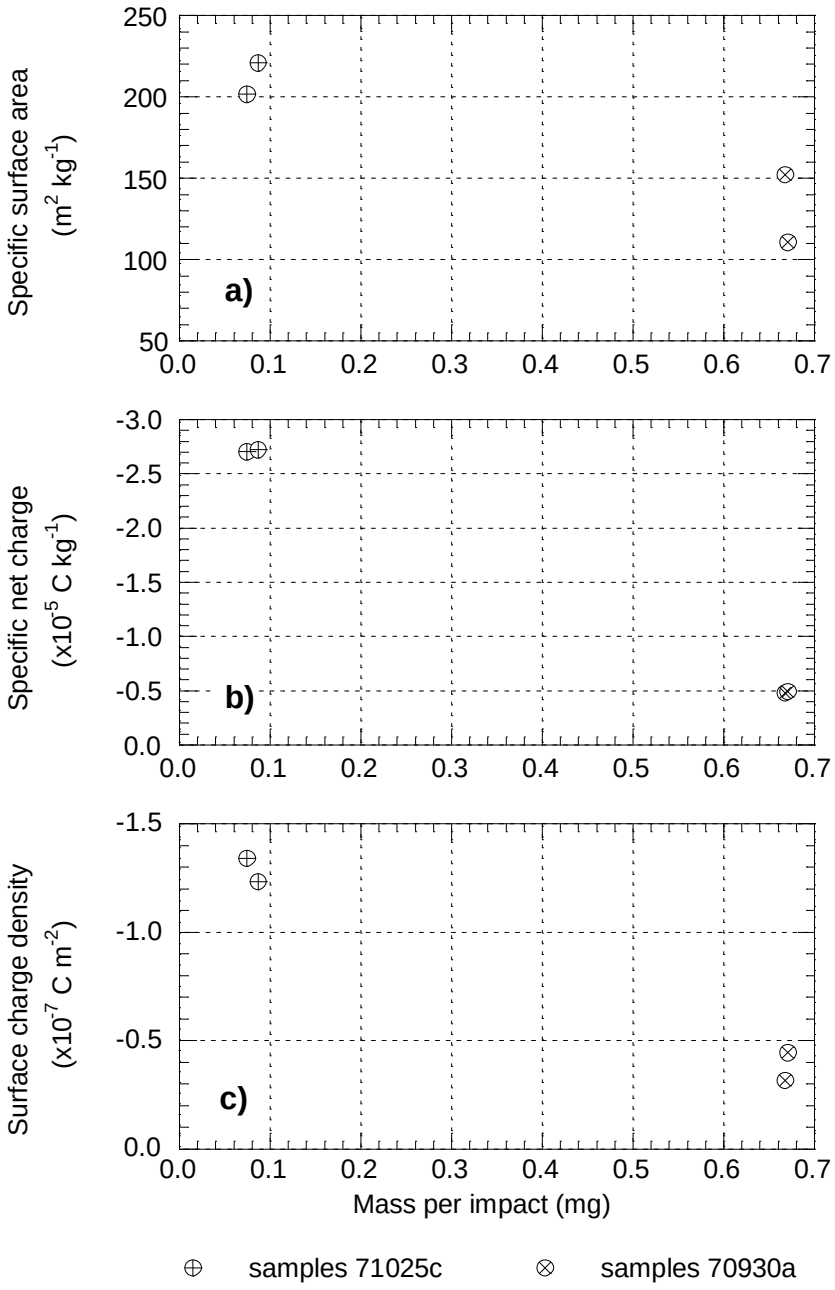

Figure 6.23 Variation in results from different samples cut from the same clast. Both samples were cut from MSH pumice, Clast 1, and all experiments were carried out at atmospheric pressure. The results shown are from experiments 71001c, 71001d, 71028c and 71028d.

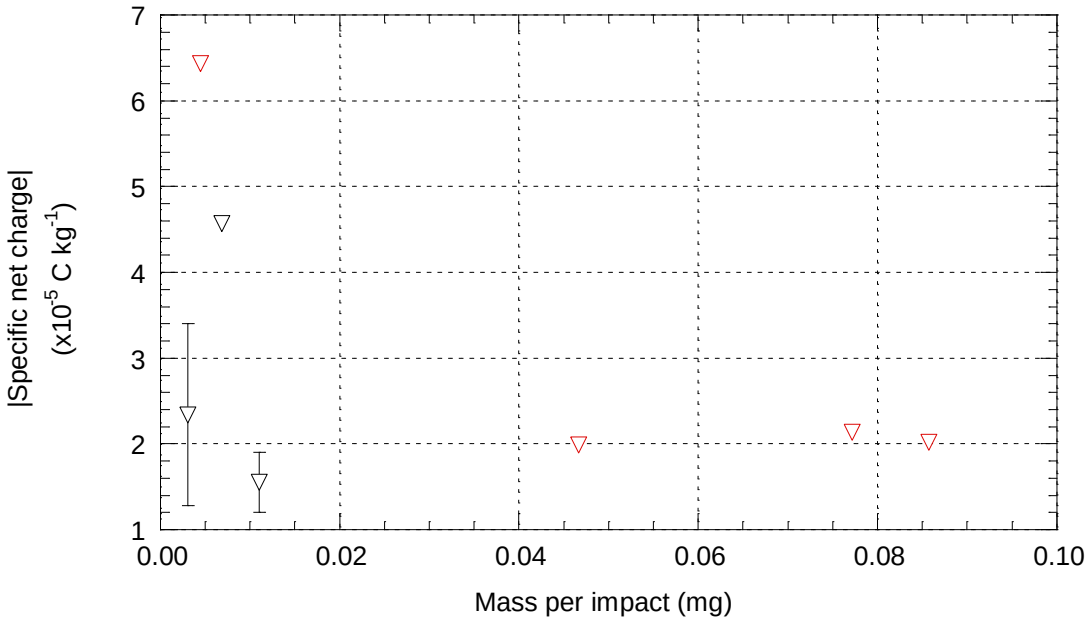

Figure 6.24 Specific net charge results from samples of two clasts of Sak 14. All experiments involved pumice–pumice impacts carried out at low pressure. The red symbols represent positive net charge results obtained from Clast 1 samples. The black symbols represent negative net charge results obtained from Clast 2 samples. The bars on the symbols show the minimum and maximum net charge that can be calculated for experiments which demonstrated a change in net ash polarity.

Variation in the magnitude of the net specific charge is observable in the results of experiments carried out with the same samples. Figure 6.25 shows the net charge results from pumice–pumice impact experiments carried out with samples 70702a, compared to all the other comparable results at low and atmospheric pressure. The 70702a experiments produced results that span more than half the range (of specific net charge and specific surface area) obtained from all the experiments, and demonstrate the heterogeneity of the charging and of the pumice samples themselves. Figure 6.25c shows the way in which the maximum volume fraction of the particles varies with their specific surface areas. The good correlation demonstrates that the particle size distribution does not change shape excessively, but is just coarser from some experiments than from others.

6.4.3 Particle mass produced per impact

Figure 6.26 shows results for the pumice–pumice impact experiments plotted against the particle mass produced per impact. The specific net charge results shown in Figure 6.26a demonstrate that at production rates of less than 0.1 mg per impact, the maximum specific net charge does not appear to be a function of the mass per impact. At rates greater than 0.1 mg per impact, a decrease in the maximum specific net charge is observed with increasing mass per impact. Although it is greatly attenuated, this decrease can also be observed in the net surface charge density results (Figure 6.26b), suggesting that coarser particles are produced at rates of more than 0.1 mg per impact. This is confirmed in Figure 6.26c by plotting the specific surface area of the particles against the mass per impact. The variation observed could be interpreted as reflecting possible differences in the size of vesicles being fractured. A sample (or area within a sample) with small vesicles may be resistant to fracturing

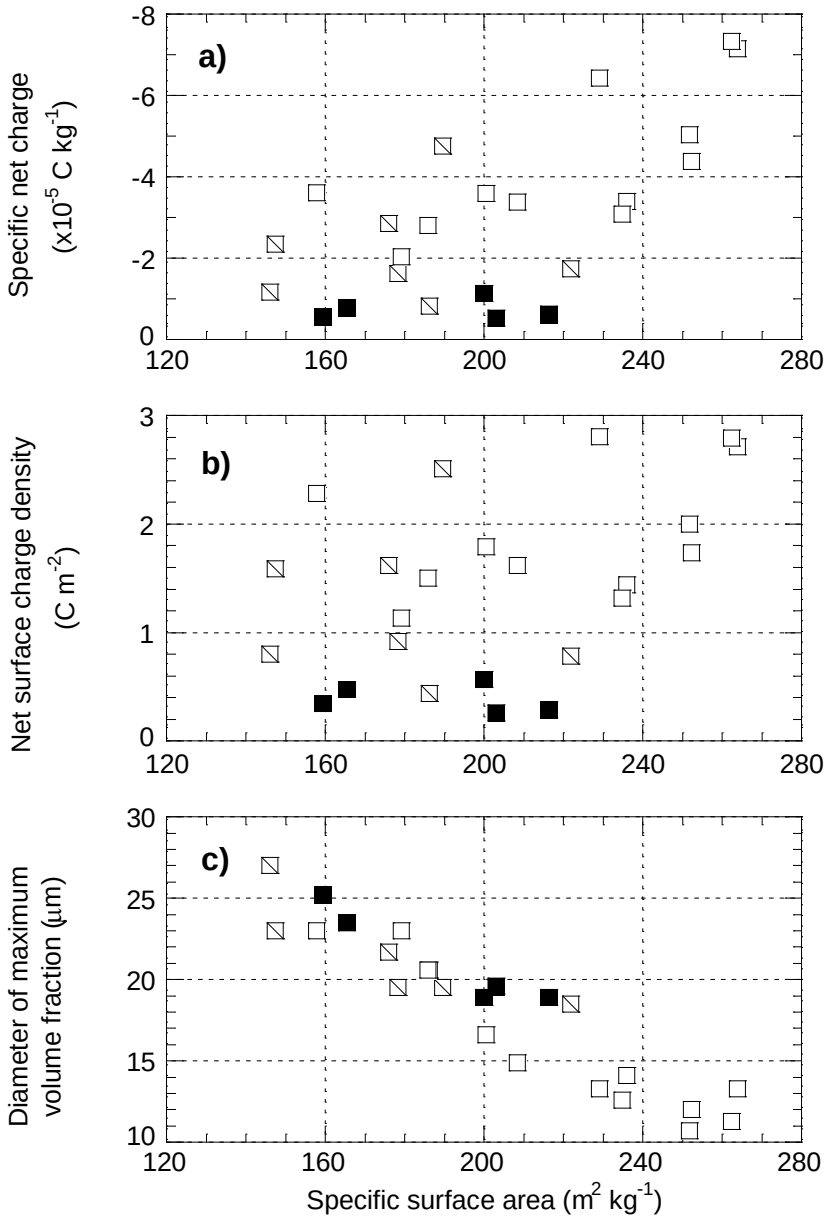

Figure 6.25 Variation between experiments carried out with the same sample. All experiments were carried out with samples of Santorini pumice, the crossed boxes all with samples 70702a. The filled boxes are the results from experiments carried out at atmospheric pressure, all other experiments were carried out at low pressure.

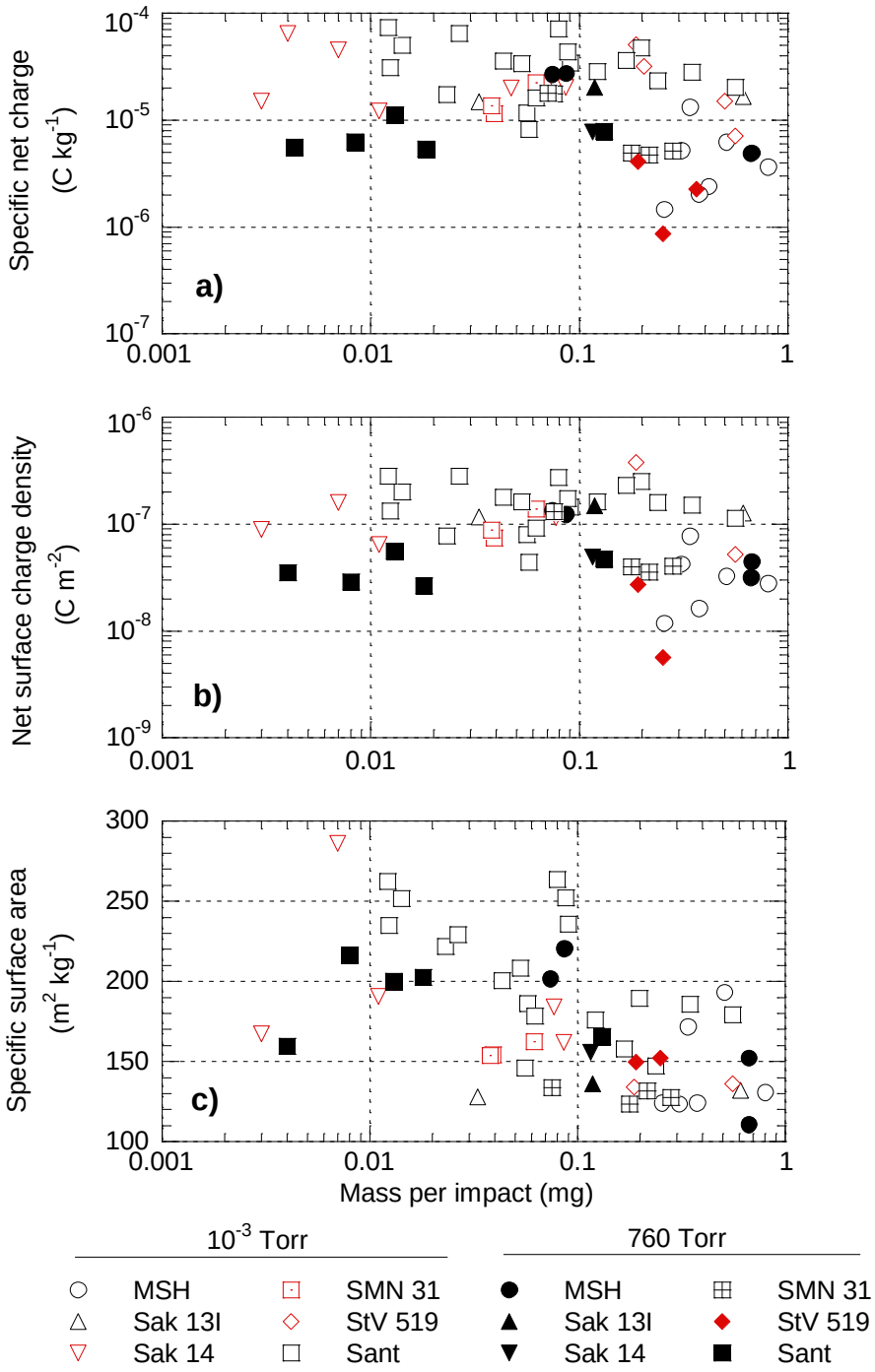

Figure 6.26 Net charge and mass per impact results for pumice–pumice collisions. Charges are given as magnitudes, the polarity is indicated by the colour of the symbol. Red symbols are for net positively charged particles; black for net negatively charged. Charges are plotted against the mass of particles produced per impact.

upon impact, but produces fine particles when it does. A pumice with coarser vesicles may produce larger particles and also be easier to fracture.

6.4.4 Effect of relative humidity and impact velocity

After having carried out particle charge experiments (Chapter 7) with a range of impact velocities and under various relative humidity (RH) conditions, attempts were made to reproduce these experiment with the net charge apparatus. However, experiments could not be carried out at very high relative humidity (90 % RH) due to the possibility of condensation forming on the sensing surfaces and electronics of the fieldmeter. Two experiments were carried out at approximately 75 % RH, and they both demonstrated a greatly increased rate of charge loss from the Faraday cup due to some condensation on the insulators. The errors in the calculated charge due to this decay rate dictated that any small change in the fieldmeter response could be neglected. Data collected during experiments carried out at high and low values of RH are given in Figure 6.27.

The specific net charge results from these experiments are shown in Figure 6.28. The points represent the calculated results, and show a decrease in the magnitude of the net charge with increasing RH. The bars on the points represent possible adjustments to the calculated specific net charge if the effect of charge dissipation over the insulators (for the points at high RH) and slow falling particles (for the points at low RH) are taken into account. Thus the perceived decrease in specific net charge with increasing RH represents a maximum value.

Figure 6.28 also shows the results from experiments carried out with a solenoid voltage of 6 V. Unlike the results for absolute particle charges (Chapter 7), a decrease in impact velocity does not appear to affect the net charge held on the particles.

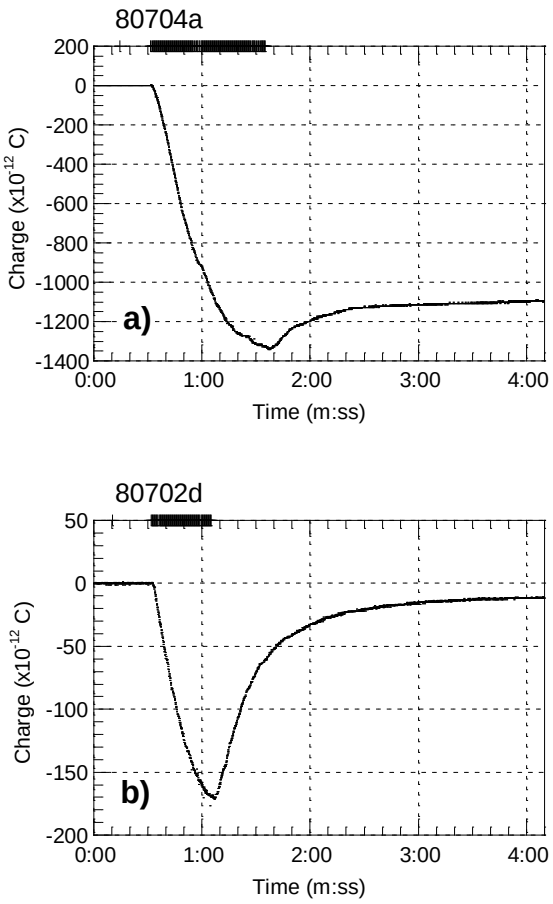

Figure 6.27 Experiments carried out at low and high values of relative humidity. With the exception of the first line (showing the release of the electrometer zero-check), vertical lines on top axes represent individual impacts and the Faraday cup data are shown in black. Both experiments consisted of pumice–pumice collisions of MSH samples at atmospheric pressure. **a)** 177 collisions under conditions of low relative humidity (19 °C, 5 % RH). **b)** 101 collisions under conditions of high relative humidity (23 °C, 76 % RH). Mesh data are not shown as they are subject to interference from the solenoid and do not reflect charge accumulation on the mesh. This was a result of failure of one electrometer, necessitating rearrangement of the output from the mesh during several experiments.

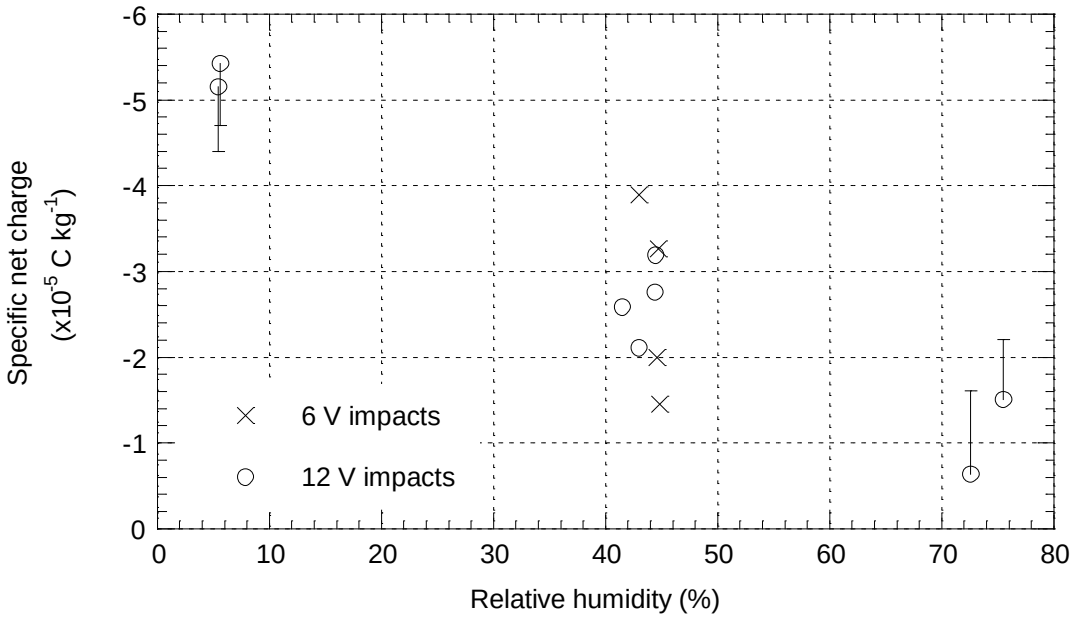

Figure 6.28 Specific net charge variations as a function of relative humidity and impact velocity. The bars represent adjusted figures due to charge held on slow falling particles (for results at RH < 10 %) and charge losses from the Faraday cup (for results at RH > 70 %).

6.5 Earthed collet impact experiments

As shown in section 6.3, many of the pumice–pumice impact experiments produced effects which were a result of charge accumulation on the samples. In particular, variation of the net ash polarity is believed to be a direct result of charge residing on the impact surfaces. The rationale behind the experiments using an earthed collet was thus to investigate the net ash charges produced by pumice fracture from impacts with a surface which maintained a zero potential.

A total of 33 experiments involving collisions between a pumice sample and an earthed collet were carried out. Of these, 16 were at atmospheric pressure, and 17 were at low pressure. For the majority of the experiments, the pumice sample was mounted on the hammer so that any charge accumulation on it could be monitored via the double line effect. Typical data collected from experiments carried out at atmospheric pressure are shown in Figure 6.29, and Figure 6.30 gives data from some low pressure experiments.

At low pressure, experiments on the various samples all produced similar graphs, with negative charge detected by the mesh and the Faraday cup. With the exception of the MSH sample, the pumice samples charged substantially, and negatively. At atmospheric pressure, the net ash charges recorded were also all negative. Very little mesh charge was detected and, with the exception of the StV 519 experiments, this was also negative. Note that polarity changes, similar to those shown in Figure 6.16, were not recorded. The specific net charges calculated from these experiments are given in Figure 6.31.

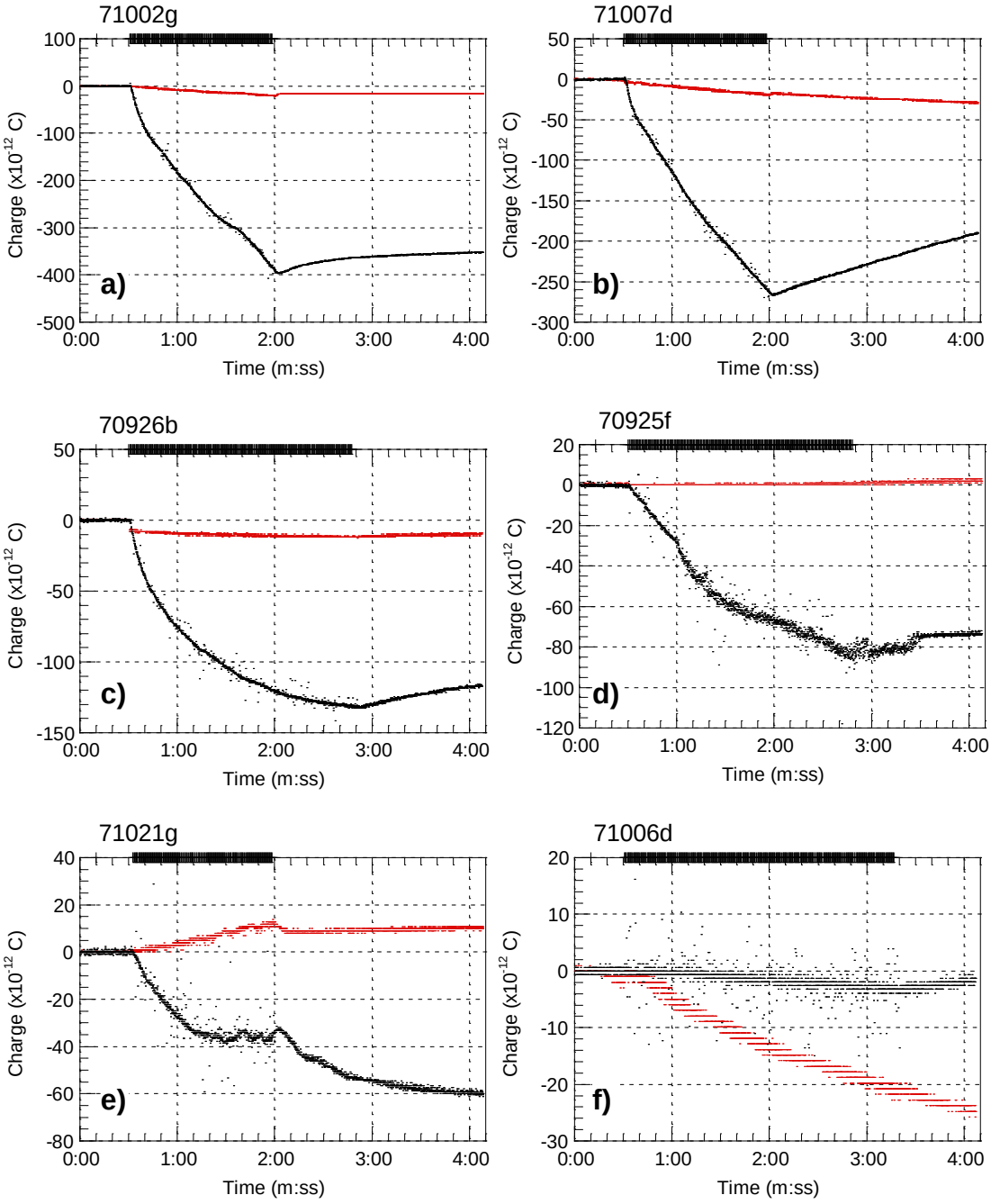

Figure 6.29 Results of impact experiments with an earthed collet at atmospheric pressure. With the exception of the first line (release of the electrometer zero-check), vertical lines on top axes represent individual impacts; mesh data are in red; Faraday cup data in black. One example is given for each pumice sample. **a)** MSH. **b)** Sak 13 I. **c)** Sak 14. **d)** SMN 31. **e)** StV 519. **f)** Santorini.

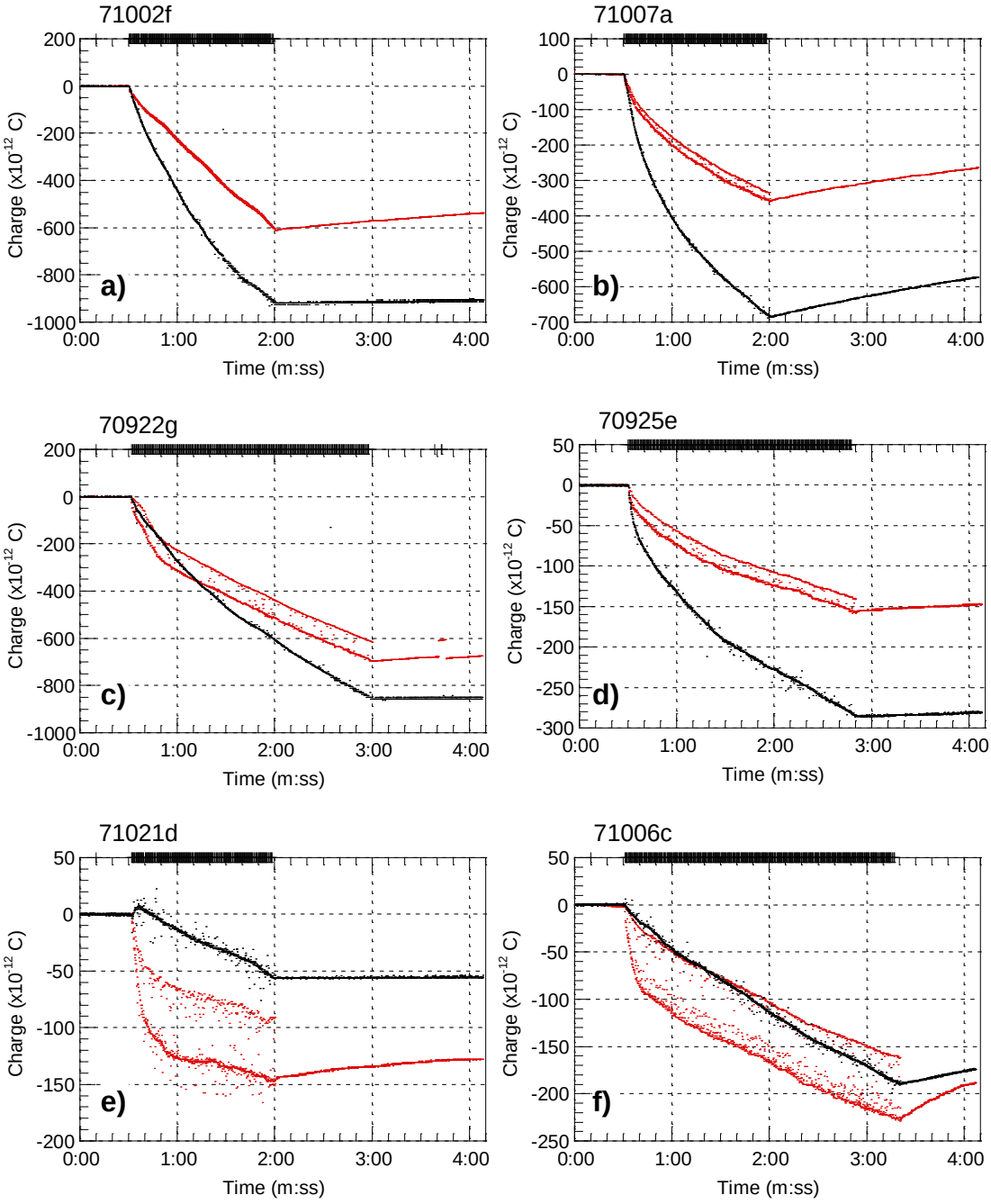

Figure 6.30 Results of impact experiments with an earthed collet at low pressure. With the exception of the first line (release of the electrometer zero-check), vertical lines on top axes represent individual impacts; mesh data are in red; Faraday cup data in black. One example is given for each pumice sample. **a)** MSH. **b)** Sak 13 I. **c)** Sak 14. **d)** SMN 31. **e)** StV 519. **f)** Santorini.

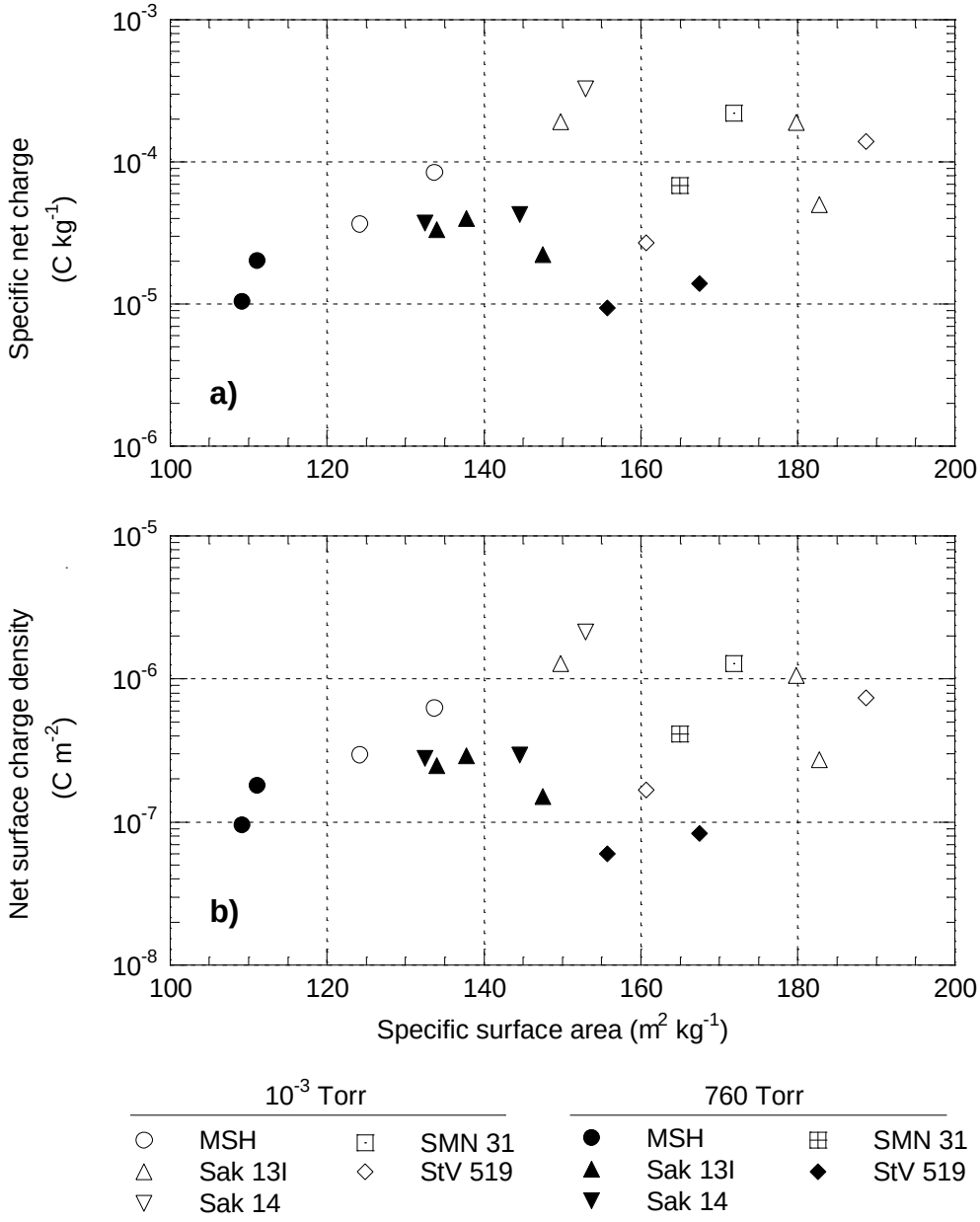

Figure 6.31 Net charge and results for impacts with an earthed collet. Charges are given as magnitudes, all charges are negative polarity. Charges are plotted against the specific surface area of the particles.

6.6 Insulated collet impact experiments

In order to examine any effect due to the earthing of the collet, the results have to be compared with those from an insulated collet. Any effect of impact with a metallic surface rather than with another pumice surface could then also be observed. 30 experiments were carried out during which impacts were initiated between a pumice sample and an insulated collet, 19 at atmospheric pressure, 11 at low pressure. Typical graphs produced are given in Figure 6.32 (for experiments carried out at atmospheric pressure) and Figure 6.33 (for experiments carried out at low pressure).

At both low and atmospheric pressure, net negatively charged ash was observed from all experiments. The mesh results demonstrated generally net positive charges, with the exception of the experiments with Santorini, Sak 14 and SMN 31 samples carried out at low pressure. The specific net charge results for these experiments are given in Figure 6.34.

6.7 Pumice–pumice rotational grinding experiments

Sixteen experiments were carried out during which particles were produced by rotational grinding of pumice samples against each other. One of these was carried out at atmospheric pressure, but produced so little charge that the others were all carried out under vacuum. Figure 6.35 shows typical results from each sample type.

The irregular traces produced by the data (especially for MSH and StV 519 samples, Figures 6.35a and 6.35e respectively) correspond to visual observations of irregular particle deposition in the cup. Particles were continuously produced, but would collect on parts of the stationary sample before avalanching into the Faraday cup at intervals of less than 10 s.

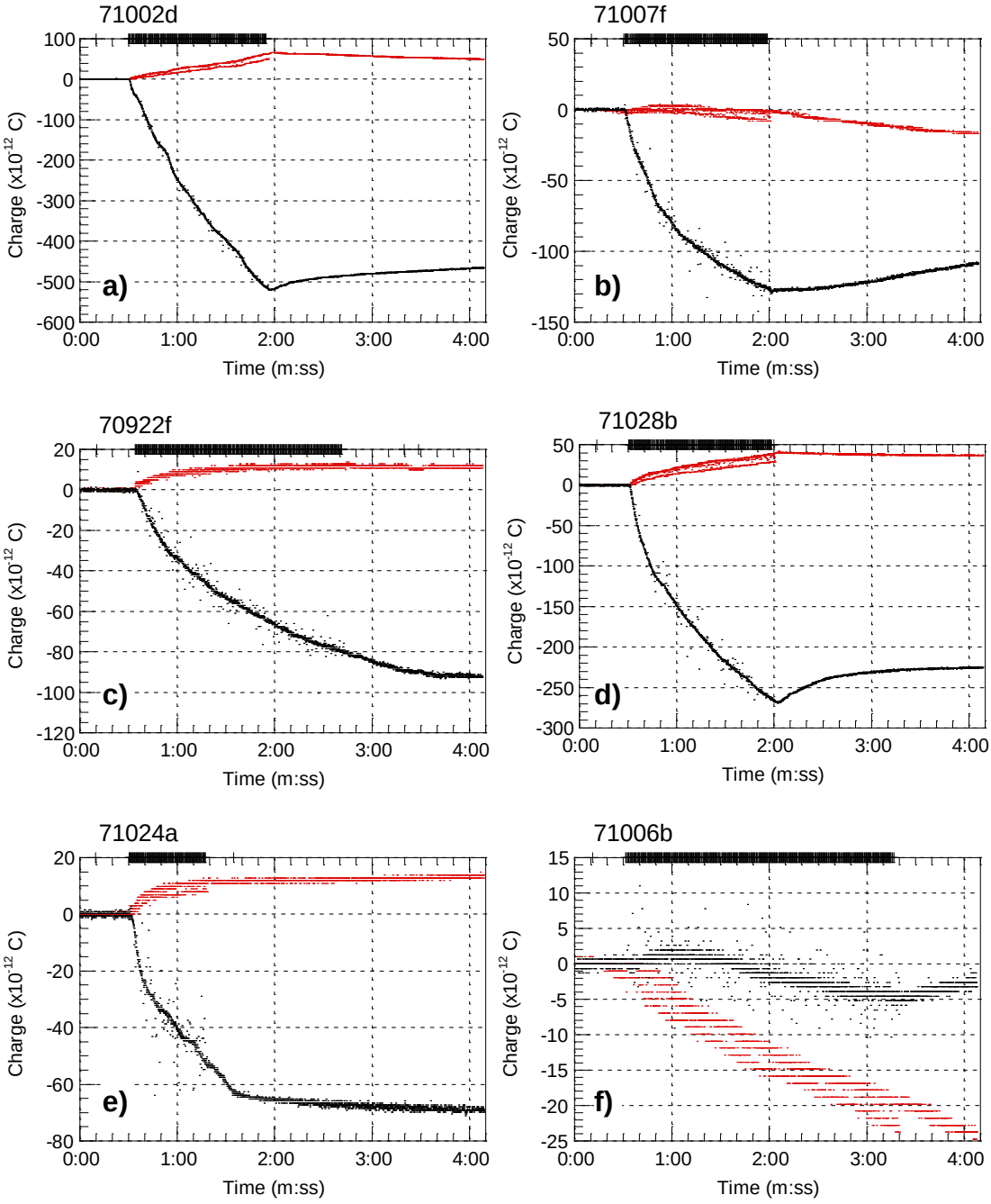

Figure 6.32 Results of impact experiments with an insulated collet at atmospheric pressure. With the exception of the first line (release of the electrometer zero-check), vertical lines on top axes represent individual impacts; mesh data are in red; Faraday cup data in black. One example is given for each pumice sample. **a)** MSH. **b)** Sak 13 I. **c)** Sak 14. **d)** SMN 31. **e)** StV 519. **f)** Santorini.

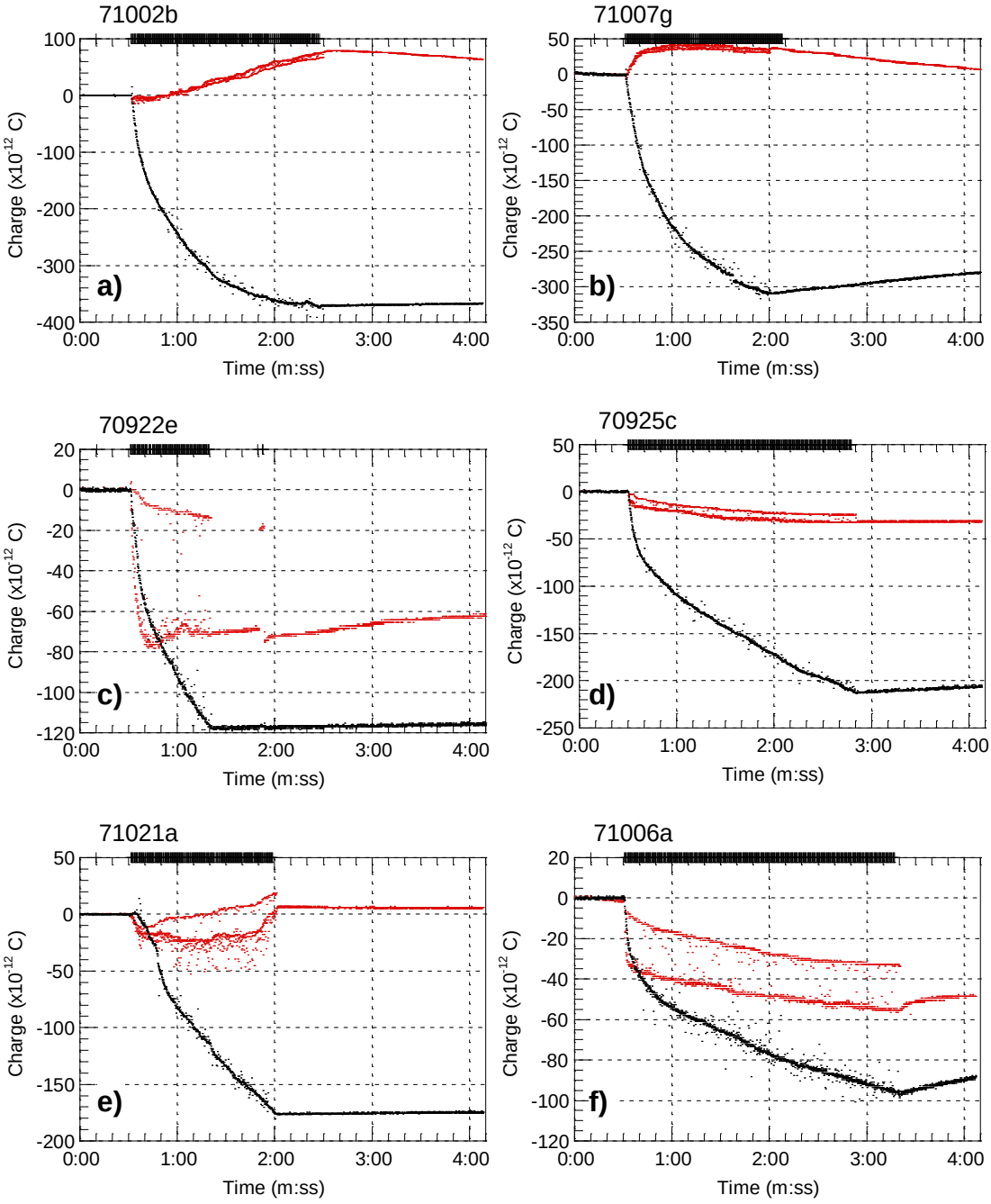

Figure 6.33 Results of impact experiments with an insulated collet at low pressure. With the exception of the first line (release of the electrometer zero-check), vertical lines on top axes represent individual impacts; mesh data are in red; Faraday cup data in black. One example is given for each pumice sample. **a)** MSH. **b)** Sak 13 I. **c)** Sak 14. **d)** SMN 31. **e)** StV 519. **f)** Santorini.

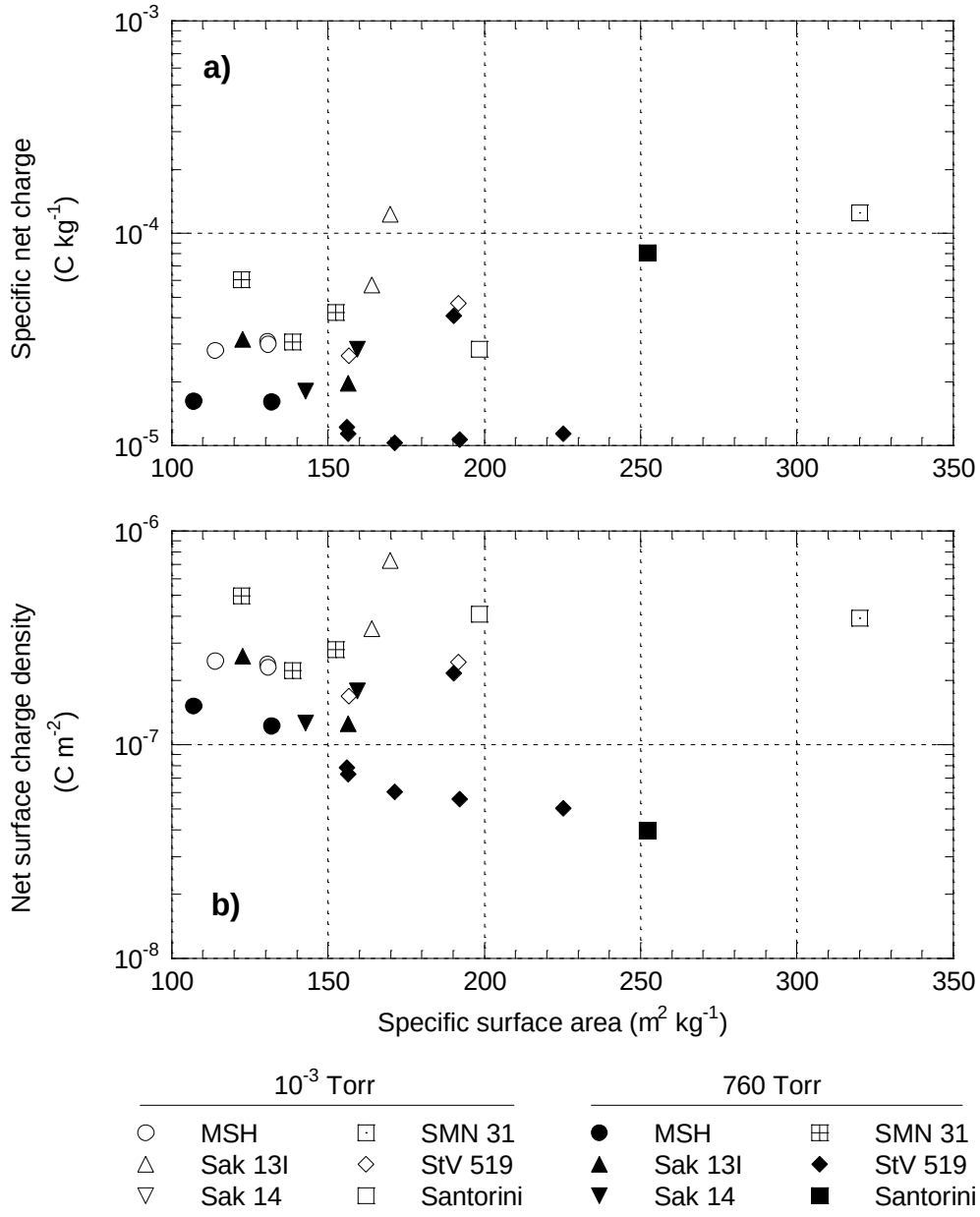

Figure 6.34 Net charge and results for impacts with an insulated collet. Charges are given as magnitudes, all charges are negative polarity. Charges are plotted against the specific surface area of the particles.

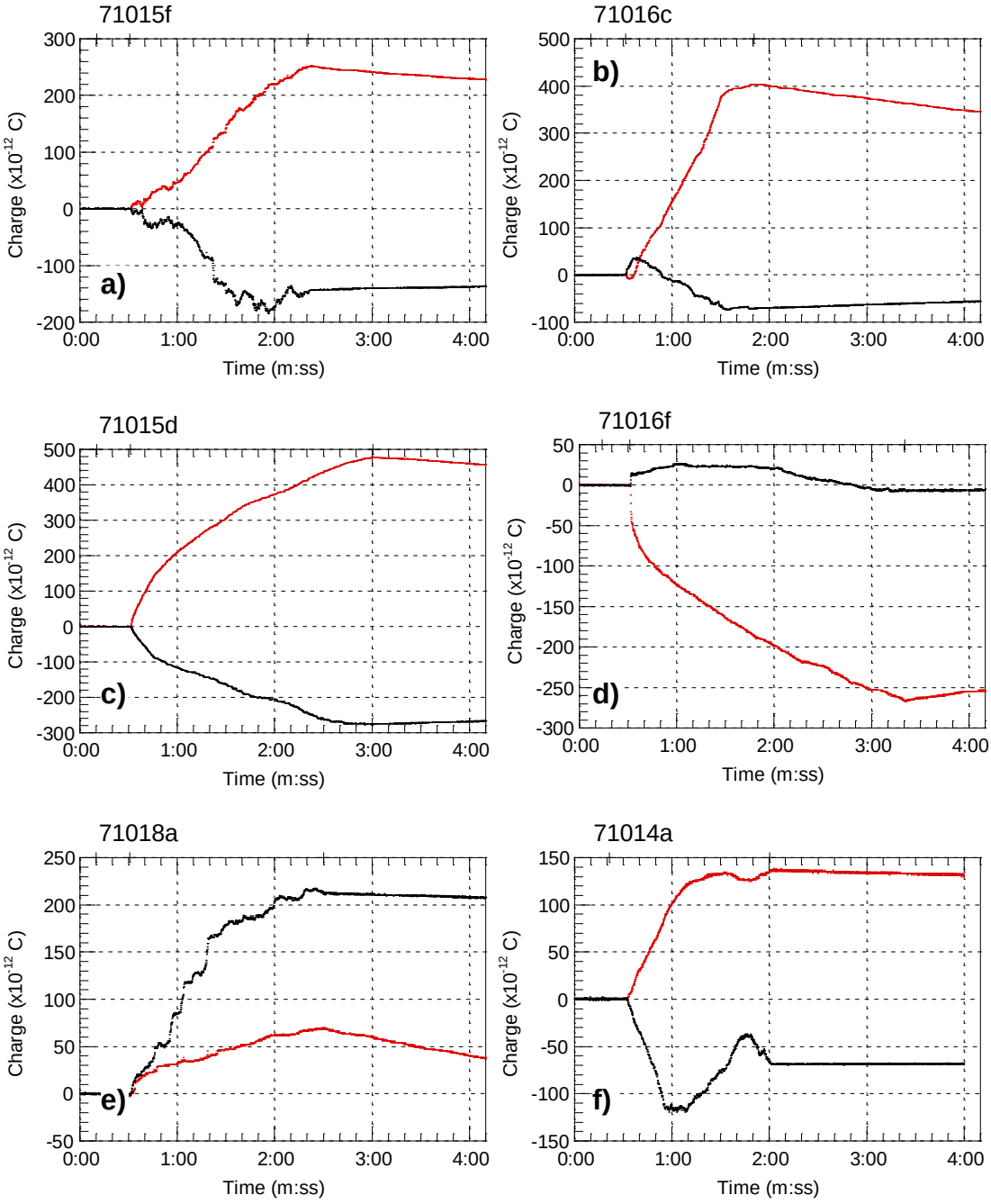

Figure 6.35 Results of pumice–pumice rotational grinding experiments at low pressure. The first vertical line on the top axes represents the release of the electrometer zero-check, the others delineate the period of grinding; mesh data are in red; Faraday cup data in black. One example is given for each pumice sample. **a)** MSH. **b)** Sak 13 I. **c)** Sak 14. **d)** SMN 31. **e)** StV 519. **f)** Santorini.

With the exception of the Sak 14 samples, and possibly also SMN 31 samples, the average net ash polarity was the same as for the pumice–pumice impact experiments for the same samples at low pressure. However, in contrast to results from the impact experiments, the grinding experiments produced mesh charges which were larger in magnitude than the charges collected in the Faraday cup (with the exception of StV 519).

Of the experiments carried out at low pressure, 11 demonstrated reasonably constant net ash polarity, and specific net charges were calculated (Figure 6.36). The one experiment carried out at atmospheric pressure (71015a) was with Santorini samples and produced ash with a specific net charge on -3.4×10^{-7} C kg^{-1}.

6.8 Pumice–earthed collet rotational grinding experiments

Six rotational grinding experiments were carried out between pumice samples and an earthed collet. All of these experiments were at low pressure and Figure 6.37 shows the data recorded.

In a similar manner to the results from impact experiments with an earthed collet, these experiments all produced both negative mesh and Faraday cup data. The particles produced were observed to be grey, and this was also observed on the sample surface after each experiment. This is thought to be a result of the brass being abraded during the grinding. Figure 6.38 gives the specific net charges calculated from these experiments.

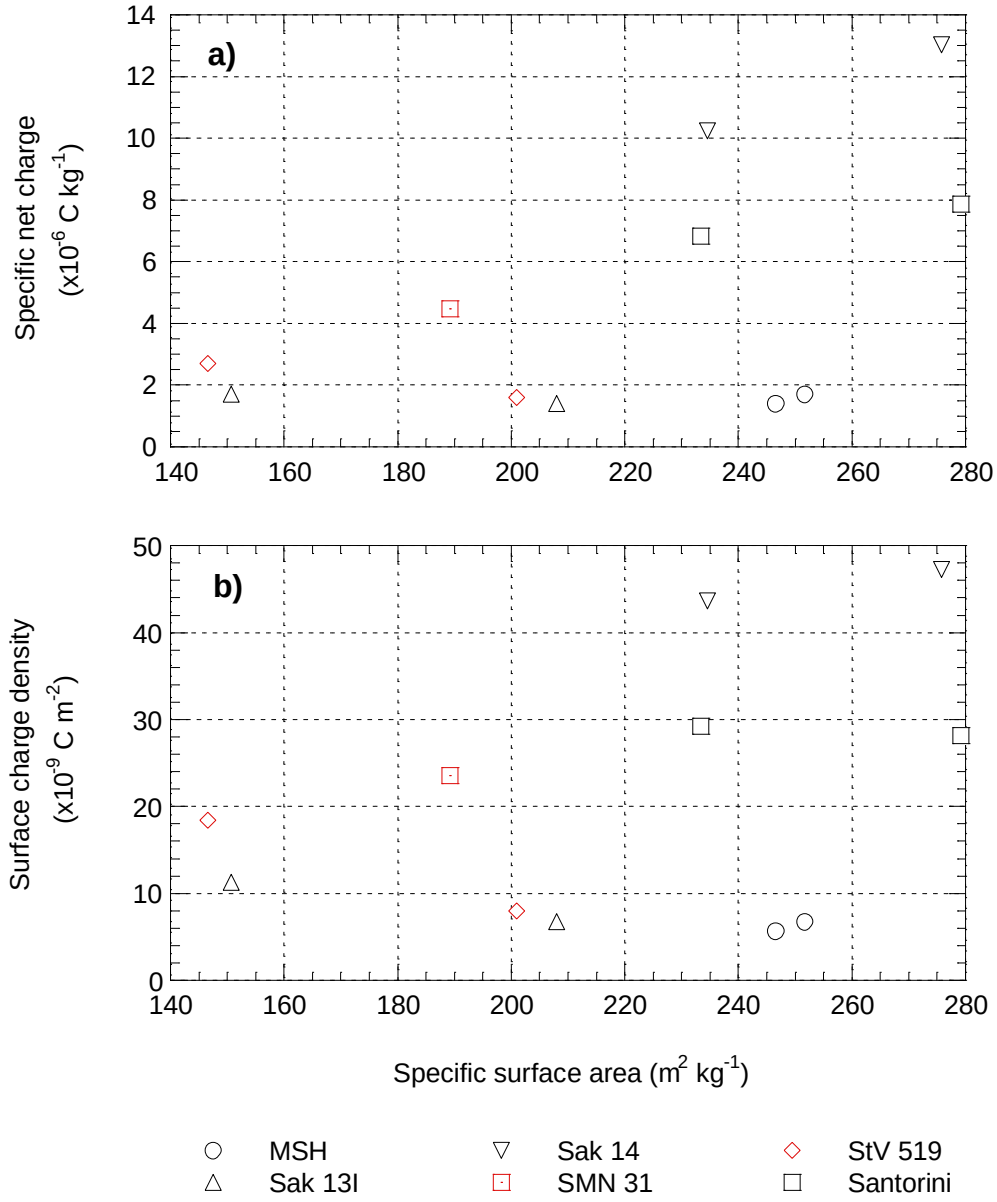

Figure 6.36 Net charge results for pumice–pumice rotational grinding experiments. Charges are given as magnitudes, the polarity is indicated by the colour of the symbol. Red symbols for net positively charged particles, black for net negatively charged. Charges are plotted against the specific surface area of the particles.

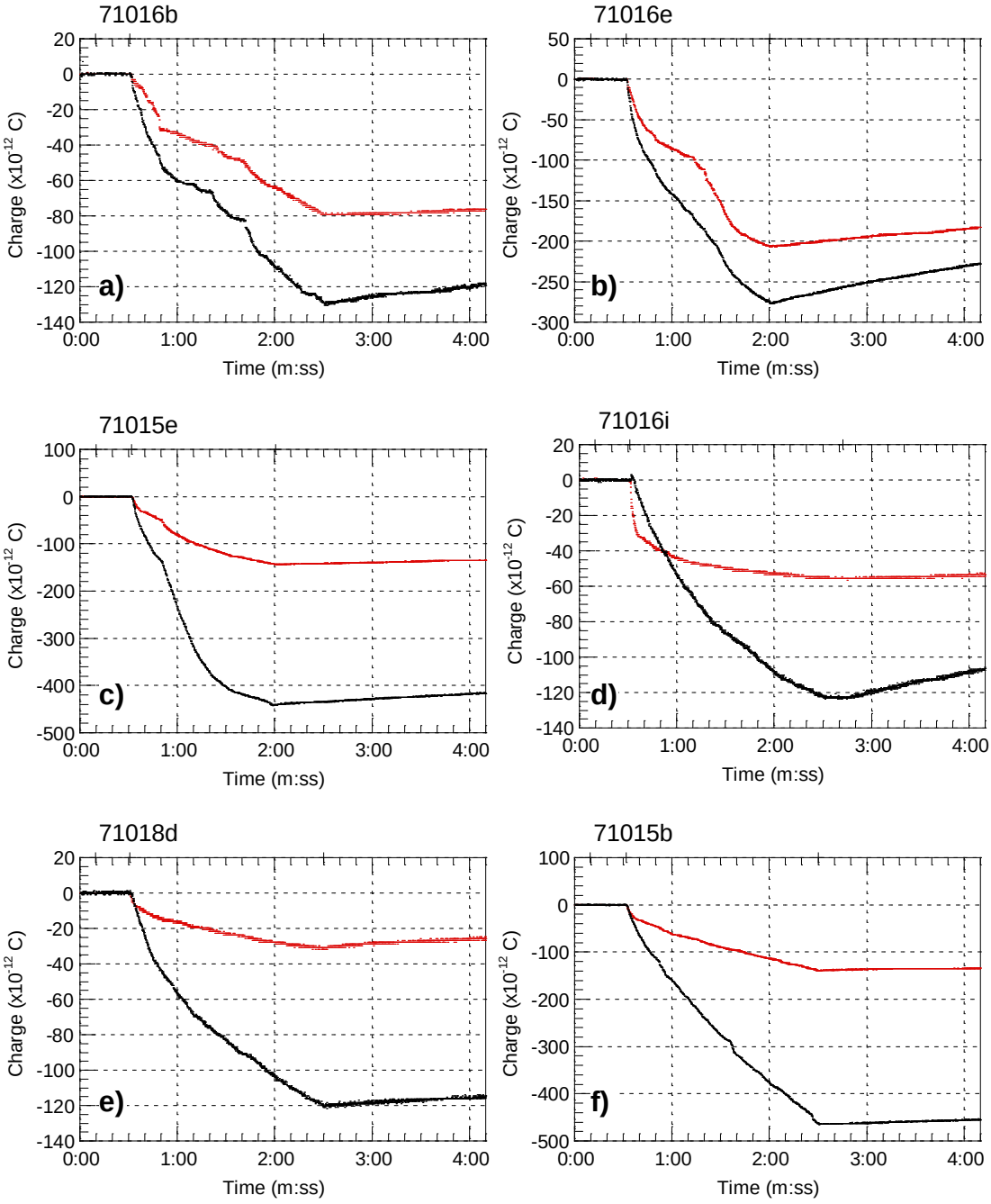

Figure 6.37 Results of rotational grinding experiments with an earthed collet carried out at low pressure. The first vertical line on the top axes represents the release of the electrometer zero-check, the others delineate the period of grinding; mesh data are in red; Faraday cup data in black. One example is given for each pumice sample. **a)** MSH. **b)** Sak 13 I. **c)** Sak 14. **d)** SMN 31. **e)** StV 519. **f)** Santorini.

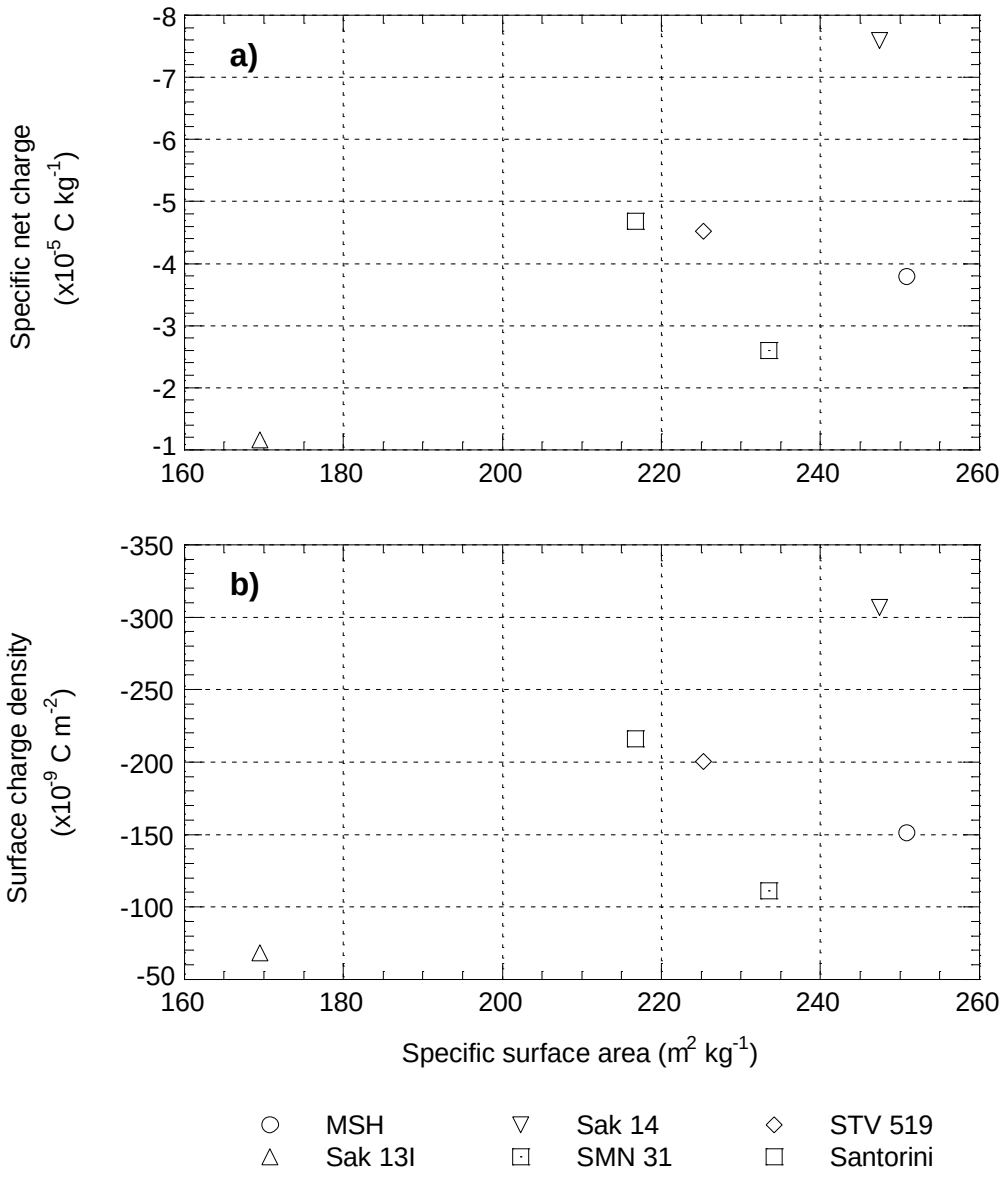

Figure 6.38 Net charge results for rotational grinding experiments with an earthed collet. Charges are plotted against the specific surface area of the particles.

6.9 Evidence for charge separation

Experiments involving pumice–pumice collisions carried out at both low and atmospheric pressure demonstrated opposite polarity charges collected by the mesh and the Faraday cup. Thus, for most experiments, a positive-above-negative gravitational separation of charge was demonstrated. StV 519 samples produced similar results, but with reversed polarity.

It is also believed that many of the changes observed in the Faraday cup charge, which occurred after impacts had ceased, also represented charge separation (section 6.3.4). In many (but not all) occurrences, these changes were of the opposite polarity to the charge on the particles already collected. Thus, gravitational sorting of particles by their fall velocities had separated small particles of opposite polarity from the rest of the particles.

6.10 Evidence for the production of ions

Although the mesh was designed to demonstrate the presence of ions by collecting 'mobile' charge, it has also been shown to be sensitive to many other types of charge (section 6.3.1). However, evidence for the presence of ions can be shown by analysis of the charge distributions produced during experiments and also the variation in the specific net ash charges produced.

6.10.1 Charge balance within pumice–pumice impact experiments

If the total charge within each experiment is assumed to be constant, at the end of an experiment the sum of the charges on the samples, the particles and any ions produced would be zero. If the unrecovered particles are assumed to hold the same net

charge as the ones that fell in to the Faraday up, then charge balance for an experiment gives

$$0 = Q_i + Q_p(1+\lambda) + Q_h + Q_a \qquad (6.7),$$

with the notation defined in section 6.3. Using equation 6.2 to produce an equation for the charge held on the samples gives

$$Q_h + Q_a = \frac{1}{\alpha}\left(Q_m + Q_i\right) \qquad (6.8),$$

which can then be substituted into equation 6.4. Thus, the ion charge is given by

$$Q_i = \frac{\alpha(1+\lambda)Q_p + Q_m}{1-\alpha} \qquad (6.9).$$

From equation 6.9 it can be seen that, if Q_p and Q_m are the same sign, then Q_i cannot be zero. This scenario was demonstrated by several experiments with Sak 13I samples (e.g. experiments 70710b and 70713a, see Figures 6.16c and 6.16e). For typical experiments carried out at atmospheric pressure, λ is less than 0.1, and Q_p and Q_m are of the opposite polarity. If α is assumed to be a maximum of 0.25, then for any experiments in which Q_m is greater than about -0.3 Q_p, Q_i is also not zero (e.g. 70804f, where the magnitude of Q_m is between 0.7 Q_p and 1.6 Q_p, see Figure 6.17a).

However, in equation 6.2, Q_i was assumed to also include any charge held on particles adhering to the mesh. Although it is not thought that particles alone could account for all of the charge required in the examples above, small amounts of fine particles were observed adhering to the mesh after some of the impact experiments. Thus a possibility exists that particle charge could be responsible for the Q_i calculated. However, the rotational grinding experiments did not produce any visible particles on the mesh because the particles generated simply fell from the samples. In all the pumice–pumice rotational experiments (except for those from StV 519) the magnitude

of the detected charge on the mesh (positive polarity) was larger than that detected by the Faraday cup (negative polarity). This demonstrates a positive Q_i which could not be the result of silicate particles on the mesh.

6.10.2 Charge balance of earthed collet impact experiments

For experiments in which the anvil sample was replaced by an earthed collet, equation 6.4 can be rewritten as

$$0 = Q_i + Q_p(1+\lambda) + Q_h + Q_E \qquad (6.10),$$

where Q_E is the charge lost to Earth through the collet. The earthed collet cannot generate any induced charge on the mesh, so the recorded mesh charge is given as

$$Q_m = Q_i + \alpha Q_h \qquad (6.11).$$

Combining equations 6.10 and 6.11 to eliminate Q_i, and then rearranging to give the charge lost to Earth through the anvil produces

$$Q_E = -\left(Q_m + Q_h(1-\alpha) + Q_p(1+\lambda)\right) \qquad (6.12).$$

The sign of the charge on the hammer sample was usually revealed to be negative by the double line effect. The experiments also demonstrated a negative net ash charge and produced negative mesh data, thus Q_E must be positive, indicating the loss of positive charge from the experiment. This could be a result of ions transferring a net positive charge to Earth by being attracted to the collet.

However, a positive charge flowing to Earth on ions cannot be distinguished from a negative charge flowing from Earth onto the ash or the samples. In this case, the presence of positive charge is demonstrated (in order to attract the negative charge from Earth), but it is not necessarily held on ions. The particle charge experiments demonstrate that the particles hold both positive and negative charges, so it is possible

that some of the positively charged particles are being partly neutralised by negative charge from Earth.

6.10.3 Specific net ash charges

Figure 6.39 shows the specific net charge results for rotational grinding and collet impact experiments carried out at low pressure. The approximate location of results from pumice–pumice impact experiments is shown by the area enclosed by the dashed line. The specific net charge of particles produced by pumice–pumice impact experiments are greater than those produced by the pumice–pumice rotational grinding experiments. This can be interpreted as smaller charges being generated by frictional processes or, alternatively, that ions are produced during fracture and have more opportunity to recombine with particles during the grinding experiments.

The specific net charge of particles produced by collet impacts was generally greater than that of particles from pumice–pumice impacts. This is probably an effect of the impacts occurring with a metal surface. However, within the collet impact results, the highest specific net charges were produced by earthed collets rather than insulated collets. This could be interpreted as positive charge being lost to Earth during impacts with earthed collets. Thus, it implies that a net positive charge is produced as a ‘mobile’ charge. However, it could also be due to negative charge flowing from the metal to neutralise positive charge on some of the ash particles. Unfortunately, again, it is not possible to distinguished between these two effects.

The results from the rotational grinding experiments with an earthed collet also show an increase in specific net charge over pumice–pumice grinding experiments. However, without being able to compare this with similar results from an insulated

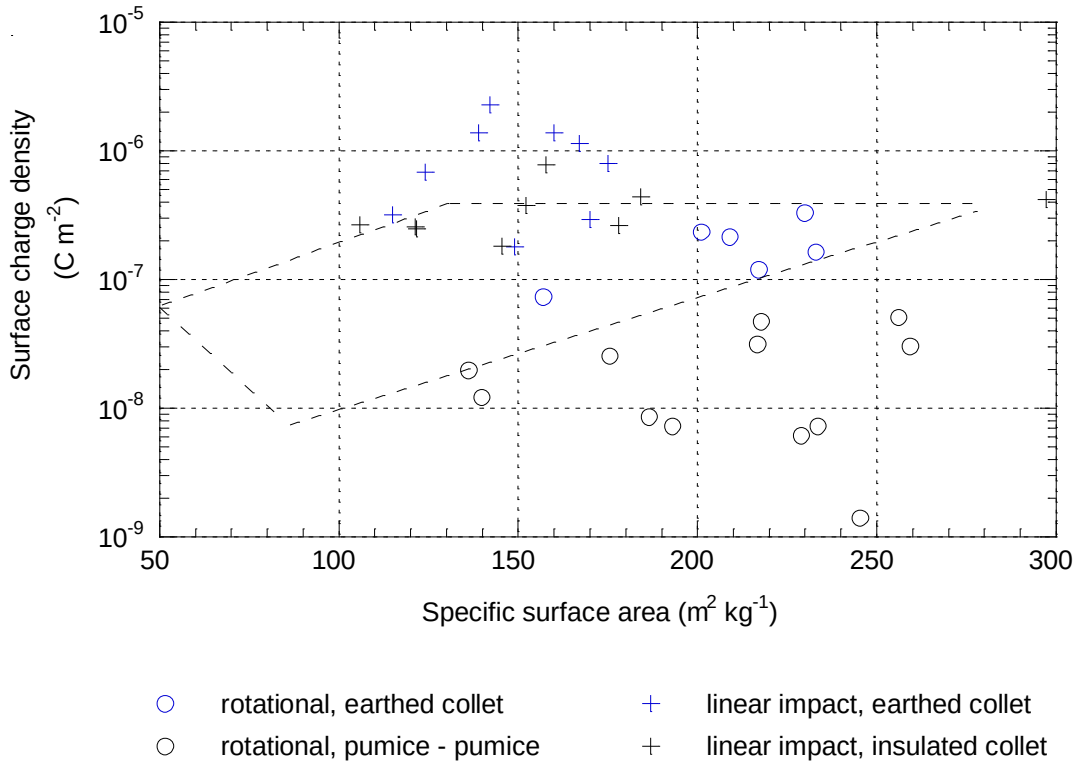

Figure 6.39 Net surface charge densities produced by different types of experiment. The dashed line represents the approximate location of the results produced from pumice–pumice impacts.

collet, this cannot be assumed to be anything more than the effect of the presence of the metal surface.

6.11 Summary

Particles have been produced by the fracture of pumice, and have been shown to hold net specific charges of the same magnitude as those measured on ashfall from volcanic plumes. The magnitude of the net charge appears to vary over approximately an order of magnitude for each pumice type, but has been shown to be a function of particle size, with smaller particles generally holding higher charge magnitudes. Relative humidity has been shown to have a small effect on the measured net charge, with only slightly decreased charges at higher values of RH. The net charges observed did not appear to vary with impact velocity of the samples.

The polarity of the net ash charge appeared to be a function of the sample geochemistry, but was also observed to change with the presence or absence of a vacuum. This may suggest a possible polarity control involving charge flow over the surface of the sample (and thus indicate the importance of surface chemistry and the presence of adsorbed species) or it may be an effect of ion scavenging.

The importance of fracto-emission processes in the charging of particles has been suggested by the detection of charge thought to be released as ions. During pumice–pumice rotational grinding experiments, particles were subject to frictional (triboelectric) charging by the nature of the grinding and produced net specific charges an order of magnitude smaller than during linear impact experiments.

7. Experimental results and interpretation: Individual particle charges

7.1 Introduction

In this chapter, the results of experiments carried out with the parallel plates apparatus (described in Chapter 5) are given and discussed. Although charge data were continuously recorded during each experiment, graphs of all the experiments are not provided for several reasons. First, no polarity variations were observed (unlike during the net ash charge experiments), because only particles of one sign were collected on the sensor plate. Thus, for each experiment, the plate data were easily summarised by a single number representing the total charge accumulated. Second, without measuring the net charge on all the particles produced, charge balance analysis cannot be carried out. There was also some uncertainty about the validity of the mesh data, which may have been susceptible to interference from the solenoid during some of the particle charge experiments. Thus, the reliable information retrievable from the mesh data was limited to the timing of the impacts.

A total of ninety eight experiments were carried out, and these are listed in Appendix IV. The results of the first ten of these will not be generally discussed because the lower slot position in the apparatus was being used and this may have induced charging or discharging of the particles (Chapter 5). The remaining results are presented here as investigations of the effect of various parameters: relative humidity (RH), number of impacts, impact velocity, particle separation field strength and net ash charge.

7.2 Results

All the experiments were carried out with particles produced by pumice–pumice impacts, mainly of Mount St. Helens (MSH) samples. This pumice was selected because it had proved reasonably easy to fragment and had provided some of the most consistent results during the net ash charge experiments. Variation was still observed within the particle charge experiments, but it was found that comparable results could be obtained from different experiments if the same samples were used continuously. This obviously created constraints on the number of experiments which could be carried out and directly compared. Several experiments were also carried out using samples from St. Vincent (StV 519) in order to compare the MSH results with data obtained from samples producing net positively charged ash.

Data collected during three different experiments are shown in Figure 7.1 as examples. In Figure 7.1a data recorded during a typical experiment involving many sample collisions are given. The kV plate was at -3.5 kV, thus negative charge was collected on the 0 V plate. Figure 7.1b shows the data recorded over 30 s during which time one sample impact was initiated. For this experiment, the kV plate was at +3.5 kV, and positive charge was collected. The operation of the solenoid was detected by the mesh and is also marked on the top axis of the graph. Charge accumulation on the 0 V plate was shown to occur over the following 8 s. These experiments can be compared with the data obtained when both of the parallel plates were earthed (thus producing no separation electric field), as shown in Figure 7.1c.

In the following sections, unless otherwise stated, the results obtained from experiments carried out with a positively charged kV plate (thus representing positive particles) are shown by red symbols. Black symbols represent the results from experiments carried out with a negatively charged kV plate. The error bars on the

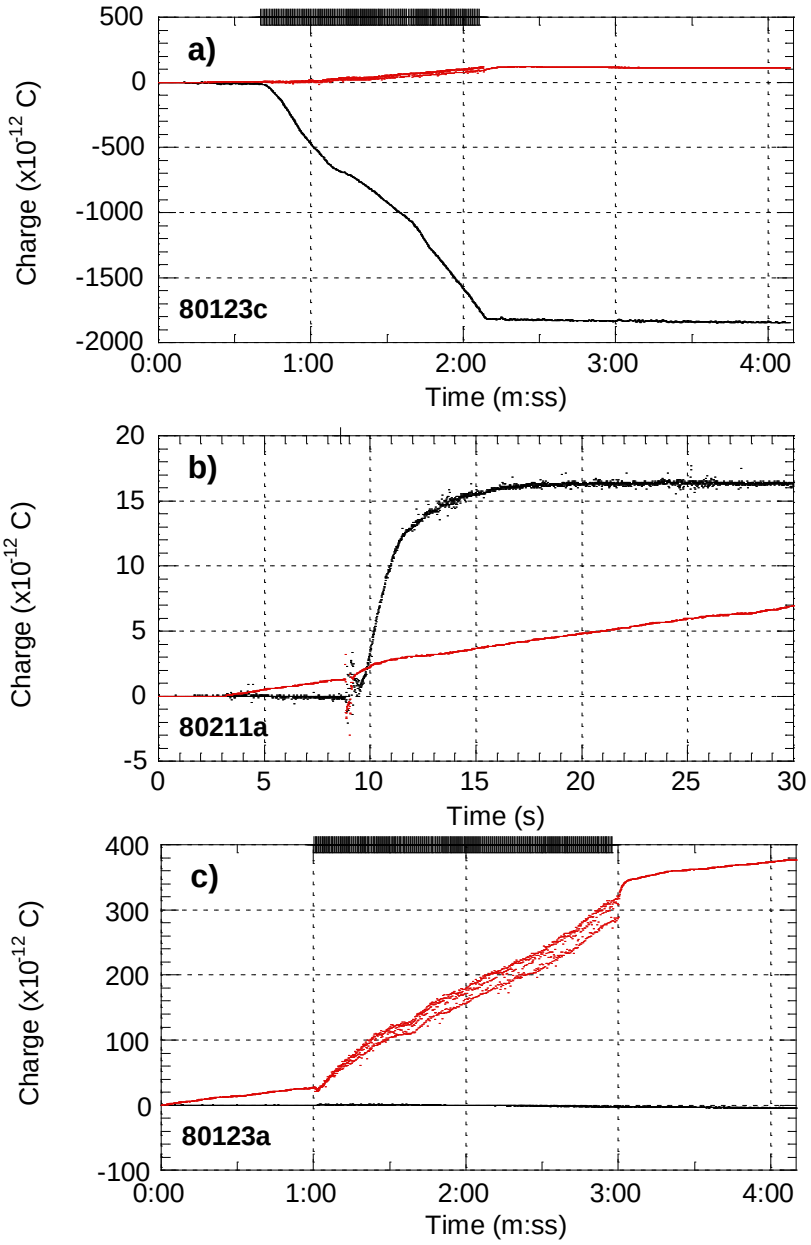

Figure 7.1 Examples of data collected during particle charge experiments. Mesh data shown in red; 0 V plate data in black. Individual sample impacts are marked by a vertical line through the top axis. **a)** An experiment with 210 impacts and the kV plate at -3.5 kV. **b)** A single impact experiment, with the kV plate at +3.5 kV and the zero-checks on the electrometers released at 3 s. **c)** An experiment with 302 impacts and the kV plate earthed. With no electric field between the plates, particles did not collect on them, and no plate charge was recorded. The mesh data show the double line effect (Chapter 6), indicating accumulation of positive charge on the hammer sample. Note the negligible drift rates of the plate data.

graphs have been calculated assuming that mass measurements were accurate to ±0.05 mg, charge measurements to ±5 % and particle specific surface areas to ±5 %. The error of ±0.05 mg for the mass measurements was chosen to represent a worst case when the mass adjustments (to account for the change in foil geometry, see Chapter 5) were taken into consideration. These adjustments dictated that, for experiments producing only small particle masses, the total error was dominated by the mass measurements. The mass adjustments also resulted in some data being discarded as a result of the calculated particle mass being less than the error. Where error bars are not shown, with the exception of specific surface area plots, the errors are smaller than represented by the symbol size. The estimated ±5 % error in the surface area data was estimated from the scatter in the results of identical analyses (Chapter 5), but has been omitted from specific surface area plots for clarity.

7.3 Effect of relative humidity

Figure 7.2a shows the specific charge results for experiments carried out under low (approximately 10 % RH or less), intermediate (between about 30 and 50 % RH) and high (approximately 90 % RH) relative humidity conditions. It includes experiments with multiple impacts (more than 200), and experiments with single impacts, carried out with the solenoid at 6 and 12 V. A collimating slot was not used during the single impact experiments, and this was shown not to affect the specific charge results (section 7.4). Difficulties with electrometer drift, noise and low signal amplitudes prevented any 6 V results being successfully recorded under conditions of high RH.

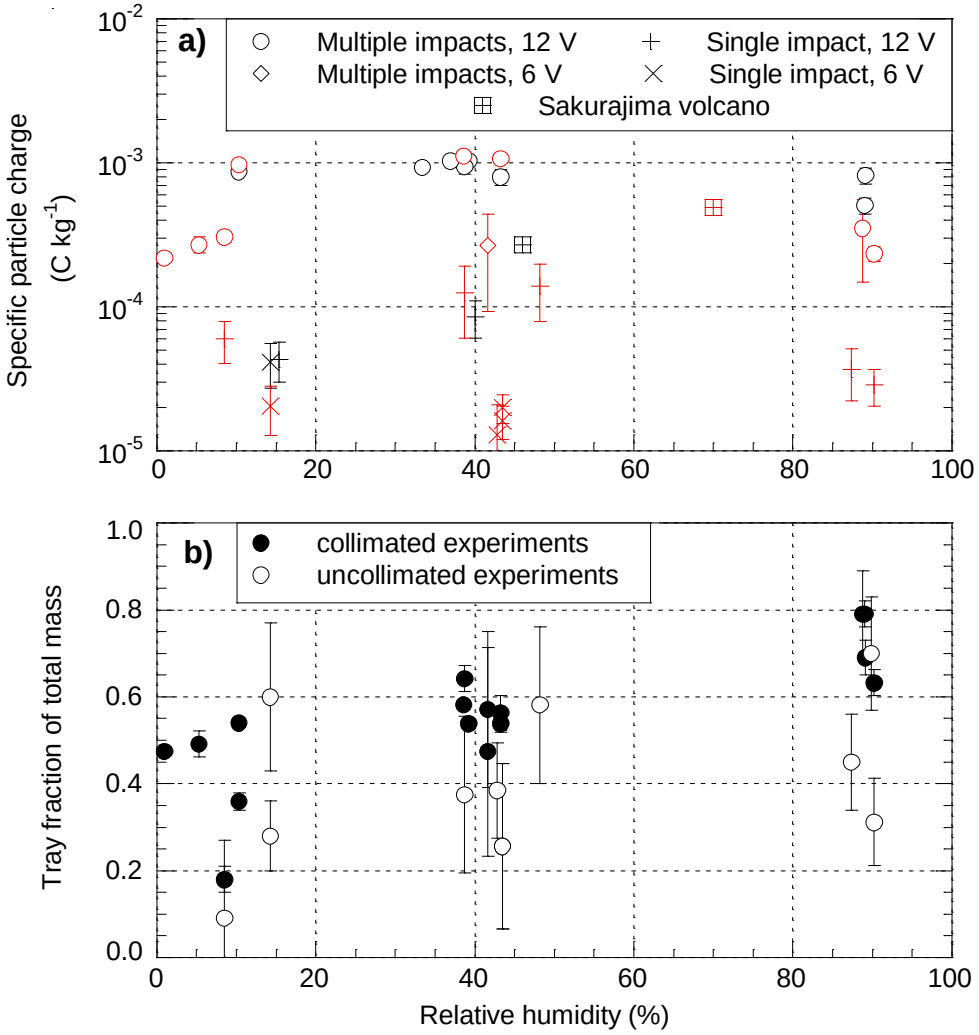

Figure 7.2 The results of particle charge experiments at different values of relative humidity. **a)** Specific particle charge. The key shows the number of impacts ('multiple impacts' refers to any experiment involving more than 100 impacts) and the voltage across the solenoid for the experiments. Red symbols represent the results of experiments carried out with the kV plate at +3.5 kV; black symbols represent experiments with the kV plate at -3.5 kV. All experiments used MSH Clast 1 samples except for the 'Sakurajima volcano' results which are from ashfall measured in the field by Gilbert *et al*. (1991). **b)** The tray fraction of the particle mass produced. During uncollimated experiments, the initial spatial distribution of the particles reaching the plates was larger, allowing more to be collected before they reached the tray.

7.3.1 Results

Intermediate humidity.

These results were obtained under 'normal' atmospheric conditions (the air inside the vacuum chamber was not deliberately dried or humidified). The specific particle charges calculated ranged from 10^{-5} to 10^{-3} C kg^{-1}, and appeared to be mainly a function of the impact velocity and the number of impacts. These factors are discussed further in sections 7.4 and 7.5.

Low humidity.

The same range of specific charges was calculated for experiments carried out at low humidity. However, the range of values from experiments carried out with the same solenoid and impact parameters varied more than they did at intermediate relative humidity. Two experiments with multiple impacts at 12 V produced results (approximately 10^{-3} C kg^{-1}) similar to experiments at intermediate humidity, suggesting that at values less than about 50 %, relative humidity has little effect. However, further experiments under conditions of less than 10 % RH produced smaller specific charge values. These experiments also demonstrated the unusual particle distribution on the kV plate observed in experiments carried out with a low collimating slit (see Chapter 5).

High humidity.

The specific charge values calculated from experiments carried out at about 90 % RH are generally smaller than those for experiments at lower humidity, but not by as much as an order of magnitude. Despite concerns about the possible effects of

charged water droplets, the results are thought to be reliable. The slightly reduced specific charge values under humid conditions are also reflected in Figure 7.2b, in which the tray mass fraction (the fraction of the total collected mass which was not caught on the plates) is plotted against relative humidity. There was a slight increase in tray fraction with increasing RH, which is most evident in the results from the collimated experiments.

During most of the multiple impact experiments, sufficient particle mass was collected on the 0 V plate for particle size analysis to be carried out. The calculated specific surface areas are shown in Figure 7.3a and, with the exception of only a few examples, the results were between 170 and 220 m^2 kg^{-1}. The implied surface charge densities are shown in Figure 7.3b.

Relative humidity has been shown to have a smaller effect on measured specific particle charges than variations of the number of impacts or the impact velocity. However, the steadily increasing tray fraction of the particles with increasing RH indicates that there is an effect which does operate over the whole RH range, even if it is only reflected in the specific charge results at high values of RH.

7.4 Number of sample impacts

Figure 7.4 shows the way in which the measured specific particle charge varied with the number of impacts during an experiment. Most experiments involving 100 impacts or less were carried out without the collimating slit in order to obtain sufficient particle numbers between the plates for accurate charge and mass measurements. An uncollimated experiment was also carried out with 220 impacts. This produced a similar specific charge value to those obtained from collimated

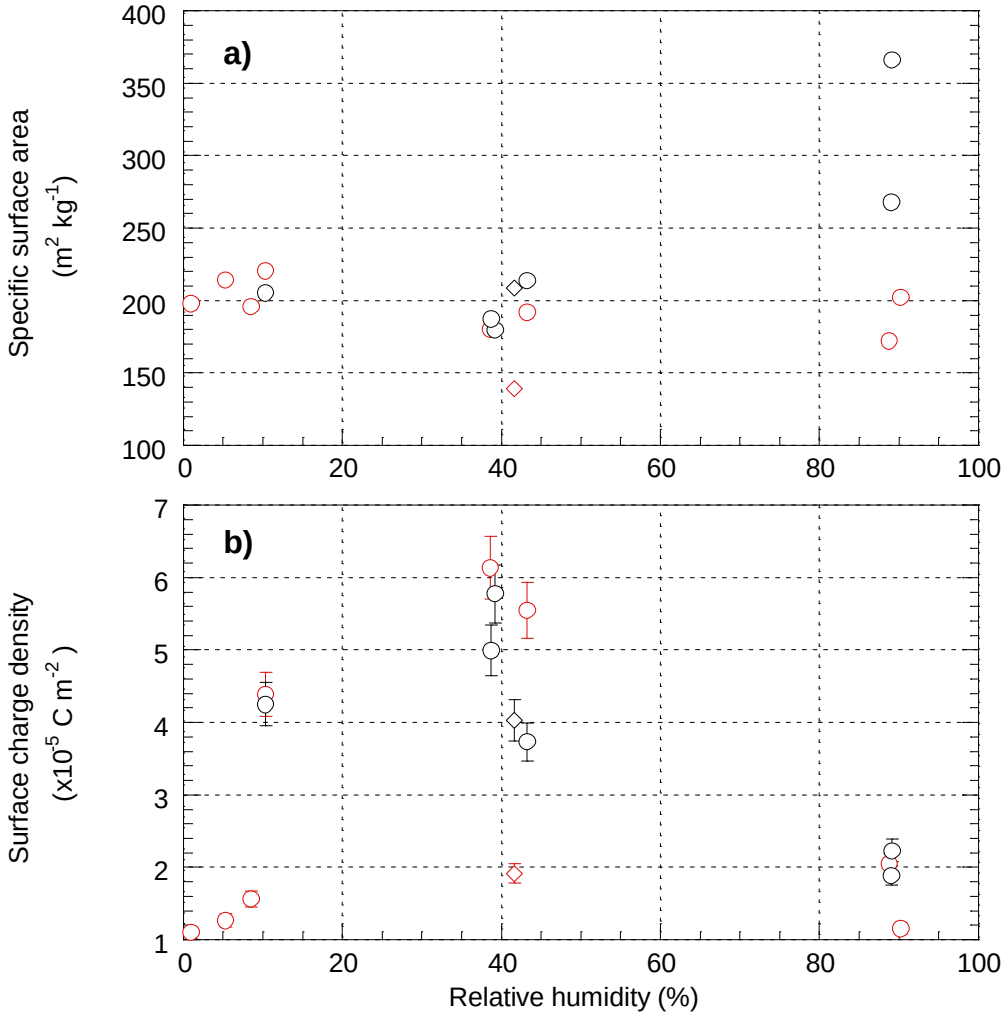

Figure 7.3 Specific surface area and surface charge density as a function of relative humidity. The graphs show results from the multiple impact experiments shown in Figure 7.2a. Circles represent experiments carried out with the solenoid at 12 V; diamonds represent 6 V. Black symbols are the results of experiments with the kV plate at -3.5 kV, red symbols +3.5 kV.

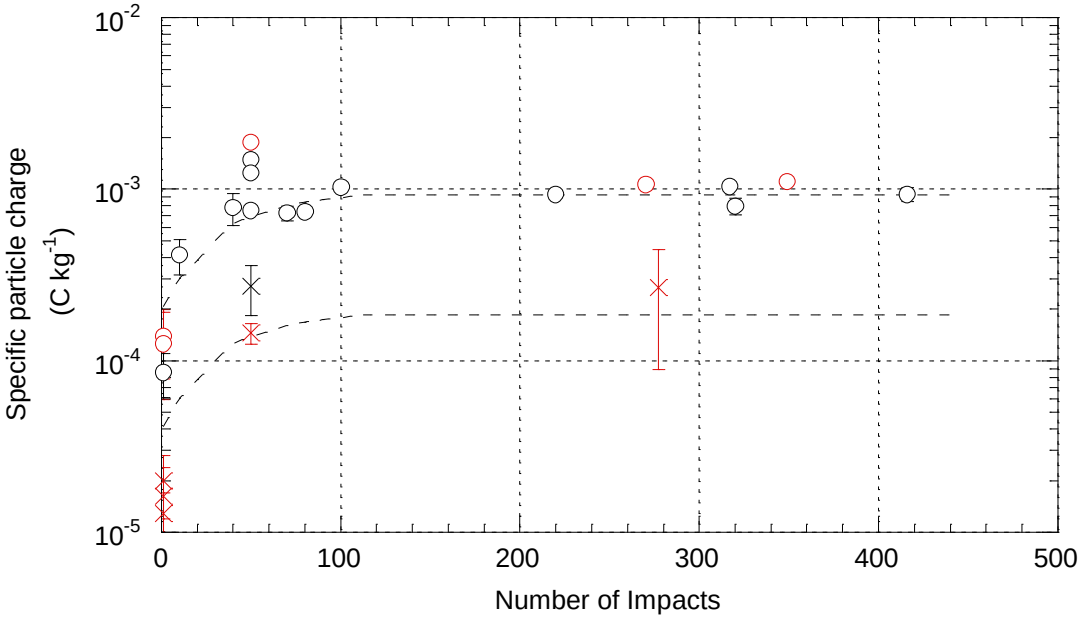

Figure 7.4 Specific particle charge as a function of the number of sample impacts. Crosses represent experiments during which impacts were initiated by the solenoid at 6 V, the circles at 12 V. Experiments with a kV plate potential of +3.5 kV are shown in red; -3.5 kV experiments are shown in black. Samples were cut from MSH Clast 1, with the exception of those used for the 50 impacts experiments, which were from MSH Clast 2. The upper dashed curve is an approximate best fit to the 12 V data. The lower curve is identical, but reduced by about a factor of 5. Experiments at 1, 10, 20, 70, 80, 100 and 210 impacts were run without a collimating slit; all others used a 3 mm slit. All experiments were carried out at atmospheric pressure (18 to 23 °C, 30 to 50 % RH).

experiments with up to 420 impacts. Thus, it was assumed that collimation had little or no effect on the measured specific charge.

7.4.1 Results

The results of experiments carried out with the solenoid at 12 V demonstrated a general trend which has been marked by a dashed line in Figure 7.4 (upper curve). The points at 50 impacts, which lie off the line, are the result of experiments carried out with MSH Clast 2 samples. All other experiments were carried out with samples from MSH Clast 1. For small numbers of impacts, the specific charge increased rapidly with the number of impacts up to about 100 impacts. However, the results of experiments carried out with more than 100 impacts suggested that the specific charge subsequently became independent of the number of impacts.

For the 12 V experiments carried out with MSH Clast 1 samples, the specific charge varied from about 10^{-4} C kg^{-1} for one impact to 10^{-3} C kg^{-1} for more than 100 impacts. The few results obtained for impacts with the solenoid at 6 V are consistent with the trend shown by the 12 V experiments, but with specific charges reduced by a factor of about five. Specific surface area and surface charge density results for some of the experiments consisting of more than 100 impacts have been given in the intermediate RH results of Figure 7.3.

Figure 7.5a shows the specific charge data from a series of experiments with 100 or less impacts, carried out with samples of MSH Clast 1. The factors influencing the shape of the curve are demonstrated in Figures 7.5b and 7.5c, which show plots of the charge generated per impact and the mass produced per impact. The 80 impacts experiment was the last in the series to be carried out, and the collision surfaces of the samples had been smoothed prior to the experiment. This produced high mass and

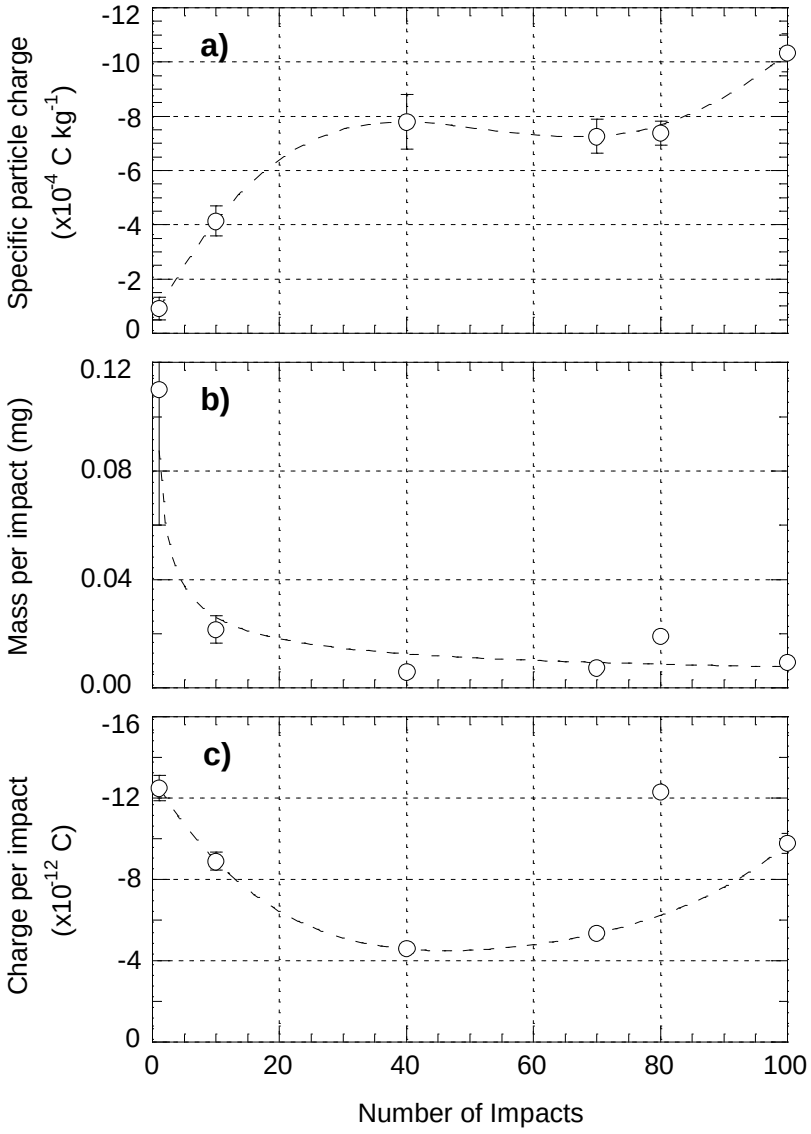

Figure 7.5 Details of experiments with low numbers of impacts. All experiments were conducted with MSH Clast 1 samples, no collimating slot, the solenoid at 12 V and the kV plate at -3.5 kV. **a)** Specific charge on particles collected by the 0 V plate. **b)** Mass of particles per impact collected on the 0 V plate. **c)** Charge collected by the 0 V plate per impact. The dashed lines represent visual guides only. All the experiments were carried out at atmospheric pressure (18 to 23 °C, 32 to 40 % RH).

charge per impact results, but a similar specific charge to the other experiments (Figure 7.5a). The single impact results represent average values from several experiments (actually carried out with the kV plate at +3.5 kV). Graphs of the total particle mass produced per impact and surface area data are given in Figure 7.6. No coherent trend was observed in the specific surface area data, and variation within the surface charge density results is dominated by the charge term.

7.4.2 Interpretation

The single impact experiments produced high mass per impact results (Figures 7.5b and 7.6a). As successive impacts occurred, the mass per impact decreased. This agreed with visual observations that the first couple of impacts appeared to be associated with more particles than following impacts. This is thought to reflect a very brief 'bedding-in' period, during which most of the weakest and pre-fractured material was removed from the impact surfaces. Much of the charge generated by the previous fracturing would have dissipated, and so the lower specific charge value would be recorded. After this period the surfaces are somewhat 'keyed' together and the particle production rate is reduced. The development of these interlocking impact surfaces was also discussed in Chapter 6 (section 6.3.3).

Figure 7.5c demonstrates that this initially high attrition rate also produced a large charge per impact for low numbers of impacts. However, unlike the mass per impact, the charge per impact increased again after about 50 impacts. This is thought to reflect the possible influence of charge accumulating on the sample surfaces. As the surface charge increases, particles produced from it also become increasingly charged. Mesh data have clearly demonstrated that the sample charging does occur, and they also imply that the charge accumulated can continue to increase (Chapter 6), even after

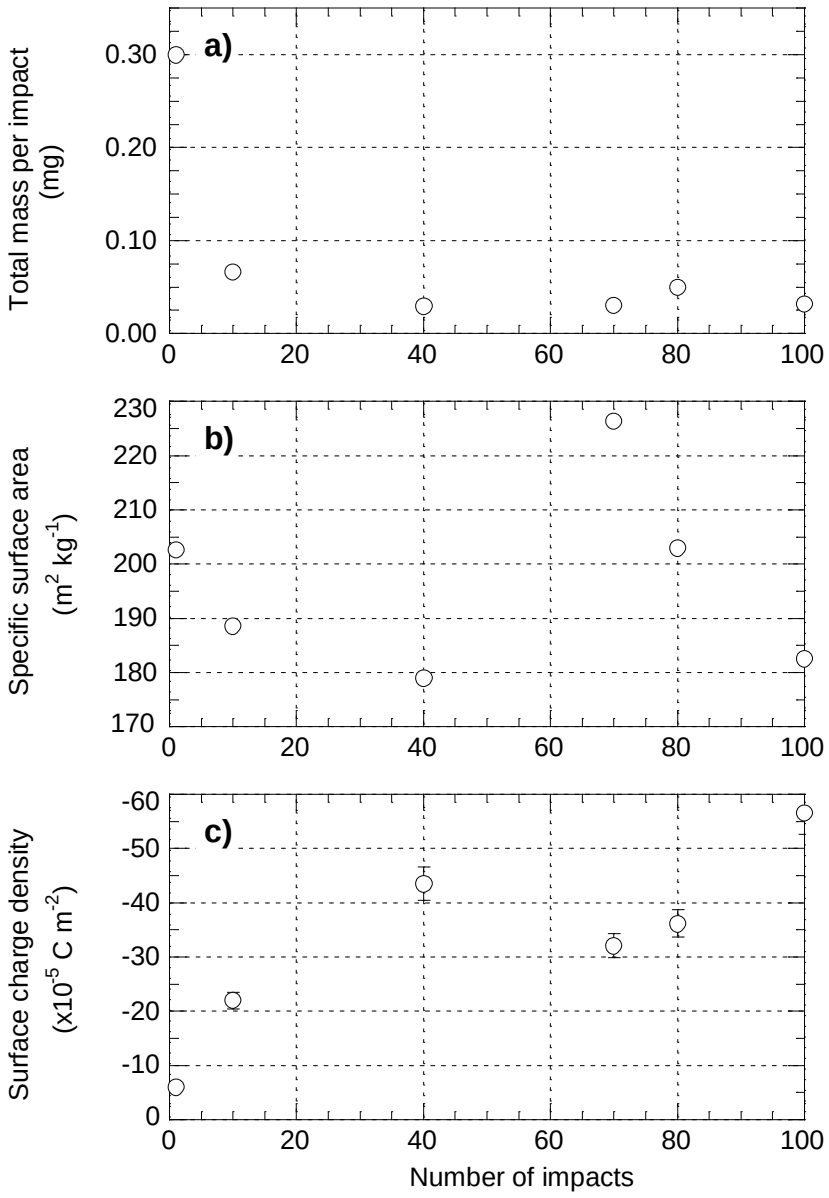

Figure 7.6 Surface area and total collected mass per impact for experiments with low numbers of impacts. **a)** Total particle mass per impact (the sum of the particle masses collected on the 0 V and kV plates and on the tray). **b)** Specific surface area of the particles collected on the 0 V plate. **c)** Calculated surface charge density of the particles collected on the 0 V plate.

400 impacts. However, if sample charge is a factor behind the increasing particle charge, its effect on the particles appeared to saturate at about 100 impacts.

7.5 Sample impact velocity

In order to minimise any possible effects from sample charging, all the following experiments were carried out with only fifty impacts. Specific charge results are shown in Figure 7.7a for experiments during which the impact velocity was varied by applying different voltages to the solenoid.

7.5.1 Results

The results demonstrated an increase in specific charge with impact velocity, and the positively charged particles appeared to have generally higher specific charge than the negative particles. This same relationship was also demonstrated by the surface charge density results (Figure 7.7b). The specific surface areas of the particles collected on the 0 V plate are shown in Figure 7.7c.

The total particle mass produced per impact for these experiments is given in Figure 7.8a, and demonstrates an increasing mass with voltage. Figure 7.8b gives the tray mass fractions, and shows an apparent change in behaviour between hammer voltages of about 8 to 9 V. At higher hammer velocities, the tray mass fraction was approximately constant between 70 and 80 %, but the lower velocity impacts produced a rapid decrease in the tray fraction.

Mass and specific surface area ratios are given in Figures 7.8c and 7.8d for the particles collected on the plates. The mass ratios show that, during the majority of experiments, a greater mass was collected on the 0 V plate than on the kV plate. Furthermore, this effect appeared to be enhanced when negative particles were being

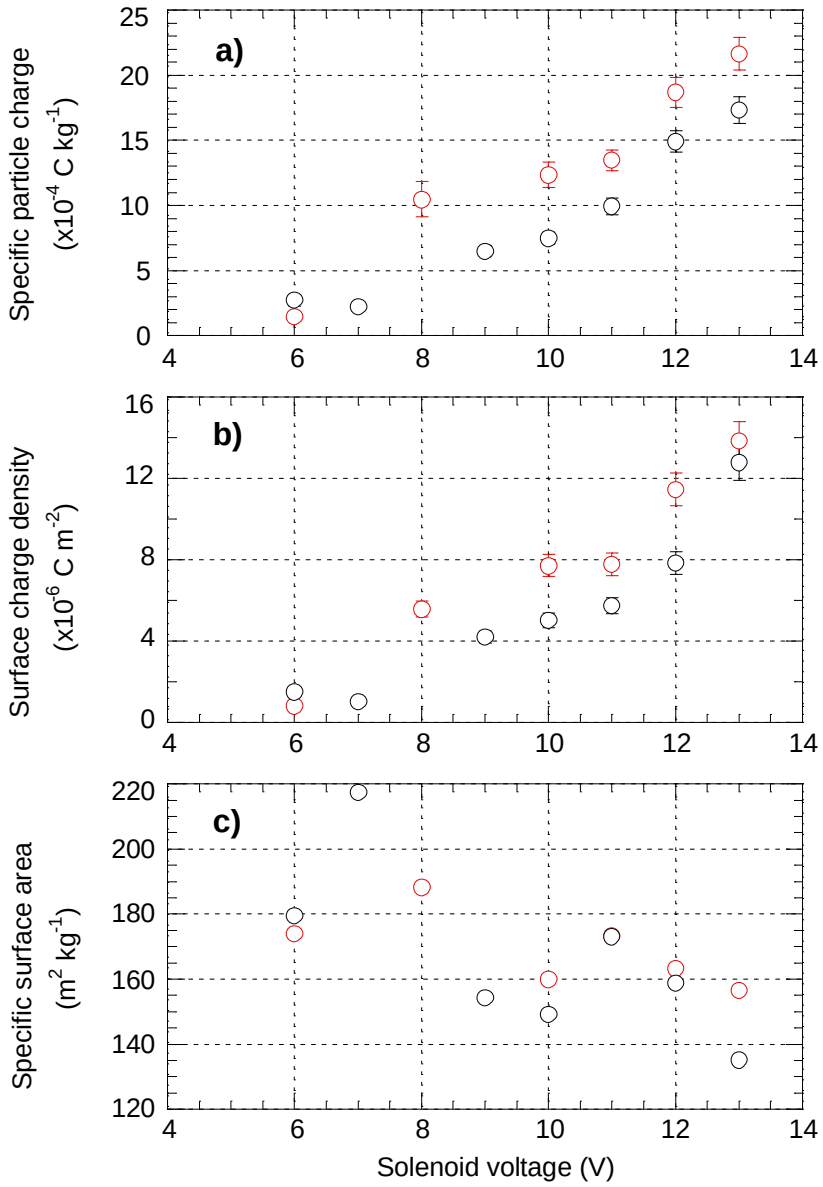

Figure 7.7 Variation of specific particle charge and surface area as a function of impact velocity. The results of experiments with a kV plate potential of +3.5 kV are shown as red circles; -3.5 kV experiments are shown as black circles. All experiments were carried out with samples cut from MSH Clast 2, and consisted of 50 impacts at atmospheric pressure (18 to 23 °C, 30 to 50 % RH). A 3 mm collimating slit was used throughout. The graphs show the results obtained for the particles collected on the 0 V plate: **a)** specific particle charge; **b)** surface charge density; and **c)** specific surface area.

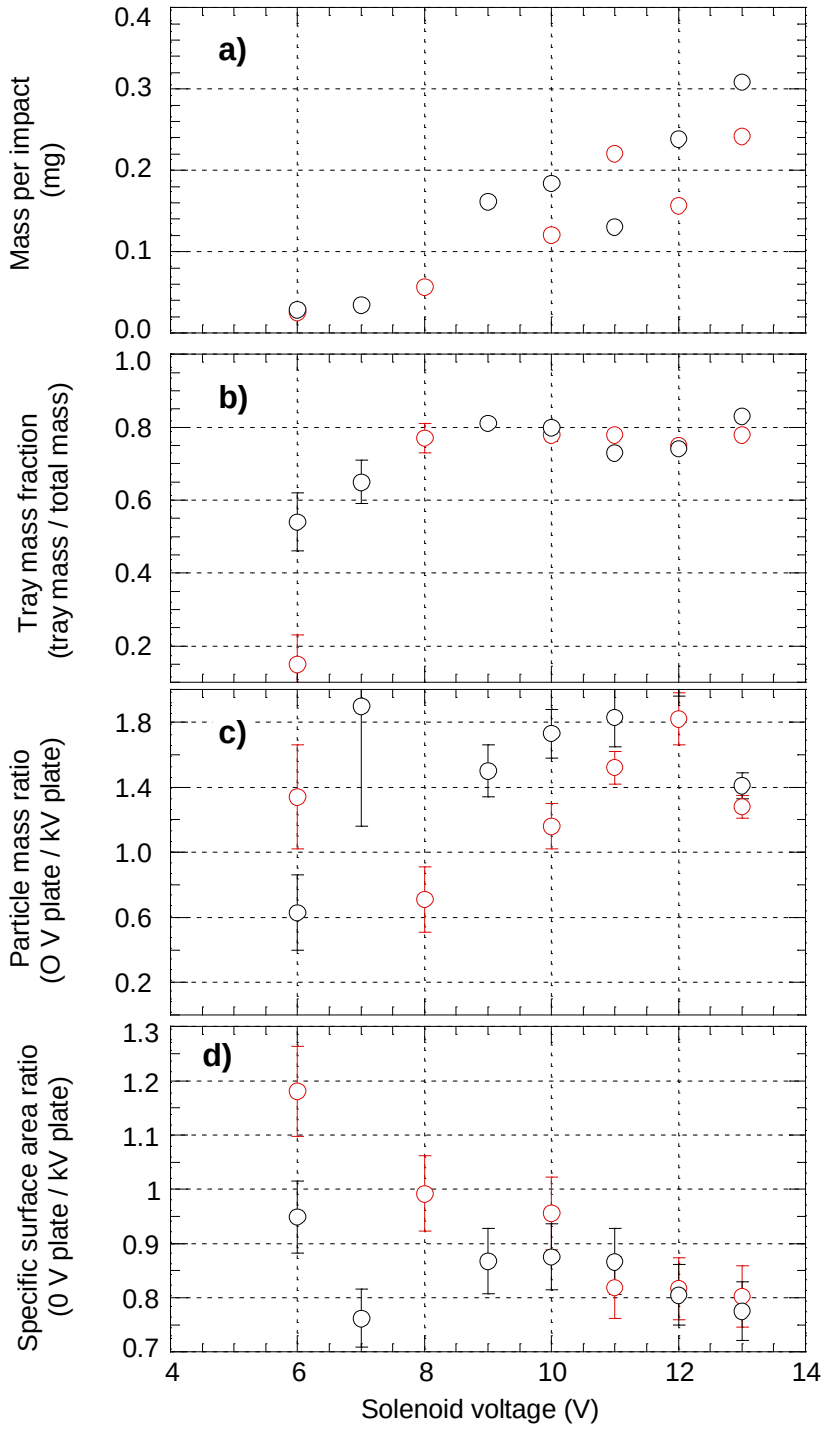

Figure 7.8 Particle mass and surface area ratio results of the impact velocity experiments. **a)** Total particle mass collected per impact. **b)** Tray fraction. **c)** Particle mass ratio (particle mass on 0 V plate divided by particle mass on the kV plate). **d)** Specific surface area ratio (specific surface area of the particles collected on the 0 V plate divided by that of the particles collected on the kV plate).

collected on the 0 V plate. There is also a suggestion that the difference in the ratios decreased with increasing impact energies. The specific surface area ratios (Figure 7.8d) demonstrated that the particles on the 0 V plate became progressively coarser than those collected on the kV plate with increasing impact velocity.

7.5.2 Particle size distributions

Figure 7.9 shows the size distributions of all the particles collected at each discrete solenoid voltage. Thus, each distribution reflects the sum of the particles caught on both plates and the tray for all experiments carried out with a certain impact velocity. The distributions have all been normalised to the same total volume. At lower voltages, the particles produced are generally finer (see also Figure 7.7c). The particle size distributions produced by solenoid voltages of 6 and 7 V are fairly similar, but the 8 V distribution contains more of the coarser particles (with diameters larger than about 30 μm) which dominate the other distributions. For voltages of 9 V and above, the size distributions are fairly constant. This appears to correlate with the relatively constant tray fraction of the experiments carried out at 9 V and above.

Examples of the particle size distributions obtained from a typical experiment are given in Figure 7.10. The tray deposits were the coarsest, and were depleted in the finer particles which had collected on the plates. The data from the experiment shown (carried out with a negatively charged kV plate) demonstrated that the kV plate collected a finer distribution of particles than the 0 V plate. However, as reflected in the surface area ratios for the particles caught on the plates (normally less than one, Figure 7.7c), the kV plate also collected finer distributions when it was maintained at a positive potential.

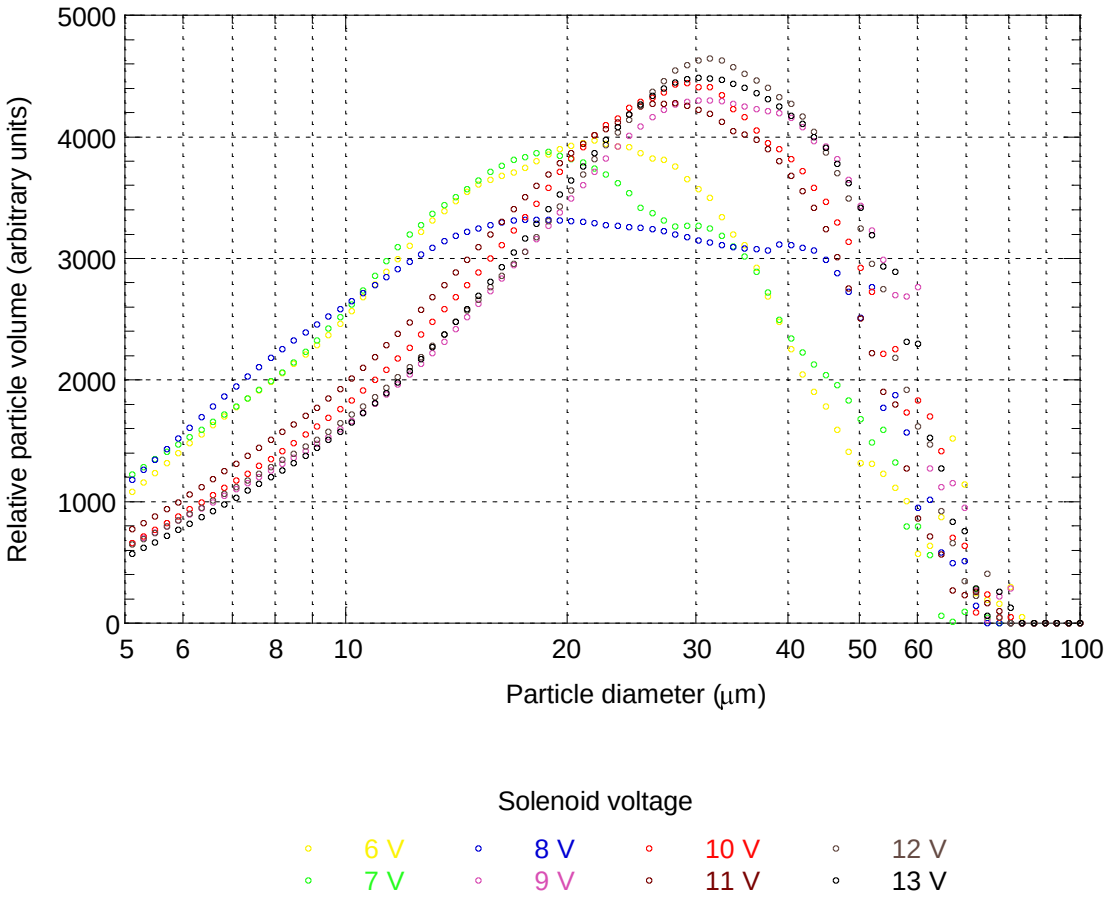

Figure 7.9 Particle size distributions for different impact velocity experiments. Each distribution represents the particles collected on the 0 V plate, the kV plate and the tray from all experiments carried out at a certain solenoid voltage. However, experiments were only included if they were carried out as part of the investigation into the effects of impact velocity.

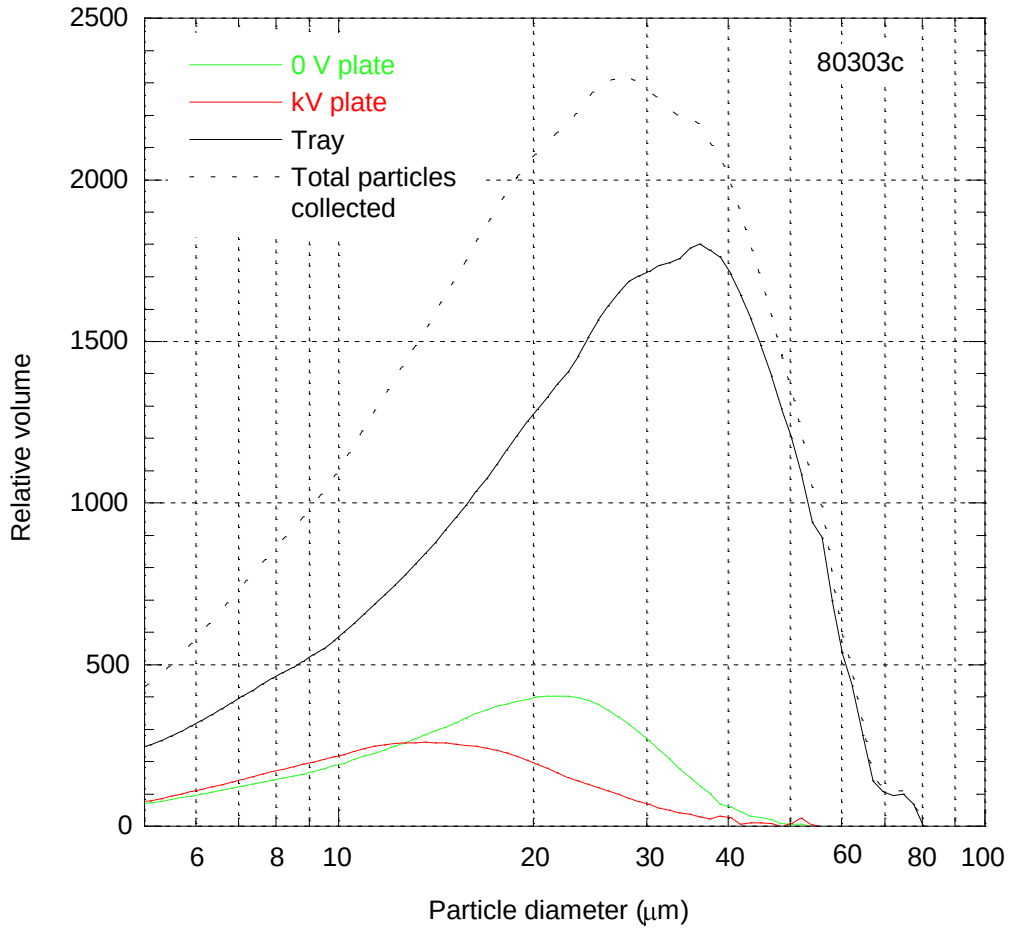

Figure 7.10 Typical particle size distributions collected during an experiment. Data are plotted on a volume basis with each distribution normalised to the relative mass of the deposit. The 'total particles collected' distribution represents the sum of the other three curves. The tray collected the coarsest particles and the majority of the mass. The 0 V plate collected a higher mass of particles than the kV plate. The extra mass was dominated by particles 20 to 40 μm in diameter, making the particles on the 0 V plate the coarser deposit. The experiment consisted of 50 impacts with the solenoid at 11 V and the kV plate at +3.5 kV.

7.5.3 Interpretation

With the exception of only two experiments, the 0 V plate collected more particle mass than the kV plate (Figure 7.8c). This suggests that, for either polarity of kV plate, particle collection is enhanced for the 0 V plate with respect to the kV plate. One possible explanation for this is the asymmetry of the separation electric field. This can be observed in the region above the plates in the cross section through the potential field generated inside the apparatus (Figure 7.11). In Figure 7.12 vectors of electric field strength are shown for this area above the plates. The asymmetry is due to the collimating slot plates being at the same (Earth) potential as the 0 V plate. Asymmetry of the vertical component of the field accelerates particles attracted to the kV plate downwards, but exerts an upwards force on particles attracted to the 0 V plate. Particles accelerated downwards have a reduced chance of being caught on the plates due to the decreased time they spend between the plates. Particles whose downwards velocity is reduced by an upwards force have an enhanced chance of capture.

This particle mass bias towards the 0 V plate was attenuated by an effect which was a function of the kV plate polarity. The plates' mass ratio was always highest for negative kV plate experiments. It is thought that this could reflect the net charge of the particles. If a net negative charge was held on the particles (as was shown for particles produced by pumice–pumice impacts of MSH samples in Chapter 6), then it is likely that a higher mass would be caught on the plate collecting the negative particles.

In order to assess any effect due to the net polarity of the ash, six experiments were carried out using StV 519 samples (71018a), previously shown to produce net positively charged particles (Chapter 6). Graphs of the results from these experiments

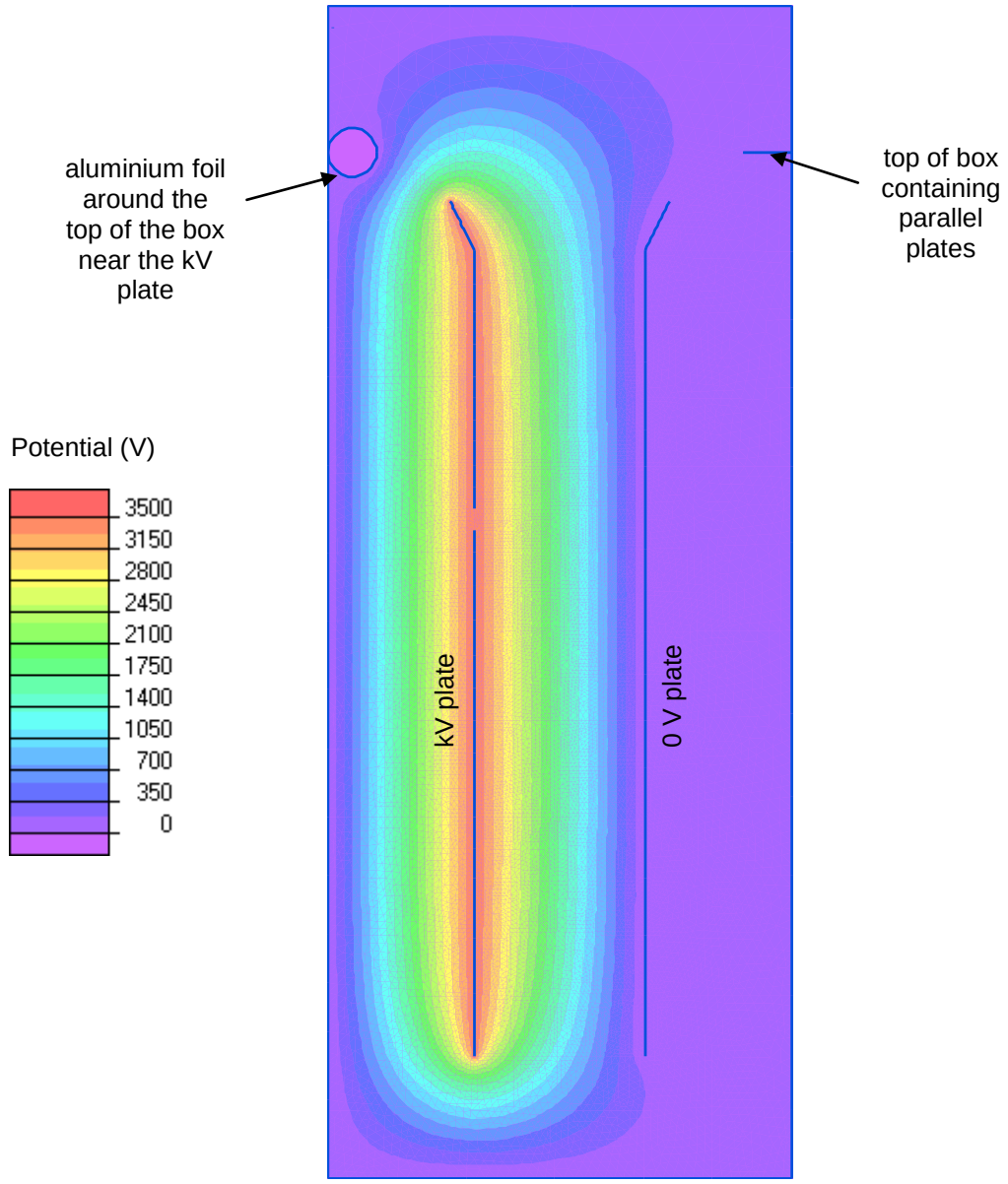

Figure 7.11 The potential field generated by the parallel plates (cross sectional diagram). This two-dimensional model was constructed and then solved in QuickField Professional (V. Podnos, *pers. comm.*). The kV plate is at +3.5 kV. The model is bounded by the earthed box around the parallel plates and an earthed plate at the top to represent the collimating slot plates.

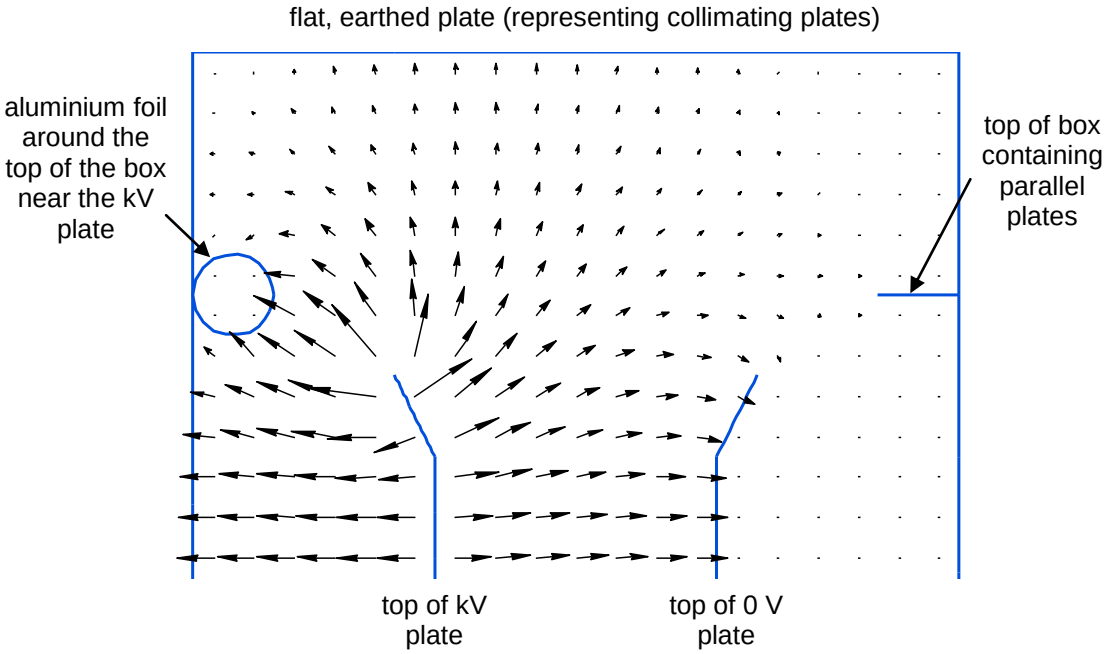

Figure 7.12 Vector arrows of the electric field in the region below the collimating slot. The kV plate is at +3.5 kV and the plates forming the collimating slot are modelled as one flat, earthed plate. (Modelled by QuickField Professional, V. Podnos, *pers. comm.*)

(equivalent to Figures 7.7 and 7.8 for MSH samples) are shown in Figures 7.13 and 7.14. Unfortunately, no coherent trend was produced by the StV 519 samples. This is thought to be partly a result of sample inhomogeneity, as demonstrated by the reduced mass per impact results obtained with a solenoid voltage of 13 V (Figure 7.14a). Another factor was particle aggregation. The particles produced were observed to be extremely aggregated, and the calculated specific surface areas were all higher than those of MSH experiments (Figures 7.7c and 7.13c).

The trends demonstrated by both the tray fractions and the particle mass ratios of experiments with the StV 519 samples (Figures 14b and 14c) were different from those observed in the MSH data. The differences are not explainable as due to positive net ash polarity or any electric field asymmetry. If all the MSH experiments are considered, then a similar range of results are observed. It is thus thought that the mass distribution is very sensitive to complex factors such as aggregation, and a simple theory cannot be used to explain results from widely differing experiments.

7.6 Separation electric field strength

Further evidence for the complex nature of the processes recorded by the experimental results was obtained by changing the magnitude of the electric field used for particle separation. Figure 7.15 shows the results of experiments involving 50 impacts carried out with plate potentials between ±1.0 and 3.5 kV. The calculated uniform field strength is shown on the top axis.

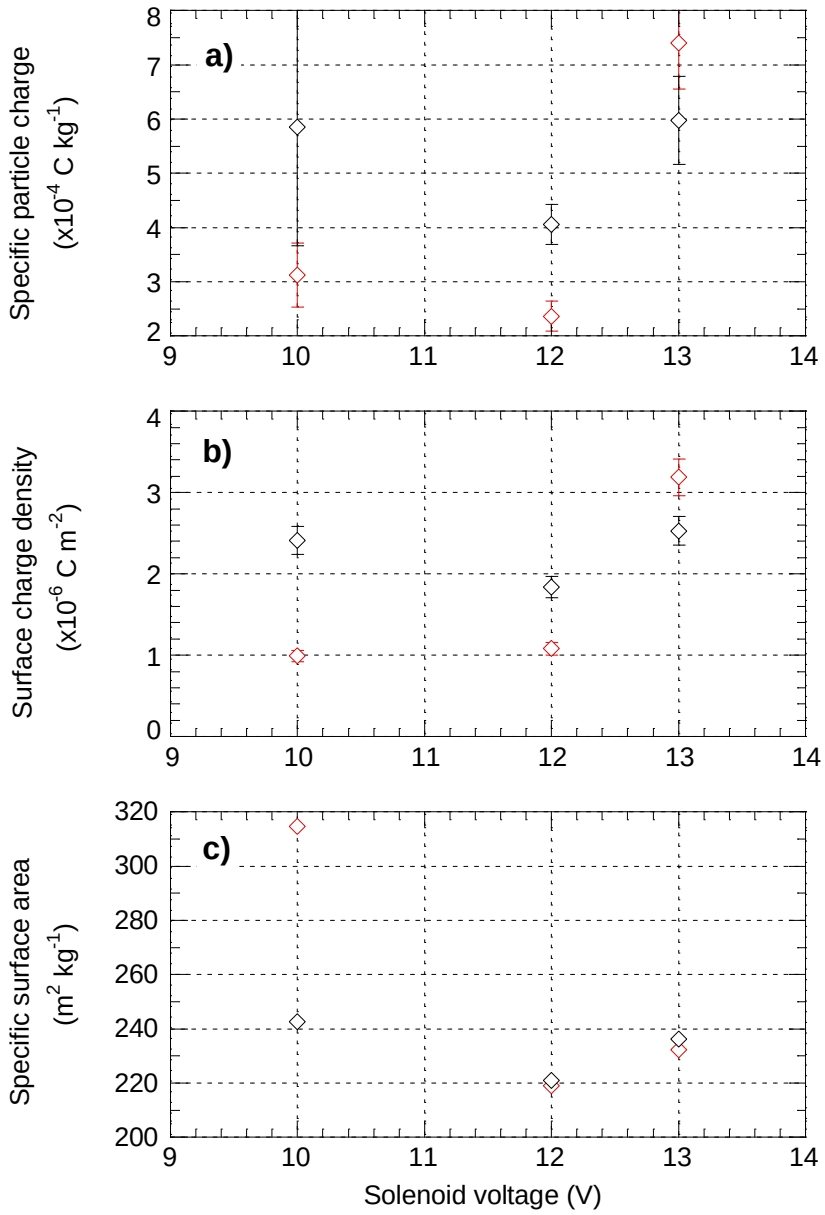

Figure 7.13 Specific particle charges and surface areas produced by StV 519 samples. The results of experiments with a kV plate potential of +3.5 kV are shown as red diamonds; -3.5 kV experiments are shown as black diamonds. All experiments were carried out with samples 71018a, and consisted of 50 impacts at atmospheric pressure (20 to 23 °C, 35 to 43 % RH). A 3 mm collimating slit was used throughout. The graphs show the results obtained for the particles collected on the 0 V plate: **a)** specific particle charge; **b)** surface charge density; and **c)** specific surface area.

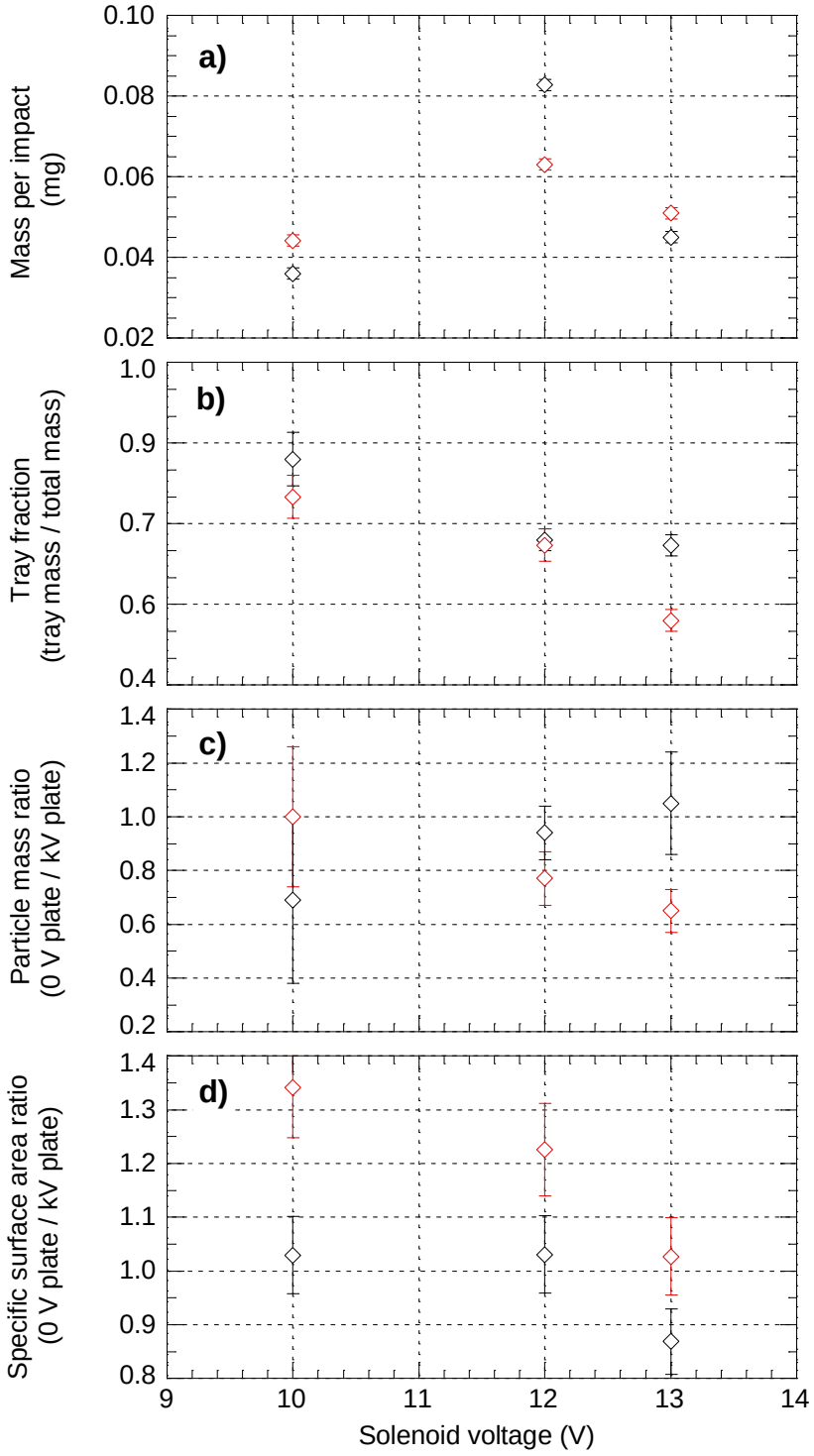

Figure 7.14 Particle mass and surface area ratio results of the impact velocity experiments with StV 519 samples. **a)** Total particle mass collected per impact. **b)** Tray fraction. **c)** Particle mass ratio. **d)** Specific surface area ratio.

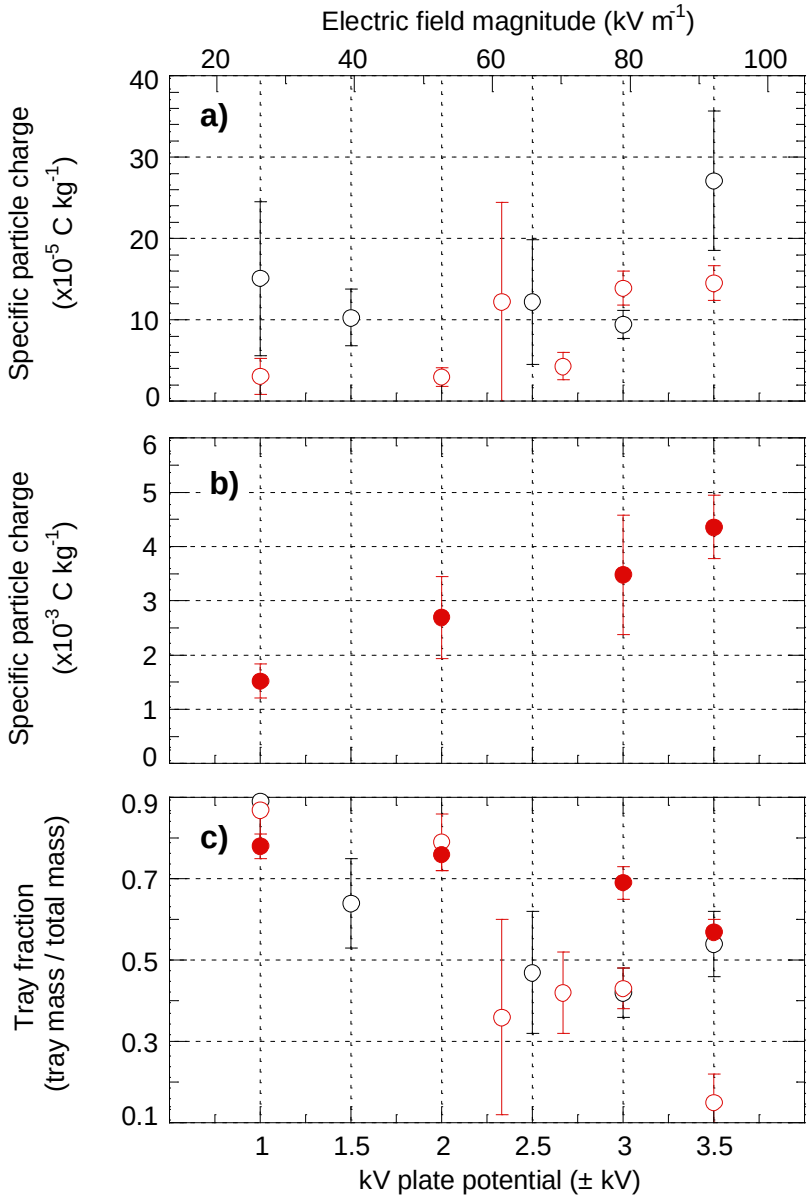

Figure 7.15 Variation of specific particle charge as a function of the separation electrical field magnitude. All experiments carried out using MSH Clast 2. **a)** Experiments carried out at atmospheric pressure (18 to 23 °C, 30 to 50 % RH). Red symbols are results from experiments with the kV plate at positive potentials and black symbols represent negative potentials. Each experiment consisted of 50 impacts with a solenoid voltage of 6 V. **b)** Experiments carried out at 10^{-4} Torr (approximately 10^{-2} Pa), with only positively biased kV plates. **c)** The tray fraction of the particle masses collected. Solid symbols represent the experiments carried out at low pressure.

7.6.1 Results

The results of experiments at atmospheric pressure are shown in Figure 7.15a. They demonstrate an approximate order of magnitude increase in the recorded specific charge, mainly over an increase in electrical field strength from about 60 to 90 kV m^{-1}. During these experiments, sub-millimetre sized aggregates were observed to be caught on the plates. Frequently, they were more evident on the plate collecting negatively charged particles, and appeared to be more abundant at the higher field strengths.

Similar experiments were carried out under vacuum (10^{-4} Torr, approximately 10^{-2} Pa). A smaller increase in specific charge with separation field strength was demonstrated (Figure 7.15b), with specific charge values increasing by only a factor of three between field strengths of about 30 to 90 kV m^{-1}. No large (sub-millimetre) aggregates were observed during these experiments and the deposits appeared to be individual particles, widely dispersed over the foils. However, it is thought that many of the larger 'individual' particles observed were actually very small (less than 100 μm in diameter) aggregates. This was verified on a few samples (by mechanically disrupting the aggregates with a fine wire), but it was not possible to obtain an estimate as to the degree of aggregation of the samples as a whole.

The tray fractions of the total collected particle masses are shown in Figure 7.15c. A greater proportion of the total particle mass accumulated on the plates with increasing separation field strengths. Note that the results of experiments carried out at atmospheric pressure demonstrate more scatter than those from the low pressure experiments, which appear to fall on a single curve.

7.6.2 Interpretation

The increase in the measured specific charge at high field strengths represents the opposite of predictions made from simple theory. At low separation field strengths, only particles with the highest specific charges should be collected. As the field strength increases, particles with lower specific charges would also be collected, decreasing the overall measured specific charge. It could be proposed that the opposite results, which were recorded, provide evidence for particle charging by ions produced within the apparatus. However, for reasons discussed in Chapter 5, this is thought not to be the case. The tray fractions demonstrate what would be expected from simple theory, with greater proportions of the mass accumulation on the plates at higher field strengths.

Some basic theoretical calculations were carried out to determine the minimum specific charge required for a particle to be trapped on a plate. The apparatus was modelled as a simple area of uniform, horizontal electric field through which the particles fell. The top of the field was designated to be at $z = 0$, and particles were assumed to be initially stationary, 7 cm above the top of the field (at $z = 0.07$ m). With the parallel plates being 18 cm long, the base of the electrostatic field was thus at $z = -0.18$ m. The air drag, F_D, on the particles was represented by Stoke's law for spherical objects where

$$F_D = 6\pi r \eta V \qquad (7.1),$$

and r is the particle radius, η is the fluid viscosity (1.83×10^{-5} Pa s for air) and V is the particle velocity. Thus, for particle of mass m, subject to a downwards gravitational acceleration of strength g, the vertical equation of motion is

$$m\ddot{z} = -mg - 6\pi r \eta \dot{z} \qquad (7.2).$$

Substituting $\gamma = 6\pi r\,\eta\, m^{-1}$, and solving for initial conditions of $z = 0.07$ and $\dot{z} = 0$ at time, $t = 0$ gives

$$z = 0.07 + \frac{g}{\gamma^2}\left(1 - \exp(\gamma t)\right) - \frac{g\,t}{\gamma} \qquad (7.3).$$

With the use of a spreadsheet application, values of t were obtained for particles entering the electrostatic field (at $z = 0$) and leaving the electrostatic field (at $z = -0.18$). Thus, the time during which the particle was subject to a horizontal electrostatic force could be found. For an electric field strength of E (directed in the positive direction of x), and a particle of charge q, the horizontal equation of motion is

$$m\ddot{x} = qE - 6\pi r\,\eta\dot{x} \qquad (7.4)$$

which, when solved for initial conditions of $x = 0$ and $\dot{x} = 0$ at $t = 0$, gives

$$x = \left(\frac{qE}{m\gamma^2}\right)\left(\exp(\gamma t) - 1\right) + \frac{qEt}{m\gamma} \qquad (7.5).$$

During the experiments, the plates were separated by a distance of 38 mm. Thus, for the calculations, particles were considered to have been captured on a plate if they were deviated more than 19 mm from the fall-line (i.e. $x \geq 0.019$) during the time in which they were exposed to the electrostatic field. For a particle to be 'just captured' it would take the full duration of its time in the field to be deviated to $x = 0.019$. Thus, by using the value of t obtained from equation 7.3, the minimum charge held on a captured particle of a particular radius and density can be found from equation 7.5.

The results of the calculations are shown in Figure 7.16. For particles sufficiently small that inertial effects are negligible over the length scale of the apparatus, the minimum specific charge for capture is only a very weak function of particle diameter. However, when inertial effects become important (for single particles, this

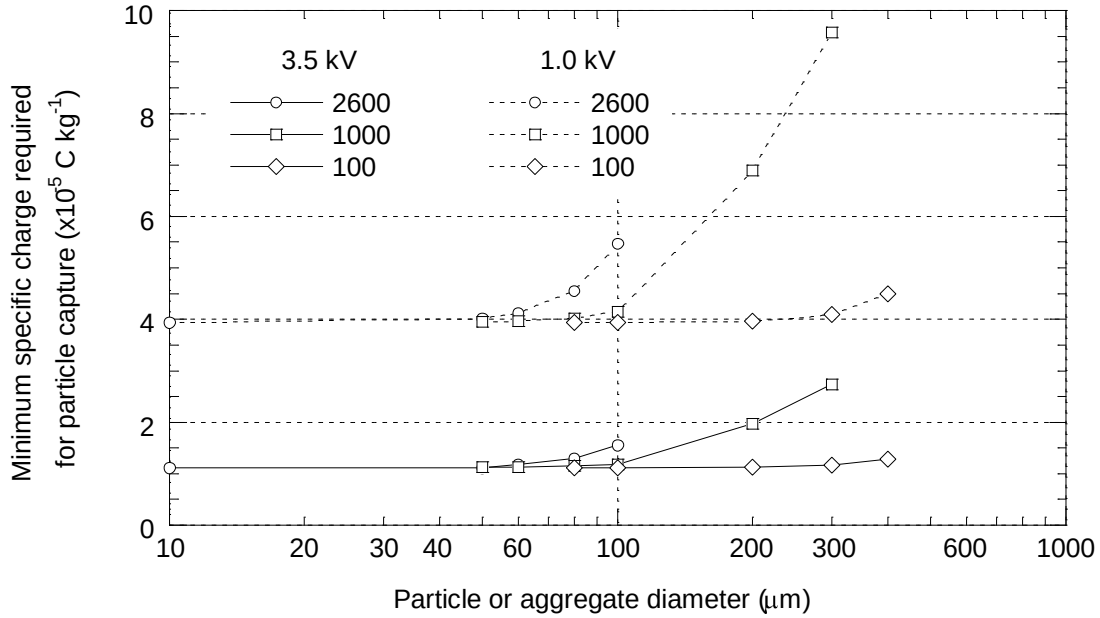

Figure 7.16 Theoretical calculation of the minimum specific charge of particles collected on the plates. Calculations have been carried out for plate potentials of 3.5 and 1.0 kV. Particles have been assumed to be represented by spheres of density 2600, 1000 and 100 kg m^{-3}. These values were chosen to represent a range between single solid silicate particles and very loosely packed aggregates.

is at diameters of about 60 μm), greater specific charges are required to trap larger particles.

The magnitude of the specific charge required for particle capture is about 10^{-5} C kg^{-1}. Thus, the fact that particles collect in the tray shows that either individual particle specific charges vary over two orders of magnitude (10^{-3} to 10^{-5} C kg^{-1}), or that many particles are scavenged by low specific charge aggregates. At low pressure, air drag can be neglected, and the minimum specific particle charge for particle capture is no longer a function of the particle radius. For a kV plate at 3.5 kV, the minimum specific charge is 3.7×10^{-5} C kg^{-1}. For lower kV plate potentials, this increases with the reciprocal of the electric field magnitude, and for a kV plate potential of 1 kV, the required specific charge is 1.3×10^{-4} C kg^{-1}. Thus, theory would predict higher specific charges to be measured at low kV plate potentials than at high kV plate potentials. Also, the difference should be greater under low pressure conditions that at atmospheric pressure. Neither of these predictions were observed in the results.

Visual observations suggested that increasing the separation field strength also increased aggregation. This was expected as it increased the transverse velocities of particles, giving them more opportunity to collide. It is possible that changes in the degree of particle aggregation were responsible for the trends observed in the specific charge data. If the electrostatic force between two equal and oppositely charged aggregate particles is modelled by point charges (of magnitude q) separated by one particle diameter d, then, from Coulomb's law, the magnitude of this binding force, F_{PP}, is given by

$$F_{PP} = \frac{q^2}{\pi \varepsilon_0 d^2} \qquad (7.6),$$

where ε_0 is the permittivity of free space (8.854×10^{-12} F m^{-1}). For a density of 2600 kg m^{-3}, and specific charge 10^{-3} C kg^{-1}, F_{PP} can be shown to vary between 10^{-13} and 10^{-9} N for particles of radius 1 to 10 μm. Each particle is also subject to a force qE exerted on it by the electric field, where E is the uniform electric field strength. Thus, particles would also be subject to a separating force of between 10^{-12} and 10^{-9} N. As a result, many of the aggregates produced may be disrupted (or be close to being disrupted) by the electric field within the apparatus. If disruption does not occur as the aggregates fall, it may be initiated by the impact exerted when the aggregate lands on the plate.

The increasing specific charge with separation strength may thus be interpreted as a result of an increasing fraction of oppositely charged particles being stripped off aggregates of the net polarity being collected. This is supported by the smaller increase observed under vacuum conditions, where aggregation was observed to be reduced. It is possible that a proportion of the general increase in the magnitude of specific charges recorded under vacuum conditions was a direct result of the reduced aggregation. It may also have been a factor in reducing the scatter in the results obtained at low pressure. The scatter in the results obtained at atmospheric pressure may represent the degree to which the experiment was sensitive to aggregation of the particles.

7.7 Summary

The measured specific charge held on particles produced by fragmentation of MSH and StV 519 samples varied between 10^{-5} and 10^{-3} C kg^{-1}. Charge magnitude has been shown to be a strong function of impact velocity and the number of impacts, and a weaker function of relative humidity.

With fewer than about 100 impacts, particles became more charged (by approximately an order of magnitude) as the number of impacts increased. This is thought to be a result of charge accumulation on the samples, but its effect on particles appeared to saturate after about 100 impacts.

Increasing the impact velocity (with solenoid voltages of between 6 to 13 V) also increased the recorded specific charge by about an order of magnitude. The impact velocity series of experiments produced some consistent trends within specific charge, collected mass ratio and particle size results. However, the trends are difficult to interpret because they could not be reproduced in other experiments or with other samples.

Experiments carried out over a range of separation electric field strengths have demonstrated the way in which particle aggregation must have also been a factor in the results. Some aggregates are thought to have been disrupted by the electric field at field strengths of about 100 kV m^{-1} (as used in the majority of experiments). Disruption may have occurred due to impact with the plate, rather than having taken place during free-fall. Differences in the aggregation occurring during experiments are thought to have been a major factor controlling the reproducibility of the results.

8. Charged volcanic plumes on Io

8.1 Introduction

This chapter presents theoretical work on Io's volcanic plumes and, using the experimentally produced particle charge magnitudes discussed in Chapters 6 and 7, investigates any effects that could be due to plume electrification. On Earth, the atmosphere dominates the dispersion of volcanic plumes and, during many eruptions, electrical discharges through the air produce spectacular lightning displays. Although blocks and bombs follow ballistic trajectories shortly after exiting the jet region of an eruption column, the paths followed by small particles are mainly controlled by gravity and the flow of the atmospheric air and volcanic gases. These influences obscure any movement due to electrostatic effects (with the exception of the formation of some aggregates).

On planets with little or no atmosphere, even small particles follow ballistic trajectories (after having exited the vent and effectively decoupled from the expanding gas stream), and the relative effect of electrostatic interactions may be enhanced. The lack of an atmosphere also permits greater amounts of charge to be held on particles, and decreases discharge rates on particles (if other factors are not considered). The only planet other than Earth known to have active volcanism is Io, and this chapter provides a brief introduction to this jovian satellite and the plumes which have been detected on it. Although the lack of atmosphere-linked convection on Io actually defines these eruptions as lava fountains, they have been commonly referred to as plumes and this convention will be adhered to here. The possible production of observable effects due to the electrostatic charging of plume particles is discussed.

One of the currently unexplained features of the plumes is spatial asymmetry, which can be observed in many images. Alternative theories to account for plume asymmetry are also discussed in section 8.4.

8.2 Volcanic plumes on Io

Io was first observed by Galileo Galilei on 7 January, 1610, along with two other jovian satellites. However, it was not until Witteborn *et al*. (1979) observed an intense, temporary brightening in Io's infrared spectrum between 2 and 5 μm during March 1979 that the presence of active volcanism was proposed. Witteborn *et al*. (1979) showed that the brightening could be modelled as produced by an isolated surface area at 600 K, surrounded by surface at the normal daytime temperature of 130 K. Peale *et al*. (1979) predicted the presence of widespread and recurrent volcanism on Io as a result of tidal heating of its interior. These developments occurred just prior to the arrival of the first satellite data from the jovian system, which were returned by the Voyager 1 mission (Stone and Lane, 1979a). Many of the images taken of Io, such as the one shown in Figure 8.1, proved Peale *et al*. correct by capturing spectacular volcanic plumes erupting from Io's surface (e.g. Morabito *et al*., 1979).

The two Voyager probes (Stone and Lane, 1979a, b) sent back a wealth of data on Io, on which much of today's knowledge of Jupiter's closest major satellite is based. Since then, further data have been obtained from surface based systems such as the Infrared Telescope Facility, Mauna Kea (Veeder *et al*., 1994), from the Hubble Space Telescope (Spencer *et al*., 1997) and, most recently, from the Galileo mission (McEwen *et al*., 1997, 1998a).

Figure 8.1 Two plumes observed on Io. This is the image which first revealed the presence of active extraterrestrial volcanism. One plume can be observed as a diffuse anomaly on the limb (the upper left), and has a maximum height of more than 260 km. The second can be observed on the terminator (the shadow between day and night), where the particles in the plume are scattering light from the rising sun. This image was taken by Voyager 1 on March 8, 1979, from a range of 4.5×10^6 km. NASA/JPL/Caltech. Image Cat. No. PIA 00379.

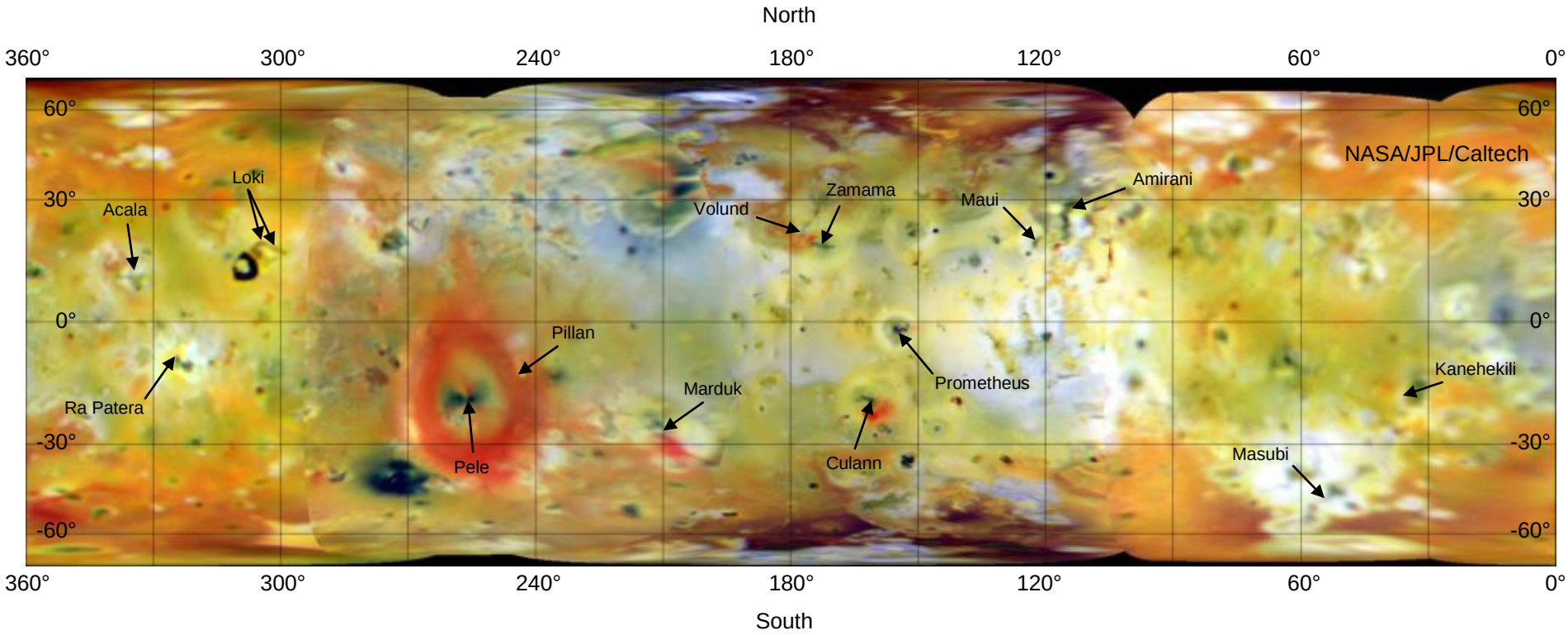

Figure 8.2 Surface map of Io. This false colour infrared composite was produced from Galileo images acquired in July and September, 1996. The area shown is 11,420 kilometres in width. The colour is composed of data taken in the near-infrared (756 nm), green and violet filters (shown as red, green, and blue respectively) of the Solid State Imaging (CCD) system. Images were obtained at resolutions ranging from 10 to 23 kilometres per pixel and phase angles from 4 to 55 degrees. The eruption sites of plumes which have been observed in Voyager and Galileo data are given. Image Cat. No. PIA00585.

Io is very similar in size to the Moon, with a radius of 1815 km and a mean density of 3.57×10^3 kg m^{-3}. The surface has a characteristic light orangey–yellow colour (Figure 8.2), revealing a sulphur-rich environment (Sagan, 1979; Pieri *et al*., 1984). Spectral analysis and experimentation has also shown the presence of an SO_2 frost in many areas (Smythe *et al*., 1979; Fanale *et al*., 1979; Hapke, 1989). A tenuous SO_2-dominated atmosphere has been detected at near-infrared (Pearl *et al*., 1979), millimetre (Lellouche *et al*., 1992) and ultraviolet (Ballester *et al*., 1994) wavelengths. The atmosphere is believed to be spatially patchy (Lellouche, 1996), with a maximum pressure the order of 10^{-6} bar (10^{-1} Pa). Its source is uncertain, but obvious candidates are sublimation from areas of SO_2 frost or produced directly from volcanism (Lellouche, 1996).

The density of the satellite and its surface topography (some areas are too high and some slopes too steep to be supported by sulphur compounds alone) suggest that Io has a silicate composition similar to that of the Earth and Moon (Clow and Carr, 1980; Moore *et al*., 1986). Thus, models of the internal structure of Io feature an Fe-FeS core and a silicate based 'mantle'. The detection of hot-spots on Io's surface at temperatures well above those of molten sulphur (Johnson *et al*., 1988) has demonstrated the presence of silicate-based volcanism. Models of thermal outbursts detected on the surface of Io (Blaney *et al*., 1995) imply that some effusive eruptions (with eruption rates of up to 3×10^5 m^3 s^{-1}) occur. Recent estimates of hot spot temperatures up to 2000 K indicate that some of the silicate lavas probably have exotic ultramafic geochemistries (McEwen *et al*., 1998b).

Just as enigmatic is the composition of the plumes detected in the Voyager and Galileo images. Nine plumes were observed in the Voyager 1 data, of which eight were still active four months later, and were observed again by Voyager 2 (Cook *et*

al., 1979; Strom *et al*., 1981). Since then, a further six have been identified from Galileo data (McEwen *et al*., 1998a). The eruption sites for these observed plumes are arrowed in Figure 8.2, and their estimated plume heights are given in Table 8.1.

Table 8.1 Observed plume eruptions on Io. See Figure 8.1 for a map of Io. Data have been collected from Strom *et al*. (1981), McEwen and Soderblom (1983) and McEwen *et al*. (1998a), with observations from V1, Voyager 1; V2 Voyager 2; G, Galileo; and HST, the Hubble Space Telescope. The plume types, Pele, Prometheus (Prom.) or hybrid are taken from McEwen and Soderblom (1983). Note that Pele has also been suggested as being a stealth plume (Johnson *et al*., 1995).

Site name	Position (Lat., Long.)	Observations	Maximum plume height (km)	Plume type
Pele	-18, 256	V1, G, HST	460	Pele
Loki (West)	+19, 305	V1, V2, G	400	Hybrid
Prometheus	-02, 152 to 154	V1, V2, G	77	Prom.
Volund	+23, 177	V1, V2, G	98	Prom.
Amirani	+24 to +28, 114	V1, V2, G	137	Prom.
Maui	+19, 122	V1, V2	148	Prom.
Marduk	-27, 210	V1, V2, G	90	Prom.
Masubi	+19, 304	V1, V2, G	50 to100	Prom.
Loki (East)	+17, 301	V1, V2, G	150	Hybrid
Culann Patera	-20, 160	G	<50	Prom.
Ra Patera	+08, 325	G	75	Prom.
Pillan Patera	-12, 244	G, HST	140	Hybrid
Kanehekili	-17, 036	G	50 to100	Prom.
Zamama	+18, 173	G	50 to 100	Prom.
Acala	+11, 334	G	200 to 300	Hybrid

From the information available in the images and the observed duration of the plume eruptions, they have been divided into two different types (McEwen and Soderblom, 1983). Type-examples, imaged over Pele and Prometheus, are shown in Figure 8.3. Pele-type eruptions were inferred to be short in duration (possibly the order of a week) but hot (~600 K) and violent, producing deposits up to 1500 km across. They contrast with the Prometheus-type eruptions which are longer lasting (e.g. constant over the two Voyager missions), less violent, (producing deposits 200 to 600 km across) and colder (~400 K). Pele-type plumes produce dark surface deposits and tend to be concentrated in the sub-jove region (between longitudes 240 and 360°), whereas the Prometheus-type are concentrated at low latitudes and produce ultraviolet bright deposits.

Theories concerning the erupted material involve silicates driven by sulphur or SO_2 volatiles (or both), or the volatiles alone without a silicate component (Kieffer, 1982). McEwen and Soderblom (1983) favoured a silicate–sulphur model for the large Pele-type plumes and a sulphur–SO_2 model for the smaller Prometheus-type plumes. More recently, a third type of plume has been proposed, consisting of gaseous SO_2 alone, produced by high entropy eruptions from the intrusion of silicate magma into buried SO_2 deposits (Johnson *et al.*, 1995). Due to the lack of solid phases in such a plume, these eruptions would have been undetectable by the Voyager instruments, and have thus been termed ‘stealth’ plumes. Evidence for the presence of these plumes may be obtained by Galileo from observations of localised auroral phenomena or localised albedo changes or from ionospheric measurements from radio occultations (Johnson *et al.*, 1995).

For some of the plumes observed, particle size and total mass estimates have been carried out. In order to do so, the optical properties of the plumes have been calculated

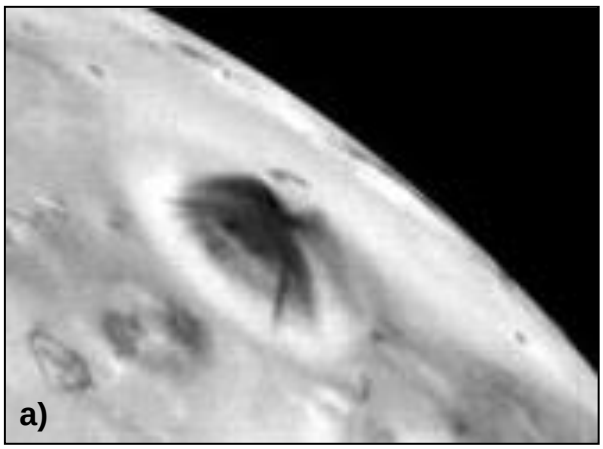

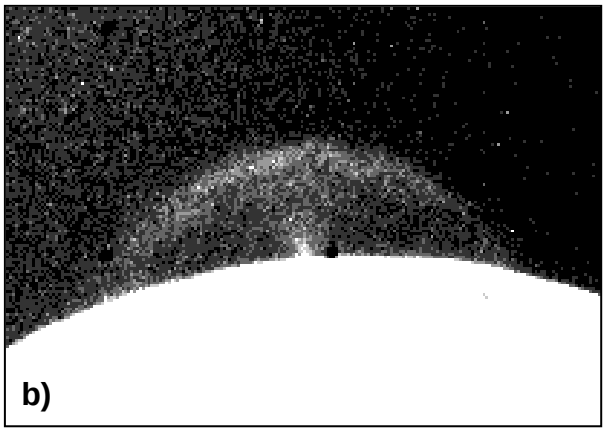

Figure 8.3 Voyager images of plumes over Prometheus and Pele. **a)** This image shows the plume over Prometheus to be composed of discrete jets of ejecta. Note that, despite the jets, the deposits form a symmetrical ring around the vent. The filamentary nature of the plume and sharp changes in the curvature of the ejecta streams suggest that, to some degree, aerodynamics control the particle distribution (Cook *et al*., 1979). NASA/JPL/Caltech. Image Cat. No. PIA00373 **b)** A faint plume over Pele, approximately 300 km high, as imaged by Voyager 1 (ultraviolet filter). The bright envelope has been interpreted as a shock front within the plume (Strom *et al*., 1981). FDS 16368.50

by representing them as gas columns (Spencer *et al*., 1997), dispersions of very small particles scattering in a Rayleigh-like fashion (Collins, 1981) and particles which are large with respect to the wavelength of light (Wilson and Head, 1981). Collins (1981) modelled a plume imaged over Loki as a central core of particles of diameter 2 to 200 μm, and a considerably more massive population of particles 0.02 to 0.002 μm in diameter extending up to an altitude of about 200 km. The smaller particles were shown to account for about 10^8 kg of the airborne mass (Collins, 1981), which is very similar to the mass derived by Pearl *et al*. (1979) who used an SO_2 gas model.

The shapes of the plumes have been modelled using two different approaches (Cook *et al*., 1979); a 'ballistic' model in which particles are assumed to be sufficiently large to disconnect rapidly from the expanding driving gas flow, and an 'aerodynamic' model where particles are small enough to be essentially locked to the gas flow despite the low pressures. The aerodynamic model was favoured by Cook *et al*. (1979) because it could account for some of the sharp bends observed in the individual dark filaments of a plume erupting from Prometheus (Figure 8.3a). However, due to its simplicity, the ballistic model was favoured by Strom *et al*. (1981), for all except the Pele plume, which exhibited a bright outer shell thought to represent a shock front (Figure 8.3b). Wilson and Head (1981) showed that, given certain eruption conditions, a bright outer shell could be reproduced by a ballistic model.

Neither of these models account for the asymmetry which can be observed in many of the plume images (Figure 8.4). Some of these images are probably due to observing a filamentary plume from the side; however, many of the deposits produced are represented by symmetric annuli located around the vent (Figure 8.5a). On the other hand, the Pele plume (one of the more symmetric plumes observed) appears to

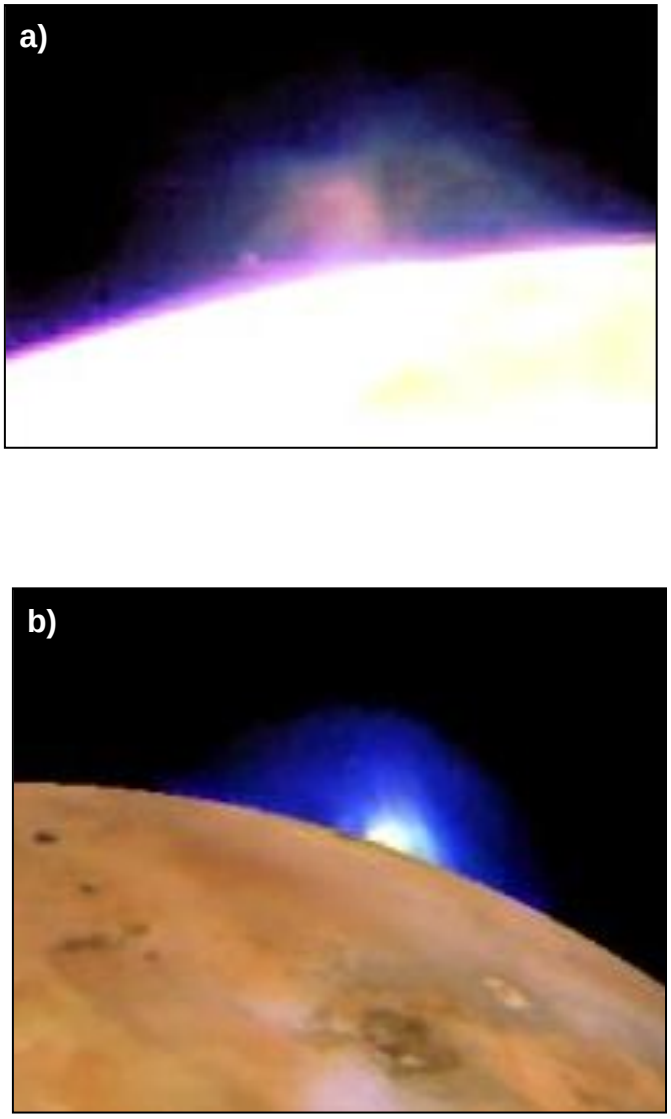

Figure 8.4 Asymmetry in plumes viewed on the limb. **a)** A plume imaged over Pillan Patera approximately 140 km high, observed by Galileo. Cat. No. PIA00703. **b)** A plume over Loki, over 200 km high, as viewed by Voyager 1. Cat. No. PIA00010. NASA/JPL/Caltech.

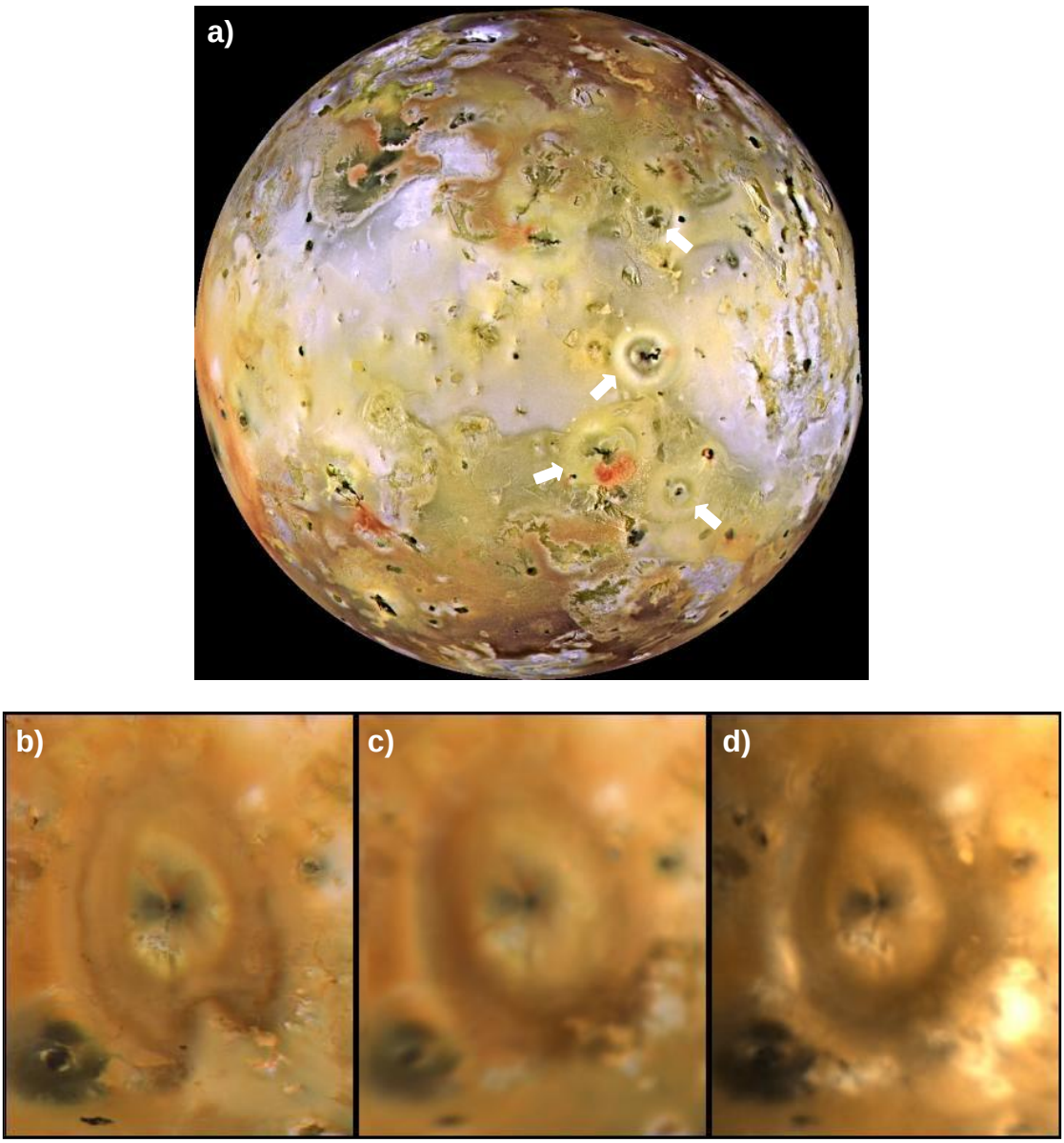

Figure 8.5 Symmetric and asymmetric deposits. Several symmetric deposits have been arrowed in the full-disc Galileo view shown in **a)** (Cat. No. PIA00583). They have been produced by Prometheus-type eruptions. The other images were obtained by **b)** Voyager 1 (1979), **c)** Voyager 2 (1979), and **d)** Galileo (1996) and demonstrate the changes of the asymmetric deposits around Pele. The shape of the outer deposits has been ascribed to asymmetry of the vent (Strom *et al.*,1981). Presumably, some sort of 'vent clearing' eruption occurred between the two Voyager images which covered the notch in the outer ring. Cat. No. PIA00717. NASA/JPL/Caltech.

have produced highly asymmetric deposits (Figure 8.5b, c, and d) which were distinctively heart-shaped in Voyager 1 images (Figure 8.5b).

8.3 Possible electrical effects

For this section it will be assumed that some of the plumes on Io do contain silicate particles, which are produced as a result of magma fragmentation. Terrestrial volcanic plumes are mainly produced by the explosive eruption of silica-rich magmas. However, on Io, low viscosity, silica-poor magmas are much more likely (McEwen *et al*., 1998b). On Earth, the fragmentation of basaltic magma during lava fountaining is predominantly not a brittle process due to its low viscosity. As a result, although explosive basaltic eruptions can form fountains 300 m high (Head and Wilson, 1987), these are not known to produce the extensive electrical effects observed during the explosive eruption of silica-rich magmas. Erupting mafic magma into a relatively low pressure environment will increase the degree of fragmentation and may have commonly produced convective plumes on Mars (Mouginis-Mark *et al*., 1992). Also, on Io, up to 25 % of the eruptive mass may be entrained as cold volatiles (S or SO_2) before eruption (L. Wilson, *pers. comm.*), thus rapid chilling of the magma may make brittle fragmentation much more common. For this reason, the charge results obtained in Chapters 6 and 7, which are based on brittle fragmentation, may be applicable.

8.3.1 Electrical discharges

Electrical discharges (lightning) during terrestrial eruptions are produced by the catastrophic breakdown of air as the local electric field exceeds the atmospheric breakdown limit (approximately 3×10^6 V m^{-1}). Other observable effects such as

corona glows are also due to strong electric fields and the presence of the atmosphere. A plume on Io erupts into a near-vacuum so, even if it is electrically charged, the production of large-scale terrestrial-style lightning is unlikely within the bulk of the plume. However, if the sub-surface pressure regimes of Io's eruptions are controlled by choked flow at the vent, then conditions within the conduit and just above the vent may to be similar to those of terrestrial eruptions. On Earth, many plume-induced electrical discharges are observed to occur close to the vent, so this may also be a feature of eruptions on Io.

Optical phenomena associated with electrical discharges occurring at low pressure are observed on Earth. High altitude observations of thunderstorms have recorded luminous features which are produced above storms, in association with lightning flashes. Two types of phenomena have been detected: blue jets (Wescott *et al*., 1995), which ascend up to 50 km above the thunderstorm top; and red sprites (Sentman *et al*., 1995) which occur in the mesospheric D region above the thunderstorm (at about 50 km altitude), and ascend to the ionosphere at up to 100 km altitude. Pressure decreases rapidly from about 10^{-2} bar (10^{3} Pa) at 30 km altitude to about 3×10^{-7} bar (3×10^{-2} Pa) at 100 km altitude (Craig, 1965). These values include part of the pressure range estimated for areas on Io (Lellouche, 1996). The effects are thought to be due to ambient electron heating, ionisation of neutrals and excitation of optical emissions as a result of quasi-electrostatic fields that exist immediately after some large lightning discharges (Pasko *et al*., 1997). Thus, on Io, discharges close to the vent could possibly produce visible effects in other parts of the plumes. However, the charge magnitudes required to model the terrestrial sprites are relatively large (e.g. 100 to 300 C; Pasko *et al*., 1997) and these may not be reached during eruptions.

Discrete optical anomalies attributable to electrical discharges within Io's plumes have yet to be captured in images. However, eclipse observations of plumes have demonstrated that they do glow in the dark (Figure 8.6). This has been attributed to the fluorescence of sulphur and oxygen ions created from SO_2 molecules split by energetic particles in the jovian magnetosphere. The molecules could also be split by particles accelerated in plume-generated electric fields (and thus the effect could be considered to be a type of glow discharge).

8.3.2 Deposit asymmetry

Of the two models which been used to explain the shapes of the imaged plumes (ballistic and aerodynamic, Cook *et al*., 1979), neither have been used in an attempt to produce the asymmetry observed in some deposits (for example, those around Pele, Figures 8.3b, 8.3c and 8.3d).

If particles making up a plume were electrically charged, interaction with a magnetic field during their flight could produce asymmetry in the deposits. This possibility was investigated using a simple ballistic plume model and a uniform magnetic field. Within a magnetic field, the motion of a charged particle is governed by the equation

$$m\mathbf{g} + q\mathbf{B} \times \mathbf{u} = m\dot{\mathbf{u}} \qquad (8.1),$$

where **g** is the acceleration due to gravity, **B** is the magnetic flux density and **u** is the particle's velocity. The particle's mass and net charge are given by m and q, respectively. In Figure 8.7 the landing positions of ejected volcanic particles are shown for this simple simulation. The particles were launched with a speed of 600 m s^{-1} at increments of 5° (up to 45°) from the vertical, and at intervals of 12.5° of

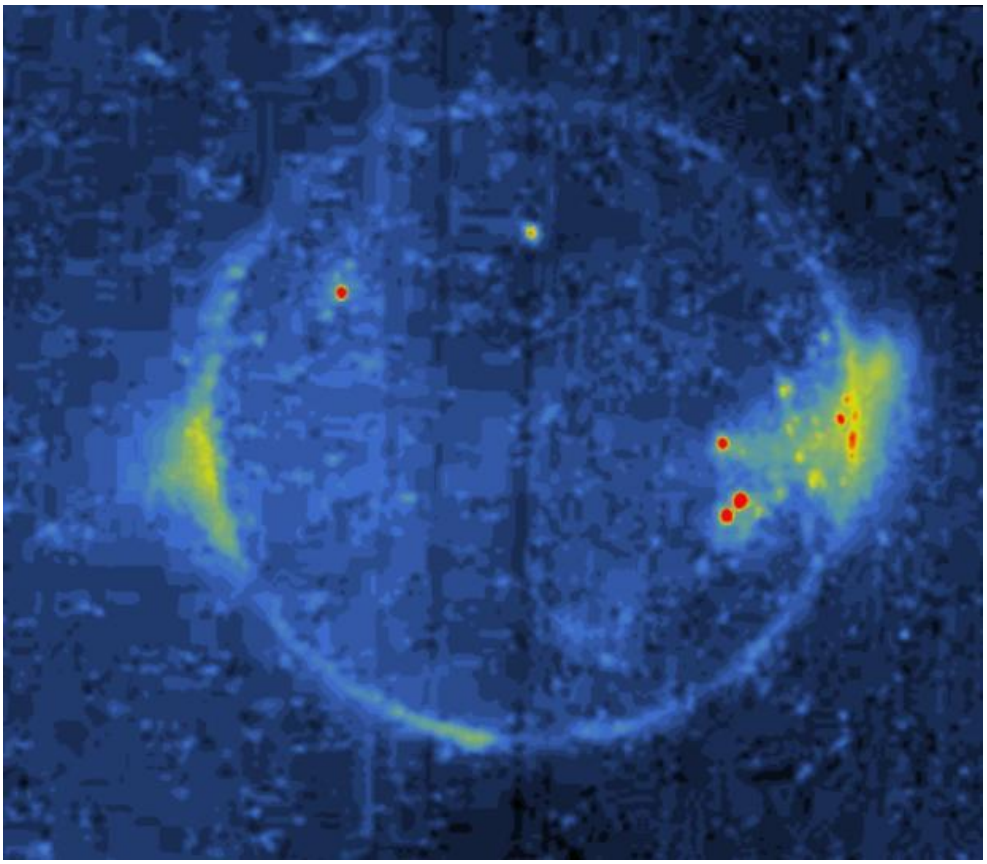

Figure 8.6 Night glow from Io's plumes. This image was acquired through a clear filter, while Io was in eclipse. The most intense features are red, while glows of lesser intensity are yellow or green, and very faint glows appear blue in this colour-coded image. The small red or yellow spots mark the sites of surface hot-spots. Extended diffuse glows are present on both equatorial limbs. The glow on the left is over Prometheus, but is nearly ten times the height of the plume over Prometheus as viewed in reflected light. The glow on the right is not correlated with a known volcanic plume. These extended glows indicate that gas (or small particles) reach much greater heights than otherwise thought, and that some sort of energetic particle reactions are occurring within them. Cat. No. PIA00704. NASA/JPL/Caltech.

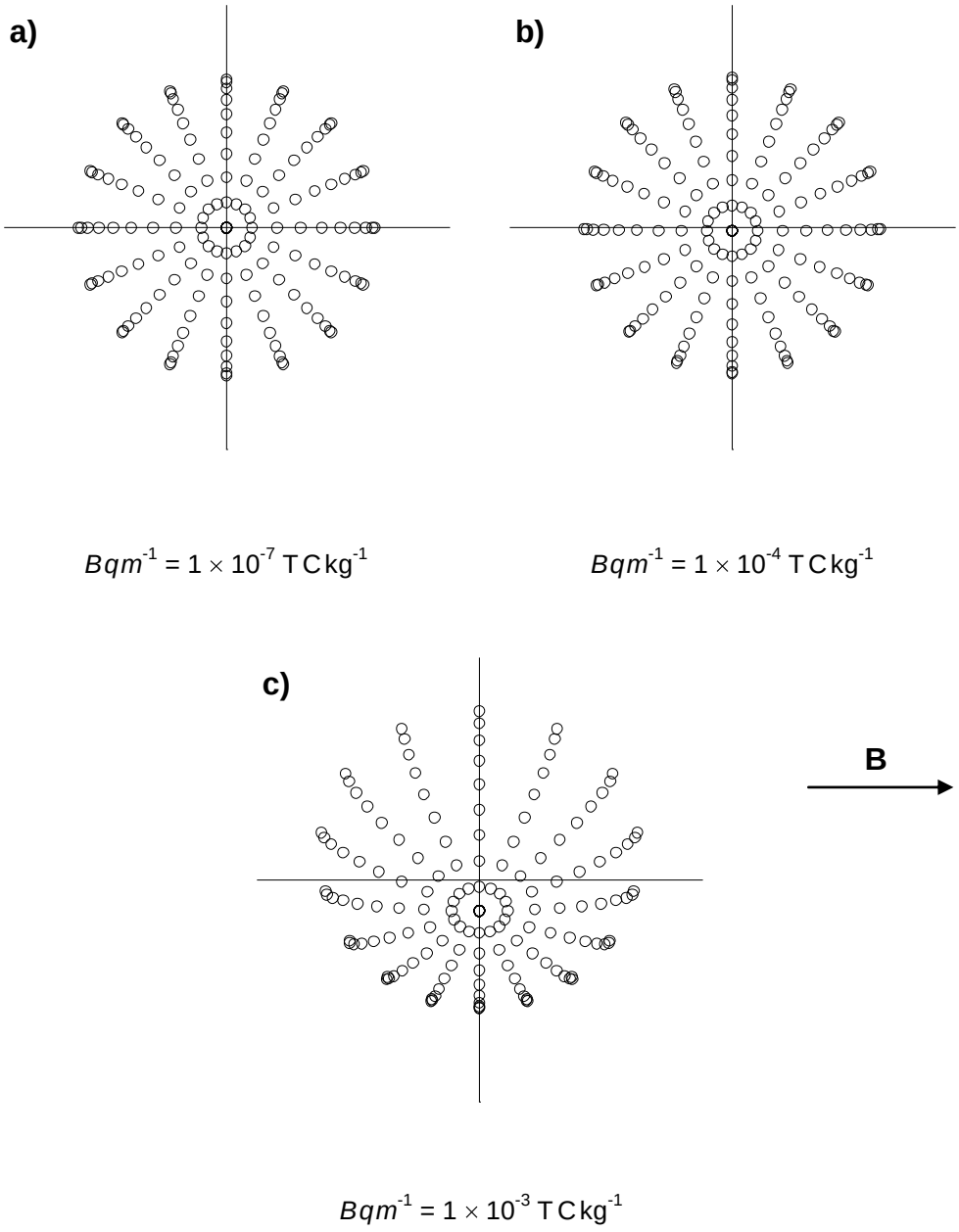

Figure 8.7 Landing positions of charged particles subject to electromagnetic interactions. The diagrams represent plan views of particles erupted at 600 m s^{-1} from a vent located at the origin. The direction of the magnetic field **B**, is shown by the arrow. The influence of this magnetic field on the particle landing positions is given by Bqm^{-1}, the product of the magnetic field strength and the particles' specific charge.

azimuth. The steady, uniform magnetic field (of magnitude B) was oriented horizontally in the direction of the x axis.

The effect of the electro-magnetic interaction on the equations of motion for particles can be represented by the quantity Bqm^{-1} (the product of the magnetic field density and the particles' specific charge). In Figure 8.7a, for $Bqm^{-1} \approx 0$, the symmetric distribution produced by particles following 'normal' ballistic trajectories can be seen. In Figure 8.7b, $Bqm^{-1} = 10^{-4}$ T C kg^{-1}, and only a very slight perturbation from the symmetric pattern is produced. With $Bqm^{-1} = 10^{-3}$ T C kg^{-1} (Figure 8.7c), considerable asymmetry can be observed.

Note that, for these simulations, any effect the plume had on the magnetic field (or the production of an electric field) was neglected, and the magnetic field did not vary with height. Any effects due to an external electric field and particle interactions with the environment were also neglected. Only particles of one value (and sign) of specific charge were considered within one model.

Calculations from Galileo magnetometer data (Kivelson *et al*., 1996a, b) have suggested that Io does possess an internal magnetic field. Although this is not the only interpretation of all the data (Frank *et al*., 1996; Neubauer, 1998), a possible surface equatorial field strength of about 1500 nT (Khurana *et al*., 1997) can be inferred. Thus, using this value, in order to obtain $Bqm^{-1} = 10^{-3}$ T C kg^{-1}, the specific charge on particles would be required to be approximately 10^{0} C kg^{-1}, which is three orders of magnitude greater than was measured during the particle charge experiments (Chapter 7). Despite the unknown eruption conditions, it is thought unlikely that silicate particles could be charged to this degree on Io.

8.3.3 Plume asymmetry

Many more plumes have been observed to be asymmetric than deposits and, in order to investigate the way in which asymmetry in the plumes could be generated by electromagnetic interactions, the model discussed in section 8.3.2 was extended to allow the particles to be tracked during their flight. This allowed the particle number density at any point in space to be calculated. For simplicity, and to maximise any observed asymmetry, the model was altered from the circular geometry of a point source, to represent a cross-section through an elongate plume erupting from a linear fissure vent. Figure 8.8 shows results from this model, with the darker shaded regions representing areas of higher particle number density. The plume was simulated by erupting particles into a vertical plane at 600 m s^{-1} and at a constant flux per angular distance, for angles up to 40° from the vertical. The magnetic field was directed into the plane of the paper.

With a near-zero value of $B\,q\,m^{-1}$ (Figure 8.8a), the plume appears essentially symmetric. No obvious visual differences can be observed for $B\,q\,m^{-1} = 10^{-4}$ T C kg^{-1} either (Figure 8.8b), but asymmetry becomes detectable for $B\,q\,m^{-1} = 10^{-3}$ T C kg^{-1} (Figure 8.8). This confirms the results of the particle landing position simulations (section 8.3.2). While the asymmetry produced does resemble that observed in images, as discussed in section 8.3.2, the value of $B\,q\,m^{-1}$ required to obtain this is believed to be unrealistically large.

8.3.4 Particle aggregation

Particle aggregation is ubiquitous within terrestrial explosive volcanic plumes (Sparks *et al*., 1997) and may be a very important effect of plume electrification on Io.

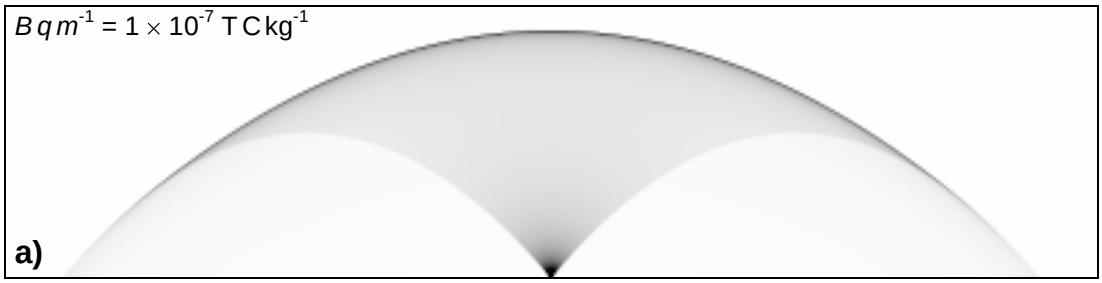

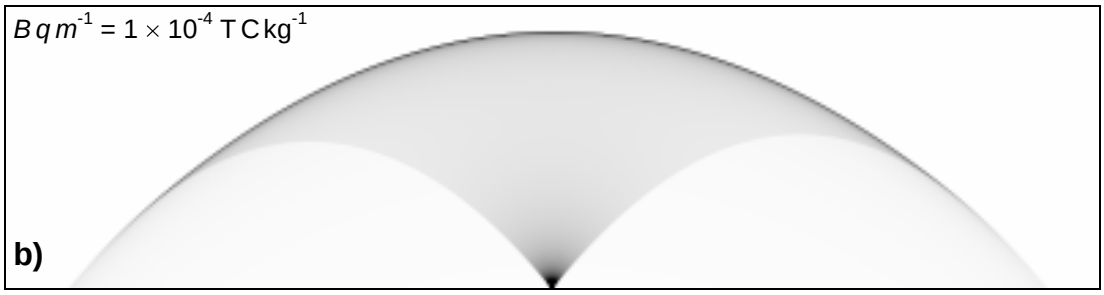

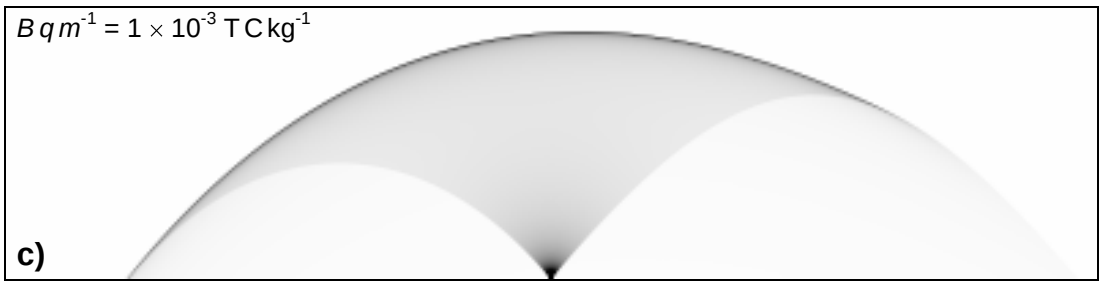

Figure 8.8 The effect of electromagnetic interactions on plumes. The images represent particle number densities in a cross-section through a plume produced from a linear fissure eruption. The particles have been erupted (from a line source) at 600 m s^{-1}, and each image represents an area of 110 × 440 km. The magnetic field is perpendicular to the page and directed into the paper. See text for further details.

Due to the lack of a dense atmosphere on Io, aggregation would have very little influence on the fall velocity of pyroclasts; however, it could have a great effect on image interpretation. Several estimates have been made of plume masses (Collins, 1981; Spencer *et al*., 1997) and of the erupted mass flux for these eruptions (Wilson and Head, 1981; James and Wilson, 1998) using optical data acquired from images. Where these calculations involve particles (rather than exclusively gas), they inevitably require particle size, number density and scattering data. All of these parameters would be altered by particle aggregation. The optical density of an aggregated particle population is much less than that of an identical, but completely dispersed, population. Thus, current calculations of particle numbers (and thus plume mass or eruption mass flux) could be invalid if aggregation played a significant role, and would be extremely difficult if the degree of aggregation was thought to vary widely within one plume.

The net ash and particle charge experiments (Chapters 6 and 7) demonstrated that visible particle aggregation was much reduced under low pressure conditions compared to at atmospheric pressure. However, it is believed that aggregates were still produced under vacuum, but that they were generally much smaller (less than 100 μm in diameter) than those produced at atmospheric pressure (Chapter 7). Aggregation has also been observed during experiments carried out under microgravity conditions onboard the Space Shuttle (Marshall, 1998), using particles charged only as a result their of initial disruption by a gas impulse. The formation of irregular clusters and elongate particulate filaments occurred rapidly after particle velocities from the initial dispersion procedure had ceased. The particles produced during explosive eruptions are likely to hold more charge than those used during these experiments, so

aggregation would be expected to be even more effective within plumes. Thus, there is little reason not to expect particle aggregation within Io's plumes.

8.3.5 Particle escape

Space-borne dust streams, probably of jovian origin, have been detected by both the Ulysses and Galileo spacecraft (Grün *et al*., 1993, 1996), and Io's plumes have been proposed as their source (Horanyi *et al*., 1993; Ip, 1996). Dust ejected from Io has also been proposed as responsible for the production of Jupiter's rings (Morfill, 1996). The dust particles act as a source of projectiles which collide with small orbital bodies such as Adrastea and Metis at the edge of the ring. The visible ring is then generated from the micron-sized ejecta released during these impacts. Particle sizes (of diameters between 0.002 and 0.02 μm) deduced for the outer regions of the Loki plume (Collins, 1981), suggest that volcanic particles from Io are suitable candidates for both these projectiles (Morfill, 1996) and for those detected as dust streams (Horanyi *et al*., 1993). Collins (1981) considered these small particles, which dominated the Loki plume, to be condensed 'snowflakes' of volcanic volatiles (SO_2).

A mechanism for the removal of this type of particle (with diameters less than 0.02 μm) from Io's gravitational field was considered by Ip (1996). After the electrostatic charging of a particle within the plasma environment of Io's ionosphere, Ip (1996) calculated whether or not electric and electromagnetic forces on the particle would allow it to escape. It was found that small particles (of diameters less than 0.02 μm) could escape even when only charged to surface potentials of about -0.5 V, and larger particles (of diameters about 0.2 μm) could only escape if charged to surface potentials of -10 V. The particle charge experiments (Chapter 7) produced particles

with maximum specific charges of the order 10^{-3} C kg^{-1}. The surface potential V_s, of these particles can be calculated from

$$V_s = \frac{q}{4\pi\varepsilon_0 r} \tag{8.2}$$

where ε_0 is the permittivity of free space (8.854×10^{-12} F m^{-1}), q is the particle charge (assuming a particle density of 2600 kg m^{-3}) and r is the particle radius. Over the range of radii investigated by Ip (1996), it can be shown that this degree of charging (10^{-3} C kg^{-1}) would not be sufficient to enable particles to escape. Thus, silicate particles are unlikely to be ejected but, if fractoemission does occur during fragmentation, then the production of ions may affect the initial charge of condensing volatiles.

8.4 Other factors influencing plume symmetry

If electromagnetic interactions are unlikely to be the reason behind the intriguing asymmetry observed in the plume images from Io, then other factors must be responsible. However, images of plumes represent only 'snap-shots' in time, but deposits represent the product of more time-averaged conditions. Thus, considering that many deposits are relatively symmetric, it is possible that observed brightness differences within plumes represent either brief, transient variations (which could produce undetectable variations within deposits), or are just an instantaneous image of a continuously varying phenomenon (with the deposits representing the average conditions). Each possible asymmetry process should then be assessed for variability with time as well as absolute magnitude.

8.4.1 Tidal effects

Io is subject to tidal forces from Jupiter just as the Earth is subject to tidal forces from the Moon. The magnitude of these tidal forces, combined with Io's orbital resonance with the other Jovian satellites, generates the heat sufficient to produce the extensive volcanism observed (Peale *et al*., 1979). As is the case for the oceans on Earth, the plumes on Io will be affected by these tidal forces. In order to obtain an estimate of the magnitude of the tidal forces, Io will be assumed to be spherical and the effect of Jupiter's gravitational field alone will be considered.

At any point on Io, the tidal force is produced by the difference in the gravitational field from Jupiter at that point and the field at Io's centre of mass (which is responsible for maintaining Io's orbit). The tidal force, F_T, on a particle of mass m at a distance r from the centre of Io (in the direction of Jupiter) is given by

$$F_T = G\,m\,M_J\left(\frac{1}{(R-r)^2} - \frac{1}{R^2}\right) \qquad (8.3),$$

where G is the universal gravitational constant (6.67×10^{-11} N m^2 kg^{-2}), M_J is the mass of Jupiter (1.9×10^{27} kg) and R is the distance between the centres of mass of Jupiter and Io (4.22×10^5 km).

For a particle 300 km above the surface of Io, in line with the centres of gravity, $F_T = 7.2 \times 10^{-3}\,m$, which represents approximately 0.5 % of the gravitational force from Io at that point. Thus, the particle motion (relative to Io) will be dominated by Io's gravity, and any plume asymmetry due to tidal effects will be too small to be detected in images.

8.4.2 Consideration of angular momentum

During Io's orbit, it maintains the same face towards Jupiter at all times. In order to do so, Io rotates on its own axis with the same 1.77 day period as its orbit. This rotational motion has not been accounted for in any previous plume models. On Earth, the Corriolis effect is well known for distorting fluid motion, and is a consequence of conservation of angular momentum. Thus, if the angular momentum of particles in a plume on Io is conserved, the plume will also appear distorted. The effect can be calculated by solving the orbital equations for erupted particles (L.Wilson, *pers. comm.*), and has the greatest influence on high plumes located on the equator.

For any particle, the degree of deviation from a simply calculated ballistic trajectory is a function of the particle flight time and maximum altitude. Thus, the particles 'deviated' the most are those which have been erupted vertically out of the vent. However, for an equatorial plume 300 km high, a vertically erupted particle is calculated to land only a maximum of 26 km from its 'simple' landing position (on the vent). When this is compared with the maximum horizontal distance to which a particle could be ejected (about 600 km) for a plume of this size, then the maximum apparent distortion is shown to be less than 5 % of the plume radius. For any one plume (i.e. at a fixed vent location), the effect would not vary with time due to the constant period of rotation. Thus, any asymmetry inferred in a plume to be due to angular momentum considerations should also be reflected in the plume deposit.

8.4.3 Vent asymmetry

If particles are erupted with an asymmetric distribution, this could readily explain many of the asymmetries observed in plume images. The main argument against this is that for long duration eruptions (such as months to years, as on Io), conduit erosion

would be expected to have removed any irregular features that could cause asymmetry. However, if plume shapes are dominated by decompression in deep craters (rather than the shape of the vents themselves), it is more feasible that irregularities could be preserved. Alternatively, steady erosion could continuously reveal further irregularities.

Kieffer (1982) suggested that complex plumes showing filamentary structures (e.g. over Prometheus, as imaged in Figure 8.3a) could be the product of eruptions from shallow craters as over-pressured jets. These irregular features would be formed by complex decompression regimes and Mach disk shocks within the plume. The directional-steering of over-pressured jets has been demonstrated for inclined vent openings for some terrestrial eruptions (Lagmay *et al*., 1998). Thus, vent and crater geometry have the potential to produce asymmetric plumes, and the effect of continuous erosion during the eruption could produce an evenly distributed deposit.

8.4.4 Optical effects

The images of plumes recorded in data returned from the Voyager and Galileo missions are produced by light being scattered by particles (or gases) within the plumes themselves. The colour and brightness of these images are complex functions of the plume's physical and chemical properties, the viewing and illumination geometry and the response of the satellite sensors. In order to investigate the effect of changing the viewing and illumination geometry, the optical properties of particulate plume models similar to those described in section 8.3.3 were calculated. Particles were assumed to erupt from a circular vent (modelled as a point source) with a constant volume flux per unit solid angle within a cone of ejection angles. This generated an array representing a 3-D distribution of particle number densities within

the plume. By considering the particles to be homogenously distributed, randomly oriented, equant and large compared to the incident wavelength, the transmission T (Hapke, 1986) of each spatial element could be calculated as

$$T = \exp\left(z \frac{n\sigma}{F} \ln(1 - F) \right) \tag{8.4}$$

for light incident orthogonal to any face, and where z is the depth of the element, n, the particle number density, σ, the average particle extinction cross section, and F, the volume fraction filled by particles.

A relative brightness image can then be constructed by considering the reflected light from an element as 1-T, and summing the light transmitted or reflected along the relevant ray path. This effectively assumes that all light which falls within the extinction cross section of any particle is reflected back along the incident direction, and thus ignores any scattering, absorption or reflection in other directions. Light scattered into a ray path from the surrounding elements is also neglected. This simple approach prevents actual brightness values from being given, but does allow the relative brightness across an image to be calculated.

Figure 8.9 shows two images of symmetric plumes constructed by this technique. The plumes have been illuminated by a light source located horizontally to the right of the plume representing a phase angle (the angle between the observer, the plume and the light source) of 90°. The properties of the plumes are identical in every respect with the exception of the volume flux, and the results can be compared with the symmetry of the image in Figure 8.9a which represents light reflected by a plume illuminated from directly behind the observer.

At a volume flux of 100 $m^3 s^{-1}$, the plume has a low optical density, allowing a

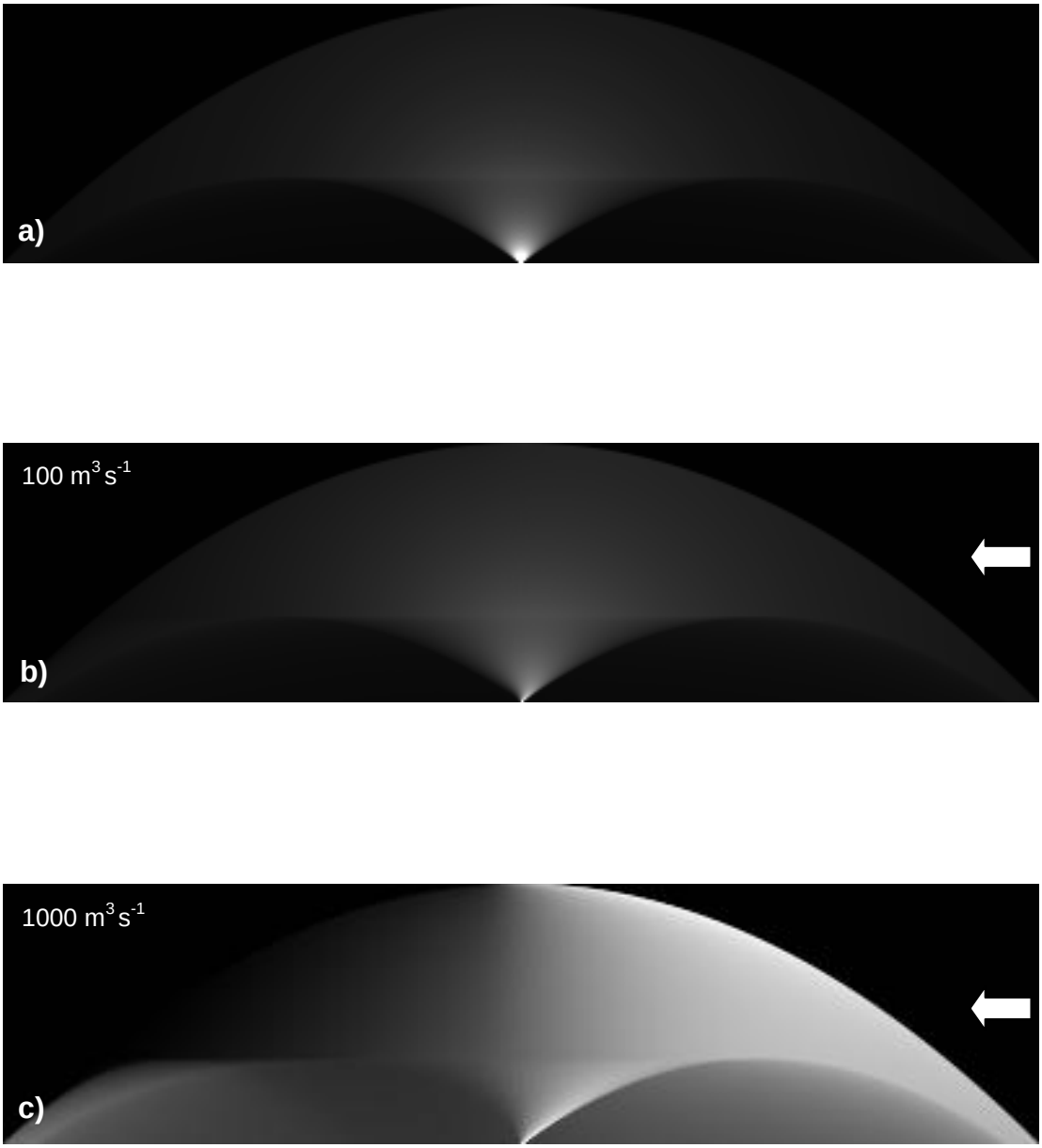

Figure 8.9 The effect of self-shadowing on the observed symmetry of plumes. **a)** A symmetric, circular plume observed with a zero phase angle (the plume is illuminated from behind the observer). In **b)** and **c)**, symmetric, circular plumes are illuminated with a phase angle of 90° (i.e. from the direction arrowed). **b)** With a volume flux of 100 $m^3 s^{-1}$, the bulk of the plume still appears symmetric due to the low optical density producing little internal shadowing. **c)** With a volume flux of 1000 $m^3 s^{-1}$, the increased optical density produces sufficient internal shadowing to make the plume appear asymmetric.

near-constant light intensity to be available throughout the plume for reflection into the direction of the observer. Thus a near-symmetric image is produced. By increasing the volume flux, and consequently also the optical density of the plume, the degree of internal shadowing is increased. The amount of illumination reaching the left hand portion of the plume is much reduced, and it appears darker, thus generating an asymmetric image.

8.5 Summary

It is highly likely that silicate particles within the volcanic plumes of Io are electrically charged, although currently this cannot be directly detected. Indirect evidence for the electrification of Io's plumes could possibly be obtained from images by the observation of luminous discharge phenomena.

The electrostatic aggregation of particles is also likely to occur, and may be an important effect when considering image interpretation. Many of the plumes are high enough to enter the plasma environment of Io's ionosphere, and this may dominate charging effects once particles have reached this altitude. Although aggregation will not be directly observable, it could pose difficulties when attempting to extract particle and mass data for plumes from their optical properties.

Simulations of plumes subject to electromagnetic interactions have shown that any asymmetry due to the presence of a magnetic field is unlikely to be detected in satellite images. The observed plume asymmetries are also unlikely to be produced by tidal or angular momentum effects, but may be a consequence of crater morphology or shocks within complex decompression regimes. Non-simple viewing geometries have been shown to be capable of generating asymmetric images of symmetric plumes.

9. Discussion and conclusions

9.1 Introduction

This chapter draws conclusions from both the experimental results and the atmospheric potential gradients measured at Sakurajima volcano. The data collected at Sakurajima are briefly reviewed in context with previous work and the implications for potential gradient measurements as a plume monitoring tool are discussed. Other plume detection techniques are also summarised and the particular areas where potential gradient monitoring could be most useful are identified. Brief reviews of the results and interpretations of the experimental work are given and their applications to processes within plumes are then discussed.

9.2 Atmospheric potential gradients at Sakurajima volcano

The results of potential gradient monitoring at Sakurajima are given in Chapter 4. During the monitoring period, a variety of plumes were produced, from white plumes of condensing gases to brown, particle-rich plumes produced by Vulcanian explosions. The data recorded support the previous conclusions made at Sakurajima (Lane and Gilbert, 1992; Lane *et al*., 1995) that sedimenting ash holds a net negative charge, plumes of condensing gases alone are only negligibly charged (thus are undetectable), and that the charge distribution within particle-rich plumes can be represented by a positive-over-negative dipole.

This positive-over-negative charge distribution has previously also been inferred from potential gradient measurements carried out at other volcanoes (e.g. Surtsey, Anderson *et al*., 1965; Unzen, Miura *et al*., 1996), but others have found evidence for

negative-over-positive charge separation (e.g. at Aso, Hatakeyama and Uchikawa, 1952). Miura *et al*. (1995) gave evidence that the ash from Sakurajima does not always hold a net negative charge, and can be charged net positively. No positive perturbations were detected during periods of ashfall in October or November 1996, thus no evidence was recorded for any net positively charged ash.

Modelling the potential gradients recorded during one Vulcanian explosion (14 November, 1996; Figure 4.31), and comparing the inferred charges with previous results (Lane *et al*., 1995) suggests that (for these small eruptions) the amount of separated charge is a strong function of the size of the eruption. Other data, collected during days of continuous gentle ash emission, demonstrate the sensitivity of the potential gradient monitoring technique by detecting even low ash concentrations dispersed over a monitoring site. The results from 10 and 13 November, 1996 (Figures 4.28 and 4.30) showed that ash held sufficient charge to be detected even when it had not been produced by a noticeably explosive eruption.

9.2.1 Charge distribution

Lane and Gilbert (1992) invoked fracto-emission as the main particle charging mechanism within plumes, producing a net negative charge on the ash and a net positive charge on the volcanic gases (ions). Gravitational separation between the ash and gases then produces the positive-over-negative dipole structure of the plume.

The other commonly quoted charge distribution theory involves charge held only on silicate particles, with their net polarity being a function of their size (e.g. Hobbs and Lyons, 1983; Hoblitt, 1994). Thus, small particles have an opposite net charge to that held on the coarser particles. This theory was originally proposed as a result of potential gradient measurements (e.g. Hatakeyama and Uchikawa, 1952) indicating

that charges residing in the upper portions of plumes had the opposite net polarity to that detected on ashfall close to the volcano. However, because fine particles separate only very slowly from the condensing gases, it would be very difficult to distinguish this theory decisively from the particles and ions charge distribution model (Lane and Gilbert, 1992) using potential gradient data alone.

9.2.2 Possible applications of plume monitoring by potential gradients

By successfully detecting even the lightest of ashfall, the data collected at Sakurajima further demonstrate the way in which the potential gradient technique could be used to monitor remotely the ash production from a volcano. One of the aims of this fieldwork was to assess the technique as a plume monitoring system by investigating any variations between data sets recorded during different eruptions. Unfortunately, this was not possible due to the low activity of the volcano. However, the data collected on 14 November, 1996 did demonstrate the same style of charge separation as shown by the data of Lane *et al*. (1995). These detected events were classed as small explosions at Sakurajima (K. Ishihara, *pers. comm.*) and, because the magnitude of the charge separation appears to be a strong function of the size of the eruption, larger eruptions should be easier to detect. Aircraft are particularly vulnerable to plumes produced by remote, unmonitored volcanoes (Sparks *et al*., 1997) and potential gradient monitoring could be used as a cheap method for detecting (in real-time) ash production at such remote volcanoes (James *et al*., 1998).

If data on dispersion direction are also needed, a monitoring array is required. As a result of the small size of the eruption on 5 November, 1996 and its dispersal direction, ash from the explosion was only detected at one monitoring site. Thus, any monitoring array required to detect eruptions of this size reliably would need either a

site closer to the vent (which could detect the vertical ascent of the plume), or a more complete azimuthal coverage of the volcano (to ensure that the dispersing plume was detected). Ideally, an array would have both, but both solutions also have associated problems. On Sakurajima, a site closer to the vent would not be feasible due to the 2 km exclusion zone, and a site to the north or northeast would probably have to be specially constructed due to the topography and vegetation cover.

Within a plume, as a result of gravitational separation, the effective charge centres move apart with time. For constant charge magnitudes, this produces larger dipole moments, and thus enhanced perturbations of the surface potential gradient. Decreasing the magnitude of one of the charges (e.g. due to sedimentation of ash) will also increase the magnitude of perturbations. So, unless both charges decay very rapidly, plumes should actually become more detectable with time. Naturally, this effect will be limited by eventual decay of the charge and the dispersal of the plume, but it does promote potential gradients as a technique which could warn of the approach of dilute plumes not necessarily detectable by other methods (e.g. radar, see next section). Thus, although currently the technique has been used only to monitor the eruption of plumes and their dispersal from a volcano, another application could be to detect the approach of plumes to a sensitive installation or location (i.e. an airport).

Similarly, it should be possible to develop the technique into an onboard warning system to alert an aircraft's crew if they flew into the vicinity of a plume (James *et al*., 1998). However, no airborne experiments have ever been carried out and, despite several near-accidents from plume encounters involving large passenger aircraft (Sparks *et al*., 1997), aircraft still have no means of detecting the presence of a plume. Before an airborne system becomes feasible, further work needs to be carried out

(initially with a permanent ground-based array) in order to fully understand variations of the charges produced by eruptions and also any meteorological effects.

9.2.3 Plume detection: other techniques

There are several techniques currently used to sense volcanic plumes remotely, but all are subject to certain limitations and drawbacks (Table 9.1).

Table 9.1 Advantages and disadvantages of plume monitoring techniques.

Technique		Advantages	Disadvantages
Radar	C-band	existing equipment and technology	limited detection capability
	Doppler	increased detection capability over C-band	expense, size of equipment
Satellite	AVHRR TOMS	wide spatial coverage	not usually real-time
Infrared radiometry		small size of equipment	cannot 'see' through meteorological cloud
Electrical techniques	lightning detection	existing technology and monitoring networks	requires sufficient charge to produce lightning; the possibility of undetected events
	potential gradients	low detection threshold, small size and low cost of equipment	insufficient research for stand-alone system

C-band radars (3.8 to 7.5 cm wavelengths) have been successfully deployed to detect plumes directly over, or close to volcanoes (e.g. Rose *et al*., 1995). However, reflectivity is a strong function of particle size, and small particles (diameters less than ~100 μm) cannot be detected. Large plumes consisting of these particles can remain in the atmosphere for several days or more and persist as a hazard to aviation. Modern

doppler radars (e.g. NEXRAD; Stone, 1994) do have improved characteristics for plume detection over C-band systems; unfortunately, standard airborne weather radar is still unable to detect ash (Stone, 1994). Radar does have the advantage over optical methods that it can provide rapid data during poor visibility conditions and at night. However, there can be difficulty in distinguishing ash reflections from those of hydrometeors or clear air reflections (Stone, 1994).

Satellite data have been utilised to detect volcanic plumes using visible and infrared wavelengths (Sparks *et al*., 1997). In the visible wavelengths it is difficult to distinguish plumes from meteorological clouds but this can be achieved by comparing two infrared bands (e.g. AVHRR bands 4 and 5; Prata, 1989). The Total Ozone Mapping Spectrometer (TOMS) has also been used to detect volcanic plumes by mapping SO_2 (Kreuger *et al*., 1994). Nevertheless, with the current coverage (although this is improving), satellite data are rarely available as a real-time plume monitoring tool. The infrared comparison technique has been developed to produce a prototype radiometry system for aircraft allowing discrimination of ash and water clouds more than 100 km away (Barton and Prata, 1994). Unfortunately, this system cannot detect plumes if they are obscured by meteorological cloud closer to the instrument.

The use of lightning detection and location has been discussed in Chapter 3, and the potential gradient technique has been shown here, and in previous work (e.g. Lane and Gilbert, 1992; see Chapter 3), to be able to detect particle-laden plumes even if no lightning is produced. The simultaneous measurement of potential gradients at different locations could provide real-time data to complement other techniques by working during most weather conditions and the night. The particular advantages over

other systems are its low cost (approximately £2,000 per site), the small size and weight of the equipment and its ability to detect even dilute plumes.

9.3 Experimental charge generation

The laboratory experiments carried out measured the net and individual charges held on silicate particles produced from pumice samples. The particles were generated by impacts between the samples at atmospheric pressure and low pressure (10^{-3} Torr, approximately 10^{-1} Pa).

9.3.1 Net charge held on particles

Particles collected from pumice impacts carried out at atmospheric pressure were shown to have specific net charges between about 10^{-6} and 10^{-5} C kg^{-1} (Chapter 6), with the finer distributions of particles holding slightly higher magnitude net charges than the coarser distributions. A variety of different effects were observed during the experiments, many of which were attributed to charge accumulating on the impact surfaces of the samples. One of the main results of this charge accumulation is thought to be changes of the net ash polarity as impacts continued during experiments, an effect to which certain pumice types appeared to be more susceptible than others. Four out of the six pumice sample types produced net negative ash. The net ash polarity for one sample varied between clasts and the lowest silica content sample (StV 519, 55.4 wt% SiO_2) produced net positively charged ash.

Many experiments carried out at atmospheric pressure provided evidence for the production of slow falling, charged particles of the opposite polarity to the net ash charge. These particles were sufficiently small that they were prevented from falling

into the Faraday cup by very small drafts and could not be observed visually. Although particle polarity being a function of particle size cannot be explained by any known physical process, some evidence for it has also been found during frictional experiments carried out in previous work (Hatakeyama and Uchikawa, 1952; Kikuchi and Endoh, 1982). However, none of this evidence can be regarded as conclusive proof that the net charge polarity varies with particle size within plumes, because these results could be limited to frictional effects alone, or be a product of aggregation processes. Within a plume, some particles may also change polarity as a result of ion scavenging (section 9.4.3).

9.3.2 Absolute particle charges

The experiments carried out with the parallel plates (Chapter 7) demonstrated that the ash produced during pumice collisions consisted of particles of both polarity, with specific charges of up to 10^{-3} C kg^{-1} and corresponding surface charge densities up to 10^{-5} C m^{-2}. Thus, the net charge held on the particles as a whole represents only a small imbalance in the sum of the individual particle charges. It was shown that specific particle charge (of either polarity) varied over an order of magnitude as a function of the number of sample impacts and the impact velocity. Relative humidity was shown to have a lesser effect, but did reduce particle charges at high values (~90 % RH). The increase in the measured particle charge with the number of impacts was thought to reflect the increasing charge held on the samples and also the decreasing particulate mass per impact produced as impacts proceeded. Although it may appear logical that specific charges would increase with increasing impact velocity (and thus impact energy), the physical process which produces this effect probably lies within

the details of the fracture process at a molecular level and, as such, cannot be addressed with the experiments carried out.

The measured specific charges were also shown to be a function of the strength of the electric field used to separate the particles, with higher specific charges being detected at higher field strengths. This unexpected result was thought to be a result of the disruption of aggregates by the electric field. Aggregates (which were ubiquitous during the experiments) effectively represent large mass, low net charge particles, so by disrupting them into their constituent small mass, high specific charge particles, the recorded specific charge increases. This result implies that some of the scatter and unpredictability within the particle charge results could be a reflection of varying degrees of aggregation and disruption.

9.3.3 Fracto-emission and ion production

The experiments carried out with the Faraday cup and mesh did provide indirect evidence for the production of ions. Direct evidence (i.e. the collection of charge from ions alone) was not possible due to the mesh also detecting induced charges and, during some experiments, collecting some very small silicate particles. The generation of ions was also suggested by the lower specific charges generated when particles were produced by grinding, rather than colliding the samples together. Although charge would still be produced by fracto-emission during the grinding process, the silicate particles then had a much longer time to recombine with ions, and thus neutralise, than if they were released rapidly as the samples moved apart after a collision. If the charge was being generated mainly by frictional effects (rather than fracture effects), then higher specific charges would be expected from grinding experiments than from impact experiments.

Supported by the extensive literature on fracto-emission (Chapter 2), the experiments have provided evidence that the brittle fragmentation of pumice releases ions as well as producing charged silicate particles. The experiments carried out using parallel plates indicated that silicate particles of both polarities were generated, so it is most likely that ions of both polarities (and probably free electrons also) are produced. To detect these (atomic) particles directly, it would be necessary to carry out dedicated fracto-emission experiments under high vacuum and with particle detectors screened from solid particle debris.

9.4 Application to explosive eruptions

These experimental results imply that if the same processes also occur during explosive eruptions, then plumes not only contain highly charged silicate particles but also ions. However, eruption conditions could not be reproduced during the experiments, so any effects due to the differences between the plume and the laboratory environments must be assessed.

9.4.1 Charge generation

Unfortunately, fragmentation processes within explosive eruptions are currently poorly understood. Thus it is not known where, or under what conditions, the majority of ash sized particles are produced. If it is within the conduit, then the high temperature and pressure conditions are far removed from the laboratory conditions. However, the classical model of fragmentation occurring at a discrete level (Sparks, 1978) is being replaced by a much more continuous process as demonstrated by decompression experiments (Mader *et al*., 1994; Phillips *et al*., 1995) and grain size

analysis of tephra (Kaminski and Jaupart, 1998). Thus, the production of ash probably continues within the eruption column where temperatures are much lower due to the entrainment of atmospheric air. If conditions within the conduit itself are not conducive to charge generation (or promote rapid discharge) then the charges detected could be the result of fragmentation within the column only (due to pumice–pumice collisions).

The experiments also demonstrated effects due to the accumulation of charge on the samples. During an eruption, the scenario of repeated impacts between the same pumice surfaces is not likely to occur. However, most pumice clasts are probably produced within a jet of gas and small particles, so are likely to have highly charged surfaces. It may be possible that the 'meshing' of the impact surfaces, as occurred during the experiments, is also required before surface charge can directly affect the net ash polarity. If the redistribution of charge over a pumice surface is important, then surface chemistry may also be a key factor. Thus, the direct effect of charged pumice surfaces is difficult to assess for the plume environment and it is likely that a wide range of surface charge conditions will exist.

9.4.2 Particle polarity

Both the experiments discussed here and previous potential gradient measurements (Hatakeyama and Uchikawa, 1952; Miura *et al*., 1995) have indicated that silicate particles are not always net negatively charged. The experiments suggest that silica content may be a factor, with low silica pumice producing net positively charged ash. However, surface chemistry rather than bulk chemistry may be the dominant factor. This would imply that the environment to which a surface is exposed (and hence the adsorbed species upon it) is highly relevant.

This may have been demonstrated during experiments carried out with one sample (SMN 31) which produced opposite polarity ash between experiments carried out at atmospheric pressure (net negative particles) and low pressure (net positive particles). Although this may indicate a sensitivity to adsorbed species on the surface of the pumice, it could also reflect a variation in the ion scavenging potential of the particles under different atmospheric pressures.

9.4.3 Ion scavenging

Inevitably, some of the ions produced during magma fragmentation will be recaptured by particles. In a number dense, particulate environment, ions will be 'mopped up' as a result of their high charge to mass ratio and image charges induced in the particles. If particle fall velocities are considered then, within the same period of time, larger particles traverse a much larger volume than smaller particles, and so could be considered capable of scavenging more efficiently. However, small ash particles provide a larger surface area and reside in the plume longer than coarse ash particles (neglecting aggregation processes). Thus, they may scavenge a greater proportion of the ions, giving the smaller particles a net positive charge (assuming that the ions represented a net positive charge). The combination of ion scavenging and long residence times of small particles in plumes could be the cause of apparent polarity changes in some plumes with increasing distance from the volcano (Hobbs and Lyons, 1983; Hoblitt, 1994; Chapter 3).

In humid plumes, ions may also be scavenged by, or condense to form, droplets of volcanic volatiles. Due to their initial small size (less than about 10 μm in diameter), liquid droplets also represent a highly significant surface area for the capture of ions. Positive potential gradients recorded by Lane and Gilbert (1992) during periods of

liquid droplet fall (formed from condensing volcanic gases) support the scavenging of ions by droplets.

Thus, some time after fragmentation has ceased, the particle-rich portion of plumes should contain relatively few free ions, and the charge will be maintained on silicate particles or liquid droplets. Ions should still exist (as atmospheric ions, Chalmers, 1967) within any gas-rich portion of the plume, segregated from the main particle-bearing plume.

9.4.4 Aggregation

Electrostatic forces are commonly quoted as a major factor in the generation of dry aggregates (Sparks *et al*., 1997), and indeed, aggregates were observed in nearly all of the experiments. No research has been carried out into the effects of aggregation on the distribution of space charge within an initially dispersed particulate medium. Although it may be expected that the net aggregate charge would reflect the original net particle charge, this has not been demonstrated.

Aggregation processes are highly complex and poorly understood, so their effect on particles of a wide range of sizes, holding a variety of charge magnitudes of both polarities, would be extremely difficult (if not impossible) to predict. Thus, even if the charge distribution on particles within a plume was known, it could be effectively changed completely by particle aggregation. Any simple model of charge distribution due to small and large particles may have to be re-thought as referring to unaggregated particles and aggregates.

9.4.5 Application to other planetary environments

The experiments carried out under low pressure (10^{-3} to 10^{-4} Torr, approximately 10^{-1} to 10^{-2} Pa) produced specific net charges of up to 10^{-4} C kg^{-1} and specific particle charges of up to 4.5×10^{-3} C kg^{-1}. Under vacuum, the charges measured during individual experiments usually showed an approximate order of magnitude increase over results obtained at atmospheric pressure. This difference is likely to reflect charge lost through local breakdown of the air around highly charged particles at atmospheric pressure.

Analysis of the possible effects this may produce within the plumes on Io (Chapter 8) suggested that luminous discharges could be generated and that particle aggregation is likely. Recent data have shown that many of Io's volcanic vents do glow to some extent, and diffuse glows associated with plumes have also been observed in eclipse. However, these have been ascribed to thermal emission (from surfaces hotter than 700 K) and particle interactions within the ionosphere respectively (McEwen *et al*., 1998a). Specific particle charges should not be sufficiently high to visibly distort the plumes and, within large plumes, particle charges may be dominated by plasma interactions within Io's ionosphere rather than fracto-electric effects. Nevertheless, large explosive silicate eruptions into low pressure atmospheres (such as probably occurred on Mars, e.g. Mouginis-Mark *et al*., 1982) are expected to have represented truly spectacular electrical events.

9.5 Summary

The technique of monitoring ground-level atmospheric potential gradients has been shown capable of detecting and tracking even dilute particulate volcanic plumes.

The equipment required is relatively cheap and could be developed into a monitoring system for volcano observatories or ash-sensitive installations, or provide an onboard warning system for aircraft. However, currently there are insufficient data on eruptions for the technique to be used independently of other geophysical monitoring tools.

Simple pumice fracture experiments have been shown to produced silicate particles charged to a similar degree as ashfall measured previously from plumes. The sign and magnitude of these charges have been shown to vary with atmospheric pressure, RH, sample geochemistry, particle size, the number of sample collisions and impact velocity. As with most particulate electrostatic problems, the processes involved appear to be highly complex and sensitive to a wide variety of factors. Charge thought to be released as ions during the fracture process has been detected, supporting the theory that fracto-emission is the dominant charging mechanism during explosive eruptions.

Unfortunately, despite these results, it is not yet possible to infer many details about the electrostatic processes within plumes due to the wide ranges of the physical parameters such as pressure, temperature and RH which exist in that environment, and the action of other complex processes such as droplet nucleation and aggregation.

References

Anderson, R., Björnsson, S., Blanchard, D.C., Gathman, S., Hughes, J., Jónasson, S., Moore, C.B., Survilas, H.J. and Vonnegut, B. (1965) Electricity in volcanic clouds. *Science*, **148**, 1179-1189.

Baker, B., Baker, M.B., Jayaratne, E.R., Latham, J. and Saunders, C.P.R. (1987) The influence of diffusional growth rates on the charge transfer accompanying rebounding collisions between ice crystals and soft hailstones. *Quart. J. Roy. Met. Soc.*, **113**, 1193-1215.

Baker, M.B. and Dash, J.G. (1989) Charge transfer in thunderstorms and the surface melting of ice. *J. Crystal Growth*, **97**, 770-776.

Ballester, G.E., McGrath, M.A., Strobel, D.F., Zhu, X., Feldman, P.D. and Moos, H.W. (1994) Detection of the SO_2 atmosphere on Io with the Hubble-Space-Telescope. *Icarus*, **111**, 2-17.

Barton, I.J. and Prata, A.J. (1994) Detection and discrimination of volcanic ash clouds by infrared radiometry-II: Experimental. In: Casadevall, T. J. (ed.) Proceedings of the first international symposium of volcanic ash and aviation safety. *U.S. Geol. Surv. Bull.*, **2047**, 313-318.

Battlo, F., Wydeven, T. and Freund, F. (1988) Mobile charge carriers in obsidian: Evidence for peroxy. *EOS, Trans. Am. Geophys. Union*, **69**, 1468.

Bering III, E.A. (1995) The global circuit: Global thermometer, weather by-product or climatic modulator? *Rev. Geophys. (suppl.)*, **33**, 845-862.

Bibhas, R.D. and Criswell, D.R. (1977) Intense localised photoelectric charging in the lunar sunset terminator region. 1). Development of potentials and fields. *J. Geophys. Res.*, **82**, 999-1004.

Björnsson, S., Blanchard, D.C. and Spencer, A.T. (1967) Charge generation due to contact of saline waters with molten lava. *J. Geophys. Res.*, **72**, 1311-1323.

Blanchard, D.C. (1964) Charge separation from saline drops on hot surfaces. *Nature*, **201**, 1164-1166.

Blaney, D.L., Johnson, T.V., Matson, D.L. and Veeder, G.J. (1995) Volcanic eruptions on Io: Heat flow, resurfacing and lava composition. *Icarus*, **113**, 220-225.

Blythe, A.R. and Reddish, W. (1979) Charges on powders and bulking effects. *Inst. Phys. Conf. Ser.*, **48**, 107-114.

Borucki, J.G. and Freund, F. (1998a) Charge carrier generation and charge cloud propagation following 100m/sec impacts on igneous rocks. In: Hayakawa, H. (ed.) *Electromagnetic phenomena related to earthquake prediction.*, Terra Sci. Publ., Tokyo. (in print)

Borucki, J.G. and Freund, F. (1998b) Impact-generated electric charges in igneous rocks. In: *Lunar Plan. Sci. XXIV*, Abstract #**1106**, Lunar and Planetary Institute, Houston. (CD-ROM)

Boschung, P. and Glor, M. (1980) Methods for investigating the electrostatic behaviour of charged particles. *J. Electrostatics*, **8**, 205-219.

Brady, B.T. and Rowell, G.A. (1986) Laboratory investigation of the electrodynamics of rock fracture. *Nature*, **321**, 488-492.

Brook, M., Moore, C.B. and Sigureirsson T. (1974) Lightning in volcanic clouds. *J. Geophys. Res.*, **79**, 472-475.

Brydson, J.A. (1982) *Plastics Materials*. Butterworth Scientific, London.

Büttner, R., Röder, H. and Zimanowski, B. (1997) Electrical effects generated by experimental volcanic explosions. *Appl. Phys. Lett.*, **70**, 1903-1905.

Caltabiano, T., Romano, R. and Budetta, G. (1994) SO_2 flux measurements at Mt. Etna (Sicily). *J. Geophys. Res.*, **99**, 12809-12819.

Caranti, J.M. and Illingworth, A.J.I. (1983) The contact potential of rimed ice. *J. Phys. Chem.*, **87**, 4125-4130.

Caranti, J.M., Avila, E.E. and Ré, M.A. (1991) Charge transfer during individual collisions in ice growing from vapor deposition. *J. Geophys. Res.*, **96**, 15365-15375.

Carey, S.N. and Sigurdsson, H. (1982) Influence of particle aggregation on deposition of distal tephra from the May 18, 1980, eruption of Mount St. Helens volcano. *J. Volcanol. Geotherm. Res.*, **7**, 7061-7072.

Carroll, J.J. and Parco, S.A. (1966) *Social organisation in a crisis situation: The Taal disaster*. Philippine Sociological Society, Manila.

Chalmers, J.A. (1967) *Atmospheric Electricity*. Pergamon Press, Oxford.

Christian, H., Holmes, C.R., Bullock, J.W., Gaskell, W., Illingworth, A.J. and Latham, J. (1980) Airborne and ground-based studies of thunderstorms in the vicinity of the Langmuir laboratory. *Quart. J. Roy. Met. Soc.*, **106**, 159-174.

Chubb, J.N. (1990) Two new designs of "field mill" type fieldmeters not requiring earthing of rotating chopper. *IEEE Trans. Industy Appl.*, **26**, 1178-1181.

Clow, G.D. and Carr, M.H. (1980) Stability of sulfur slopes on Io. *Icarus*, **44**, 268-279.

Cobb, W.F. (1980) Electric fields and lightning in the Mount St. Helens volcanic cloud. *EOS, Trans. Am. Geophys. Union*, **61**, 978. (abstr.)

Collins, S.A. (1981) Spatial color variations in the volcanic plume at Loki, on Io. *J. Geophys. Res.*, **86**, 8621-8626.

COMVOL (1975) Commission on Volcanology, Mayon volcano.

Cook, A.F., Shoemaker, E.M. and Smith, B.A. (1979) Dynamics of volcanic plumes on Io. *Nature*, **280**, 743-746.

Corwin, R.F. and Morrison, H.F. (1977) Self-potential variations preceding earthquakes in central California. *Geophys. Res. Lett.*, **4**, 171-174.

Craig, R.A. (1965) *The upper atmosphere meteorology and physics.* International Geophysics Series, Academic Press, New York.

Cress, G.O., Brady, B.T. and Rowell, G.A. (1987) Sources of electromagnetic radiation from fracture of rock samples in the laboratory. *Geophys. Res. Lett.*, **14**, 331-334.

Criswell, D.R. and De., B.R. (1977) Intense localized photoelectric charging in the lunar sunset terminator region. 1. Development of potentials and fields. *J. Geophys. Res.*, **82**, 999-1004.

Cross, J.A. (1987) *Electrostatics: Principles, Problems and Applications*. IOP Publishing, Bristol.

Cross, J.A. and Farrer, D. (1982) *Dust explosions*. Plenum, New York.

De, B.R. and Criswell, D.R. (1977) Intense localized photoelectric charging in the lunar sunset terminator region. 1. Development of potentials and fields. *J. Geophys. Res.*, **82**, 999-1004.

Derr, J.S. (1973) Earthquake lights: A review of observations and present theories. *Bull. Seismol. Soc. Am.*, **63**, 2177-2187.

Dickinson, J.T., Donaldson, E.E. and Park, M.K. (1981a) The emission of electrons and positive ions from fracture of materials. *J. Mat. Sci.*, **16**, 2897-2908.

Dickinson, J.T., Donaldson, E.E. and Snyder, D.B. (1981b) Emission of electrons and positive ions upon fracture of oxide films. *J. Vac. Sci. Technol.*, **18**, 238-242.

Dickinson, J.T., Jenson, L.C. and Bhattacharya, S.K. (1985a) Fractoemission from the failure of metal/epoxy interfaces. *J. Vac. Sci. Technol. A*, **3**, 1398-1402.

Dickinson, J.T., Jenson, L.C. and Jahan-Latibari, A. (1984) Fracto-emission: The role of charge separation. *J. Vac. Sci. Technol. A*, **2**, 1112-1116.

Dickinson, J.T., Jensen, L.C. and Langford, S.C. (1991a) Atomic and molecular emission accompanying fracture of single-crystal Ge: A dislocation driven process. *Phys. Rev. Lett.*, **66**, 2120-2123.

Dickinson, J.T., Jenson, L.C. and Williams, W.D. (1985b) Fractoemission from lead zirconate-titanate. *J. Am. Ceram. Soc.*, **65**, 235-240.

Dickinson, J.T., Jensen, L.C., Langford, S.C. and Hirth, J.P. (1991b) Atomic and molecular emission following fracture of alkali halides: A dislocation driven process. *J. Mater. Res.*, **6**, 112-125.

Dickinson, J.T., Jensen, L.C., Langford, S.C. and Rosenberg, P.E. (1992) Fracture-induced emission of alkali atoms from feldspar. *Phys. Chem. Minerals*, **18**, 453-459.

Dickinson, J.T., Jensen, L.C., Langford, S.C., Rosenberg, P.E. and Blanchard, D.L. (1991c) CO_2 emission accompanying the fracture of calcite. *Phys. Chem. Minerals.*, **18**, 320-325.

Dickinson, J.T., Jensen, L.C., Langford, S.C., Ryan, R.R. and Garcia, E. (1990) Fracto-emission from deuterated titanium: Supporting evidence for a fracto-fusion mechanism. *J. Mater. Res.*, **5**, 109-122.

Dickinson, J.T., Langford, S.C., Jensen, L.C., McVay, G.L., Kelso, J.F. and Pantano, C.G. (1988) Fractoemission from fused silica and sodium silicate glasses. *J. Vac. Sci. Technol. A*, **6**, 1084-1089.

Dickinson, J.T., Park, M.K., Donaldson, E.E. and Jensen, L.C. (1982) Fracto-emission accompanying adhesive failure. *J. Vac. Sci. Technol.*, **22**, 436-439.

Dietz, R.S. (1954) The explosive birth of Myojin Island. *The Nat. Geogr. Mag.*, **105**, 117-128.

Doering, D.L., Dickinson, J.T., Langford, S.C. and Xiong-Skiba, P. (1990) Fracto-emission during the interfacial failure of a metal-oxide-semiconductor system: Au-SiO_2-Si. *J. Vac. Sci. Technol. A*, **8**, 2401-2406.

Donaldson, E.E., Dickinson, J.T. and Bhattacharya, S.K. (1988) Production and properties of ejecta released by fracture of materials. *J. Adhesion*, **25**, 281-302.

Druitt, T., Lanphere, M. and Vougiokalakis, G. (1996) *Santorini*. IAVCEI, Commission on Explosive Volcanism, Field workshop handbook. (unpub.)

DuBard, J.L. and Nichols, G.B. (1990) Diagnosis of electrical operation of electrostatic precipitators. *J. Electrostatics*, **25**, 75-96.

Duffin, W.J. (1990) *Electricity and magnetism*. McGraw-Hill Book Company, London.

Dzurisin, D., Anderson, L.A., Eaton, G.P., Koyanaguchi, R.Y., Lipman, P.W., Lockwood, J.P., Okamura, R.T., Puniwai, G.S., Sako, M.K. and Yamashita, K.M. (1980) Geophysical observations of Kilauea volcano, Hawaii, 2, Constraints on the magma supply during November 1975 - September 1977. *J. Volcanol. Geotherm. Res.*, **7**, 241-269.

Eden, H.F. (1973) Electrostatic nuisances and hazards. In: Moore, A.D. (ed.) *Electrostatics and its Applications*. John Wiley & Sons, Inc., New York.

Elster, J. and Geitel, H. (1913) Zur influenztheorie der niederschlagselectrizität. *Phys. Z.*, **14**, 1287-1292.

Enomoto, Y. and Hashimoto, H. (1990) Emission of charged particles from indentation fracture of rocks. *Nature*, **346**, 641-463.

Fanale, F.P., Brown, R.H., Cruikshank, D.P. and Clark, R.N. (1979) Significance of absorption features in Io's IR reflectance spectrum. *Nature*, **280**, 761-763.

Fedotov, S.A., Chirkov, A.M., Gusev, N.A., Kovalev, G.N. and Slezin, Y.B. (1980) The large fissure eruption in the region of Plosky Tolbchik Volcano in Kamchatka, 1975-1976. *Bull. Volcanol.*, **43**, 47-60.

Finkelstein, D. and Powell, J. (1970) Earthquake lightning. *Nature*, **228**, 759-760.

Frank, L.A., Paterson, W.R., Ackerson, K.L., Vasyliunas, V.M., Coroniti, F.V. and Bolton, S.J. (1996) Plasma observations at Io with the Galileo spacecraft. *Science*, **274**, 394-395.

Freund, F. (1985) Conversion of dissolved “water” into molecular hydrogen and peroxy linkages. *J. Non-Crys. Solids*, **71**, 195-202.

Freund, F., Batllo, F. and LeRoy, R.C. (1988) Sparks from olivine: Simulation of earthquake lights and electromagnetic emissions. *EOS, Trans. Am. Geophys. Union*, **69**, 1300.

Freund, F., Gupta, A., Butow, S.J. and Tenn, S. (1998) Molecular hydrogen and dormant charge carriers in minerals and rocks. In: Hayakawa, H. (ed.) *Electromagnetic phenomena related to earthquake prediction.*, Terra Sci. Publ., Tokyo. (in print)

Freund, F., Whang, E.-J. and Lee, J. (1994b) Highly mobile hole charge carriers in minerals: Key to the enigmatic electrical earthquake phenomenon? In: Hayakawa, M. and Fujinawa, Y (eds.) *Electromagnetic Phenomena Related to Earthquake prediction.* Terra Sci. Publ., Tokyo, 271-292.

Freund, F., Whang, E.-J., Batllo, F., Desgranges, L., Desgranges, C. and Freund, M.M. (1994a) Positive hole-type charge carriers in oxide materials. *Ceram. Trans.*, **41**, 263-278.

Freund, M.M., Freund, F. and Batllo, F. (1989) Highly mobile oxygen holes in magnesium oxide. *Phys. Rev. Lett.*, **63**, 2096-2099.

Fujinawa, Y. and Takahashi, K. (1990) Emission of electromagnetic radiation preceding the Ito seismic swarm of 1989. *Nature*, **347**, 376-378.

Fujinawa, Y., Kumagai, T. and Takahashi, K. (1992) A study of anomalous underground electric field variations associated with a volcanic eruption. *Geophys. Res. Lett.*, **19**, 9-12.

Furhmann, J. and Kurschner, J. (1981) Time dependent transient and intermittent contact electrification. *J. Electrostatics*, **10**, 115-120.

Gaskell, W. and Illingworth, A.J.I. (1980) Charge transfer accompanying individual collisions between ice particles and its role in thunderstorm electrification. *Quart. J. Roy. Met. Soc.*, **106**, 841-854.

Gilbert, J.G., Lane, S.J., Sparks, R.S.J. and Koyaguchi, T. (1991) Charge measurements on particle fallout from a volcanic plume. *Nature*, **349**, 598-600.

Gill, E.W.B. and Alfrey, G.F. (1952) Production of electric charge on water drops. *Nature*, **169**, 203-204.

Geller, R.J. (1996) (ed.) Debate on VAN. *Geophys. Res. Lett.*, **23**, 1291-1452.

Gokhberg, M.B., Morgounov, V.A., Yoshino, T. and Tomizawa, I. (1982) Experimental measurement of electromagnetic emissions possibly related to earthquakes in Japan. *J. Geophys. Res.*, **87**, 7824-7828.

Green, J.A. (1944) Paricutín, the cornfield that grew a volcano. *The Nat. Geogr. Mag.*, **85**, 129-156.

Grün, E., Baguhl, M., Hamilton, D.P., Riemann, R., Zook, H.A., Dermott, S., Fechtig, H., Gustafson, B.A., Hanner, M.S., Horányi, M., Khurana, K.K., Kissel, J., Kivelson, M., Lindblad, B.A., Linkert, D., Linkert, G., Mann, I., McDonnell, J.A.M., Morfill, G.E., Polanskey, C., Schwehm, G. and Srama, R. (1996) Constraints from Galileo observations on the origin of jovian dust streams. *Nature*, **381**, 395-398.

Grün, E., Zook, H.A., Baguhl, M., Balogh, A., Bame, S.J., Fechtig, H., Forsyth, R., Hanner, M.S., Horanyi, M., Kissel, J., Lindblad, B.-A., Linkert, D., Linkert, G., Mann, I., McDonnell, J.A.M., Morfill, G.E., Phillips, J.L., Polanskey, C., Schwehm, G. Siddique, N., Staubach, P., Svestka, J. and Taylor, A. (1993) Discovery of jovian dust streams and interstellar grains by the Ulysses spacecraft. *Nature*, **362**, 428-430.

Hadfield, P. (1996) Quake warning comes in blue and red. *New Scientist*, **2017**, 16.

Hadjicontis, V. and Mavramatou, C. (1994) Transient electric signals prior to rock failure under uniaxial compression. *Geophys. Res. Lett.*, **21**, 1687-1690.

Hamamoto, N., Nakajima, Y. and Sato, T. (1992) Experimental discussion on maximum surface charge density of fine particles sustainable in normal atmosphere. *J. Electrostatics*, **28**, 161-173.

Hamilton, W. (1772) *Observations on Mt Vesuvius, Mt Etna and other volcanoes*. Cadell, London.

Hapke, B. (1986) Bidirectional Reflectance Spectroscopy 4. The extinction coefficient and the opposition effect. *Icarus*, **67**, 264-280.

Hapke, B. (1989) The surface of Io: A new model. *Icarus*, **79**, 56-74.

Harper, W.R. (1967) *Contact and frictional electrification*. Oxford University Press, London.

Harris, D.M., Rose, W.I., Roe, R. and Thompson, M.R. (1981) Radar observations of ash eruptions. In: Lipman, P.W. and Mullineaux, D.R. (eds.) The 1980 Eruptions of Mount St. Helens, Washington. *U.S. Geol. Surv. Prof. Paper*, **1250**, 201-207.

Hatakeyama, H. (1943) On the variation of atmospheric potential gradient caused by the cloud of smoke of the volcano Asama. *2nd Report J. Met. Soc. Japan II*, **21,** 420-426.

Hatakeyama, H. (1949) On the disturbance of the atmospheric potential gradient caused by the smoke-cloud of the volcano Yake-yama. *J. Geomag. Geoelect.*, **1,** 48-51.

Hatakeyama, H. (1958) On the disturbance of the atmospheric electric field caused by the smoke-cloud of the volcano Asama-yama. *Pap. Meteor. Geophys.*, **8**, 302-315.

Hatakeyama, H. and Uchikawa, K. (1952) On the disturbance of the atmospheric potential gradient caused by the eruption smoke of the volcano Aso. *Pap. Meteor. Geophys.*, **2**, 85-89.

Head, J.W. and Wilson, L. (1987) Lava fountain heights at Pu'u 'O'o, Kilauea, Hawaii: Indicators of amount and variations of exolved magma volatiles. *J. Geophys. Res.*, **92**, 13715-13719.

Heath, E. (1997) *Genesis and evolution of calc-alkaline magmas at Soufriere volcano, St. Vincent, Lesser Antilles arc*. PhD. Thesis, Lancaster University.

Hedervari, P. and Noszticzius, Z. (1985) Recent results concerning earthquake lights. *Ann. Geophys.*, **3**, 705-708.

Hobbs, P.V. and Lyons J.H. (1983) Electrical activity associated with the May 18, 1980 volcanic eruption of Mount St. Helens. *Final report to IRT Corporation*. (unpub.)

Hoblitt, R.P. (1994) An experiment to detect and locate lightning associated with eruptions of Redoubt volcano. *J. Volcanol. Geotherm. Res.*, **62**, 499-517.

Holasek, R.E., Woods, A.W. and Self, S. (1996) Experiments on gas-ash separation processes in volcanic umbrella plumes. *J. Volcanol. Geotherm. Res.*, **70**, 169-181.

Horányi, M. and Cravens, T.E. (1996) The structure and dynamics of Jupiter's ring. *Nature*, **381**, 293-295.

Horanyi, M., Morfill, G. and Grün, E. (1993) Mechanism for the acceleration and ejection of dust grains from Jupiter's magnetosphere. *Nature*, **363**, 144-146.

Huang, L. and Hanzen, D. (1979) *Earthquake light*. Earthquake Press Beijing, China, 1-140.

Hunter, R.J. (1981) *Zeta potential in colloid science*. Academic, San Diego, California.

Inculet, I.I. and Criswell, D.R. (1979) Electrostatic benefication of ores on the Moon surface. In: Lowell, J (ed.) *Electrostatics 1979*. Institute of Physics, London, 45-54.

Ip, W.H. (1996) The dust halo of Io. *Geophys. Res. Letts.*, **23**, 3671-3674.

Ishikawa, G., Kadena, M. and Misake, M. (1951) On the charge distribution in volcanic smoke. *J. Geomag. Geoelect*, **1**, 9-17.

Jaggar, T.A. (1906) The volcano Vesuvius in 1906. *Technol. Quart. and Proc*., **19**, 104-115.

James, M.R. and Wilson, L. (1998) An optical model for ballistic plumes on Io. In: *Lunar Plan. Sci. XXIX*, Abstract #**1349**, Lunar and Planetary Institute, Houston. (CD-ROM)

James, M.R., Lane, S.J. and Gilbert, J.S. (1998) Volcanic plume monitoring using atmospheric electric potential gradients. *J. Geol. Soc. Lond.*, **155**, 587-590.

Jayaratne, E.R., Saunders, C.P.R. and Hallett, J. (1983) Laboratory studies of the charging of soft-hail during ice crystal interactions. *Quart. J. Roy. Met. Soc.*, **109**, 609-630.

Jiang, Y.G., Shan, F.K., Jin, H.M. and Zhou, L.W. (1998) A method for measuring electrokinetic coefficients of porous media and its potential application in hydrocarbon exploration. *Geophys. Res. Lett.,* **25**, 1581-1584.

Johnson, T.V., Matson, D.L., Blaney, D.L. and Veeder, G.J. (1995) Stealth plumes on Io. *Geophys. Res. Letts.*, 3293-3296.

Johnson, T.V., Veeder, G.J., Matson, D.L., Brown, R.H., Nelson, R.M. and Morrison, D. (1988) Io: Evidence for silicate volcanism in 1986. *Science*, **242**, 1280.

Jouniaux, L. and Pozzi, J.-P. (1997) Laboratory measurements anomalous 0.1-0.5 Hz streaming potential under geochemical changes: Implications for electrotelluric precursors to earthquakes. *J. Geophys. Res.*, **102**, 15335-15342.

K'singham, L.A., Dickinson, J.T. and Jensen, L.C. (1985) Fractoemission from failure of metal/glass interfaces. *J. Am. Ceram. Soc.*, **68**, 510-514.

Kaminski, E. and Jaupart, C. (1998) The size distribution of pyroclasts and the fragmentation sequence in explosive volcanic eruptions. *Geoscience 98,* The Geological Society, 93. (abstr.)

Kamra, A.K. (1969a) Effect of wind on diurnal and seasonal variations of atmospheric electric field. *J. Atmos. Terr. Phys.*, **31**, 1281-1286.

Kamra, A.K. (1969b) Electrification in an Indian dust storm. *Weather*, **24**, 145-146.

Kamra, A.K. (1973) Experimental study of the electrification produced by dispersion of dust into the air. *J. Appl. Phys.*, **44**, 125-131.

Kanagy, S.P. and Mann, C.J. (1994) Electrical properties of eolian sand and silt. *Earth Sci. Rev.*, **36**, 181-204.

Kawaguchi, Y. (1995) Time-resolved fractoluminescence spectra of silica glass in a vacuum and nitrogen atmosphere. *Phys. Rev. B*, **52**, 9224-9228.

Keiffer, S.W. (1982) Ionian volcanism. In: Morrison, D. (ed.) *Satellites of Jupiter*. Univ. Arizona Press, Tuscon.

Keith, W.D. and Saunders, C.P.R. (1988) Light emission from colliding ice particles. *Nature*, **336**, 362-364.

Keith, W.D. and Saunders, C.P.R. (1990) Further laboratory studies of the charging of graupel during ice crystal interactions. *Atmos. Res.*, **25**, 445-464.

Khatiashvilli, N.G. and Perel'man, M.E. (1989) On the mechanism of seismo-electromagnetic phenomena and their possible role in the electromagnetic radiation during periods of earthquakes, foreshocks and aftershocks. *Phys. Earth Plan. Int.*, **57**, 169-177.

Khurana, K., Kivelson, M.G. and Russell, C.T. (1997) Interaction of Io with its torus: Does Io have an internal magnetic field? *Geophys. Res. Letts.*, **19**, 2391-2394.

Kikuchi, K and Endoh, T. (1982) Atmospheric electrical properties of volcanic ash particles in the eruption of Mt. Usu volcano, 1977. *J. Meteor. Soc. Japan.*, **60**, 548-561.

Kivelson, M.G., Khurana, K.K., Walker, R.J., Russell, C.T., Linker, J.A., Southwood, D.J. and Polanskey, C. (1996a) A magnetic signature at Io: Initial report from the Galileo magnetometer. *Science*, **273**, 337-340.

Kivelson, M.G., Khurana, K.K., Walker, R.J., Warnecke, J., Russell, C.T., Linker, J.A., Southwood, D.J. and Polanskey, C. (1996b) Io's interaction with the plasma torus: Galileo magnetometer report. *Science*, **274**, 396-398.

Kreuger, A.J., Doiron, S.R., Bluth, G.S.J., Walter, L.S. and Schnetzler, C.C. (1994) Volcanic hazard detection with the Total Ozone Mapping Spectrometer (TOMS). In: Casadevall, T. J. (ed.) Proceedings of the first international symposium of volcanic ash and aviation safety. *U.S. Geol. Surv. Bull.*, **2047**, 367-372.

Lagmay, M.A., Pyle, D.M., Dade, B. and Oppenheimer, C. (1998) A reinterpretation of the origin of the fatal May 8th 1902 Mount Pelée nuée ardentes. *Volcanic and Magmatic Studies Group Ann. Meeting*. (abstr.)

Lane, S.J. (1994) Logit: User-friendly data logging. *Terra Nova*, **6**, 202-206.

Lane, S.J. and Gilbert, J.S. (1992) Electric potential gradient changes during explosive activity at Sakurajima volcano, Japan. *Bulletin of Volcanology*, **54**, 590-594.

Lane, S.J., Gilbert, J.S. and Kemp, A.J. (1995) Electrical and chemical properties of eruption plumes at Sakurajima volcano, Japan. In: *8th Report of Geophysical and Geochemical Observations at Sakurajima Volcano*, 105-127.

Langford, S.C., Dickinson, J.T. and Jensen, L.C. (1987) Simultaneous measurements of the electron and photon emission accompanying fracture of single-crystal MgO. *J. Appl. Phys.*, **62**, 1437-1449.

Langford, S.C., Jensen, L.C., Dickinson, J.T. and Pederson, L.R. (1991) Alkali emission accompanying fracture of sodium silicate glasses. *J. Mater. Res.*, **6**, 1358-1368.

Latham, J. and Mason, B.J. (1961) Electric charge transfer associated with temperature gradients in ice. *Proc. Roy. Soc. A*, **260**, 523-536.

Latham, J. and Mason, B.J. (1962) Electrical charging of hail pellets in a polarizing electric field. *Proc. Roy. Soc. A*, **266**, 387-401.

Lawver, J.E. and Dyrenforth, W.P. (1973) Electrostatic separation. In: Moore, A.D. (ed.) *Electrostatics and its Applications*. John Wiley & Sons, Inc., New York.

Lellouche, E. (1996) Io's atmosphere: Not yet understood. *Icarus*, **124**, 1-21.

Lellouche, E., Belton, M., DePater, I., Paubert, G., Gulkis, S. and Encrenaz, T. (1992) The structure, stability and global distribution of Io's atmosphere. *Icarus*, **98**, 271-295.

Lenard, P. (1892) Über die elektrizität der wasserfälle. *Ann. Phys.*, **46**, 584-636.

Lipman, P.W., Norton, D.R., Taggart Jr., S.R., Brandt, E.L. and Engleman, E.E. (1981) Compositional variations in 1980 magmatic deposits. In Lipman, P.W. and Mullineaux, D.R. (eds.) The 1980 Eruptions of Mount St. Helens, Washington. *U.S. Geol. Surv. Prof. Paper*, **1250**, 631-640.

Lockner, D.A., Johnston, M.J.S. and Byerlee, J.D. (1983) A mechanism to explain the generation of earthquake lights. *Nature*, **302**, 28-33.

Lowell, J. (1976) The electrification of polymers by metals. *J. Phys. D: Appl. Phys.*, **9**, 1571-1585.

Lupton, J., Klinkhammer, G., Normark, W., Haymon, R., MacDonald, K., Wein, R. and Craig, H. (1980) Helium-3 and manganese at the 21º N East Pacific Rise hydrothermal site. *Earth Plan. Sci. Lett.*, **50**, 115-127.

Lynch, J.S. and Stephens, G. (1996) Mount Pinatubo: A satellite perspective of the June 1991 eruptions. In: Newhall, C.G. and Punongbayan, S. (eds.) *Fire and mud: Eruptions and lahars on Mount Pinatubo, Philippines*. University of Washington Press, Seattle.

Ma, Z.-Y. and Dickinson, J.T. (1991) Fracto-emission from embedded interfaces. *J. Appl. Phys.*, **70**, 4797-4807.

Mader, H.M., Zhang, Y., Phillips, J.C., Sparks, R.S.J., Sturtevant, B. and Stolper, E. (1994) Experimental simulations of explosive degassing of magma. *Nature*, **372**, 85-88.

Marshall, J.R. (1998) "Electrostructural phase changes" in charged particulate clouds: Planetary and astrophysical implications. In: *Lunar Plan. Sci. XXIX*, Abstract #**1132**, Lunar and Planetary Institute, Houston. (CD-ROM)

Marshall, T.C. and Winn, W.P. (1982) Measurements of charged precipitation in a New Mexico thunderstorm: Lower positive charge centres. *J. Geophys. Res.*, **87**, 7141-7157.

Marshall, T.C., Rust, W.D., Winn, W.P. and Gilbert, K.E. (1989) Electrical structure in two thunderstorm anvil clouds. *J. Geophys. Res.*, **94**, 2171-2181.

Mason, B.J. (1988) The generation of electric charges and fields in thunderstorms. *Proc. Roy. Soc. Lond. A*, **415**, 303-315.

Mathison, J.P., Langford, S.C. and Dickinson, J.T. (1989) The role of damage in post-emission of electrons from cleavage surfaces of single-crystal LiF. *J. Appl. Phys.*, **65**, 1923-1928.

McEwen, A., Spencer, J., Simonelli, D., Johnson, T., Belton, M., Keszthelyi, L. and the Galileo SSI team (1997) Io plume observations from Galileo and HST. In: *Lunar Plan. Sci. XXVIII*, Abstract #**826**, Lunar and Planetary Institute, Houston. (CD-ROM)

McEwen, A.S. and Soderblom, L.A. (1983). Two classes of volcanic plumes on Io. *Icarus*, **55**, 191-217.

McEwen, A.S., Keszthelyi, L., Geissler, P., Simonelli, D.P., Carr, M.H., Johnson, T.V., Klaasen, K.P., Breneman, H.H., Jones, T.J., Kaufman, J.M., Magee, K.P., Senske, D.A., Belton, M.J.S. and Schubert, G. (1998a) Active volcanism on Io as seen by Galileo SSI. *Icarus*, **135**, 181-219.

McEwen, A.S., Keszthelyi, L., Spencer, J.R., Schubert, G., Matson, D.L., Lopes-Gautier, R., Klaasen, K.P., Johnson, T.V., Head, J.W., Geissler, P., Fagents, S., Davies, A.G., Carr, M.H., Breneman, H.H. and Belton, M.J.S. (1998b) High-temperature silicate volcanism on Jupiter's moon Io. *Science*, **281**, 87-90.

Miles, M.H., Dickinson, J.T. and Jensen, L.C. (1985) Fractoemission from single crystal pentaerythritol tetranitrate. *J. Appl. Phys.*, **57**, 5048-5055.

Mills, A.A. (1977) Dust clouds and frictional generation of glow discharges on Mars. *Nature*, **268**, 614.

Miura, T., Koyaguchi, T. and Tanaka, Y. (1995) Simultaneous measurement of the changing of the atmospheric electric field and the relative electric charge on ash caused by the eruption of Sakurajima Volcano. In: *8th Report of Geophysical and Geochemical Observations at Sakurajima Volcano*, 89-104. (in Japanese)

Miura, T., Koyaguchi, T. and Tanaka, Y. (1996) Atmospheric electric potential gradient measurements of ash clouds generated by pyroclastic flows at Unzen volcano, Japan. *Geophys. Res. Letts.*, **23**, 1789-1792.

Moore, A.D. (1973) *Electrostatics and its Applications*. John Wiley & Sons, Inc., New York.

Moore, C.B., Vonnegut, B. and Holden, D.N. (1989) Anomalous electric fields associated with clouds growing over a source of negative space charge. *J. Geophys. Res.*, **94**, 13127-13134.

Moore, J.M., McEwen, A.S., Albin, E.F. and Greeley, R. (1986) Topographic evidence for shield volcanism on Io. *Icarus*, **67**, 181-183.

Morabito, L.A., Synnott, S.P., Kupferman, P.M. and Collins, S.A. (1979) Discovery of currently active extraterrestrial volcanism. *Science*, **204**, 972.

Morfill, G. (1996) The enigma of Jupiter's ring. *Nature*, **381**, 279-280.

Mouginis-Mark, P.J., Wilson, L. and Head III, J.W. (1982) Explosive volcanism on Hecates Tholus, Mars: investigation of eruptive conditions. *J. Geophys. Res.*, **87**, 9890-9904.

Mouginis-Mark, P.J., Wilson, L. and Zuber, M.T. (1992) The physical volcanology of Mars. In: Keiffer, H.H., Jakosky, B.M., Snyder, C.W. and Matthews, M.S. (eds.) *Mars*. Univ. Arizona Press, Tucson.

Nagata, T., Hirao, K., Fukushima, M. and Takahashi, T. (1946) The change in point discharge current due to the volcanic smoke of Sakura-jima. *Bull. Earthq. Res. Inst.*, **24**, 221-227. (in Japanese)

Nalivikin, D.V. (1983) *Hurricanes, Storms and Tornadoes*. A.A. Balkema, Rotterdam.

Neubauer, F.M. (1998) Comment on “Interaction of Io with its torus: Does Io have an internal magnetic field?” by Krishan K. Khurana, Margaret G. Kivelson and Christopher T. Russell. *Geophys. Res. Letts.*, **25**, 2349.

Nitsan, U. (1977) Electromagnetic emission accompanying fracture of quartz-bearing rocks. *Geophys. Res. Lett.*, **4**, 333-336.

Ogawa, T., Oike, K. and Miura, T. (1985) Electromagnetic radiation from rocks. *J. Geophys. Res.*, **90**, 6245-6249.

Ohuchi, F. and Holloway, P.H. (1982) General model of sodium desorption and diffusion during electron bombardment of glass. *J. Vac. Sci. Technol.*, **20**, 863-867.

Ouellet, M. (1990) Earthquake lights and seismicity. *Nature*, **348**, 492.

Palmieri, L. (1873) *The eruption of Vesuvius in 1872*. (translation) Asher & Co., London.

Paskievitch, J.F., Murray, T.L., Hoblitt, R.P. and Neal, C.A. (1995) Lightning associated with the August 18, 1992, eruption of Crater Peak vent, Mount Spurr volcano, Alaska. In: Keith, T.E.C. (ed.) *The 1992 eruptions of Crater Peak vent, Mount Spurr volcano, Alaska*. United States Geological Survey Bulletin, **2139**, 179-182.

Pasko, V.P., Inan, U.S., Bell, T.F. and Taranenko, Y.N. (1997) Sprites produced by quasi-electrostatic heating and ionisation in the lower ionosphere. *J. Geophys. Res.*, **102**, 4529-4561.

Peale, S.J., Cassen, P. and Reynolds, R.T. (1979) Melting of Io by tidal dissipation. *Science*, **203**, 892-894.

Pearl, J., Hanel, R., Kunde, V., Maguire, W., Fox, K., Gupta, S., Ponnamperuma, C. and Raulin, F. (1979) Identification of gaseous SO_2 and new upper limits for the other gases on Io. *Nature*, **280**, 755-758.

Phillips, J.C., Lane, S.J., Lejeune, A.-M. and Hilton, M. (1995) Gum rosin-acetone system as an analogue to the degassing behaviour of hydrated magmas. *Bull. Volc.*, **57**, 263-268.

Pierce, E.T. (1970) *Waterfalls, Bathrooms and Perhaps Supertanker Explosions*. Stanford Research Institute Report 4454 to O.N.R. Contract No. 14-71-C-0106.

Pieri, D.C., Baloga, S.M., Nelson, R.M. and Sagan, C. (1984) Sulfur flows of Ra Patera. *Icarus*, **60**, 685-700.

Pliny (79AD) Book VI, Letter XX to C. Tacitus. In: Warmington, E.H. (1969) (ed.) *Pliny, Letters and panegyricus.* William Heinemann Ltd., London. (translation by B. Radice)

Prata, A.J. (1989) Observations of volcanic ash clouds in the 10-12 μm window using AVHRR/2 data. *Int. J. Remote Sensing*, **10**, 751-761.

Pratt, W.E. (1911) The eruption of Taal volcano, January 30, 1911. *Philippine J. Sci.*, **6**, 63-86.

Perret, F.A. (1924) *The Vesuvious eruption of 1906.* Carnegie Institute of Washington, Washington.

Pond, J.A. and Smith, S.P. (1886) Observations on the eruption of Mount Tarawera, Bay of Plenty, New Zealand, 10th June, 1886. *New Zealand Inst, Trans. and Proc*., **19**, 342-371.

Pounder, C. (1972) Electrification from salt water on heated metals. *J. Phys. D: Appl. Phys.*, **5**, 753-755.

Pounder, C. (1978) *Investigation of a reproducible boiling phenomenon with relevance to volcanic lightning*. Ph.D. Thesis, Open University.

Pounder, C. (1980a) Charge carrying particles from Leidenfrost boiling (an aspect of saline contact charging). Part II. The electrical properties of Leidenfrost drops and associated particles. *J. Electrostatics*, **9**, 177-182.

Pounder, C. (1980b) Volcanic lightning. *Weather*, **35**, 357-360.

Pounder, C. (1984) Solution contact charging with respect to earthquake lights. *Nature*, **307**, 389.

Rennilson, J.J. and Criswell, D.R. (1974) Surveyor observations of lunar horizon glow. *Moon*, **10**, 121.

Reynolds, S.E., Brook, M. and Gourly, M.F. (1957) Thunderstorm charge separation. *J. Meteor.*, **14**, 426-437.

Robinson, M. (1973) Electrostatic precipitation. In: Moore, A.D. (ed.) *Electrostatics and its Applications*. John Wiley & Sons, Inc., New York.

Rose, W.I., Kostinski, A.B. and Kelley, L. (1995) Real-time C-Band radar observations of 1992 eruption clouds from Crater Peak, Mount Spurr volcano, Alaska. In: Keith, T.E.C. (ed.) The 1992 eruptions of Crater Peak vent, Mount Spurr volcano, Alaska. *U.S. Geol. Surv. Bull.*, **2139**, 19-26.

Rosenbaum, J.G. and Waitt Jr., R.B. (1981) Summary of eyewitness accounts of the May 18 eruption. In: Lipman, P.W. and Mullineaux, D.R. (eds.) The 1980 Eruptions of Mount St. Helens, Washington. *U.S. Geol. Surv. Prof. Paper*, **1250**, 53-67.

Sabit, J.P., Pigtain, R.C. and de la Cruz, E.G. (1996) The West-Side story: Observations of the 1991 Mount Pinatubo Eruptions from the West. In: Newhall, C.G. and Punongbayan, S. (eds.) *Fire and mud: Eruptions and lahars on Mount Pinatubo, Philippines*. University of Washington Press, Seattle.

Sagan, C. (1979) Sulphur flows on Io. *Nature*, **280**, 750-753.

Saunders, C.P.R., Keith, W.D. and Mitzeva, R.P. (1991) The effect of liquid water on thunderstorm charging. *J. Geophys. Res.*, **96**, 11007-11017.

Schloessin, H.H. (1985) Experiments on the electrification and luminescence of minerals and possible origins of EQLs and sferics. *Ann. Geophys.*, **3**, 709-720.

SEAN (1981) *Smithsonian Institution Scientific Event Alert Network Bulletin*, **6**, no. 10, 4.

Sentman, D.D., Wescott, E.M., Osborne, D.L., Hampton, D.L. and Heavner, M.J. (1995) Preliminary results from the Sprites ’94 aircraft campaign: Red sprites. *Geophys. Res. Letts.*, **22**, 1205-1208.

Sheldon, J.W. (1974) Charge separation from drops of NaCl solution on a heated metal. *J. Phys. D: Appl. Phys.*, **7**, 91-93.

Shepherd, J.B. Aspinall, W.P., Rowley, K.C., Pereira, J., Sigurdsson, H., Fiske, R.S. and Tomblin, J.F. (1979) The eruption of Soufriere volcano, St. Vincent, April-June 1979. *Nature*, **282**, 24-28.

SIBGVN (1994) *Smithsonian Institution Bulletin of the Global Volcanism Network*, **19**, no. 8, 2-6.

Simkin, T. and Fiske, R.S. (1983) *Krakatau 1883 - the volcanic eruption and its effects*. Smithsonian Institution Press, Washington D.C.

Simkin, T. and Howard, K.A. (1970) Caldera collapse in the Galapagos Islands, 1968. *Science*, **169**, 429-437.

Simpson, B. (1966) *Rocks and minerals*. Pergamon, New York.

Smythe, W.D., Nelson, R.M. and Nash, D.B. (1979) Spectral evidence for SO_2 frost or adsorbate on Io's surface. *Nature*, **280**, 766.

Sparks, R.S.J. (1978) The dynamics of bubble formation and growth in magmas - a review and analysis. *J. Volc. Geotherm. Res.*, **3**, 1-37.

Sparks, R.S.J., Bursic, M.I., Carey, S.N., Gilbert, J.S., Glaze, L.S., Sigurdsson, H. and Woods, A.W. (1997) *Volcanic plumes*. John Wiley & Sons Ltd., Chichester.

Spencer, J.R., Sartoretti, P., Ballester, G.E., McEwen, A.S., Clarke, J.T. and McGrath M.A. (1997) The Pele plume (Io): Observations with the Hubble Space Telescope. *Geophys. Res. Letts.*, **24**, 2471-2474.

Stehn, C.E. (1933) Funfzig jahre Krakatau. *Umschau*, **37**, 659-663.

Stone, E.C. and Lane, A.L. (1979a) Voyager 1 encounter with the Jovian system. *Science*, 204, 945-948.

Stone, E.C. and Lane, A.L. (1979b) Voyager 2 encounter with the Jovian system. *Science*, 206, 925-927.

Stone, M.L. (1994) Application of contemporary ground-based and airborne radar for the observation of volcanic ash. In: Casadevall, T.J. (ed.) Proceedings of the first international symposium of volcanic ash and aviation safety. *U.S. Geol. Surv. Bull*., **2047**, 419-428.

Strom, R.G., Schneider, N.M., Terrile, R.J., Cook, A.F. and Hansen, C. (1981) Volcanic eruptions on Io. *J. Geophys. Res.*, **86**, 8593-8620.

Takahashi, T. (1978) Riming electrification as a charge generation mechanism in thunderstorms. *J. Atmos. Sci.*, **35**, 1536-1548.

Tate, J. and Daily, W. (1989) Evidence of electro-seismic phenomena. *Phys. Earth Plan. Int.*, **57**, 1-10.

Tsukuda, T. (1997) Sizes and some features of luminous sources associated with the 1995 Hyogo-ken Nanbu earthquake. *J. Phys. Earth*, **45**, 73-82.

Uman, M.A. (1984) *Lightning*. Dover Publications Inc., New York.

Varotsos, P. and Alexopoulos, K. (1984a) Physical properties of the variations of the electric field of the earth preceding earthquakes. *Tectonophys.*, **110**, 73-98.

Varotsos, P. and Alexopoulos, K. (1984b) Physical properties of the variations of the electric field of the earth preceding earthquakes, determination of epicentre and magnitude. *Tectonophys.*, **110**, 99-125.

Veeder, G.J., Matson, D.L., Johnson, T.V., Blaney, D.L., and Goguen, J.D. (1994) Io's heat flow from infrared radiometry: 1983-1993. *J. Geophys. Res.,* **99**, 17095-17162.

Verbeek, R.D.M. (1885) *Krakatau, Imprimerie de l'Etat*. Government of Batavia. *Translated in*: Simkin, T. and Fiske, R.S. (1983) *Krakatau 1883 - the volcanic eruption and its effects*. Smithsonian Institution Press, Washington D.C.

Vereshagin, I.P., Morozov, V.S., Kyrylenko, I.I., Mirzabekyan, G.Z., Orlov, A.V. and Petukhov, V.S. (1989) An automatic control system of atmospheric electricity. *J. Electrostatics*, **23**, 357-360.

Wagner, P.B. and Telford, J.W. (1981) Cloud dynamics and an electric charge separation mechanism in convective clouds. *J. Rech. Atmos*., **15**, 97-120.

Warwick, J.W., Stoker, C. and Meyer, T.R. (1982) Radio emission associated with rock fracture: Possible application to the great Chilean earthquake of May 22, 1960. *J. Geophys. Res.*, **87**, 2851-2859.

Wescott, E.M., Sentman, D.D., Osborne, D.L., Hampton, D.L. and Heavner, M.J. (1995) Preliminary results from the Sprites '94 aircraft campaign: Blue jets. *Geophys. Res. Letts.*, **22**, 1209-1212.

Williams, T.J. and Bailey, A.G. (1989) Neutralization of particle charge using unipolar and bipolar space charge. *J. Electrostatics*, **23**, 341-350.

Wilson, L. and Head, J.W. (1981) Io volcanic eruptions: Mass eruption rate estimates. *Lunar Plan. Sci. Conf. XII*, 1191-1193. (abstr.)

Wilson, L. and Self, S. (1980) Volcanic explosion clouds: density temperature and particle content estimates from cloud motion. *J. Geophys. Res.*, **85**, 2567-2572.

Witteborn, F.C., Bregman, J.D. and Pollack, J.B. (1979) Io: An intense brightening near 5 micrometers. *Science*, **203**, 643-646.

Wollbrandt, J., Bruckner, U. and Linke, E. (1983) Investigations of mechanically induced excited states on cleavage planes of ionic crystals. *Phys. Stat. Solidi (A).*, **78**, 163-168.

Woodcock, A.H. and Spencer, A.T. (1961) Lava-sea-air contact areas as sources of sea-salt particles in the atmosphere. *J. Geophys. Res.*, **66**, 2873-2887.

Workman, E.J. and Reynolds, S.E. (1948) A suggested mechanism for the generation of thunderstorm electricity. *Phys. Rev*., **74**, 709.

Workman, E.J. and Reynolds, S.E. (1950) Electrical phenomena occurring during the freezing of dilute aqueous solutions and their possible relationship to thunderstorm electricity. *Phys. Rev*., **78**, 254-259.

Xiong-Skiba, P., Doering, D.L. and Siek, K.H. (1991) Characterization of the interfacial failure of metal thin films on oxidized silicon using fracto-emission. *J. Vac. Sci. Technol.*, **9**, 2563-2565.

Yamada, I., Masuda, K. and Mizutani, H. (1989) Electromagnetic and acoustic emission associated with rock fracture. *Phys. Earth Plan. Int.*, **57**, 157-168.

Yasui, Y. (1968) A study on the luminous phenomena accompanied with earthquakes. I. *Proc. Kakioka Magn. Obs.*, **13**, 23-33.

Yasui, Y. (1971) A study on the luminous phenomena accompanied with earthquakes. II. *Proc. Kakioka Magn. Obs.*, **14**, 67-78.

Yoshino, T. and Tomizawa, I. (1990) Observation results of low frequency electromagnetic emissions as precursors of volcanic eruption at Mt. Mihara in November, 1986. *J. Geomag. Geoelectr*., **42**, 225-235.

Zlotnicki, J. and Le Mouël, J.L. (1990) Possible electrokinetic origin of large magnetic variations at La Fournaise volcano. *Nature*, **343**, 633-636.

Zwikker, C. (1954) *Physical Properties of Solid Materials*. Interscience, New York.

Appendix I. Equipment specifications

AI.1 Electrostatic fieldmeters

The electrostatic fieldmeters used (Figure AI.1) were two different models of rotating chopper field-mill, JCI 111 and JCI 121. Both types were produced by John Chubb Instruments but had been modified by the manufacturer from their original specifications (listed below in Table AI.1 for the JCI 111). The analogue outputs representing the measured electric field were decreased from ±2 V full scale deflection, to ±1 V for compatibility with the LogIT data loggers. The JCI 111 meter was converted to allow an external ±7.5 V battery supply and the JCI 121 meters were supplied with an extended 2 m cable. One JCI 111 and five JCI 121 fieldmeters were used during atmospheric potential gradient monitoring at Sakurajima volcano (Chapter 4). One JCI 121 fieldmeter was used for the experimental work described in Chapter 5.

Figure AI.1 JCI electrostatic fieldmeters. JCI 111 (centre) with two JCI 121 model fieldmeters either side. The rotating chopper and LCD display are visible on the JCI 111. Both JCI 121 units display the sensing aperture within which the rotating chopper is located.

Table AI.1 JCI 111 electrostatic fieldmeter specifications.

Manufacturer	John Chubb Instrumentation (http://www.jci.co.uk/)
Sensitivity ranges	autoranging: ± 2, 20, 200, 2000 kV m^{-1}
Accuracy and linearity	±1 % of each range full scale deflection zero offset stable within ±50 V m^{-1} noise within ±10 V m^{-1}
Display	3½ digit LCD giving electric field in kV m^{-1}, polarity and low battery warning
Outputs	4 pin connector with various options including: earth, ±2 V electric field analogue signal, sensitivity range, RS 423 interface, alarm, calibration
Power requirements	internal NiCd rechargeable battery giving about 4 hours continuous operation integral regulated mains power supply / battery charger
Mounting	¼" Whit thread tripod mounting bush
Dimensions and weight	65 × 65 × 240 mm, 900 g

The JCI 121 has similar response characteristics to the JCI 111. However, it is cylindrical in shape, 50 mm in diameter and 85 mm long, and does not have an LCD display. Electrical connections (including the ±7.5 V power supply) are made by a 15 way D-type plug. Mounting is achieved by three M4 blind tapped screw holes in the base of the unit. The electrical connections for both fieldmeters are given below in Tables AI.2 and AI.3.

Table AI.2 Connections at 15 pin D-type connector plug of cable to JCI 121 fieldmeter head unit.

Pin	Connection		Pin	Connection	
1	frame earth to cable sheath	(green/yellow)	8	+V motor	(red)
			9	range control: bit 1	(yellow)
2	0 V	(black)	10	0 V	(pale blue)
3	0V	(slate)	11	n/c	
4	signal earth	(green)	12	n/c	
5	signal	(white)	13	-V circuit	(orange)
6	+V circuit	(pink)	14	range control: bit 2	(brown)
7	zero adjust	(violet)	15	-V motor	(blue)

Table AI.3 Connections at 9 pin D-type connector plug of cable to JCI 111 fieldmeter.

Pin	Connection		Pin	Connection	
1	n/c		5	signal	(red, signal cable)
2	0 V	(green)	6	+V	(blue)
3	signal earth	(black, signal cable)	7	n/c	
4	range	(blue, signal cable)	8	n/c	
	analogue: 0.25, 0.5, 0.75 or 1 V		9	-V	(red)

AI.2 Electrometers

Two Keithley Model 614 electrometers were used during the experimental work. These have the capability to measure voltage, current, resistance and charge. Specifications for the charge measurement function are given in Table AI.4.

Table AI.4 Keithley 614 electrometer specifications. (lsd is the lowest significant digit on the LED display).

Manufacturer		Keithley Instruments Inc. (http://www.keithley.com/)
Input connector		triaxial BNC-type
Display		4½ digits LED display
Output		±2 V analogue output
Charge measurements	Ranges	± 0.2, 2.0, 20 nC
	Resolution and accuracy	0.2 nC range: 10 fC ±(5 % + 50 lsd) 2.0 nC range: 100 fC ±(5 % + 5 lsd) 20 nC range: 1 pC ±(5 % + 1 lsd)
	Input bias current	< 60 fA at 23 °C
Power requirements		mains or internal rechargeable battery
Environmental conditions		0 – 35 °C 0 – 70 % RH
Dimensions and weight		127 × 216 × 359 mm, 3.3 kg

AI.3 Data loggers

Two types of data logger were employed: LogIT SL and Pico ADC-100. The LogIT data loggers (Table AI.5) are capable of being programmed from a PC for remote logging, allowing the data to be downloaded later. The Pico ADC-100 (Table AI.6) runs directly from a PC and is not capable of operating remotely. Logging is controlled by PicoLog software, but the logger can also be used as a 'virtual oscilloscope' with PicoScope software.

Table AI.5 LogIT SL specifications.

Manufacturer		DCP Microdevelopments Ltd. (http://www.dcpmicro.com/)
Sensor inputs		3 DIN sockets, each with one analogue and one digital input
Power requirements		8.3 V rechargeable battery (PP3 size) or external 9 to 13.5 V d.c. supply
Data link		serial via DBus socket RS 232/423 compatible interface 9600 Baud
Analogue inputs	Resolution	12 bit
	Accuracy	±1 % (nominal)
	Max. sampling rate	300 samples per second
Voltage reference		2.5 V precision IC source
Dimensions and weight		120 × 67 × 32 mm, 195 g

Table AI.6 Pico ADC-100 specifications.

Manufacturer	Pico Technology Ltd (http://www.picotech.co.uk/)
Resolution	12 bit
Number of input channels	2, either AC or DC
Input voltage ranges	software selectable: ± 20, 10, 5, 2, 1 V, ± 500, 200 mV
Max sampling rate	computer dependent: 120 k samples per second with 486-66 100 k samples per second with 386-33
Repeatability	±4 lsb at 25 °C
Absolute accuracy	±1 % typical at 25 °C ±3 % worst case over operating temp. range
Input impedance	1 MΩ
Input connectors	BNC
Output connector	25-way male D-type to computer parallel port
Power requirements	all power sourced from output connector
Environmental conditions	0 to 70 °C 0 to 95 % RH

A1.4 High voltage power supplies

The EHT supply for the parallel plates was provided by two Brandenburg 390 series miniature high voltage power supply modules. One supplied 0 to +3.5 kV and the other -3.5 to 0 kV. Their specifications are provided in Table AI.7.

Table AI.7 EHT power supply specifications.

Manufacturer	Brandenburg (http://www.brandenburg.co.uk)	
Model number	390-108	390-208
Polarity	positive	negative
Output voltage	0 to 3.5 kV	
Output current	1.5 mA	
Input voltage	24 V	
Output control	internal potentiometer	
Output ripple (peak to peak, at maximum output and full load)	350 mV	
Temperature coefficient (maximum)	300 ppm per °C	

Appendix II. Fieldmeter zero values

Table AII.1 (overleaf) Zero offsets of the fieldmeters used at Sakurajima. The numbers represent the output voltage (in volts) of the fieldmeters with the zero-check chamber over the sensing aperture. The symbol '?' indicates that an unsteady zero-value was obtained, and '-' indicates that a zero not taken. The asterisk indicates where the broken fieldmeter D was replaced by fieldmeter F. For each fieldmeter, 'start' refers to the zeros taken (in the field) before each day of monitoring, and 'end' refers to the zeros taken (in the field) at the end of the day of monitoring. 'Lab.' refers to the zeros taken at Sakurajima Volcano Research Center during the evening.

Date	Fieldmeter A			Fieldmeter B			Fieldmeter C			Fieldmeter D (F)			Fieldmeter E		
	Start	End	Lab.	Start	End	Lab.	Start	End	Lab.	Start	End	Lab.	Start	End	Lab.
16/10/96	0.12	0.40	0.04	0.15	0.20	0.19	-0.10	?	0.17	-0.01	0.18	-0.20	-	-	-
17/10/96	0.03	0.01	0.06	0.18	0.17	0.17	0.13	0.21	0.23	-0.22	-0.22	-0.21	-	-	-
18/10/96	-0.10	0.06	0.08	0.16	0.14	0.13	0.19	0.20	0.22	-0.18	-0.21	-0.19	-	-	-
19/10/96	0.11	?	0.11	0.08	0.08	0.11	0.25	0.22	0.33	-0.18	-	-0.02 *	-	-	
21/10/96	0.39	0.34	0.11	0.12	0.19	0.16	0.35	0.22	0.25	-0.02	0.00	0.00	-0.05	-0.03	-
22/10/96	?	0.40	0.12	0.19	-	0.21	0.28	0.43	0.44	-0.01	-0.01	-0.01	-	-	-
23/10/96	0.13	0.04	-	?	0.15	-	0.39	0.24	-	-	-	-	-0.05	-0.01	-
24/10/96	0.14	-	0.22	0.28	0.25	0.29	0.36	0.28	0.42	0.00	-	0.03	-0.01	-0.16	-0.03
26/10/96	0.19	0.20	0.19	0.25	-	0.24	0.49	0.61	0.72	0.04	0.01	0.01	-	-	-
27/10/96	0.15	0.08	0.08	0.21	0.19	0.21	0.72	0.59	0.69	0.01	0.00	0.01	-	-	-
29/10/96	0.01	-	0.05	0.19	-	0.28	0.58	0.48	0.55	0.04	0.01	0.04	-	-	-
30/10/96	0.06	-0.04	0.02	0.28	0.22	0.26	0.42	0.36	0.66	0.07	0.03	0.03	-0.04	-0.05	-0.06
31/10/96	-0.01	-0.02	0.03	0.27	0.26	0.26	0.53	0.50	0.50	0.06	0.04	0.09	-	-	-
02/11/96	-0.05	-0.01	-0.39	0.22	0.17	0.20	0.22	0.71	0.75	0.08	0.04	0.04	-	-	-
03/11/96	0.02	-	0.02	0.22	0.15	0.19	0.73	0.53	0.68	0.06	-0.04	0.02	-	-	-
04/11/96	0.01	-	-0.01	0.19	-	0.21	?	-	0.52	0.00	-	-0.01	-0.10	-0.28	-0.19
05/11/96	?	-	-0.03	0.24	-	0.25	0.65	0.52	0.56	-	-	-	-0.17	-0.14	-0.13
06/11/96	0.07	-	0.13	0.24	0.17	0.21	0.54	0.50	0.65	0.02	-0.03	0.00	-0.11	-0.13	-0.16
07/11/96	0.16	0.16	0.09	0.22	-	0.20	?	0.61	0.60	-0.01	-0.04	-0.04	-0.13	-0.37	-0.16
08/11/96	0.00	0.00	0.03	0.21	0.17	0.23	?	-	0.51	-0.02	-0.01	0.00	-0.16	?	-0.16
09/11/96	0.14	-	0.15	0.22	0.23	0.25	-	-	0.41	0.02	-0.02	0.02	-0.13	-0.14	-0.13
10/11/96	0.17	-0.04	0.02	0.24	0.17	0.24	0.36	0.48	0.47	0.03	-0.02	0.00	-0.12	-0.13	-0.11
12/11/96	0.10	0.12	0.12	0.19	0.15	0.18	0.40	0.55	0.67	0.05	-0.04	-0.02	-0.13	-0.14	-0.10
13/11/96	0.12	0.22	0.25	0.18	0.13	0.16	0.54	0.44	0.54	-0.02	-0.04	-0.04	-0.09	-0.14	-0.12
14/11/96	0.17	0.33	0.28	0.19	0.08	0.17	?	0.45	0.76	-0.02	-0.04	-0.12	-0.11	-0.15	-0.13
15/11/96	0.22	-	0.22	0.21	0.15	0.19	?	0.62	0.70	-0.04	-0.08	-0.07	-0.12	-0.11	-0.12
16/11/96	0.23	0.38	0.23	0.20	0.13	0.16	0.72	-	0.72	-0.05	-0.08	-0.05	-0.15	-0.15	-0.13
18/11/96	0.13	0.24	0.16	0.19	0.16	0.18	0.73	0.79	0.72	-0.03	-0.06	-0.05	-0.12	-0.13	-0.13
19/11/96	0.25	-	0.27	0.16	-	0.16	?	0.52	0.68	-0.06	-0.06	-0.03	-0.13	-0.15	-0.13
20/11/96	0.25	-	0.22	0.21	0.15	0.18	?	0.62	0.76	-0.04	-0.04	0.01	-	-	-
21/11/96	0.19	0.29	0.28	0.20	0.20	0.16	0.64	0.59	0.66	0.00	-0.04	-0.03	-0.12	-0.15	-0.13

Appendix III. Calibration data for experiments

Table AIII.1 Fieldmeter calibration data for the net ash charge experiments. A.P. is the applied potential to the Faraday cup, and ADC is the average of the ADC counts of the fieldmeter output logged for each potential. Plotting ADC against A.P. produces straight lines for each experiment, and the reciprocal gradients required for calibration are given. The 02/06/98 experiment marked with an asterisk, was carried out under vacuum (10^{-3} Torr).

28/06/97				31/07/97		09/10/97		02/06/98		02/06/98*	
A.P.	ADC	A.P.	ADC	A.P.	ADC	A.P.	ADC	A.P.	ADC	A.P.	ADC
0.000	0.0	18.28	463.3	0.090	1.8	0.000	0.0	0.000	0.6	0.000	0.0
0.087	1.7	18.33	464.2	0.57	13.7	0.000	-0.1	1.645	40.4	0.000	0.0
0.176	4.3	19.3	488.4	1.12	28.1	0.080	1.5	2.263	56.2	0.555	14.5
0.406	10.3	20.16	511.0	1.37	34.3	0.38	7.7	3.022	75.6	1.587	41.3
0.666	17.0	20.3	513.4	1.67	40.5	0.55	12.2	3.541	88.5	1.650	43.2
0.666	17.1	20.81	527.3	1.71	42.8	1.05	25.5	4.85	122.2	2.347	60.4
1.077	27.6	21.65	548.4	1.92	47.7	2.21	53.6	5.93	148.9	2.999	76.1
1.554	40.0	22.07	559.7	2.31	58.4	3.14	77.4	6.05	152.7	4.67	120.2
2.589	65.5	22.51	569.9	2.72	68.3	4.09	100.4	7.68	194.4	5.43	138.4
2.876	73.4	23.34	591.6	2.75	68.3	4.99	123.8	9.38	236.2	6.09	155.8
3.531	89.6	24.09	610.2	4.51	113.5	6.06	150.4	9.54	241.0	7.61	193.1
4.25	109.7	24.24	614.0	5.04	125.3	6.23	155.0	11.14	281.5	8.37	213.4
4.41	112.4	25.29	640.6	5.52	138.7	7.13	177.9	11.39	288.1	9.7	247.6
5.53	140.4	25.85	655.3	6.19	155.3	7.26	180.1	13.37	338.3	9.96	252.2
5.52	141.6	26.13	661.9	6.69	167.4	8.39	209.7	13.4	338.5	11.88	302.1
6.75	171.2	27.46	695.7	7.98	199.6	8.63	215.0	14.74	372.3	12.72	323.0
6.7	171.3	27.68	701.3	8.96	224.0	9.62	240.8	15.61	394.3	14.41	366.3
7.45	188.9	28.59	723.8	9.03	226.7	10.23	255.7	16.39	414.5	14.76	376.3
7.61	193.8	28.98	734.6	9.9	248.6	11.34	282.6	17.65	445.8	16.8	426.4
8.3	209.9	29.12	737.4	11.03	276.1	11.84	294.2	17.67	446.8	16.97	431.0
8.94	227.1	31.16	788.5	11.18	280.1	12.5	311.9	19.69	497.6	18.88	478.8
9.15	232.2			11.86	296.8	13.48	336.5	19.83	500.7	19.08	484.1
10.13	256.8			12.19	305.3	14.3	355.3	21.3	538.0	20.14	510.4
10.33	261.6			12.8	319.7	14.39	357.8	21.92	553.3	20.76	527.2
11.33	287.7			13	324.9	15.57	387.6	22.92	579.7	22.12	562.4
11.48	290.2			13.74	344.3	16.2	403.9	23.68	597.9	22.13	562.3
11.86	300.4			13.79	345.9	17.23	429.8	24.15	611.3	23.19	588.7
12.52	317.1			15.1	378.4	17.27	430.8	25.28	639.3	24.32	617.9
13.11	332.7			15.42	385.1	18.57	463.6	25.47	644.2	25.69	652.1
13.31	336.9			17.07	427.8	18.79	468.3	26.51	670.4	26.56	673.9
13.89	352.1			17.11	427.6	19.72	491.5	27.38	691.9	27.33	694.4
14.54	368.3			17.57	440.2	19.90	496.9	28.32	715.2	28.43	722.4
15.35	388.6			17.82	444.7			30.50	771.2	30.12	764.0
15.39	389.9			18.93	474.0					30.53	774.7
16.64	420.9			19.41	484.4						
17.22	436.2			20.09	502.7						
17.58	445.1			20.38	508.5						
Gradient^{-1} (V adc^{-1})		0.0395		0.0400		0.0400		0.0395		0.0394	

Table AIII.2 Verification of internal calibration of the mass balance.

Mass measurements of 1.0024 g calibrated check weight (g)		
Test no.	18/05/98	21/05/98
1	1.00251	1.00244
2	1.00245	1.00244
3	1.00248	1.00244
4	1.00246	1.00244
5	1.00246	1.00244
6	1.00245	1.00245
7	1.00244	1.00245
8	1.00247	1.00244
9	1.00246	1.00243
10	1.00244	1.00243
Mean	1.002462	1.002440
Standard deviation, σ_{n-1} (mg)	0.013	0.007

Table AIII.3 Repeatability of five figure mass measurements of the particle charge experiment foils.

Repeated mass measurements (g)		
Measurement no.	Plate foil	Tray foil
1	0.64139	0.46408
2	0.64141	0.46407
3	0.64142	0.46404
4	0.64142	0.46406
5	0.64141	0.46407
6	0.64142	0.46408
7		0.46406
8		0.46409
9		0.46407
10		0.46405
Mean	0.641412	0.464067
Standard deviation, σ_{n-1} (mg)	0.012	0.015

Table AIII.4 Measurements of the apparent increases in foil mass. The apparent measured mass increases of foils after folding are shown in mg.

Foil number	Mass of plate foils (g)			Mass of tray foils (g)		
	Before folding	After folding	Mass increase (mg)	Before folding	After folding	Mass increase (mg)
1	0.64277	0.64295	0.18	0.47472	0.47494	0.22
2	0.65528	0.65547	0.19	0.45065	0.45082	0.17
3	0.62162	0.62178	0.16	0.50319	0.50333	0.14
4	0.59834	0.59851	0.17	0.47466	0.47486	0.20
5	0.60217	0.60237	0.20	0.46409	0.46425	0.16
6	0.60314	0.60330	0.16	0.47485	0.47509	0.24
7	0.60622	0.60646	0.24	0.47948	0.47965	0.17
8	0.60557	0.60573	0.16	0.47778	0.47801	0.23
9	0.66111	0.66127	0.16	0.47584	0.47602	0.18
10	0.59959	0.59981	0.22	0.49254	0.49276	0.22
11	0.60041	0.60057	0.16			
12	0.59419	0.59445	0.26			
13	0.60608	0.60628	0.20			
14	0.60136	0.60154	0.18			
15	0.60850	0.60866	0.16			
16	0.59736	0.59753	0.17			
17	0.60047	0.60060	0.13			
18	0.60954	0.60971	0.17			
19	0.60019	0.60038	0.19			
20	0.59713	0.59737	0.24			
Average			0.185			0.193
Standard deviation, σ_{n-1}			0.033			0.034

Table AIII.5 Statistics for repeated size analyses of particles produced from Mount St. Helens pumice. The given surface area is the particle surface area (in units of 10^{-12} m^2) calculated by PDI software for a total particulate volume of 1×10^{-13} m^{-3}. All other statistics also provided by the PDI software, with the exception of the specific surface area (calculated assuming a particle density of 2600 kg m^{-3}).

	Test 1	Test 2	Test 3	Test 4	Test 5
Geometric mean diameter	16.14	15.16	15.27	15.81	15.49
Arithmetic mean diameter	19.18	18.35	18.11	18.76	18.50
Median diameter	16.65	16.05	16.07	16.63	16.08
Modal diameter	20.25	18.74	18.31	21.01	18.00
Standard deviation	1.827	1.907	1.849	1.833	1.856
Coefficient of variance	11.32	12.58	12.11	11.59	11.98
Skewness	-2.253	-1.877	-1.643	-2.833	-1.351
Given surface area	11234	12464	12083	11530	11902
Calculated specific surface area ($m^2 kg^{-1}$)	173.0	191.9	186.1	177.6	183.3

Appendix IV: Experiment results

AIV.1 Net ash charge experiments

In this section, the details of the experiments carried out with the Faraday cup apparatus are given. The experiments were catalogued by an experiment ID comprised of the date on which each was carried out, given by *ymmdd* (where *y*, indicates the year, 7, for 1997, or 8 for 1998, *mm*, for the month and *dd*, for the day) followed by a letter (to delineate different experiments carried out on the same day). Each pair of pumice samples were similarly catalogued, and usually given the same name as the experiment in which they were first used. For further information on the pumice types see Appendix V and Chapter 6. The details and results of the net charge experiments are given in Table AIV.1. Graphs of all these experiments are provided at the end of this appendix, in Figure AIV.1.

AIV.2 Particle charge experiments

Table AIV.2 provides the details and summarised results for the particle charge experiments. The experiments were given ID's of the same format as the net ash charge experiments.

Table AIV.1 Net charge experiments: details and results summary. Abbreviations used in the table are: li, linear impact; rg, rotational grinding; pp, pumice–pumice; ih, insulated hammer; ea, earthed anvil; eh, earthed hammer; P, pressure in Torr, (760 Torr for atmospheric pressure); T, temperature (°C); RH, relative humidity (%); PM, collected particle mass (in mg); λ, mass loss fraction; Q, net charge recorded for the Faraday cup (in units of 10^{-12} C), Q_{sp}, specific net charge (in units of 10^{-5} C kg^{-1}); SSA, specific surface area (in m^2 kg^{-1}) and SCD, effective surface charge density (in units of 10^{-7} C m^2). For linear impact experiments, the number of impacts are given in the experiment type column. The samples are described by pumice type, clast number, and sample ID.

Exp. ID	Samples	Exp. Type	P	T	RH	PM	λ	Q	Q_{sp}	SSA	ESCD	Notes
70702a	Santorini, 1, 70702a	li, pp, 193	10^{-3}	-	-	46.0	0.09	-1076	-2.34	147.4	-1.59	logging the fieldmeter over ±1 V (data lost as it approached range change) logging every 50 ms
70702b	Santorini, 1, 70702b	li, pp, 119	10^{-3}	-	-	66.6	0.07	-1349	-2.03	179.1	-1.13	logging the fieldmeter over ±1 V (data lost as it approached range change) logging every 50 ms
70703a	Santorini, 1, 70703a	li, pp, 190	10^{-3}	-	-	17.2	0.12	-586	-3.41	235.9	-1.44	no data recorded by LogIT due to battery failure 90 seconds of solenoid activity, number of impacts estimated
70703b	Santorini, 1, 70703b	li, pp, 182	10^{-3}	-	-	16.0	0.06	-699	-4.37	252.2	-1.73	
70707a	Santorini, 1, 70707a	li, pp, 206	10^{-3}	-	-	10.9	0.06	-367	-3.37	208.4	-1.62	sudden offsets in the mesh data probably due to the body of the solenoid touching the top of the Faraday cup shielding
70707b	Santorini, 1, 70707b	li, pp, 207	10^{-3}	-	-	16.5	0.09	-1180	-7.15	263.8	-2.71	sample contact appeared to occur only in limited areas, represented by white patches, covered with very fine particles
70707c	Santorini, 1, 70707c	li, pp, 205	10^{-3}	-	-	2.9	0.35	-146	-5.03	251.8	-2.00	sample contact appears to have been in very limited areas
70708a	Sak 13I, 1, 70708a	li, pp, 211	10^{-3}	-	-	42.3	0.21	?	-	-	-	samples orientated along direction of vesicle elongation
70708b	Sak 13I, 1, 70707b	li, pp, 5	10^{-3}	-	-	-	-	?	-	-	-	after a couple of collisions, hammer sample broke and landed on mesh vibrations cause it to move around on the mesh, producing a few more particles
70708c	Sak 13I, 1, 70708a	li, pp, 228	10^{-3}	-	-	49.5	0.23	?	-	-	-	
70709a	Santorini, 1, 70802a	li, pp, 183	10^{-3}	-	-	63.4	0.12	-1775	-2.80	186	-1.51	
70709b	Sak 13I, 2, 70709b	li, pp, 193	10^{-3}	-	-	28.1	0.32	?	-	-	-	variable net ash polarity
70709c	Sak 13I, 2, 70709b	li, pp, 273	10^{-3}	-	-	34.2	0.08	?	-	-	-	fixed anvil (no recoil), variable net ash polarity
70710a	Sak 13I, 2, 70709b	li, pp, 368	10^{-3}	-	-	62.5	0.13	?	-	-	-	sample dried at 10^{-3} Torr for over 4 hours before experiment electrometer problem towards end of experiment
70710b	Sak 13I, 2, 70709b	li, pp, 271	10^{-3}	-	-	33.0	0.06	?	-	-	-	low anvil recoil to ensure that hammer slider was not colliding with stop variable net ash polarity
70712a	Sak 13I, 2, 70709b	li, pp, 351	10^{-3}	-	-	40.9	0.07	?	-	-	-	low recoil to ensure that hammer slider was not colliding with stop mesh logging failed, but mesh charge follwed pattern recorded in 70709c with and end value of 165×10^{-12} C; variable net ash polarity

Table AIV.1 continued..

Exp. ID	Samples	Exp. Type	P	T	RH	PM	λ	Q	Q_{sp}	SSA	ESCD	Notes
70712b	Sak 13I, 2, 70709b	li, pp, 306	10^{-3}	-	-	43.2	-	?	-	-	-	samples not removed after experiment to allow assessment of 'bedding in' of the contact surfaces, variable net ash polarity mesh extended to include horizontal mesh below the samples
70713a	Sak 13I, 2, 70709b	li, pp, 269	10^{-3}	-	-	13.6	-	?	-	-	-	samples not removed since last experiment in order to see if 'bedding in' of the contact surfaces is a factor, variable net ash polarity
70713b	Sak 13I, 2, 70709b	li, pp, 10	10^{-3}	-	-	6.1	-	-102	-1.67	132.1	-1.27	samples not removed since last experiment, but anvil rotated round by 180° impacts stopped when visible particle production ceased
70715a	Sak 13I, 2, 70709b	li, pp, 374	10^{-3}	-	-	12.3	0.04	-183	-1.49	127.8	-1.16	samples insulated by mounting on two layers on insulating tape; slowing down of the charge generation probably due to decreasing attrition rate; unknown cause for offset in mesh data
70715b	Sak 13I, 2, 70709b	li, pp, 359	10^{-3}	-	-	17.8	-	?	-	-	-	sample faces flattened since last experiment variable net ash polarity, samples not removed after experiment
70715c	Sak 13I, 2, 70709b	li, pp, 289	10^{-3}	-	-	8.7	-	?	-	-	-	samples not removed since previous experiment; variable net charge polarity
70715d	Sak 13I, 2, 70709b	li, pp, 383	10^{-3}	-	-	13.5	0.04	?	-	-	-	sample faces flattened since previous experiment; unknown source of offset in mesh data variable net ash polarity
70716a	Sak 14, 1, 70716a	li, pp, 408	10^{-3}	-	-	4.5	0.16	?	-	190.7	-	samples dried under vacuum overnight before experiment; variable net ash polarity
70716b	Sak 14, 1, 70716a	li, pp, 305	10^{-3}	-	-	2.1	-0.10	-96	-4.57	286	-1.60	particles produced not visible during experiment small white patches produced where impacts were actually taking place (implies small particles, and low rates of production)
70716c	Sak 14, 1, 70716a	li, pp, 323	10^{-3}	-	-	1.0	1.20	?	-	167.5	-	surfaces of samples flattened since last experiment; variable net ash polarity
70721a	Santorini, 1, 70702a	li, pp, 245	10^{-3}	-	-	29.8	0.18	-849	-2.85	176	-1.62	sample surfaces flattened since last experiment
70721b	Santorini, 1, 70702a	li, pp, 332	10^{-3}	-	-	7.7	0.21	-133	-1.73	221.7	-0.78	sample surfaces flattened since last experiment; horizontal section of the mesh removed
70722a	Santorini, 1, 70702a	li, pp, 312	10^{-3}	-	-	17.9	0.24	-146	-0.82	186.2	-0.44	
70722b	Santorini, 1, 70702a	li, pp, 334	10^{-3}	-	-	18.7	0.17	-218	-1.17	146	-0.80	horizontal section of the mesh re-attached
70724a	Santorini, 1, 70702a	li, pp, 233	10^{-3}	-	-	14.5	0.19	-236	-1.63	178.2	-0.91	horizontal section of the mesh removed
70724b	Santorini, 1, 70702a	li, pp, 74	10^{-3}	-	-	14.7	0.22	-700	-4.76	189.6	-2.51	impacts stopped when the anvil stopped recoiling, showing that the hammer was reaching its stop
70724c	Sak 13I, 3, 70724c	li, pp, 91	10^{-3}	-	-	65.8	0.15	?	-	-	-	horizontal section of the mesh attached for this experiment; variable net ash polarity
70724d	Sak 13I, 3, 70724c	li, pp, 75	10^{-3}	-	-	42.1	0.39	?	-	-	-	ash sample lost; variable net ash polarity
70725a	Sak 13I, 3, 70724c	li, pp,	10^{-3}	-	-	41.5	0.12	?	-	-	-	initial impacts with solenoid on 6 V, when charge accumulation stopped, voltage increased to 10 V; sharp change in rate of charge production corresponded to rapid increase in anvil recoil; variable net ash polarity
70725b	Sak 13I, 3, 70724c	li, pp, 450	10^{-3}	-	-	61.3	0.10	?	-	-	-	solenoid voltage increased from 6 V, to 9 V then 12 V, marked by sharp increases in Faraday cup charge; sharp change in rate of charge production at 3:20 corresponded to rapid increase in recoil of anvil; variable net ash polarity
70729a	StV 519, 1, 70729a	li, pp, 66	10^{-3}	-	-	32.8	0.10	497	1.52	-	-	horizontal section of the mesh re-attached; anvil sample broke
70729b	StV 519, 1, 70729a	li, pp, 142	10^{-3}	-	-	79.2	0.03	566	0.71	136.3	0.52	particles produced included one of several mm in diameter (0.0387 g)
70729c	Sak 13I, 3, 70729c	li, eh,	10^{-3}	-	-	70.7	0.15	1310	1.85	-	-	

Table AIV.1 continued..

Exp. ID	Samples	Exp. Type	P	T	RH	PM	λ	Q	Q_{sp}	SSA	ESCD	Notes
70729d	Sak 13I, 3, 70729c	li, eh,	10^{-3}	-	-	39.9	0.22	1510	3.78	-	-	horizontal section of the mesh removed
70729e	Sak 13I, 3, 70729c	li, ih,	10^{-3}	-	-	81.9	0.11	?	-	-	-	variable net ash polarity
70730a	Sak 13I, 3, 70729c	li, pp, 20	10^{-3}	-	-	11.2	0.14	-35	-0.31	-	-	20 impacts only to prevent excessive charging of the sample
70730b	Sak 14, 2, 70730b	li, pp, 358	10^{-3}	-	-	1.6	0.50	103	6.44	-	-	horizontal section of the mesh re-attached
70730c	Santorini, 1, 70702b	li, pp, 270	760	22.1	47.5	35.4	0.09	-278	-0.79	165.4	-0.47	
70730d	Santorini, 1, 70702b	li, pp, 164	10^{-3}	-	-	27.5	0.14	-992	-3.61	157.8	-2.29	
70804a	SMN 31, 1, 70804a	li, pp, 184	10^{-3}	-	-	11.4	0.70	255	2.24	162.6	1.38	anvil sample broke near the end of the experiment (producing the offset observed in the mesh data)
70804b	SMN 31, 1, 70804a	li, pp, 368	10^{-3}	-	-	14.4	0.38	166	1.15	154.1	0.75	
70804c	SMN 31, 1, 70804a	li, pp, 311	10^{-3}	-	-	11.8	0.33	160	1.36	153.8	0.88	
70804d	SMN 31, 1, 70804a	li, pp, 241	760	22.3	42.3	17.1	0.06	-304	-1.78	-	-	
70804e	SMN 31, 1, 70804a	li, pp, 352	10^{-3}	-	-	33.8	0.47	?	-	-	-	variable net ash polarity
70804f	SMN 31, 1, 70804a	li, pp, 150	760	21.9	44.3	42.1	0.02	-216	-0.51	127.6	-0.40	rate of particle production decreases rapidly towards end of experiment
70805a	StV 519, 1, 70729a	li, pp, 20	760	20.6	48.0	41.6	1.78	-19	-0.05	-	-	
70805b	Sak 14, 2, 70730b	li, pp, 305	760	20.7	47.3	2.3	0.00	?	-	-	-	unusual mesh data
70805c	Sak 13I, 1, 70708a	li, pp, 404	760	21.2	50.0	47.8	0.06	-970	-2.03	136.3	-1.49	one large particle produced (0.0074 g)
70808a	Sak 13I, 3, 70729c	li, eh, 117	10^{-3}	-	-	11.9	0.29	-596	-5.01	-	-	horizontal section of the mesh removed
70808b	Sak 13I, 3, 70729c	li, eh, 121	760	27.4	40.5	60.9	0.12	-906	-1.49	-	-	
70808c	Sak 13I, 3, 70729c	li, eh,	760	27.2	43.0	7.2	0.06	-65	-0.90	-	-	unusual mesh data
70808d	Sak 13I, 3, 70729c	li, eh, 130	760	27.1	43.1	71.6	0.04	-615	-0.86	-	-	unusual mesh data; samples held together between times: 1:08 to 1:20, 1:57 to 2:11, 3:17 to 3:28
70918a	Santorini, 3, 70918a	li, eh, 245	760	17.0	59.3	2.3	0.13	?	-	-	-	
70918b	Santorini, 3, 70918a	li, eh, 244	760	17.3	57.9	1.1	0.27	?	-	-	-	variable net ash polarity
70918c	Santorini, 3, 70918a	li, pp, 267	10^{-3}	-	-	3.3	0.39	-102	-3.09	234.8	-1.32	
70918d	Santorini, 3, 70918a	li, pp, 184	760	17.6	57.0	2.4	0.33	-27	-1.13	200	-0.56	
70918e	Santorini, 3, 70918a	li, ea,	760	17.5	55.8	3.2	0.03	-9	-0.28	-	-	
70922a	Sak 14, 2, 70922a	li, pp, 375	10^{-3}	-	-	17.5	0.12	348	1.99	-	-	
70922b	Sak 14, 2, 70922a	li, pp, 127	10^{-3}	-	-	9.8	0.36	209	2.13	184	1.16	
70922c	Sak 14, 2, 70922a	li, pp, 56	10^{-3}	-	-	4.8	0.31	97	2.02	162	1.25	
70922d	Sak 14, 2, 70922a	li, pp, 157	760	19.3	40.3	18.2	0.09	-140	-0.77	156.2	-0.49	
70922e	Sak 14, 2, 70922a	li, ih, 116	10^{-3}	-	-	2.1	0.29	-117	-5.57	-	-	
70922f	Sak 14, 2, 70922a	li, ih, 296	760	19.2	42.2	5.0	0.30	-91	-1.82	142.7	-1.28	
70922g	Sak 14, 2, 70922a	li, ea, 295	10^{-3}	-	-	3.9	0.77	-856	-21.95	-	-	
70922h	Sak 14, 2, 70922a	li, ea, 296	760	18.9	45.9	2.6	0.23	-95	-3.65	132.5	-2.76	unusual Faraday cup data
70923a	Sak 14, 2, 70922a	li, ea, 380	10^{-3}	-	-	2.9	0.52	-944	-32.55	153	-21.28	

Table AIV.1 continued..

Exp. ID	Samples	Exp. Type	P	T	RH	PM	λ	Q	Q_{sp}	SSA	ESCD	Notes
70925a	SMN 31, 1, 70925a	li, pp, 338	10^{-3}	-	-	19.4	0.36	?	-	-	-	variable net ash polarity
70925b	SMN 31, 1, 70925a	li, pp, 288	760	22.5	41.2	21.7	0.07	-380	-1.75	133.9	-1.31	
70925c	SMN 31, 1, 70925a	li, ih, 321	10^{-3}	-	-	1.7	0.41	-212	-12.47	319.9	-3.90	
70925d	SMN 31, 1, 70925a	li, ih, 277	760	21.2	43.8	1.7	0.18	-72	-4.24	152.5	-2.78	
70925e	SMN 31, 1, 70925a	li, ea, 318	10^{-3}	-	-	1.3	0.46	-286	-22.00	171.9	-12.80	
70925f	SMN 31, 1, 70925a	li, ea, 311	760	21.0	43.9	1.2	0.00	-82	-6.83	165	-4.14	
70926a	Sak 14, 2, 70922a	li, ih, 320	760	17.3	50.0	1.9	0.21	-54	-2.84	159.5	-1.78	
70926b	Sak 14, 2, 70922a	li, ea, 341	760	17.3	50.0	3.1	0.03	-132	-4.26	144.6	-2.94	
70930a	MSH, 1, 70930a	li, pp, 259	10^{-3}	-	-	80.0	0.15	-418	-0.52	123.3	-0.42	variable net ash polarity
70930b	MSH, 1, 70930a	li, pp, 10	10^{-3}	-	-	5.1	0.04	-32	-0.63	193.2	-0.32	
70930c	MSH, 1, 70930a	li, pp, 10	10^{-3}	-	-	4.2	0.48	-10	-0.24	241.3	-0.10	10 impacts, but exact timing of impacts unreliable for this experiment
70930d	MSH, 1, 70930a	li, pp, 20	10^{-3}	-	-	6.8	0.06	-90	-1.32	171.9	-0.77	
70930e	MSH, 1, 70930a	li, pp, 160	10^{-3}	-	-	40.9	0.32	-60	-0.15	124.3	-0.12	variable net ash polarity
70930f	MSH, 1, 70930a	li, pp, 185	10^{-3}	-	-	69.6	0.28	-141	-0.20	124.2	-0.16	variable net ash polarity; particle polarity appeared to be a function of particle production rate: positive during periods of low mass production
71001a	MSH, 1, 70930a	li, pp, 49	10^{-3}	-	-	26.2	0.30	25	0.10	-	-	variable net ash polarity
71001b	MSH, 1, 70930a	li, pp, 55	10^{-3}	-	-	44.3	0.12	-162	-0.37	131	-0.28	
71001c	MSH, 1, 70930a	li, pp, 119	760	18.8	62.0	79.8	0.18	-394	-0.49	110.8	-0.45	
71001d	MSH, 1, 70930a	li, pp, 136	760	17.2	61.3	90.8	0.12	-438	-0.48	152.3	-0.32	
71002a	MSH, 1, 70930a	li, ih, 228	10^{-3}	-	-	13.0	0.26	-404	-3.11	130.6	-2.38	-10 s offset in the timing of the impacts
71002b	MSH, 1, 70930a	li, ih, 309	10^{-3}	-	-	13.3	0.23	-374	-2.81	113.9	-2.47	
71002c	MSH, 1, 70930a	li, ih, 256	10^{-3}	-	-	13.5	0.19	-406	-3.01	130.8	-2.30	
71002d	MSH, 1, 70930a	li, ih, 217	760	19.3	47.9	32.1	0.16	-520	-1.62	106.8	-1.52	
71002e	MSH, 1, 70930a	li, ih, 235	760	18.9	48.7	17.5	0.12	-283	-1.62	131.9	-1.23	
71002f	MSH, 1, 70930a	li, ea, 233	10^{-3}	-	-	10.9	0.28	-920	-8.44	133.6	-6.32	
71002g	MSH, 1, 70930a	li, ea, 230	760	17.1	53.2	19.6	0.15	-395	-2.02	111.1	-1.81	
71003a	MSH, 1, 70930a	li, ea, 236	760	17.0	66.8	35.8	0.12	-374	-1.04	109.2	-0.96	
71003b	MSH, 1, 70930a	li, ea, 166	10^{-3}	-	-	17.8	0.47	-657	-3.69	124.2	-2.97	
71004a	Santorini, 3, 71004a	li, pp, 422	10^{-3}	-	-	11.2	0.38	-720	-6.43	229.1	-2.81	
71004b	Santorini, 3, 71004a	li, pp, 419	760	19.0	62.6	1.8	0.33	-10	-0.56	159.4	-0.35	fine particles observed to form small 'snowflake' aggregations which were easily visible to the eye as they fell
71004c	Santorini, 3, 71004a	li, pp, 419	10^{-3}	-	-	5.1	0.41	-374	-7.33	262.3	-2.80	
71004d	Santorini, 3, 71004a	li, pp, 286	760	19.2	63.0	2.4	-0.33	-15	-0.62	216.3	-0.29	
71006a	Santorini, 3, 71004a	li, ih, 395	10^{-3}	-	-	1.2	0.92	-97	-8.08	198.4	-4.07	
71006b	Santorini, 3, 71004a	li, ih, 414	760	17.1	64.1	2.0	9.85	-20	-1.00	252.1	-0.40	variable net ash polarity

Table AIV.1 continued..

Exp. ID	Samples	Exp. Type	P	T	RH	PM	λ	Q	Q_{sp}	SSA	ESCD	Notes
71006c	Santorini, 3, 71004a	li, ea, 404	10^{-3}	-	-	1.1	1.00	-189	-17.18	-	-	
71006d	Santorini, 3, 71004a	li, ea, 417	760	16.9	68.2	0.6	-0.17	?	-	-	-	
71006e	Sak 13I, 1, 70708a	li, ea, 167	10^{-3}	-	-	10.6	0.64	-528	-4.98	182.7	-2.73	unknown reason for high charge decay rate
71006f	Sak 13I, 1, 70708a	li, ea, 232	760	16.6	67.8	9.5	0.17	-211	-2.22	147.5	-1.51	unknown reason for high charge decay rate
71007a	Sak 13I, 1, 70708a	li, ea, 222	10^{-3}	-	-	3.6	0.44	-684	-19.00	179.8	-10.57	
71007b	Sak 13I, 1, 70708a	li, ea, 243	760	15.2	62.1	6.7	3.88	-272	-4.06	137.7	-2.95	unknown reason for high charge decay rate
71007c	Sak 13I, 1, 70708a	li, ea, 233	10^{-3}	-	-	3.3	0.39	-635	-19.24	149.8	-12.85	
71007d	Sak 13I, 1, 70708a	li, ea, 234	760	16.4	59.4	8.0	0.78	-267	-3.34	134	-2.49	unknown reason for high charge decay rate
71007e	Sak 13I, 1, 70708a	li, ih, 242	10^{-3}	-	-	5.8	0.86	-331	-5.71	163.9	-3.48	
71007f	Sak 13I, 1, 70708a	li, ih, 252	760	17.1	56.2	6.5	0.05	-128	-1.97	156.5	-1.26	
71007g	Sak 13I, 1, 70708a	li, ih,	10^{-3}	-	-	2.5	0.48	-308	-12.32	169.7	-7.26	
71007h	Sak 13I, 1, 70708a	li, ih, 242	760	17.0	56.6	4.0	0.20	-127	-3.17	122.7	-2.59	
71010a	Santorini, 4, 71010a	li, pp, 238	10^{-3}	-	-	10.3	0.44	-370	-3.59	200.5	-1.79	
71010b	Santorini, 4, 71010a	li, pp, 414	760	19.2	54.8	7.6	0.04	-41	-0.54	203	-0.27	
71014a	Santorini, 4, 71010a	rg, pp	10^{-3}	-	-	50.5	0.09	?	-	-	-	variable net ash polarity
71014b	Santorini, 4, 71010a	rg, pp	10^{-3}	-	-	16.7	0.21	-114	-0.68	233.4	-0.29	
71014c	Santorini, 4, 71010a	rg, pp	10^{-3}	-	-	9.4	0.36	-74	-0.79	279.2	-0.28	
71015a	Santorini, 4, 71010a	rg, pp	760	13.2	62.1	40.8	0.17	-14	-0.03	264.3	-0.01	
71015b	Santorini, 4, 71010a	rg, sc	10^{-3}	-	-	9.9	0.76	-464	-4.69	216.7	-2.16	
71015c	Sak 14, 2, 70922a	rg, pp	10^{-3}	-	-	16.3	0.56	-167	-1.02	234.5	-0.44	
71015d	Sak 14, 2, 70922a	rg, pp	10^{-3}	-	-	21.1	0.32	-275	-1.30	275.8	-0.47	
71015e	Sak 14, 2, 70922a	rg, sc	10^{-3}	-	-	5.8	0.45	-440	-7.59	247.5	-3.07	
71015f	MSH, 1, 71015a	rg, pp	10^{-3}	-	-	103.5	0.15	150	0.14	246.5	0.06	variable net ash polarity; unsteady rate of particles falling off the samples into the FC
71016a	MSH, 1, 71015a	rg, pp	10^{-3}	-	-	93.2	0.13	-163	-0.17	251.7	-0.07	variable net ash polarity; unsteady rate of particles falling off the samples into the FC
71016b	MSH, 1, 71015a	rg, sc	10^{-3}	-	-	3.4	0.38	-129	-3.79	250.9	-1.51	
71016c	Sak 13I, 1, 70708a	rg, pp	10^{-3}	-	-	83.8	0.13	?	-	207.9	-	variable net ash polarity
71016d	Sak 13I, 1, 70708a	rg, pp	10^{-3}	-	-	90.1	0.09	?	-	150.8	-	variable net ash polarity; unsteady rate of particles falling off the samples into the FC
71016e	Sak 13I, 1, 70708a	rg, sc	10^{-3}	-	-	23.9	0.03	-277	-1.16	169.5	-0.68	
71016f	SMN 31, 1, 70925a	rg, pp	10^{-3}	-	-	30.9	0.26	?	-	-	-	contact surfaces of samples roughened before start of experiment
71016g	SMN 31, 1, 70925a	rg, pp	10^{-3}	-	-	25.2	0.23	?	-	-	-	variable net ash polarity; unsteady rate of particles falling off the samples into the FC
71016h	SMN 31, 1, 70925a	rg, pp	10^{-3}	-	-	5.6	0.57	25	0.45	189.2	0.24	contact surfaces of samples roughened since last experiment
71016I	SMN 31, 1, 70925a	rg, sc	10^{-3}	-	-	4.7	0.40	-123	-2.62	233.5	-1.12	
71018a	StV 519, 2, 71018a	rg, pp	10^{-3}	-	-	133.9	0.16	216	0.16	200.9	0.08	variable net ash polarity; unsteady rate of particles falling off the samples into the FC
71018b	StV 519, 2, 71018a	rg, pp	10^{-3}	-	-	57.1	-	?	-	-	-	rotating hammer broke during experiment
71018c	StV 519, 2, 71018a	rg, pp	10^{-3}	-	-	93.8	0.15	250	0.27	146.6	0.18	

Table AIV.1 continued..

Exp. ID	Samples	Exp. Type	P	T	RH	PM	λ	Q	Q_{sp}	SSA	ESCD	Notes
71018d	StV 519, 2, 71018a	rg, sc	10^{-3}	-	-	2.7	0.00	-122	-4.52	225.3	-2.01	
71020a	StV 519, 2, 71020a	li, pp, 226	10^{-3}	-	-	46.2	0.55	1477	3.20	134.2	2.38	
71020b	StV 519, 2, 71020a	li, pp, 159	10^{-3}	-	-	29.8	0.80	1510	5.07	-	-	
71020c	StV 519, 2, 71020a	li, pp, 173	760	16.3	41.1	51.1	0.08	?	-	-	-	anvil recoil stops, possibly when the mesh data calm down; mesh data thought to be due to an undetermined problem; variable net ash polarity
71020d	StV 519, 2, 71020a	li, pp, 282	760	17.2	39.6	70.8	0.13	61	0.09	152	0.06	particle generation rate decreased towards end of experiment
71020e	StV 519, 2, 71020a	li, ih,	10^{-3}	-	-	1.5	0.80	-70	-4.67	191.5	-2.44	problem with LogIT data, only beginning and end of period of impacts recorded unusual mesh data
71021a	StV 519, 2, 71020a	li, ih, 223	10^{-3}	-	-	6.7	0.34	-177	-2.64	156.7	-1.69	unusual mesh data
71021b	StV 519, 2, 71020a	li, ih, 219	760	17.8	37.0	7.9	0.14	-90	-1.14	156.5	-0.73	
71021c	StV 519, 2, 71020a	li, ih, 295	760	18.6	35.4	4.1	0.24	-45	-1.10	156	-0.70	
71021d	StV 519, 2, 71020a	li, ea, 224	10^{-3}	-	-	2.0	0.60	-55	-2.75	160.7	-1.71	unusual mesh data
71021e	StV 519, 2, 71020a	li, ea, 241	760	18.6	34.1	4.2	0.02	-60	-1.43	167.5	-0.85	variable net ash polarity?
71021f	StV 519, 2, 71020a	li, ea, 267	10^{-3}	-	-	0.8	0.63	-114	-14.25	188.7	-7.55	unusual mesh data
71021g	StV 519, 2, 71020a	li, ea, 230	760	18.3	33.8	6.4	0.27	-60	-0.94	155.7	-0.60	variable net ash polarity
71021h	StV 519, 2, 71020a	li, ih,	760	17.8	36.2	5.0	2.30	-57	-1.14	225.3	-0.51	experiment carried out with the glass vacuum chamber removed; after impacts, a foil was placed over the hole above the Faraday cup; only the beginning and end of impacts shown
71021I	StV 519, 2, 71020a	li, ih,	760	17.7	36.4	3.4	0.53	-51	-1.50	-	-	experiment carried out with the glass vacuum chamber removed only the beginning and end of impacts shown by LogIT data
71021j	StV 519, 2, 71020a	li, ih, 239	760	17.7	36.6	4.1	0.27	-44	-1.07	192	-0.56	
71021k	StV 519, 2, 71020a	li, ih,	760	17.8	36.2	4.7	0.30	?	-	-	-	after impacts stopped a foil was placed over the hole above the Faraday cup (time denoted by last mark); variable net ash polarity
71021l	StV 519, 2, 71020a	li, ea,	10^{-3}	-	-	0.3	1.33	?	-	-	-	experiment to investigate unusual mesh data, logging every 20 ms
71022a	StV 519, 2, 71020a	li, ea, 40	10^{-3}	-	-	0.6	0.00	?	-	-	-	experiment to investigate unusual mesh data, logging every 1 ms; Faraday cup data offset by 50×10^{-12} C; samples held together: 13 to 15 s and 18 to 20 s
71024a	StV 519, 2, 71020a	li, ih, 136	760	16.1	37.6	5.8	0.17	-60	-1.03	171.3	-0.60	after impacts stopped, a foil was placed over the hole above the Faraday cup (time denoted by last mark)
71027a	StV 519, 2, 71020a	li, ih,	760	15.7	48.0	5.6	0.30	?	-	-	-	after impacts stopped a foil was placed over the hole above the Faraday cup
71027b	StV 519, 2, 71020a	li, ih, 244	760			5.2	0.23	-212	-4.08	190.2	-2.14	after impacts stopped a foil was placed over the hole above the Faraday cup
71027c	SMN 31, 1, 70925a	li, pp, 244	760	15.7	50.0	43.3	0.06	-213	-0.49	123.5	-0.40	
71027d	SMN 31, 1, 70925a	li, pp, 229	760	15.9	49.6	49.7	0.06	-233	-0.47	131.7	-0.36	after impacts stopped a foil was placed over the hole above the Faraday cup
71028a	SMN 31, 1, 70925a	li, ih, 241	760	15.4	42.1	14.3	0.11	-439	-3.07	138.6	-2.21	
71028b	SMN 31, 1, 70925a	li, ih, 230	760	15.0	28.8	4.4	0.16	-267	-6.07	122.3	-4.96	
71028c	MSH, 1, 71028c	li, pp, 113	760	14.7	23.9	9.8	0.08	-267	-2.72	220.8	-1.23	anvil sample became loose during experiment

Table AIV.1 continued..

Exp. ID	Samples	Exp. Type	P	T	RH	PM	λ	Q	Q_{sp}	SSA	ESCD	Notes
71028d	MSH, 1, 71028c	li, pp, 221	760	14.9	22.7	16.4	0.10	-444	-2.71	201.8	-1.34	after impacts stopped a foil was placed over the hole above the Faraday cup
71028e	StV 519, 2, 71020a	li, pp, 220	760	14.5	24.0	80.1	0.38	180	0.22	-	-	
71028f	StV 519, 2, 71020a	li, pp, 238	760	14.1	25.5	45.4	0.25	185	0.41	149.8	0.27	
80701a	MSH, 3, 80504a	li, pp, 247	760	22.7	44.8	2.2	0.00	-32	-1.45	166.8	-0.87	mesh data (not shown on graph) taken via unshielded lead-through and is nearly entirely dominated by interference from solenoid operation
80701b	MSH, 3, 80504a	li, pp, 317	760	22.5	43.0	21.8	0.16	-461	-2.11	170.4	-1.24	mesh data (not shown on graph) taken via unshielded lead-through and is nearly entirely dominated by interference from solenoid operation
80701c	MSH, 3, 80504a	li, pp, 281	760	22.1	43.0	1.9	0.00	-74	-3.89	181.4	-2.15	mesh data (not shown on graph) taken via unshielded lead-through and is nearly entirely dominated by interference from solenoid operation
80701d	MSH, 3, 80504a	li, pp, 284	760	21.9	44.6	1.3	-0.15	-26	-2.00	180.4	-1.11	mesh data (not shown on graph) taken via unshielded lead-through and is nearly entirely dominated by interference from solenoid operation
80701e	MSH, 3, 80504a	li, pp, 292	760	21.8	44.5	27.1	0.09	-866	-3.20	169.8	-1.88	mesh data (not shown on graph) taken via unshielded lead-through and is nearly entirely dominated by interference from solenoid operation
80701f	MSH, 3, 80504a	li, pp, 299	760	21.7	44.7	2.3	0.13	-75	-3.26	193.7	-1.68	mesh data (not shown on graph) taken via unshielded lead-through and is nearly entirely dominated by interference from solenoid operation
80702a	MSH, 3, 80504a	li, pp, 316	760	20.0	44.4	23.5	0.26	-649	-2.76	183.5	-1.51	mesh data (not shown on graph) taken via unshielded lead-through and is nearly entirely dominated by interference from solenoid operation
80702b	MSH, 3, 80504a	li, pp, 216	760	21.4	41.5	22.3	0.19	-577	-2.59	177.9	-1.45	mesh data (not shown on graph) taken via unshielded lead-through and is nearly entirely dominated by interference from solenoid operation
80702c	MSH, 3, 80504a	li, pp, 235	760	22.5	72.6	26.6	0.13	-169	-0.64	169.0	-0.38	mesh data (not shown on graph) taken via unshielded lead-through and is nearly entirely dominated by interference from solenoid operation
80702d	MSH, 3, 80504a	li, pp, 101	760	22.7	75.5	11.3	0.20	-170	-1.50	180.5	-0.83	mesh data (not shown on graph) taken via unshielded lead-through and is nearly entirely dominated by interference from solenoid operation low no of impacts to ensure high rate of particle production
80703a	MSH, 3, 80504a	li, pp, 273	760	20.2	5.6	28.0	0.21	-1519	-5.43	169.4	-3.20	mesh data (not shown on graph) taken via unshielded lead-through and is nearly entirely dominated by interference from solenoid operation particle production rate decreases towards end of experiment
80704a	MSH, 3, 80504a	li, pp, 177	760	19.0	5.4	25.9	0.17	-1334	-5.15	168.1	-3.06	mesh data (not shown on graph) taken via unshielded lead-through and is nearly entirely dominated by interference from solenoid operation low number of impacts to ensure high particle production rates

Table AIV.2 Particle charge experiments: details and results summary. Abbreviations used in the table are: kV, the potential of the kV plate, (in kiloVolts); V, the solenoid voltage, (in Volts); NI, the number of impacts; P, pressure in Torr, (760 Torr for atmospheric pressure); T, temperature (°C); RH, relative humidity (%); PM_{0V}, PM_{kV}, and $PM_{Tr,}$ the particle masses collected on the 0 V plate, the kV plate, and the tray respectively, (in mg); Q, the charge collected on the 0 V plate, (in units of 10^{-12} C); Q_{sp}, the calculated specific charge (in units of 10^{-4} C kg^{-1}); SCD, the calculated surface charge density for the particles on the 0 V plate (in units of 10^{-5} C m^{-2}); SSA_{0V}, SSA_{kV} and SSA_{Tr}, the specific surface areas of the particles collected on the 0 V plate, the kV plate and on the tray respectively. Particle masses are given as the actual measured values without adjustment for the folding of the foils. The mass adjustments have been carried out before calculation of the specific charge and surface charge density. The samples are described by pumice type, clast number, and sample ID.

Exp. ID	Samples	kV	V	NI	P	T	RH	PM_{0V}	PM_{kV}	PM_{Tr}	Q	Q_{sp}	SCD	SSA_{0V}	SSA_{kV}	SSA_{Tr}	Notes
80123a	MSH, 1, 71028c	0	12	302	760	18.2	39.4	-	-	1.40	0	0	-	-	-	-	no particles visible on plates, plate foils not weighed
80123b	MSH, 1, 71028c	-3.5	12	379	760	18.5	37.8	0.35	0.42	2.70	-40	-2.4	-	-	-	-	
80123c	MSH, 1, 71028c	-3.5	12	210	760	18.7	37.0	2.11	1.48	6.00	-1800	-9.4	-	-	-	-	
80124a	MSH, 1, 71028c	0	12	152	760	17.5	33.7	-	-	13.40	-10	-	-	-	-	-	plate separation 18 mm, some ash detected, but not visible on plates, plate foils not weighed
80124b	MSH, 1, 71028c	-3.5	12	47	760	17.6	33.8	1.13	0.65	0.50	-1900	-20.1	-	-	-	-	plate separation 18 mm
80124c	MSH, 1, 71028c	-3.5	12	143	760	17.5	32.8	1.71	1.22	1.80	-5400	-35.4	-	-	-	-	plate separation 18 mm
80124d	StV 519, 2, 71020a	-3.5	12	329	760	17.6	33.1	5.20	3.68	5.60	-19700	-39.3	-	-	-	-	plate separation 18 mm
80125a	StV 519, 2, 71020a	-3.5	12	412	760	16.3	29.6	6.80	4.64	11.50	-12265	-18.5	-	-	-	-	plate separation 28 mm
80126a	StV 519, 2, 71020a	-3.5	12	326	760	15.2	31.2	2.28	2.68	17.60	-1970	-9.4	-	-	-	-	
80127a	StV 519, 2, 71020a	-1.7	12	169	760	14.9	29.2	2.20	1.04	15.20	-1966	-9.8	-	-	-	-	plate separation 18 mm
80205a	MSH, 1, 71028c	-3.5	12	1	760	18.6	40.0	0.36	0.32	-	-15	-0.9	-	-	-	-	top cut off earthed box, no collimating slit, logging over 30 s @ 10 ms intervals, note no tray collected
80205b	MSH, 1, 71028c	-3.5	12	1	760	18.6	40.0	0.12	0.22	0.19	-12	-	-	-	-	-	no collimating slit, logging over 30 s @ 10 ms intervals
80206f	MSH, 1, 71028c	-3.5	12	1	760	18.3	38.7	0.16	0.13	0.18	-13	-	-	-	-	-	no collimating slit, logging over 30 s @ 10 ms intervals
80211a	MSH, 1, 71028c	3.5	12	1	760	19.2	48.2	0.30	0.24	0.43	16	1.4	6.87	202.6	291.3	-	no collimating slit, logging over 30 s @ 10 ms intervals
80212a	MSH, 1, 71028c	3.5	12	1	760	18.3	38.7	0.28	0.30	0.32	12	1.3	-	-	-	-	no collimating slit, logging over 30 s @ 10 ms intervals
80214a	MSH, 1, 71028c	3.5	12	1	760	20.9	90.2	0.36	0.42	0.38	5	0.3	-	-	-	-	no collimating slit, logging over 30 s @ 10 ms intervals
80216a	MSH, 1, 71028c	3.5	6	1	760	20.4	43.5	0.31	0.28	0.27	2.5	0.2	-	-	-	-	no collimating slit, logging over 30 s @ 10 ms intervals
80217a	MSH, 1, 71028c	3.5	6	1	760	19.2	42.8	0.34	0.36	0.40	2	0.1	-	-	153.3	-	no collimating slit, logging over 30 s @ 10 ms intervals

Table AIV.2 continued..

Exp. ID	Samples	kV	V	NI	P	T	RH	PM_{0V}	PM_{kV}	PM_{Tr}	Q	Q_{sp}	SCD	SSA_{0V}	SSA_{kV}	SSA_{Tr}	Notes
80217b	MSH, 1, 71028c	3.5	6	1	760	19.7	43.5	0.29	0.30	0.27	1.7	0.2	-	-	-	-	no collimating slit, logging over 30 s @ 10 ms intervals
80218a	MSH, 1, 71028c	3.5	12	270	760	19.9	43.2	1.00	0.79	1.85	868	10.7	55.48	192.0	251.3	213	raised collimating slot, 1.5 mm slot width
80218b	MSH, 1, 71028c	-3.5	12	320	760	19.9	43.2	0.62	0.46	1.11	-347	-8.0	-37.31	213.8	251.2	245	1.5 mm collimating slot width
80218c	MSH, 1, 71028c	-3.5	12	317	760	20.9	39.2	2.04	1.54	3.95	-1922	-10.4	-57.72	179.5	196.4	195	3.0 mm collimating slot width
80218d	MSH, 1, 71028c	-3.5	12	416	760	20.5	38.7	0.71	0.69	2.04	-492	-9.4	-49.94	187.6	195.0	197	
80218e	MSH, 1, 71028c	3.5	12	349	760	20.4	38.6	1.99	1.53	4.56	1995	11.1	61.37	180.1	209.8	216	some particles observed at base of kV foil impact surfaces of pumice flattened before experiment
80219a	MSH, 1, 71028c	3.5	6	277	760	20.5	41.6	0.26	0.28	0.42	20	2.7	19.14	139.3	142.5	-	
80219b	MSH, 1, 71028c	-3.5	6	294	760	20.5	41.6	0.21	0.30	0.32	-21	-8.4	-40.29	208.5	-	-	
80219c	MSH, 1, 71028c	-3.5	12	318	760	21.0	89.0	0.62	0.42	2.72	-220	-5.1	-18.83	268.6	233.5	233	
80219d	MSH, 1, 71028c	3.5	12	318	760	21.2	88.8	0.27	0.28	0.87	30	3.5	20.47	172.4	201.4	306	
80223a	MSH, 1, 71028c	3.5	12	1	760	20.3	89.9	-	-	-	?	-	-	-	-	-	plate data too noisy, particle masses not recorded
80223b	MSH, 1, 71028c	-3.5	12	1	760	20.8	87.9	-	-	-	?	-	-	-	-	-	plate data too noisy, particle masses not recorded
80224a	MSH, 1, 71028c	-3.5	12	1	760	21.2	15.4	0.35	0.31	0.48	-7.2	-0.4	-	-	-	-	no collimating slot
80224b	MSH, 1, 71028c	-3.5	12	310	760	21.2	10.3	2.46	1.15	3.99	-1990	-8.7	-42.54	205.6	264.6	194	
80224c	MSH, 1, 71028c	-3.5	12	1	760	21.2	89.9	0.20	0.35	0.61	-9.5	-6.3	-	-	-	-	no collimating slot
80225a	MSH, 1, 71028c	3.5	12	299	760	19.6	5.3	0.62	0.74	1.15	118	2.7	12.68	214.0	269.9	-	unusual particle distribution on kV plate
80225b	MSH, 1, 71028c	3.5	12	1	760	20.0	8.5	0.34	0.29	0.22	9.3	0.6	-	-	-	-	no collimating slot
80226a	MSH, 1, 71028c	3.5	12	300	760	20.1	8.5	0.99	1.00	0.55	246	3.1	15.62	195.6	244.3	188	unusual particle distribution on kV plate
80226b	MSH, 1, 71028c	-3.5	6	1	760	20.3	14.3	0.33	0.21	0.45	-6	-0.4	-	-	-	-	no collimating slot
80226c	MSH, 1, 71028c	3.5	6	1	760	20.3	14.3	0.42	0.43	0.38	4.8	0.2	-	-	-	-	no collimating slot
80227a	MSH, 1, 71028c	3.5	12	290	760	19.5	10.3	1.22	1.53	1.53	1003	9.7	43.89	220.8	244.8	220	unusual particle distribution on kV plate
80227b	MSH, 1, 71028c	-3.5	12	289	760	20.4	89.1	0.61	0.40	1.63	-347	-8.2	-22.30	366.2	250.3	211	
80227c	MSH, 1, 71028c	3.5	12	291	760	20.8	90.2	0.66	0.76	2.00	111	2.3	11.55	202.3	248.3	218	
80227d	MSH, 1, 71028c	3.5	12	1	760	20.0	87.3	0.31	0.37	0.45	4.6	0.4	-	-	-	-	
80227e	MSH, 1, 71028c	-3.5	12	1	760	21.2	89.6	0.11	0.06	0.17	?	-	-	-	-	-	no collimating slot, plate data too noisy
80228a	MSH, 1, 71028c	3.5	12	283	760	18.9	0.9	2.05	1.64	3.19	407	2.2	11.00	198.3	246.1	214	unusual particle distribution on kV plate
80228b	MSH, 1, 71028c	-3.5	12	1	760	20.1	88.3	0.15	0.17	0.50	-9	-	-	-	-	-	
80228c	MSH, 1, 71028c	-3.5	12	100	760	19.7	36.9	1.13	0.56	2.03	-977	-10.3	-56.62	182.6	248.7	185	
80228d	MSH, 1, 71028c	-3.5	12	10	760	19.9	34.7	0.40	0.38	0.44	-89	-4.1	-21.95	188.6	-	-	
80228e	MSH, 1, 71028c	-3.5	12	70	760	20.2	34.5	0.70	0.57	1.42	-374	-7.3	-32.09	226.3	174.0	-	

Table AIV.2 continued..

Exp. ID	Samples	kV	V	NI	P	T	RH	PM_{0V}	PM_{kV}	PM_{Tr}	Q	Q_{sp}	SCD	SSA_{0V}	SSA_{kV}	SSA_{Tr}	Notes
80228f	MSH, 1, 71028c	-3.5	12	40	760	20.2	34.8	0.42	0.45	0.87	-183	-7.8	-43.50	179.0	310.4	-	
80228g	MSH, 1, 71028c	-3.5	12	220	760	19.7	33.4	1.20	0.97	3.55	-949	-9.3	-49.67	188.2	198.8	182	
80228h	MSH, 1, 71028c	-3.5	12	80	760	19.7	32.6	1.52	0.87	2.17	-985	-7.4	-36.21	203.8	-	-	
80302a	MSH, 1, 71028c	3.5	12	295	760	18.6	1.8	1.56	1.98	4.67	503	3.7	-	-	-	-	foil put over rear wall of box, but unusual mass distribution still produced on KV plate
80302b	MSH, 2, 80302b	3.5	6	50	760	19.3	39.7	0.54	0.45	0.29	51.5	1.5	8.34	174.0	147.4	154	
80302c	MSH, 2, 80302b	3.5	12	50	760	19.3	39.7	1.38	0.84	5.61	2235	18.7	114.60	163.2	199.9	125	
80302d	MSH, 2, 80302b	3.5	8	50	760	19.7	40.2	0.41	0.50	1.92	236	10.5	55.71	188.3	189.8	155	
80302e	MSH, 2, 80302b	3.5	10	50	760	19.7	40.2	0.83	0.74	4.46	797	12.4	77.23	160.0	167.4	122	
80302f	MSH, 2, 80302b	-3.5	7	50	760	19.1	41.8	0.46	0.33	0.96	-61	-2.2	-10.20	217.5	285.2	147	
80302g	MSH, 2, 80302b	-3.5	11	50	760	19.0	42.8	1.24	0.76	4.54	-1048	-9.9	-57.37	173.1	199.8	119	
80303a	MSH, 2, 80302b	-3.5	9	50	760	19.1	48.9	1.05	0.76	6.29	-561	-6.5	-42.05	154.2	177.8	123	
80303b	MSH, 2, 80302b	-3.5	13	50	760	19.1	48.9	1.69	1.25	12.48	-2607	-17.3	-128.13	135.2	174.5	114	
80303c	MSH, 2, 80302b	3.5	11	50	760	19.6	47.7	1.60	1.11	8.31	1901	13.5	77.80	173.3	211.6	146	impact surfaces of pumice flattened before experiment
80303d	MSH, 2, 80302b	3.5	13	50	760	19.6	47.7	1.63	1.31	9.14	3128	21.6	138.36	156.5	195.0	155	
80303e	MSH, 2, 80302b	-3.5	10	50	760	19.9	45.5	1.30	0.83	7.08	-834	-7.5	-50.18	149.1	170.3	124	
80303f	MSH, 2, 80302b	-3.5	12	50	760	19.9	45.5	1.88	1.19	11.40	-1277	-7.5	-	-	-	-	vacuum chamber lid removed, increased air-flow and apparatus vibration
80303g	MSH, 2, 80302b	-3.5	12	50	760	19.8	43.3	2.17	1.14	8.61	-2960	-14.9	-93.95	158.7	197.1	121	
80305a	MSH, 2, 80302b	-1	6	50	760	19.2	39.0	0.26	0.21	0.96	-11.3	-1.5	-	-	-	-	
80305b	MSH, 2, 80302b	1	6	50	760	19.5	37.0	0.26	0.27	1.22	2.3	0.3	-	-	-	-	
80305c	MSH, 2, 80302b	2	6	50	760	19.6	37.5	0.32	0.31	1.13	4	0.3	-	-	-	-	
80305d	MSH, 2, 80302b	-2	6	50	760	19.5	36.3	0.18	0.17	0.29	-3.1	-	-	-	-	-	
80305e	MSH, 2, 80302b	-3	6	50	760	19.3	35.0	0.46	0.56	0.65	-26	-0.9	-	-	-	-	
80305f	MSH, 2, 80302b	3	6	50	760	19.3	35.0	0.53	0.56	0.72	48	1.4	-	-	-	-	
80306a	MSH, 2, 80306a	-3.5	6	50	760	16.5	32.0	0.34	0.44	0.66	-42	-2.7	-15.11	179.4	224.9	189	
80306b	MSH, 2, 80306a	3	6	50	760	16.4	34.0	0.25	0.20	0.42	26.5	4.1	-	-	-	-	
80306c	MSH, 2, 80306a	2.3	6	50	760	16.7	36.6	0.23	0.30	0.27	5.5	1.2	-	-	-	-	
80306d	MSH, 2, 80306a	2.7	6	50	760	16.8	37.1	0.32	0.42	0.45	5.8	0.4	-	-	-	-	
80306e	MSH, 2, 80306a	2.9	6	50	760	16.9	38.5	0.30	0.34	0.94	41.1	3.6	-	-	-	-	
80323a	MSH, 2, 80306a	3.5	12	50	10^{-4}	-	-	0.58	0.91	1.68	?	-	-	-	-	-	no aggregation of particles observable by eye electrometer problem - no data recorded
80323b	MSH, 2, 80306a	3.5	12	60	10^{-4}	-	-	0.44	0.90	2.95	1113	43.6	301.46	144.8	182.4	-	no aggregation of particles observable by eye
80323c	MSH, 2, 80306a	1	12	50	10^{-4}	-	-	0.44	0.64	2.66	388	15.2	65.57	232.1	225.0	99	4 small aggregates observed on kV plate, none on O V plate
80324a	MSH, 2, 80306a	2	12	50	10^{-4}	-	-	0.37	0.49	1.69	497	26.9	-	-	-	-	

Table AIV.2 continued..

Exp. ID	Samples	kV	V	NI	P	T	RH	PM_{0V}	PM_{kV}	PM_{Tr}	Q	Q_{sp}	SCD	SSA_{0V}	SSA_{kV}	SSA_{Tr}	Notes

80324b	MSH, 2, 80306a	3	12	50	10^{-4}	-	-	0.35	0.61	1.45	575	34.8	-	-	-	-	
80324c	MSH, 2, 80324c	-1.5	12	50	760	22.1	32.2	0.38	0.39	-3.83	-19.5	-1.0	-	-	-	-	no aggregates visible on plates, 3 observed in tray
80324d	MSH, 2, 80324c	-1.5	12	50	760	22.1	32.2	0.49	0.56	0.76	-25.2	-0.8	-	-	-	-	about 3 small aggregates visible on kV plate, 4 larger ones on 0 V plate, and 6 on tray, near 0 V plate
80324e	MSH, 2, 80324c	-2.5	12	50	760	21.5	35.9	1.70	1.31	4.75	-1015	-6.7	-	-	-	-	no large aggregates on kV plate, but many observed on 0 V plate and in tray
80324f	MSH, 2, 80324c	-3.5	12	50	760	21.5	35.9	2.12	2.00	4.24	-2410	-12.5	-	-	-	-	plenty of aggregates on all foils
80325a	MSH, 2, 80324c	-2.5	6	50	760	20.4	43.6	0.27	0.33	0.38	-10.4	-1.2	-	-	-	-	particles on 0 V plate dominantly in aggregates note that this plate visually appeared to collect more mass than kV plate, but in fact had less
80325b	MSH, 2, 80324c	-1.5	6	50	760	20.8	39.8	0.33	0.29	0.62	-14.9	-1.0	-	-	-	-	a few aggregates visible on the 0 V plate and tray only
80405a	MSH, 3, 80504a	-1	12	50	760	20.8	90.9	0.29	0.34	1.72	?	-	-	-	-	-	high noise ratio prevented charge determination high aggregation of particles in tray
80406a	MSH, 3, 80504a	-1	12	50	760	19.5	87.7	0.21	0.21	7.58	-30	-12.0	-	-	-	-	about 3 small aggregates on 0V plate, none on kV. as before, particles concentrated on lower half of plates noisy plate data
80406b	MSH, 3, 80504a	-3.5	12	50	760	19.9	89.0	0.28	0.38	3.05	?	-	-	-	-	-	barely anything visible at all on the 0V plate, a few small particles on the lower half of the kV plate plate data too noisy to obtain charge
80406c	MSH, 3, 80504a	-3.5	12	50	760	20.8	90.5	0.46	0.76	1.69	-75	-2.7	-	-	-	-	a few aggregates visible on plates
80509a	StV 519, 2, 71018a	3.5	12	50	760	22.5	41.4	0.65	0.79	2.27	110	2.4	10.80	219.0	196.5	184	particles on both plates very highly aggregated
80509b	StV 519, 2, 71018a	-3.5	12	50	760	22.5	41.4	0.85	0.89	2.96	-270	-4.1	-16.70	243.2	235.9	194	particles on both plates very highly aggregated
80510a	StV 519, 2, 71018a	-3.5	10	50	760	20.7	35.4	0.32	0.38	1.66	-79	-5.9	-21.93	266.8	259.2	261	particles on both plates very highly aggregated
80510b	StV 519, 2, 71018a	3.5	10	50	760	20.7	35.4	0.46	0.46	1.85	86	3.1	9.94	314.7	258.1	245	particles on both plates very highly aggregated
80511a	StV 519, 2, 71018a	3.5	13	50	760	20.1	43.8	0.67	0.93	1.51	359	7.4	31.87	232.2	248.8	250	distinctly less aggregation observed than during previous experiment
80511b	StV 519, 2, 71018a	-3.5	13	50	760	20.6	42.9	0.58	0.56	1.67	-236	-6.0	-23.01	259.7	298.9	243	similarly reduced number of visible aggregates

Figure AIV.1 (overleaf) Graphs showing data recorded during the net charge experiments. All the graphs show the mesh data in red, and the Faraday cup data in black. The first line across the top axis shows the release of the electrometer zero-check; for the impact experiments, other lines indicate individual collisions. For rotational experiments, the other lines delineate the period of grinding. Each graph is identified by the experiment ID.

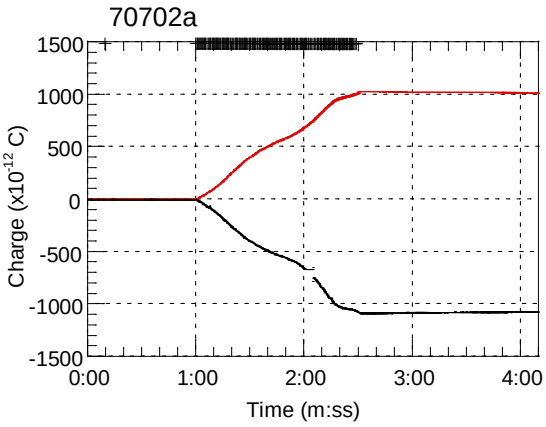
70702a
Charge (x10-12 C)
Time (m:ss)

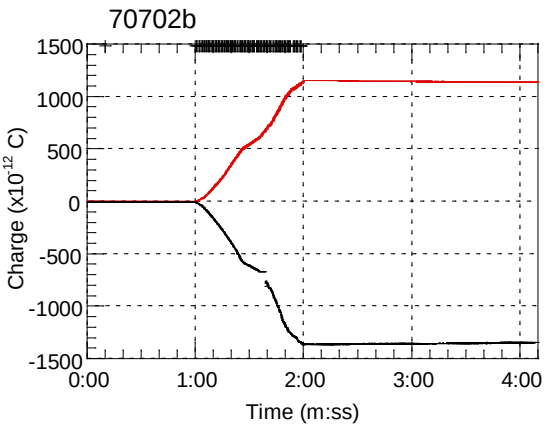
70702b
Charge (x10-12 C)
Time (m:ss)

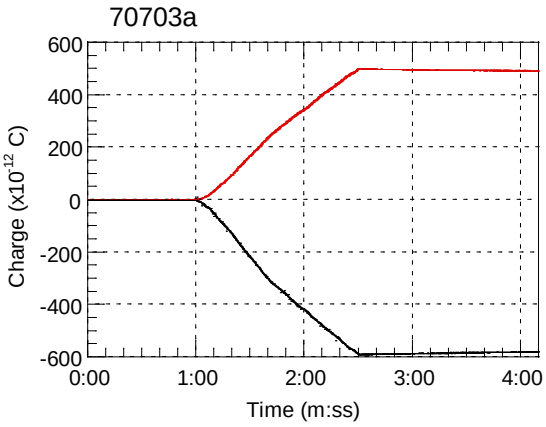
70703a
Charge (x10-12 C)
Time (m:ss)

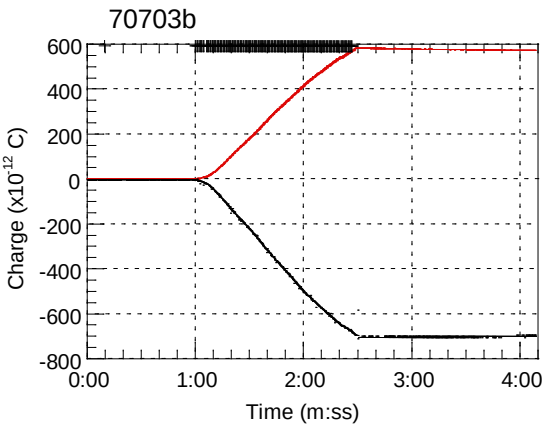
70703b
Charge (x10-12 C)
Time (m:ss)

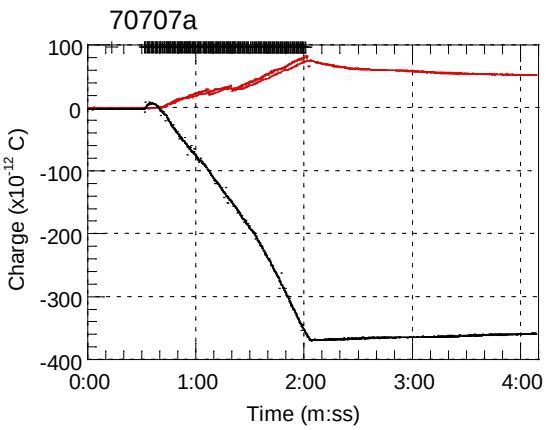
70707a
Charge (x10-12 C)
Time (m:ss)

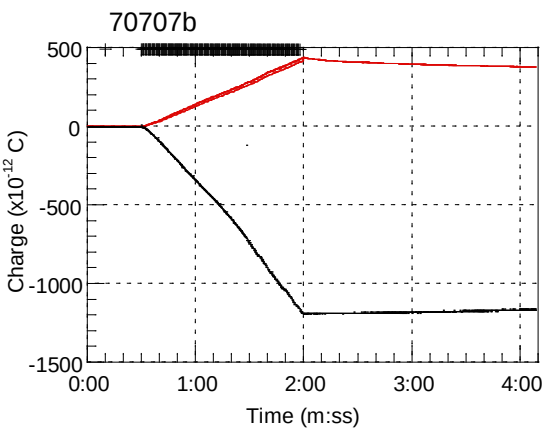
70707b
Charge (x10-12 C)
Time (m:ss)

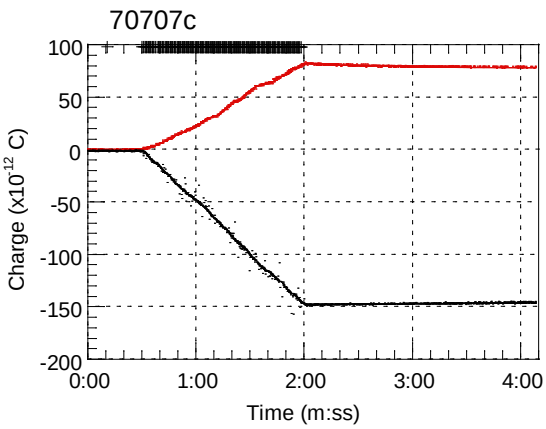
70707c
Charge (x10-12 C)
Time (m:ss)

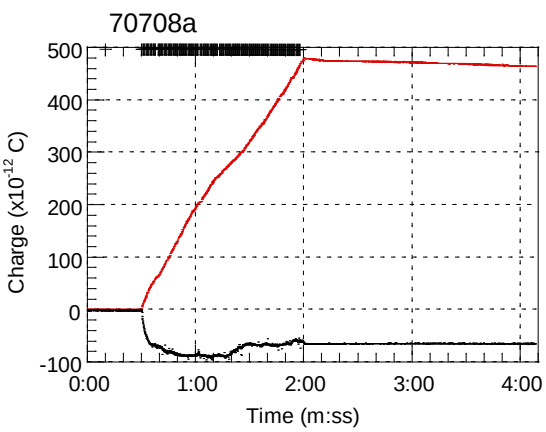
70708a
Charge (x10-12 C)
Time (m:ss)

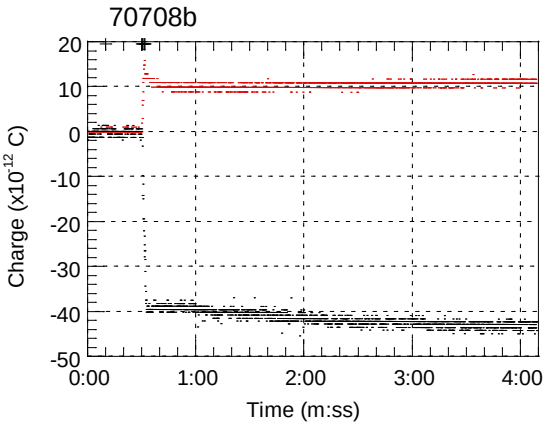
70708b
Charge (x10^{-12} C)
Time (m:ss)

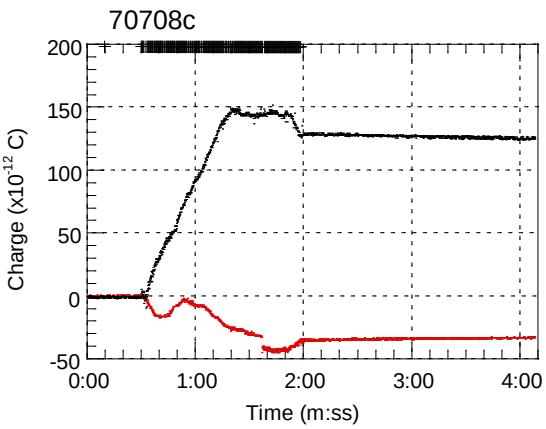
70708c
Charge (x10^{-12} C)
Time (m:ss)

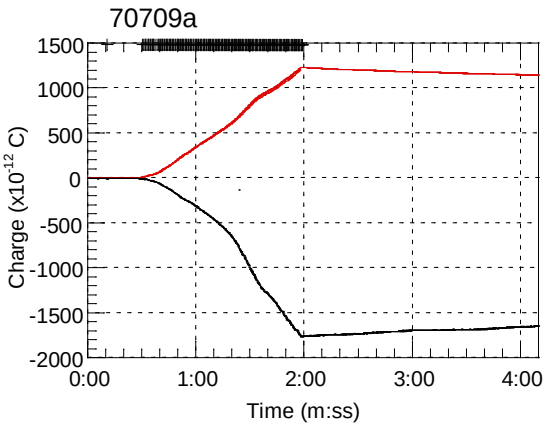
70709a
Charge (x10^{-12} C)
Time (m:ss)

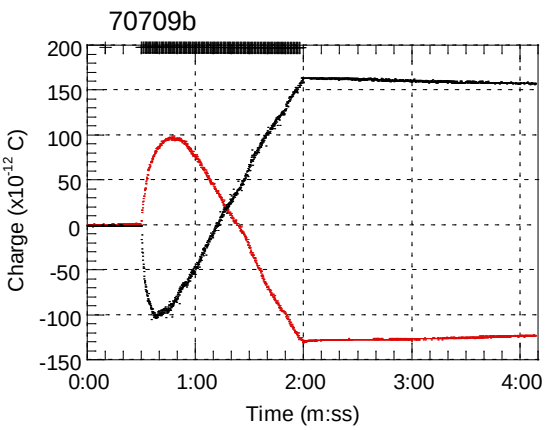
70709b
Charge (x10^{-12} C)
Time (m:ss)

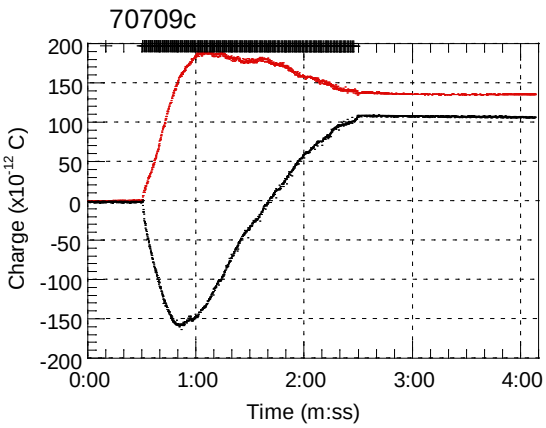
70709c
Charge (x10^{-12} C)
Time (m:ss)

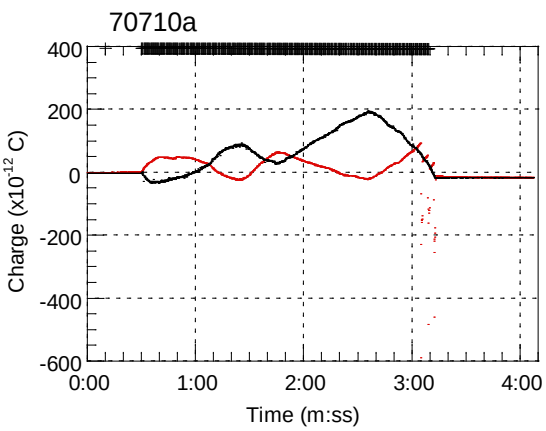
70710a
Charge (x10^{-12} C)
Time (m:ss)

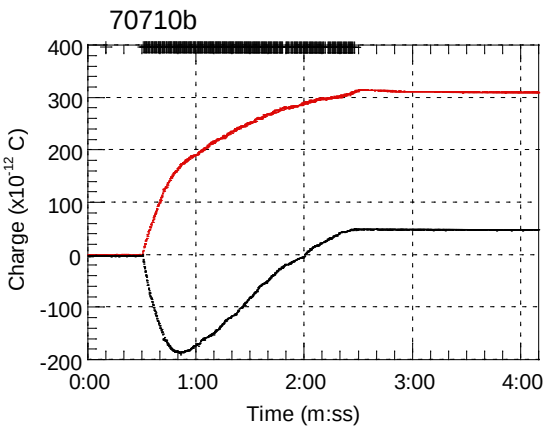
70710b
Charge (x10^{-12} C)
Time (m:ss)

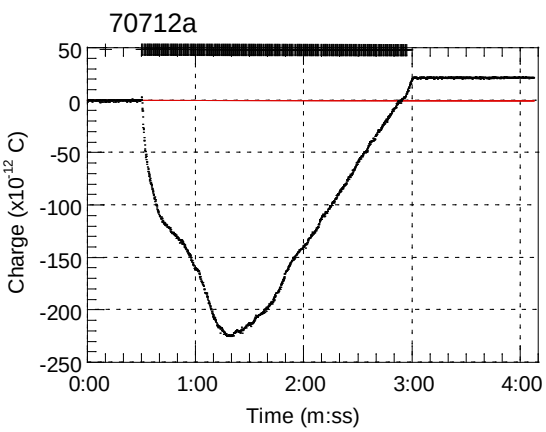
70712a
Charge (x10^{-12} C)
Time (m:ss)

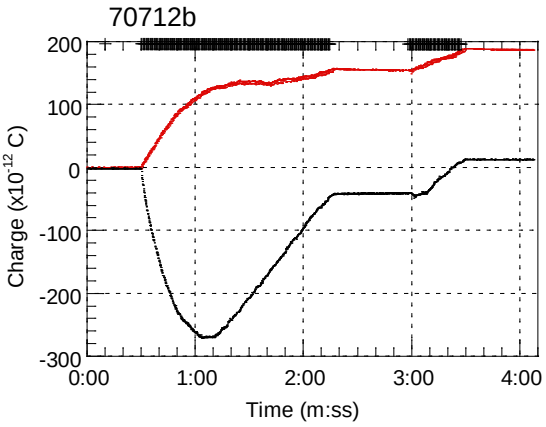
70712b
Charge (x10-12 C)
Time (m:ss)

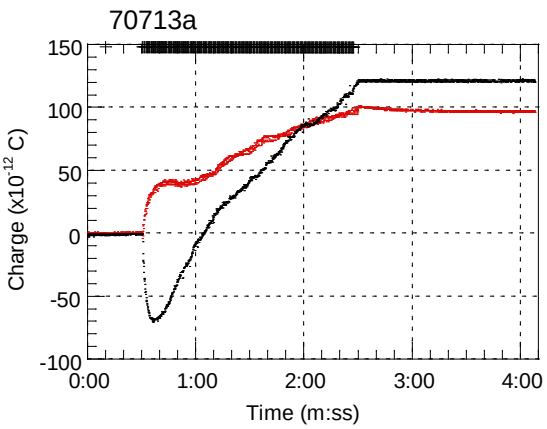
70713a
Charge (x10-12 C)
Time (m:ss)

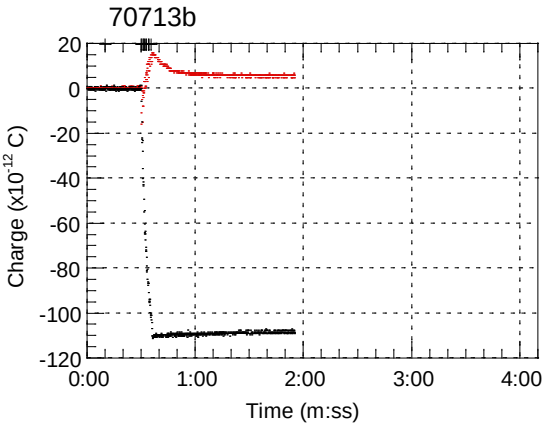
70713b
Charge (x10-12 C)
Time (m:ss)

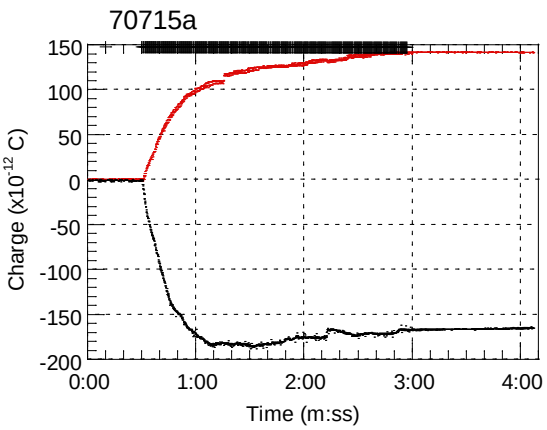
70715a
Charge (x10-12 C)
Time (m:ss)

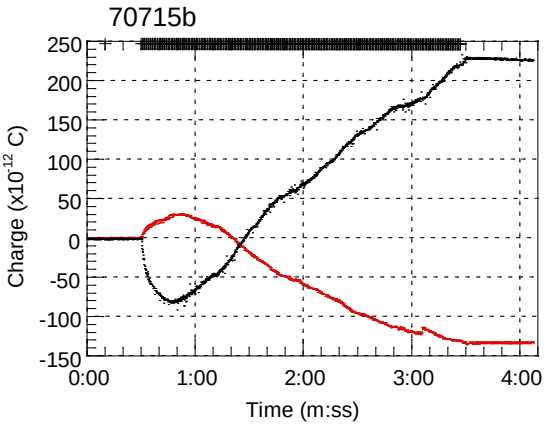
70715b
Charge (x10-12 C)
Time (m:ss)

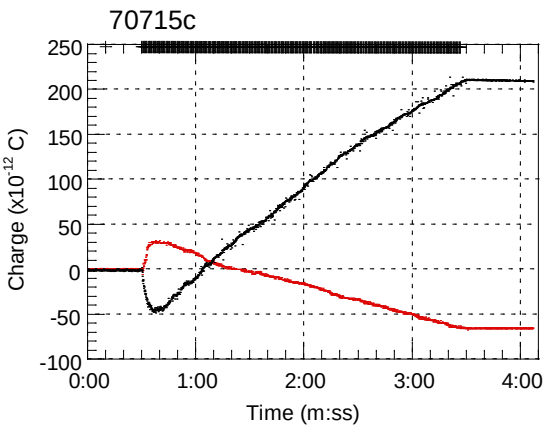
70715c
Charge (x10-12 C)
Time (m:ss)

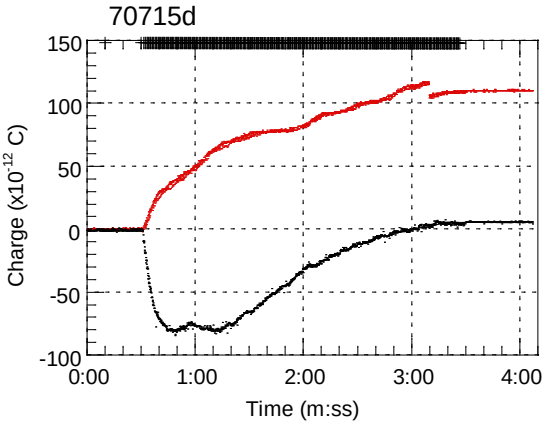
70715d
Charge (x10-12 C)
Time (m:ss)

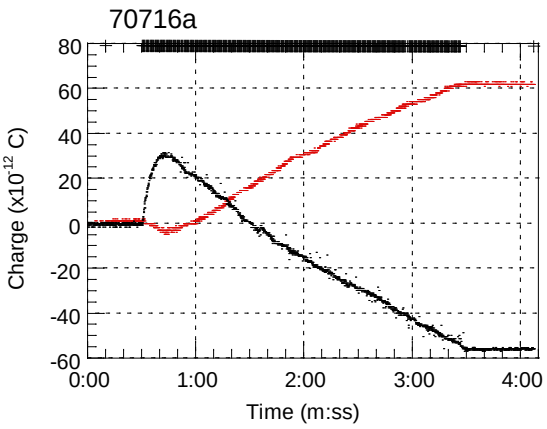
70716a
Charge (x10-12 C)
Time (m:ss)

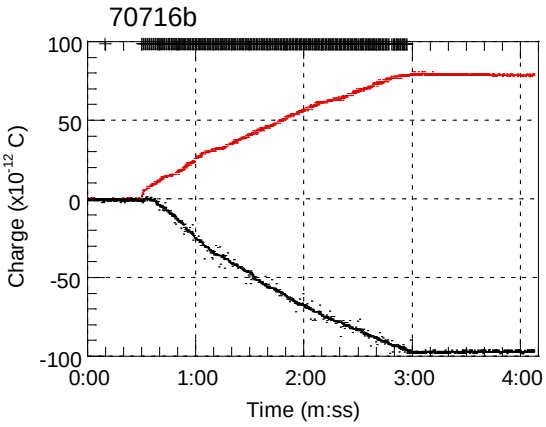
70716b
Charge (x10-12 C)
Time (m:ss)

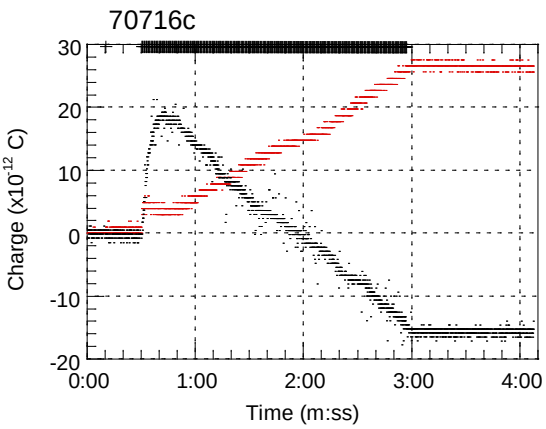
70716c
Charge (x10-12 C)
Time (m:ss)

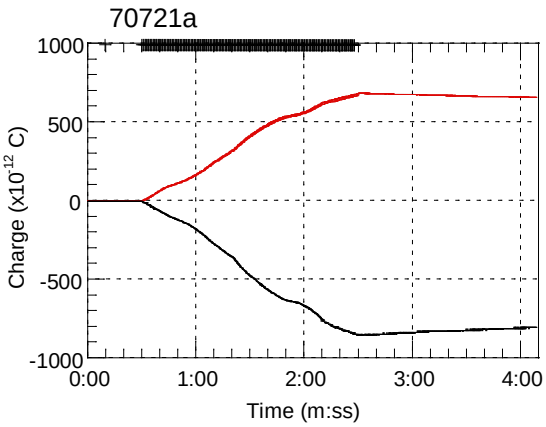
70721a
Charge (x10-12 C)
Time (m:ss)

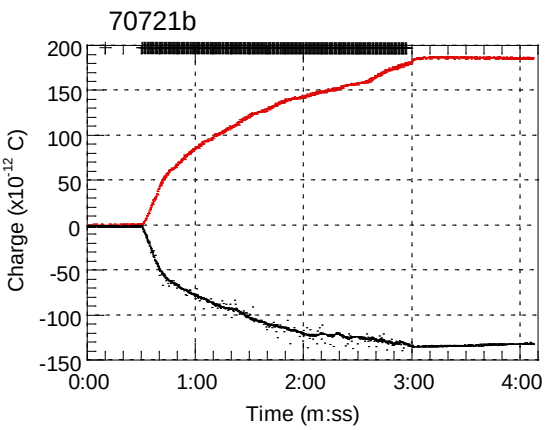
70721b
Charge (x10-12 C)
Time (m:ss)

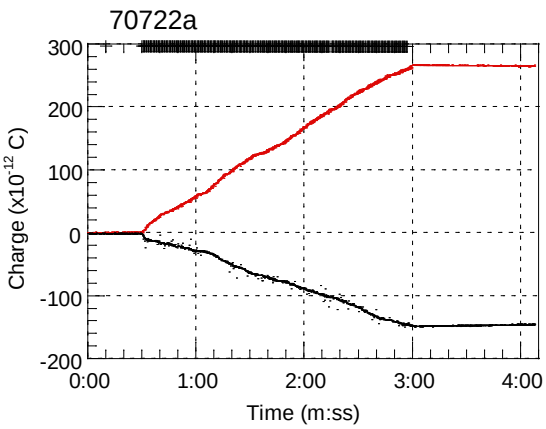
70722a
Charge (x10-12 C)
Time (m:ss)

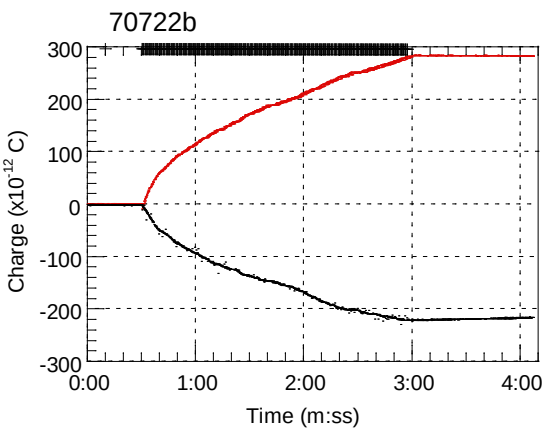
70722b
Charge (x10-12 C)
Time (m:ss)

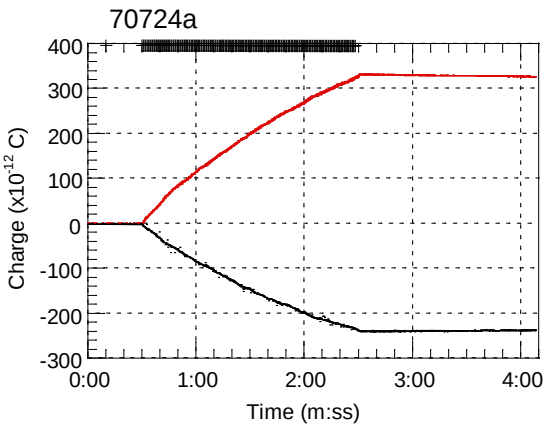
70724a
Charge (x10-12 C)
Time (m:ss)

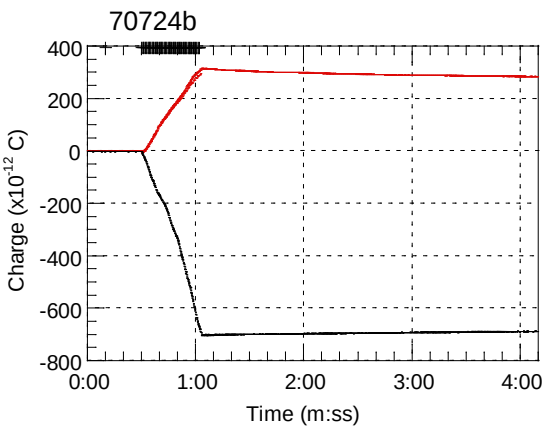
70724b
Charge (x10-12 C)
Time (m:ss)

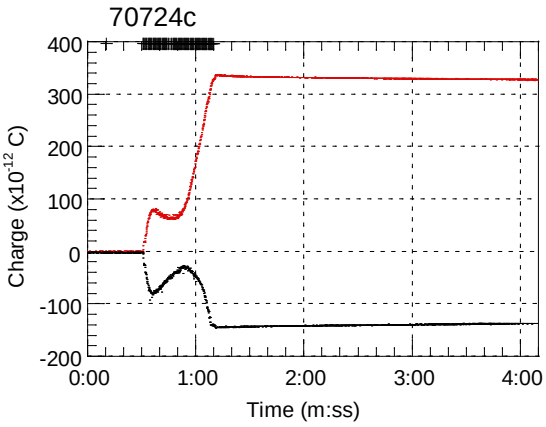
70724c
Charge (x10-12 C)
Time (m:ss)

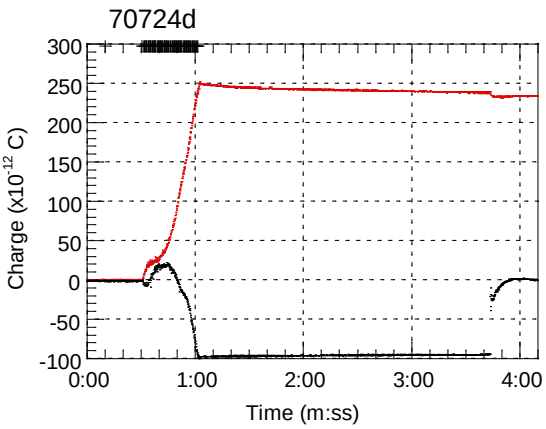
70724d
Charge (x10-12 C)
Time (m:ss)

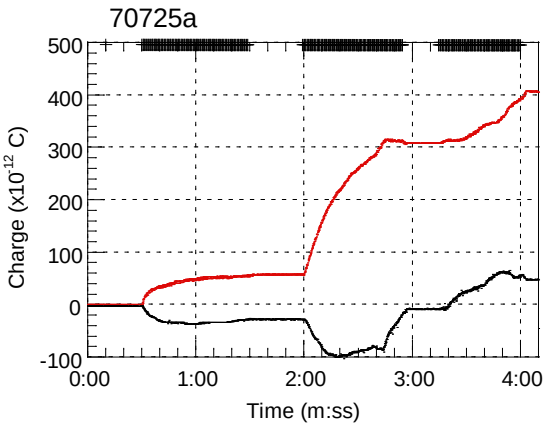
70725a
Charge (x10-12 C)
Time (m:ss)

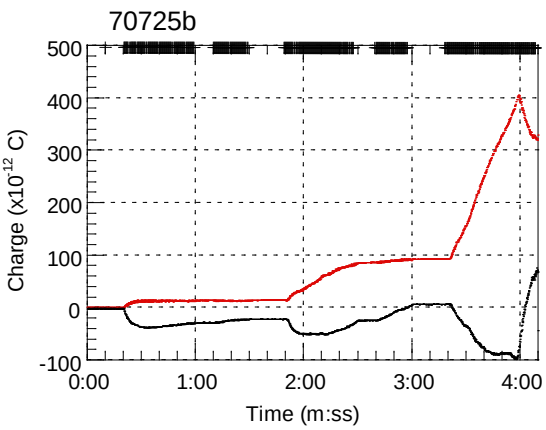
70725b
Charge (x10-12 C)
Time (m:ss)

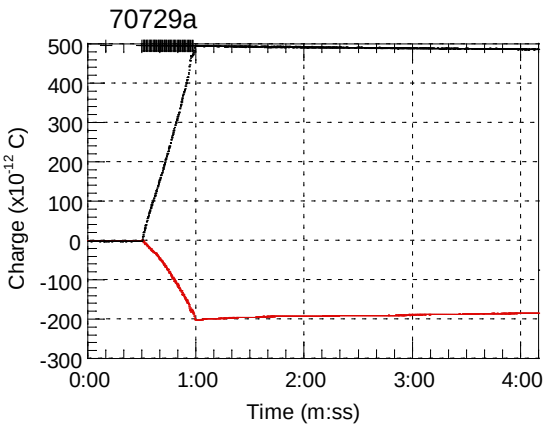
70729a
Charge (x10-12 C)
Time (m:ss)

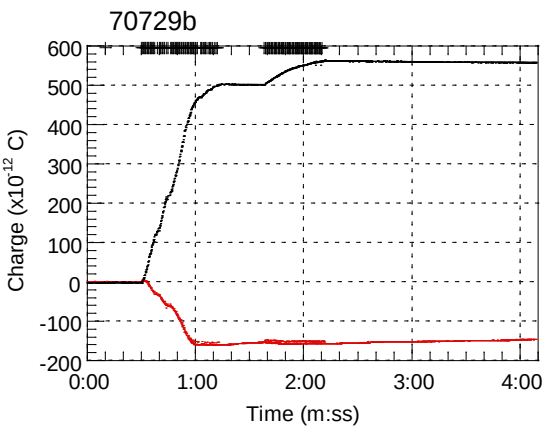
70729b
Charge (x10-12 C)
Time (m:ss)

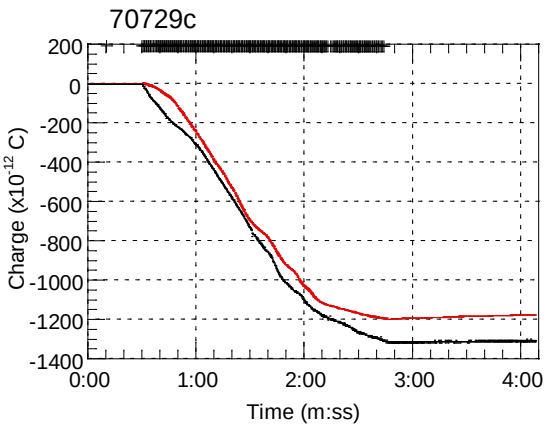
70729c
Charge (x10-12 C)
Time (m:ss)

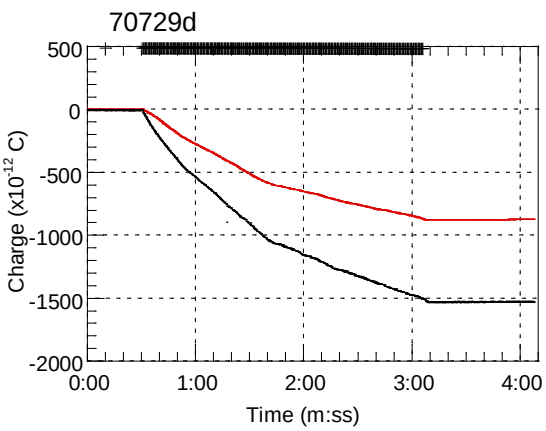
70729d
Charge (x10-12 C)
Time (m:ss)

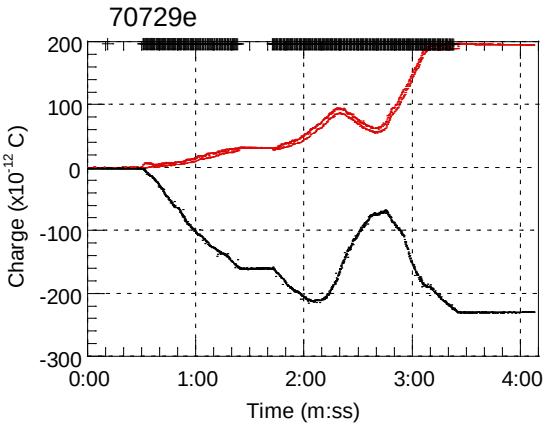
70729e
Charge (x10-12 C)
Time (m:ss)

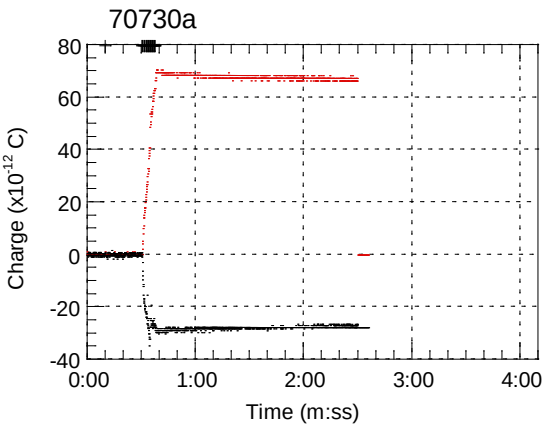
70730a
Charge (x10-12 C)
Time (m:ss)

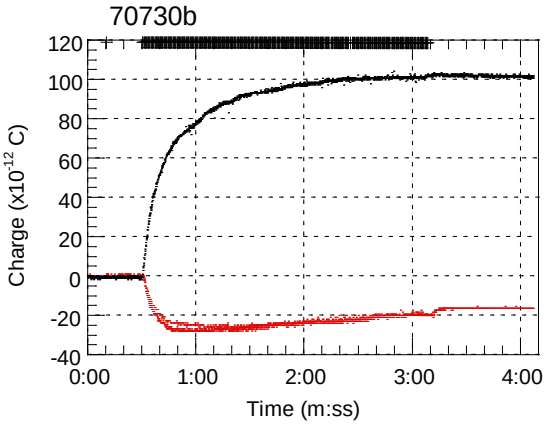
70730b
Charge (x10-12 C)
Time (m:ss)

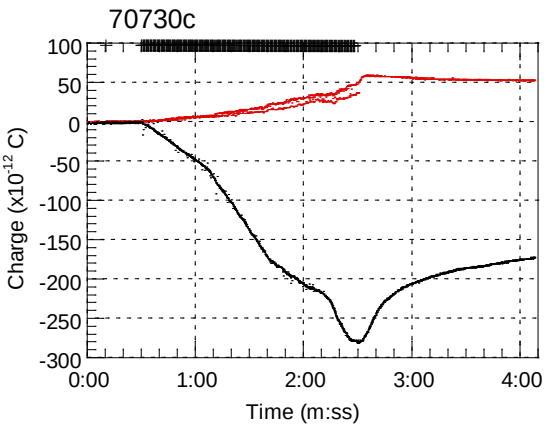
70730c
Charge (x10-12 C)
Time (m:ss)

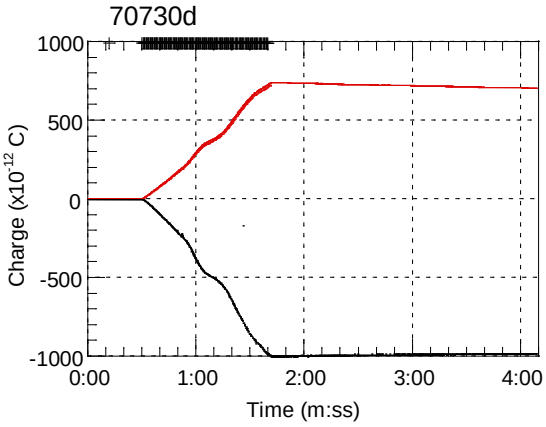
70730d
Charge (x10-12 C)
Time (m:ss)

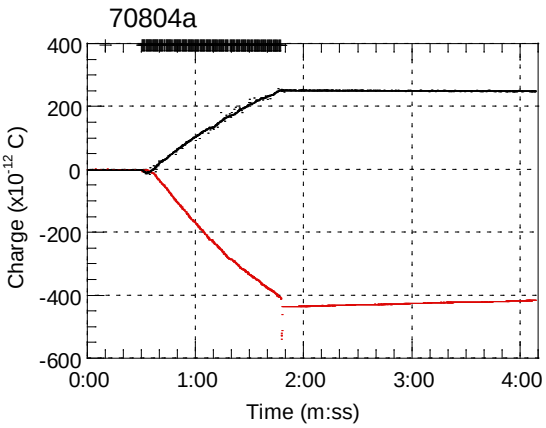
70804a
Charge (x10-12 C)
Time (m:ss)

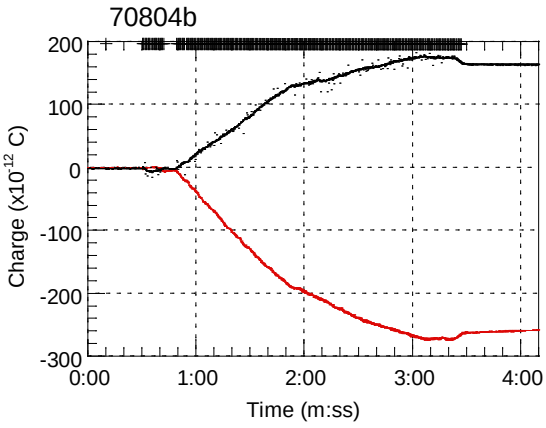
70804b
Charge (x10-12 C)
Time (m:ss)

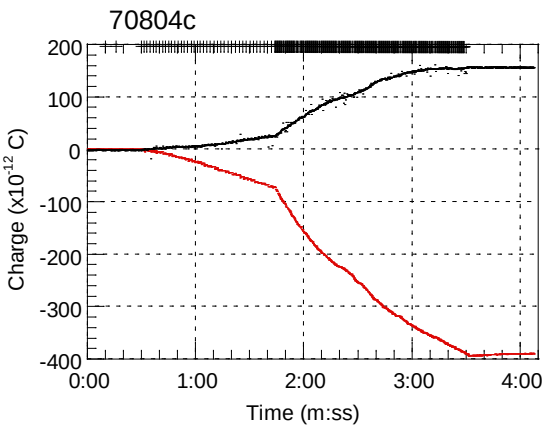
70804c
Charge (x10-12 C)
Time (m:ss)

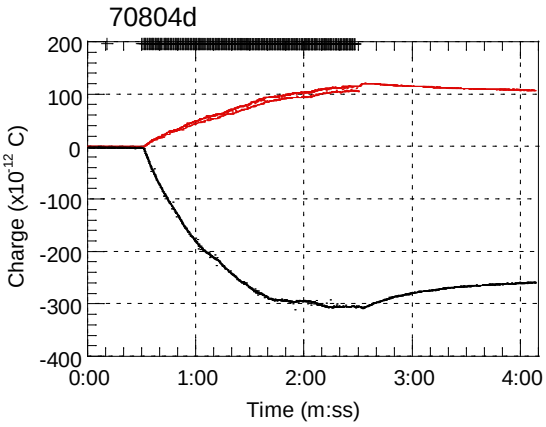
70804d
Charge (x10-12 C)
Time (m:ss)

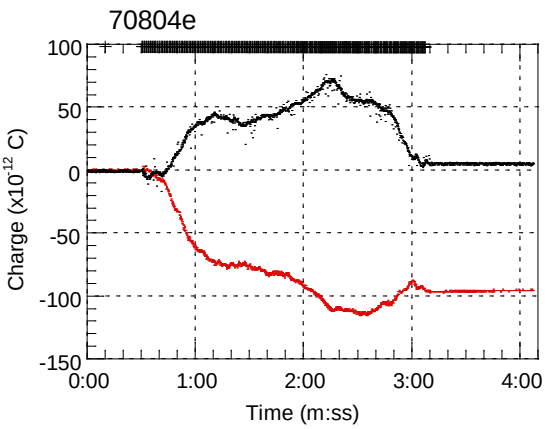
70804e
Charge (x10-12 C)
Time (m:ss)

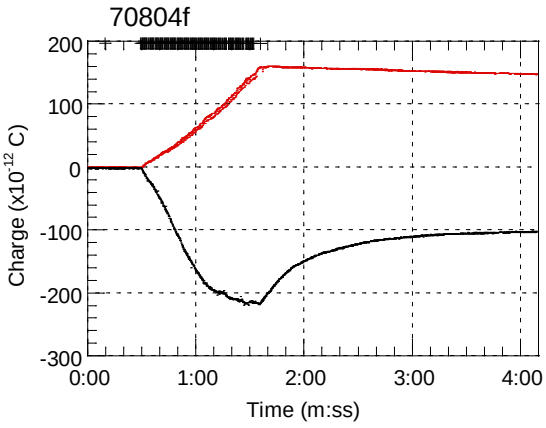
70804f
Charge (x10-12 C)
Time (m:ss)

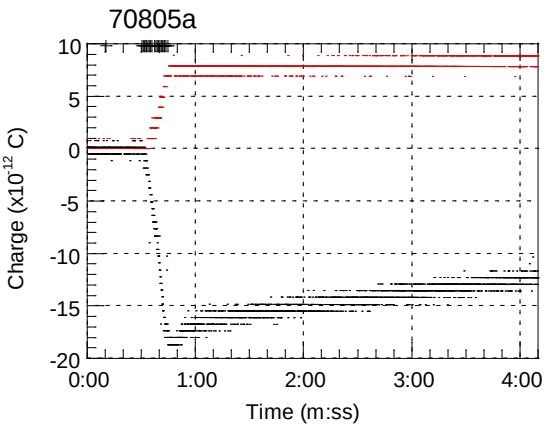
70805a
Charge (x10-12 C)
Time (m:ss)

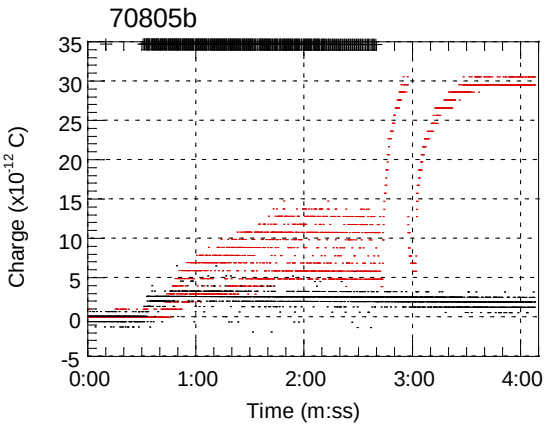
70805b
Charge (x10-12 C)
Time (m:ss)

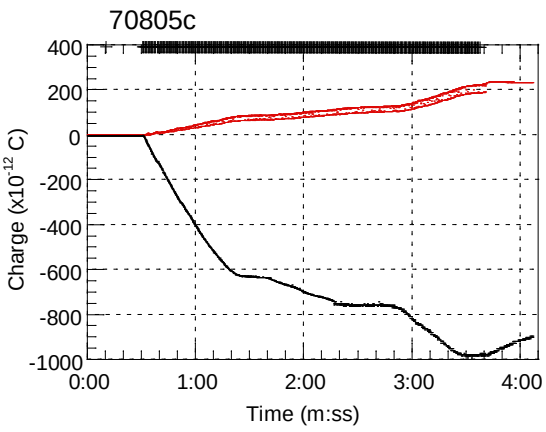
70805c
Charge (x10-12 C)
Time (m:ss)

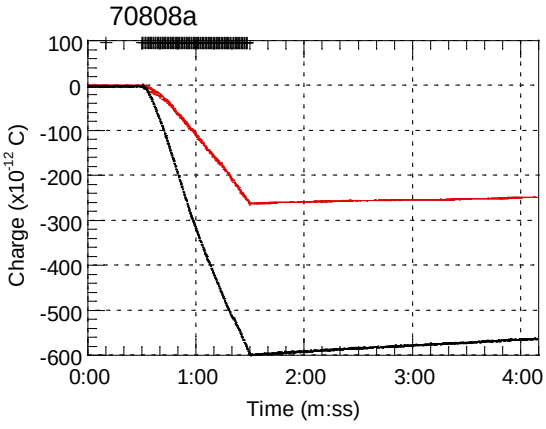
70808a
Charge (x10-12 C)
Time (m:ss)

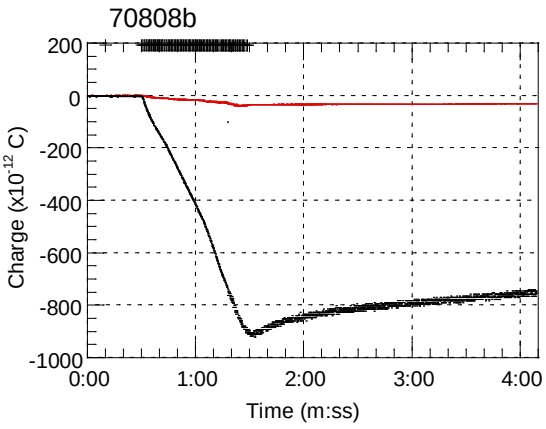
70808b
Charge (x10-12 C)
Time (m:ss)

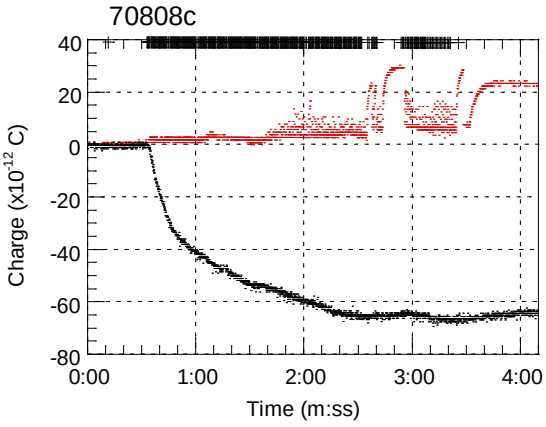
70808c
Charge (x10-12 C)
Time (m:ss)

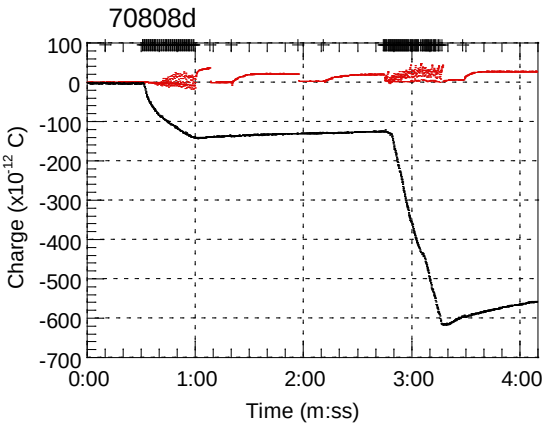
70808d
Charge (x10-12 C)
Time (m:ss)

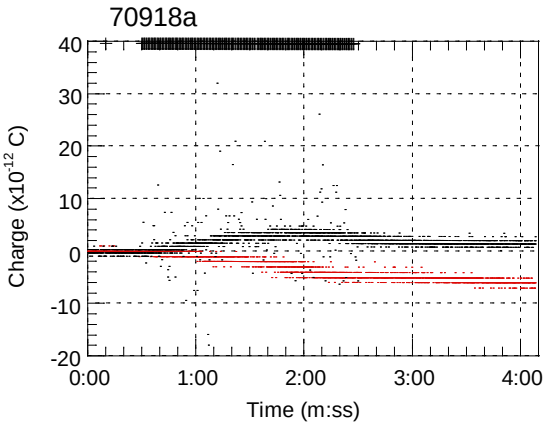
70918a
Charge (x10-12 C)
Time (m:ss)

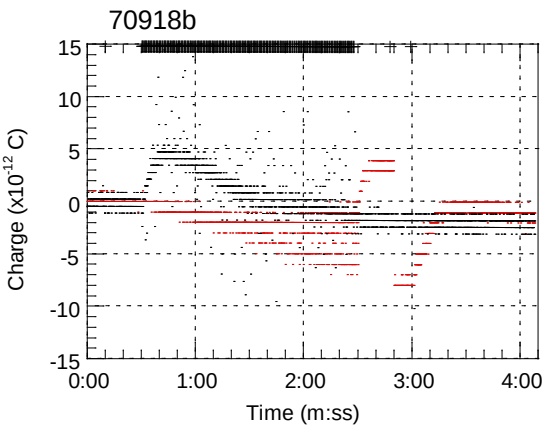
70918b
Charge (x10-12 C)
Time (m:ss)

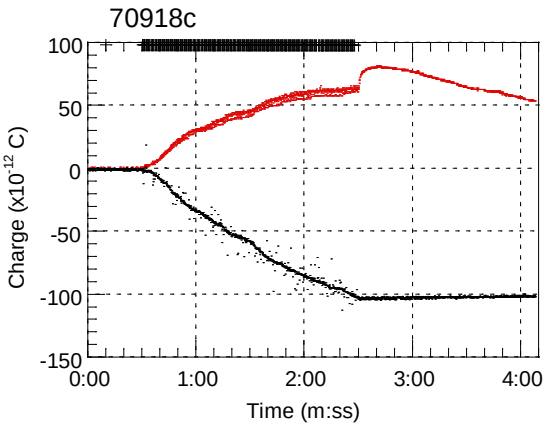
70918c
Charge (x10-12 C)
Time (m:ss)

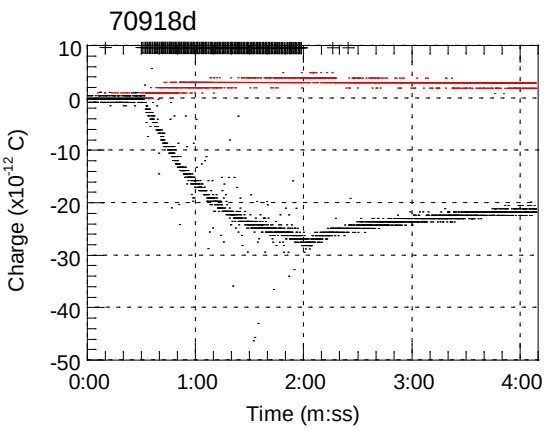
70918d
Charge (x10-12 C)
Time (m:ss)

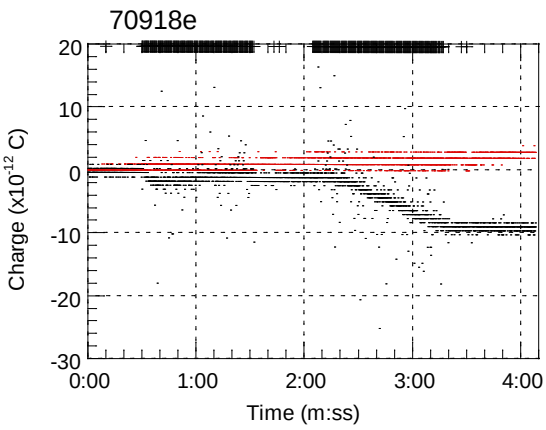
70918e
Charge (x10-12 C)
Time (m:ss)

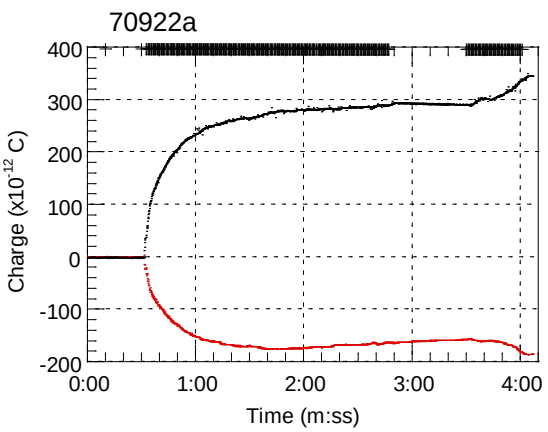
70922a
Charge (x10-12 C)
Time (m:ss)

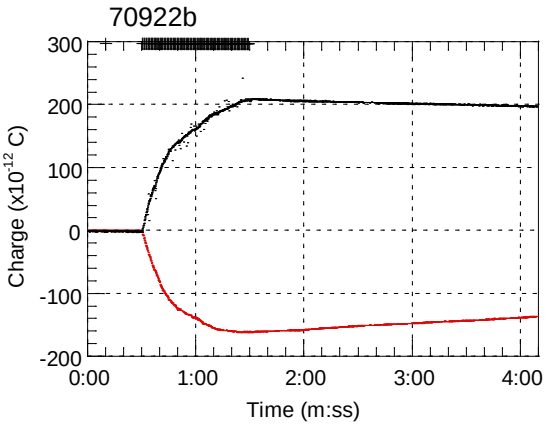
70922b
Charge (x10-12 C)
300
200
100
0
-100
-200
0:00
1:00
2:00
3:00
4:00
Time (m:ss)

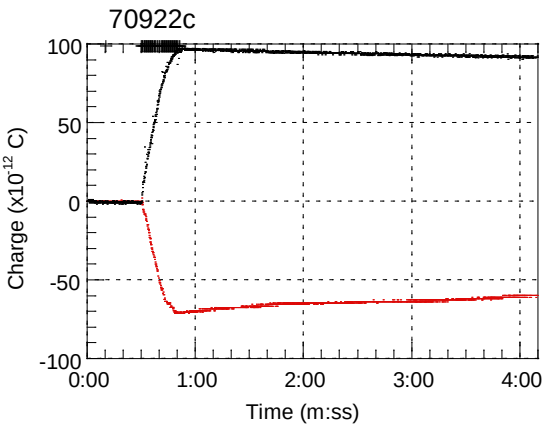
70922c
Charge (x10-12 C)
100
50
0
-50
-100
0:00
1:00
2:00
3:00
4:00
Time (m:ss)

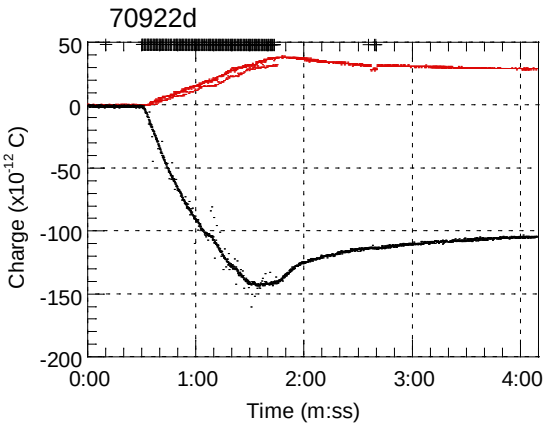
70922d
Charge (x10-12 C)
50
0
-50
-100
-150
-200
0:00
1:00
2:00
3:00
4:00
Time (m:ss)

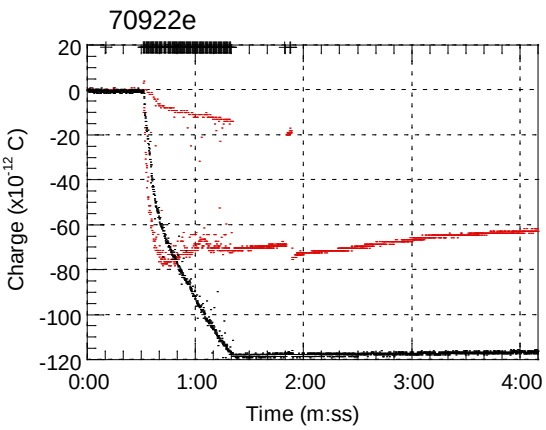
70922e
Charge (x10-12 C)
20
0
-20
-40
-60
-80
-100
-120
0:00
1:00
2:00
3:00
4:00
Time (m:ss)

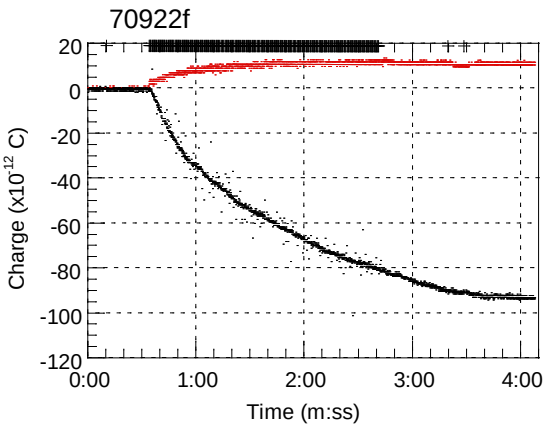
70922f
Charge (x10-12 C)
20
0
-20
-40
-60
-80
-100
-120
0:00
1:00
2:00
3:00
4:00
Time (m:ss)

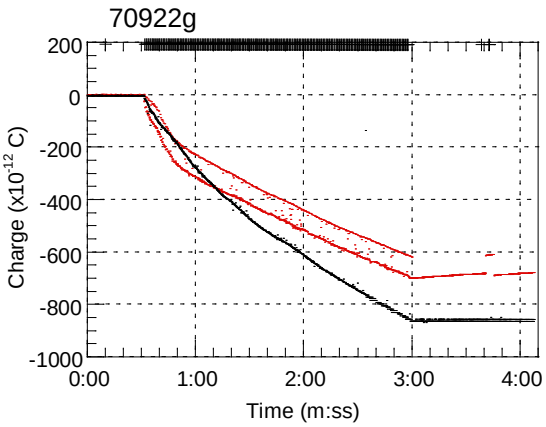
70922g
Charge (x10-12 C)
200
0
-200
-400
-600
-800
-1000
0:00
1:00
2:00
3:00
4:00
Time (m:ss)

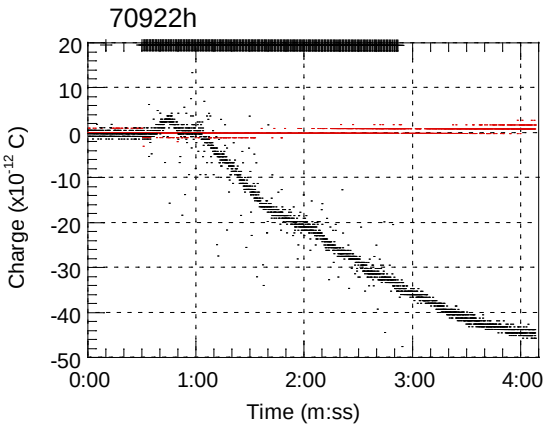
70922h
Charge (x10-12 C)
20
10
0
-10
-20
-30
-40
-50
0:00
1:00
2:00
3:00
4:00
Time (m:ss)

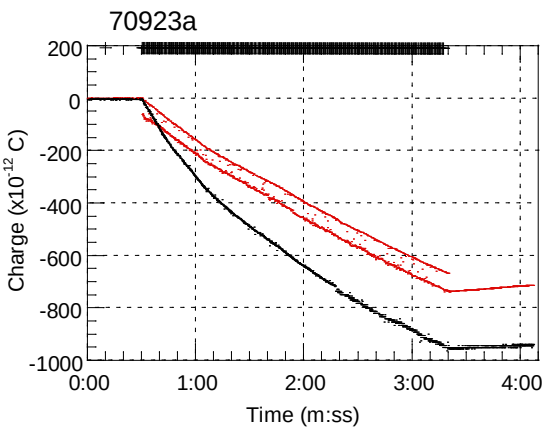
70923a
Charge (x10-12 C)
200
0
-200
-400
-600
-800
-1000
0:00
1:00
2:00
3:00
4:00
Time (m:ss)

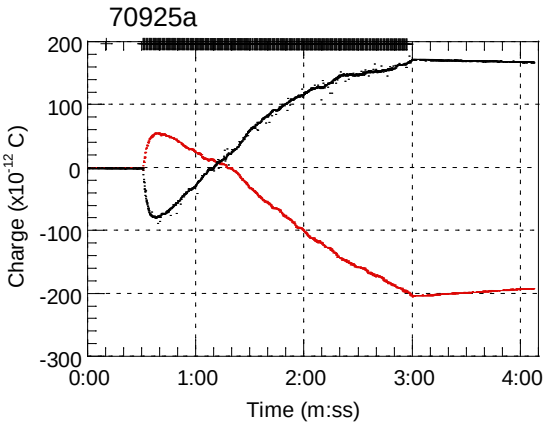
70925a
Charge (x10^{-12} C)
Time (m:ss)

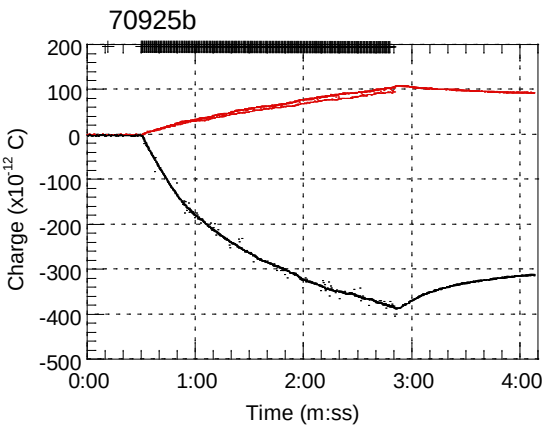
70925b
Charge (x10^{-12} C)
Time (m:ss)

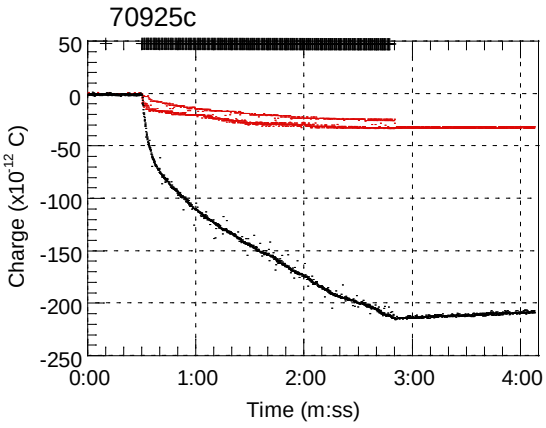
70925c
Charge (x10^{-12} C)
Time (m:ss)

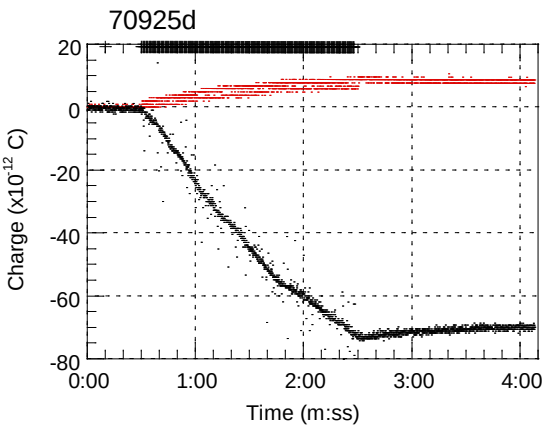
70925d
Charge (x10^{-12} C)
Time (m:ss)

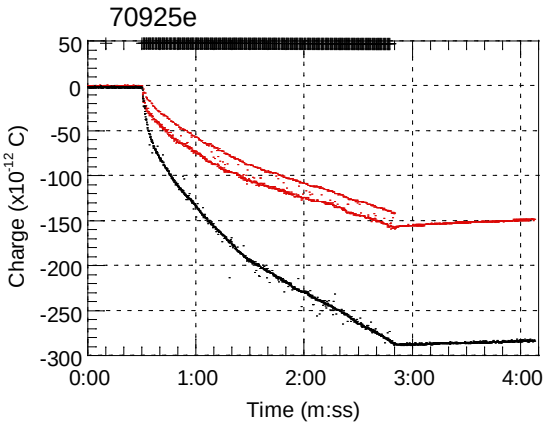
70925e
Charge (x10^{-12} C)
Time (m:ss)

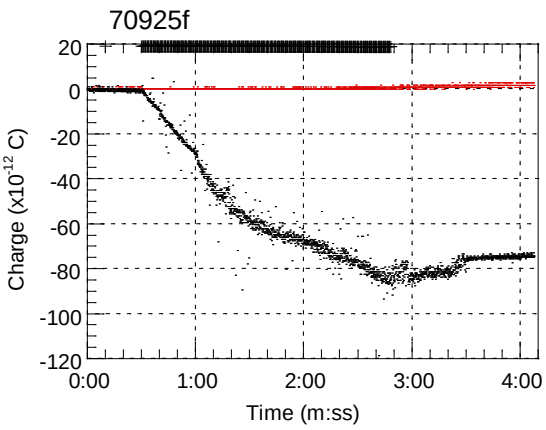
70925f
Charge (x10^{-12} C)
Time (m:ss)

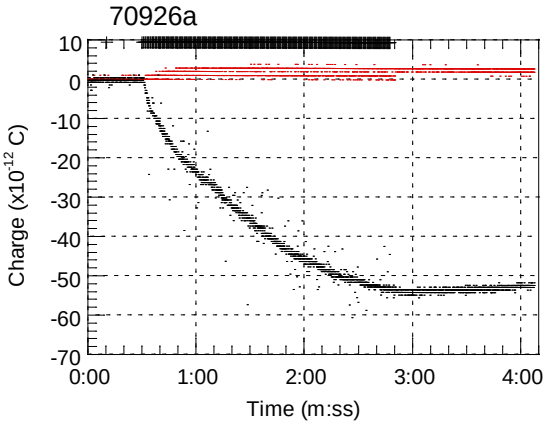
70926a
Charge (x10^{-12} C)
Time (m:ss)

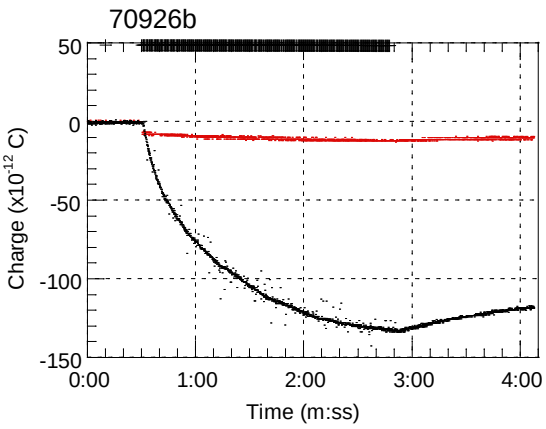
70926b
Charge (x10^{-12} C)
Time (m:ss)

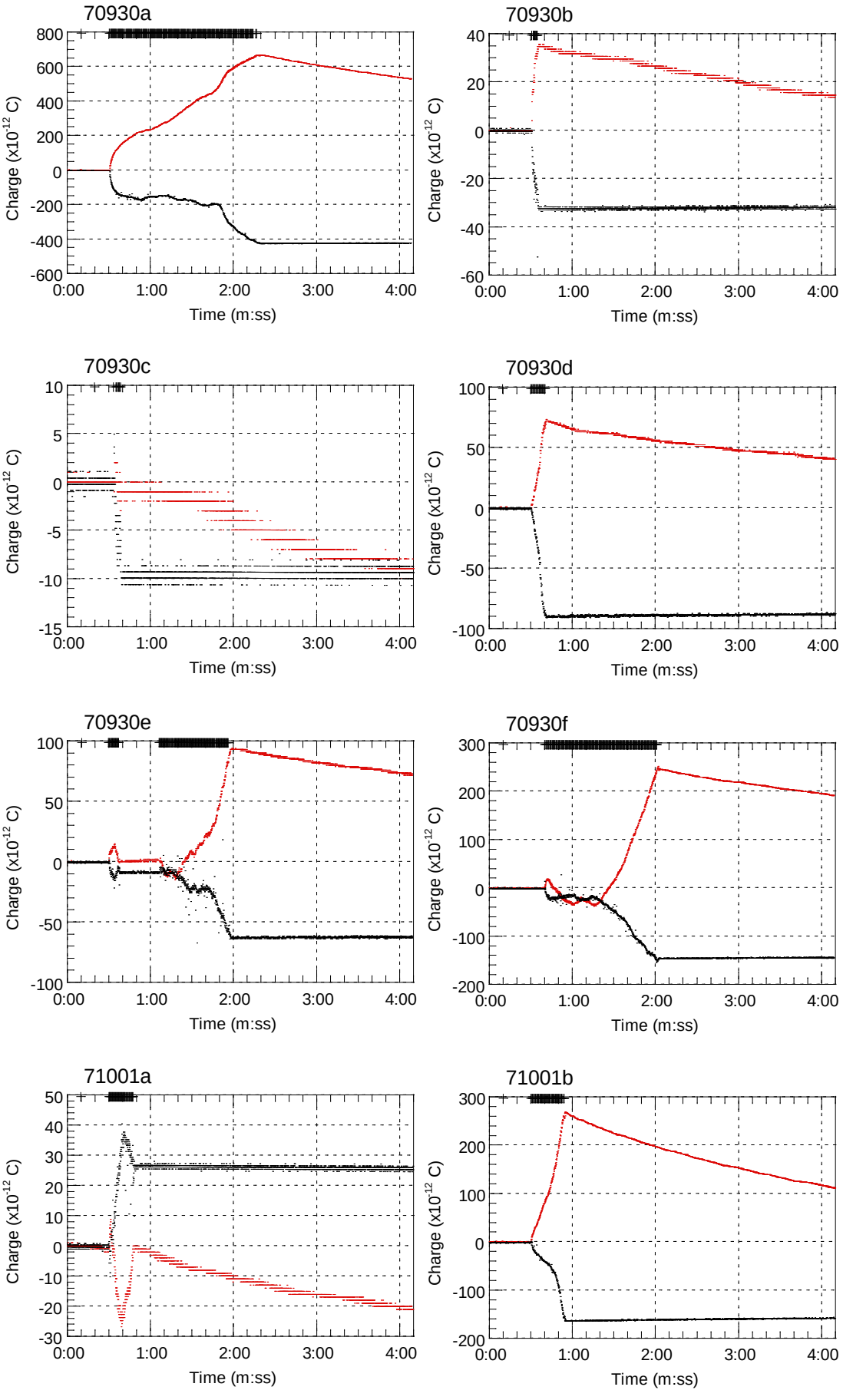
70930a
70930b
70930c
70930d
70930e
70930f
71001a
71001b
Charge (x10-12 C)
Time (m:ss)
0:00
1:00
2:00
3:00
4:00

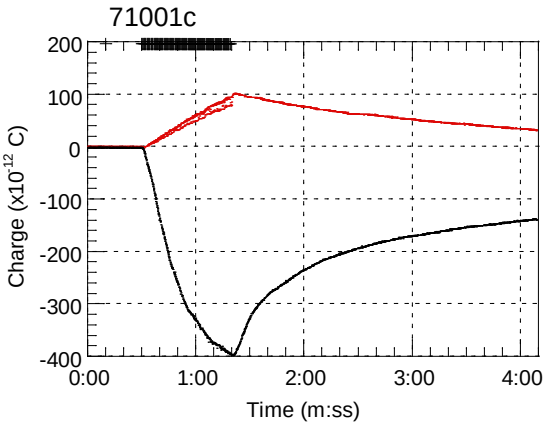
71001c
Charge (x10-12 C)
Time (m:ss)

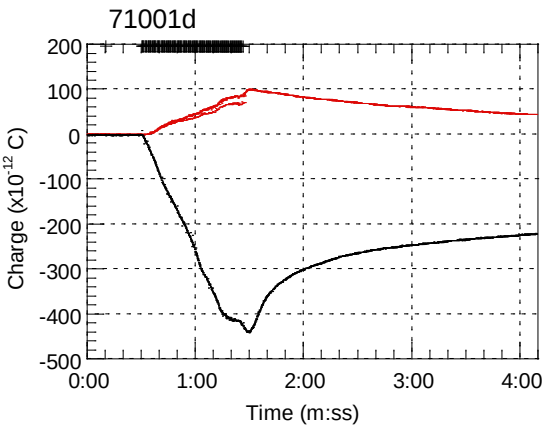
71001d
Charge (x10-12 C)
Time (m:ss)

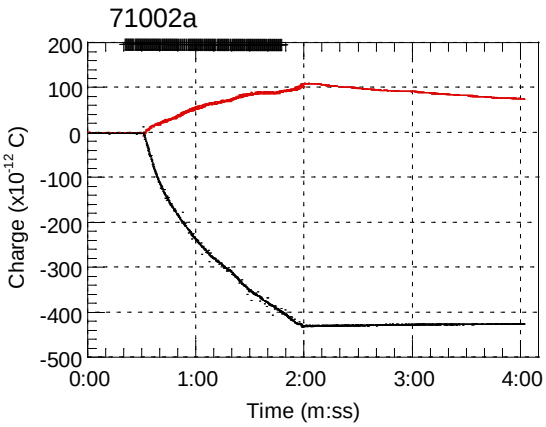
71002a
Charge (x10-12 C)
Time (m:ss)

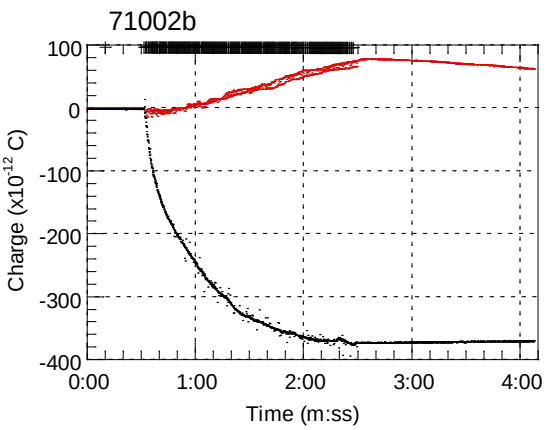
71002b
Charge (x10-12 C)
Time (m:ss)

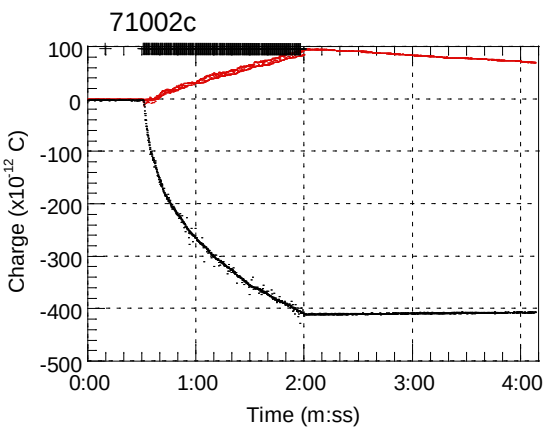
71002c
Charge (x10-12 C)
Time (m:ss)

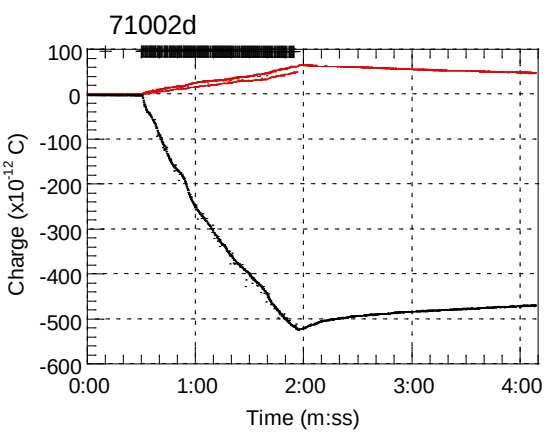
71002d
Charge (x10-12 C)
Time (m:ss)

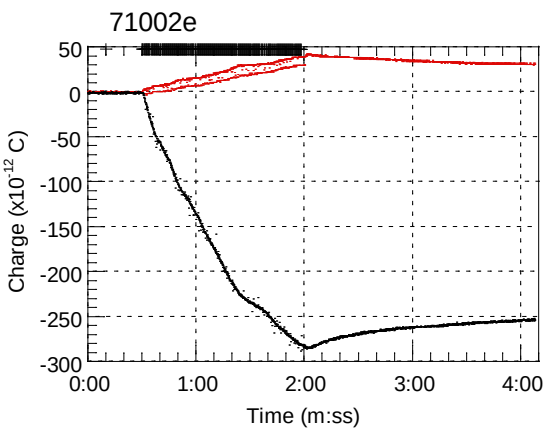
71002e
Charge (x10-12 C)
Time (m:ss)

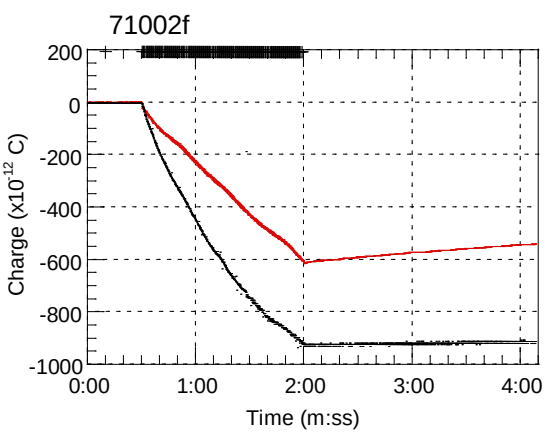
71002f
Charge (x10-12 C)
Time (m:ss)

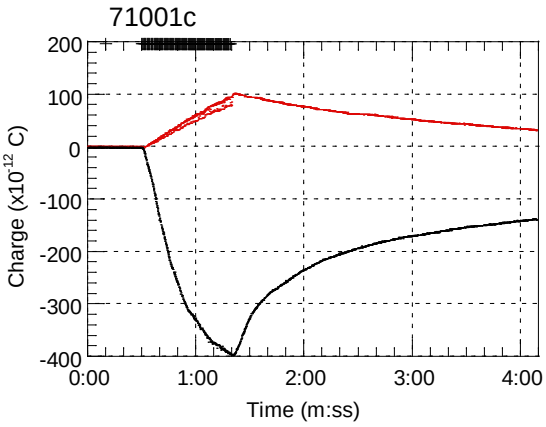
71001c
Charge (x10-12 C)
Time (m:ss)

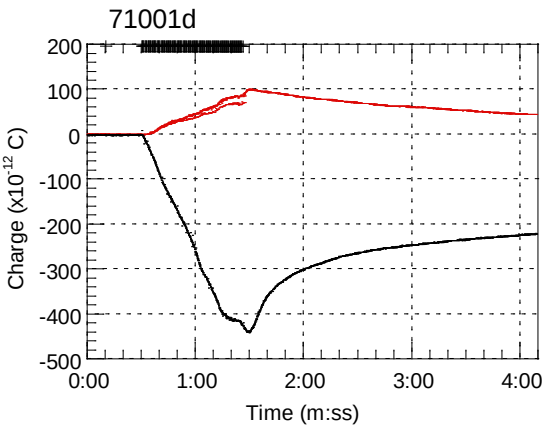
71001d
Charge (x10-12 C)
Time (m:ss)

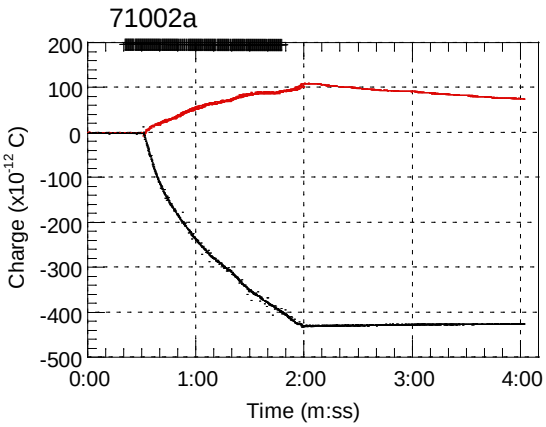
71002a
Charge (x10-12 C)
Time (m:ss)

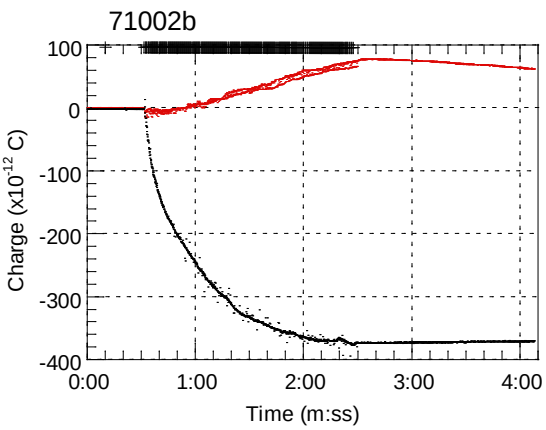
71002b
Charge (x10-12 C)
Time (m:ss)

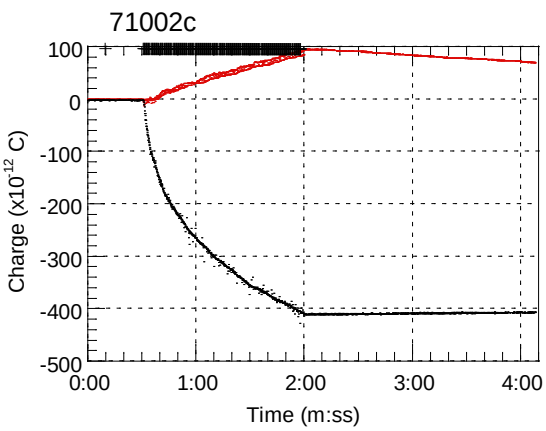
71002c
Charge (x10-12 C)
Time (m:ss)

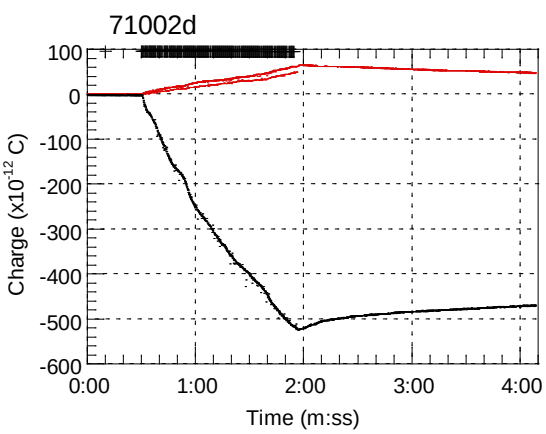
71002d
Charge (x10-12 C)
Time (m:ss)

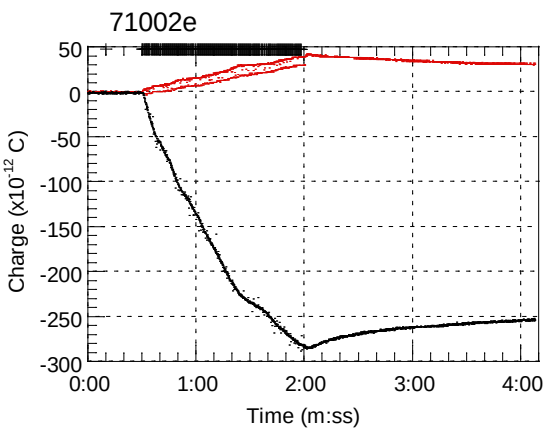
71002e
Charge (x10-12 C)
Time (m:ss)

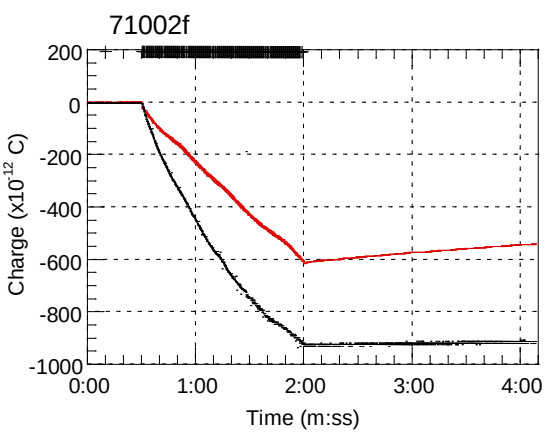
71002f
Charge (x10-12 C)
Time (m:ss)

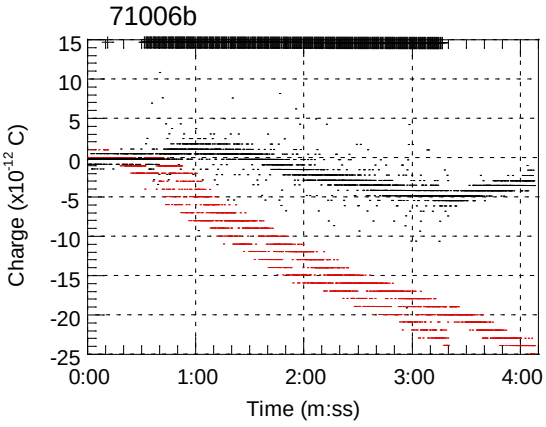
71006b
Charge (x10^{-12} C)
Time (m:ss)

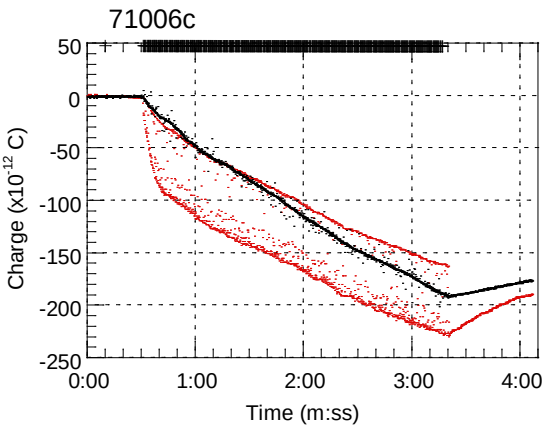
71006c
Charge (x10^{-12} C)
Time (m:ss)

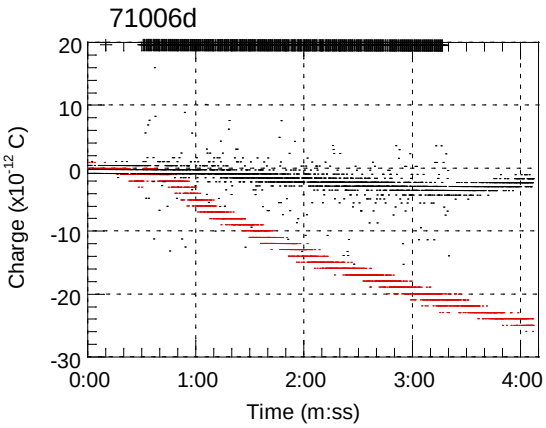
71006d
Charge (x10^{-12} C)
Time (m:ss)

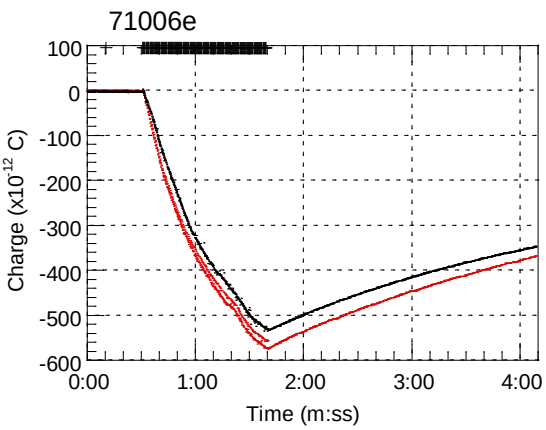
71006e
Charge (x10^{-12} C)
Time (m:ss)

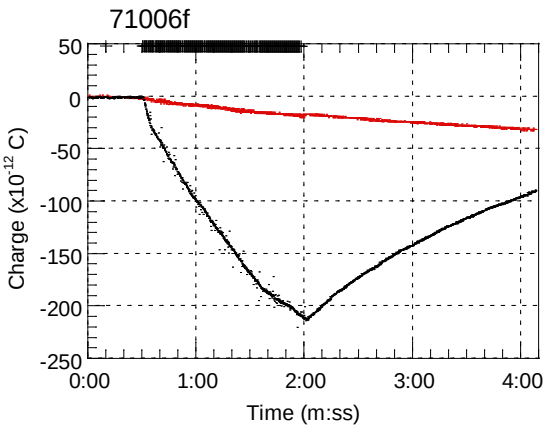
71006f
Charge (x10^{-12} C)
Time (m:ss)

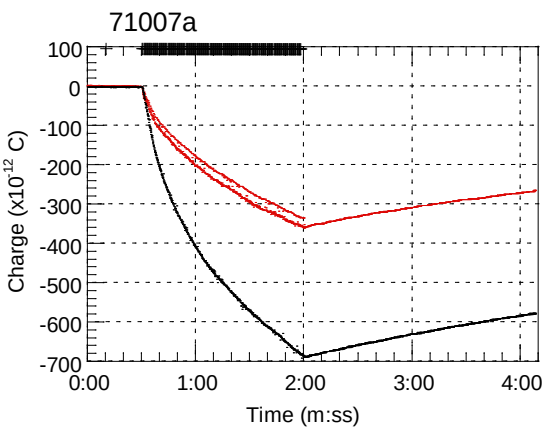
71007a
Charge (x10^{-12} C)
Time (m:ss)

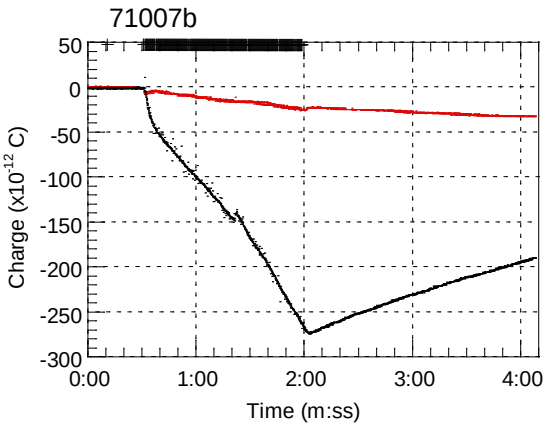
71007b
Charge (x10^{-12} C)
Time (m:ss)

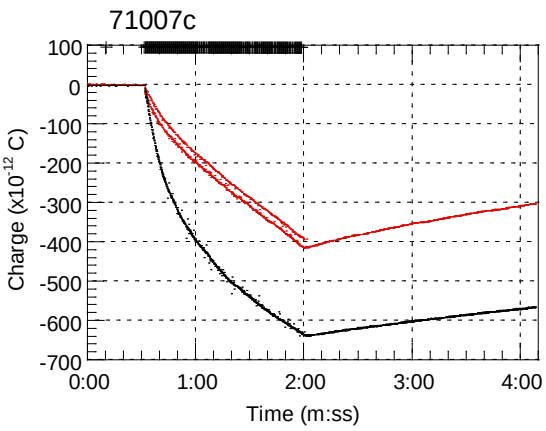
71007c
Charge (x10^{-12} C)
Time (m:ss)

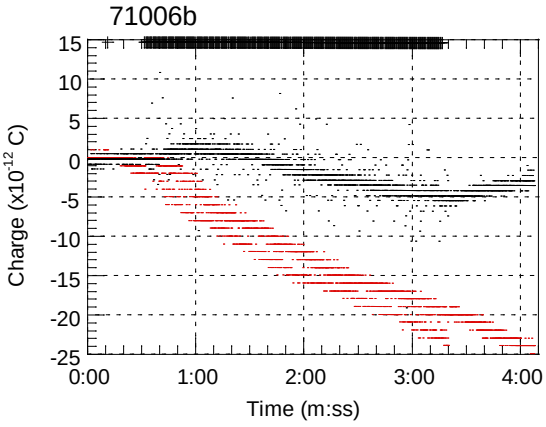
71006b
Charge (x10^{-12} C)
Time (m:ss)

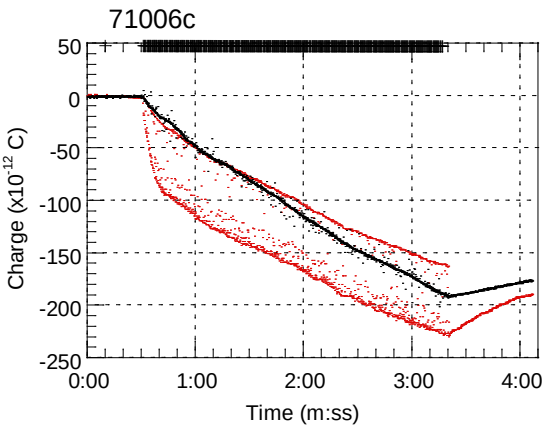
71006c
Charge (x10^{-12} C)
Time (m:ss)

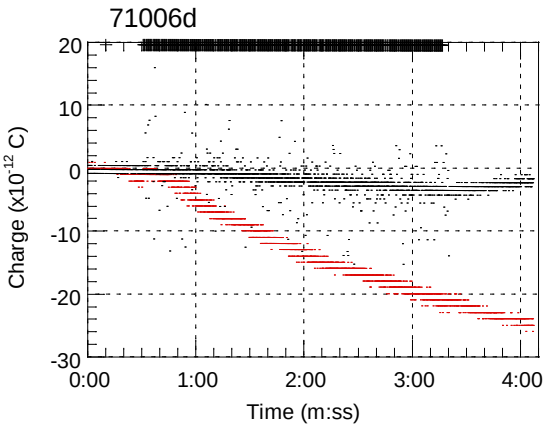
71006d
Charge (x10^{-12} C)
Time (m:ss)

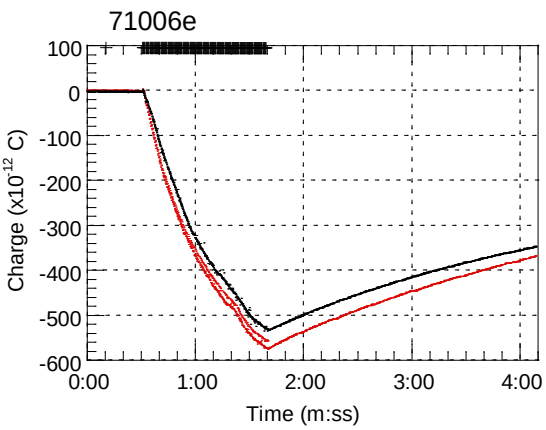
71006e
Charge (x10^{-12} C)
Time (m:ss)

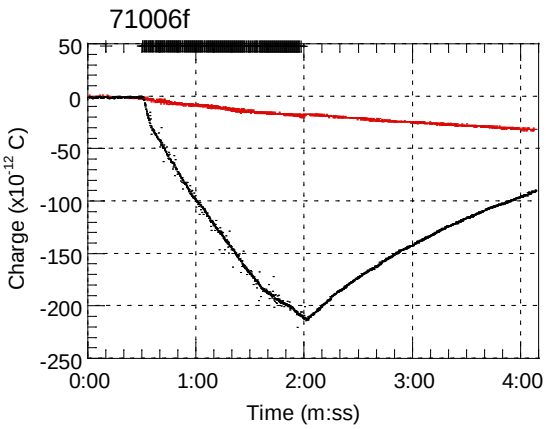
71006f
Charge (x10^{-12} C)
Time (m:ss)

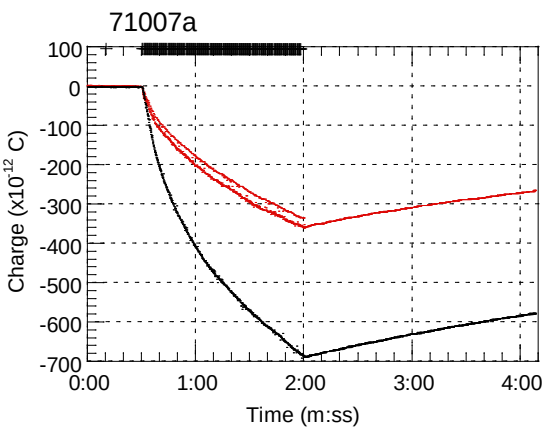
71007a
Charge (x10^{-12} C)
Time (m:ss)

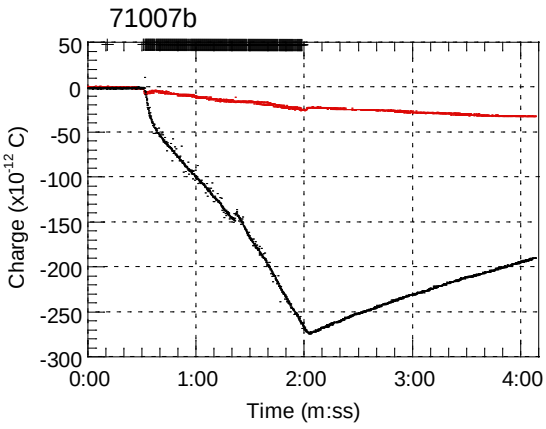
71007b
Charge (x10^{-12} C)
Time (m:ss)

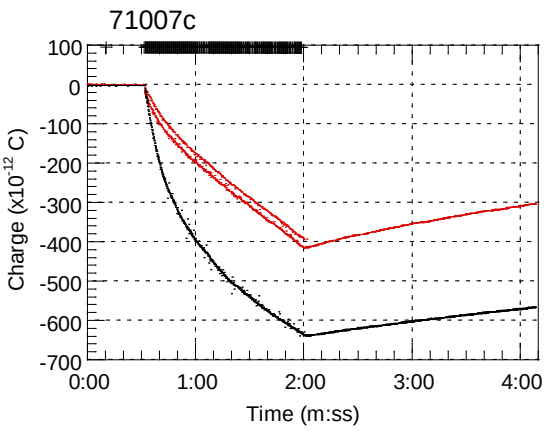
71007c
Charge (x10^{-12} C)
Time (m:ss)

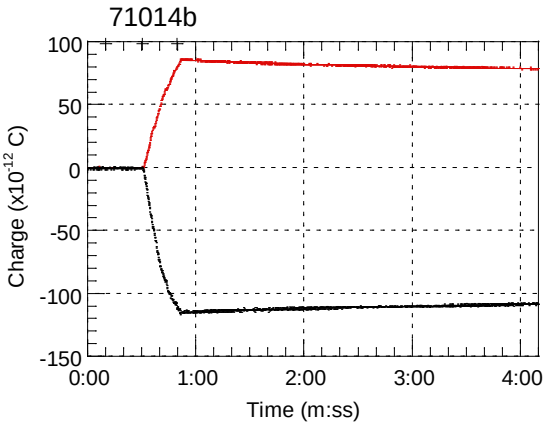
71014b
Charge (x10-12 C)
Time (m:ss)

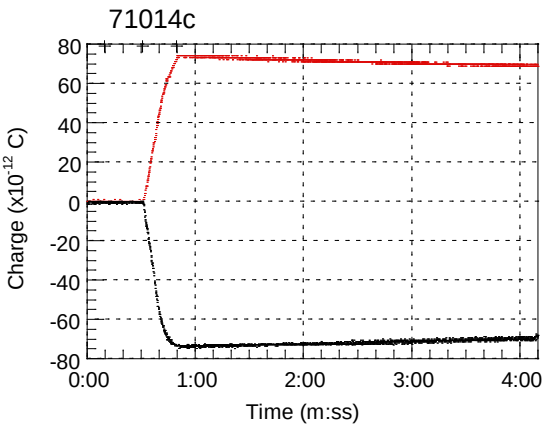
71014c
Charge (x10-12 C)
Time (m:ss)

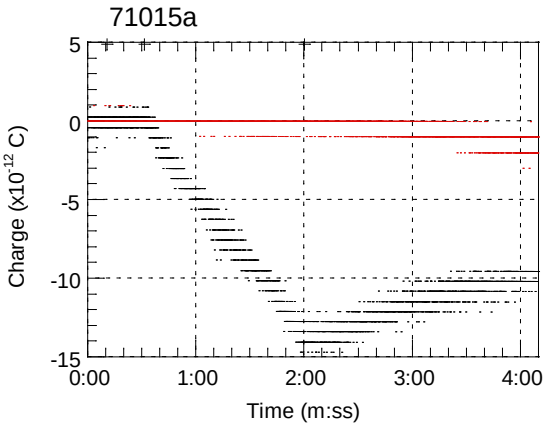
71015a
Charge (x10-12 C)
Time (m:ss)

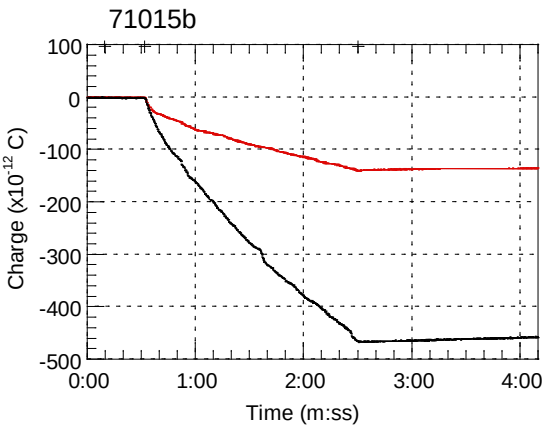
71015b
Charge (x10-12 C)
Time (m:ss)

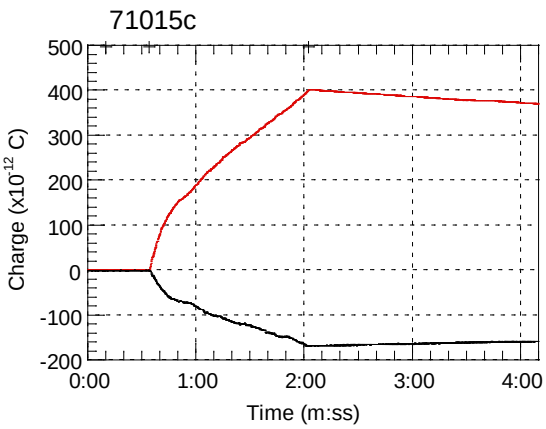
71015c
Charge (x10-12 C)
Time (m:ss)

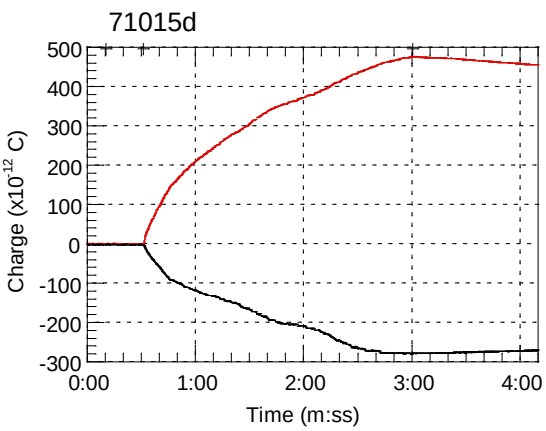
71015d
Charge (x10-12 C)
Time (m:ss)

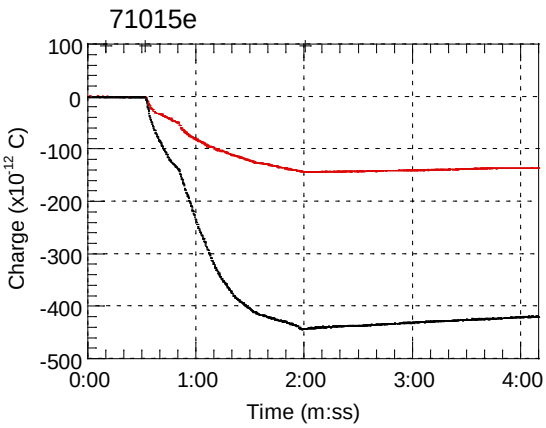
71015e
Charge (x10-12 C)
Time (m:ss)

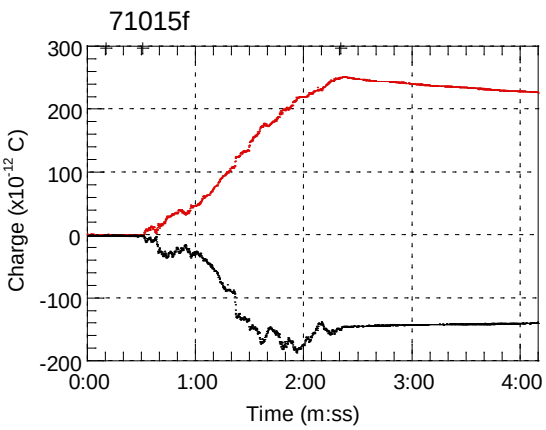
71015f
Charge (x10-12 C)
Time (m:ss)

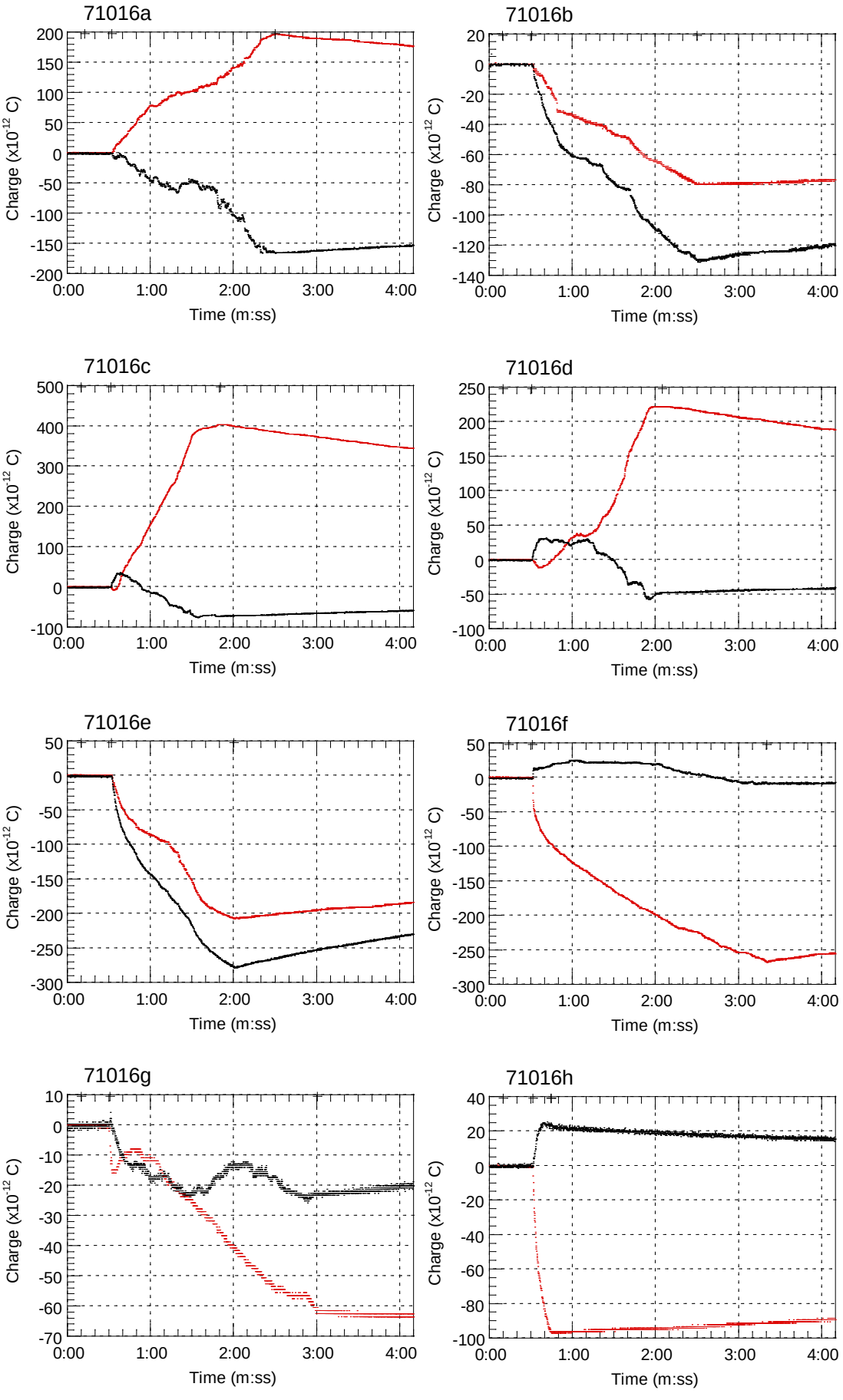
71016a
71016b
71016c
71016d
71016e
71016f
71016g
71016h
Charge (x10^{-12} C)
Time (m:ss)
0:00
1:00
2:00
3:00
4:00

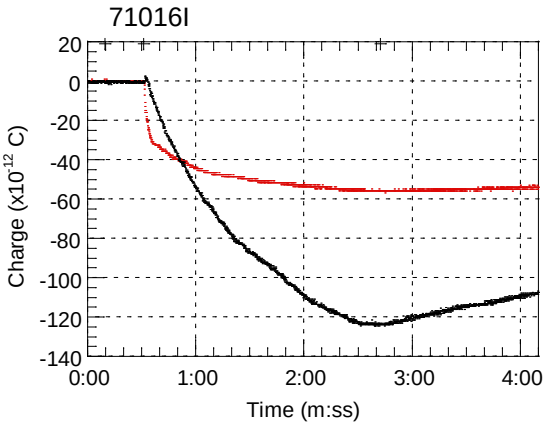
71016l
Charge (x10-12 C)
Time (m:ss)

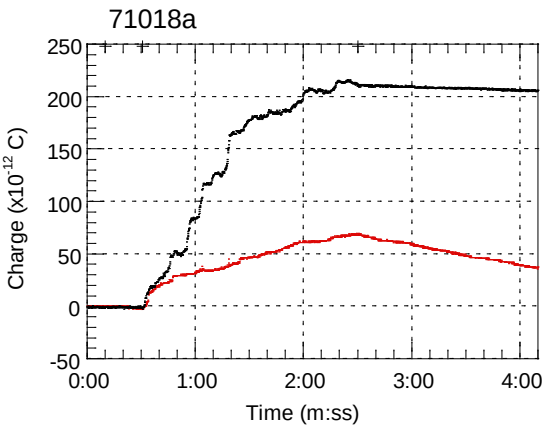
71018a
Charge (x10-12 C)
Time (m:ss)

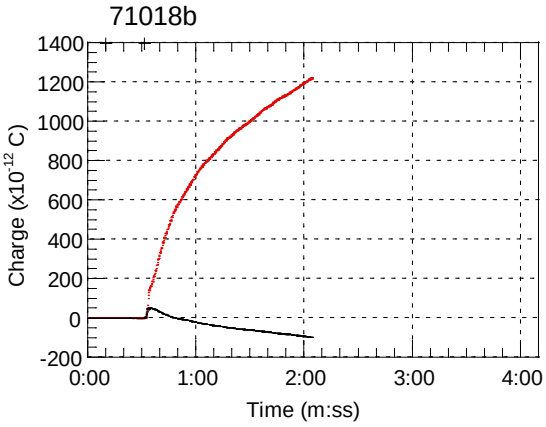
71018b
Charge (x10-12 C)
Time (m:ss)

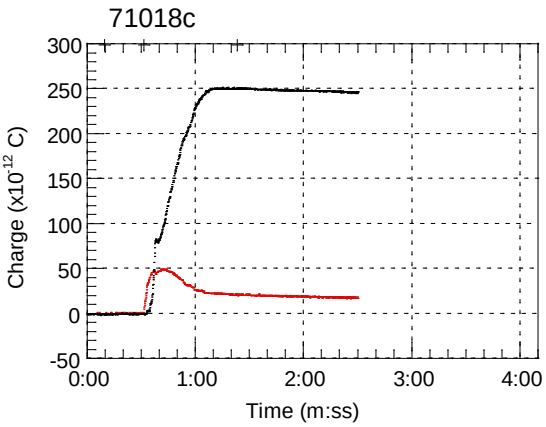
71018c
Charge (x10-12 C)
Time (m:ss)

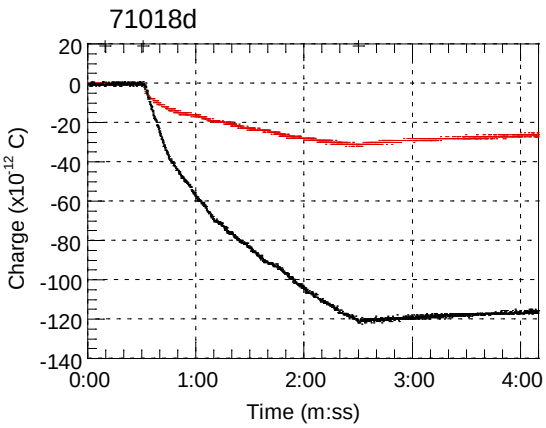
71018d
Charge (x10-12 C)
Time (m:ss)

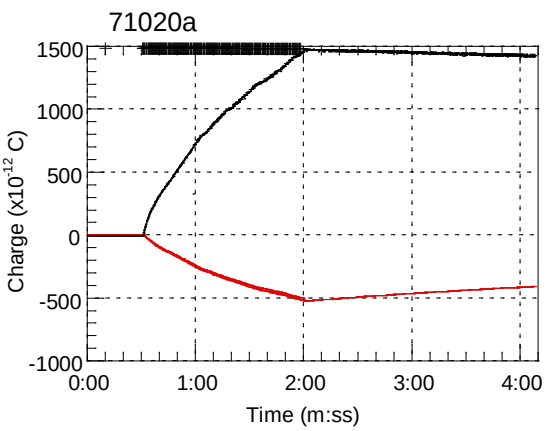
71020a
Charge (x10-12 C)
Time (m:ss)

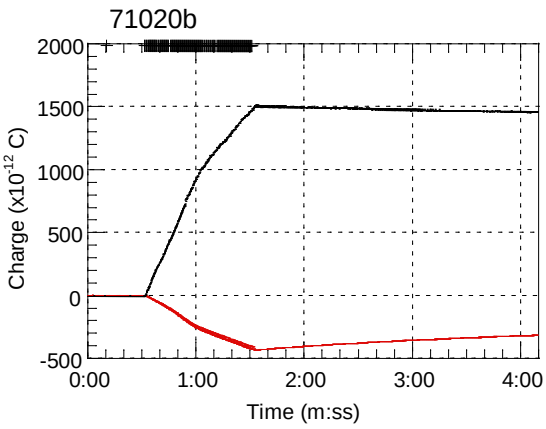
71020b
Charge (x10-12 C)
Time (m:ss)

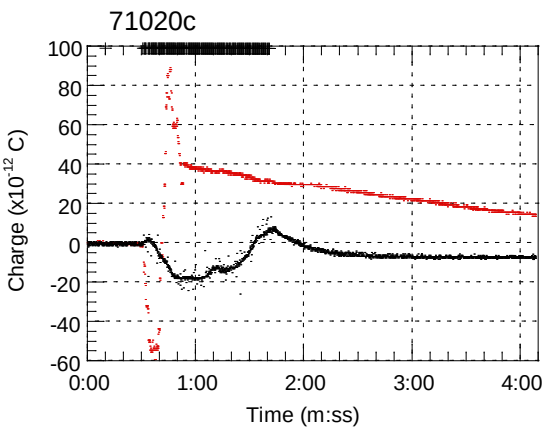
71020c
Charge (x10-12 C)
Time (m:ss)

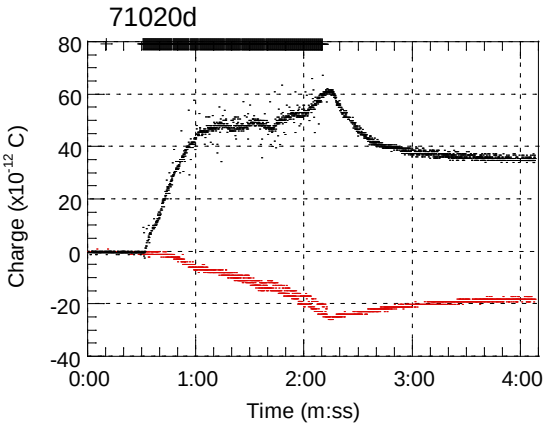
71020d
Charge (x10^{-12} C)
Time (m:ss)

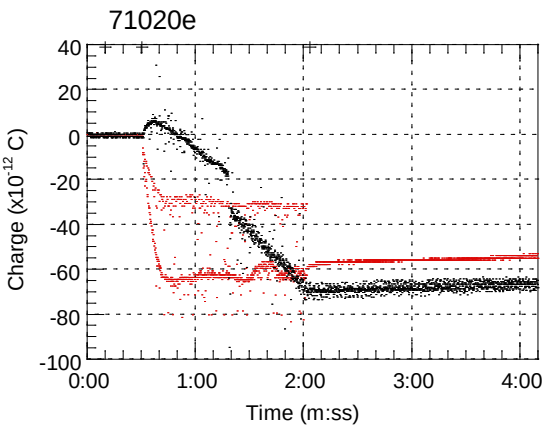
71020e
Charge (x10^{-12} C)
Time (m:ss)

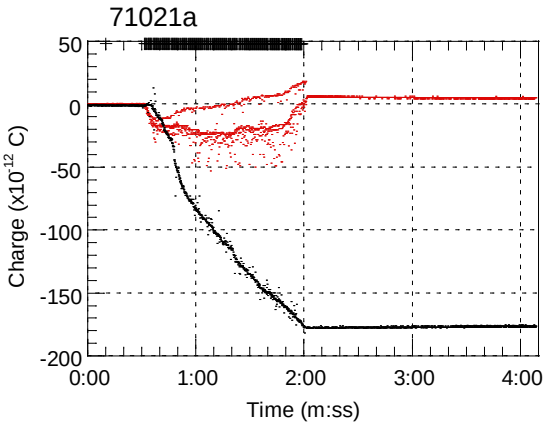
71021a
Charge (x10^{-12} C)
Time (m:ss)

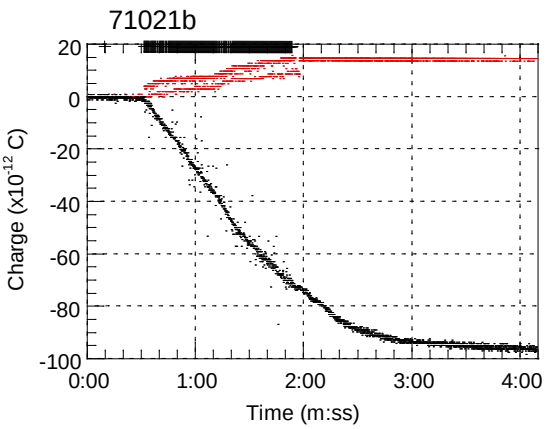
71021b
Charge (x10^{-12} C)
Time (m:ss)

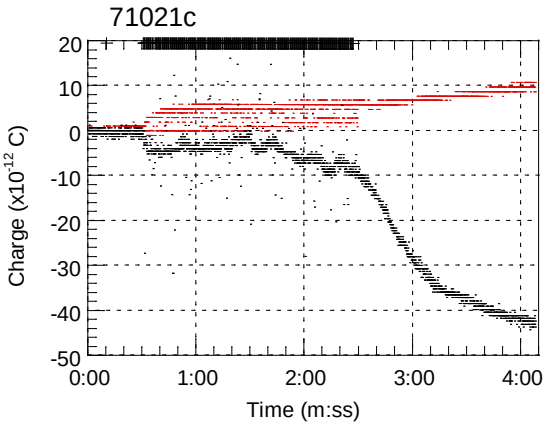
71021c
Charge (x10^{-12} C)
Time (m:ss)

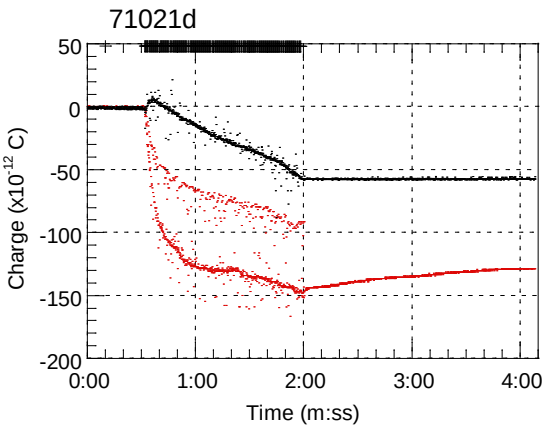
71021d
Charge (x10^{-12} C)
Time (m:ss)

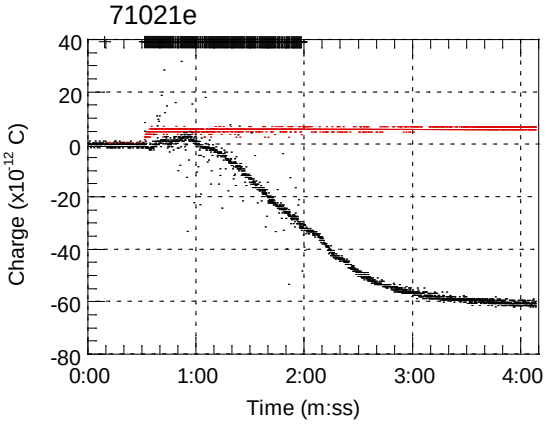
71021e
Charge (x10^{-12} C)
Time (m:ss)

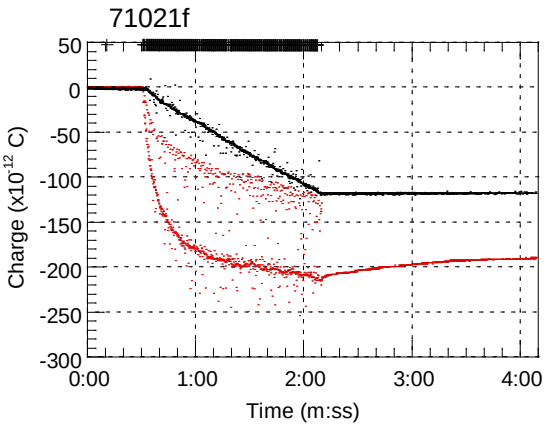
71021f
Charge (x10^{-12} C)
Time (m:ss)

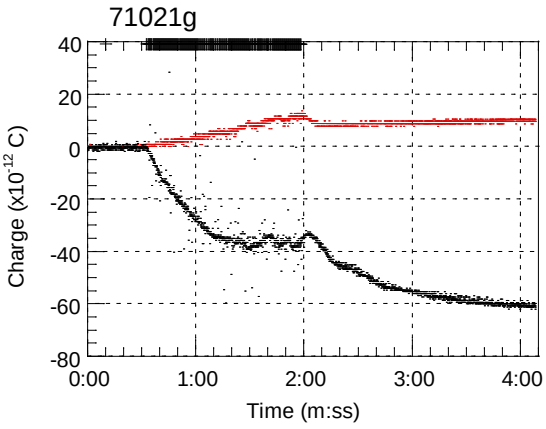
71021g
Charge (x10^{-12} C)
Time (m:ss)

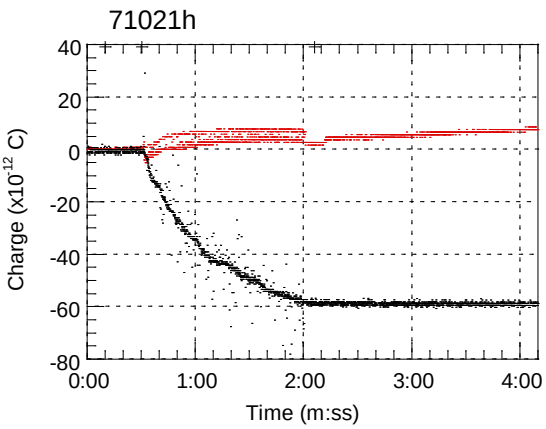
71021h
Charge (x10^{-12} C)
Time (m:ss)

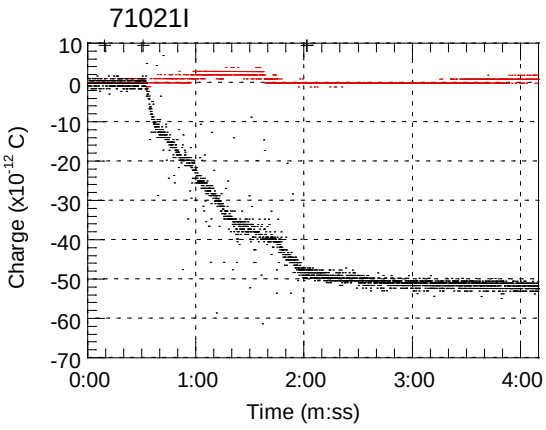
71021I
Charge (x10^{-12} C)
Time (m:ss)

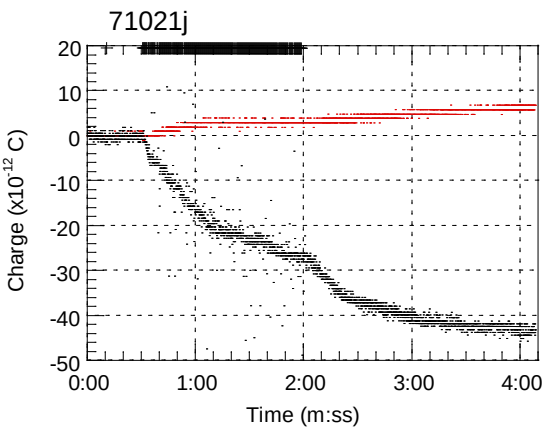
71021j
Charge (x10^{-12} C)
Time (m:ss)

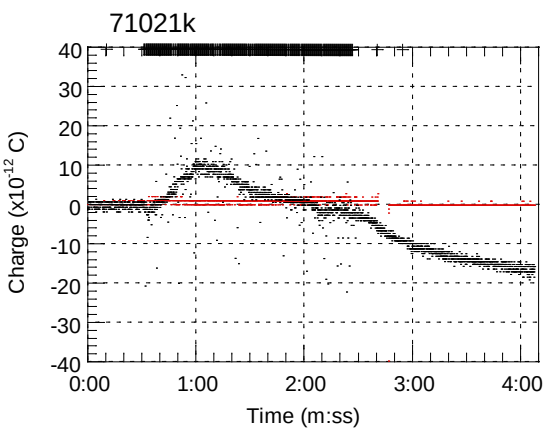
71021k
Charge (x10^{-12} C)
Time (m:ss)

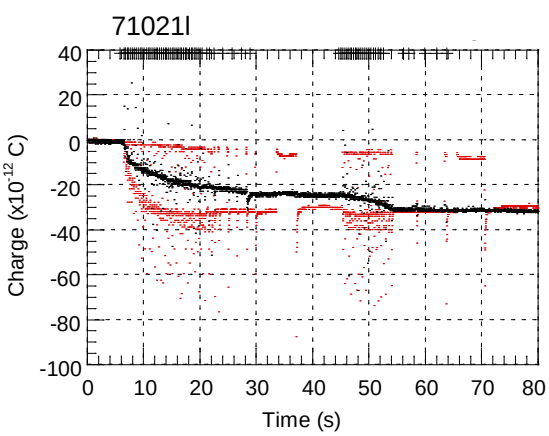
71021l
Charge (x10^{-12} C)
Time (s)

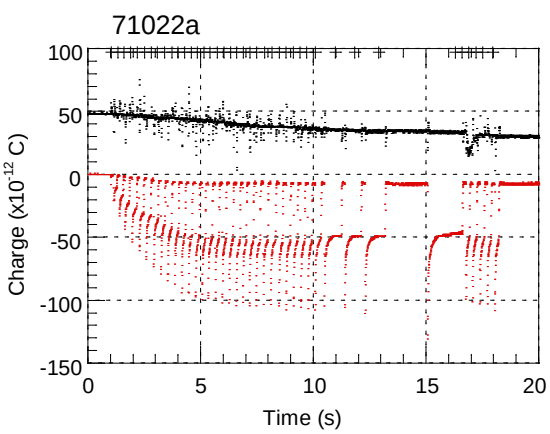
71022a
Charge (x10^{-12} C)
Time (s)

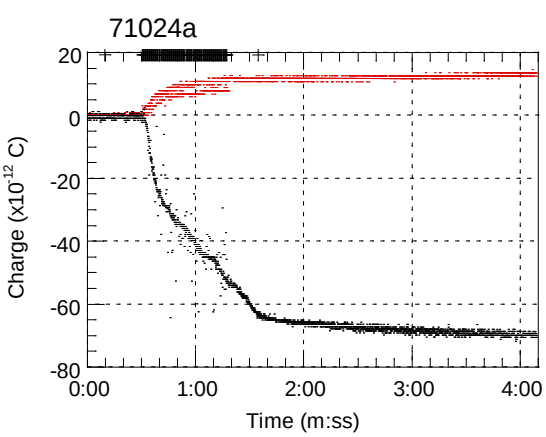
71024a
Charge (x10^{-12} C)
Time (m:ss)

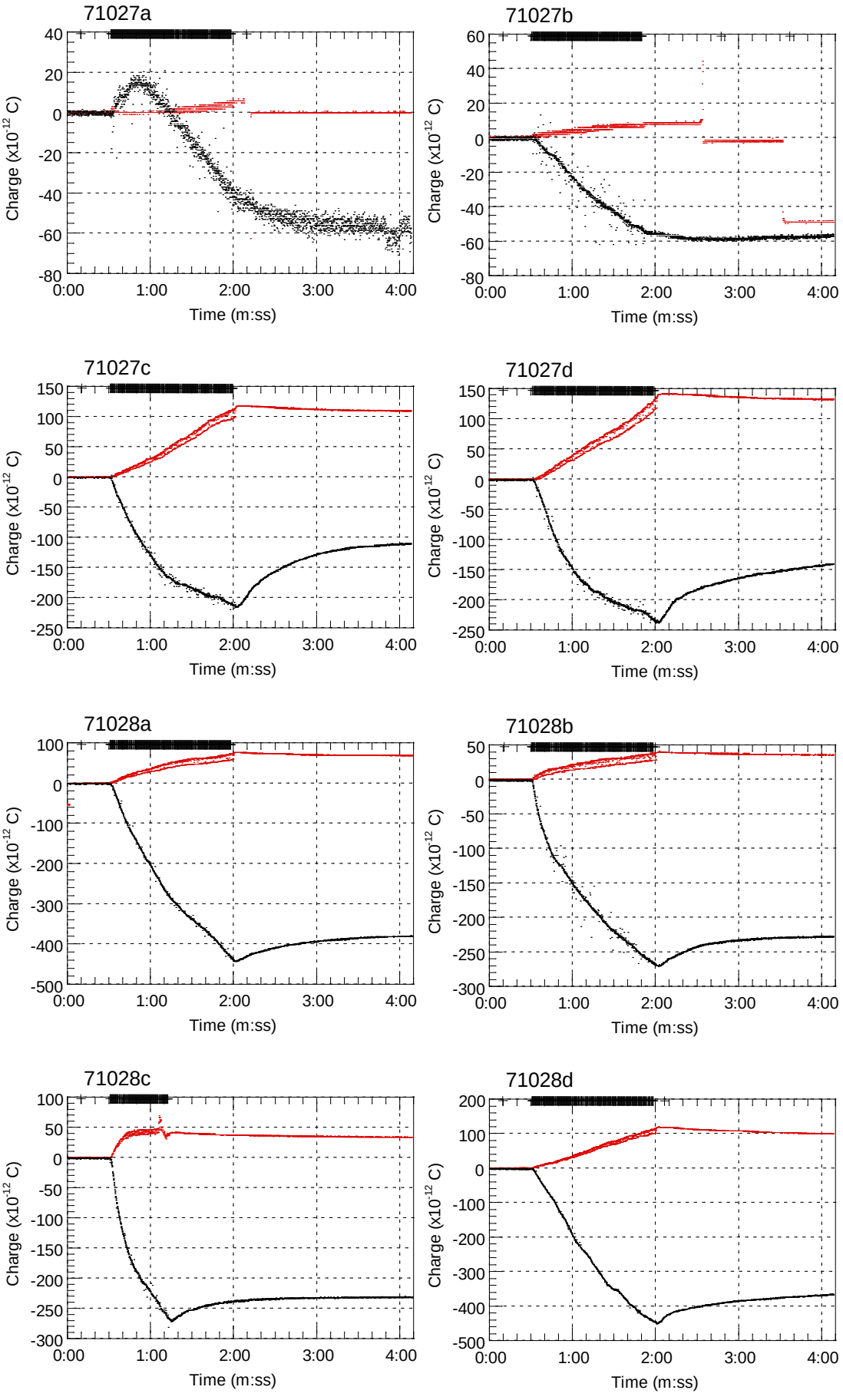
71027a
71027b
71027c
71027d
71028a
71028b
71028c
71028d
Charge (x10^{-12} C)
Time (m:ss)
0:00
1:00
2:00
3:00
4:00

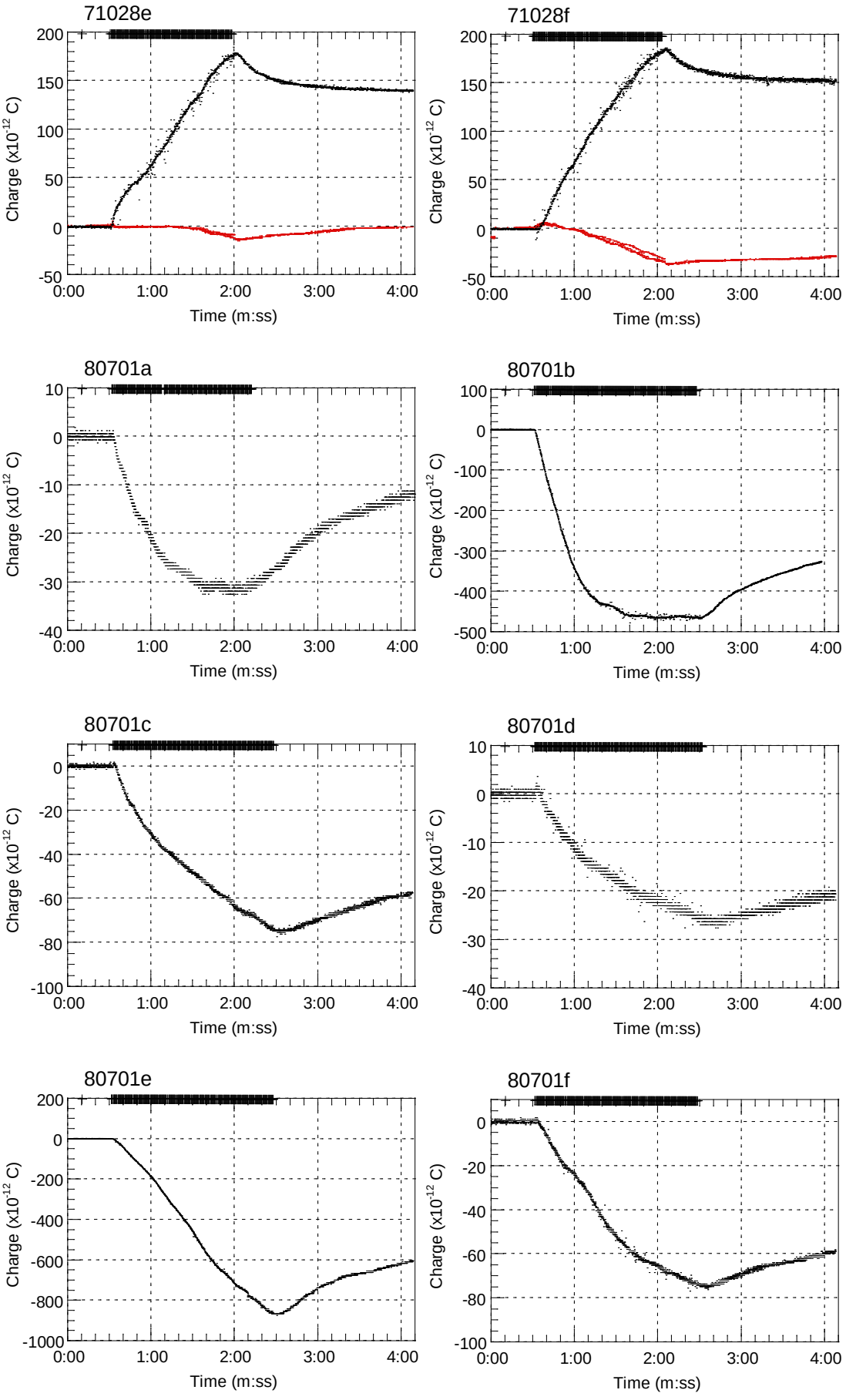
71028e
71028f
80701a
80701b
80701c
80701d
80701e
80701f
Charge (x10-12 C)
Time (m:ss)
0:00
1:00
2:00
3:00
4:00

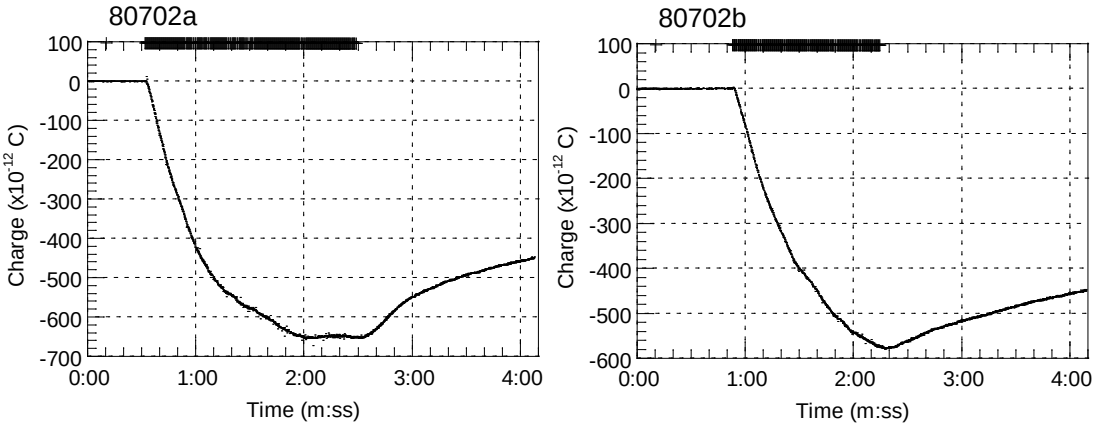
80702a
Charge (x10-12 C)
100
0
-100
-200
-300
-400
-500
-600
-700
0:00
1:00
2:00
3:00
4:00
Time (m:ss)

80702b
Charge (x10-12 C)
100
0
-100
-200
-300
-400
-500
-600
0:00
1:00
2:00
3:00
4:00
Time (m:ss)

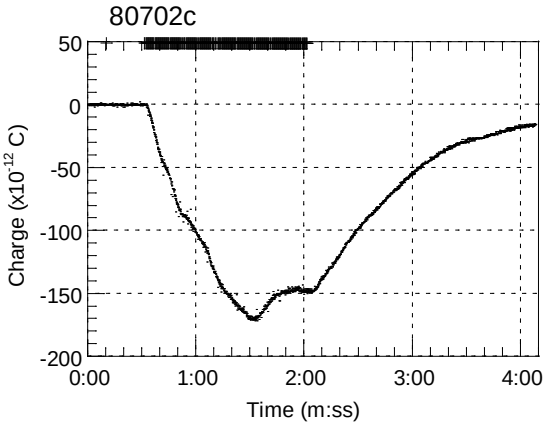
80702c
Charge (x10-12 C)
50
0
-50
-100
-150
-200
0:00
1:00
2:00
3:00
4:00
Time (m:ss)

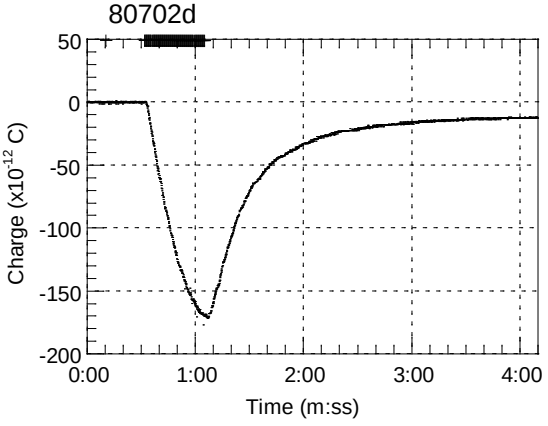
80702d
Charge (x10-12 C)
50
0
-50
-100
-150
-200
0:00
1:00
2:00
3:00
4:00
Time (m:ss)

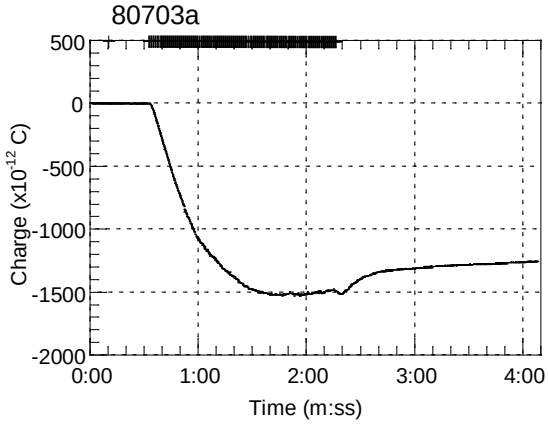
80703a
Charge (x10-12 C)
500
0
-500
-1000
-1500
-2000
0:00
1:00
2:00
3:00
4:00
Time (m:ss)

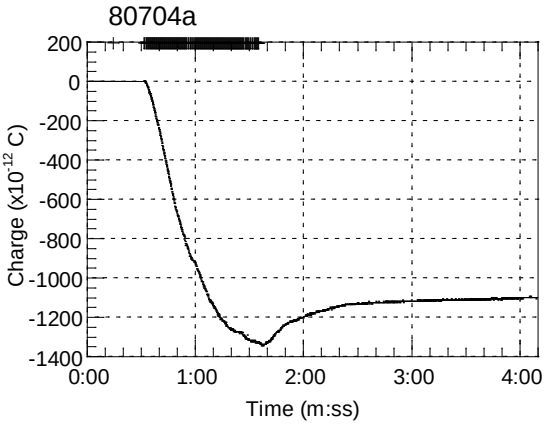
80704a
Charge (x10-12 C)
200
0
-200
-400
-600
-800
-1000
-1200
-1400
0:00
1:00
2:00
3:00
4:00
Time (m:ss)

Appendix V: Sample details and geochemistry

The samples used during the experiments are described in Chapter 6. This appendix provides further details and geochemical data for the samples.

Table AV.1 Major element sample geochemistry. Data obtained by XRF analyses (with all Fe given as Fe_2O_3) with the exception of the MSH data (obtained by wet chemical technique). Loss on ignition (LOI) data are provided where available.

	SMN 31	Santorini	Sak 14	MSH	StV 519	Sak 13I
SiO_2	71.55	68.26	72.74	63.66	55.39	67.3
TiO_2	0.17	0.39	0.90	0.64	0.68	0.76
Al_2O_3	10.54	13.90	15.37	17.45	16.61	16.8
Fe_2O_3	4.37	3.00	2.21	4.52	6.64	4.81
MnO	0.06	0.08	0.10	0.07	0.16	0.13
MgO	0.01	0.58	0.10	1.93	5.55	1.65
CaO	0.46	2.12	2.59	5.03	7.77	2.09
Na_2O	5.15	4.69	1.10	4.57	3.23	1.20
K_2O	4.60	3.03	2.05	1.30	0.54	2.78
P_2O_5	-	0.08	-	0.09	0.14	-
LOI	3.10	3.78	-	-	2.56	-
Totals	100.0	99.9	97.1	99.3	100.0	97.5

SMN 31

Collected from Gorge Farm, Naivasha, Kenya by S. Marshall. Geochemical data also provided by S. Marshall.

Santorini

Collected from pyroclastic flow deposits of the Minoan eruption, Santorini. Geochemical data obtained from Druitt *et al*. (1996).

Sak 14

Collected from the Osumi pumice, Sakurajima, by S. Black and J.S. Gilbert. Geochemical data provided by S. Black.

MSH

Sampled from the pumice fall deposit of the May 18, 1980 eruption of Mount St. Helens (collected at Windy Ridge). Geochemical data from Table 69 of Lipman *et al*. (1991).

StV 519

Collected from the Yellow Tuff formation, St. Vincent, by J. Toothill. Geochemistry given in Table AV1 is from sample STV 377 (Heath, 1997) of the Yellow Tuff, collected from the same site.

Sak 13I

Collected from the base of the Bunmei tephra, Sakurajima by S. Black and J.S. Gilbert. Geochemical data provided by S. Black.